

## Robust Automatic Pumping Cycle Operation of Airborne Wind Energy Systems

Rapp, S.

**DOI**

[10.4233/uuid:ab2adf33-ef5d-413c-b403-2cfb4f9b6bae](https://doi.org/10.4233/uuid:ab2adf33-ef5d-413c-b403-2cfb4f9b6bae)

**Publication date**

2021

**Document Version**

Final published version

**Citation (APA)**

Rapp, S. (2021). *Robust Automatic Pumping Cycle Operation of Airborne Wind Energy Systems*. [Dissertation (TU Delft), Delft University of Technology]. <https://doi.org/10.4233/uuid:ab2adf33-ef5d-413c-b403-2cfb4f9b6bae>

**Important note**

To cite this publication, please use the final published version (if applicable). Please check the document version above.

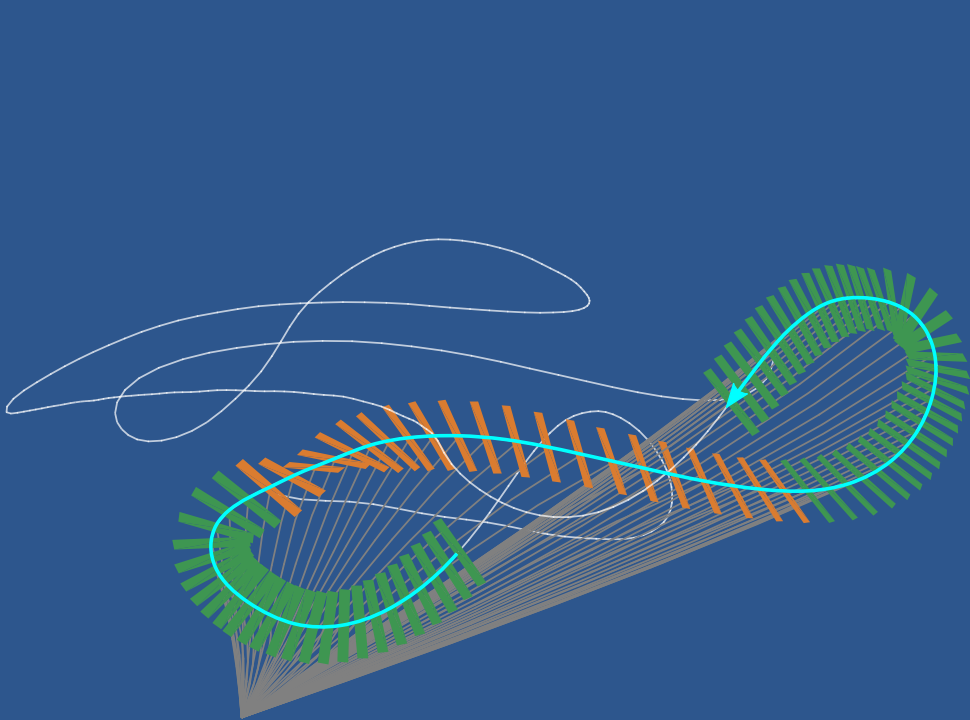
**Copyright**

Other than for strictly personal use, it is not permitted to download, forward or distribute the text or part of it, without the consent of the author(s) and/or copyright holder(s), unless the work is under an open content license such as Creative Commons.

**Takedown policy**

Please contact us and provide details if you believe this document breaches copyrights. We will remove access to the work immediately and investigate your claim.

# Robust Automatic Pumping Cycle Operation of Airborne Wind Energy Systems



Sebastian Rapp



# **Robust Automatic Pumping Cycle Operation of Airborne Wind Energy Systems**

## **Dissertation**

for the purpose of obtaining the degree of doctor  
at Delft University of Technology  
by the authority of the Rector Magnificus, prof. dr. ir. T.H.J.J. van der Hagen,  
chair of the Board for Doctorates  
to be defended publicly on  
Wednesday 3 March 2021 at 12:30 o'clock

by

**Sebastian RAPP**

Master of Science in Aerospace Engineering,  
Technical University of Munich, Munich, Germany,  
born in Albstadt-Ebingen, Germany.

This dissertation has been approved by the promoters.

Composition of the doctoral committee:

Rector Magnificus,	chairperson
Prof. dr. G.J.W. van Bussel	Delft University of Technology, promoter
Dr.-Ing. R. Schmehl	Delft University of Technology, copromotor

Independent members:

Prof. dr. G.C.H.E. de Croon	Delft University of Technology
Prof. dr. M. Diehl	University of Freiburg, Germany
Prof. dr. S. Gros	Norwegian University of Science and Technology, Norway
Dr. L.M. Fagiano	Polytechnic University of Milan, Italy
Dr. C. Vermillion	North Carolina State University, USA
Prof. dr. S.J. Watson	Delft University of Technology, reserve member

This research has been supported financially by the project AWESCO (H2020-ITN-642682), funded by the European Union's Horizon 2020 research and innovation program under the Marie Skłodowska-Curie grant agreement No. 642682.



*Keywords:* Airborne Wind Energy, Flight Control, Robustness, Monte Carlo Simulations

*Printed by:* <http://www.proefschriftmaken.nl>

*Front:* Flight path during a pumping cycle with tether rupture avoidance maneuver.

Copyright © 2021 by S. Rapp

ISBN 978-94-6423-148-9

An electronic version of this dissertation is available at  
<http://repository.tudelft.nl/>.

# Contents

<b>Summary</b>	<b>ix</b>
<b>Samenvatting</b>	<b>xi</b>
<b>Abbreviations</b>	<b>xiii</b>
<b>Nomenclature</b>	<b>xv</b>
<b>1 Introduction</b>	<b>1</b>
1.1 Motivation . . . . .	1
1.2 Robust Automatic Pumping Cycle Operation . . . . .	5
1.3 Literature Review . . . . .	8
1.4 Research Questions . . . . .	16
1.5 Thesis Outline, Reading Order and Methodology Overview . . . . .	16
<b>2 Simulation Framework and Models</b>	<b>21</b>
2.1 Notation . . . . .	21
2.2 Reference Frames . . . . .	22
2.3 Simulation Models . . . . .	29
2.3.1 Aircraft Model . . . . .	29
2.3.2 Ground Station, Tether and Wind Field Models . . . . .	33
2.4 Summary . . . . .	36
<b>3 Linearization and Flight Dynamic Analysis</b>	<b>37</b>
3.1 Traction Phase . . . . .	37
3.1.1 Model Equations for Trimming and Linearizing . . . . .	37
3.1.2 Traction Phase Operating Point Analysis . . . . .	40
3.1.3 Traction Phase Eigenmode Analysis . . . . .	44
3.2 Retraction Phase . . . . .	47
3.2.1 Model Equations for Trimming and Linearizing . . . . .	47
3.2.2 Retraction Phase Operating Point Analysis . . . . .	47
3.2.3 Retraction Phase Eigenmode Analysis . . . . .	50
3.3 Summary . . . . .	51
<b>4 Control System Design</b>	<b>63</b>
4.1 Theoretical Preliminaries . . . . .	63
4.1.1 Linear Quadratic Regulator and $\mathcal{H}_2$ -optimal Control . . . . .	64
4.1.2 Eigenstructure Assignment . . . . .	66
4.1.3 Nonlinear Dynamic Inversion . . . . .	68

4.2	State Machine . . . . .	72
4.3	Guidance Strategies . . . . .	74
4.3.1	Traction Phase Guidance . . . . .	74
4.3.2	Retraction Phase Guidance . . . . .	89
4.3.3	Transition Strategy from the Retraction to the Traction Phase . . . . .	92
4.4	Path Following Loop . . . . .	94
4.4.1	Traction Phase . . . . .	94
4.4.2	Retraction Phase . . . . .	97
4.5	Winch Controller . . . . .	99
4.6	Outer Loop Controller Verification . . . . .	100
4.7	Linear Inner Loop Design . . . . .	111
4.7.1	Traction Phase . . . . .	111
4.7.2	Retraction Phase . . . . .	131
4.8	Nonlinear Inner Loop Design . . . . .	143
4.8.1	Attitude Loop . . . . .	143
4.8.2	Rate Loop . . . . .	144
4.8.3	Control Allocation . . . . .	144
4.8.4	Filter and Gain Design . . . . .	145
4.9	Inner Loop Performance during Figure of Eight Flight . . . . .	148
4.9.1	Comparison of Path Following Capabilities . . . . .	150
4.10	Optimization of High Level Parameters . . . . .	151
4.11	Summary . . . . .	159
<b>5</b>	<b>Control Performance Analysis in Presence of Uncertainty</b>	<b>163</b>
5.1	Preliminaries . . . . .	163
5.2	Results . . . . .	168
5.2.1	Impact of Time Delays . . . . .	168
5.2.2	Impact of Turbulence . . . . .	171
5.2.3	Impact of Model Uncertainties . . . . .	190
5.2.4	Sensitivity Analysis . . . . .	196
5.2.5	Detailed Control Performance Analysis . . . . .	203
5.3	Summary . . . . .	219
<b>6</b>	<b>Upset Condition Generation, Prediction and Avoidance</b>	<b>223</b>
6.1	Preliminaries . . . . .	223
6.2	Upset Condition Generation, Prediction and Avoidance Framework . . . . .	224
6.2.1	Upset Condition Generation . . . . .	225
6.2.2	Upset Condition Prediction . . . . .	228
6.2.3	Upset Condition Avoidance . . . . .	234
6.3	Application: Generate, Predict and Avoid Tether Rupture . . . . .	234
6.3.1	Setup . . . . .	234
6.3.2	Results . . . . .	237
6.3.3	Discussion of Model Validity . . . . .	247
6.4	Summary . . . . .	248

---

<b>7 Conclusion and Perspective</b>	<b>251</b>
7.1 Conclusion . . . . .	251
7.2 Perspective . . . . .	255
<b>Bibliography</b>	<b>258</b>
<b>A Appendix</b>	<b>273</b>
A.1 Transformation Matrices . . . . .	273
A.2 State-space Models for Control Design . . . . .	275
A.2.1 Traction Phase Longitudinal Dynamics . . . . .	275
A.2.2 Traction Phase Lateral Dynamics . . . . .	277
A.2.3 Retraction Phase Longitudinal Dynamics . . . . .	279
A.2.4 Retraction Phase Lateral Dynamics . . . . .	280
A.3 Cost Function Terms . . . . .	282
A.4 Asymptotic Confidence Interval for Quantiles. . . . .	282
<b>Acknowledgements</b>	<b>285</b>
<b>Curriculum Vitæ</b>	<b>287</b>
<b>List of Publications</b>	<b>289</b>



# Summary

Airborne wind energy (AWE) is a novel technology that aims at accessing wind resources at higher altitudes which cannot be reached with conventional wind turbines. This technological challenge is accomplished using tethered aircraft or kites in combination with either onboard or ground-based generators. In the former case, the kinetic energy of the air flow is transformed into electricity and transmitted via a conductive cable to the ground. In the latter case, the aerodynamic force of the aircraft or kite is translated into tether tension. The pulling force uncoils the tether from a drum which turns a generator and hence transforms the mechanical torque into electrical power on the ground. In this case two operational modes are required: In the first mode, the tether is reeled out until the maximum length is reached. It follows a reeling in phase where the aircraft or kite glides back towards the ground station and a fraction of the generated power is used to wind the tether again onto the drum of the winch. The cycle restarts as soon as the minimum tether length is reached. These two modes combined constitute a so-called pumping cycle.

Reliability is a key system property that will decide over the success of AWE as a commercially feasible technology. To reach this goal, a well designed control system is required that can achieve the nominal control objectives as well as handle disturbances such as atmospheric turbulence and mismatches between the model used for the controller derivation and the real plant. In light of these challenges, the present work tries to make a contribution to bring AWE closer to commercial success. More specifically, a workflow to design a modular control architecture for a rigid wing AWE system operated in pumping cycle mode is presented. The thesis introduces models of different fidelity that are either directly used for the controller synthesis or in order to verify if the designed controller is able to meet its objectives. A quasi-stationary analysis is performed to describe the operational flight envelope and to derive linear state space models for the longitudinal and lateral flight controller synthesis. A generic outer loop controller, independent of the specific aircraft actuation, is designed which guides the system along the traction and retraction phase reference flight paths. A ground based winch controller is used to track the tether tension and hence the radial motion of the aircraft. To track the outer loop guidance commands several linear and nonlinear inner loop flight controllers are proposed. All controller designs are verified in detail using Monte Carlo simulations. The resulting distributions of critical metrics are used to quantify performance as well as robustness of the controllers in the presence of stochastic variations in the wind field and model uncertainties.

In the last part of this thesis a methodology is proposed that can be used to systematically generate conditions in which the AWE control system is failing. The generated knowledge can be leveraged to create an analytic model that is able to predict during operation a critical flight state. Ultimately, this allows to trigger a mitigation maneuver to avoid the failure. Different prediction strategies are presented and eventually the

methodology is specifically applied to the case of tether rupture condition generation, prediction and avoidance.

# Samenvatting

Airborne Wind Energy (AWE) is een nieuwe technologie waarmee geprobeerd wordt om windenergie op grote hoogtes, boven het bereik van reguliere windturbines toegankelijk te maken. Deze technologie maakt gebruik van aangeliende vliegtuigen of vliegers met elektriciteitsgeneratoren ofwel aan boord of op de grond. In het eerste geval, wordt de kinetische energie van de luchtstroom aan boord omgezet in elektriciteit en vervolgens wordt de elektriciteit via een geleidend kabel naar de grond gebracht. In het tweede geval, worden de aerodynamische krachten op de vlieger of het vliegtuig overgebracht via de kabel van de lier naar een liertrommel. Deze trekkracht rolt de kabel van de trommel af en drijft daarmee de generator aan in de liertrommel op de grond waardoor deze elektriciteit opwekt. Hierbij zijn twee operationele fases te onderscheiden: in de eerste fase wordt de liertrommel afgerold totdat de maximale kabellengte is bereikt. Daarna volgt een fase waarin de vlieger richting het grondstation glijdt en de kabel actief wordt ingehaald. En dit gebeurt met een fractie van het gegenereerde vermogen van de eerste fase. De cyclus begint opnieuw zodra de minimale kabellengte is bereikt, en deze twee operationele fases samen wordt een pompcyclus genoemd.

Betrouwbaarheid is een beslissende factor in de haalbaarheid van AWE als commerciële technologie. Om dit doel te bereiken is een goed ontworpen besturingssysteem vereist dat de vlieger naar behoren stuurt en dat verstoringen zoals veroorzaakt door turbulentie kan opvangen. Het besturingssysteem moet ook robuust zijn, zodat het kan omgaan met verschillen tussen de praktijk en het theoretische model dat gebruikt is voor het ontwerp ervan. Dit proefschrift richt zich op de verbetering van de besturing van AWE systemen met een pompcyclus en levert daarmee een bijdrage aan het dichterbij brengen van een commercieel succes van AWE. De specifieke bijdrage van het proefschrift is een systematische workflow met een modulaire architectuur voor het ontwikkelen van een besturingssysteem voor de pompcyclus van een AWE-systeem. Modellen van verschillende betrouwbaarheid worden geïntroduceerd en worden ofwel direct gebruikt voor het ontwerpen, of om te verifiëren of de ontworpen regelaar aan de eisen voldoet. Met behulp van een quasi-stationaire analyse worden de operationele limieten bepaald en worden lineaire modellen afgeleid voor de longitudinale en laterale vliegmechanica. Een generieke buitenste lus van de regelaar zorgt ervoor dat de vlieger het referentie traject van de desbetreffende fase volgt. De regelaar voor de lier op de grond wordt gebruikt om de kabelspanning te controleren en daarmee de uitrolsnelheid en dus de uitwaartse beweging van het vliegtuig of de vlieger. Verschillende lineaire en niet-lineaire regelaars voor de binnenste lus worden ontwikkeld die de commando's volgen van de regelaar van de buitenste lus. Alle regelaars worden geverifieerd met behulp van Monte Carlo-simulaties. De resulterende verdelingen van indicatoren voor de kritieke vluchttoestand worden gebruikt om de prestaties van de regelaar te kwantificeren zoals de robuustheid bij stochastische variaties in het windveld en de prestaties bij modelonzekerheden.

In het laatste deel van dit proefschrift wordt een methodologie gepresenteerd om systematisch situaties te genereren waarbij het besturingssysteem faalt. De daarmee opgedane kennis kan worden gebruikt voor het creëren van een analytisch model dat voorspelt wanneer een kritieke vluchttoestand zich zal voordoen en hoe deze te vermijden door het inzetten van een ontwijkende manoeuvre. Verschillende voorspellingsstrategieën worden gepresenteerd en de toepasbaarheid van de ontwikkelde methodologie voor het genereren, voorspellen en vermijden van kabelbreukgevallen wordt gedemonstreerd.

# Abbreviations

AWE	Airborne wind energy
CDF	Cumulative distribution function
CG	Center of gravity
CI	Confidence interval
DoF	Degree of freedom
DR	Dutch roll
ESA	Eigenstructure assignment
EVa(s)	Eigenvalue(s)
EVe(s)	Eigenvector(s)
FMEA	Failure mode and effect analysis
FTA	Fault tree analysis
GMST	Global mean surface temperature
GS	Ground station
HTOL	Horizontal take-off and landing
iid	Identically and independently distributed
ILC	Iterative learning control
IPCC	Intergovernmental Panel on Climate Change
LB	Lower bound
LHS	Left hand side
LMI	Linear matrix inequality
LQG	Linear-quadratic Gaussian
LQR	Linear-quadratic regulator
MCC	Matthews correlation coefficient
MPC	Model predictive control
NDI	Nonlinear dynamic inversion
NED	North, East, Down
o.w.	Otherwise
PCH	Pseudo control hedging
PI	Proportional-integral
PMF	Probability mass function

RHS	Right hand side
rms	Root mean square
SMOTE	Synthetic minority over-sampling technique
SS	Subset simulation(s)
SVM	Support vector machine
TR	Transition rule
UAV	Unmanned aerial vehicle
UB	Upper bound
VTOL	Vertical take-off and landing
WCS	Winch Control System
w.r.t.	with respect to

# Nomenclature

Note that all symbols are also defined in the text where they occur for the first time.

## Greek letters

Symbol	Meaning	Unit
$\alpha$	Level of significance in a statistical experiment	[-]
$\alpha_{a/e}$	Aerodynamic/kinematic angle of attack	[rad]
$\alpha_{L,j}$	Lagrange multiplier in a SVM predictor	[-]
$\beta_{a/k}$	Aerodynamic/kinematic sideslip angle	[rad]
$\gamma_{a/k/\tau}$	Aerodynamic/kinematic/tangential path angle	[rad]
$\gamma_{k,path}$	Descend angle of the retraction path	[rad]
$\Gamma(s)$	Figure-8 path given in Cartesian coordinates	[m]
$\mathbb{I}_{\mathcal{F}}$	Indicates a reference path related quantity	[-]
$\delta$	Cross track error on a sphere	[rad]
$\delta_0$	Defines the $\delta$ that commands a 45° path intercept	[rad]
$\delta_{a/e/r}$	Aileron/elevator/rudder deflection	[rad]
$\delta_{a/e/r,lim}$	Aileron/elevator/rudder deflection limit	[rad]
$\delta_{mp}$	Multiplicative uncertainty	[-]
$\Delta$	Model mismatch	[-]
$\Delta\phi$	Angle between the aircraft position vector and the horizontal	[rad]
$\Delta_{s,1}$	Defines the interval in which the retraction point lays	[rad]
$\Delta T_{nop}$	Idle time of the AWE system due to a failure	[s]
$\Delta T_s$	Time shift of adjacent signal segments	[s]
$\Delta T_r$	Reaction time shift before an upset	[s]
$\Delta\chi_\tau$	Parallel course correction value	[rad]
$\pm\Delta X$	Defines an uncertainty interval	[-]
$\Delta z_i$	ith segment of a signal $z$	[-]
$\zeta$	Relative damping in a second order system	[-]
$\boldsymbol{\eta}$	Normal vector of a hyperplane	[-]
$\boldsymbol{\eta}_{T,i}$	ith test vector in the sensitivity analysis	[-]
$\theta$	Angle between $\mathbf{b}^G$ and $\mathbf{v}_{k,\tau}$	[rad]

$\Theta$	Pitch angle	[rad]
$\theta$	Realization of the random variable $\Theta$	[-]
$\tilde{\theta}$	A $\theta$ that is an element of an intermediate failure domain	[-]
$\Theta_{\text{sp}}$	The space of the random variable $\Theta$	[-]
$\Theta_{\tau}$	Tangential plane pitch angle	[rad]
$\iota$	Indicates if the aircraft is on the LHS or RHS of the path	[-]
$\bar{\kappa}$	Path curvature	[1/m]
$\kappa_{\text{W}}$	Viscous friction coefficient of the winch	[kgm/s]
$\lambda$	Small earth longitude	[rad]
$\lambda_{\text{FP/FN}}$	False positive/negative rate	[-]
$\lambda_i$	ith Eigenvalue of a matrix	[-]
$\mu_{\text{a/k}}$	Aerodynamic/kinematic bank angle	[rad]
$\mu^*$	Rotational angle between the $K$ and the $K^*$ frame	[rad]
$\mu_{\Delta}$	Structured singular value	[-]
$\mathbf{v}$	Pseudo-control input	[-]
$\xi$	Wind direction (from North)	[rad]
$\Xi$	Time reversal asymmetry statistic	[-]
$\rho$	Air density	[kg/m <sup>3</sup> ]
$\rho_{\text{T}}$	Tether mass density	[kg/m <sup>3</sup> ]
$\sigma$	The sign operator	[-]
$\sigma_{\text{d,p}}$	Defines if the aircraft is on the LHS or RHS of the retraction path	[-]
$\sigma_{\text{SVM}}$	Standard deviation of a SVM Gaussian kernel	[-]
$\tau$	Denotes the tangential plane (frame)	[-]
$\tau_{\text{r}}$	Time constant of the transition phase	[s]
$\bar{\tau}_{\text{FCS}}$	FCS time delay margin	[s]
$\tau_{\text{TRA}}$	Time reversal asymmetry time constant	[s]
$Y$	Limit function value in SS	[-]
$Y^*$	Maximum limit function value in SS	[-]
$Y_{\text{T}}$	Chosen fixed threshold value for upset prediction	[-]
$\phi$	Small earth latitude	[rad]
$\Phi$	Roll angle	[rad]
$\tilde{\Phi}$	Gaussian CDF	[-]
$\phi_0$	Initial mean path elevation angle during the traction phase	[rad]
$\phi_{\text{f,i}}$	Feature vector of sample i	[-]
$\tilde{\phi}_{\text{f,i}}$	Reduced feature vector of sample i	[-]
$\phi_{\text{r}}$	Rotational angle of figure-8 around $y_{\text{W}}$	[rad]

$\phi_{SV,j}$	Support vector in a SVM	[-]
$\Phi_\tau$	Tangential plane roll angle	[rad]
$\chi_{a/k/\tau}$	Aerodynamic/kinematic/tangential course angle	[rad]
$\chi_{k,path}$	Orientation of the retraction path in the $x_W y_W$ plane	[rad]
$\chi_{\parallel}$	Course in the tangential plane parallel to the figure-8	[rad]
$\Psi$	Azimuth angle	[rad]
$\Psi_\tau$	Tangential plane azimuth angle	[rad]
$\omega_{0,X}$	Natural frequency of a model further specified by X	[rad/s]
$\omega_{a/e/r,0}$	Bandwidth of the aileron/elevator/rudder model	[rad/s]
$\omega_\tau$	Inverse of the transition time constant $\tau_\tau$	[rad/s]
$(\omega)_i^{jj}$	Rotational velocity of the i frame w.r.t. the j frame given in the i frame	[rad/s]
$\omega_{i,j}^{kj}$	i-th component of a rotational velocity given in frame j relative to k	[rad/s]
$\omega_W$	Winch rotational speed	[rad/s]

### Latin letters

Symbol	Meaning	Unit
$\{\dots\}^a$	Indicates an achievable quantity in the context of ESA	[-]
<b>A</b>	Denotes the aerodynamic frame	[-]
<b>A</b>	Denotes the dynamic matrix in a state space model	[-]
<b>A(x)</b>	Input affine part of the input/output dynamics	[-]
$\tilde{A}$	Denotes the rotated aerodynamic frame	[-]
$a_{i,X}$	Aircraft acceleration in i direction given in a frame X	[m/s <sup>2</sup> ]
$a_{path}$	Path shape parameter (controls the height of the figure-8)	[-]
$a_W$	Winch acceleration	[m/s <sup>2</sup> ]
$b$	Wingspan	[m]
<b>B</b>	Denotes the body-fixed frame	[-]
<b>B</b>	Denotes the input matrix in a state space model	[-]
<b>b(x)</b>	Input independent part of the input/output dynamics	[-]
<b>b<sup>G</sup></b>	Tangent vector that points to the closest point on the path	[m]
$b_{path}$	Path shape parameter (controls the width of the figure-8)	[-]
<b>(b)<sub>W</sub></b>	Retraction phase glide path	[m]
<b>(<math>\tilde{b}</math>)<sub>W</sub></b>	Identical to <b>(b)<sub>W</sub></b> except that the third element is zero	[m]
$\{\dots\}_{Bernoulli}$	Subscript that indicates the Lemniscate of Bernoulli	[-]

$\text{[]}_{\text{Booth}}$	Subscript that indicates the Lemniscate of Booth	[-]
$\text{[]}_c$	Subscript that indicates a commanded value	[-]
$\bar{c}$	Mean wing chord length	[m]
<b>C</b>	Denotes the measurement matrix in a state space model	[-]
$c_j$	Error feedback coefficients	[-]
$c'/\tilde{c}'$	Nominal/perturbed element in a state space model	[-]
$C_{d,t}$	Tether drag coefficient	[-]
$C_L$	Lift coefficient	[-]
$C_{l/m/n}$	Resultant aerodynamic roll/pitch/yaw moment coefficient	[-]
$C_{l/m/n,j,\alpha^i}$	$i$ th polynomial coefficient of $C_{l/m/n,j}$	[-]
$C_{l/m/n,j}$	Aerodynamic roll/pitch/yaw moment derivative w.r.t. $j$	[-]
$c_T$	Spring stiffness of the tether model	[N/m]
$C_{x/y/z}$	Resultant aerodynamic force coefficient in $x_B/y_B/z_B$ direction	[-]
$C_{x/y/z,j}$	Aerodynamic force derivative in $x_B/y_B/z_B$ direction w.r.t. $j$	[-]
$C_{x/y/z,j,\alpha^i}$	$i$ th polynomial coefficient of $C_{x/y/z,j}$	[-]
<b>C<sub>z</sub></b>	State weights in the $\mathcal{H}_2$ -norm optimal design approach	[-]
<b>D</b>	Aerodynamic drag	[N]
$\mathcal{D}$	Denotes a data set	[-]
$d_p$	Cross track error to the retraction path in the horizontal plane	[m]
$d_t$	Tether diameter	[m]
$d_T$	Damping coefficient of the tether model	[N s/m]
$d_Z$	Vertical distance of the aircraft to the retraction path	[m]
$d_\theta$	Dimension of the random variable vector $\Theta$	[-]
<b>D<sub>z</sub></b>	Weights controls in the $\mathcal{H}_2$ -norm optimal approach	[-]
<b>E</b>	Input matrix in a state space model for uncontrolled inputs	[-]
<b>E</b>	Expected value operator	[-]
$E_{em}$	Energy loss through an emergency maneuver	[kJ]
$E_{FP/FN}$	Energy loss through false positives/negatives	[kJ]
$E_{misc}$	Not further specified energy losses due to a failure	[kJ]
$\mathbf{e}_{i,j}$	Unit vector of frame $j$ in $i$ direction given in the $W$ frame	[-]
$e_{i,X}$	Integrated tracking error of $X$	[-]
$e_j$	Tracking error of output $j$	[-]
$e_p$	Path following error	[m]
$E_{pc}$	On average generated net energy per pumping cycle	[kJ]
$E_{tot}$	Total expected energy loss until failure	[kJ]

<b>F</b>	Transfer function matrix from $\mathbf{w}$ to $\mathbf{z}$	[-]
$\tilde{f}_{i,K}$	Resultant force in $i$ direction given in the $K$ frame	[N]
$\hat{f}_P$	Binary predictor based on a SVM	[-]
<b>f(x)</b>	Nonlinear input independent part of a state space model	[-]
$(\mathbf{F}_a)_B$	Denotes the aerodynamic force given in the $B$ frame	[N]
$F_i$	$i$ th intermediate failure	[-]
$(\mathbf{F}_g)_B$	Denotes the gravitational force given in the $B$ frame	[N]
$F_t$	Tether force magnitude	[N]
$(\mathbf{F}_t)_B$	Denotes the tether force given in the $B$ frame	[N]
$(\mathbf{F}_{t,d})_\tau$	Denotes the tether drag force given in the $\tau$ frame	[N]
$(\mathbf{F}_{tot})_B$	Denotes the resultant force given in the $B$ frame	[N]
$f_X(x)$	PDF of random a variable $X$ evaluated at $x$	[-]
$f'_X(x)$	PDF of a standard normally distributed random variable	[-]
$F_X(x)$	Cumulative distribution function of the random variable $X$	[-]
$g$	Gravitational acceleration	[m/s <sup>2</sup> ]
<b>g(x)</b>	Nonlinear, input affine part of a states space model	[-]
$\square^G$	Indicates a CG located scalar or vector	[-]
$h$	Aircraft altitude above ground	[m]
$\square_h$	Indicates a hedged signal	[-]
<b>h(x)</b>	Nonlinear measurement matrix	[-]
$h_\tau$	Radial distance of the aircraft to the ground station	[m]
$\mathcal{I}$	The indicator function	[-]
<b>J</b>	Inertia tensor of the aircraft	[kg m <sup>2</sup> ]
$J_W$	Winch drum inertia	[kg m <sup>2</sup> ]
<b>K</b>	Denotes the kinematic frame	[-]
<b>K</b>	Denotes a controller gain	[-]
$\bar{K}$	Denotes the rotated kinematic frame w.r.t. the ground	[-]
$K^*$	Denotes the rotated kinematic frame w.r.t. the $\tau$ plane	[-]
$k_{rt,\gamma}$	Parameter for the commanded retraction descend angle	[-]
$k_{rt,\chi}$	Parameter for the commanded retraction course angle	[-]
$k_{p,X}$	Proportional tracking error gain for $X$	[-]
$k_{i,X}$	Integral tracking error gain for $X$	[-]
$\square_{lo/la}$	Indicates longitudinal/lateral dynamics	[-]
<b>O</b>	Denotes the NED frame	[-]
$L$	Aerodynamic lift	[N]
$\square_{Lissa}$	Indicates a Lissajous figure	[-]

$l_{i/j}$	Binary label of the $i$ th/ $j$ th sample	[-]
$l_t$	Tether length	[m]
$l_{t,p}$	Predicted tether length after half a figure-8	[m]
$\mathbf{l}_j$	Parameter vector	[-]
$\mathcal{L}_i h$	Lie-derivative of $h$ along $i$	[-]
$m$	The number of controllable inputs	[-]
$\mathbf{M}_0$	Non-aerodynamic moment around the CG of the aircraft	[Nm]
$\square_m$	Indicates a measured quantity	[-]
$m_a$	Mass of the aircraft	[kg]
$\mathbf{M}_a$	Resultant aerodynamic moment around the CG	[Nm]
$\mathbf{M}_{a,0}$	Input independent aerodynamic moment around the CG	[Nm]
$\mathbf{M}_{a,\delta}$	Input dependent aerodynamic moment around the CG	[Nm]
$m_f$	Feature vector dimension	[-]
$\square_{\min/\max}$	Indicates a minimum/maximum value	[-]
$m_{LM}$	Number of non-zero Lagrange multipliers	[-]
$m_s$	Number of epochs in a SS run	[-]
$\mathbf{M}_{tot}$	Resultant moment around the CG	[Nm]
$M_{W,set}$	Winch control moment	[Nm]
$\mathbf{M}_{YX}$	Transformation matrix from the X to the Y frame.	[-]
$n_f$	Total number of failures in $n_{mc}$ simulations	[-]
$n_{f,j}$	Number of failures with sampled uncertainty $j$	[-]
$n_{f,ss}$	Number of failures in an intermediate failure domain	[-]
$n_{FP/FN}$	Number of false positives/negatives	[-]
$\tilde{\mathbf{N}}_j$	Columns correspond to base vectors of the nullspace	[-]
$\hat{\mathbf{N}}_j$	Rows of $\tilde{\mathbf{N}}_j$ are used to define desired EVes	[-]
$\mathbf{N}_j$	Completes $\tilde{\mathbf{N}}_j$ with $\hat{\mathbf{N}}_j$	[-]
$n_{pc}$	Number of pumping cycles until failure	[-]
$n_{mc}$	Number of Monte Carlo simulations	[-]
$n_{mpc}$	Number of missed pumping cycles due to a failure	[-]
$n_s$	Sample size	[-]
$n_T$	Amount of tether particles	[-]
$n_{train}$	Number of training samples	[-]
$n_z$	Number of signal segments	[-]
$n_z^+$	Number of synthetically generated segments	[-]
$O_W$	Origin of the W frame	[-]
$p$	Roll rate	[rad/s]

<b>p</b>	Position of the CG of the aircraft	[m]
<b>P</b>	Denotes the path frame	[-]
<b>P</b>	Positive definite (Lyapunov) matrix	[-]
$\mathcal{P}$	Denotes the generalized plant	[-]
$P_{em}$	Power loss equivalent of an emergency maneuver	[kW]
$p_f$	Failure probability	[-]
$p_i$	State space model at trim point $i \in 1, 2, 3, 4, 5$	[-]
$\mathbf{p}_i$	Initial aircraft position during the retraction phase	[m]
$P_{mech}$	Instantaneous mechanical power	[kW]
$\mathbf{p}_P$	Figure-8 definition in the path frame	[m]
$P_{pc}$	Average mechanical power converted in one pumping cycle	[kW]
$\mathbf{p}_{rel}$	Relative vector of the aircraft position and $\mathbf{p}_i$	[m]
$\tilde{\mathbf{p}}_{rel}$	Equal to $\mathbf{p}_{rel}$ but the third element is set to zero	[m]
$p_s$	Fraction of samples that initiate the next subset in SS	[-]
$\mathbf{p}_t$	Retraction phase target point	[m]
$p_Z(z)$	The PMF of the random variable $Z$ evaluated at $z$	[-]
$Pr(F_i)$	Probability of an intermediate failure $F_i$	[-]
$Pr_i$	Probability of obtaining a lower value than the quantile $q_i$	[-]
$q$	Pitch rate	[rad/s]
<b>Q</b>	State vector weight matrix utilized for the design of a LQR	[-]
$\bar{q}$	Dynamic pressure	[kg/m/s <sup>2</sup> ]
$q_\alpha$	$\alpha$ -quantile	[-]
$r$	Yaw rate	[rad/s]
<b>R</b>	Input vector weight matrix utilized for the design of a LQR	[-]
$r_i$	Relative degree of the output $i$	[-]
$\mathbf{r}^{ij}$	Relative position vector from $i$ to $j$	[m]
$\square_{ref}$	Indicates a reference value	[-]
$r_W$	Winch drum radius	[m]
$\square_{rt}$	Indicates a retraction phase quantity	[-]
$\square^s$	Denotes an specifiable quantity in an ESA	[-]
$s$	Lemniscate path parameter or Laplace variable	[rad]/[-]
$\square_{set}$	Indicates a set point	[-]
$S_{ref}$	Wing reference area	[m <sup>2</sup> ]
$t$	Time	[s]
$\mathcal{T}$	Intermediate threshold in a SS	[-]
$\mathbf{t}(s)$	Tangent on the path at $s$	[-]

$\mathbf{t}'(s)$	Total derivative of $\mathbf{t}(s)$ w.r.t. $s$	[-]
$t_{pc}$	Average time of a pumping-cycle	[s]
$\mathbf{u}$	Plant control input	[rad]
$\mathbf{u}_c$	Actuator input	[rad]
$\mathbf{v}_{a/k/w}$	Aerodynamic/kinematic/wind velocity	[m/s]
$v_{a/k/w}$	Magnitude of the aerodynamic/kinematic/wind velocity	[m/s]
$\mathbf{v}_i, \mathbf{v}_j$	ith/jth eigenvector of a matrix	[-]
$\mathbf{v}_{k,\tau/r}$	Tangential/radial kinematic velocity	[m/s]
$v_{k/a/w,x/y/z,X}$	Kinematic/aerodyn./wind speed in x/y/z direction in frame X	[m/s]
$v_{k,xy}$	Kinematic aircraft speed in the horizontal plane	[m/s]
$v_r$	Reel-out/in speed of the tether	[m/s]
$v_w$	Winch speed	[m/s]
$v_{w,ref}$	Reference wind speed at 6 m altitude	[m/s]
$\mathcal{V}$	Asymptotic variance	[-]
$\mathbf{w}$	Uncontrolled (exogenous) input in a state space model	[-]
$W$	Denotes the wind frame	[-]
$\mathbf{W}$	Positive definite matrix used in the $\mathcal{H}_2$ -optimal design	[-]
$\mathbf{x}$	State vector	[-]
$\tilde{\mathbf{x}}$	Transformed state vector (decoupled state space model)	[-]
$x_{f,i}$	Defines the start of the flare maneuver	[-]
$x_i, y_i$ and $z_i$	Denote the orthonormal basis of coordinate frame $i$	[-]
$\begin{bmatrix} \cdot \\ \cdot \\ \cdot \end{bmatrix}_x, \begin{bmatrix} \cdot \\ \cdot \\ \cdot \end{bmatrix}_y$ and $\begin{bmatrix} \cdot \\ \cdot \\ \cdot \end{bmatrix}_z$	Denote the first, second and third component of a vector in $\mathbb{R}^3$	[-]
$X_i$	Denotes a random variable	[-]
$\mathbf{y}$	The output of a state space model	[-]
$Y$	Aerodynamic sideforce	[N]
$\mathbf{z}$	Performance measure for an $\mathcal{H}_2$ -norm optimal design	[-]
$\mathbf{Z}$	Matrix used to derive LMIs for the $\mathcal{H}_2$ -optimal design	[-]
$z_{sig}$	An example signal	[-]
$Z_{ber,i}$	A Bernoulli random variable	[-]
$Z_j$	Hypergeometrically distributed random variable	[-]
$\mathbf{z}_j^*$	Linear combination of the columns of $\mathbf{N}_j$	[-]

**Miscellaneous**

Symbol	Meaning	Unit
$\dot{\square}$	Time derivative	[-]
$\square^*$	Desired quantity if not o.w. defined	[-]
$\square_{\perp}$	Normal projection if not o.w. defined	[-]
$\square^{\max}$	Maximum value if not o.w. defined	[-]
$\hat{\square}$	Estimated or predicted quantity if not o.w. defined	[-]
$\ \square\ _2$	The 2-norm of a vector	[-]



# 1

## Introduction

### 1.1. Motivation

In 2018 the *Intergovernmental Panel on Climate Change* (IPCC) published an alarming report on the consequences of an increase of global mean surface temperature (GMST) by 1.5°C above the pre-industrial level [76]. The report encompasses over 600 pages, based on 6000 peer-reviewed and mostly recently published scientific articles. It comes to a serious conclusion: Already now the increase of the GMST by 1°C impacts the life of people and ecosystems worldwide leading to longer extreme heat waves, wildfires, droughts, increasing heavy precipitation, ocean acidification as well as rising sea levels [67]. In fact, 2015 to 2018 were the warmest years ever recorded [164]. Alarmingly, this heating process might become irreversible if the right counter measures are not taken immediately. Specifically, anthropogenic (i.e. man-made) global warming is estimated, with high confidence, to lead to a GMST increase of 0.2°C every ten years. Fortunately, tackling the challenge of limiting the temperature increase to 1.5°C, is still possible but requires radically reducing the emission of greenhouse gases in the coming years. Otherwise, this irreversible process will reduce biodiversity significantly and destroy entire ecosystems on land and in the ocean. This will impact first geographically less favorable regions and most often less developed countries that after all did not contribute significantly to the global greenhouse gas emissions. However, it eventually will affect the planet and humanity as a whole. As a result, global world poverty and inequality will rise, food and water availability will shrink and the number of geopolitical conflicts will increase [138, 130, 76, 67, 164].

Around two thirds of the greenhouse gas emissions stem from the energy sector. Therefore, the IPCC report urges the acceleration of the transformation from fossil fuels towards renewable energies. This is in particular a challenge because of the growing global energy demand, which jeopardizes the goal to reach the net zero carbon dioxide emission goal by 2050 [76, 77, 164]. The authors in [77] estimate that until 2050 the electrical energy consumption will rise by 130% to 55000 TWh relative to 2016. Fortunately, the amount of investments into renewable energy technologies is increasing as well. This

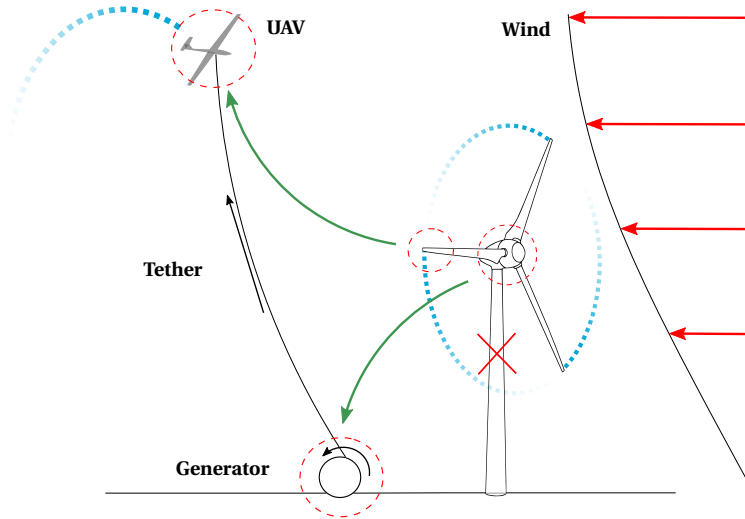


Figure 1.1: Making high altitude wind energy resources accessible through tethered UAVs.

trend is imperative to reduce greenhouse gas emissions and to achieve the goal stated in Article 2 (a) of the Paris Climate Agreement of 2015, namely "Holding the increase in the global average temperature to well below 2°C above pre-industrial levels and pursuing efforts to limit the temperature increase to 1.5°C above pre-industrial levels, recognizing that this would significantly reduce the risks and impacts of climate change;" [147]. The authors in [77] state that "at least two-thirds of the total final energy supply" needs to be renewables until 2050 to reach this goal. It is noteworthy that limiting the GMST might ultimately be economically less severe than the costs associated with the consequences of a GMST increase beyond 1.5°C, according to [67].

Besides solar photovoltaic, wind energy is and will play an important role in the overall renewable energy mix. [77]. According to the *Wind Technology Market Report* (see [158]) more than 591 GW of cumulative wind power capacity was installed world wide in 2018. In 2019 the cumulative wind power increased to around 651 GW, an increase of over 10%, and this trend will most likely continue in the years to come [58]. Nevertheless, the globally available wind resources are far from being completely exploited. As a relatively new technology, Airborne Wind Energy (AWE) systems aim to augment the existing wind energy technology portfolio. The goal is to increase the global wind energy capacity factor or even provide cheaper solutions compared to conventional wind turbines, especially at location with low near-ground wind speeds or deep offshore.

The advantage that AWE systems offer compared to conventional wind turbines can be described using the visualization in Fig. 1.1. In general, the wind speed increases with altitude, which is abstractly depicted on the right hand side of Fig. 1.1. This motivates making the wind resources accessible that are available in several hundreds meter of altitude where the wind is not only stronger but also more consistent. Potentially, this increases the capacity factor of these systems compared to conventional wind turbines

installed at the same location.

Making high altitude wind resources accessible with conventional wind turbines is a great technological challenge. The worlds tallest wind turbine, the Haliade-X, is installed in Rotterdam-Maasvlakte and measures 260m from the base to the tip of the blades [84], [159]. It is an impressive construction, only a bit shorter than the Eiffel Tower (324 m) in Paris. The three blades measure each 107 m, approximately the length of a football field, and create enough torque to turn a 12MW generator installed on top of the 150m tall tower. This makes the turbine not only the tallest but also the most powerful wind turbine in the world. Although it is still a prototype it seems to be a reasonable benchmark for the size of future offshore wind turbines. This manifests itself as well in the response of lead engineer Vincent Schelling to a question regarding the design goal: "What is the biggest rotor we would still feel comfortable with?" [85]. The quote indicates that the growing size of wind turbines is not unlimited. However, conceptual design studies predict even larger turbines. The conceptual benchmark is set by the 20MW turbine of the UpWind project which is taller than 270m (base to blade tip) with blades that are over 120m long [151]. Constructing buildings that are several hundreds of meters tall is in general possible, e.g. the tallest building in the world, the Burj Khalifa, in Dubai is over 800m tall [146]. However, it is unlikely that in the near future wind turbines that reach this height will be constructed. The logistic challenges to transport the turbine components as well as the technical challenges involved with building the towers such that they can support several hundreds of tons of blade and nacelle weight on top, while operating safely for several years, are high and certainly not feasible with today's technologies [159]. For instance, the envisioned turbine of the UpWind project leads to a nacelle weight of 800t and a rotor mass of 770t while the tower weighs 2780 t. Nevertheless, the UpWind project report concludes that such a 20MW turbine is feasible, however is not realizable by simply up-scaling existing turbines and technologies, hence more research and tailored designs are required [151].

In contrast to that, AWE systems do not require a large and heavy tower as well as long blades. In AWE these components are replaced by a strong tether as well as an unmanned aerial vehicle with a sufficiently large lifting surface (i.e. a wing). This means that the overall structural size is reduced significantly, which is visible in Fig. 1.2. On the left, a current prototype of the company TwingTec (see [107]), is depicted next to a wind turbine with a comparable rated power output. On the right, a rendered visualization of the 2MW concept of Ampyx Power is depicted, again next to a wind turbine with comparable power output [90]. These two examples clearly show the reduced material costs associated to AWE systems compared to wind turbines. Besides the material costs itself also the logistic challenges are reduced, since no large turbine blades need to be transported over long distances. Furthermore, since the tether cannot transmit any bending moments, the requirements on the foundations are less demanding which also makes it easier to install AWE systems offshore, for instance on floating platforms. Ultimately, AWE systems can operate in several hundreds meter of altitude already with the currently available technology and hence are able to provide access to wind resources which are not accessible to ground-based wind turbines.

The concept depicted in Fig. 1.1 belongs to the class of AWE systems that produce electricity on the ground. However, since this technology is still in an early development



Figure 1.2: Comparison of conventional wind turbines to AWE systems with similar rated power output: The left picture shows the TwingTec prototype [107], the right picture shows a rendering of AP4 which has a rated power of 2 MW and is designed by Ampyx Power [90].



Figure 1.3: Selected AWE prototypes operated by: Kitepower, TwingTec, Ampyx Power and Makani Power (from left to right) (photos from [135]).

stage several concepts are investigated at the moment. A selection of current prototypes is depicted in Fig. 1.3 and a more complete concept classification is given in Fig. 1.4 (obtained from [131]). Most of the existing prototypes produce electricity with a fixed ground station (GS) where the traction force in the tether is transformed into electrical power through a generator on the ground. In fact, the first four systems from left to right in Fig. 1.3 belong to this class. A further subdivision into different types of flight operation is possible. The most prominent type is crosswind flight operation, but also tether aligned as well as rotational concepts are investigated. More exotic concepts consist of a moving ground station on a rail, for instance the KiteGen carousel concept [78]. A third concept class is represented by AWE systems that mount the generators on the wing. The most prominent companies pursuing this approach are Makani Power [109], whose 600 kW prototype is depicted on the right in Fig. 1.3, and Altaeros [4].

Although AWE systems have the advantage of reaching high altitude wind energy resources they are significantly more difficult to operate autonomously compared to conventional wind turbines. In order to become commercially attractive, AWE systems need to be capable of launching and landing autonomously as well as being in power produc-

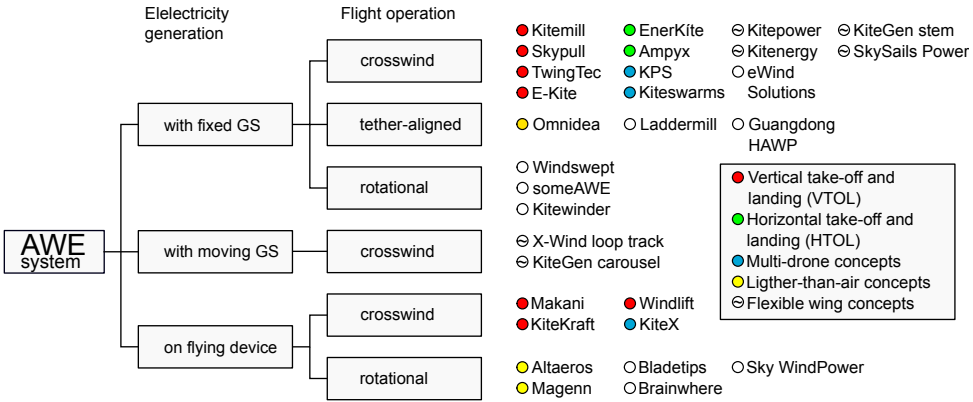


Figure 1.4: High level classification of AWE concepts [131].

tion mode continuously while being exposed to varying wind conditions. Autonomous operation can only be achieved with a reliable control system that is robust to changing wind conditions which motivates the research that led to this dissertation. More specifically, a control design methodology for fixed wing AWE systems with ground based electricity generation is proposed in the present work. On the one hand, a complete control design workflow is presented leading to a novel control architecture. A detailed robustness study is presented that analysis different control designs in presence of uncertainties. On the other hand, a data-driven methodology is presented that allows generating, predicting and preventing failure conditions systematically in order to increase the long term reliability of AWE systems. In total, this work aims to facilitate the control design process in the future for AWE systems and also tries serving as a self-contained basis for further research in this field. Although the author of this work also investigated autonomous launching and landing, see [117], the scope of this dissertation is limited to the control system design and verification for autonomous pumping cycle operation.

## 1.2. Robust Automatic Pumping Cycle Operation

In the following, the general control objective that needs to be achieved to robustly and automatically operate an AWE system in pumping cycle mode is described. The main parts of the control objective and the key words that describe the challenges are visualized in Fig. 1.5. The control objective for such a system can be subdivided into a tangential and a radial direction control task. On the one hand, the aircraft needs to follow a prescribed flight path, for instance a figure of eight or a circular pattern during the traction phase and, on the other hand, a straight line glide path during the retraction phase similar to the ones visualized in Fig. 1.6. In order to follow these reference paths, the aircraft needs to continuously adapt its aerodynamic force in magnitude and direction as a function of the path curvature, the deviation of the flight direction from the reference path, airspeed as well as the required tether tension. The corresponding commanded aerodynamic force that needs to be tracked by the control system consists of a part that

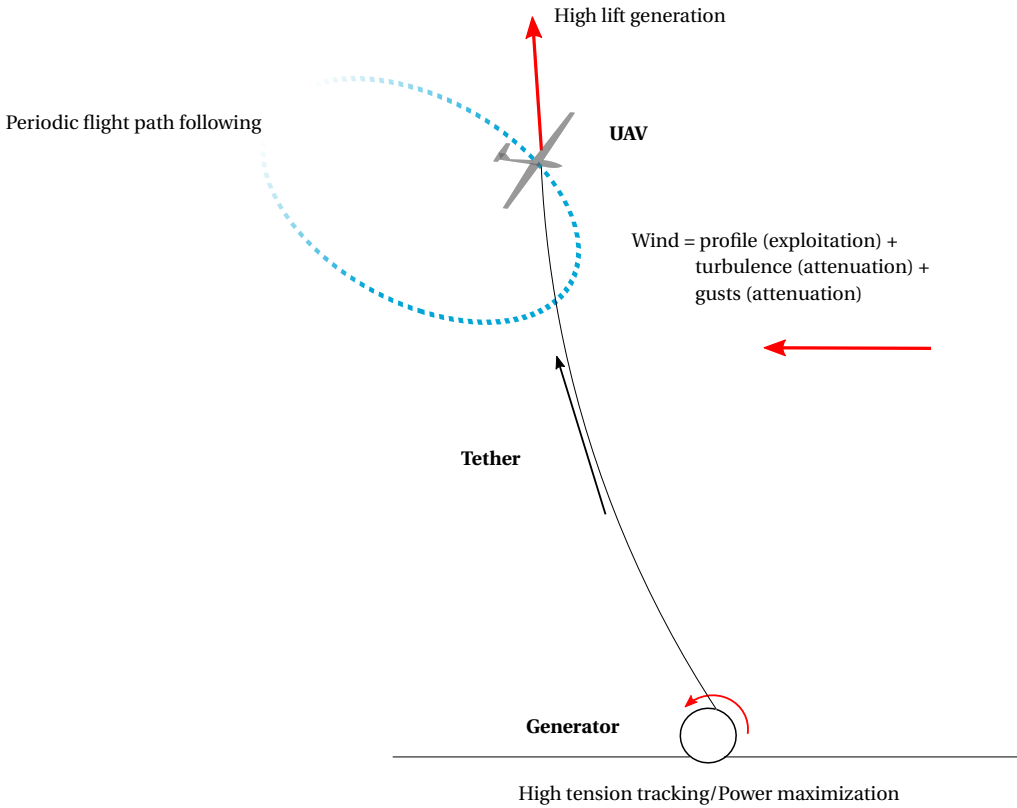


Figure 1.5: Components and high level control objectives.

accounts for gravity and tether tension as well as a part that creates the centripetal force required to follow the reference path. In combination this usually leads to flight maneuvers at high angles of attack close to the stall point. Hence, a reliable control system is required that tracks the angle of attack accurately and prevents large overshoots to avoid entering the post-stall flight regime. On the ground, the winch and the generator have the objective to adjust the reeling in or out speed of the tether in order to track the tether tension. Besides the high tension tracking it is paramount that the winch is able to keep the tension below the critical value beyond which the tether breaks. These two failure scenarios, stall and tether rupture, are investigated in depth in this work. Additionally, during the retraction phase the tether tension needs to be kept low in order to minimize the consumed power.

Arguably the major challenge that needs to be overcome for reliable AWE system operation is to design a control system that can handle the uncertainties of the wind field. In Fig. 1.5 the "wind" is split up into three parts. The mean wind speed is usually modeled through the wind speed profile which is also depicted on the right hand side of Fig. 1.1. This part of the wind component can be regarded as the "propelling force" of

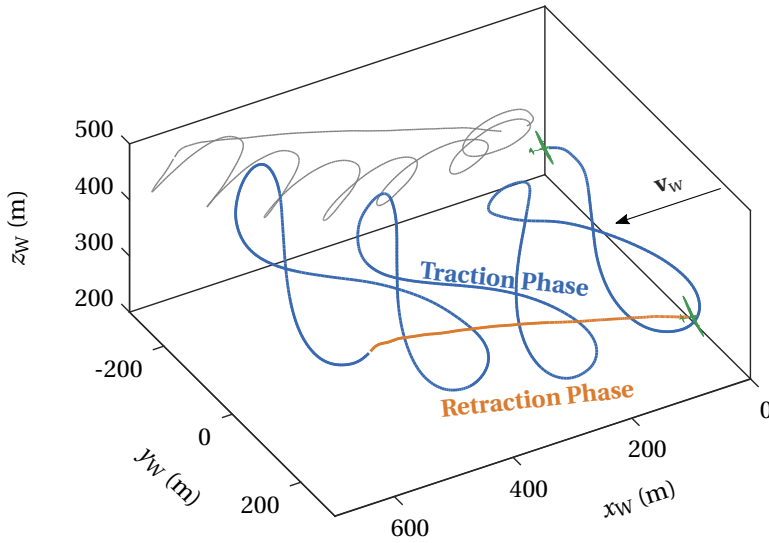


Figure 1.6: Generic pumping cycle trajectory. The tether is not shown for visualization purposes.

the AWE system. The atmospheric turbulence as well as the wind gusts can be regarded as the disturbances that the control system needs to account for. The dilemma is hence that, on the one hand side, the beneficial part of the wind needs to be exploited in order to propel the aircraft but, on the other hand, the effect of the harmful part of the wind needs to be attenuated to ensure safe operation.

Note that in the area of robust control system design and analysis the term *robustness* is usually utilized with respect to the *robust stability* as well as the *robust performance* properties of the closed loop plant (see [140, p.269]). In order to analyze these properties an uncertainty model for a linearized representation of the plant is created. It allows to incorporate mathematically the "known unknowns" such as inexact model parameters. Design paradigms such as  $\mathcal{H}_\infty$  robust control can then be utilized to derive a controller that guarantees stability and performance within the specified uncertainty set. Moreover, measures such as the gain and the phase margin (see [140, p.34]) or the structured singular value (see [140, p.331]) can then be used to quantify the robustness properties of the closed loop plant in a mathematically rigorous way. These concepts are well understood and applicable especially for linear time invariant systems. However, it is challenging to apply these concepts directly to plants with highly nonlinear behavior as well to as nonlinear controllers such as the ones utilized in the present context. Therefore, robust analysis tools, such as the structure singular value, are in this work only utilized in the innermost loop for which reasonable linear time invariant plant models and, therefore, also linear controllers can be derived. Furthermore, a linear matrix inequality approach is utilized to design linear inner loop controllers with guaranteed stability and performance properties for a set of plant models. This indirectly results in a control design that is more resilient towards parametric uncertainties in the plant. More im-

portantly, however, is that the global stability and performance properties are eventually analyzed in a statistical sense using Monte Carlo simulations and models of different fidelity. Since analytical stability proofs of the utilized closed loop nonlinear systems are intractable, the controllers are assessed using a probabilistic approach. More specifically, probabilities are calculated that quantify the likelihood that critical requirements are met. Overall, the term *robustness* is in this work, hence, related to the probability of performing pumping cycle operations without violating these requirements to ensure the integrity of the AWE system.

### 1.3. Literature Review

In light of the presented challenges this section reviews the existing AWE control literature. Since the seminal work of Miles Loyd in the 1970s (see [104] and also [102], [103]) different research groups and companies contributed to the technological and scientific progress of AWE. The revised literature that is presented in this section focuses on the areas that are important for control system design in particular for AWE systems that are operated in pumping cycle mode. The review paper [24] compares in detail the different concepts on a system level which is not repeated in this work. The physical fundamentals of AWE are not introduced in this work either since they are explained in [3, p.3-22]. Latest technological advances can be found in [132].

Controlling AWE systems requires to tackle fundamental challenges that are shared by all autonomous (flying) systems (see [7], [114]). Specifically, all autonomous systems need to achieve their specific objective while being exposed to varying disturbances and uncertainties and need to be able to recover from adverse conditions. In general, autonomy is achieved by creating a hierarchical control structure similar to the one proposed in [7]. At the highest level decisions are made that, for instance, define the current operational mode while at the lowest level the system interacts with its environment using actuators. In the highest layer of an AWE control system the current active controller or operational mode (i.e. launching/landing/power generation) is selected while the middle layer defines, for instance, the reference flight path that is potentially optimized during the operation. Eventually, the lowest level consists of the control system that calculates the actuator commands to follow the reference path. Such a hierarchical or cascaded structure offers the advantage that the individual layers can be designed to the largest extend individually while complying to the interfaces of the adjacent layers. This approach is especially necessary if the operational modes differ significantly from each other. For example, in AWE a different controller is required for the launching/landing phase as well as the power generation mode. For most AWE systems launching and landing is supported by an onboard propulsion system which is switched off after a successful launch. Clearly, this requires a different control strategy compared to crosswind flight where the systems are solely propelled by the wind. In addition, for systems operated in pumping cycle mode a different controller for the traction and the retraction phase might be implemented. Cascaded control approaches also offer a convenient way to "divide and conquer" the complex control problem by transforming it into smaller sub-problems that are easier to handle individually. Other strategies try to tackle the control problem at once by formulating an optimization problem where the entire system dynamics and limitations are included in form of equality and inequality constraints and

then either offline or online an optimal, with respect to the defined cost function, control input is calculated. Nevertheless, even if the latter approach is chosen it is necessary to solve separate optimization problems for the different operational modes and connect the resulting "optimal" controllers. This shows that basically every control system of a complex technical system is hierarchically implemented.

To that end, the review section is structured as follows. First, the AWE control literature for systems with flexible wings (i.e. kites) is reviewed followed by a review of control system designs for rigid wings (i.e. tethered aircraft). Next, winch control strategies are presented. Subsequently, a concise overview of optimal control approaches is given. Lastly, automatic launching and landing is discussed. Note, a complete review of existing flight control techniques for UAVs is out of the scope of this section. However, reference [153] provides a detailed overview of the different linear and nonlinear control techniques for UAVs for the interested reader.

### Cascaded Control Approaches for Flexible Wing AWE Systems

The first fundamental challenge that needs to be tackled is to design an outer loop that guides the kite (or aircraft) in a periodic manner on a spherical surface (tangential direction control objective). In the literature this challenge is usually solved using target point based guidance approaches. It is shown in [39, 40, 44, 45, 169, 41, 167, 128, 46, 15, 136] that periodic figure of eight flight patterns can already be achieved by defining only two target points. The guidance law is simply realized by switching between two target points, which leads to alternating left and right turns. Notably, in [39] the turn-rate law is introduced which essentially defines the relationship between the tangential plane course rate of a flexible kite with its steering input. In [52, 50] four waypoints are used that are connected with arcs and great circles to further shape the figure of eight flight pattern. This approach is also implemented for the TU Delft kite power system as presented in [154]. In [35] power optimal flight paths are calculated for a given control structure, designed by the company Skysails (see [142]) and published in [39]. The yaw angle set-points, used to steer the kite in a figure-8 shaped manner, for the low-level controller are optimized using Gaussian Processes such that the towing forces is maximized while complying with an altitude constraint.

The authors of [43, 45] propose the velocity-angle guidance strategy employing two target points similar to the one proposed in [39]. A simple proportional feedback law calculates based on the velocity angle tracking error the steering input for the kite. A simple stability proof involving the linear actuator dynamics as well as the velocity angle tracking error dynamics is carried out invoking the notion of quadratic stability [122, p. 31-92].

In [169] the traction phase controller proposed in [45] is augmented by a retraction phase controller to enable full pumping cycle control for a flexible kite system. Simulations as well as experimental results are used to verify the proposed control strategies. Similar to [45] robust stability is shown using Lyapunov equations evaluated at the vertices of the convex hull of the closed loop system matrix. This approach is further developed in [169] to adapt the paths online solely based on the measured tether tension. The study additionally shows that the path shape itself is of minor importance with respect to the power output in contrast to the location of the path with respect to the wind direction. Although the results are intuitive they provide a theoretical justification that the

flight path should be centered in the wind window, hence needs to rotate with the mean wind direction, and the optimal elevation angle is a function of the wind speed profile.

In [162] the control method is based on the work of [45, 169, 160] and augmented by an online identification method which is used to adapt the gain and time delay in the kite steering model. The controller performance for figure-8 flight is verified experimentally in a tow test experiment.

The work in [31] proposes an adaptive control scheme for a flexible kite. An online system identification procedure is used to adapt the proportional-differential flight controller gains in the course error feedback law during figure-8 flight. The same flight path planner as in [52] is utilized.

A drawback of the two or four waypoint based approaches is that the resulting path shape is harder to prescribe. However, due to its simplicity these guidance approaches are easy to implement and are computationally cheap which makes them attractive in practice. Some authors try to improve the predictability of the resulting path shape by calculating the waypoints through a discretization of a continuous curve. From a practical point of view the resulting controller complexity is similar to the one with two or more target points but offers the advantage that the flown curve can be defined more precisely. Such an approach is adopted by the authors in [161] (also in [124] but for a rigid wing system). In [161] a cascaded approach is chosen, where the outer-loop calculates the desired flight direction and the inner loop determines the actuator input given by the line angle difference. A Smith predictor is used to incorporate time delay information into the calculation of the velocity angle reference value. To calculate the reference velocity vector orientation a receding horizon LQR is used that uses the linearized unicycle model on the path as the input and then calculates the reference velocity vector orientation sequence that minimizes the deviation of the kite from the reference path over a specified time horizon. Note, the paper mainly focuses on the tangential control objective. In radial direction a constant reeling out velocity is considered and the controller is verified in simulations. In addition, the changing model parameters are estimated using an online least-squares method.

Other approaches use a continuous path parameterization (see [11, 80, 123, 35, 163]). In [11] a nonlinear Lyapunov-based adaptive controller is proposed and validated using a point-mass (flexible) kite model. The path is defined as a curve parameterized through the path length. A formal stability proof is carried out and the concept is validated using simulations. Note, only the reeling-out phase is considered and no explicit winch control system is implemented. Furthermore, in [80] a figure-8 path following controller for a flexible kite power system is proposed (only traction phase). Through an inversion of the turn rate law the steering input is calculated. The controller is verified experimentally. Note, the outer loop of this work also serves as a foundation of the guidance module in the present thesis.

[123] propose a path-following controller for a flexible kite that takes into account time-delays by adapting the turn-rate law. A least-mean-squares approach is used to fit a linear filter that better approximates the turn rate dynamics online and hence allows to predict the future kite state in order to compensate for delays. The guidance law is realized as a virtual target following approach and the steering input is calculated based on a proportional feedback of the course tracking error. Experimental results of the figure-8

following performance are presented with fixed tether length.

In [2] a stability analysis for figure of eight flight based on contraction theory is presented including model uncertainties. The results show that the region of attraction correlates inversely with the model uncertainties. The work uses the uni-cycle model without radial dynamics.

Note, all of these publications that use a continuous reference curve tackle only the figure of eight path following problem either with a fixed or varying line length but do not consider full pumping cycle operation.

### Cascaded Control Approaches for Rigid Wing AWE Systems

All the previous discussed results were directed towards controlling flexible wing kite power systems with a cascaded control architecture. The turn-rate law shows that flexible kite systems are conveniently controlled by exploiting the proportionality of the required turn-rate to follow a reference path and the kite steering input. Rigid wing AWE systems are essentially tethered aircraft with conventional actuation devices on board i.e. ailerons, elevator and rudder, hence the turn rate law does not apply here. This section reviews the cascaded control approaches for rigid wings.

In [124] a high-level description of the Ampyx Power [5] control system is given. The path-following problem is solved using a discretization of a continuous curve. The desired flight direction is then given by a look-ahead distance that selects the current target waypoint on the curve. In this approach a fixed elevator is used, similar to the power setting of a flexible wing system. The disadvantage of this approach is therefore that one control degree of freedom is not used and the aerodynamic force can only be changed through the airspeed and hence through the reeling speed. This makes it more difficult to ensure that the tether tension does not exceed its limit value if for instance the winch is saturating. The lateral controller maps the desired flight direction into a roll angle relative to the tangential plane and the corresponding tracking error is mapped into a roll rate whose tracking error is allocated to an aileron deflection. However, the exact controller structure, most likely a PI controller, is not presented in detail.

In [65] the authors propose a Lyapunov function based approach for the controller design to stabilize the attitude and rate error dynamics, yielding a proportional-differential control law. The tension in the tether is assumed to be a control input, hence tether dynamics and an additional winch control system are not considered. Figure-8 flight paths are flown by periodically switching between roll, pitch and yaw set points that are tracked by the attitude loop. The retraction phase is flown with a constant negative pitch angle. It is not clear, however, how the controller performs in presence of disturbances since the attitude reference points are fixed and most likely lead to an uncontrolled deviation of the aircraft from the desired figure-of-eight pattern in a more realistic environment. This control approach is also applied by the same authors in [64] to control an AWE system with onboard generators. In contrast to [65] fixed angle of attack and sideslip angle set points are defined and mapped to the corresponding Euler angles. The Euler angles are then tracked using a second order dynamic inversion of the attitude dynamics. Similar to [65], however, the robustness of this approach towards uncertainties is not investigated. Also the implications on the resulting tether force are neglected. The authors publish the same controller in [93] for an AWE system with ground based gen-

erator. In [94] the authors of [65, 64, 93] further compare the different proposed attitude control strategies with each other.

In [148] a flight controller for a rigid wing AWE is proposed that can fly figure of eight maneuvers in the horizontal plane as part of a vertical takeoff and landing control architecture. Hence, the flight path is followed while using the onboard propellers and no pumping cycles are performed. The inner loop is implemented in a cascaded manner, where attitude reference angles are tracked using a proportional tracking error feedback law which is then mapped to rate commands and ultimately to control surface deflections. The figure-8 pattern is realized through switching between target points, similar to [44] but in this work at a constant altitude.

Recently, [149] proposes a control architecture for full cycle control including launching and landing that extends the work in [148]. The flight path controller is based on the work published in [41] and [44], the inner loop is based on [148]. The authors show full cycle control capabilities with this approach.

Besides crosswind patterns some authors propose pumping cycle control approaches in which the motion of the airborne system is only in the downwind direction [62, 105]. In addition, [61] tries to exploit the Magnus effect to create high tether tension. Common in these approaches is that no crosswind patterns are flown, hence only a radial direction control system is required that tracks the tension in the tether for optimal power output. It is, however, debatable if these approaches on a large scale can be competitive compared to crosswind flight due to the lower achievable airspeed.

### Winch Control

The previous two sections mainly reviewed control strategies to achieve the tangential direction control problem i.e. how to steer the kite or the aircraft between waypoints or along a continuous curve. However, as discussed in section 1.2, for full autonomous cycle also the radial control objective needs to be solved. This is mainly done by the winch control system. Similar to the flight controller implementation different strategies are presented in the literature. In [102] the notion of an optimal reeling out speed is introduced, which is defined as a third of the projected wind speed in tether direction. Note, the notion of optimality in this publication is derived from simplified models based on assumptions such as a constant reeling out speed as well as simplified system dynamics, i.e. point-mass dynamics and neglected tether dynamics. Based on the concept of this "optimal" reeling-out speed [169] proposes to directly calculate the reference motor torque which applied to the winch adapts the current reeling speed accordingly. In the retraction phase a constant reference torque is chosen to achieve a high reeling in speed to reduce the retraction phase time for a higher net power output. In contrast to determining directly the motor torque, [51] introduces a feed-forward winch control strategy in combination with a tether force tracking error feedback controller to calculate a set-point for the reeling speed. The feed-forward part is determined based on a force equilibrium. The reeling speed set point is then tracked by a speed controller. In [41] a similar approach is used where the radial direction is controlled using a reeling speed tracking controller. As a safety feature, in order to avoid too high tether tension, the maximum current in the electrical motor/generator is limited. However, the exact implementation of this limiter and its effectiveness to avoid overload is not shown in

this work. The reeling speed set point in the traction phase is again determined using the optimal reeling speed "rule". In the retraction phase the winch speed set point is scheduled as a function of the current elevation angle. The authors in [149] use the optimal generator torque proposed in [169] to control the radial direction during the traction phase. In the retraction phase the motor torque is calculated using a proportional error feedback of a reeling in speed set point that needs to be tuned for optimal pumping cycle efficiency.

### Optimal Control Approaches

A large part of the AWE literature addresses the challenge of flight path optimization. In this section the optimal control literature is reviewed in which the entire AWE system dynamics (airborne system and ground system) are embedded into an optimization problem. Different strategies are proposed ranging from offline path optimization, model predictive control (MPC) as well as iterative learning control (ILC). Since these strategies fundamentally differ from the cascaded approach utilized in this work only a concise description of the existing publications is given without going too much into detail.

Offline optimization offers a systematic way to predict the expected power output of a given AWE system for a given wind speed profile or even a distribution of the wind speeds at a given location. It hence allows to predict the expected power output while considering the dynamic constraints imposed by the AWE system itself (see e.g. [95]). In the context of AWE, the optimal control problem is usually posed such the average power output of the system is maximized which is studied extensively in the literature [72, 157, 144, 71, 137, 92, 97]. Other approaches maximize the total energy that is generated [21, 53, 10]. Also the incorporation of other, for instance safety constraints, can be incorporated into the optimization problem [73, 127, 160]. Besides using optimal control techniques for the power generation phase, optimization techniques can also be applied to calculate optimal launching and landing trajectories (see e.g. [87] and [20]). For the solution of the optimal control problem several open-source tools are available: CasADi [6], the open Optimal Control Library openOCL [88], LAgrangian Kite Simulators LAKSA [126], and the awebox [30].

Besides the offline optimization of autonomous AWE operation numerous publications that use online optimal control i.e. model-predictive control (MPC) are available. Nonlinear periodic MPC was applied to AWE in [34, 32, 33] for a simple tethered wing and extended to AWE systems operated in pumping cycle mode in [21, 22, 75, 35]. In [163] a predictive guidance controller is presented with varying line length and the impact of actuator delay is explicitly accounted for using a Smith predictor. The proposed controller in [163] is further developed by also taking into account changing kite velocity. The controller is ultimately experimentally verified in a tow test and results are presented in [160] but no complete pumping cycles are performed. The results of other real-time capable studies are proposed in [21, 54, 60, 165] and [166]. The former applied MPC to single kite systems whereas the latter applied it to control dual-kite systems. Recently robust MPC techniques were developed (e.g. [108, 82]). Due to its computational complexity most of the proposed control methods are verified within a simulation environment. Available publications that deal with real-world implementation of MPC usually use a simplified experimental setup (see e.g. [160, 155]). Drawback of the MPC approaches is that they

rely on accurate models as well as knowledge regarding the surrounding wind conditions in time and space and are in general computationally more demanding.

In addition to MPC, ILC is another optimal control techniques that can be used to optimize the power output of AWE systems. The application of this techniques is motivated by the fact that AWE systems are operated in a periodic, or repetitive, manner. In this context, a new ILC variant (economic ILC) is proposed in [27]. Economic ILC is applied to systems with ground-based generators in [26] but also for on-board power generation in [27].

### Launching and Landing

Although this work focuses on the design of pumping cycle control systems the available literature regarding autonomous launching and landing is concisely reviewed in the following for completeness. Clearly, without a reliable launching and landing strategy AWE will not be commercially feasible on a large scale, for instance realized as large offshore parks where multiple AWE systems are operated next to each other. The importance of launching and landing is motivated by the fact that although it is desirable to design the control systems such that the aircraft can stay in the air for long periods of time the wind conditions might force the aircraft to land and hence also takeoff again from time to time. If the system is not able to achieve this without manual intervention the technology will be too expensive to become a viable part of the renewable energy technologies portfolio. Since there is still no consensus in the AWE community which launching and landing strategy is the most reliable one, several studies are published where different concepts are compared to each other [16, 66, 42, 46, 149, 74, 117].

The most popular approach is to use an onboard propulsion system that allows vertical takeoff and landing, which is also a concept pursued by most of the companies in the field (see e.g. [86], [106], [110]). VTOL concepts are also assessed in simulation for flexible systems in [13] and [117] as well as for rigid wings in [149].

The disadvantage of the VTOL concept is that the additional mass of the VTOL systems needs to be carried onboard. Therefore, Ampyx Power [5] pursues a horizontal launching and landing strategy from a platform using a combination of a catapult mechanism and onboard propellers.

For flexible kite systems a telescopic mast approach has been proposed by the company Skysails [141]. Another mast based launching concept for flexible wings has been investigated by the University of Technology in Delft. In this approach the kite hangs initially upside down from a mast. If the wind speed is sufficiently high it performs a swing-up motion while the tether is reeled out. Footage of the launching process can be found in [133, 134].

The company EnerKite pursues a rotational launch and landing concept where the wing is accelerated through a rotating arm until takeoff speed where the controller switches into crosswind flight [37]. Landing is performed in a similar manner.

Recently, in [129] another multicopter based launching and landing strategy for a rigid wing is presented. The controller is implemented as a trajectory tracking controller and verified using two-dimensional simulations. A linear set point change from the initial values of elevation angle and radial position to their final desired values is implemented. In addition, a constant tether force set point is chosen. The trajectory and

the tension is tracked using the ground based winch as well as the thrust of the multi-copter. The aerodynamic forces are regarded as disturbances that the controller needs to compensate. Since the model is only two-dimensional and the tether dynamics are neglected, the control scheme needs to be verified further using models with higher fidelity, or experimentally, in the future.

### Summary Literature Study

The results of this literature study show that most of the available publications address the challenge of flexible-wing (i.e. kite) control system design and/or optimal control approaches. Among these contributions either complex nonlinear, sometimes adaptive, control schemes are derived for simplified point-mass models and analyzed in simulations using simple models. More practical controllers, also derived using point-mass models, notably using the uni-cycle model, are proposed that often are also verified experimentally. In contrast to that, cascaded full-cycle control schemes for rigid wing systems were not published at the start of this research. One exception is the work published in [124] which is, however, only presenting the control system on a high level without detailed derivations. Overall this result is surprising since most of the AWE companies operate rigid wing systems and is an indication that more research in this field is required to fill the gap between academia and industry. Furthermore, most of the existing publications deal with the path-following problem especially in the traction phase, hence the radial control objective, i.e. reliable tether force tracking is to the largest extent discarded or simplified by assuming a constant reeling out speed. This simplifies the overall control objective, since especially the radial motion control approach is paramount for robust pumping cycle operation as will be shown later in this work. Therefore, one contribution of the present work is a novel cascaded control approach for rigid wing AWE systems similar to the ones developed for flexible wing (i.e. kites) systems for full pumping cycle control.

Another challenge that is so far not addressed in the literature, except for the work published in [125], is reliability and safety. In fact, the revised literature does not provide any statistical assessment of pumping cycle control systems. Note, in [125] a high level safety assessment is performed and published for a flexible kite system using fault-tree (FTA) and failure mode and effect analysis (FMEA). In the published literature the control systems are usually designed to maximize the power output and verified for a specific wind condition with or without turbulence. However, they are not assessed under varying environmental conditions and model uncertainties to create distributions that more accurately approximate the robustness of the closed loop system. For that reason the present thesis puts emphasize on robustness in the sense that the controllers are not necessarily derived in order to obtain the most power optimal control solution. Instead, the controllers are designed and assessed in terms of their statistical compliance with specific requirements, such as keeping the tether force below a limit value, under varying wind conditions as well as in presence of model uncertainties. Where deemed necessary, confidence intervals are used to quantify the expected variability of the obtained results for completeness and to judge if sufficiently high sample sizes are utilized to assess the controller robustness.

Besides standard Monte Carlo simulations also a more advanced technique based on the *subset simulation* method is used in this work to systematically generate conditions

under which the overall control system will fail. Generating this information systematically allows to leverage knowledge of failure conditions in order to be able to predict and prevent the violation of a critical requirement that jeopardizes reliable pumping cycle operation. Ultimately, this will substantially improve long term robust autonomous operation of AWE systems.

## 1.4. Research Questions

Based on the identified gaps in the revised literature the following high-level research questions are stated which are answered in the subsequent chapters:

1. What makes AWE systems more difficult to control than conventional UAVs?
2. How should robustness and performance of AWE control systems be assessed?
3. How can decoupled linear state feedback flight controllers for robust figure-8 flight be systematically designed and how do they perform compared to a nonlinear flight controller?
4. How can the derivative term in the pseudo-control input for the inversion of the path-dynamics during figure-8 flight be calculated without relying on linear reference filters?
5. How can the transition from the retraction to the traction phase be shaped in order to damp tether tension peaks during the transients and how does the transition strategy enable to trade-off performance and robustness?
6. How can upset conditions in the context of AWE be defined and systematically generated if the probability of encountering one per pumping cycle is low in simulations and how can they be predicted and prevented?

These research questions are partially answered in the publications of the author of this dissertation. A complete publication list can be found at the end of this thesis. Naturally, the subsequent chapters overlap partially with the published work. Note that, if instructive, the results and derivations are displayed in greater detail in this thesis, but also novel material is presented.

## 1.5. Thesis Outline, Reading Order and Methodology Overview

The thesis is structured as follows. In chapter 2 the utilized notation and coordinate reference frames are introduced and the mathematical models required for the control system design and to perform pumping cycle simulations are presented. In chapter 3 the AWE system dynamics are linearized and a flight dynamic analysis in quasi-stationary operating points is performed. Chapter 4 contains the control system design part of this work. The outer flight guidance loop, linear and nonlinear inner loop flight controllers as well as the winch controller are derived. In chapter 5 the control performance is assessed in presence of different time delay combinations as well as model uncertainties and changing wind conditions. In chapter 6 an upset condition generation, prediction

and avoidance methodology is introduced. Within this framework critical flight conditions are systematically generated in order to be able to train a prediction model. The predictor is able to foresee requirement violations before they occur and can trigger appropriate avoidance maneuvers. Finally, chapter 7 concludes this thesis and provides ideas for further research directions.

For completeness Fig. 1.7 is provided which displays possible reading orders for this thesis. Naturally, the thesis can be read from the first to the last page (blue route) but it is also possible to skip chapters that are not of interest for a particular reader. In general, it is recommended to read through Chapter 1, since it explains the context into which the present work is embedded. Readers that are familiar with the existing literature can of course skip the review section. Furthermore, a reader that is familiar with flight mechanics as well as AWE related models can additionally skip Chapter 2. The red highlighted reading order is recommended if the reader is interested in the control system design and verification process. Note, in this case the linear analysis as well as the derivation of the models that are used for the controller synthesis are skipped. Since Chapter 6 is a self-contained part of this work it is not required to read all the preceding chapters in order to understand the content (green route). All other possible reading order combinations can be deduced from the figure.

The overall control system design workflow is concisely summarized in the following and visualized in Fig. 1.8. The figure also graphically illustrates how the individual chapters of this thesis are connected to each other in more detail. Due to the cascaded structure of the flight controller it is helpful to design the controller from the outer to the inner loop and verify the performance using models with appropriate fidelity. In the first step, the implementation of the guidance loop can be verified using only a kinematic model which does not require any specific model parameters and is therefore a step that can be taken at an early design stage. In Fig. 1.8 this corresponds to Step 1. Next, since the path-following controller is mainly derived from the three-degree-of-freedom dynamics (3-DoF) it is reasonable to use a 3-DoF model to verify it. In this case a model for the aerodynamic forces acting on the aircraft is required. The path-following controller calculates the required attitude angles to create the lift force, that on the one hand, creates the required maneuver force (i.e. centripetal force) to follow the reference curve and, on the other hand, compensates gravity as well as the tether force. In the 3-DoF model the attitude commands are then directly applied to the model. In order to account for the attitude dynamics, linear second order filters can be used to smooth these commands which also leads to a better approximation of the real 6-DoF dynamics. This makes later on the transition from the 3-DoF to the 6-DoF model easier since the additional delay induced by the closed loop attitude dynamics is already roughly approximated by the filters.

The second step can be further subdivided into intermediate steps. In the first intermediate step the traction phase path-following controller can be designed and verified using a perfect tether tension tracking assumption. In this case the traction phase path-following controller can be tested separately from the winch controller and without the additional complexity of the tether dynamics. If the path-following controller leads to an acceptable tracking performance the tether dynamics can be switched on and the winch controller can be tuned in the second intermediate step. Both intermediate steps are

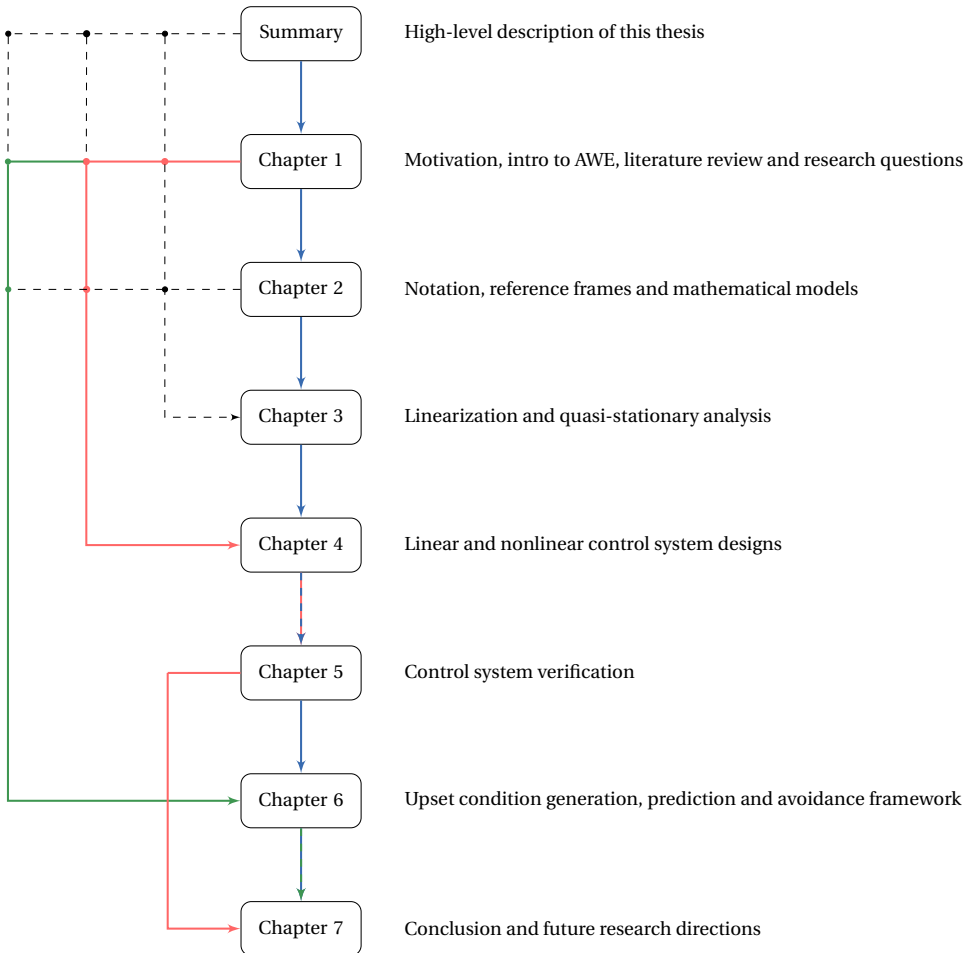


Figure 1.7: Thesis reading guideline. The arrows indicate suggested reading orders. Besides reading the complete thesis (blue route) it is also possible to read only the parts that are of interest for the reader. Exemplary the reading order for the control system design and verification process is highlighted in red and for the upset generation, prediction and avoidance framework the suggested reading order is highlighted in green.

denoted with Step 2.1 and Step 2.2 in Fig. 1.8.

In Step 3 of the framework the inner loop controller is designed and verified. In this work different inner loop design strategies, linear and nonlinear, are proposed and compared to each other with respect to performance and robustness. In this step either the attitude angle commands of Step 2 can be used for tuning or simple step commands. The latter offers the advantage that time domain characteristics such as overshoot, rise time and settling time can be used to specify the controller performance. Note, in order to perform this step the full aerodynamic model of the aircraft needs to be available.

In Step 4 the outer and inner flight control loops are combined and verified with the 6-DoF aircraft simulation model. Note, this step offers again the possibility to first test

the flight controller with perfect tether force tracking and without the tether dynamics. As soon as an acceptable performance is achieved the tether dynamics can be switched on and the winch gains can be adjusted if necessary. This intermediate step is essentially used to test if the inner loop is able to track the outer loop commands given the limited bandwidth of the flight control system. In general, this procedure is only carried out for the traction phase controller since it demands a higher bandwidth than the retraction phase controller.

In Step 5 the complete control architecture is assessed using the 6-DoF aircraft model as well as tether and winch dynamics in a statistical manner using Monte-Carlo simulations. Note, the entire process is in general iterative and hence requires several re-design steps until all performance specifications are met.

As an optional step (Step 6), the control system can be stressed with respect to specific failure conditions, for instance tether rupture or stall. If the control system is well designed through Step 1 to Step 5, these failure conditions are most likely rare and hence only encountered once every hundreds of pumping cycle simulations (or even less). Therefore, in Step 6 these failure conditions can be generated more systematically than with "brute-force" Monte Carlo simulations in order to be able to learn from the counter examples where the controller does not satisfy critical requirements. Ultimately, a prediction and prevention strategy can be derived that further increases the reliability of the control system.

Note, as indicated in Fig. 1.8 every step consists of a design phase (boxes with round corners) as well as a verification task (boxes in bold with sharp corners). If the verification output does not meet the desired performance criteria another iteration of the corresponding design phase is necessary. This procedure is especially applicable in Step 1, Step 2, Step 3 and Step 6. Step 4 and Step 5 do not contain a specific design phase. In fact, Step 4 verifies if the inner loop controller design in Step 3 (linear or nonlinear) can follow a specific figure of eight or a retraction path geometry. If the inner loop controller is not able to track the corresponding outer loop commands with acceptable accuracy another inner loop design iteration is required. If, however, the inner loop operates already close to the maximum bandwidth or any other hard constraint, the iteration loop needs also to include Step 2. In this case, it might be required to alter the path geometry. It is therefore instructive to already verify in Step 2 if the outer loop is able to follow different path shapes. In Step 3 the path shape that leads to the best performance can then be selected without requiring an additional iteration that includes Step 2. The same procedure needs to be conducted if the Monte Carlo simulations in Step 5 do not lead to satisfactory results. Note, it is shown later in this work that already modifications in the high level set point parameters can improve the reliability without requiring to redesign the controller gains.

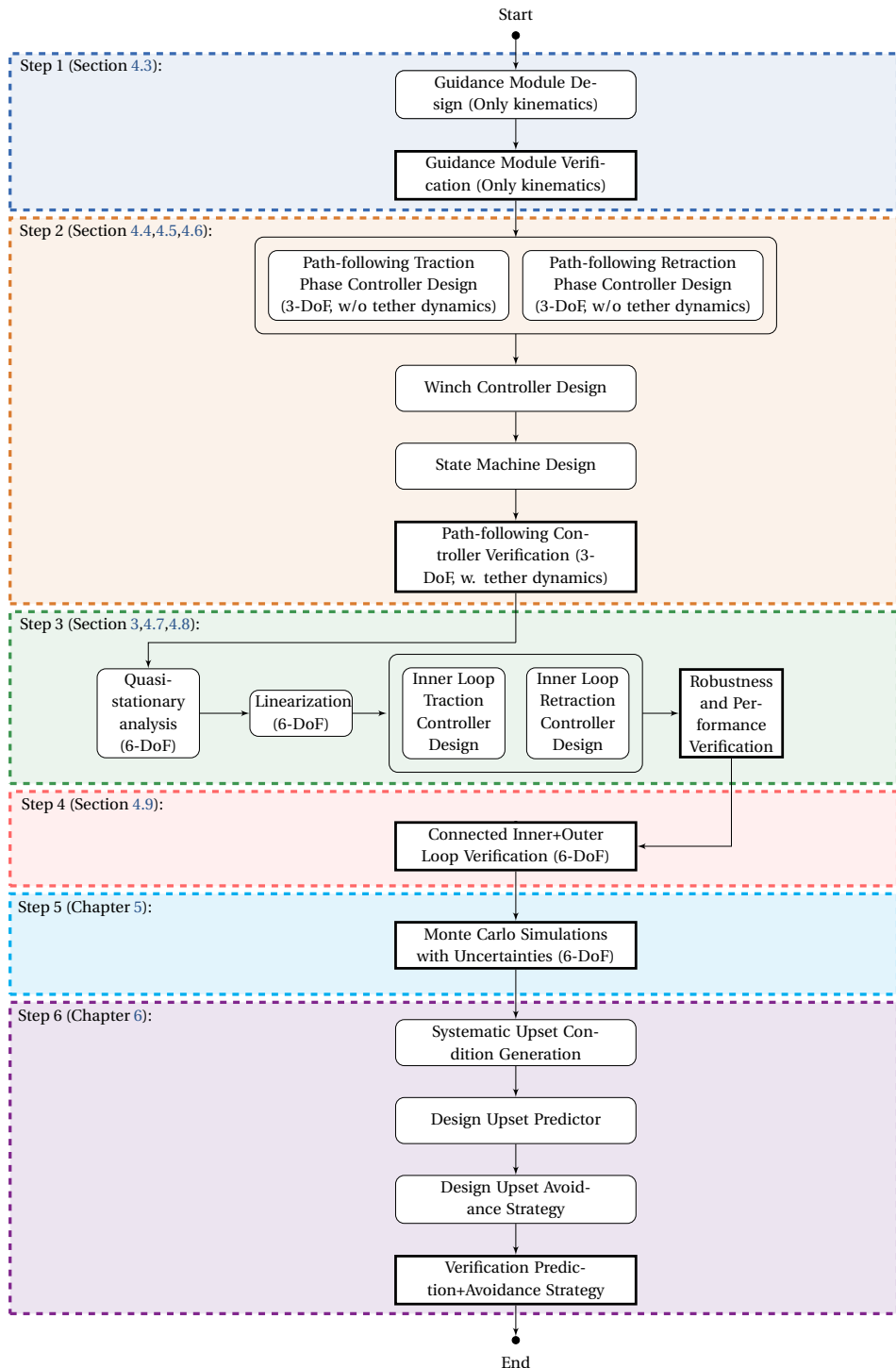


Figure 1.8: Control design and verification workflow using models with appropriate fidelity. Note, possible design iterations are not displayed for visualization purposes but are explained in the text. The individual parts are discussed in greater detail throughout this thesis (see indicated section and chapter numbers). Blocks with round corners indicate design tasks, sharp corners indicate verification tasks.

# 2

## Simulation Framework and Models

In the first part of this chapter the utilized notation in this thesis as well as the frames of reference are introduced. Subsequently, the mathematical models that are used to design the controllers and to perform the simulations are presented.

### 2.1. Notation

The following notation is utilized in this work: Vectors and matrices are written in bold letters. Moreover, the frame in which a vector is given is indicated by the subscript outside the brackets. For instance,  $(\mathbf{v})_B$  indicates that the vector  $\mathbf{v}$  is given in the B frame. Transformation matrices are denoted with a capital, bold  $\mathbf{M}$  as well as a subscript that specifies the transformation. For instance,  $\mathbf{M}_{AB}$  denotes the transformation matrix from the B to the A frame and hence a coordinate transformation from B to A is given by

$$(\mathbf{v})_A = \mathbf{M}_{AB} (\mathbf{v})_B \quad (2.1)$$

If necessary additional sub- and superscripts are utilized. Concretely, the subscript "k" indicates a kinematic entity and "a" an aerodynamic entity if not otherwise specified. For instance,  $(\mathbf{v}_a)_A$  denotes the aerodynamic velocity given in the A frame. In some cases it is instructive to further specify the affiliation of a vector. For instance,  $(\mathbf{v}_k^G)_A$  denotes the kinematic velocity of point G given in the A frame. Relative rotational velocities of reference frames are also indicated by superscripts. For instance,  $(\boldsymbol{\omega})_B^{OB}$  denotes the rotational velocity of the B frame relative to the O frame given in the B frame. A specific component of a vector in a given frame is specified according to the right hand side of Eq. (2.2):

$$(\mathbf{v}_k)_B = \begin{pmatrix} v_{k,x,B} \\ v_{k,y,B} \\ v_{k,z,B} \end{pmatrix} \quad (2.2)$$

In general, if three subscripts are used the first letter further specifies the scalar (here  $k$  indicates that the scalar is a kinematic quantity), the second letter defines one of the three components of the corresponding vector ( $x, y$  or  $z$ ), and the last letter indicates the frame in which the corresponding vector is given (here B frame). In case only two subscripts are used, the first letter specifies the component and the second letter the reference frame.

## 2.2. Reference Frames

In this thesis a variety of different coordinate frames is utilized to conveniently express vectors. To the largest extent the coordinate frames are equivalent to the conventional reference frames utilized in the flight mechanics literature. Besides the well known reference frames also AWE specific coordinate frames are required and linked to the conventional reference frames in the following. All utilized reference frames are introduced in this section and serve as a reference for the rest of the thesis. Note that all transformation matrices that are used in this work are listed in the appendix.

### The Wind Frame

For the flight path definition as well as the positioning of the aircraft a locally fixed reference frame is utilized and denoted as the  $W$  or Wind frame. Note, that this frame is not to be confused with the Wind frame that is sometimes used in the flight mechanics literature where it denotes a frame fixed at the aircraft and utilized to describe the orientation of the aircraft with respect to the relative airflow. Instead, in this work, the frame is fixed at the ground station. The  $x$  axis of the  $W$  frame points into the direction of the mean wind direction (denoted with  $\xi$ ), the  $z$  axis points upwards and the  $y$  axis forms a right hand reference frame with the  $x$  and  $z$  axis. The orientation of the  $W$  frame is defined by the wind direction which is defined relatively to the North direction. This allows to connect the  $W$  frame with the well-known North-East-Down (NED or  $O$ ) frame. Since the movement of the aircraft is spatially constraint to a few hundred meters around the ground station, the NED frame can be regarded as a fixed coordinate frame at the origin of the ground station as well (see Fig. 2.1).

### The Tangential Plane Frame

Since the aircraft flies during the traction phase on a sphere with time varying radius, the guidance problem can be solved conveniently using a spherical coordinate frame. In fact, using a "small Earth" analogy this spherical coordinate frame is similar to the  $O$  frame with respect to the Earth-centered-earth fixed frame. The spherical frame, called tangential plane frame, is denoted with  $\tau$  in this work. Its  $x$  axis points to the small Earth North direction (also called the zenith position), the  $z$ -axis points towards the origin of the  $W$  frame and the  $y$  axis completes the basis of the right-hand frame. The  $\tau$  frame moves together with the aircraft and hence its location is defined by the longitude and latitude angles,  $\lambda$  and  $\phi$  as well as the Euclidean distance of the aircraft with respect to the origin of the  $W$  frame. These definitions are visualized in Fig. 2.1.

### The Kinematic Frames

For the guidance problem definition and its solution it is instructive to define kinematic frames that can be used to express the kinematic velocity vector conveniently. In Fig. 2.1

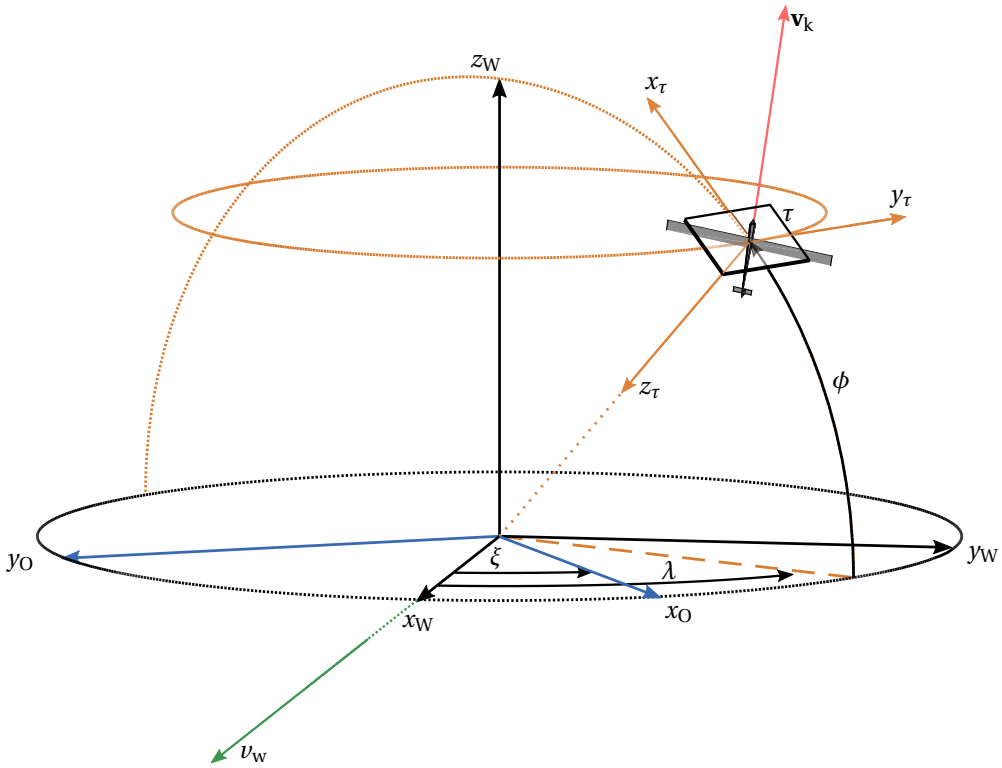


Figure 2.1: Visualization of the tangential plane frame  $\tau$ , the wind frame  $W$  and the NED/ $O$  frame. Note, the aircraft orientation is chosen arbitrarily and the vectors are scaled individually for visualization purposes. Furthermore, the  $z$  axis of the  $O$  frame, pointing into the ground, is not displayed.

the kinematic velocity is indicated with  $\mathbf{v}_k$ , its orientation and magnitude is chosen arbitrarily in the figure for illustration purposes. As already mentioned, during the traction phase the aircraft is steered with respect to the tangential plane  $\tau$ . In this case it is convenient to define a tangential plane course  $\chi_\tau$  and path angle  $\gamma_\tau$  similar to its conventional definition with respect to the  $O$  frame. Furthermore, this allows to decompose the kinematic velocity into a radial and a tangential component. On the other hand, during the retraction phase it is more convenient to use the conventional definitions of course  $\chi_k$  and path angle  $\gamma_k$  to define the desired flight direction. The relationship between these coordinate frames is visualized in Fig. 2.2. The tangential plane course angle  $\chi_\tau$  defines the orientation of the tangential component  $\mathbf{v}_{k,\tau}$  of the velocity with respect to the virtual (small Earth) north direction. The tangential plane path angle  $\gamma_\tau$  defines the radial component  $\mathbf{v}_{k,r}$ . For the guidance law an intermediate kinematic reference frame is required which is denoted with  $K^*$ . Intuitively, it is the equivalent to the rotated kinematic frame  $\bar{K}$ . The  $K^*$  frame is defined such that its  $x$  axis is aligned with the kinematic velocity vector, identical to the  $\bar{K}$  and  $K$  frame. However, the  $y$  axis lies in the tangential plane similar to the  $K$  frame who's  $y$  axis lies in the  $xy$  plane of the  $O$  frame. The kinematic frame  $K$  and the  $K^*$  frame are connected through a rotation around the kinematic velocity vector

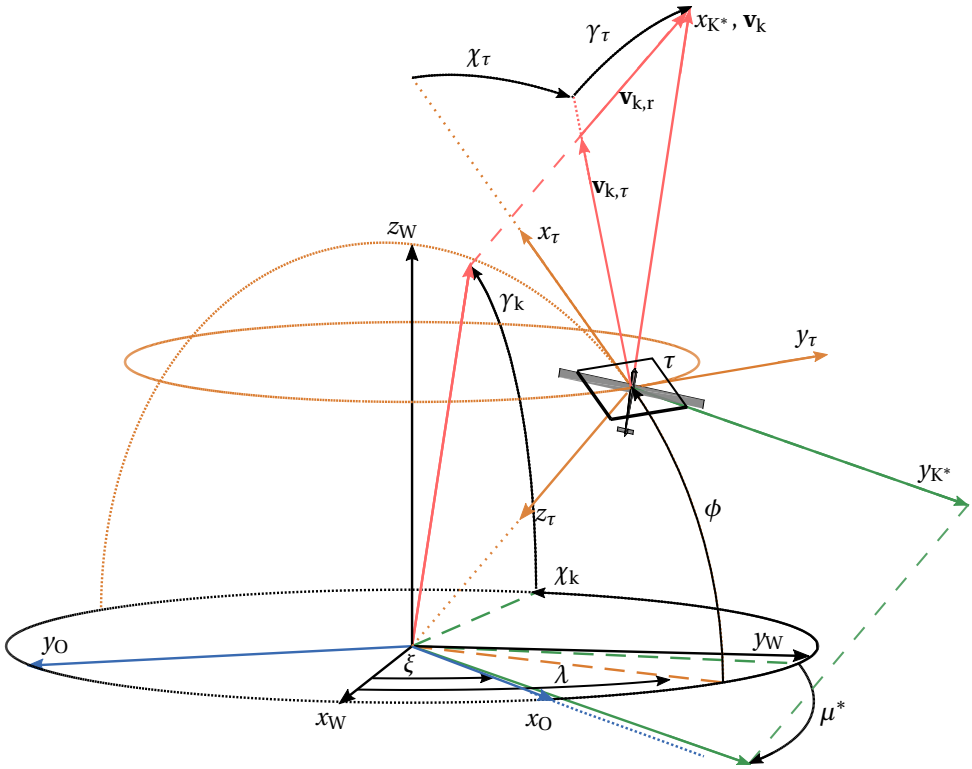


Figure 2.2: Visualization of the tangential plane frame, the wind frame, the  $O$  frame and the rotated kinematic frame  $K^*$ . Note, for visualization purposes the  $z$ -axis of the  $O$  and the  $K^*$  is not displayed.

by the angle  $\mu^*$ . In this sense the  $K^*$  frame is just another rotated kinematic reference frame but in contrast to the  $\bar{K}$  frame the rotational angle is always defined such that the  $y_{K^*}$  axis lies in the tangential plane.

### Reference Frames for Attitude Parameterizations

The orientation of the aircraft in this thesis is defined using Euler angles. In fact, two sets of Euler angles are used. On the one hand, the orientation can be given with respect to the  $O$  frame which yields the conventional attitude parameterization of an aircraft using roll angle  $\Phi$ , pitch angle  $\Theta$  and azimuth/yaw angle  $\Psi$  that define the required three rotations of the  $O$  frame to reach the body fixed frame  $B$ . On the other hand, the orientation can also be given with respect to the tangential plane. This leads to the definition of the tangential plane roll angle  $\Phi_\tau$ , tangential plane pitch angle  $\Theta_\tau$  as well as the tangential plane azimuth/yaw angle  $\Psi_\tau$ . The definitions of the conventional Euler angles are depicted in Fig. 2.3, the definitions of the tangential plane Euler angles are visualized in Fig. 2.4.

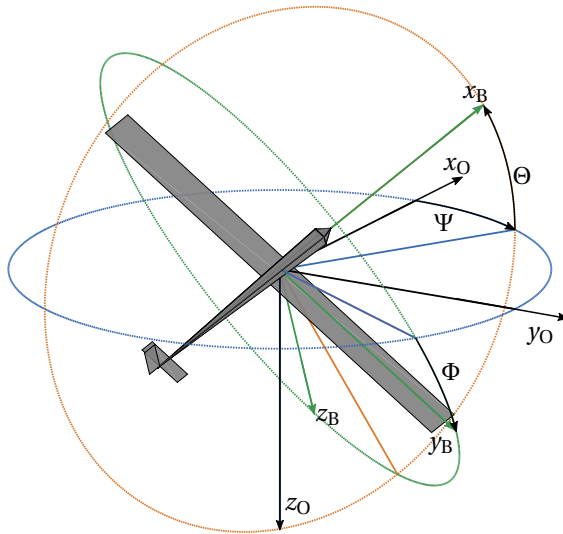


Figure 2.3: Body fixed frame with respect to the  $O$  frame. The chosen rotational order is first a rotation by  $\Psi$  then by  $\Theta$  and finally by  $\Phi$ .

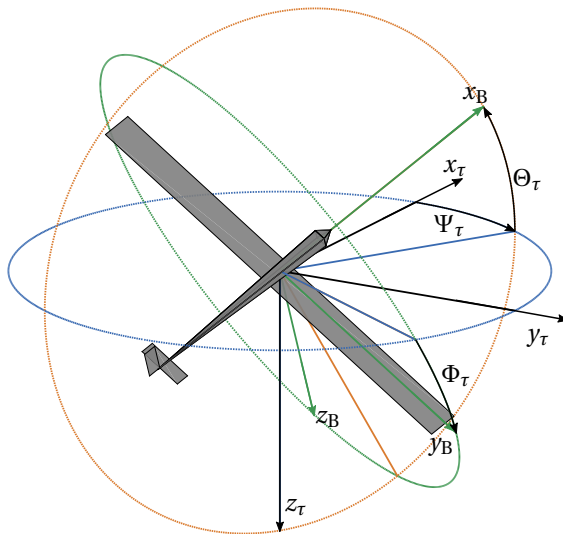


Figure 2.4: Body fixed frame with respect to the  $\tau$  frame. The chosen rotational order is first a rotation by  $\Psi_\tau$  then by  $\Theta_\tau$  and finally by  $\Phi_\tau$ .

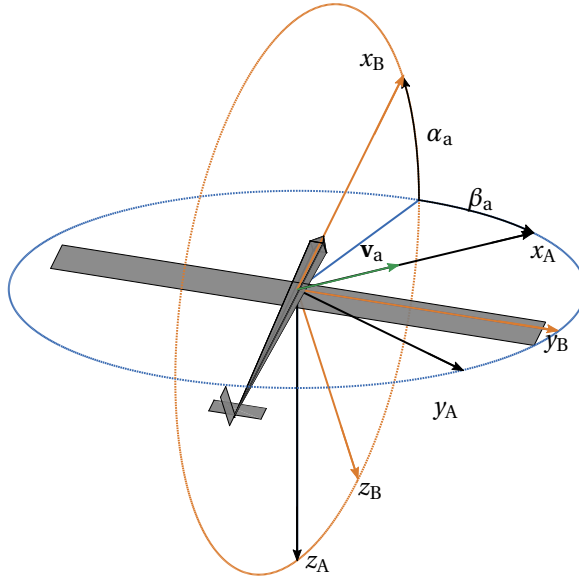


Figure 2.5: Body fixed frame with respect to the A frame. The chosen rotational order is first a rotation by  $-\beta_a$  then by  $\alpha_a$ .

### The Aerodynamic Frames

Naturally, wind plays an important role in this work. Therefore, in order to clearly distinguish between the kinematic velocity  $\mathbf{v}_k$  and the relative flow velocity  $\mathbf{v}_a$  (aerodynamic velocity) as well as their relative orientation with respect to the B frame, the aerodynamic frame A as well as the rotated aerodynamic frame  $\bar{A}$  is defined. Note, by convention, the rotated kinematic frame  $\bar{K}$  is analogously defined as the A frame and the kinematic frame K is defined analogously as the  $\bar{A}$  frame. The definition of the aerodynamics frame with respect to the B frame is depicted in Fig. 2.5 and contains the conventional definitions of angle of attack  $\alpha_a$  as well as sideslip angle  $\beta_a$ . The subscript a is used to distinguish the two angles from their kinematic counterparts shown in Fig. 2.6. With these definitions the kinematic and the aerodynamic velocity form the velocity triangle defined by

$$\mathbf{v}_k = \mathbf{v}_a + \mathbf{v}_w \quad (2.3)$$

where  $\mathbf{v}_w$  is the wind velocity. Note, since this relationship holds in general no specific coordinate frame in which the vectors are given is indicated. In case of neglected wind the aerodynamic frame and the kinematic frame coincide which allows to drop the a and k indices. This simplification is in general not made in this work if it is not indicated otherwise. Finally, the definitions of the aerodynamic course angle  $\chi_a$ , aerodynamic path angle  $\gamma_a$  as well as the aerodynamic bank angle  $\mu_a$  are depicted in Fig. 2.7. They connect the A frame with the O frame.

As a summary all transformation paths between the individual frames are depicted in Fig. 2.9. The required transformation matrices are listed in the appendix of this thesis (see A).

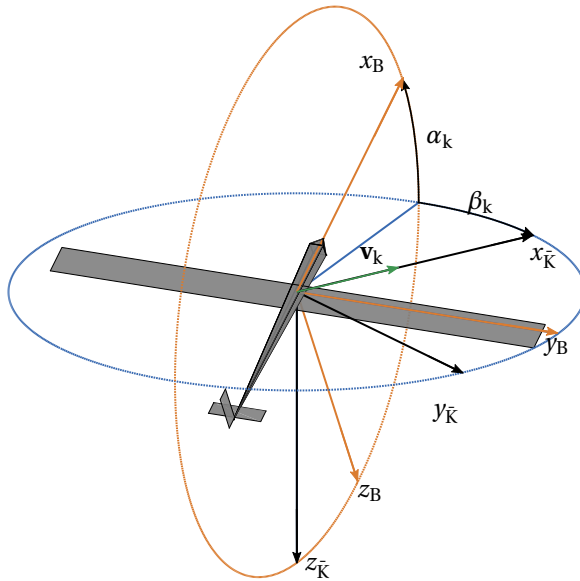


Figure 2.6: Body fixed frame with respect to the rotated kinematic frame. The chosen rotational order is first a rotation by  $-\beta_k$  then by  $\alpha_k$ .

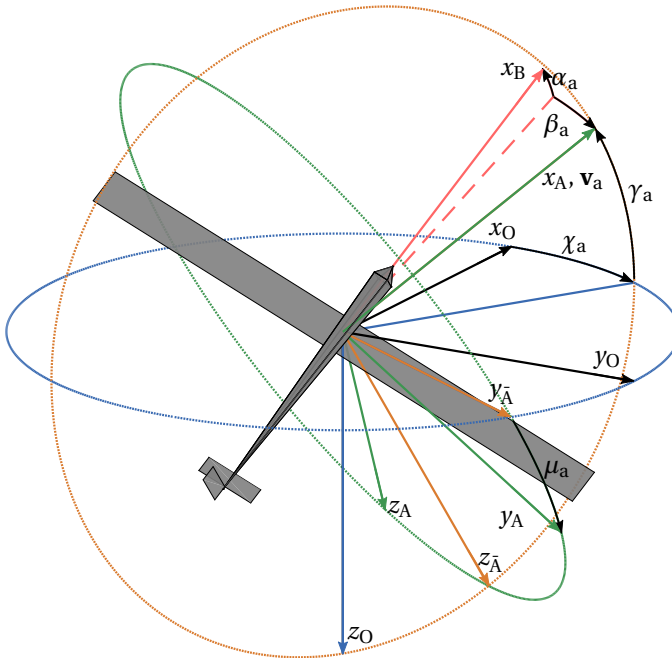


Figure 2.7: Rotated aerodynamic frame with respect to the O frame. The chosen rotational order is first a rotation by  $\chi_a$ ,  $\gamma_a$  then by  $\mu_a$ . The rotated aerodynamic frame is indicated by the  $\bar{A}$  indices, the  $x_{\bar{A}}$  axis coincides with the  $x_A$  axis. In addition, the angle of attack and sideslip angle are included.

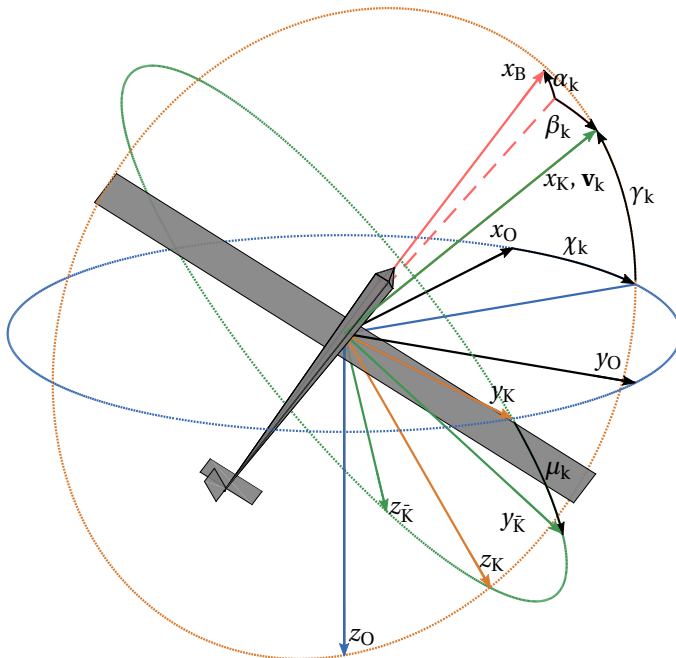


Figure 2.8: Rotated kinematic frame with respect to the O frame. The chosen rotational order is first a rotation by  $\lambda_k, \gamma_k$  then by  $\mu_k$ . The rotated kinematic frame is indicated by the  $\bar{K}$  indices, the  $x_{\bar{K}}$  axis coincides with the  $x_K$  axis. In addition, the kinematic angle of attack and kinematic sideslip angle are included.

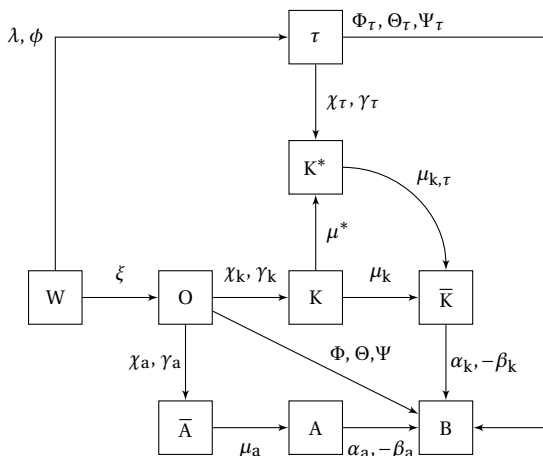


Figure 2.9: Relationships between the different utilized reference frames in this work. The corresponding transformation matrices are listed in the appendix.

## 2.3. Simulation Models

### 2.3.1. Aircraft Model

The aircraft utilized in this work is modeled as a generic rigid body with six degrees of freedom (6-DoF). Its geometric and aerodynamic properties are based on the values in [96] and [111], hence the aircraft model approximates the AP2 system of Ampyx Power [5].

#### Aircraft Translational Dynamics

The translational dynamics in the body-fixed reference frame, as for instance derived in [145], are given by

$$(\dot{\mathbf{v}}_k^G)_B = -(\boldsymbol{\omega})_B^{OB} \times (\mathbf{v}_k^G)_B + \frac{(\mathbf{F}_{tot})_B}{m_a} \quad (2.4)$$

with

$$(\mathbf{F}_{tot})_B = (\mathbf{F}_a)_B + (\mathbf{F}_g)_B + (\mathbf{F}_t)_B \quad (2.5)$$

where  $(\dot{\mathbf{v}}_k^G)_B$ ,  $(\mathbf{v}_k^G)_B$ ,  $(\boldsymbol{\omega})_B^{OB}$  and  $m_a$  represent the kinematic acceleration, the kinematic velocity, the rotational rate of the aircraft with respect to the NED reference frame and the total mass of the aircraft, respectively. Note, for notational convenience the superscript "G" is mostly neglected in the remainder of this work unless it is required to clearly distinguish it with a velocity given at a different point than the center of gravity (CG) of the aircraft. The total force acting in the CG of the aircraft consists of the resulting aerodynamic force  $(\mathbf{F}_a)_B$ , the weight  $(\mathbf{F}_g)_B$  and the tether force  $(\mathbf{F}_t)_B$ . More specifically, the gravitational force is defined by

$$(\mathbf{F}_g)_B = \mathbf{M}_{BO} \begin{pmatrix} 0 \\ 0 \\ m_a g \end{pmatrix}_O \quad (2.6)$$

where  $g$  is the gravitational constant. The tether force is defined in the subsequent section. The aerodynamic force of the aircraft is implemented as defined in [96] and [111]:

$$(\mathbf{F}_a)_B = \frac{1}{2} \rho S_{ref} v_a^2 \begin{pmatrix} C_x \\ C_y \\ C_z \end{pmatrix} \quad (2.7)$$

with

$$\begin{pmatrix} C_x \\ C_y \\ C_z \end{pmatrix} = \begin{pmatrix} C_{x,0}(\alpha_a) + C_{x,q}(\alpha_a) \frac{\dot{c}q}{2v_a} + C_{x,\delta_e}(\alpha_a) \delta_e \\ C_{y,\beta}(\alpha_a) \beta + C_{y,p}(\alpha_a) \frac{b \cdot p}{2v_a} + C_{y,r}(\alpha_a) \frac{b \cdot r}{2v_a} + C_{y,\delta_a}(\alpha_a) \delta_a + C_{y,\delta_r}(\alpha_a) \delta_r \\ C_{z,0}(\alpha_a) + C_{z,q}(\alpha_a) \frac{\dot{c}q}{2v_a} + C_{z,\delta_e}(\alpha_a) \delta_e \end{pmatrix} \quad (2.8)$$

where all  $\alpha_a$  dependent coefficients are second order polynomials. For instance:

$$C_{x,0}(\alpha_a) = C_{x,0,0} + C_{x,0,\alpha} \alpha_a + C_{x,0,\alpha^2} \alpha_a^2 \quad (2.9)$$

Note, if the tether is implemented using a straight tether approximation without dynamics the drag contribution of the tether needs to be added to the aerodynamic force. The tether drag approximation is derived in the next section.

### Alternative Formulations of the Point-mass Dynamics

For the derivation of the guidance law in the next chapter the translational dynamics in the kinematic frame (K) or the rotated aerodynamic frame ( $\bar{A}$ ) are required. Since both represent another way to represent the point-mass dynamics they are also introduced in this section. Note, they can also be used to simulate the three degree of freedom (3-DoF) dynamics of the tethered aircraft. The translational dynamics in the kinematic frame are derived for instance in [19, p. 210-212] where the additional contribution of the tether (tension and drag) needs to be added to the total force vector. This leads to:

$$\begin{pmatrix} \dot{v}_k \\ \dot{\chi}_k \\ \dot{\gamma}_k \end{pmatrix}_K = \frac{1}{m_a} \begin{pmatrix} 1 & 0 & 0 \\ 0 & \frac{1}{v_k \cos \gamma_k} & 0 \\ 0 & 0 & -\frac{1}{v_k} \end{pmatrix} (\mathbf{M}_{KO}(\chi_k, \gamma_k) ((\mathbf{F}_g)_O + (\mathbf{F}_t)_O) + \mathbf{M}_{K\bar{K}}(\mu_k) (\mathbf{F}_a)_{\bar{K}}) \quad (2.10)$$

where  $(\mathbf{F}_a)_{\bar{K}}$  is the resultant aerodynamic force (including tether drag) in the rotated kinematic frame. Note, if the kinematic equations are invoked it is commonly assumed that  $\bar{K} \approx A$ , which essentially assumes that the wind velocity is negligible with respect to the kinematic velocity (this also implies  $\alpha_k \approx \alpha_a$ ). In this case

$$(\mathbf{F}_a)_{\bar{K}} = (\mathbf{F}_a)_A = \mathbf{M}_{AB} (\mathbf{F}_a)_B = \begin{pmatrix} -D \\ Y \\ -L \end{pmatrix} \quad (2.11)$$

where  $D$ ,  $Y$  and  $L$  denote the aerodynamic drag, side and lift force. For the point-mass simulations  $\mu_k$  and  $\alpha_k$  are then the (pseudo-) inputs that allow to control the motion of the aircraft.

Since the derivation of the translational dynamics using  $v_a$ ,  $\chi_a$  and  $\gamma_a$ , where the assumption that the wind velocity is negligible compared to the kinematic velocity is dropped, has not been found in the literature it is derived in the following. In the O frame the kinematic velocity can be written as:

$$(\mathbf{v}_k)_O = (\mathbf{v}_a)_O + (\mathbf{v}_w)_O \quad (2.12)$$

The aerodynamic velocity can be expressed more conveniently in the  $\bar{A}$  frame which yields

$$(\mathbf{v}_k)_O = \mathbf{M}_{O\bar{A}} \begin{pmatrix} v_a \\ 0 \\ 0 \end{pmatrix}_{\bar{A}} + (\mathbf{v}_w)_O \quad (2.13)$$

The time derivative with respect to the O frame (here assumed to be inertial) yields

$$\left( \frac{d}{dt} \right)^O (\mathbf{v}_k)_O = \dot{\mathbf{M}}_{O\bar{A}} \begin{pmatrix} v_a \\ 0 \\ 0 \end{pmatrix}_{\bar{A}} + \mathbf{M}_{O\bar{A}} \begin{pmatrix} \dot{v}_a \\ 0 \\ 0 \end{pmatrix}_{\bar{A}} + \left( \frac{d}{dt} \right)^O (\mathbf{v}_w)_O \quad (2.14)$$

Invoking Newton's second law and transforming the equation into the  $\bar{A}$  frame yields

$$\begin{aligned}
 \frac{(\mathbf{F}_{\text{tot}})_{\bar{A}}}{m_a} &= \mathbf{M}_{\bar{A}O} \dot{\mathbf{M}}_{O\bar{A}} \begin{pmatrix} v_a \\ 0 \\ 0 \end{pmatrix}_{\bar{A}} + \begin{pmatrix} \dot{v}_a \\ 0 \\ 0 \end{pmatrix}_{\bar{A}} + \mathbf{M}_{\bar{A}O} \left( \frac{d}{dt} \right)^O (\mathbf{v}_w)_O \\
 &= (\boldsymbol{\omega})_{\bar{A}}^{O\bar{A}} \times \begin{pmatrix} v_a \\ 0 \\ 0 \end{pmatrix}_{\bar{A}} + \begin{pmatrix} \dot{v}_a \\ 0 \\ 0 \end{pmatrix}_{\bar{A}} + \mathbf{M}_{\bar{A}O} \left( \frac{d}{dt} \right)^O (\mathbf{v}_w)_O \\
 &= \begin{pmatrix} \dot{v}_a \\ \dot{\chi}_a \cos \gamma_a v_a \\ -\dot{\gamma}_a v_a \end{pmatrix}_{\bar{A}} + \mathbf{M}_{\bar{A}O} \left( \frac{d}{dt} \right)^O (\mathbf{v}_w)_O
 \end{aligned} \tag{2.15}$$

This equation fully describes the point-mass dynamics in a non-stationary and spatially varying wind field in the  $\bar{A}$  frame. The equation can be further simplified if certain assumptions about the wind field are made. Note that the total derivative of the wind velocity can be split into (see also [19, p. 181])

$$\left( \frac{d}{dt} \right)^O (\mathbf{v}_w)_O = \frac{\partial (\mathbf{v}_w)_O}{\partial t} + (\nabla (\mathbf{v}_w)_O)^\top (\mathbf{v}_w)_O \tag{2.16}$$

where the Jacobi matrix  $\nabla (\mathbf{v}_w)_O$  contains the spatial derivatives of the wind velocity in the O frame. Note, if the wind field is assumed to be stationary and not changing spatially the 3-DoF equations of motion simplify and yield a similar form compared to the purely kinematic description of the point-mass dynamics. Expanding the total force vector and solving for the derivatives yields:

$$\begin{pmatrix} \dot{v}_a \\ \dot{\chi}_a \\ \dot{\gamma}_a \end{pmatrix}_{\bar{A}} = \frac{1}{m_a} \begin{pmatrix} 1 & 0 & 0 \\ 0 & \frac{1}{v_a \cos \gamma_a} & 0 \\ 0 & 0 & -\frac{1}{v_a} \end{pmatrix} (\mathbf{M}_{\bar{A}O} (\chi_a, \gamma_a) ((\mathbf{F}_g)_O + (\mathbf{F}_t)_O) + \mathbf{M}_{\bar{A}A} (\mu_a) (\mathbf{F}_a)_A) \tag{2.17}$$

Note, this form of the 3-DoF dynamics is later on also used to derive the path following controller for the retraction phase where, due to the potentially low kinematic speed, the aerodynamic and kinematic entities are distinguishable especially in high wind speed conditions. The input variables to control the 3-DoF dynamics are in this case the aerodynamic bank angle  $\mu_a$  as well as the angle of attack  $\alpha_a$ .

### Aircraft Rotational Dynamics

The rotational dynamics given in the body-fixed frame are derived for instance in [145] and are defined by

$$(\dot{\boldsymbol{\omega}})_B^{OB} = -\mathbf{J}^{-1} ((\boldsymbol{\omega})_B^{OB} \times \mathbf{J} (\boldsymbol{\omega})_B^{OB} - (\mathbf{M}_{\text{tot}})_B) \tag{2.18}$$

where  $(\dot{\boldsymbol{\omega}})_B^{OB}$  and  $\mathbf{J}$  denote the rotational acceleration and the inertia tensor. The resultant moment is defined by

$$(\mathbf{M}_{\text{tot}})_B = (\mathbf{M}_a)_B + (\mathbf{r}^{\text{GT}})_B \times (\mathbf{F}_t)_B \tag{2.19}$$

where  $(\mathbf{M}_a)_B$  is the resulting aerodynamic moment acting in the center of mass and  $(\mathbf{r}^{\text{GT}})_B \times (\mathbf{F}_t)_B$  is the potential contribution of the tether force to the moment equation

if the tether attachment point (T) is not located in the CG of the aircraft. The aerodynamic moment is implemented as defined in [96] and [111]:

$$(\mathbf{M}_a)_B = \frac{1}{2} \rho S_{\text{ref}} v_a^2 \begin{pmatrix} b \cdot C_l \\ \bar{c} \cdot C_m \\ b \cdot C_n \end{pmatrix} \quad (2.20)$$

where  $\bar{c}$  is the mean wing chord length and  $b$  is the wing span. The roll-, pitch- and yaw moment coefficients are implemented according to:

$$\begin{pmatrix} C_l \\ C_m \\ C_n \end{pmatrix} = \begin{pmatrix} C_{l,\beta}(\alpha_a) \beta_a + C_{l,p}(\alpha_a) \frac{b \cdot p}{2v_a} + C_{l,r}(\alpha_a) \frac{b \cdot r}{2v_a} + C_{l,\delta_a}(\alpha_a) \delta_a + C_{l,\delta_r}(\alpha_a) \delta_r \\ C_{m,0}(\alpha_a) + C_{m,q}(\alpha_a) \frac{\bar{c} \cdot q}{2v_a} + C_{m,\delta_e}(\alpha_a) \delta_e \\ C_{n,\beta}(\alpha_a) \beta_a + C_{n,p}(\alpha_a) \frac{b \cdot p}{2v_a} + C_{n,r}(\alpha_a) \frac{b \cdot r}{2v_a} + C_{n,\delta_a}(\alpha_a) \delta_a + C_{n,\delta_r}(\alpha_a) \delta_r \end{pmatrix} \quad (2.21)$$

where all  $\alpha_a$  dependent coefficients are again second order polynomials. The roll-, pitch- and yaw rate are defined by  $p, q$  and  $r$ .  $\delta_a, \delta_e$  and  $\delta_r$  represent the aileron, elevator and rudder deflections.

### Attitude Parameterization

The attitude for the simulation model is parameterized using conventional Euler angles  $\Phi, \Theta$  and  $\Psi$  that define the orientation of the B frame with respect to the O frame (see Fig. 2.3). The attitude propagation equation is then given by:

$$\begin{pmatrix} \dot{\Phi} \\ \dot{\Theta} \\ \dot{\Psi} \end{pmatrix} = \begin{pmatrix} 1 & \sin \Psi \tan \Theta & \cos \Phi \tan \Theta \\ 0 & \cos \Phi & -\sin \Phi \\ 0 & \frac{\sin \Phi}{\cos \Theta} & \frac{\cos \Phi}{\cos \Theta} \end{pmatrix} (\boldsymbol{\omega})_B^{\text{OB}} \quad (2.22)$$

Note, a second attitude parameterization with respect to the tangential plane frame is derived in the next chapter which is used to derive the linear models for the traction phase controller synthesis.

### Aircraft Position Propagation

The position of the aircraft is given in the W frame using the (small Earth) longitude  $\lambda$  and latitude  $\phi$  angles as well as the radial distance  $h_\tau$ , which is defined as the Euclidean distance between the CG of the aircraft and the ground station (origin of the W frame). Therefore, the position is propagated according to:

$$\begin{aligned} \dot{\lambda} &= \frac{v_{k,y,\tau}}{\cos \phi h_\tau} \\ \dot{\phi} &= \frac{v_{k,x,\tau}}{h_\tau} \\ \dot{h}_\tau &= -v_{k,z,\tau} \end{aligned} \quad (2.23)$$

$v_{k,x,\tau}$  and  $v_{k,y,\tau}$  are the first two components of the kinematic velocity in the  $\tau$  reference frame which are calculated using the integrated accelerations in Eq. (2.4) transformed into the  $\tau$  frame.

$$(\mathbf{v}_k)_\tau = \mathbf{M}_{\tau B} (\mathbf{v}_k)_B \quad (2.24)$$

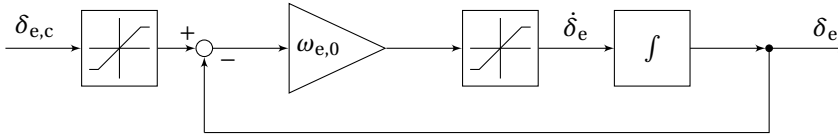


Figure 2.10: First order reference filters are used to model the actuator dynamics (here elevator). Saturation blocks ensure that the actuator rates and the deflections do not exceed the specified limits.

Table 2.1: First order actuator model parameters.

Parameters	Values	Units
Bandwidth aileron $\omega_{a,0}$	35	$\text{rad s}^{-1}$
Aileron deflection limit $\delta_{a,\text{lim}}$	$\pm 20$	$^\circ$
Aileron rate limit $\dot{\delta}_{a,\text{lim}}$	$\pm 115$	$^\circ \text{s}^{-1}$
Bandwidth elevator $\omega_{e,0}$	35	$\text{rad s}^{-1}$
Elevator deflection limit $\delta_{e,\text{lim}}$	$\pm 20$	$^\circ$
Elevator rate limit $\dot{\delta}_{e,\text{lim}}$	$\pm 115$	$^\circ \text{s}^{-1}$
Bandwidth rudder $\omega_{r,0}$	35	$\text{rad s}^{-1}$
Rudder deflection limit $\delta_{r,\text{lim}}$	$\pm 30$	$^\circ$
Rudder rate limit $\dot{\delta}_{r,\text{lim}}$	$\pm 115$	$^\circ \text{s}^{-1}$

### Actuator Models

The actuator dynamics for ailerons, elevator and rudder are approximated as first order filters including bandwidth, rate and deflection limits. Exemplary, the elevator actuator model including the limiters for the deflections as well as the rates is depicted Fig. 2.10. The utilized values for all three actuator models are summarized in Table 2.1.

### 2.3.2. Ground Station, Tether and Wind Field Models

In this section the mathematical models for the ground station, the tether and the wind field are presented.

#### Ground Station Model

The ground station is modeled as in [119] and given by a simple scalar first order system:

$$\dot{\omega}_W = J_W^{-1} (-\kappa_W \omega_W + M_{W,c} + r_W F_t) \quad (2.25)$$

where  $J_W$  is the winch inertia,  $\kappa_W$  is the friction coefficient,  $r_W$  is the winch radius,  $F_t$  is the absolute value of the tether force at the winch,  $M_{W,c}$  is the commanded mechanical torque and  $\omega_W$  is the rotational speed of the winch. Note, the electrical drive system is not modeled in this work explicitly. Instead, a time delay is used to delay the requested torque from the controller and the point in time where it is applied to the winch. The utilized winch parameter values are summarized in Table 2.2.

### Tether Model

For the simulations the discretized tether model of [49] is implemented and the utilized tether parameters are displayed in Table 2.3. Since the equations of motion of the tether are derived in detail in [49] they will not be repeated here. This tether model accounts for aerodynamic drag, mass as well as elasticity.

Besides the discretized tether model also a simpler model is used in this work for different purposes. On the one hand, for the calculation of quasi-stationary operating points and the generation of linear state space models. On the other hand, the tether is simplified for simulations where it is desired to remove the additional complexity coming from the tether dynamics and the winch control system for instance in order to verify the flight control system alone (e.g. in the first sub-step of Step 2 as shown in Fig. 1.8). In this case a perfect tether tension tracking control system is assumed which allows to include the tether force as an additional external input. In addition, it is assumed that the tether is straight and hence the force points to the ground station. Besides the tensile force also tether drag is included. Note, if the discretized tether model is implemented the tether drag is explicitly included for each particle. For the straight tether model it is assumed that the tether drag force points into the opposite direction of the perpendicular part of the incoming relative airflow with respect to the tether. Mathematically, this corresponds to the aerodynamic velocity projected into the tangential plane. Integrating the drag moment increments along the tether and setting the integral equal to the equivalent tether drag moment at the aircraft (see [8]) results in the following expression for the tether drag in the tangential plane frame:

$$(\mathbf{F}_{t,d})_{\tau} = -\frac{1}{8}\rho C_{d,t}d_t l_t \sqrt{v_{a,x,\tau}^2 + v_{a,y,\tau}^2} \begin{pmatrix} v_{a,x,\tau} \\ v_{a,y,\tau} \\ 0 \end{pmatrix}_{\tau} \quad (2.26)$$

The aerodynamic speed in the  $\tau$  frame is obtained through the following coordinate transformation:

$$\begin{pmatrix} v_{a,x,\tau} \\ v_{a,y,\tau} \\ v_{a,z,\tau} \end{pmatrix}_{\tau} = \mathbf{M}_{\tau B} \mathbf{M}_{BA} \begin{pmatrix} v_a \\ 0 \\ 0 \end{pmatrix}_A = \mathbf{M}_{\tau W} \mathbf{M}_{WO} \mathbf{M}_{OB} \mathbf{M}_{BA} \begin{pmatrix} v_a \\ 0 \\ 0 \end{pmatrix}_A \quad (2.27)$$

where  $v_a$  is the airspeed of the aircraft. In the A frame the tether drag is given by:

$$(\mathbf{F}_{t,d})_A = \mathbf{M}_{AB} \mathbf{M}_{B\tau} (\mathbf{F}_{t,d})_{\tau} \quad (2.28)$$

Table 2.2: Ground station parameters.

Parameters	Values	Units
Inertia $J_W$	0.08	kgm <sup>2</sup>
Radius $r_W$	0.1	m
Viscous friction $\kappa_W$	0.6	kgms <sup>-1</sup>
Acceleration limits $a_{W,\min/\max}$	±5	ms <sup>-2</sup>
Maximum speed $v_{W,\max}$	20	ms <sup>-1</sup>
Minimum speed $v_{W,\min}$	-15	ms <sup>-1</sup>

Table 2.3: Tether parameters.

Parameters	Values	Units
Particles $n_T$	5	-
Mass Density $\rho_T$	0.0046	$\text{kg m}^{-3}$
Diameter $d_T$	0.0025	m
Drag coefficient $C_{d,T}$	1.2	-
Stiffness $c_T$	10243	$\text{Nm}^{-1}$
Damping $d_T$	7.8833	$\text{Ns m}^{-1}$

which can then be added to the aircraft aerodynamic force ( $\mathbf{F}_a$ )<sub>A</sub>.

### Wind Model

Wind conditions are simulated using the wind speed profile and the discrete Dryden turbulence model provided by the Matlab Aerospace Toolbox [1]. The utilized wind shear profile in the present work as a function of altitude is given by

$$v_w = v_{w,\text{ref}} \frac{\ln\left(\frac{h}{z_0}\right)}{\ln\left(\frac{20}{z_0}\right)} \quad (2.29)$$

where  $h$  is the altitude of the aircraft (here in feet),  $v_{w,\text{ref}}$  is the reference speed at approximately 6 m (20 feet) altitude and  $z_0$  is a constant set to 0.15 feet according to [1]. Example wind speed profiles for three different reference wind speeds (without turbulence) are depicted in Fig. 2.11. The control designs in this work are usually assessed for the two "extreme" wind conditions defined with  $v_{w,\text{ref}} = 4 \text{ m s}^{-1}$  and  $v_{w,\text{ref}} = 9 \text{ m s}^{-1}$ . These values are used to demonstrate that the controller is working in low as well as high wind speed conditions.

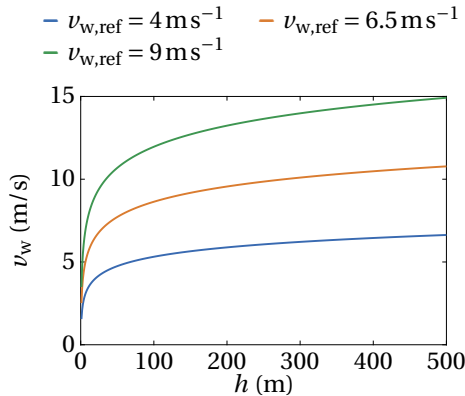


Figure 2.11: Wind speed profiles as a function of altitude with different reference wind speeds at 6m.

For the turbulence scale lengths in low- (below 305 m), medium-, and high-altitudes (above 610 m) the MIL-F-8785C (see [55]) specification values are used. The formulas

can also be found in the documentation of [1]. Similarly, the turbulence intensities as stated in [1] are used.

## 2.4. Summary

This chapter lays the foundation on which the subsequent chapters are built upon. The utilized mathematical notation as well as the necessary coordinate reference frames, which are used throughout this thesis, are introduced. The relation between the coordinate frames is graphically depicted. Notice that all required coordinate transformation matrices are listed in the appendix. Furthermore, all mathematical models are presented that are either used for simulation or control design purposes in this work.

# 3

## Linearization and Flight Dynamic Analysis

In this chapter the necessary equations and conditions to determine (quasi-) stationary operating points during a pumping cycle using the nonlinear equations of motion introduced in chapter 2 are presented. This is done separately for the traction and the retraction phase due to slightly different attitude parameterizations. The determined operating points are then used, on the one hand, to characterize the operational envelope of the system and, on the other hand, to derive linear state space models that are later on used to derive linear state feedback controllers. To simplify the controller synthesis it is investigated if it is justified to decouple the longitudinal and lateral motion during figure of eight flight as well as during the retraction phase. Additionally, the characteristic eigenmodes at one particular operating point during the traction and retraction phase are investigated and qualitatively compared to the characteristic eigenmodes of untethered aircraft.

### 3.1. Traction Phase

#### 3.1.1. Model Equations for Trimming and Linearizing

For the open loop analysis the aircraft model can be linearized at any point on the figure of eight reference flight path. Before the model can be linearized the "trim" states and inputs need to be calculated. The trim values are determined such that translational and rotational accelerations are zero. For the rotational dynamics the rigid body equations of motion as stated in chapter 2 are utilized. For the translational equations of motion a slightly different representation compared to chapter 2 is chosen such that the derivatives of angle of attack  $\alpha_a$ , airspeed  $v_a$  and sideslip angle  $\beta_a$  can be forced to be zero. Since usually in the flight mechanics literature the differential equations for true airspeed, angle of attack and sideslip angle are derived without wind, a derivation with wind is presented subsequently. This is required since it is desired to investigate how the wind conditions in this application impact the quasi-stationary operating points.

The kinematic acceleration given in the body-fixed reference frame can be expressed as

$$(\dot{\mathbf{v}}_k)_B^O = (\dot{\mathbf{v}}_k)_B^B + (\boldsymbol{\omega})_B^{OB} \times (\mathbf{v}_k)_B = \frac{(\mathbf{F}_{\text{tot}})_B}{m_a} \quad (3.1)$$

Since the derivative is taken with respect to the (assumed) inertial frame O, Newton's second law can be invoked. The acceleration  $(\dot{\mathbf{v}}_k)_B^B$  can be expressed as

$$\begin{aligned} (\dot{\mathbf{v}}_k)_B^B &= (\dot{\mathbf{v}}_a)_B^B + (\dot{\mathbf{v}}_w)_B^B \\ &= (\dot{\mathbf{v}}_a)_B^B + \mathbf{M}_{BO} (\dot{\mathbf{v}}_w)_O^B \end{aligned} \quad (3.2)$$

The derivative of the wind vector can be written as

$$(\dot{\mathbf{v}}_w)_O^B = (\dot{\mathbf{v}}_w)_O^O + (\boldsymbol{\omega})_O^{BO} \times (\mathbf{v}_w)_O \quad (3.3)$$

Substituting back in Eq. (3.1) yields

$$(\dot{\mathbf{v}}_k)_B^B = (\dot{\mathbf{v}}_a)_B^B + \mathbf{M}_{BO} ((\dot{\mathbf{v}}_w)_O^O + (\boldsymbol{\omega})_O^{BO} \times (\mathbf{v}_w)_O) + (\boldsymbol{\omega})_B^{OB} \times (\mathbf{v}_k)_B = \frac{(\mathbf{F}_{\text{tot}})_B}{m_a} \quad (3.4)$$

Transforming Eq. (3.4) into the aerodynamic frame yields

$$(\dot{\mathbf{v}}_a)_A^B + \mathbf{M}_{AB} (\mathbf{M}_{BO} ((\dot{\mathbf{v}}_w)_O^O + (\boldsymbol{\omega})_O^{BO} \times (\mathbf{v}_w)_O) + (\boldsymbol{\omega})_B^{OB} \times (\mathbf{v}_k)_B) = \frac{(\mathbf{F}_{\text{tot}})_A}{m_a} \quad (3.5)$$

With the identity

$$(\boldsymbol{\omega})_O^{BO} \times (\mathbf{v}_w)_O = -(\boldsymbol{\omega})_O^{OB} \times (\mathbf{v}_w)_O \quad (3.6)$$

this leads to

$$\begin{aligned} (\dot{\mathbf{v}}_a)_A^B + \mathbf{M}_{AB} (\mathbf{M}_{BO} ((\dot{\mathbf{v}}_w)_O^O - (\boldsymbol{\omega})_O^{OB} \times (\mathbf{v}_w)_O) + (\boldsymbol{\omega})_B^{OB} \times (\mathbf{v}_k)_B) &= \frac{(\mathbf{F}_{\text{tot}})_A}{m_a} \\ (\dot{\mathbf{v}}_a)_A^B + \mathbf{M}_{AB} (\mathbf{M}_{BO} (\dot{\mathbf{v}}_w)_O^O - (\boldsymbol{\omega})_B^{OB} \times (\mathbf{v}_w)_B + (\boldsymbol{\omega})_B^{OB} \times (\mathbf{v}_k)_B) &= \frac{(\mathbf{F}_{\text{tot}})_A}{m_a} \\ (\dot{\mathbf{v}}_a)_A^B + \mathbf{M}_{AB} (\mathbf{M}_{BO} (\dot{\mathbf{v}}_w)_O^O - (\boldsymbol{\omega})_B^{OB} \times (\mathbf{v}_w)_B + (\boldsymbol{\omega})_B^{OB} \times ((\mathbf{v}_a)_B + (\mathbf{v}_w)_B)) &= \frac{(\mathbf{F}_{\text{tot}})_A}{m_a} \\ (\dot{\mathbf{v}}_a)_A^B + \mathbf{M}_{AB} (\mathbf{M}_{BO} (\dot{\mathbf{v}}_w)_O^O + (\boldsymbol{\omega})_B^{OB} \times (\mathbf{v}_a)_B) &= \frac{(\mathbf{F}_{\text{tot}})_A}{m_a} \\ (\dot{\mathbf{v}}_a)_A^B + \mathbf{M}_{AB} \mathbf{M}_{BO} (\dot{\mathbf{v}}_w)_O^O + (\boldsymbol{\omega})_A^{OB} \times (\mathbf{v}_a)_A &= \frac{(\mathbf{F}_{\text{tot}})_A}{m_a} \end{aligned} \quad (3.7)$$

The first acceleration term can be expressed as

$$\begin{aligned} (\dot{\mathbf{v}}_a)_A^B &= (\dot{\mathbf{v}}_a)_A^A + (\boldsymbol{\omega})_A^{BA} \times (\mathbf{v}_a)_A^A \\ &= \begin{pmatrix} \dot{v}_a \\ 0 \\ 0 \end{pmatrix}_A + \begin{pmatrix} -\dot{\alpha}_a \sin \beta_a \\ -\dot{\alpha}_a \cos \beta_a \\ \dot{\beta}_a \end{pmatrix}_A \times \begin{pmatrix} v_a \\ 0 \\ 0 \end{pmatrix}_A \end{aligned} \quad (3.8)$$

Substituting Eq. (3.8) in Eq. (3.7) yields

$$\begin{pmatrix} \dot{v}_a \\ v_a \dot{\beta}_a \\ v_a \cos \beta_a \dot{\alpha}_a \end{pmatrix}_A + \mathbf{M}_{AB} \mathbf{M}_{BO} (\dot{\mathbf{v}}_w)_O^O + (\boldsymbol{\omega})_A^{OB} \times (\mathbf{v}_a)_A = \frac{(\mathbf{F}_{tot})_A}{m_a} \quad (3.9)$$

Solving for the derivatives leads to the desired differential equations:

$$\begin{pmatrix} \dot{v}_a \\ \dot{\beta}_a \\ \dot{\alpha}_a \end{pmatrix}_A = \begin{pmatrix} 1 & 0 & 0 \\ 0 & \frac{1}{v_a} & 0 \\ 0 & 0 & \frac{1}{\cos \beta_a v_a} \end{pmatrix} \left( -\mathbf{M}_{AB} \mathbf{M}_{BO} (\dot{\mathbf{v}}_w)_O^O - (\boldsymbol{\omega})_A^{OB} \times (\mathbf{v}_a)_A + \frac{(\mathbf{F}_{tot})_A}{m_a} \right) \quad (3.10)$$

where the derivative of the wind velocity can be calculated using Eq. (2.16). Note, for the trim analysis the wind field is assumed to be stationary and homogeneous, hence  $(\dot{\mathbf{v}}_w)_O = 0$ . Hence,

$$\begin{pmatrix} \dot{v}_a \\ \dot{\beta}_a \\ \dot{\alpha}_a \end{pmatrix}_A = \begin{pmatrix} 1 & 0 & 0 \\ 0 & \frac{1}{v_a} & 0 \\ 0 & 0 & \frac{1}{\cos \beta_a v_a} \end{pmatrix} \left( -(\boldsymbol{\omega})_A^{OB} \times (\mathbf{v}_a)_A + \frac{(\mathbf{F}_{tot})_A}{m_a} \right) \quad (3.11)$$

Simplifying yields

$$\begin{pmatrix} \dot{v}_a \\ \dot{\beta}_a \\ \dot{\alpha}_a \end{pmatrix}_A = \begin{pmatrix} \frac{F_{tot,x,A}}{m_a} \\ \sin \alpha_a p - \cos \alpha_a r + \frac{F_{tot,y,A}}{m_a v_a} \\ q - \tan \beta_a (\cos \alpha_a p + \sin \alpha_a r) + \frac{F_{tot,z,A}}{m_a \cos \beta_a v_a} \end{pmatrix} \quad (3.12)$$

where  $p$ ,  $q$ , and  $r$  represent roll-, pitch-, and yaw rate, respectively. It can be observed that Eq. (3.12) is equivalent to the case without wind if the gradient of the wind field in time and space is set to zero and  $v_a$ ,  $\alpha_a$ , and  $\beta_a$  are replaced by their kinematic equivalent. The total force vector in this model consists of the gravitational force, aircraft aerodynamic force and the contributions of the tether using a straight tether approximation, including drag, the mass of the tether is neglected. In total:

$$(\mathbf{F}_{tot})_A = \mathbf{M}_{AB} \mathbf{M}_{B\tau} \mathbf{M}_{\tau W} \mathbf{M}_{WO} \left( (\mathbf{F}_g)_O - \frac{(\mathbf{p})_O}{\|(\mathbf{p})_O\|_2} F_t \right) + (\mathbf{F}_a)_A + (\mathbf{F}_{t,d})_A \quad (3.13)$$

One important difference compared to the linearization model used for conventional aerial vehicles is the different attitude parameterization in order to derive linear models for the traction phase. Since during the traction phase the aircraft is steered on a spherical surface it is more reasonable to parameterize the attitude with respect to the tangential plane frame using "tangential plane Euler angles". Such an attitude re-parameterization leads to more reasonable linear state space models for the traction phase, since the attitude angles vary less relative to the tangential plane (see also [124]). Due to the small-Earth analogy the attitude propagation equation is defined analogously to the conventional case where Euler angles between the O and B frame are utilized. If the attitude is parameterized with respect to the tangential plane the role of the O frame

is replaced by the  $\tau$  frame. This yields the *strapdown equation* (see [145, p. 45]) with respect to the tangential plane:

$$\begin{pmatrix} \dot{\Phi}_\tau \\ \dot{\Theta}_\tau \\ \dot{\Psi}_\tau \end{pmatrix} = \begin{pmatrix} 1 & \sin \Psi_\tau \tan \Theta_\tau & \cos \Phi_\tau \tan \Theta_\tau \\ 0 & \cos \Phi_\tau & -\sin \Phi_\tau \\ 0 & \frac{\sin \Phi_\tau}{\cos \Theta_\tau} & \frac{\cos \Phi_\tau}{\cos \Theta_\tau} \end{pmatrix} (\boldsymbol{\omega})_B^{\tau B} \quad (3.14)$$

with

$$\begin{aligned} (\boldsymbol{\omega})_B^{\tau B} &= (\boldsymbol{\omega})_B^{\text{OB}} - \mathbf{M}_{B\tau} (\boldsymbol{\omega})_\tau^{\text{O}\tau} \\ &= (\boldsymbol{\omega})_B^{\text{OB}} - \mathbf{M}_{B\tau} ((\boldsymbol{\omega})_\tau^{\text{OW}} + (\boldsymbol{\omega})_\tau^{\text{W}\tau}) \\ &= (\boldsymbol{\omega})_B^{\text{OB}} - \mathbf{M}_{B\tau} (\mathbf{M}_{\tau W} (\boldsymbol{\omega})_W^{\text{OW}} + (\boldsymbol{\omega})_\tau^{\text{W}\tau}) \\ &= (\boldsymbol{\omega})_B^{\text{OB}} - \mathbf{M}_{B\tau} \begin{pmatrix} \dot{\lambda} \cos \phi \\ -\dot{\phi} \\ -\dot{\lambda} \sin \phi \end{pmatrix}_\tau \end{aligned} \quad (3.15)$$

In the last step it is assumed that the rotation of the mean wind direction is small compared to  $(\boldsymbol{\omega})_B^{\text{OB}}$  and the tangential plane transport rate  $(\boldsymbol{\omega})_\tau^{\text{W}\tau}$ , hence  $(\boldsymbol{\omega})_W^{\text{OW}} \approx 0$ . This assumption is of course made without restriction to generality. The rates of longitude and latitude can be obtained directly from the position propagation equation given by Eq. (2.23). However, since in this case the kinematic velocity is not directly calculated through integration of the translational equations of motion (translational states are now  $v_a$ ,  $\alpha_a$  and  $\beta_a$ ) it needs to be calculated using the wind velocity:

$$\begin{aligned} (\mathbf{v}_k)_\tau &= \mathbf{M}_{\tau B} (\mathbf{v}_a)_B + \mathbf{M}_{\tau W} (\mathbf{v}_w)_W \\ &= \mathbf{M}_{\tau B} \mathbf{M}_{BA} (\mathbf{v}_a)_A + \mathbf{M}_{\tau W} (\mathbf{v}_w)_W \end{aligned} \quad (3.16)$$

### 3.1.2. Traction Phase Operating Point Analysis

In order to calculate the quasi-stationary operating points an optimization problem is formulated. Its solution yields the values for the inputs  $\delta_a$ ,  $\delta_e$ , and  $\delta_r$  as well as the states  $p$ ,  $q$ ,  $r$ ,  $\Phi_\tau$ ,  $\Theta_\tau$ ,  $\Psi_\tau$ , and  $v_a$  such that the accelerations are zero and the equality constraints for  $\chi_\tau$ ,  $\dot{\chi}_k$ ,  $\dot{\gamma}_k$ ,  $\alpha_a$ ,  $\beta_a$ , and  $F_t$  are satisfied. In general, the cost function that the optimizer tries to minimize is given by the residuals of the desired and the achieved state vector derivatives i.e.:

$$\mathbf{r}_{\text{trim}} = \dot{\mathbf{x}} - \dot{\mathbf{x}}_{\text{des}} = \mathbf{f}(\mathbf{x}, \mathbf{u}) - \dot{\mathbf{x}}_{\text{des}} \quad (3.17)$$

For a conventional aircraft the trim points usually reflect characteristic operating points such as horizontal cruise flight. In this case the trim point reflects a quasi-stationary flight state that is maintained without external disturbances. Defining such a characteristic operating point is more challenging in AWE since a stable quasi-stationary trim point like horizontal cruise does not exist. Therefore, a trim point is in the following more generally denoted as a quasi-stationary state that can be defined for any point on the flight path in which all accelerations are rendered zero through an appropriate choice of state and input values. Naturally, these points are unstable equilibrium points,

but nonetheless allow to linearize the equations of motions around them. Given a certain wind speed this allows then to calculate linear state space models that can be used to analyze the dynamic characteristics of the open loop system as well as to derive linear state feedback controllers. In addition, this analysis can be used to characterize the operational envelope of the system. For example, the required reeling speeds in different wind conditions and for different tether forces can be determined that lead to a force and moment equilibrium. Ultimately, these results can be used to define high level requirements for instance for the ground station i.e. the required reeling velocities in specific wind conditions.

The following procedure allows to calculate a quasi-stationary point on any point on the figure of eight path but it is exemplified for the center point of the figure of eight. This point can be regarded as a characteristic flight state since, on the one hand, the downward flight segments passing through the center can be regarded as the horizontal flight state in conventional aviation due to the analogy of the  $\tau$  and  $O$  frame and, on the other hand, the great circle flight segment passing through the center reflects the majority of the figure of eight flight. Therefore, it is expected that the linear state-space models derived at this quasi-stationary point represent reasonable models for the controller design. Per definition a quasi-stationary point is defined by a state and input vector that renders all accelerations zero. The latter equality constraint is mathematically simply written as:

$$\begin{aligned}\dot{v}_a &= 0 \\ \dot{\beta}_a &= 0 \\ \dot{\alpha}_a &= 0 \\ (\dot{\omega})_B^{OB} &= 0\end{aligned}\tag{3.18}$$

The derivatives of the attitude angles ( $\dot{\Phi}_\tau$ ,  $\dot{\Theta}_\tau$  and  $\dot{\Psi}_\tau$ ) as well as the derivatives of the position  $\dot{\lambda}$  and  $\dot{\phi}$  are allowed to vary since they do not represent accelerations. In order to fully characterize the flight state, the following additional constraints are defined. The desired sideslip angle is set to zero to achieve a coordinated turn and the angle of attack is equal to a specified value corresponding to a desired *power setting*. In addition, the "fourth input"  $F_t$  is set to the desired traction phase set point. Mathematically:

$$\begin{aligned}\beta_a &= 0 \\ \alpha_a &= \alpha_a^* \\ F_t &= F_t^*\end{aligned}\tag{3.19}$$

Three additional conditions are required that define the desired flight direction as well as the course and path angle rates corresponding to the path curvature at the chosen path position:

$$\begin{aligned}\chi_\tau &= \chi_\tau^* \\ \dot{\chi}_k &= \dot{\chi}_k^* \\ \dot{\gamma}_k &= \dot{\gamma}_k^*\end{aligned}\tag{3.20}$$

Note, in chapter 4 formulas are derived that allow to calculate the desired course and path angle rates  $\dot{\lambda}_k^*$  and  $\dot{\gamma}_k^*$  given the kinematic speed of the aircraft and the path geometry for a specified path point. In order to link these rates to the dynamics of the aircraft two additional outputs in the model are defined. Concretely, in addition to the model equations the course and path angle dynamics as defined in Eq. (2.10) are implemented and set equal to the desired course and path angle rates  $\dot{\lambda}_k^*$  and  $\dot{\gamma}_k^*$ , respectively. Additional boundary conditions are the position on the path given by the small earth longitude and latitude angles:

$$\begin{aligned}\lambda &= \lambda^* \\ \phi &= \phi^*\end{aligned}\quad (3.21)$$

as well as the wind velocity:

$$(\mathbf{v}_w)_W = \begin{pmatrix} v_{w,x,W} \\ 0 \\ 0 \end{pmatrix}_W \quad (3.22)$$

The wind speed  $v_{w,x,W}$  is set to a fixed value. This allows to study quasi-stationary points for different wind conditions. Furthermore, note that the trim result is dependent on the position for two reasons. First, the direction of the tether force depends on the position of the aircraft. Second, the angles and rates of the course and path angle are a function of the path parameter  $s$  and hence also a function of the position.

The optimization problem is solved in Matlab 2018b using the *findop* routine. Reasonable initial conditions need to be chosen otherwise the optimizer might not find a solution. In addition, for every state and input, limits are defined such that only physically reasonable solutions are returned by the optimization algorithm. Note, the required course and path angle rates depend on the other trim states through the unknown kinematic speed, hence an iterative trim process is required. Concretely, the trim process is started with an initial guess for the course and path angle rate based on the initial condition of the kinematic speed. After convergence the optimizer returns the trim states and inputs that comply with the initial course and path angle rate. However, since the obtained trim state is not guaranteed to require the same course and path angle rate, simply because the kinematic speed might have changed, the resulting course and path angle rate need to be recalculated and compared with the initial rates. Therefore, the process needs to be repeated until the course and path angle rates obtained after the optimization match the rates that were defined as the boundary conditions of the previous step. If the residual is small enough the trim procedure is finished and the nonlinear equations of motion can be linearized around the returned quasi-stationary operating point.

The numerical linearization is again conducted in Matlab 2018b using the *linearize* routine. The output of the linearization process is a state space model with 12 states and 4 inputs given by:

$$\begin{aligned}\dot{\mathbf{x}} &= \mathbf{Ax} + \mathbf{Bu} \\ \mathbf{x}^\top &= (v_a \quad \beta_a \quad \alpha_a \quad \Phi_\tau \quad \Theta_\tau \quad \Psi_\tau \quad p \quad q \quad r \quad \lambda \quad \phi \quad h_\tau) \\ \mathbf{u}^\top &= (\delta_a \quad \delta_e \quad \delta_r \quad F_t)\end{aligned}\quad (3.23)$$

where  $h_r$  is the radial distance of the aircraft to the origin of the W reference frame. For the flight control design it is beneficial to separate the tether force from the control surface deflections, hence

$$\dot{\mathbf{x}} = \mathbf{Ax} + \mathbf{B}_1 \begin{pmatrix} \delta_a \\ \delta_e \\ \delta_r \end{pmatrix} + \mathbf{B}_2 F_t = \mathbf{Ax} + \mathbf{B}_1 \mathbf{u} + \mathbf{B}_2 F_t \quad (3.24)$$

Since the position is controlled by the outer loop, the corresponding differential equations are removed. Furthermore, the orientation of the aircraft given by  $\Psi_\tau$  needs to be removed since the orientation of the aircraft on the tangential plane is intrinsically controlled using the outer loop course tracking controller. Eventually, this leads to the final coupled state space model that can be used for the inner loop control design. The to be tracked outputs are defined by  $\mathbf{y}_c$ :

$$\begin{aligned} \dot{\mathbf{x}} &= \mathbf{Ax} + \mathbf{B}_1 \mathbf{u} + \mathbf{B}_2 F_t \\ \mathbf{x}^\top &= (v_a \quad \beta_a \quad \alpha_a \quad \Phi_\tau \quad \Theta_\tau \quad p \quad q \quad r) \\ \mathbf{u}^\top &= (\delta_a \quad \delta_e \quad \delta_r) \\ \mathbf{y}_c = \mathbf{C}_c \mathbf{x} &= \begin{pmatrix} 0 & 1 & 0 & 0 & 0 & 0 & 0 & 0 \\ 0 & 0 & 1 & 0 & 0 & 0 & 0 & 0 \\ 0 & 0 & 0 & 1 & 0 & 0 & 0 & 0 \end{pmatrix} \mathbf{x} = \begin{pmatrix} \beta_a \\ \alpha_a \\ \Phi_\tau \end{pmatrix} \end{aligned} \quad (3.25)$$

In the subsequent section it is analyzed whether it is reasonable to decouple the state-space model into two models that describe the longitudinal and lateral motion separately. This requires to split up the state vector into the longitudinal states  $v_a$ ,  $\alpha_a$ ,  $\Theta_\tau$  and  $q$  as well as into the lateral states consisting of  $\beta_a$ ,  $\Phi_\tau$ ,  $p$  and  $r$ . The longitudinal motion is controlled with the elevator deflection  $\delta_e$  and the lateral motion by the aileron and rudder deflection  $\delta_a$  and  $\delta_r$ . As an additional external input the tether force appears in both state-space models. The resulting longitudinal state-space model is then defined by

$$\begin{aligned} \begin{pmatrix} \dot{v}_a \\ \dot{\alpha}_a \\ \dot{\Theta}_\tau \\ \dot{q} \end{pmatrix} &= \mathbf{A}_{l0} \mathbf{x}_{l0} + \mathbf{B}_{l0,1} \delta_e + \mathbf{B}_{l0,2} F_t \\ y_{l0} &= \alpha_a \end{aligned} \quad (3.26)$$

The tracked output of the longitudinal model is the angle of attack  $\alpha_a$ . The lateral state-space model is given by

$$\begin{aligned} \begin{pmatrix} \dot{\beta}_a \\ \dot{\Phi}_\tau \\ \dot{p} \\ \dot{r} \end{pmatrix} &= \mathbf{A}_{la} \mathbf{x}_{la} + \mathbf{B}_{la,1} \begin{pmatrix} \delta_a \\ \delta_r \end{pmatrix} + \mathbf{B}_{la,2} F_t \\ \mathbf{y}_{la} &= \begin{pmatrix} \beta_a \\ \Phi_\tau \end{pmatrix} \end{aligned} \quad (3.27)$$

The tracked outputs of the lateral model are the sideslip angle  $\beta_a$  and the tangential plane roll angle  $\Phi_\tau$ .

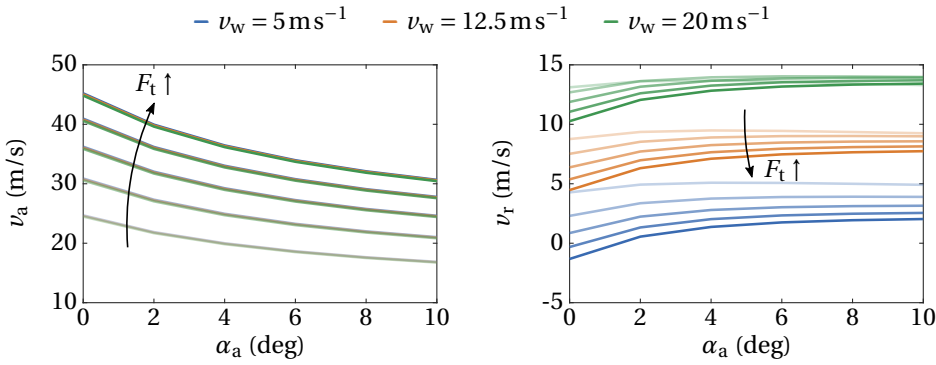
In order to calculate the numerical values of the state-space matrices a grid of different tether force inputs and angle of attacks (power settings) is created at a fixed mean elevation angle of  $35^\circ$ . This angle is considered as a center point of the interval of expected mean path elevation angles. In order to limit the scope of this section the analysis is carried out exemplary for a path shape with  $a_{\text{path}} = 0.6$  and  $b_{\text{path}} = 160$ . The exact definition of these parameters is given in chapter 4. For now it is sufficient to know that  $a_{\text{path}}$  controls the height and  $b_{\text{path}}$  controls the width of the reference path. Note, since the system is in the following only linearized at the center point of the figure of eight, the path shape itself has no significant impact on the trim result. Naturally, if the equations are linearized around any other point on the path, the path shape has an impact through the required course and path angle rates. The angle of attack is varied between  $0^\circ$  and  $10^\circ$  which covers the angle of attack range that is likely to be encountered in the traction phase. This can be verified using the results in Step 2 of the design workflow (see Fig. 1.8) which are presented in the following chapter. Similarly, the tether force is varied between 0.4kN and 2kN. This range is conservatively chosen, in order to investigate the impact of the tether force on the quasi-stationary operating point. The same grid is created for three different wind conditions i.e.  $5 \text{ ms}^{-1}$ ,  $12.5 \text{ ms}^{-1}$  and  $20 \text{ ms}^{-1}$ . The trim results are analyzed with respect to the resulting airspeed as well as the resulting reeling out (or in) velocity.

The obtained results are depicted in Fig. 3.1a and Fig. 3.1b. The color gradient from bright to dark colors indicates the increase in the tether force. This is also indicated by the arrow in the figure. The green, orange and blue curves represent the results for  $5 \text{ ms}^{-1}$ ,  $12.5 \text{ ms}^{-1}$  and  $20 \text{ ms}^{-1}$  wind speed, respectively. It can be observed that the steady state airspeed is basically independent of the wind speed since the three curves representing the three wind conditions are overlapping. The reason for the invariance of steady state airspeed with respect to the wind is that the reeling speed is adapted as can be seen in Fig. 3.1b. With increasing wind speed (from blue to green) the reeling speed increases as well and hence keeps the airspeed constant. Similarly, the reeling speed increases for a fixed wind speed if the tether force is decreased. As expected, for larger angle of attacks the steady state airspeed decreases.

### 3.1.3. Traction Phase Eigenmode Analysis

In this section the open loop dynamics of the aircraft are analyzed using the linearization results of the previous section. The goal of this section is to assess how well the decoupled longitudinal and lateral dynamics approximate the coupled dynamics in order to decide if the longitudinal and the lateral controller can be designed independently. Furthermore, it is investigated how the characteristic eigenmodes compare qualitatively to the modes of untethered aircraft. The analysis is carried out with a fixed wind speed of  $12.5 \text{ ms}^{-1}$  and varying angles of attack between  $0^\circ$  and  $10^\circ$  which results in airspeeds between  $29 \text{ ms}^{-1}$  and  $43 \text{ ms}^{-1}$ . The tether force is fixed to 1.8kN which corresponds to the traction force set point that is later on used in the simulations.

Figure 3.2 shows the resulting location of the eigenvalues in the complex plain. In general, the marker size correlates with increasing airspeed and decreasing angle of at-



(a) Airspeed over angle of attack in a quasi-stationary state. The color gradient (bright to dark) indicates increasing tether force from  $F_t = 0.4 \text{ kN}$  to  $F_t = 2 \text{ kN}$ . Path parameters are  $a_{\text{path}} = 0.6$  and  $b_{\text{path}} = 160$ .

(b) Reeling speed over angle of attack in a quasi-stationary state. The color gradient (bright to dark) indicates increasing tether force from  $F_t = 0.4 \text{ kN}$  to  $F_t = 2 \text{ kN}$ . Path parameters are  $a_{\text{path}} = 0.6$  and  $b_{\text{path}} = 160$ .

Figure 3.1: Quasi-stationary points for varying wind speeds and tether force set points at 35° elevation angle.

tack. This is also indicated by the arrows. Furthermore, the blue colored circular markers indicate the location of the eigenvalues obtained with the coupled model, the orange crosses indicate the location of the eigenvalues of the longitudinal model and the green squares represent the location of the eigenvalues of the lateral model.

The locations of the eigenvalues indicate that in total two aperiodic modes, corresponding to the eigenvalue on the real axis, and three oscillatory modes, corresponding to the three complex conjugate eigenvalues, exist. In general, this characteristic distribution of the eigenvalues is comparable to the distribution of the eigenvalues of an untethered aircraft linearized around a steady state straight flight state (see [19, p. 307-308]). The fastest aperiodic mode can be associated to the roll mode, the slow aperiodic and slightly unstable mode corresponds to the spiral mode. The oscillatory mode with the highest damping across all airspeeds is the short period mode and the mode with a similar frequency but lower damping can be associated to the dutch-roll mode. Finally, the phugoid motion can be associated with the low frequency oscillatory mode with decreasing damping for decreasing airspeed.

As stated in [19, p. 309], besides the description of the eigenvalue location, it is important to also analyze which states contribute most to each of the modes. Both results can then for instance be used to justify the decoupling of the longitudinal and the lateral dynamics for the controller synthesis. One intuitive approach to carry out this analysis is to use eigenvectors where the magnitude of the elements of each eigenvector indicates how much the corresponding state contributes to a specific mode relative to the other states [19, p. 310]. Mathematically, this can be deduced from the homogeneous solution

of a linear state-space model, i.e. the solution to:

$$\dot{\mathbf{x}} = \mathbf{A}\mathbf{x} \quad (3.28)$$

where  $\mathbf{A}$  is the dynamic matrix. Since the derivation can be found in any control theory textbook (for instance see [57, pp. 282-283]) only the solution is presented in Eq. (3.29):

$$\mathbf{x}(t) = \sum_{i=1}^n \mathbf{v}_i e^{\lambda_i t} \tilde{x}_i(0) \quad (3.29)$$

with

$$\begin{pmatrix} \tilde{x}_1(0) \\ \vdots \\ \tilde{x}_n(0) \end{pmatrix} = (\mathbf{v}_1 \cdots \mathbf{v}_n)^{-1} \begin{pmatrix} x_1(0) \\ \vdots \\ x_n(0) \end{pmatrix} \quad (3.30)$$

Here  $\mathbf{x}(t)$  is the state vector,  $\mathbf{v}_i$  is the  $i$ th eigenvector corresponding to the  $i$ th eigenvalue  $\lambda_i$  (of  $\mathbf{A}$ ) and  $x_i(0)$  is the initial condition of the  $i$ th state. Each  $\mathbf{v}_i e^{\lambda_i t}$  term in the sum of Eq. (3.29) is called a "mode" of the system. Clearly, the elements of  $\mathbf{v}_i$  can be interpreted as weights of the states of the  $i$ th mode. Hence, large elements in  $\mathbf{v}_i$  indicate that the corresponding states dominate the  $i$ th mode.

Graphically, this can be illustrated using so called *eigenvector stars* (see [69, p. 58-60]). The eigenvector stars are created for the decoupled model (longitudinal and lateral) as well as for the fully coupled model. For each mode the corresponding eigenvector is extracted and the elements of the vector are drawn in terms of its phase and magnitude. Additionally, the eigenvectors are rotated such that the largest element has a phase of  $0^\circ$ . Since only a qualitative analysis is carried out and the eigenvector stars do not change significantly across the selected airspeed range, only the results for  $\alpha_a = 0^\circ$  are depicted in Fig. 3.3a-Fig. 3.7b. In Fig. 3.3a and Fig. 3.3b the eigenvector stars corresponding to the fast oscillatory mode are depicted. Similar to a conventional aircraft the pitch rate is the dominant state in this mode, followed by the angle of attack. Furthermore, both eigenvectors obtained with the decoupled model and with the full model are nearly identical. In Fig. 3.4a and Fig. 3.4b the elements of the eigenvector corresponding to the slow and weakly damped oscillatory mode are depicted. In this case, a difference to the conventional phugoid mode can be observed, since also here the pitch rate is the dominating state followed closely by the airspeed and the tangential plane pitch angle. The eigenvector star obtained with the fully coupled model is again nearly identical.

The remaining three modes can be attributed to the lateral motion of the tethered aircraft. The dominating state in Fig. 3.5a and Fig. 3.5b is clearly the roll rate and hence corresponds to the well known roll mode. Both decoupled and coupled model lead to nearly identical results. In Fig. 3.6a and Fig. 3.6b the oscillatory mode of the lateral motion is depicted (i.e. the dutch roll). Similar to a conventional aircraft the dominating states are lateral states. The most dominant state is the yaw rate followed by roll-rate and sideslip angle which indicates the characteristic roll-yaw motion of this aircraft mode. Finally, Fig. 3.7a and Fig. 3.7b represent the slightly unstable and slow spiral mode. Although the contributing states, i.e. yaw rate and roll angle, are similar to the ones in a conventional aircraft configuration, the impact of the yaw rate is usually less dominant

than the the roll angle. Both models, the coupled and the decoupled one, lead again to nearly identical results.

In combination with the overlapping locations of the eigenvalues that are obtained with the two decoupled models as well as the fully coupled model the following conclusion can be drawn. Using the utilized attitude parameterization indeed allows to decouple the longitudinal and the lateral motion, since the eigenmodes obtained with the decoupled models are approximately identical to the modes obtained with the coupled model. The contributing states, as shown by the eigenvector stars, can be clearly separated and associated to either a longitudinal or a lateral motion state. On the other hand, the analysis of the phygoid motion shows that further decoupling the longitudinal motion into the short period and the phygoid motion for the control design is not recommended. The reason for this is that the pitch rate contributes not only to the fast but also to the slow oscillatory mode of the longitudinal dynamics (phygoid mode). This decision is reinforced by the fact that in this application only one aircraft control input for the longitudinal motion through the elevator is available. Hence, controlling the phygoid and short period motion separately, through for instance the throttle and elevator, is not realizable in this application. Therefore, using a combined control approach of short period and phygoid mode seems to be a more appropriate choice in this work.

## 3.2. Retraction Phase

### 3.2.1. Model Equations for Trimming and Linearizing

Similarly to the traction phase, quasi-stationary operating points can be calculated for the retraction phase in order to derive state-space models for the controller synthesis. Since the retraction phase is characterized by a flight trajectory with a negative path angle, pointing into the opposite direction as the mean wind velocity, a slightly different model for the quasi-stationary point calculation is required. In fact, the attitude can be parameterized using Euler angles not with respect to the tangential plane but with respect to the ground. More specifically, Eq. (3.14) needs to be replaced by Eq. (2.22). The remaining equations are the same as for the model that is used to linearize the model during the traction phase.

### 3.2.2. Retraction Phase Operating Point Analysis

Besides the model equations also the optimization problem needs to be stated differently. Therefore, the equality constraints for the optimization problem are adjusted. To simplify the analysis it is assumed that the retraction phase is a straight flight path starting at the center of the figure of eight. Naturally, any other point on the figure of eight could be chosen as a starting point. However, in light of the subsequent derivation of the linear state-space models, this would lead to significant asymmetries due to the changing tether force direction. It turns out that in this case it is more reasonable to chose the center of the figure of eight as a starting point which leads to a symmetric flight state for which the state-space models and eventually the controller is derived. Moreover, since in the retraction state the course and path angle rates are zero (straight line flight) they are removed from the equality constraints as well. In addition, the tangential plane course is removed and replaced by the conventional course and path angle. Note, the tether force

is not a fixed parameter anymore since no obvious value for the tether tension that leads to a quasi-stationary flight state during the retraction phase, for a specific descend path and a specific wind speed, can be defined a priori.

Since a symmetric flight state is chosen the number of unknown states is reduced compared to the traction phase. In this case,  $v_a$ ,  $\Theta$ ,  $q$ ,  $\delta_{a,e,r}$  and  $F_t$  need to be determined such that the translational and rotational accelerations are zero:

$$\begin{aligned}\dot{v}_a &= 0 \\ \dot{\beta}_a &= 0 \\ \dot{\alpha}_a &= 0 \\ (\dot{\omega})_B^{OB} &= 0\end{aligned}\tag{3.31}$$

Furthermore, the desired values for the roll angle and roll rate as well as the yaw rate are set zero.

$$\Phi, p, r = 0\tag{3.32}$$

Additionally, the desired sideslip angle is set to zero to achieve a coordinate flight state and the angle of attack is set to the desired power setting:

$$\begin{aligned}\beta_a &= 0 \\ \alpha_a &= \alpha_a^*\end{aligned}\tag{3.33}$$

Since the retraction phase flight path is a straight line, no required course and path angle rates need to be defined. Moreover, the retraction is flown against the wind, therefore the azimuth and course angle are identical and defined by

$$\begin{aligned}\chi_k &= \Psi = \xi - \pi \\ \gamma_k &= \gamma_k^*\end{aligned}\tag{3.34}$$

Without loss of generality the wind direction can be set to zero. The optimization problem is solved again with the *findop* routine using Matlab 2018b.

Similarly to the traction phase the quasi-stationary operating points are calculated for three different wind conditions. In contrast to the fixed flight direction for the steady state calculation during the traction phase, different path angles ranging from  $-5^\circ$  to  $-10^\circ$  are chosen. This is due to the fact that later on the retraction path angle is chosen adaptively depending on the minimum tether length as well as the point where the retraction phase is triggered. Therefore it is reasonable to calculate operating points for various descend angles. The results of the trim calculations are summarized in Fig. 3.8a to Fig. 3.8f. Since the resulting airspeed over angle of attack curves are overlapping for the three wind conditions they are displayed in separate figures. The results show that within the defined boundary condition grid, i.e.  $\alpha_a \in [-4.5^\circ, 0^\circ]$  and  $\gamma_k \in [-10^\circ, -5^\circ]$ , not all points lead to a steady state solution. This is especially visible in the low wind condition case (i.e.  $5 \text{ ms}^{-1}$ ) where for instance a solution for  $\gamma_k = -10^\circ$  only at  $\alpha_a = -4.5^\circ$ ,  $\alpha_a = -4^\circ$ ,  $\alpha_a = -3.5^\circ$  and  $\alpha_a = -3^\circ$  exists. For a wind speed of  $12.5 \text{ ms}^{-1}$  and  $20 \text{ ms}^{-1}$  all airspeed and angle of attack pairs enable the optimizer to find a quasi-stationary point. Qualitatively, for the converged points, similar airspeed over angle of attack curves result across the three wind speeds. This is again due to the fact that the reeling speed is

adapted to the wind speed. In general, for high wind speed conditions lower reeling in speeds are required, as expected. Furthermore, decreasing the angle of attack leads to an increase in airspeed which results in a higher reeling in speed.

Additionally, it is instructive to analyze the required tension in the tether (see Fig. 3.9a-Fig. 3.9c). Qualitatively, the required tension decreases with increasing angle of attack. This is due to the fact that in the chosen angle of attack range the lift coefficient increases monotonously with the angle of attack. Hence, if the angle of attack increases the resultant aerodynamic force increases as well. This requires a higher tether tension to achieve the desired force equilibrium.

In each of the obtained quasi-stationary operating points the nonlinear aircraft equations of motion can be linearized. The state space model is defined by:

$$\begin{aligned}\dot{\mathbf{x}} &= \mathbf{Ax} + \mathbf{Bu} \\ \mathbf{x}^\top &= (v_a \quad \beta_a \quad \alpha_a \quad \Phi \quad \Theta \quad \Psi \quad p \quad q \quad r \quad \lambda \quad \phi \quad h_r) \\ \mathbf{u}^\top &= (\delta_a \quad \delta_e \quad \delta_r \quad F_t)\end{aligned}\quad (3.35)$$

Following a similar argumentation as for the traction phase the state space model reduces to

$$\begin{aligned}\dot{\mathbf{x}} &= \mathbf{Ax} + \mathbf{B}_1\mathbf{u} + \mathbf{B}_2F_t \\ \mathbf{x}^\top &= (v_a \quad \beta_a \quad \alpha_a \quad \Phi \quad \Theta \quad p \quad q \quad r) \\ \mathbf{u}^\top &= (\delta_a \quad \delta_e \quad \delta_r) \\ \mathbf{y}_c = \mathbf{C}_c\mathbf{x} &= \begin{pmatrix} 0 & 1 & 0 & 0 & 0 & 0 & 0 & 0 \\ 0 & 0 & 1 & 0 & 0 & 0 & 0 & 0 \\ 0 & 0 & 0 & 1 & 0 & 0 & 0 & 0 \end{pmatrix} \mathbf{x} = \begin{pmatrix} \beta_a \\ \alpha_a \\ \Phi \end{pmatrix}\end{aligned}\quad (3.36)$$

In this case the tracked outputs are  $\beta_a$ ,  $\alpha_a$  and the roll angle  $\Phi$ . Note, compared to the traction phase the state vector contains now the Euler angles with respect to the ground and not with respect to the tangential plane.

The decoupled state space models that describe the longitudinal and the lateral motion are defined analogously to the traction phase models:

$$\begin{aligned}\begin{pmatrix} \dot{v}_a \\ \dot{\alpha}_a \\ \dot{\Theta} \\ \dot{q} \end{pmatrix} &= \mathbf{A}_{lo,rt}\mathbf{x}_{lo,rt} + \mathbf{B}_{lo,rt,1}\delta_e + \mathbf{B}_{lo,rt,2}F_t \\ \gamma_{lo,rt} &= \alpha_a\end{aligned}\quad (3.37)$$

The tracked output of the longitudinal model is the angle of attack  $\alpha_a$ . The lateral state space model is given by

$$\begin{aligned}\begin{pmatrix} \dot{\beta}_a \\ \dot{\Phi} \\ \dot{p} \\ \dot{r} \end{pmatrix} &= \mathbf{A}_{la,rt}\mathbf{x}_{la,rt} + \mathbf{B}_{la,rt,1} \begin{pmatrix} \delta_a \\ \delta_r \end{pmatrix} + \mathbf{B}_{la,rt,2}F_t \\ \mathbf{y}_{la,rt} &= \begin{pmatrix} \beta_a \\ \Phi \end{pmatrix}\end{aligned}\quad (3.38)$$

The tracked outputs of the lateral model are the sideslip angle  $\beta_a$  and the roll angle  $\Phi$ .

### 3.2.3. Retraction Phase Eigenmode Analysis

In the following an eigenmode analysis is exemplified for a constant flight path angle of  $\gamma_k = -7.5^\circ$  with varying airspeed between  $19.7 \text{ m s}^{-1}$  and  $37.7 \text{ m s}^{-1}$  in combination with an angle of attack varying between  $-4^\circ$  and  $0^\circ$ . The wind speed is fixed to  $12.5 \text{ m s}^{-1}$ .

Linearizing the system in the obtained quasi-stationary points and calculating the eigenvalues of the resulting state space models yields the results depicted in Fig. 3.10. Similar to the traction phase the marker size correlates with increasing airspeed and decreasing angle of attack. Furthermore, the blue colored circular markers indicate the location of the eigenvalues obtained with the coupled model, the orange crosses indicate the location of the eigenvalues of the longitudinal model and the green squares represent the location of the eigenvalues of the lateral model. The location of the eigenvalues show that in total two aperiodic modes, corresponding to the eigenvalue on the real axis, and three oscillatory modes, corresponding to the three complex conjugate eigenvalues, exist. Since the retraction phase is approximately a symmetric flight state in which the aircraft glides back in negative  $x_W$  direction it is expected that the eigenmodes resemble the eigenmodes of a conventional aircraft which is linearized in a stationary and straight descending flight state. Concretely, the two oscillatory eigenmodes of the longitudinal motion are visible and represent the fast and well damped short period mode as well as the slow and weakly damped phugoid mode. Similar to the traction phase the fast roll mode and the oscillatory dutch-roll mode as well as the slightly unstable spiral mode are visible. The location of the eigenvalues obtained with the decoupled models and the fully coupled model are again nearly identical. The corresponding eigenvector stars are displayed in Fig. 3.11a-Fig. 3.15b. The short period mode is dominated, as expected, by the pitch rate, followed by the angle of attack. In contrast to the traction phase the phugoid is now mainly dominated by the airspeed and the pitch angle similar to phugoid mode of an untethered aircraft. In both cases the longitudinal modes obtained with the decoupled and the fully coupled model are basically identical.

The results that are obtained for the lateral eigenmodes are comparable to the lateral mode shapes of an untethered aircraft, as well. The fast roll mode is dominated by the roll rate, the dutch-roll is influenced by the yaw-rate, roll-rate as well as the sideslip angle. Finally, the spiral mode is mainly influenced by the roll angle and yaw rate.

Based on these results it can be concluded that the longitudinal and the lateral retraction phase controller can be designed independently. This is justified by the fact that the mode analyses conducted, on the one hand, for the decoupled longitudinal and lateral models and, on the other hand, for the fully coupled model lead to nearly identical results. In both cases the eigenvalue locations as well as the eigenvector stars overlap sufficiently. Overall, this result is not surprising since the retraction phase flight state is similar to a stationary descending flight state of a conventional aircraft for instance during a landing maneuver. In this case, it is common to design the longitudinal and lateral control system independently also due to the symmetric flight state that naturally decouples the longitudinal from the lateral motion.

### 3.3. Summary

The results in this chapter serve as a basis for the control design process that is presented in the subsequent chapter. A preliminary analysis of the operational envelope is conducted by linearizing the nonlinear AWE system model around characteristic operating points during the traction and the retraction phase. Using linear state space models a flight dynamic analysis based on the location of Eigenvalues as well as Eigenvector stars is performed. The findings of this analysis are used in the next chapter to derive different flight controllers.

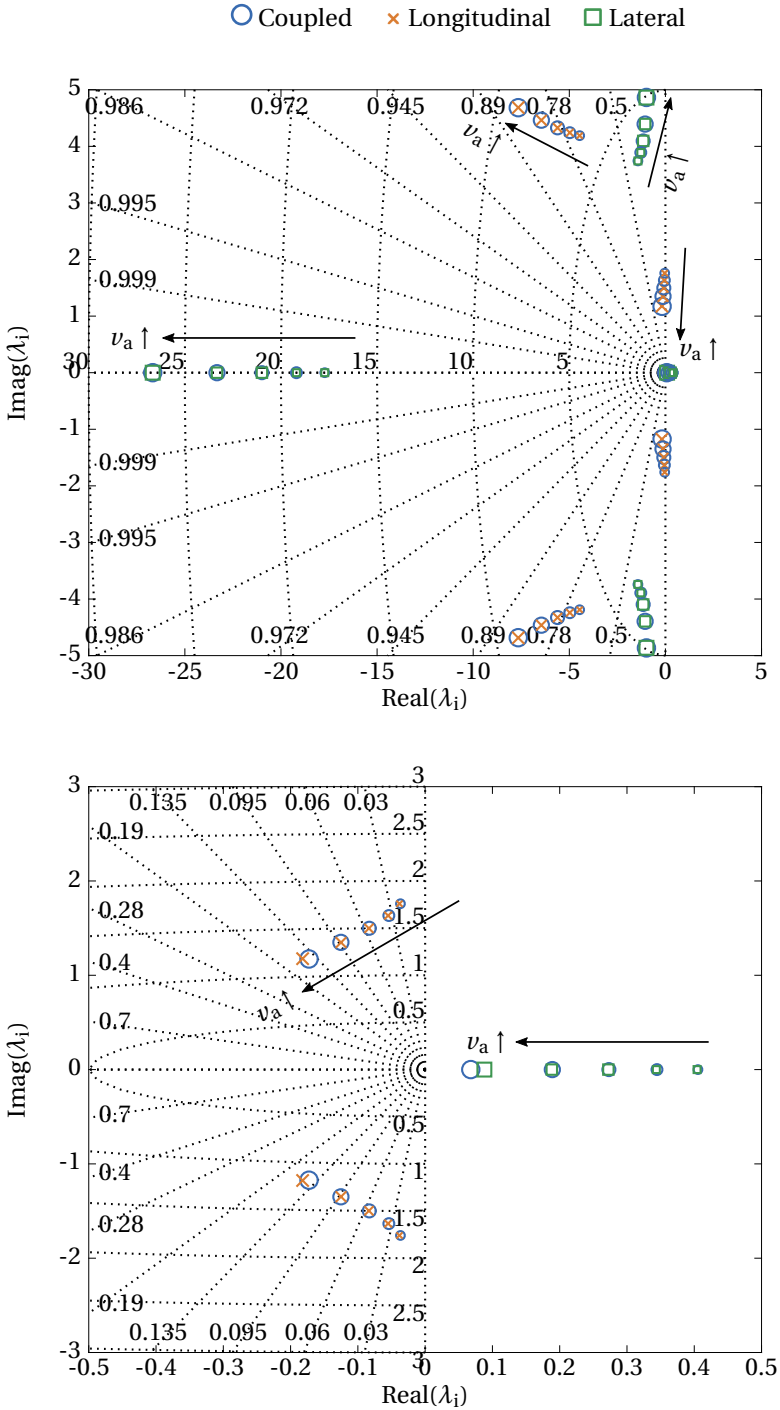


Figure 3.2: Eigenvalues of the coupled dynamics for  $F_t = 1.8\text{kN}$ . Linearization point is at the center of the figure-8 during the traction phase. Increasing marker size indicates increasing airspeed and decreasing angle of attack. The lower plot magnifies the area around the origin.

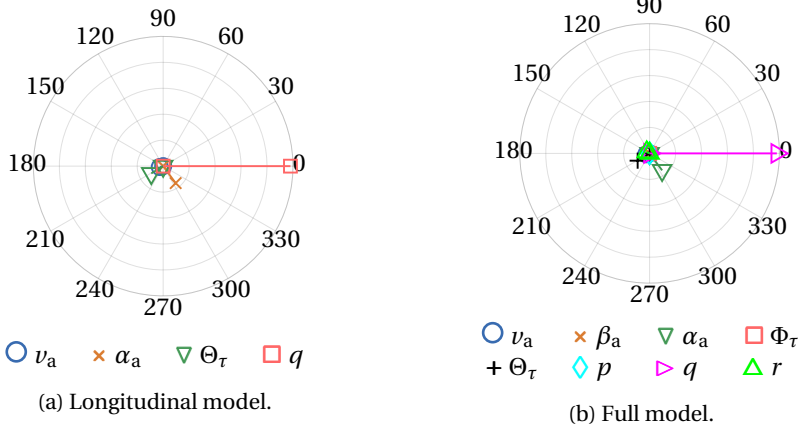


Figure 3.3: Eigenvector components corresponding to the short period mode (traction phase).

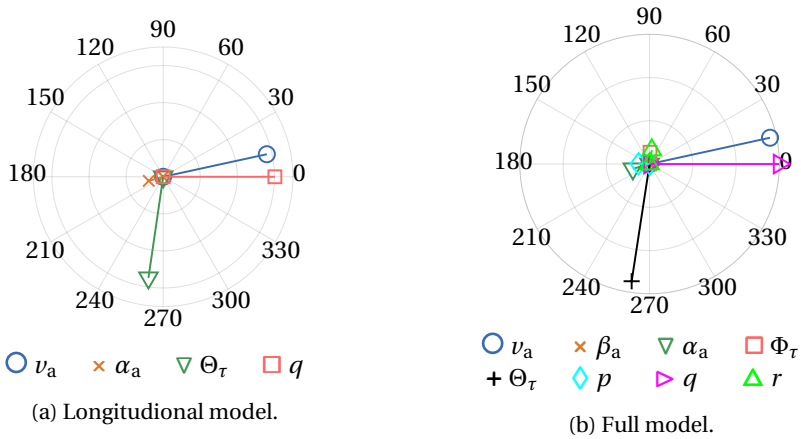


Figure 3.4: Eigenvector components corresponding to the phygoid mode (traction phase).

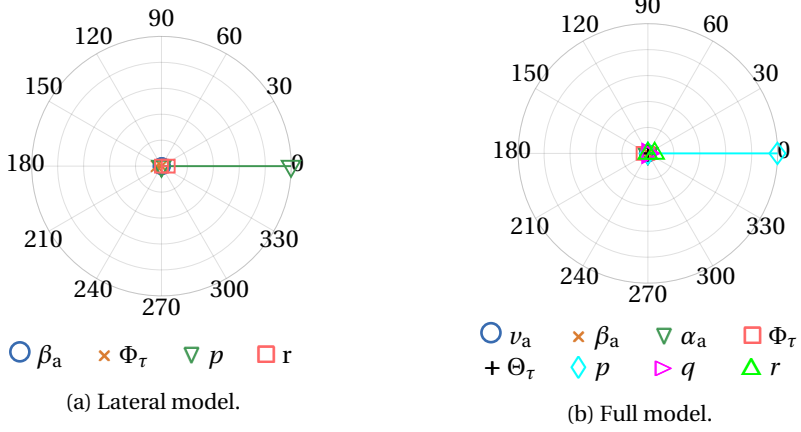


Figure 3.5: Eigenvector components corresponding to the roll mode (traction phase).

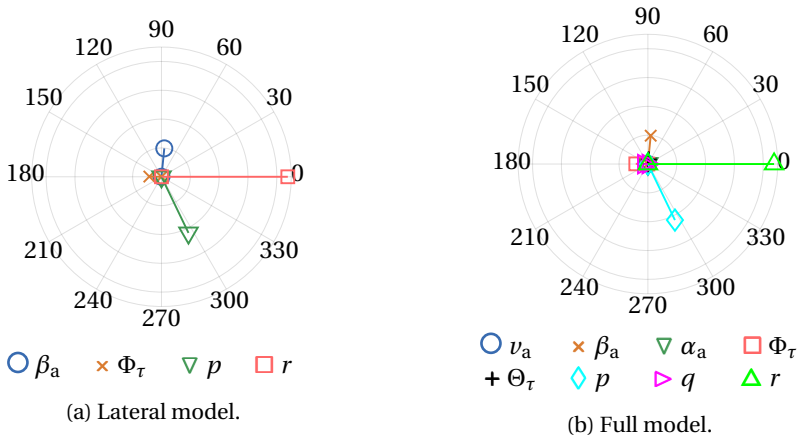


Figure 3.6: Eigenvector components corresponding to the dutch-roll mode (traction phase).

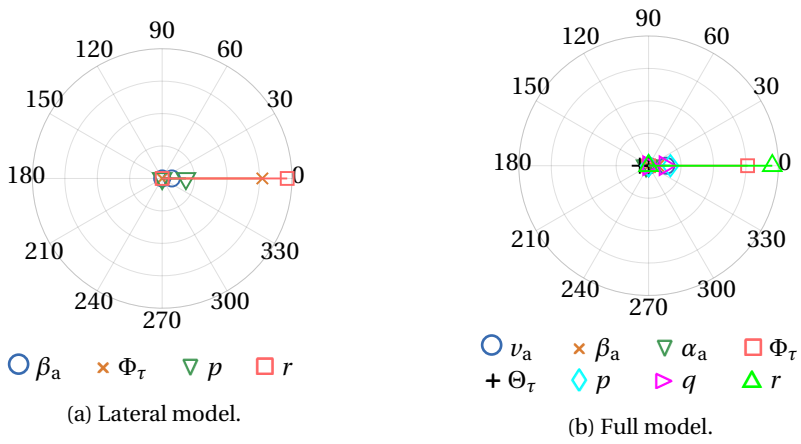
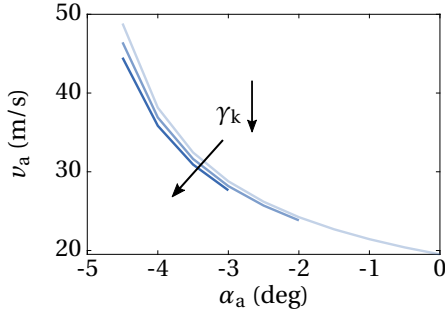
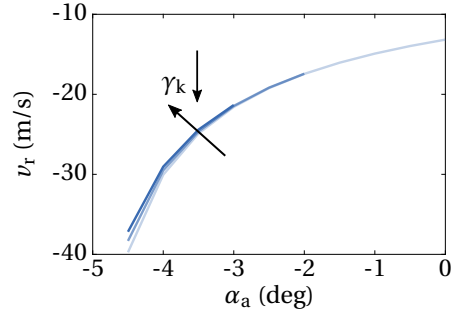


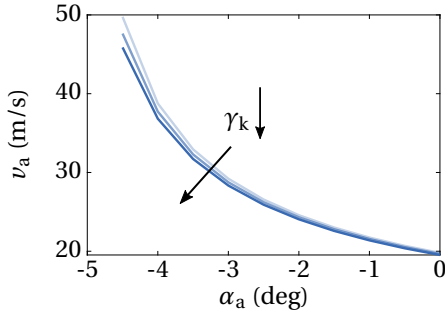
Figure 3.7: Eigenvector components corresponding to the spiral mode (traction phase).



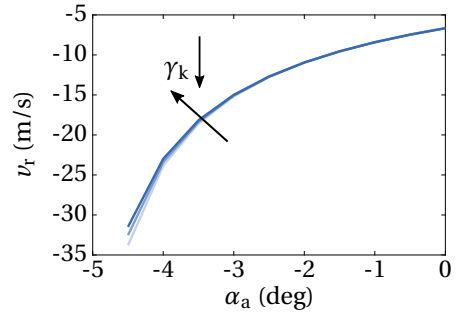
(a) Airspeed over angle of attack in a quasi-stationary state during the retraction phase for  $v_w = 5 \text{ m s}^{-1}$ .



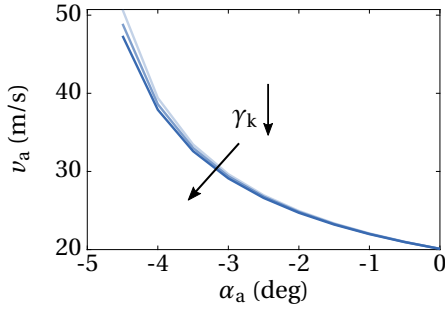
(b) Reeling speed over angle of attack in a quasi-stationary state during the retraction phase for  $v_w = 5 \text{ m s}^{-1}$ .



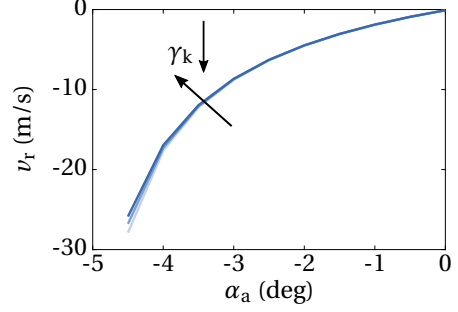
(c) Airspeed over angle of attack in a quasi-stationary state during the retraction phase for  $v_w = 12.5 \text{ m s}^{-1}$ .



(d) Reeling speed over angle of attack in a quasi-stationary state during the retraction phase for  $v_w = 12.5 \text{ m s}^{-1}$ .

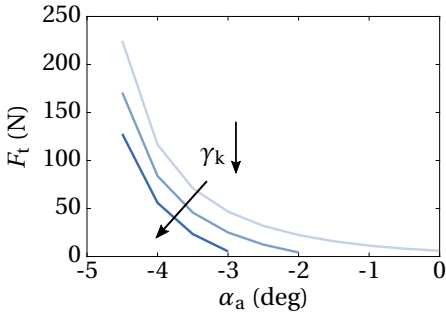


(e) Airspeed over angle of attack in a quasi-stationary state during the retraction phase for  $v_w = 20 \text{ m s}^{-1}$ .

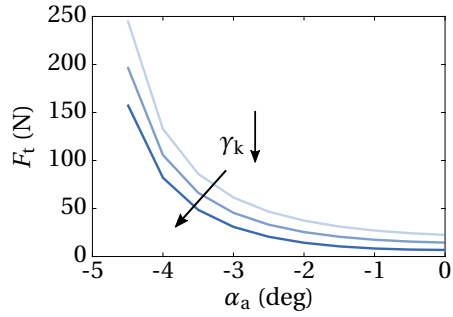


(f) Reeling speed over angle of attack in a quasi-stationary state during the retraction phase for  $v_w = 20 \text{ m s}^{-1}$ .

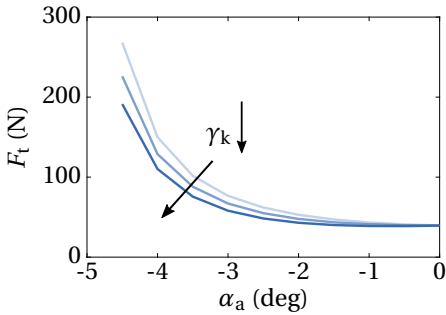
Figure 3.8: Quasi-stationary states during the retraction phase for different wind speeds. The color gradient (bright to dark) indicates steeper path angles i.e.  $\gamma_k = -5^\circ \rightarrow \gamma_k = -7.5^\circ \rightarrow \gamma_k = -10^\circ$ .



(a) Tether force over angle of attack in a quasi-stationary state during the retraction phase for  $v_w = 5 \text{ m s}^{-1}$ .



(b) Tether force over angle of attack in a quasi-stationary state during the retraction phase for  $v_w = 12.5 \text{ m s}^{-1}$ .



(c) Tether force over angle of attack in a quasi-stationary state during the retraction phase for  $v_w = 20 \text{ m s}^{-1}$ .

Figure 3.9: Required tether force over angle of attack during the retraction phase for different wind speeds. The color gradient (bright to dark) indicates steeper path angles i.e.  $\gamma_k = -5^\circ \rightarrow \gamma_k = -7.5^\circ \rightarrow \gamma_k = -10^\circ$ .

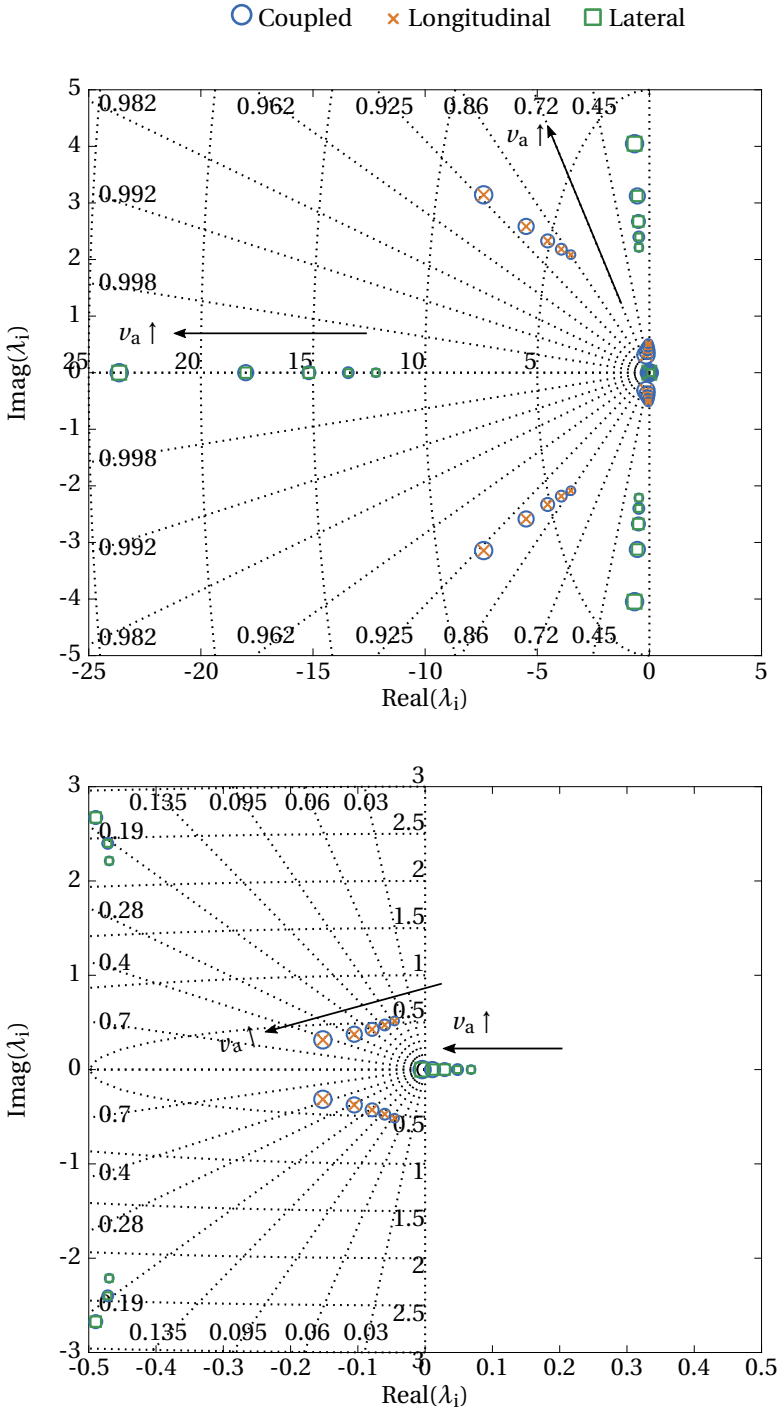


Figure 3.10: Eigenvalues as a function of airspeed at a constant descend path angle  $\gamma_k = -7.5^\circ$ . Increasing marker size indicates increasing airspeed and decreasing angle of attack. The lower plot magnifies the area around the origin.

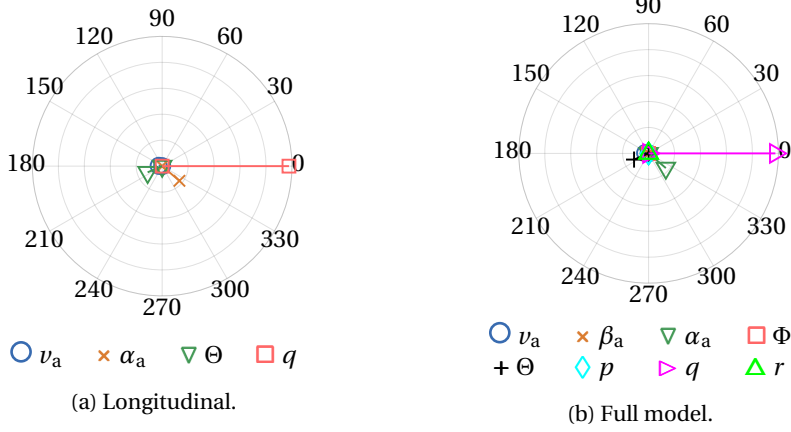


Figure 3.11: Eigenvector components corresponding to the short period mode (retraction phase).

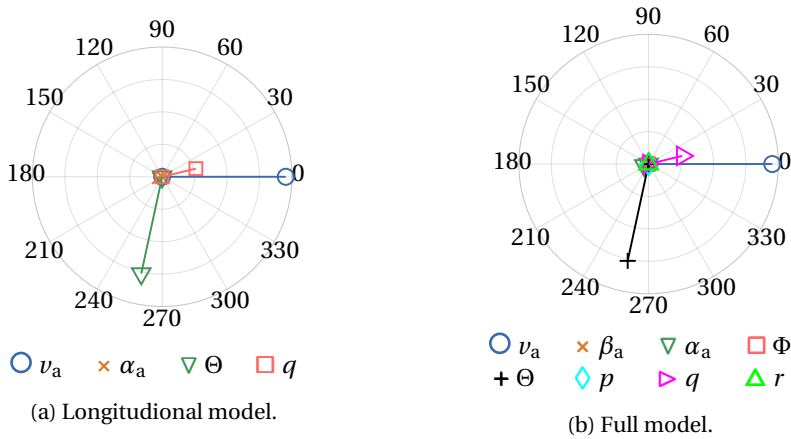


Figure 3.12: Eigenvector components corresponding to the phygoid mode (retraction phase).

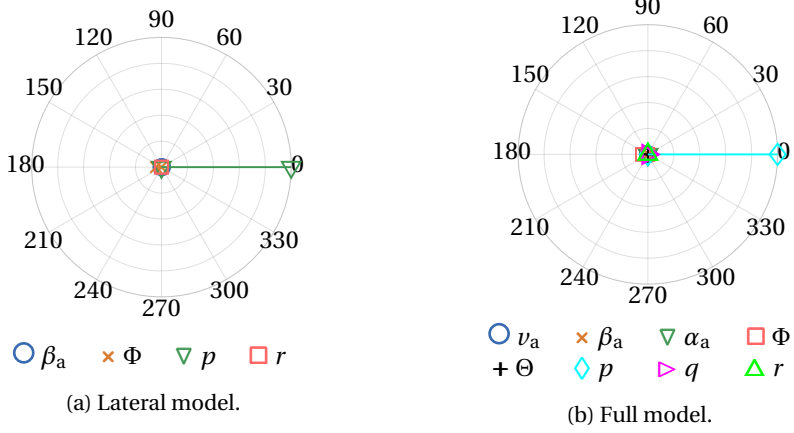


Figure 3.13: Eigenvector components corresponding to the roll mode (retraction phase).

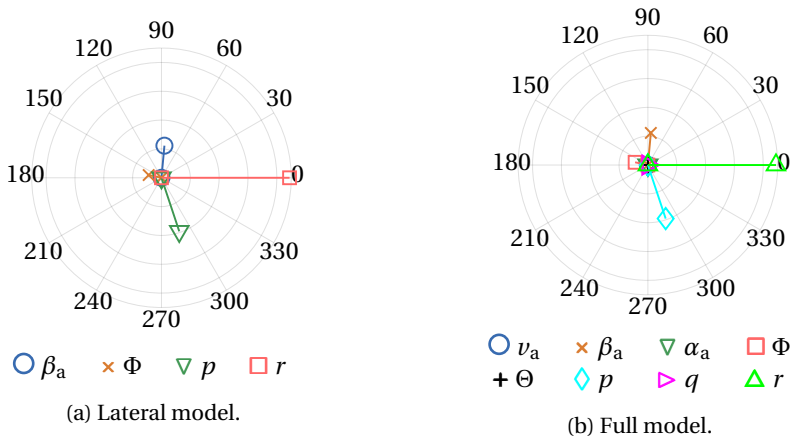


Figure 3.14: Eigenvector components corresponding to the dutch-roll mode (retraction phase).

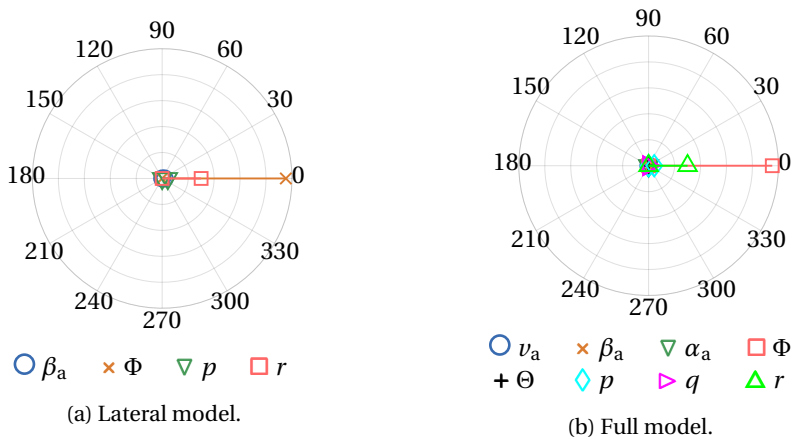


Figure 3.15: Eigenvector components corresponding to the spiral mode (retraction phase).



# 4

## Control System Design

This chapter presents in detail the control system design methodology, in particular Step 1 to Step 4, depicted in Fig. 1.8. The controllers are synthesized using the models presented in chapter 2 and 3. In the first section a concise introduction to the theoretical preliminaries for the different control design strategies is presented. Note, this section does not intend to reproduce existing theory from other sources in great detail. It rather provides the reader with enough information to understand the main properties of the different design paradigms in order to be able to implement and tune the controllers in the context of this work or for a different system. The subsequent sections build up the control system following the process diagram in Fig. 1.8. In this thesis three linear inner loop flight control designs as well as one nonlinear design are developed and analyzed. During the design phase (Step 3) the performance is assessed with respect to the step response characteristics (rise time, overshoot and settling time). Robustness is assessed with respect to parametric model uncertainties and their impact on the step response. In the last part of this chapter the performances of the different inner loop controllers are verified including the outer loop (Step 4) which allows to study the tracking performance of time varying reference signals. In the subsequent chapter the controllers are assessed in more detail with respect to stochastic uncertainties.

Note that the traction phase guidance and the path following loop as well as the nonlinear inner loop control design are partially based on published work of the author of this dissertation (see [118, 119]).

### 4.1. Theoretical Preliminaries

In this section a concise overview of the control theory is given that is utilized to derive the inner loop controllers that are presented in the subsequent section. Note, for the controller synthesis in this work state feedback is assumed.

### 4.1.1. Linear Quadratic Regulator and $\mathcal{H}_2$ -optimal Control

For the controller synthesis in this section the plant is defined as

$$\begin{aligned}\dot{\mathbf{x}}(t) &= \mathbf{A}\mathbf{x}(t) + \mathbf{B}\mathbf{u}(t) + \mathbf{E}\mathbf{w}(t) \\ \mathbf{y}(t) &= \mathbf{C}\mathbf{x}(t) \\ \mathbf{z}(t) &= \mathbf{C}_z\mathbf{x}(t) + \mathbf{D}_z\mathbf{u}(t)\end{aligned}\quad (4.1)$$

with  $\mathbf{A} \in \mathbb{R}^{n \times n}$ ,  $\mathbf{B} \in \mathbb{R}^{n \times m}$ ,  $\mathbf{C} \in \mathbb{R}^{r \times n}$ ,  $\mathbf{x} \in \mathbb{R}^n$ ,  $\mathbf{y} \in \mathbb{R}^r$ ,  $\mathbf{u} \in \mathbb{R}^m$ ,  $\mathbf{E} \in \mathbb{R}^{n \times m}$  and  $\mathbf{w} \in \mathbb{R}^m$  where  $\mathbf{w}$  is an exogenous input (e.g. a disturbance).  $\mathbf{z}(t)$  represents a performance measure where  $\mathbf{C}_z$  and  $\mathbf{D}_z$  are specified weights on the states and inputs. The linear quadratic regulator (LQR) is the linear optimal controller for the system defined in Eq.(4.1) that minimizes the following quadratic cost function

$$J = \int_0^{\infty} (\mathbf{x}^\top(t)\mathbf{Q}\mathbf{x}(t) + \mathbf{u}^\top(t)\mathbf{R}\mathbf{u}(t)) dt \quad (4.2)$$

with weighting matrices  $\mathbf{Q} \in \mathbb{R}^{n \times n}$  and  $\mathbf{R} \in \mathbb{R}^m$ . Note, for the derivation  $\mathbf{w}$  is set to zero. The solution of this optimization problem can for instance be obtained by solving an algebraic Riccati equation [91, p. 39]. This yields the optimized controller gain matrix  $\mathbf{K}$  and the state-feedback law is defined by:

$$\mathbf{u} = -\mathbf{K}\mathbf{x} \quad (4.3)$$

Besides the Riccati equation approach the LQR can also be synthesized by solving the following convex optimization problem involving linear matrix inequalities (LMIs) [36, p.188-207]:

$$\underset{\mathbf{P}, \mathbf{Z}}{\text{minimize}} \text{trace}(\mathbf{W}) \quad (4.4)$$

subject to

$$\begin{pmatrix} \mathbf{A} & \mathbf{B} \end{pmatrix} \begin{pmatrix} \mathbf{P} \\ \mathbf{Z} \end{pmatrix} + \begin{pmatrix} \mathbf{P} & \mathbf{Z}^\top \end{pmatrix} \begin{pmatrix} \mathbf{A}^\top \\ \mathbf{B}^\top \end{pmatrix} < 0 \quad (4.5)$$

$$\begin{pmatrix} \mathbf{P} & (\mathbf{C}_z\mathbf{P} + \mathbf{D}_z\mathbf{Z})^\top \\ \mathbf{C}_z\mathbf{P} + \mathbf{D}_z\mathbf{Z} & \mathbf{W} \end{pmatrix} > 0 \quad (4.6)$$

with  $\mathbf{P} \in \mathbb{R}^{n \times n}$ ,  $\mathbf{Z} \in \mathbb{R}^{m \times n}$  and  $\mathbf{W} \in \mathbb{R}^{(n+m) \times (n+m)}$ . Additionally,  $\mathbf{P}$  needs to be a positive definite matrix. The controller gain for the same control law as defined in Eq. (4.3) is eventually obtained by

$$\mathbf{K} = -\mathbf{Z}\mathbf{P}^{-1} \quad (4.7)$$

This optimization problem is usually derived in the context of  $H_2$ -optimal control [36, p.188-207]. In fact, it can be shown that the  $H_2$ -optimal controller is equivalent to the linear quadratic Gaussian (LQG) controller [140, p. 355-356] and naturally leads to the same state-feedback law as the LQR if the system is assumed to be deterministic and if the weighting matrices of the performance output  $\mathbf{z}$  are chosen according to:

$$\mathbf{C}_z = \begin{pmatrix} \sqrt{\mathbf{Q}} \\ \mathbf{0} \end{pmatrix} \quad (4.8)$$

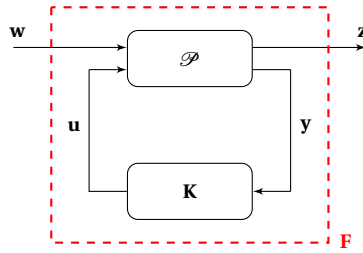


Figure 4.1: General control configuration.

and

$$\mathbf{D}_z = \begin{pmatrix} \mathbf{0} \\ \sqrt{\mathbf{R}} \end{pmatrix} \quad (4.9)$$

To further elaborate on the intuition of  $H_2$ -optimality it is instructive to define the interconnection structure displayed in Fig. 4.1, where  $\mathcal{P}$  denotes the generalized plant [140, p. 104]. An  $H_2$ -optimal controller minimizes then the  $H_2$ -norm of the linear fractional transformation of the interconnection shown in Fig. 4.1 and hence tries to mitigate the impact of the exogenous signal  $\mathbf{w}$  on the output  $\mathbf{z}$ . Mathematically, the  $H_2$ -norm is defined by

$$\|\mathbf{F}\|_{\mathcal{H}_2} = \sqrt{\frac{1}{2\pi} \int_{-\infty}^{\infty} \text{trace}(\mathbf{F}(j\omega)\mathbf{F}(j\omega)^H)} \quad (4.10)$$

There are several interpretations of the  $H_2$ -norm. For instance, if  $\mathbf{w}$  is regarded as a unit impulse the  $H_2$ -norm represents the output energy. The stochastic interpretations leads in the end to the equivalence of an  $H_2$ - and a LQG-controller and assumes that  $\mathbf{w}$  is white noise with unit intensity. In this case the controller minimizes the output variance [140].

The advantage of the LMI formulation to calculate the state feedback gain is that it allows to derive a fixed state-feedback controller that simultaneously stabilizes multiple plants while ensuring that the common upper bound of the  $H_2$ -norm of all plants is minimized. Note, in the AWE literature, in particular in [45, 168], the LMI defined by Eq. (4.5) is used to proof stability of a given controller for a set of plants. However, if the optimization problem in Eq. (4.4) is solved subject to Eq. (4.5) and Eq. (4.6), not only stability is guaranteed but at the same time the controller is optimal in the  $H_2$ -norm sense. Equation (4.5) needs to be formulated for each state-space model  $(\mathbf{A}_i, \mathbf{B}_i)$  in a defined set, the other LMIs remain unchanged. The resulting controller guarantees stability and optimal performance with respect to the  $H_2$ -norm at all considered operating points. Note, if the operating points are far away from each other, in terms of their quasi steady state values, the controller can become conservative. As usual, a trade-off needs to be made between robustness, i.e. covering a large domain of the operational envelope, and performance, i.e. only a small part is covered but the control performance (e.g. short rise time and small overshoot) is high. Furthermore, note that the resulting controller only guarantees, in a mathematical sense, stability at these considered operating points.

All LMIs in this work are implemented and solved using the MATLAB toolbox YALMIP [100] in combination with the semidefinite programming solver SDPT3 [150].

#### 4.1.2. Eigenstructure Assignment

For comparison a second linear flight control approach based on *eigenstructure assignment* (ESA) is implemented. The algorithm for the synthesis is taken from [70] and concisely described in the following. The idea of ESA is to shape the closed loop dynamics according to desired eigenvalues and eigenvectors. Note, the elements of the eigenvectors define the contribution of the states to a certain eigenmode which is shown in section 3.1.3. Hence, by choosing appropriate eigenvectors the ESA method allows to decouple different modes from each other. The closed loop dynamics with controller  $\mathbf{K}$  are defined as

$$\dot{\mathbf{x}} = (\mathbf{A} - \mathbf{B}\mathbf{K})\mathbf{x} = \mathbf{A}^*\mathbf{x} \quad (4.11)$$

The matrix  $\mathbf{A}^*$  defines the desired closed loop dynamics, achieved through the state feedback controller  $\mathbf{K}$ . Each desired eigenvalue  $\lambda_j^*$  and its corresponding eigenvector  $\mathbf{v}_j^*$  fulfills then Eq. (4.12):

$$\lambda_j^* \mathbf{v}_j^* = \mathbf{A}^* \mathbf{v}_j^* \quad (4.12)$$

This can be rewritten as

$$\begin{pmatrix} \lambda_j^* \mathbf{1} - \mathbf{A} & \mathbf{B} \end{pmatrix} \begin{pmatrix} \mathbf{v}_j^* \\ \mathbf{K}\mathbf{C}\mathbf{v}_j^* \end{pmatrix} = \mathbf{M}_j \begin{pmatrix} \mathbf{v}_j^* \\ \mathbf{z}_j^* \end{pmatrix} = 0 \quad (4.13)$$

hence, the vector composed of  $\mathbf{v}_j^*$  and  $\mathbf{z}_j^*$  lies in the nullspace of  $\mathbf{M}_j$ . Denote the nullspace of  $\mathbf{M}_j$  with  $\tilde{\mathbf{N}}_j$  and furthermore partition the base vectors of the nullspace into

$$\tilde{\mathbf{N}}_j = \begin{pmatrix} \hat{\mathbf{N}}_j \\ \mathbf{N}_j \end{pmatrix} \in \mathbb{R}^{n+m \times m} \quad (4.14)$$

with  $\hat{\mathbf{N}}_j \in \mathbb{R}^{n \times n+m}$  and  $\mathbf{N}_j \in \mathbb{R}^{m \times n+m}$ . The nullspace basis vectors are then calculated for every desired eigenvalue  $\lambda_j^*$ . Note that the solution of Eq. (4.13) can be written as a linear combination of the basis vectors of the nullspace given by the columns of  $\tilde{\mathbf{N}}$ . Mathematically, this can be expressed as

$$\begin{pmatrix} \mathbf{v}_j^* \\ \mathbf{z}_j^* \end{pmatrix} = \begin{pmatrix} \hat{\mathbf{N}}_j \\ \mathbf{N}_j \end{pmatrix} \mathbf{I}_j \quad (4.15)$$

where  $\mathbf{I}_j \in \mathbb{R}^m$  is a to be determined parameter vector. The desired procedure would be now to first calculate the nullspace of  $\mathbf{M}_j$ , then invert the first row in Eq. (4.15) to calculate  $\mathbf{I}_j$  and then  $\mathbf{z}_j^*$ . Using Eq.(4.13) would allow to calculate the controller gain  $\mathbf{K}$ . However,  $\tilde{\mathbf{N}}_j$  is in general not quadratic, hence inverting the first row using the Moore-Penrose Pseudo-Inverse would only lead to an approximate (least-squares) solution. With a simple trick, proposed in [70], an exact solution can be obtained by only specifying a certain

number of elements per eigenvector and allow the others to vary freely. For an exact solution the number of specifiable elements per eigenvectors  $s$  is bounded by the number of inputs  $m$ . Concretely, the desired elements of an eigenvector can be extracted by

$$\mathbf{v}_j^s = \mathbf{P}_j \mathbf{v}_j^* = \mathbf{P}_j \hat{\mathbf{N}}_j \mathbf{l}_j = \hat{\mathbf{N}}_j^s \mathbf{l}_j \quad (4.16)$$

where  $\mathbf{P}_j \in \mathbb{R}^{s \times n}$  selects per row the desired element in the eigenvector e.g. by setting a "1" at the appropriate location and a "0" otherwise. In the following it is assumed that  $s=m$ . Practically, all other elements in the desired eigenvector can be set to an arbitrary value. Note,  $\hat{\mathbf{N}}_j^s$  is now a quadratic matrix with dimension  $m \times m$ , hence

$$\mathbf{l}_j = \left( \hat{\mathbf{N}}_j^s \right)^{-1} \mathbf{v}_j^s \quad (4.17)$$

Hence,

$$\begin{pmatrix} \mathbf{v}_j^a \\ \mathbf{z}_j^* \end{pmatrix} = \begin{pmatrix} \hat{\mathbf{N}}_j \\ \mathbf{N}_j \end{pmatrix} \left( \hat{\mathbf{N}}_j^s \right)^{-1} \mathbf{v}_j^s \quad (4.18)$$

Note,  $\mathbf{v}_j^a$  represents now the achieved eigenvector for the  $j$ th eigenvalue and will contain the  $m$  desired elements. The remaining  $n-m$  elements are chosen according to Eq. (4.18). Evaluating Eq. (4.18) for all  $r$  eigenvectors allows to calculate the controller gain  $\mathbf{K}$ . Invoking Eq. (4.13) for each achieved eigenvector yields  $r$  equations:

$$\begin{aligned} \mathbf{z}_1^* &= \mathbf{K} \mathbf{C} \mathbf{v}_1^a \\ \mathbf{z}_2^* &= \mathbf{K} \mathbf{C} \mathbf{v}_2^a \\ &\vdots \\ \mathbf{z}_r^* &= \mathbf{K} \mathbf{C} \mathbf{v}_r^a \end{aligned} \quad (4.19)$$

which can be written as one equation:

$$\begin{pmatrix} \mathbf{z}_1^* & \mathbf{z}_2^* & \cdots & \mathbf{z}_r^* \end{pmatrix} = \mathbf{K} \mathbf{C} \begin{pmatrix} \mathbf{v}_1^a & \mathbf{v}_2^a & \cdots & \mathbf{v}_r^a \end{pmatrix} \quad (4.20)$$

inverting yields the controller gain  $\mathbf{K}$

$$\mathbf{K} = \begin{pmatrix} \mathbf{z}_1^* & \mathbf{z}_2^* & \cdots & \mathbf{z}_r^* \end{pmatrix} \left( \mathbf{C} \begin{pmatrix} \mathbf{v}_1^a & \mathbf{v}_2^a & \cdots & \mathbf{v}_r^a \end{pmatrix} \right)^{-1} \quad (4.21)$$

where all the  $\mathbf{z}_j^*$ 's and  $\mathbf{v}_j^a$ 's are calculated using Eq. (4.18).

Tuning parameters in this approach are the locations of the eigenvalues as well as the  $m$  elements of each eigenvector. Usually, the elements in the eigenvectors are chosen such that certain modes are decoupled which will be shown later in this work. Note that in contrast to the LQR or the  $H_2$ -norm optimal controller the insights from the linear analysis can be used more effectively in the ESA design approach, since specific mode shapes can be altered and others can be left nearly unchanged (nearly, because only  $m$  elements of each eigenvector can be chosen). If certain modes in the open loop plant are already satisfactory the corresponding eigenvalues do not have to be moved and the choose-able elements of the corresponding eigenvectors can be set equal to the open loop values.

### 4.1.3. Nonlinear Dynamic Inversion

Besides the three linear control designs a nonlinear dynamic inversion (NDI) based controller is synthesized for the inner loop. NDI is a popular nonlinear control approach especially for aerospace applications (see for instance [38, 120, 18, 101, 68]). For a detailed theoretical introduction of this control approach it is referred to [79, p.219-291]. In the following only a concise introduction is given, which is also limited to systems with a total relative degree equal to the order of the system and hence without inner dynamics.

The considered nonlinear models utilized for control design in this work are mathematically given in the form specified in Eq. (4.22):

$$\begin{aligned}\dot{\mathbf{x}} &= \mathbf{f}(\mathbf{x}) + \mathbf{g}(\mathbf{x}) \mathbf{u} \\ \mathbf{y} &= \mathbf{h}(\mathbf{x})\end{aligned}\quad (4.22)$$

where  $\mathbf{x} \in \mathbb{R}^n$  is the state vector,  $\mathbf{u} \in \mathbb{R}^m$  is the input and  $\mathbf{y} \in \mathbb{R}^m$  is the output. Note, it is assumed that the nonlinear system is affine in the input and the number of control variables is equal to the controlled outputs. In order to derive the NDI control law every output is differentiated with respect to time until the input appears. This procedure can be written compactly using Lie derivatives. For instance, the  $i$ th output is given by

$$y_i = h_i(\mathbf{x}) \quad (4.23)$$

Differentiating with respect to time yields

$$\dot{y}_i = \left( \frac{\partial h_i}{\partial \mathbf{x}} \right)^\top \dot{\mathbf{x}} = \left( \frac{\partial h_i}{\partial \mathbf{x}} \right)^\top \mathbf{f}(\mathbf{x}) + \left( \frac{\partial h_i}{\partial \mathbf{x}} \right)^\top \mathbf{g}(\mathbf{x}) \mathbf{u} = \mathcal{L}_{\mathbf{f}} h_i + \mathcal{L}_{\mathbf{g}} h_i \mathbf{u} \quad (4.24)$$

where  $\mathcal{L}_{\mathbf{f}} h_i$  and  $\mathcal{L}_{\mathbf{g}} h_i$  are the Lie derivatives of  $h_i$  relative to  $\mathbf{f}$  and  $\mathbf{g}$ . Assuming that  $\mathcal{L}_{\mathbf{g}} h_i$  is zero the output needs to be differentiated again.

$$\ddot{y}_i = \frac{\partial \mathcal{L}_{\mathbf{f}} h_i}{\partial \mathbf{x}} \dot{\mathbf{x}} = \frac{\partial \mathcal{L}_{\mathbf{f}} h_i}{\partial \mathbf{x}} \mathbf{f}(\mathbf{x}) + \frac{\partial \mathcal{L}_{\mathbf{f}} h_i}{\partial \mathbf{x}} \mathbf{g}(\mathbf{x}) \mathbf{u} = \mathcal{L}_{\mathbf{f}}^2 h_i + \mathcal{L}_{\mathbf{g}} \mathcal{L}_{\mathbf{f}} h_i \mathbf{u} \quad (4.25)$$

If  $\mathcal{L}_{\mathbf{g}} \mathcal{L}_{\mathbf{f}} h_i$  is again zero another derivative is necessary. This procedure continues until the first time the matrix in front of  $\mathbf{u}$  does not vanish, which yields:

$$y_i^{(r_i)} = \mathcal{L}_{\mathbf{f}}^{r_i} h_i + \mathcal{L}_{\mathbf{g}} \mathcal{L}_{\mathbf{f}}^{r_i-1} h_i \mathbf{u} \quad (4.26)$$

The number of necessary derivatives constitutes the relative degree  $r_i$  of the output  $i$ . The same procedure needs to be conducted for all the outputs and the sum of all relative degrees forms the vectorial relative degree. In this work all the models will have a vectorial degree which is equal to the number of states. In total the following input/output dynamics are obtained:

$$\begin{aligned}y_1^{(r_1)} &= \mathcal{L}_{\mathbf{f}}^{r_1} h_1 + \mathcal{L}_{\mathbf{g}} \mathcal{L}_{\mathbf{f}}^{r_1-1} h_1 \mathbf{u} \\ y_2^{(r_2)} &= \mathcal{L}_{\mathbf{f}}^{r_2} h_2 + \mathcal{L}_{\mathbf{g}} \mathcal{L}_{\mathbf{f}}^{r_2-1} h_2 \mathbf{u} \\ &\vdots \\ y_m^{(r_m)} &= \mathcal{L}_{\mathbf{f}}^{r_m} h_m + \mathcal{L}_{\mathbf{g}} \mathcal{L}_{\mathbf{f}}^{r_m-1} h_m \mathbf{u}\end{aligned}\quad (4.27)$$

which can be written more compactly as

$$\begin{pmatrix} y_1^{(r_1)} \\ y_2^{(r_2)} \\ \vdots \\ y_m^{(r_m)} \end{pmatrix} = \mathbf{b}(\mathbf{x}) + \mathbf{A}(\mathbf{x}) \mathbf{u} \quad (4.28)$$

The following feedback law linearizes and decouples the dynamics:

$$\mathbf{u} = \mathbf{A}^{-1}(\mathbf{x}) (\mathbf{v} - \mathbf{b}(\mathbf{x})) \quad (4.29)$$

where  $\mathbf{v}$  is the so called pseudo-control input. It essentially allows to shape the output dynamics. In case of perfect state measurements and a perfect model it can be seen that this feedback law enforces the model to follow a reference trajectory. Naturally, it is required that the reference trajectory for each output  $i$  is at least  $r_i$  times differentiable. Note, in reality model uncertainties, measurement delays, sensor noise, neglected dynamics and external disturbances lead to an imperfect inversion. The corresponding feedback law is therefore given by

$$\mathbf{u} = \hat{\mathbf{A}}^{-1}(\hat{\mathbf{x}}) (\mathbf{v} - \hat{\mathbf{b}}(\hat{\mathbf{x}})) \quad (4.30)$$

where the "hat" operator indicates an estimation of the corresponding model term.

The model mismatch, i.e. the difference between the real and the estimated plant, can be defined as

$$\Delta = \begin{pmatrix} y_1^{(r_1)} \\ y_2^{(r_2)} \\ \vdots \\ y_m^{(r_m)} \end{pmatrix} - \begin{pmatrix} \hat{y}_1^{(r_1)} \\ \hat{y}_2^{(r_2)} \\ \vdots \\ \hat{y}_m^{(r_m)} \end{pmatrix} = \mathbf{b}(\mathbf{x}) - \hat{\mathbf{b}}(\hat{\mathbf{x}}) + (\mathbf{A}(\mathbf{x}) - \hat{\mathbf{A}}(\hat{\mathbf{x}})) \mathbf{u} \quad (4.31)$$

Inserting the feedback law given by Eq. (4.30) yields

$$\begin{aligned} \Delta &= \mathbf{b}(\mathbf{x}) - \hat{\mathbf{b}}(\hat{\mathbf{x}}) + (\mathbf{A}(\mathbf{x}) - \hat{\mathbf{A}}(\hat{\mathbf{x}})) \hat{\mathbf{A}}^{-1}(\hat{\mathbf{x}}) (\mathbf{v} - \hat{\mathbf{b}}(\hat{\mathbf{x}})) \\ \Delta &= \mathbf{b}(\mathbf{x}) + \mathbf{A}(\mathbf{x}) \hat{\mathbf{A}}^{-1}(\hat{\mathbf{x}}) (\mathbf{v} - \hat{\mathbf{b}}(\hat{\mathbf{x}})) - \mathbf{v} \\ \Delta &= \begin{pmatrix} y_1^{(r_1)} \\ y_2^{(r_2)} \\ \vdots \\ y_m^{(r_m)} \end{pmatrix} - \mathbf{v} \end{aligned} \quad (4.32)$$

Hence,

$$\begin{pmatrix} (r_1) \\ y_1 \\ (r_2) \\ y_2 \\ \vdots \\ (r_m) \\ y_m \end{pmatrix} = \mathbf{v} + \Delta \quad (4.33)$$

Equation (4.33) indicates that in presence of uncertainties, i.e.  $\Delta \neq 0$ , the output derivatives, including the output itself, are not following perfectly the pseudo-control input  $\mathbf{v}$  and its derivatives. Speaking differently, the error dynamics of each output tracking error  $e_i = y_{\text{ref},i} - y_i$  are excited by the model mismatch term  $\Delta$ . Therefore, using just the model inversion as a control law will not stabilize the plant. However, since  $\mathbf{v}$  is a control input it can be augmented with an additional error feedback part. Hence, for each output:

$$y_i^{(r_i)} = v_i + \Delta_i = v_{\text{ref},i} + c_{r_i-1} e_i^{(r_i-1)} + \dots + c_0 e_i + \Delta_i \quad (4.34)$$

with

$$\begin{aligned} \mathbf{v} &= \left( v_1 \quad \dots \quad v_i \quad \dots \quad v_m \right)^T \\ \mathbf{v}_{\text{ref}} &= \left( v_{\text{ref},1} \quad \dots \quad v_{\text{ref},i} \quad \dots \quad v_{\text{ref},m} \right)^T \end{aligned} \quad (4.35)$$

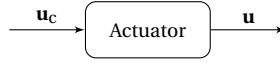
and the subscript "ref" indicates a reference signal. With this feedback law the error dynamics are stable for a bounded model mismatch  $\Delta$  and for positively chosen coefficients  $c_j$ . Hence, the design variables in the NDI approach are the reference models that generate the desired output signals and its derivatives as well as the error feedback coefficients  $c_j$ . Note, in this form of the NDI controller each  $v_{\text{ref},i}$  is equal to  $y_{i,\text{ref}}^{(r_i)}$ . In the following a small adaption is presented that can be used to hide the impact of actuator limitations on the error dynamics.

### Pseudo-Control Hedging

Pseudo-Control hedging (PCH) is an advanced anti-windup scheme that adapts the reference filter in case the control signal is altered before it is applied to the real plant (e.g. through an actuator). In fact, it hedges (hides) any actuator dynamics in front of the error dynamics. In a cascaded control approach it also allows to handle state limitations of states that are tracked by an inner loop. In this case limiters represent the pseudo actuator dynamics. The scheme was originally proposed in [81] and is concisely reviewed in the following.

To distinguish the actuator input and output in the following,  $\mathbf{u}_c$  denotes the commanded actuator input and  $\mathbf{u}$  denotes the actuator output (see Fig. 4.2). The pseudo-control hedging signal is then defined as the difference between the pseudo-control input  $\mathbf{v}$  that is commanded as well as the expected pseudo-control input that takes into account the actuator dynamics. Note, if the actuator output cannot be measured, an actuator model is required. With the measured or estimated actuator output the dynamic inversion can be reversed and the expected pseudo-control input  $\hat{\mathbf{v}}$  can be calculated:

$$\hat{\mathbf{v}} = \hat{\mathbf{A}}(\hat{\mathbf{x}}) \mathbf{u} + \hat{\mathbf{b}}(\hat{\mathbf{x}}) \quad (4.36)$$

Figure 4.2: Definition of  $\mathbf{u}_c$  and  $\mathbf{u}$ 

with

$$\hat{\mathbf{v}} = \left( \hat{v}_1 \quad \cdots \quad \hat{v}_i \quad \cdots \quad \hat{v}_m \right)^\top \quad (4.37)$$

The hedging signal can then be calculated according to

$$\mathbf{v}_h = \mathbf{v} - \hat{\mathbf{v}} \quad (4.38)$$

Each reference model output is then adapted according to the corresponding hedging value:

$$y_{i,\text{ref}}^{(r_i)} = v_{\text{ref},i} - v_{h,i} \quad (4.39)$$

Intuitively, the hedging signal slows down or speeds up the reference model if the commanded and the expected pseudo control input deviate from each other i.e. if the hedging signal is not zero. With this hedging approach the influence of the actuator dynamics on the tracking error dynamics is removed (hedged) which can be shown as follows. The model mismatch of the  $i$ th output channel can be written as:

$$y_i^{(r_i)}(\mathbf{u}) - \hat{y}_i^{(r_i)}(\mathbf{u}_c) = y_i^{(r_i)}(\mathbf{u}) - \hat{y}_i^{(r_i)}(\mathbf{u}) + \hat{y}_i^{(r_i)}(\mathbf{u}) - \hat{y}_i^{(r_i)}(\mathbf{u}_c) \quad (4.40)$$

The first difference on the right hand side is the model mismatch due to model uncertainties (see Eq. 4.31), the second difference is the model mismatch due to the actuator. Rearranging yields:

$$y_i^{(r_i)}(\mathbf{u}) = \hat{y}_i^{(r_i)}(\mathbf{u}_c) + \Delta_i + \hat{y}_i^{(r_i)}(\mathbf{u}) - \hat{y}_i^{(r_i)}(\mathbf{u}_c) \quad (4.41)$$

The first term and the last term in the sum on the right hand side corresponds to the pseudo control input  $v_i$  while the third term is the expected pseudo control input  $\hat{v}_i$ . This leads to

$$y_i^{(r_i)}(\mathbf{u}) = v_i + \Delta_i + \hat{v}_i - v_i \quad (4.42)$$

with Eq. (4.38) the last difference can be replaced by the negative hedging signal of the  $i$ th output channel and  $v_i$  can be substituted using Eq. (4.34). This yields:

$$y_i^{(r_i)}(\mathbf{u}) = v_{\text{ref},i} + c_{r_i-1} e_i^{(r_i-1)} + \cdots + c_0 e_i + \Delta_i - v_{h,i} \quad (4.43)$$

Invoking Eq. (4.39) cancels the hedging signal. This results in the same error dynamics as without actuator. Hence, the error dynamics are again only excited by the model mismatch but not by the difference between the commanded and actual control signal:

$$y_i^{(r_i)}(\mathbf{u}) = y_{i,\text{ref}}^{(r_i)} + c_{r_i-1} e_i^{(r_i-1)} + \cdots + c_0 e_i + \Delta_i \quad (4.44)$$

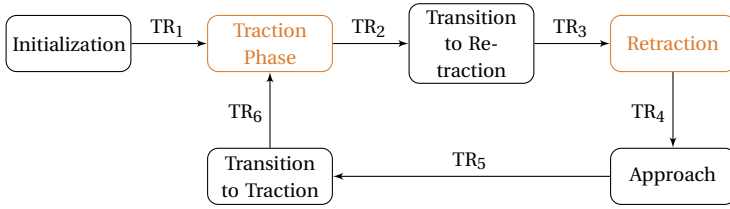


Figure 4.3: State machine. The transition rules  $TR_1$  to  $TR_6$  are explained in the text.

## 4.2. State Machine

The highest layer of the control architecture is represented by the state machine. It consists of two principal states corresponding to the traction and the retraction phase of a pumping cycle as well as sub-states that are active during the transition phases. The complete state machine is depicted in Fig. 4.3. The initial transition rule  $TR_1$  (and also  $TR_6$ ) is satisfied if the aircraft is close to the center of the figure of eight. Mathematically this is implemented as

$$TR_{1,6} = \begin{cases} 1, & \text{for } \text{mod}(s, \pi) \leq \bar{s} \\ 0, & \text{otherwise} \end{cases} \quad (4.45)$$

where  $\text{mod}$  is the modulo operation and  $\bar{s}$  is chosen to be 0.1. Note,  $s$  is the curve parameter that uniquely defines a position on the figure of eight path. The exact curve definition is introduced in the subsequent section. Note, for the results presented in this work the aircraft is initialized at a chosen trim point at the center of the figure of eight path, hence this condition is immediately satisfied if the simulation is started. It will become more important if the pumping cycle controller is augmented with a launching and landing strategy. In this case  $TR_1$  can define the switch between the takeoff and the pumping cycle controller.

The transition rule  $TR_2$  is active if the end of the traction phase is reached. Usually the retraction is initialized as soon as the maximum tether length is reached. However, in this case the retraction phase can be triggered from any point on the path. For safety reasons it is better to choose a fixed point on the path that allows so smoothly leave the figure of eight and intercept the retraction glide path. In general, the two outer most points (i.e.  $s=\pi/2$  and  $s=3/2\pi$ ) on the path have this property. The drawback is that the tether length at which the retraction phase is triggered can vary especially in high wind conditions that require a high reeling out speed. Naturally, the maximum tether length should not be exceeded. Hence, as soon as the aircraft reaches one of the two potential retraction points the increment in tether length, that is required to reach the subsequent retraction point, is predicted. In case this increment plus the current tether length exceeds the maximum tether length the retraction phase is already triggered at the current retraction point. The decision logic for  $TR_2$  is implemented as a second state machine, depicted in Fig. 4.4. The transition rule  $TR_1^{(2)}$  activates the prediction logic as

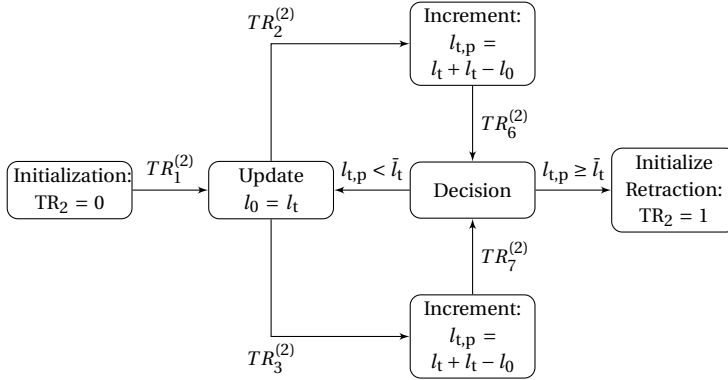


Figure 4.4: State machine for  $TR_2$ . The transition rules are explained in the text. The superscripts in the brackets indicate that the transition rule is part of the overall "global" transition rule  $TR_2$ .

soon as the aircraft passes one of the two potential retraction points:

$$TR_1^{(2)} = \begin{cases} 1, & \text{for } s \in \left[\frac{\pi}{2} - \Delta_{s,1}, \frac{\pi}{2} + \Delta_{s,1}\right] \text{ or } s \in \left[\frac{3\pi}{2} - \Delta_{s,1}, \frac{3\pi}{2} + \Delta_{s,1}\right] \\ 0, & \text{otherwise} \end{cases} \quad (4.46)$$

where  $\Delta_{s,1} = 5^\circ \cdot \pi / 180^\circ$ . Next, whenever the aircraft passes a potential retraction point either  $TR_2^{(2)}$  or  $TR_3^{(2)}$  is activated. In the state "Increment" the predicted tether length  $l_{t,p}$  is continuously updated by calculating the difference between the current tether length and the current value of  $l_0$  and adding it to the current tether length.

$$TR_{2,7}^{(2)} = \begin{cases} 1, & \text{for } s \in \left[\frac{\pi}{2} - \Delta_{s,1}, \frac{\pi}{2} + \Delta_{s,1}\right] \\ 0, & \text{otherwise} \end{cases} \quad (4.47)$$

$$TR_{3,6}^{(2)} = \begin{cases} 1, & \text{for } s \in \left[\frac{3\pi}{2} - \Delta_{s,1}, \frac{3\pi}{2} + \Delta_{s,1}\right] \\ 0, & \text{otherwise} \end{cases} \quad (4.48)$$

As soon as the aircraft passes the next retraction point either  $TR_6^{(2)}$  or  $TR_7^{(2)}$  are activated and the state "Decision" is reached. If in this state  $l_{t,p}$  is larger than the maximum tether length  $\bar{l}_t$  the transition to the retraction phase is initialized, i.e.  $TR_2 = 1$ , otherwise  $l_0$  is updated with the current tether length and the cycle starts again.

In the transition state the set point of the tether force is set to the retraction phase tether force set point. Note, the aircraft will at first continue to follow the figure of eight until the tether tension drops below a selected threshold which will activate  $TR_3$ . This is usually happening shortly after the set point change but allows to first reduce the tension in the tether before the flight controller switches into retraction mode. This prevents the aircraft from increasing its elevation angle due to the pulling force of the tether. In this work a threshold of 80% of the traction set point is chosen to activate  $TR_3$ .

The "Approach" state is activated, i.e.  $TR_4 = 1$ , if at least one of the two following conditions is met: Either the aircraft reaches the target point of the retraction phase or the

airspeed drops below a selected threshold that does not ensure a safe gliding flight. Usually this happens towards the end of the retraction phase and in particular in low wind speed conditions. In the "Approach" state the aircraft stays in the retraction mode if it has not yet reached the target point but the tether force set point is already set to the traction phase set point and hence the tension in the tether rises again which also increases the airspeed of the aircraft. If the aircraft reaches the target point, TR<sub>5</sub> is activated and the transition to the traction phase is initiated.

In the state "Transition to Traction" the flight controller switches back to figure of eight flight. For a smooth transition the reference flight path is in this phase rotated to a higher elevation angle (e.g. 80°). This is explained in more detail in the subsequent section. In this state the path is not yet rotated into the power zone in order to allow the aircraft first to converge towards the path and to regulate tracking errors that are a result of the switching between the retraction and traction phase controllers. As soon as the aircraft passes through the center point of the figure of eight (see condition in Eq. (4.45)) TR<sub>6</sub> becomes active and the traction phase starts again.

### 4.3. Guidance Strategies

This section is subdivided into three parts. In the first part the traction phase guidance module is presented that calculates the directional angles and angular rates to follow a figure of eight shaped flight path during the traction phase. The second part introduces the retraction phase guidance module. Similar to the first part directional angles are calculated such that the aircraft follows a straight gliding path against the wind while the tether is reeled-in. Finally, the guidance module for the transition strategy from the retraction to the traction phase is presented. The latter enables a smooth transition from the retraction phase into the figure of eight flight pattern.

#### 4.3.1. Traction Phase Guidance

Assuming a straight and taut tether the aircraft flies during the traction phase on a sphere where the radius is equal to the current tether length. In fact, if a fixed radius (e.g. equal to one) is chosen and the aircraft position is projected in radial direction onto this sphere the guidance problem can be simplified. Using this strategy requires to define a path on a sphere without any radial component. Essentially, the three dimensional path following problem is translated into a two dimensional path following problem with respect to the spherical coordinate system. This approach is adopted by all researchers and practitioners in the AWE community (see chapter 1.3).

Separating the radial and the tangential motion of the aircraft allows to state the control objectives for the traction phase as follows. On the one hand, the radial direction needs to be controlled by the winch such that the tether force set point is tracked. Moreover, the radial direction controller needs to ensure that the maximum tether tension is not exceeded to avoid tether rupture or aircraft damage. On the other hand, the flight controller needs to follow a predefined flight path on a sphere. The reference path on the unit sphere is adapted proportionally to the distance of the aircraft to the ground station such that the real path the aircraft traces has a constant shape during the reel-out phase in case of perfect path-following performance.

In the existing AWE literature the tethered aircraft is steered according to the tangential plane set point  $\chi_{\tau,c}$ , which is also sometimes called the velocity angle. It is defined as the angle between the  $x_{\tau}$  axis of the tangential plane frame  $\tau$  and the velocity vector projected into the tangential plane as depicted in Fig. 2.2. Originally, this strategy is chosen because a direct relationship between the steering input of a flexible kite and the tangential plane course rate can be derived (see for instance [39]) which allows to directly calculate the steering input based on the course rate. In this work the guidance problem is solved as well by first calculating the desired  $\chi_{\tau}$  set point, which will be then, however, transformed into a corresponding set point for the course  $\chi_k$  and path angle  $\gamma_k$ , which specify the orientation of the  $K$  frame relatively to the  $O$  frame (see Fig. 2.2). The reason for this approach is that a model for the path dynamics as defined in Eq.(2.10) can be used to translate the guidance module outputs into desired set points for the inner loop (i.e. attitude commands). An additional advantage of this approach is that the same inner loop control structure for the retraction phase can be used which is later on exploited by the nonlinear inner loop flight controller.

In this work the figure of eight guidance approach presented in [80], where it is used to steer a flexible kite along a prescribed path, is adopted and further extended. As an addition to [80] a novel predictive part is presented, which takes the current path curvature into account to improve the path following capabilities. Concretely, the path curvature in combination with the current kinematic speed allows to calculate the required tangential plane course rate to follow the path. Furthermore, the interface to a rigid wing aircraft path-following controller will be presented taking into account a generalization of the rotational rate vector  $(\omega)_{K^*}^{\tau}$  which describes the relative rotation between the rotated kinematic frame  $K^*$  and the tangential plane frame  $\tau$ . Furthermore, a kinematic transformation between the tangential plane course rate and the conventional course and flight path angle rates is presented which ultimately allows to link the "turning-rate-law" (e.g. [39]) to the point-mass dynamics as defined in Eq.(2.10). Since the terminology slightly deviates from [80] the main steps of the derivation will be presented again in addition to the novel extensions for completeness.

The objective of the traction phase guidance module is twofold. First, it needs to calculate the flight direction that leads to a reduction of the distance  $\delta$  (i.e. the cross track error) as defined by the arc length between the projected aircraft position on the unit sphere  $\mathbf{p}_{\perp}^G$  and the path  $\Gamma$ . Second, for zero cross-track error the kinematic velocity vector projected onto the tangential plane  $\mathbf{v}_{k,\tau}$  needs to be aligned with the path direction as defined by the tangent vector  $\mathbf{t}$ . For clarification, all relevant vectors are depicted in Fig. 4.5-Fig. 4.7. The acting forces on the aircraft during the traction flight are visualized in Fig. 4.8. The reference flight path  $\Gamma$  is defined in spherical coordinates on the unit sphere. Hence, a point on the path is fully defined by its longitude  $\lambda_{\Gamma}$  and latitude  $\phi_{\Gamma}$ . Note, in the following all vectors are given in the  $W$  reference frame, if not indicated otherwise. In Cartesian coordinates the path is given by

$$\mathbf{\Gamma}(s) = \begin{pmatrix} \cos \lambda_{\Gamma}(s) \cos \phi_{\Gamma}(s) \\ \sin \lambda_{\Gamma}(s) \cos \phi_{\Gamma}(s) \\ \sin \phi_{\Gamma}(s) \end{pmatrix} \quad (4.49)$$

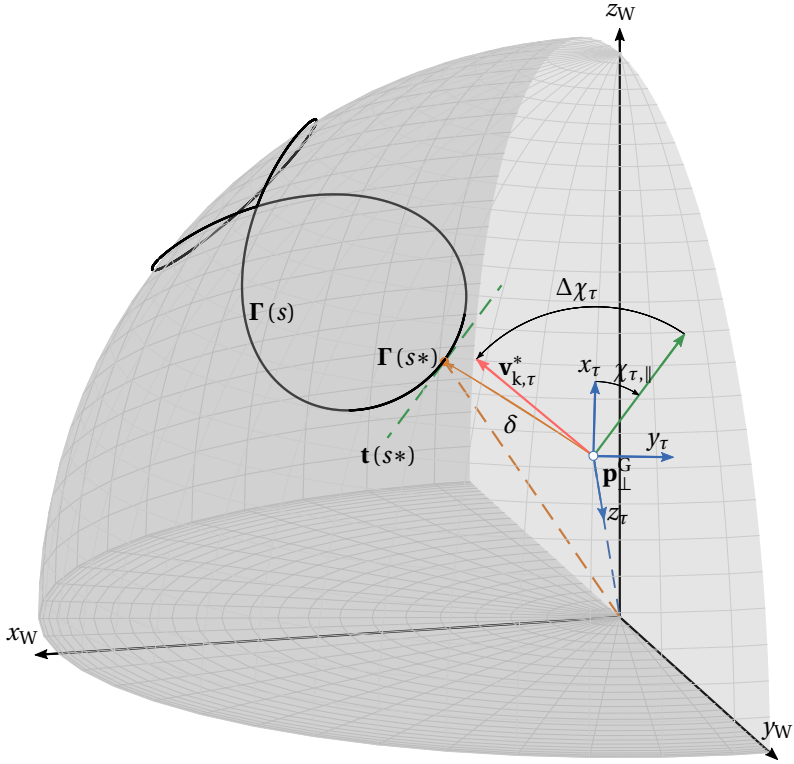


Figure 4.5: Guidance strategy kinematics: The further the aircraft is away from the path the more perpendicular, with respect to the tangential direction, the desired flight direction becomes.

For subsequent calculations the tangent and its derivative need to be known. The tangent can be calculated according to

$$\mathbf{t}(s) = \frac{d\Gamma}{ds} = \frac{\partial\Gamma}{\partial\lambda_\Gamma} \frac{d\lambda_\Gamma}{ds} + \frac{\partial\Gamma}{\partial\phi_\Gamma} \frac{d\phi_\Gamma}{ds} \quad (4.50)$$

and its derivative is given by

$$\begin{aligned} \frac{d\mathbf{t}(s)}{ds} \mathbf{t}'(s) = & \frac{\partial^2\Gamma}{\partial\lambda_\Gamma^2} \left( \frac{d\lambda_\Gamma}{ds} \right)^2 + \\ & 2 \frac{\partial^2\Gamma}{\partial\phi_\Gamma\partial\lambda_\Gamma} \frac{d\phi_\Gamma}{ds} \frac{d\lambda_\Gamma}{ds} + \frac{\partial^2\Gamma}{\partial\phi_\Gamma^2} \left( \frac{d\phi_\Gamma}{ds} \right)^2 + \frac{\partial\mathbf{t}}{\partial s} \end{aligned} \quad (4.51)$$

The last partial derivative is given by

$$\frac{\partial\mathbf{t}}{\partial s} = \frac{\partial\Gamma}{\partial\lambda_\Gamma} \frac{d^2\lambda_\Gamma}{ds^2} + \frac{\partial\Gamma}{\partial\phi_\Gamma} \frac{d^2\phi_\Gamma}{ds^2} \quad (4.52)$$

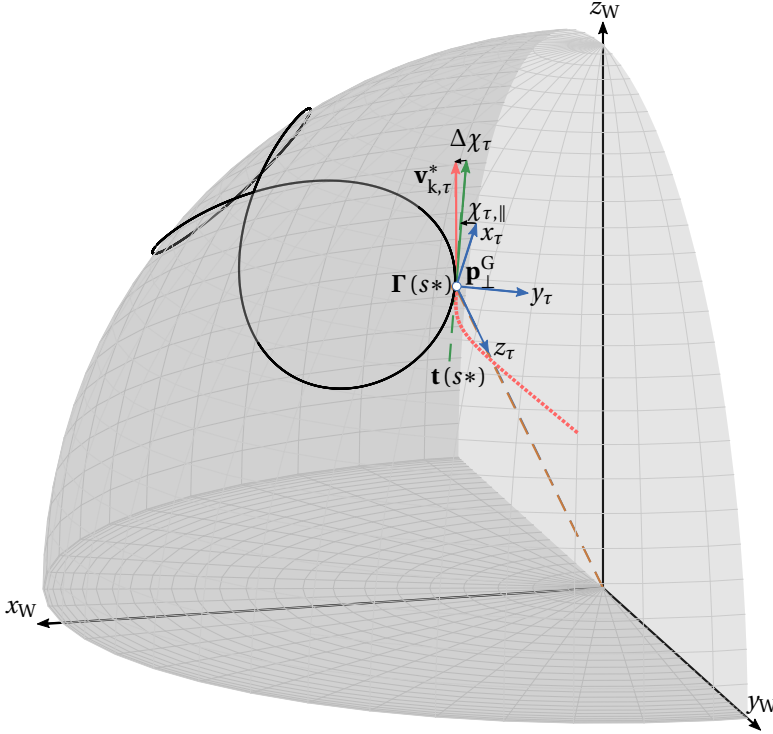


Figure 4.6: Guidance strategy kinematics: As the aircraft flies towards the path the desired flight direction aligns more with the tangent at the target point on the path.

Furthermore, the speed of the path parameter  $s$  is denoted with  $ds/dt = \dot{s}$  and is given by the projection of the velocity vector onto the path tangent:

$$\frac{ds}{dt} = \dot{s} = \frac{\mathbf{t}^\top \mathbf{v}_k^G}{\|\mathbf{t}\|_2 \|\mathbf{p}^G\|_2} = \frac{\mathbf{t}^\top \mathbf{v}_k^G}{\|\mathbf{t}\|_2 h_\tau} \quad (4.53)$$

For convenience, the path can be first defined as a planar curve using scalar functions of  $s$  for longitude and latitude and then transform it into spherical coordinates.

In this work the flight path is given by a laying eight which is a common shape for the reference path in AWE. One advantage for instance over a circular path is that it allows to continuously fly the figure of eight maneuver without twisting the cable. An additional advantage is that the aircraft flies through the power zone which potentially leads to a higher power output. This has however not been verified yet. In the following three different parameterizations for the figure of eight are discussed. One possible parameterization is given by a Lissajous curve which is defined as

$$\begin{aligned} \lambda_\Gamma(s) &= \frac{a_{Lissa}}{h_\tau} \sin s \\ \phi_\Gamma(s) &= \frac{b_{Lissa}}{h_\tau} \sin 2s \end{aligned} \quad (4.54)$$

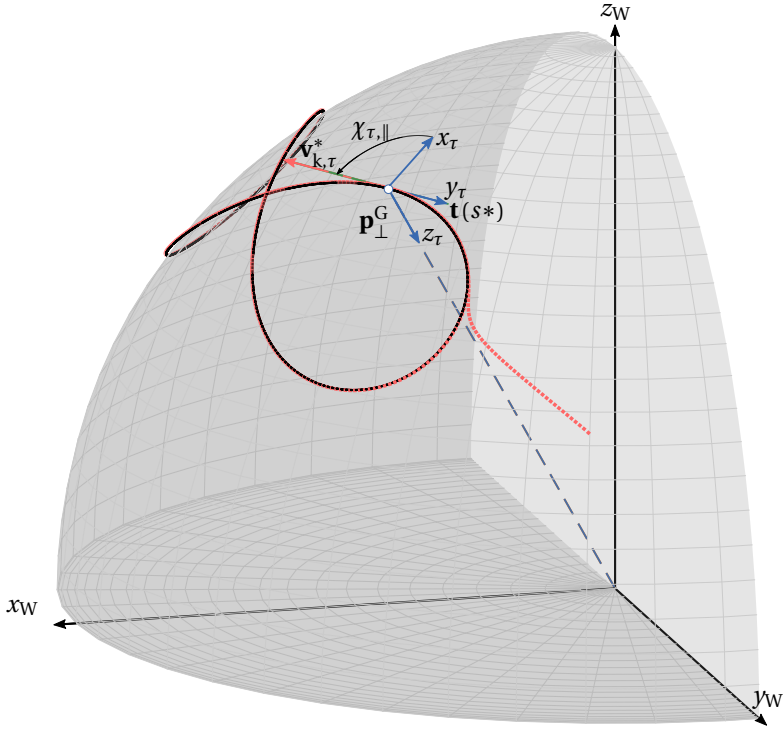


Figure 4.7: Guidance strategy kinematics: If the aircraft is on the path the desired flight direction is aligned with the path tangent.

where  $a_{\text{Lissa}}$  defines the width of the curve and  $b_{\text{Lissa}}$  defines the height [59, p.70]. Since the guidance problem is solved on the unit sphere the path shape is scaled by the current distance of the aircraft to the origin of the  $W$  frame, given by  $h_\tau$ . Defining the path as a Lissajous figure is appealing due to its simplicity and is also chosen in [80]. Other parameterizations include for instance the Lemniscate of Bernoulli [59, p. 52], defined by

$$\begin{aligned}\lambda_\Gamma(s) &= \frac{1}{h_\tau} \frac{a_{\text{Bernoulli}} \sqrt{2} \cos s}{1 + \sin^2 s} \\ \phi_\Gamma(s) &= \frac{1}{h_\tau} \frac{a_{\text{Bernoulli}} \sqrt{2} \sin s \cos s}{1 + \sin^2 s}\end{aligned}\tag{4.55}$$

where  $a_{\text{Bernoulli}}$  can be used to tune the width of the curve. Finally, the Lemniscate of

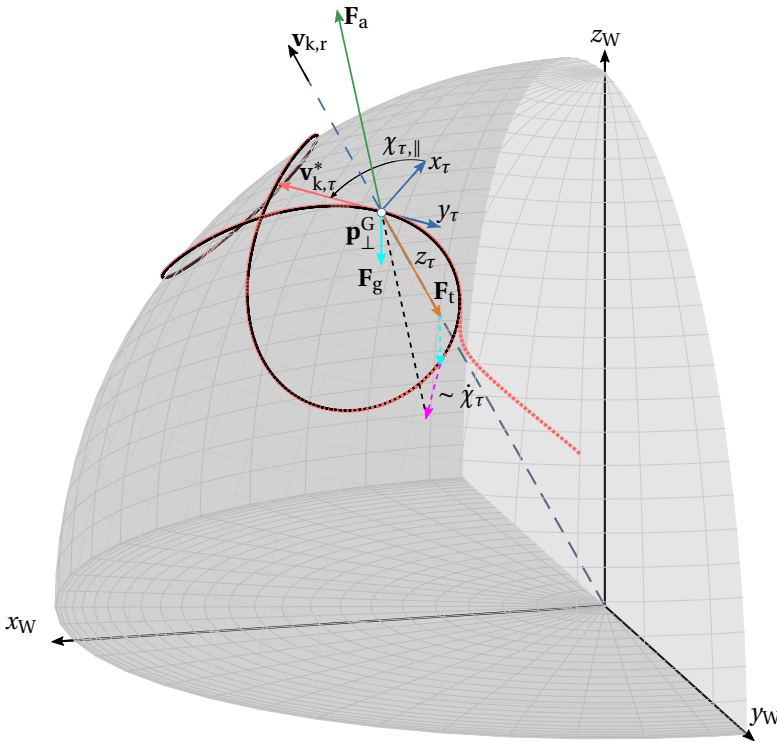


Figure 4.8: Acting forces on the aircraft during the traction phase. The aerodynamic force  $F_a$  needs to compensate gravity  $F_g$  and tether force  $F_t$  as well as the maneuver forces, which are proportional to  $\dot{\chi}_\tau$  (and potentially  $\dot{\gamma}_\tau$ ), in order to follow the flight path.

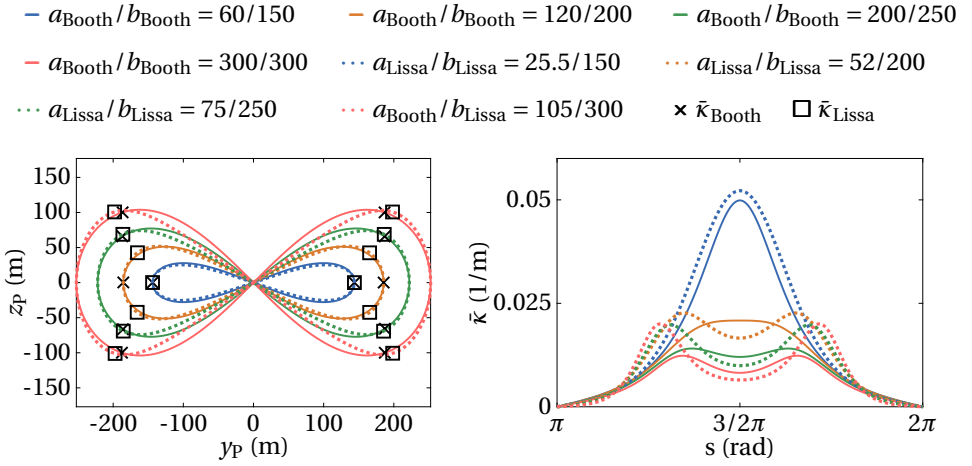
Booth can be used which is defined by

$$\lambda_\Gamma(s) = \frac{1}{h_\tau} \frac{b_{\text{Booth}} \sin s}{1 + \left(\frac{a_{\text{Booth}}}{b_{\text{Booth}}}\right)^2 \cos^2 s}$$

$$\phi_\Gamma(s) = \frac{1}{h_\tau} \frac{a_{\text{Booth}} \sin s \cos s}{1 + \left(\frac{a_{\text{Booth}}}{b_{\text{Booth}}}\right)^2 \cos^2 s}$$
(4.56)

It can be derived from the equation of a hyperbolic Lemniscate as for instance described in [17, p.164].  $a_{\text{Booth}}$  and  $b_{\text{Booth}}$  are parameters that define the height and width of the curve. Different parameter combinations and the resulting curves are depicted in Fig.4.9a.

The Lemniscate of Bernoulli can be regarded as a special case of the Lemniscate of Booth, since if  $a_{\text{booth}}$  and  $b_{\text{booth}}$  are chosen to be equal to  $\sqrt{2}a_{\text{Bernoulli}}$  both curve shapes are identical. Therefore, Booth's Lemniscate provides more flexibility in choosing a certain path shape and therefore only the Lemniscate of Booth and the Lissajous figure parameterizations are compared with each other in the following. For comparison, four different shapes are calculated for each of the two curves. Note, since the curves are com-



(a) Lemniscates and Lissajous curves.

(b) Curvature plots.

Figure 4.9: Paths and corresponding curvatures for different path parameterizations.

pared in this step relative to each other only a planar analysis is conducted. In Fig.4.9a the different path shapes are depicted, where the dotted curves represent the Lissajous curves and the solid lines indicate the Lemniscates. In addition, the planar path curvature is calculated at every point on the path and the result is depicted in Fig.4.9b. Note, due to the symmetry only the left hand side of the figure of eight curvature is shown. The square and the cross markers indicate the points of maximum curvature. The formula for the planar curvature is given by

$$\bar{\kappa} = \frac{\frac{d\Gamma_y(s)}{ds} \frac{d^2\Gamma_z(s)}{ds^2} - \frac{d\Gamma_z(s)}{ds} \frac{d^2\Gamma_y(s)}{ds^2}}{h_r \left( \left( \frac{d\Gamma_y(s)}{ds} \right)^2 + \left( \frac{d\Gamma_z(s)}{ds} \right)^2 \right)^{\frac{3}{2}}} \quad (4.57)$$

where  $\Gamma_y(s)$  and  $\Gamma_z(s)$  represent the y and z coordinate of  $\Gamma(s)$ , respectively. Note, the y and z components are used since the curves are defined in the path frame which is essentially a rotated W frame by the elevation angle.  $h_r$  corresponds to the radius of the sphere which is for this analysis chosen arbitrarily to be 300m. The curvature plots corresponding to the different path shapes show that the curvature peaks of the Lissajous figure are higher than the ones obtained with the Lemniscate. Furthermore, for larger paths significant local maxima in the Lemniscate curvature occur. In this sense the Lemniscate of Booth leads to a smoother path with a less oscillatory curvature. From a control perspective the Lemniscate parameterization possesses advantages over the Lissajous figure for the following reasons. First, the lower curvature peaks require lower maneuver forces. Hence, less aerodynamic force is required to follow the path. This "gain" in lift can then instead be converted in tether tension or can be regarded as a safety reserve to carry out potential emergency maneuvers. Second, the oscillatory curvature of the Lissajous fig-

ure also requires a higher control activity since the bank angle needs to be changed more actively in the utilized bank-to-turn strategy which will be explained later in this work. These advantages of the Lemniscate over the Lissajous curve come, however, at the expense of increased complexity which is especially visible in the derivative terms of the curve parameterization (i.e.  $\mathbf{t}$  and  $\mathbf{t}'$ ). Nevertheless, this drawback is considered to be minor and for that reason the Lemniscate of Booth is chosen in this work to parameterize the figure of eight reference path during the traction phase. The path parameters in the remainder of this work are denoted with  $a_{\text{path}}$  and  $b_{\text{path}}$ , instead of  $a_{\text{booth}}$  and  $b_{\text{booth}}$ , respectively.

Having picked a parameterization for  $\Gamma$  the path following problem can be solved as follows (see also [80]). The distance between any point on the curve and the aircraft position can be calculated using the definition of the arc length on the unit sphere.

$$\delta(s) = \arccos(\mathbf{p}_{\perp}^G \cdot \Gamma(s)) \quad (4.58)$$

where  $\mathbf{p}_{\perp}^G$  is the normal projection of the aircraft position onto the sphere. To determine the closest point (defined by  $s^*$ ) requires to solve

$$\left. \frac{d\delta}{ds} \right|_{s=s^*} = 0 \quad (4.59)$$

where the derivative is given by

$$\frac{d\delta}{ds} = -\frac{1}{\sin\delta} \frac{d(\mathbf{p}_{\perp}^G \cdot \Gamma(s))}{ds} = -\frac{\mathbf{p}_{\perp}^G \cdot \mathbf{t}(s)}{\sin\delta} \quad (4.60)$$

Eventually, the following root-finding problem needs to be solved:

$$\mathbf{p}_{\perp}^G \cdot \mathbf{t}(s) = 0 \quad (4.61)$$

The solution can be determined using for instance *Newton's* method. With

$$\left( \frac{d}{ds} \right) \mathbf{p}_{\perp}^G \cdot \mathbf{t}(s) = \mathbf{p}_{\perp}^G \cdot \frac{d\mathbf{t}(s)}{ds} \quad (4.62)$$

the update equation for *Newton's* method is then

$$s^+ = s^- - \frac{\mathbf{p}_{\perp}^G \cdot \mathbf{t}(s)}{\mathbf{p}_{\perp}^G \cdot \mathbf{t}'(s)} \quad (4.63)$$

In the conducted simulations the method usually converged quickly after two to three iterations if the previous solution is selected as a starting point. For the initialization of the simulation the starting point is chosen manually based on the initial position of the aircraft. In this work, the aircraft is initialized at the trim point at  $s = 0$  which then also represents the initial solution for the root-finding problem. Note, after the retraction phase the guidance module needs to be reinitialized. Depending on if the retraction is flown on the right hand or on the left hand side of the wind window the initial value is selected to be either  $\frac{\pi}{2}$  or  $\frac{3\pi}{2}$ , respectively.

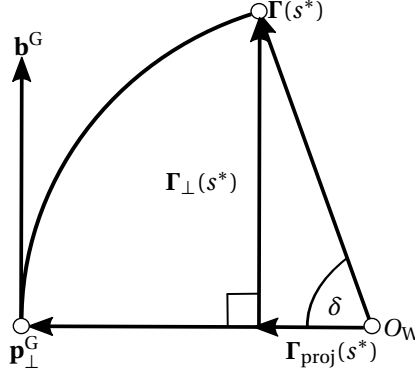


Figure 4.10: Guidance strategy kinematics.

Knowing the closest point on the curve relative to the current aircraft position enables to calculate the desired flight direction. The vector at the current aircraft position pointing towards  $\Gamma(s^*)$  perpendicularly along a great circle can be expressed as

$$\mathbf{b}^G = \frac{\Gamma(s^*) - \cos \delta \mathbf{p}_{\perp}^G}{\sin \delta} \quad (4.64)$$

This can be derived simply by looking at the normal projection of  $\Gamma(s^*)$  onto  $\mathbf{p}_{\perp}^G$  (see Fig. 4.10) given by

$$\Gamma_{\text{proj}}(s^*) = \cos \delta \|\Gamma(s^*)\|_2 \mathbf{p}_{\perp}^G = \cos \delta \mathbf{p}_{\perp}^G \quad (4.65)$$

and

$$\Gamma_{\perp}(s^*) = \Gamma(s^*) - \Gamma_{\text{proj}}(s^*) \quad (4.66)$$

where  $-\Gamma_{\perp}(s^*)$  denotes the vector of the projection direction, which is by definition perpendicular to  $\mathbf{p}_{\perp}^G$ . Normalizing  $\Gamma_{\perp}(s^*)$  yields:

$$\mathbf{b}^G = \frac{\Gamma(s^*) - \Gamma_{\text{proj}}(s^*)}{\|\Gamma(s^*) - \Gamma_{\text{proj}}(s^*)\|_2} = \frac{\Gamma(s^*) - \cos \delta \mathbf{p}_{\perp}^G}{\sin \delta} \quad (4.67)$$

Equation (4.61) can be rewritten using Eq. (4.67):

$$\frac{\Gamma(s^*) \cdot \mathbf{t}(s^*) - \sin \delta (\mathbf{b}^G \cdot \mathbf{t}(s^*))}{\cos \delta} = 0 \quad (4.68)$$

The first scalar product is zero, since  $\Gamma(s^*)$  is perpendicular to the tangent vector, which yields

$$\tan \delta (\mathbf{b}^G \cdot \mathbf{t}(s^*)) = 0 \quad (4.69)$$

If this equation is divided by  $\tan \delta$  and bearing in mind that the only relevant singularity is located at  $\delta = 0$  this yields for  $\delta \neq 0$

$$\mathbf{b}^G \cdot \mathbf{t}(s^*) = 0 \quad (4.70)$$

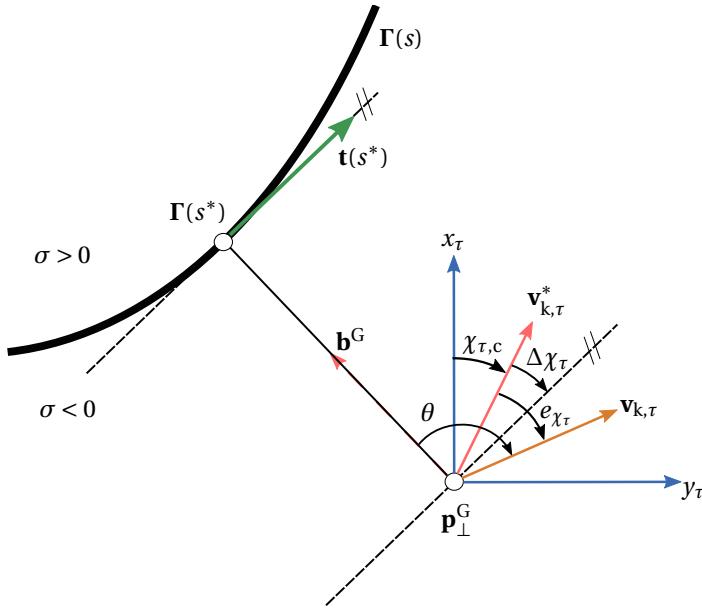


Figure 4.11: Guidance strategy kinematics (detailed). See also Fig. 4.5 for the three dimensional picture.

which proves that the direction vector pointing towards the path is indeed orthogonal to the tangent at  $\Gamma(s^*)$ . Hence, if the kite would fly in  $\mathbf{b}^G$  direction it would intercept the path perpendicularly. From a practical point of view it is, however, not desirable that the aircraft intercepts the path perpendicularly. Instead, the commanded flight direction needs to smoothly transition from an orthogonal interception if the aircraft is farther away from the curve to a tangential, hence, curve aligned flight direction (see also Fig. 4.5-Fig. 4.7). If the aircraft is on the path it is required that the path controller tracks the directional angle of the tangent vector on the curve. This behavior can be achieved as follows: If  $\delta \neq 0$  the course angle  $\chi_{\tau,\parallel}$ , which can be obtained from the orientation of the tangent on the path with respect to the  $x_\tau$  direction, has to be adapted such that the distance to the curve  $\delta$  decreases over time. In [80] the following set point definition is proposed, which is utilized in this work as well:

$$\chi_{\tau,c} = \chi_{\tau,\parallel} + \Delta\chi_\tau \quad (4.71)$$

with

$$\Delta\chi_\tau = \arctan_2(-\sigma(\iota)\delta, \delta_0) \quad (4.72)$$

and

$$\iota = (\mathbf{t}(s^*) \times \Gamma(s^*)) \cdot (\mathbf{p}_\perp^G - \Gamma(s^*)) \quad (4.73)$$

where  $\sigma$  denotes the sign of  $\iota$ . Depending if the aircraft is on the left or the right hand side of the path, as depicted in Fig. 4.11, the sign of  $\Delta\chi_\tau$  is adapted accordingly.

If the course as defined in Eq. (4.71) is tracked by the flight control system, the relative distance  $\delta$  between aircraft and path decreases over time, i.e.  $\dot{\delta} < 0$  with can be

proven as follows. Taking the derivative of Eq. (4.58) with respect to time at  $s = s^*$  yields

$$\dot{\delta} = -\frac{1}{\sqrt{1 - \cos^2 \delta}} (\dot{\mathbf{p}}_{\perp}^G \cdot \boldsymbol{\Gamma}(s^*) + \mathbf{p}_{\perp}^G \cdot \dot{\boldsymbol{\Gamma}}(s^*)) \quad (4.74)$$

with

$$\dot{\boldsymbol{\Gamma}}(s^*) = \mathbf{t}(s^*) \dot{s}^* \quad (4.75)$$

$\mathbf{p}_{\perp}^G \cdot \mathbf{t}(s^*)$  is zero, therefore,

$$\dot{\delta} = -\frac{1}{\sin \delta} (\dot{\mathbf{p}}_{\perp}^G \cdot \boldsymbol{\Gamma}(s^*)) \quad (4.76)$$

With Eq. (4.67) the dot product can be written as

$$\dot{\mathbf{p}}_{\perp}^G \cdot \boldsymbol{\Gamma}(s^*) = \dot{\mathbf{p}}_{\perp}^G \cdot \mathbf{b}^G \sin \delta + \dot{\mathbf{p}}_{\perp}^G \cdot \mathbf{p}_{\perp}^G \cos \delta \quad (4.77)$$

Per definition, the second scalar product on the right hand side is zero. Inserting the result into Eq. (4.76) yields

$$\dot{\delta} = -\dot{\mathbf{p}}_{\perp}^G \cdot \mathbf{b}^G \quad (4.78)$$

This can be further simplified to

$$\dot{\delta} = -v_{k,\tau} \cos \theta \quad (4.79)$$

where  $v_{k,\tau}$  is the magnitude of  $\mathbf{v}_{k,\tau} = \dot{\mathbf{p}}_{\perp}^G$  and  $\theta$  denotes the angle between the vector pointing perpendicularly to  $\boldsymbol{\Gamma}(s^*)$ ,  $\mathbf{b}^G$ , and the projected aircraft velocity on the tangential plane. To calculate  $\theta$  two cases have to be distinguished:

$$\theta = \begin{cases} \pi/2 - \Delta\chi_{\tau} + e_{\chi_{\tau}}, & \text{for } \sigma < 0 \\ \pi/2 + \Delta\chi_{\tau} - e_{\chi_{\tau}}, & \text{for } \sigma > 0 \end{cases} \quad (4.80)$$

where  $e_{\chi_{\tau}}$  is the difference between the desired and the current tangential plane course angle. This yields for  $\dot{\delta}$

$$\dot{\delta} = \begin{cases} -v_{k,\tau} \sin(\Delta\chi_{\tau} - e_{\chi_{\tau}}), & \text{for } \sigma < 0 \\ -v_{k,\tau} \sin(-\Delta\chi_{\tau} + e_{\chi_{\tau}}), & \text{for } \sigma > 0 \end{cases} \quad (4.81)$$

with Eq. (4.72) it follows

$$\begin{aligned} \dot{\delta} &= -\sigma v_{k,\tau} \sin(-\Delta\chi_{\tau} + e_{\chi_{\tau}}) \\ &= -\sigma v_{k,\tau} (-\sin \Delta\chi_{\tau} \cos e_{\chi_{\tau}} + \cos \Delta\chi_{\tau} \sin e_{\chi_{\tau}}) \\ &= -\sigma v_{k,\tau} \left( \frac{\sigma \delta / \delta_0 \cos e_{\chi_{\tau}}}{\sqrt{1 + (\delta / \delta_0)^2}} + \frac{\sin e_{\chi_{\tau}}}{\sqrt{1 + (\delta / \delta_0)^2}} \right) \\ &= \frac{-\sigma v_{k,\tau}}{\sqrt{1 + (\delta / \delta_0)^2}} (\sigma \delta / \delta_0 \cos e_{\chi_{\tau}} + \sin e_{\chi_{\tau}}) \end{aligned} \quad (4.82)$$

where the identities

$$\begin{aligned} \sin(\arctan(x)) &= x / \sqrt{1 + x^2} \\ \cos(\arctan(x)) &= 1 / \sqrt{1 + x^2} \\ \sin(x + y) &= \sin(x) \cos(y) + \cos(x) \sin(y) \end{aligned} \quad (4.83)$$

have been utilized. If the course error dynamics are asymptotically stable i.e.  $e_{\chi_\tau} \rightarrow 0$  then

$$\dot{\delta} = -v_{k,\tau} \frac{\delta/\delta_0}{\sqrt{1 + (\delta/\delta_0)^2}} \quad (4.84)$$

where the fact that  $\sigma^2 = 1$  has been exploited. Equation (4.84) shows that if the commanded course according to Eq. (4.71) is tracked, the distance  $\delta$  strictly decreases over time, which concludes the proof.

The input signal to the path-following controller will be the desired course and flight path angle rates. In an inversion based control approach these rates are usually obtained by filtering the corresponding course and flight path angles. From a geometrical point of view, the reference course rate contains information about the future course angle and hence is linked to the curvature of the path that needs to be followed. If the rate of a reference filter is used only an approximation is obtained if the to be followed path is not a straight line, or a combination thereof. In this case switching between one straight line segment to another simply results in step commands in the course reference angle. This only requires a course rate in the transients which can be reasonably shaped by a linear filter. If the path curvature is not zero the approximated rate of the filter will not keep the system on the path since in general the rate of the filter does not correspond to the rate imposed by the geometry of the path. Hence, although the path-following controller would steer the aircraft towards the path, once the aircraft is on the path it would leave the path again, which can lead to unnecessary control effort and oscillations of the aircraft around the path. Theoretically, this effect can be minimized with high gain tracking error feedback, which, however, can lead to the usual issues of high gain feedback (e.g. instability). Therefore, a different approach is pursued subsequently where the exact required course rate based on the path geometry will be calculated analytically instead of numerically using a filter. The following derivation is also an extension to the work in [80].

The commanded tangential plane course rate is given by  $\chi_{\tau,c}$ , hence the commanded rate can be calculated by taking the derivative of the terms in Eq. (4.71) which yields

$$\dot{\chi}_{\tau,c} = \dot{\chi}_{\tau,\parallel} + \Delta\dot{\chi}_\tau \quad (4.85)$$

with

$$\Delta\dot{\chi}_\tau = -\frac{\sigma/\delta_0}{1 + (\delta/\delta_0)^2} \dot{\delta} \quad (4.86)$$

with Eq. (4.84) this leads to

$$\dot{\chi}_{\tau,c} = \frac{v_{k,\tau} \sigma / \delta_0^2}{(1 + (\delta/\delta_0)^2)^{3/2}} \delta \quad (4.87)$$

It can be seen that for decreasing  $\delta$ , hence small  $\delta/\delta_0$ , the contribution of  $\Delta\dot{\chi}_\tau$  converges linearly to zero. Note,  $\Delta\dot{\chi}_\tau$  is not linked to the path geometry directly. It improves however the path-following performance if  $\delta \neq 0$ . If  $\Delta\dot{\chi}_\tau$  would be neglected only the course error feedback part would adapt  $\dot{\chi}_{\tau,\parallel}$  such that the commanded course rate does not only contain a component that would keep the aircraft parallel to the path. Since this contribution is mainly required for  $\delta \neq 0$ , a too high gain for the course tracking feedback

would probably dominate also  $\dot{\chi}_{\tau,\parallel}$  for  $\delta = 0$ . Hence, using a small gain for the course error feedback in combination with  $\Delta\chi_{\tau}$  increases the performance of the path-following controller. The derivative of  $\chi_{\tau,\parallel}$  is given by

$$\dot{\chi}_{\tau,\parallel} = \frac{d}{dt} \arctan\left(\frac{\mathbf{e}_{y,\tau} \cdot \mathbf{t}^G}{\mathbf{e}_{x,\tau} \cdot \mathbf{t}^G}\right) \quad (4.88)$$

Simplifying yields:

$$\begin{aligned} \dot{\chi}_{\tau,\parallel} &= \frac{1}{1 + \left(\frac{\mathbf{e}_{y,\tau} \cdot \mathbf{t}^G}{\mathbf{e}_{x,\tau} \cdot \mathbf{t}^G}\right)^2} \frac{\frac{d}{dt}(\mathbf{e}_{y,\tau} \cdot \mathbf{t}^G)(\mathbf{e}_{x,\tau} \cdot \mathbf{t}^G) - (\mathbf{e}_{y,\tau} \cdot \mathbf{t}^G) \frac{d}{dt}(\mathbf{e}_{x,\tau} \cdot \mathbf{t}^G)}{(\mathbf{e}_{x,\tau} \cdot \mathbf{t}^G)^2} \\ &= \frac{\frac{d}{dt}(\mathbf{e}_{y,\tau} \cdot \mathbf{t}^G)(\mathbf{e}_{x,\tau} \cdot \mathbf{t}^G) - (\mathbf{e}_{y,\tau} \cdot \mathbf{t}^G) \frac{d}{dt}(\mathbf{e}_{x,\tau} \cdot \mathbf{t}^G)}{(\mathbf{e}_{x,\tau} \cdot \mathbf{t}^G)^2 + (\mathbf{e}_{y,\tau} \cdot \mathbf{t}^G)^2} \\ &= \frac{\frac{d}{dt}(\mathbf{e}_{y,\tau} \cdot \mathbf{t}^G)(\mathbf{e}_{x,\tau} \cdot \mathbf{t}^G) - (\mathbf{e}_{y,\tau} \cdot \mathbf{t}^G) \frac{d}{dt}(\mathbf{e}_{x,\tau} \cdot \mathbf{t}^G)}{\mathbf{t}^G \cdot \mathbf{t}^G} \end{aligned} \quad (4.89)$$

The derivatives in the numerator are given by

$$\begin{aligned} \frac{d}{dt}(\mathbf{e}_{y,\tau} \cdot \mathbf{t}^G) &= \frac{d\mathbf{e}_{y,\tau}}{dt} \cdot \mathbf{t}^G + \mathbf{e}_{y,\tau} \cdot \frac{d\mathbf{t}^G}{dt} \\ \frac{d}{dt}(\mathbf{e}_{x,\tau} \cdot \mathbf{t}^G) &= \frac{d\mathbf{e}_{x,\tau}}{dt} \cdot \mathbf{t}^G + \mathbf{e}_{x,\tau} \cdot \frac{d\mathbf{t}^G}{dt} \end{aligned} \quad (4.90)$$

For the derivatives of the basis vectors the local rate, i.e. at the aircraft, of the longitude and latitude has to be taken into account, which yields

$$\begin{aligned} \frac{d\mathbf{e}_{x,\tau}}{dt} &= \frac{\partial \mathbf{e}_{x,\tau}}{\partial \lambda} \dot{\lambda} + \frac{\partial \mathbf{e}_{x,\tau}}{\partial \phi} \dot{\phi} \\ \frac{d\mathbf{e}_{y,\tau}}{dt} &= \frac{\partial \mathbf{e}_{y,\tau}}{\partial \lambda} \dot{\lambda} + \frac{\partial \mathbf{e}_{y,\tau}}{\partial \phi} \dot{\phi} \end{aligned} \quad (4.91)$$

where the dot represent a derivative with respect to time. The derivative of the tangent vector is given by

$$\frac{d\mathbf{t}^G}{dt} = \frac{d\mathbf{t}^G}{ds} \dot{s} \quad (4.92)$$

This yields

$$\begin{aligned}
\dot{\chi}_{\tau,\parallel} &= \frac{\left(\frac{d\mathbf{e}_{y,\tau}}{dt} \cdot \mathbf{t}^G + \mathbf{e}_{y,\tau} \cdot \frac{d\mathbf{t}^G}{ds} \dot{s}\right) (\mathbf{e}_{x,\tau} \cdot \mathbf{t}^G) - (\mathbf{e}_{y,\tau} \cdot \mathbf{t}^G) \left(\frac{d\mathbf{e}_{x,\tau}}{dt} \cdot \mathbf{t}^G + \mathbf{e}_{x,\tau} \cdot \frac{d\mathbf{t}^G}{ds} \dot{s}\right)}{\mathbf{t}^G \cdot \mathbf{t}^G} \\
&= \frac{\left(\frac{d\mathbf{e}_{y,\tau}}{dt} \cdot \mathbf{t}^G + \mathbf{e}_{y,\tau} \cdot \frac{d\mathbf{t}^G}{ds} \dot{s}\right) \cos(\chi_{\tau,\parallel}) \|\mathbf{t}^G\| - \sin(\chi_{\tau,\parallel}) \|\mathbf{t}^G\| \left(\frac{d\mathbf{e}_{x,\tau}}{dt} \cdot \mathbf{t}^G + \mathbf{e}_{x,\tau} \cdot \frac{d\mathbf{t}^G}{ds} \dot{s}\right)}{\mathbf{t}^G \cdot \mathbf{t}^G} \\
&= \frac{\left(\frac{d\mathbf{e}_{y,\tau}}{dt} \cdot \mathbf{t}^G + \mathbf{e}_{y,\tau} \cdot \frac{d\mathbf{t}^G}{ds} \dot{s}\right) \cos(\chi_{\tau,\parallel}) - \sin(\chi_{\tau,\parallel}) \left(\frac{d\mathbf{e}_{x,\tau}}{dt} \cdot \mathbf{t}^G + \mathbf{e}_{x,\tau} \cdot \frac{d\mathbf{t}^G}{ds} \dot{s}\right)}{\|\mathbf{t}^G\|} \quad (4.93) \\
&= \frac{\begin{pmatrix} \cos(\chi_{\tau,\parallel}) & -\sin(\chi_{\tau,\parallel}) \end{pmatrix} \begin{pmatrix} \left(\frac{\partial \mathbf{e}_{y,\tau}}{\partial \lambda} \dot{\lambda} + \frac{\partial \mathbf{e}_{y,\tau}}{\partial \phi} \dot{\phi}\right) \cdot \mathbf{t}^G + \mathbf{e}_{y,\tau} \cdot \frac{d\mathbf{t}^G}{ds} \dot{s} \\ \left(\frac{\partial \mathbf{e}_{x,\tau}}{\partial \lambda} \dot{\lambda} + \frac{\partial \mathbf{e}_{x,\tau}}{\partial \phi} \dot{\phi}\right) \cdot \mathbf{t}^G + \mathbf{e}_{x,\tau} \cdot \frac{d\mathbf{t}^G}{ds} \dot{s} \end{pmatrix}}{\|\mathbf{t}^G\|}
\end{aligned}$$

with

$$\mathbf{e}_{x,\tau} = \begin{pmatrix} -\sin \phi \cos \lambda \\ -\sin \phi \sin \lambda \\ \cos \phi \end{pmatrix}, \quad \mathbf{e}_{y,\tau} = \begin{pmatrix} -\sin \lambda \\ \cos \lambda \\ 0 \end{pmatrix} \quad (4.94)$$

Equation (4.93) defines the rate with which the angle between the tangent vector  $\mathbf{t}^G$  at the aircraft and the basis vector of the tangent plane frame  $\mathbf{e}_{x,\tau}$  changes as a function of path geometry and aircraft velocity. It hence corresponds to the required course rate to follow a given path geometry with a given kinematic velocity.

The lower level path-following controller requires the course and flight path angle rate  $\dot{\chi}_{k,c}$ ,  $\dot{\gamma}_{k,c}$  as well as the desired flight direction defined by the course and the path angle  $\chi_{k,c}$  and  $\gamma_{k,c}$  from the guidance module, in order to calculate the set points for the attitude controller consisting of aerodynamic bank angle  $\mu_{a,c}$  as well as the angle of attack  $\alpha_{a,c}$ . For this reason it is required that the tangential plane course rate  $\dot{\chi}_{\tau,c}$  is transformed into the corresponding rates for the course and flight path angle  $\dot{\chi}_{k,c}$  and  $\dot{\gamma}_{k,c}$ , respectively. This is achieved using the following kinematic manipulations. The tangential plane course rate occurs in the angular velocity vector between the  $\tau$  and the  $K^*$  frame, for instance given in the rotated kinematic frame  $K^*$ :

$$\left(\boldsymbol{\omega}_{K^*}^{\tau K^*}\right)^{\top} = \begin{pmatrix} -\dot{\chi}_{\tau} \sin \gamma_{\tau} & \dot{\gamma}_{\tau} & \dot{\chi}_{\tau} \cos \gamma_{\tau} \end{pmatrix}_{K^*} \quad (4.95)$$

Note, in [80] it is assumed that  $\gamma_{\tau} \approx 0$  which is only justified if the reeling-out speed is small compared to the onto the tangential plane projected kinematic velocity vector. This is a reasonable assumption for soft-wing kites but not for the considered rigid-wing system considered in this work. Hence, Eq. (4.95) generalizes the result in [80]. Furthermore, Eq. (4.95) offers through  $\dot{\gamma}_{\tau}$  another control degree of freedom that can be used to assist the winch controller in the radial direction motion control. In this work this has not been further investigated, hence  $\dot{\gamma}_{\tau,c}$  is set to zero.  $\left(\boldsymbol{\omega}_{K^*}^{\tau K^*}\right)^{\top}$  can be converted into the angular velocity vector between the O and  $K^*$  frame, denoted with  $\left(\boldsymbol{\omega}_{K^*}^{\text{OK}^*}\right)^{\top}$  according to

$$\left(\boldsymbol{\omega}_{K^*}^{\text{OK}^*}\right)^{\top} = \mathbf{M}_{K^*O} \left(\boldsymbol{\omega}_O^{\text{OW}} + \mathbf{M}_{\text{OW}} \left(\boldsymbol{\omega}_W^{\text{W}\tau}\right) + \left(\boldsymbol{\omega}_{K^*}^{\tau K^*}\right)^{\top}\right) \quad (4.96)$$

It is reasonable to assume that the mean wind direction changes much slower than the transport rate  $(\boldsymbol{\omega})_W^{W\tau}$  and the course rate vector  $(\boldsymbol{\omega})_{K^*}^{TK^*}$ . Hence,  $(\boldsymbol{\omega})_K^{OW}$  can be set to zero. This yields

$$\begin{aligned} (\boldsymbol{\omega})_{K^*}^{OK^*} &= \mathbf{M}_{K^*O} \mathbf{M}_{OW} (\boldsymbol{\omega})_W^{W\tau} + (\boldsymbol{\omega})_{K^*}^{TK^*} \\ &= \begin{pmatrix} \dot{\mu}^* - \dot{\chi}_{k,c} \sin \gamma_k \\ \dot{\gamma}_{k,c} \cos \mu^* + \dot{\chi}_{k,c} \sin \mu^* \cos \gamma_k \\ -\dot{\gamma}_{k,c} \sin \mu^* + \dot{\chi}_{k,c} \cos \mu^* \cos \gamma_k \end{pmatrix}_{K^*} \end{aligned} \quad (4.97)$$

with

$$((\boldsymbol{\omega})_W^{W\tau})^\top = \begin{pmatrix} \dot{\phi} \sin \lambda & -\dot{\phi} \cos \lambda & \dot{\lambda} \end{pmatrix}_W \quad (4.98)$$

Note, the second equality in Eq. (4.97) is a generic expression which can be obtained from the literature for instance from [19, p. 75]. The transformation matrix  $\mathbf{M}_{K^*O}$  can be calculated using the knowledge of the course and the path angle as well as the position of the aircraft in the W frame. With

$$\begin{aligned} (\mathbf{e}_{x,K^*})_O &= \begin{pmatrix} \cos \chi_k \cos \gamma_k \\ \sin \chi_k \cos \gamma_k \\ -\sin \gamma_k \end{pmatrix} \\ (\mathbf{e}_{y,K^*})_O &= \frac{-\mathbf{M}_{OW}(\mathbf{p}^G)_W \times (\mathbf{e}_{x,K^*})_O}{\|-\mathbf{M}_{OW}(\mathbf{p}^G)_W \times (\mathbf{e}_{x,K^*})_O\|_2} \\ (\mathbf{e}_{z,K^*})_O &= (\mathbf{e}_{x,K^*})_O \times (\mathbf{e}_{y,K^*})_O \end{aligned} \quad (4.99)$$

this yields

$$\mathbf{M}_{K^*O} = \begin{pmatrix} (\mathbf{e}_{x,K^*})_O^\top \\ (\mathbf{e}_{y,K^*})_O^\top \\ (\mathbf{e}_{z,K^*})_O^\top \end{pmatrix} \quad (4.100)$$

Ultimately, the desired course and path angle rates can be calculated by solving Eq. (4.97):

$$\begin{aligned} \dot{\chi}_{k,c} &= \frac{\omega_{y,K^*}^{OK^*} \sin \mu_k^* + \omega_{z,K^*}^{OK^*} \cos \mu_k^*}{\cos \gamma_k} \\ \dot{\gamma}_{k,c} &= \omega_{y,K^*}^{OK^*} \cos \mu_k^* - \omega_{z,K^*}^{OK^*} \sin \mu_k^* \end{aligned} \quad (4.101)$$

with

$$\mu^* = \arctan \left( \frac{M_{K^*O,23}}{M_{K^*O,33}} \right) \quad (4.102)$$

where  $M_{K^*O,23}$  and  $M_{K^*O,33}$  denote the elements in the second row and third column as well as in the third row and third column of  $\mathbf{M}_{K^*O}$ , respectively.

The traction phase guidance module can be verified by simulating the tangential plane kinematics. By integrating Eq. (4.85) it can be verified if the reference course rate

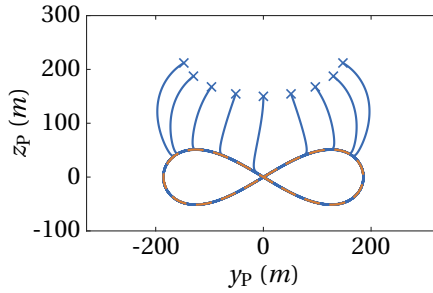


Figure 4.12: Guidance strategy verification. The crosses represent different initial positions, the dashed orange line is the reference path. The trajectories are the projections of the flight path into the path frame, hence the flight paths are curved.

is correctly calculated. In Fig. 4.12 the resulting flight path with different initial positions is depicted. It can be observed that the kinematic model indeed converges towards the path and stays on it. Note, due to the numerical integration of the course rate a small tracking error feedback part needs to be added to Eq. (4.85). Otherwise the numerical error will grow and the model can diverge from the path.

#### 4.3.2. Retraction Phase Guidance

The retraction phase guidance module is separated from the traction phase module since the aircraft is required to fly a straight gliding path instead of a path on a virtual sphere. The supervisory logic switches to the retraction phase according to the high-level state machine status (see Fig. 4.3). The outputs of the retraction guidance module are again course and path angle commands. The gliding path is calculated as soon as the state machine switches into retraction mode. The path is then defined by the connecting line of the position at which the retraction phase got triggered and the target point. Since the retraction phase can be triggered either on the left or the right hand side of the wind window the target point needs to be chosen accordingly: either on the left or the right hand side of the wind window. With the implemented transition strategy no additional guidance module between the retraction and the traction phase is required. Hence, as a target point, a point on the Lemniscate can be chosen. Since the retraction is triggered at either  $s = \pi/2$  or  $s = 3\pi/2$  it makes sense to choose these points as targets for the retraction phase as well, but corresponding to the minimum tether length and the higher elevation angle. The reason for the higher elevation angle will be explained in the next section. The reference course and descend angle are calculated as follows. Denoting the target point with  $(\mathbf{p}_t)_W$  and the initial position where the retraction phase got triggered with  $(\mathbf{p}_i)_W$ . The direction of the gliding path is then simply given by

$$(\mathbf{b})_W = (\mathbf{p}_t)_W - (\mathbf{p}_i)_W \quad (4.103)$$

transforming this vector into the O frame allows to calculate the directional angle of the glide path

$$\chi_{k,\text{path}} = \tan^{-1} \left( \frac{b_{y,O}}{b_{x,O}} \right) \quad (4.104)$$

where  $b_{y,O}$  and  $b_{z,O}$  are the y and z component of the glidepath vector given in the O frame. The current relative position of the aircraft with respect to  $(\mathbf{p}_i)_W$  is given by

$$(\mathbf{p}_{\text{rel}})_W = (\mathbf{p}^G)_W - (\mathbf{p}_i)_W \quad (4.105)$$

In order to regulate the horizontal distance to the path the relative position of the aircraft and the path vector are both projected into the xy plane of the wind frame. Both projected vectors are denoted with  $(\tilde{\mathbf{p}}_{\text{rel}})_W$  and  $(\tilde{\mathbf{b}})_W$ , respectively. The normal projection of the relative aircraft position in the xy plane on the projected retraction path is then given by

$$(\tilde{\mathbf{p}}_{\text{rel},\perp})_W = \frac{(\tilde{\mathbf{p}}_{\text{rel}})_W \cdot (\tilde{\mathbf{b}})_W}{\|(\tilde{\mathbf{b}})_W\|_2^2} (\tilde{\mathbf{b}})_W \quad (4.106)$$

The cross-track error can then be calculated according to:

$$d_p = \|(\tilde{\mathbf{p}}_{\text{rel},\perp})_W - (\tilde{\mathbf{p}}_{\text{rel}})_W\|_2 \quad (4.107)$$

The sign of the cross-track error, that defines if the aircraft is on the left or right hand side of the path can be calculated with Eq. (4.108):

$$\sigma_{d,p} = \text{sign} \left( \begin{pmatrix} 0 \\ 0 \\ 1 \end{pmatrix} \cdot ((\tilde{\mathbf{b}})_W \times (\tilde{\mathbf{p}}_{\text{rel},\perp})_W) \right) \quad (4.108)$$

Denoting further the projection of the kinematic aircraft velocity in the xy-plane of the W frame with  $v_{k,xy}$ , the commanded course angle can finally be calculated using Eq. (4.109):

$$\chi_{k,c} = \chi_{k,\text{path}} + \sigma_{d,p} \arcsin \left( \min \left( \max \left( \frac{k_{rt,\chi} d_p}{v_{k,xy}}, -1 \right), 1 \right) \right) \quad (4.109)$$

The second term regulates the horizontal distance to the reference path to zero as a function of the cross-track error  $d_p$  as well as the horizontal kinematic speed  $v_{k,xy}$ . The parameter  $k_{rt,\chi} > 0$  is a tuning parameter. For large values of  $k_{rt,\chi}$  the approach towards the path is more perpendicular while for smaller values it is more tangential. In this work a value of 0.1 leads to acceptable results.

The descend angle command is obtained in a similar manner. The descend angle of the path is given by

$$\gamma_{k,\text{path}} = -\arctan \left( \frac{p_{i,z,W} - p_{t,z,W}}{\sqrt{((p_{i,x,W} - p_{t,x,W})^2 + (p_{i,y,W} - p_{t,y,W})^2)}} \right) \quad (4.110)$$

where  $p_{i,z,W}$  and  $p_{t,z,W}$  are the initial and target altitudes, respectively. The projection of the relative position of the aircraft onto the descend path is given by

$$(\mathbf{p}_{\text{rel},\perp})_W = \frac{(\mathbf{p}_{\text{rel}})_W \cdot (\mathbf{b})_W}{\|(\mathbf{b})_W\|_2^2} (\mathbf{b})_W \quad (4.111)$$

The vertical distance  $d_z$  to the path is then simply given by the difference of the third components of  $(\mathbf{p}_{\text{rel},\perp})_W$  and  $(\mathbf{p}_{\text{rel}})_W$ . Eventually, the descend angle command can be calculated using Eq. (4.112).

$$\gamma_{k,c} = \gamma_{k,\text{path}} + \arcsin \left( \min \left( \max \left( \frac{k_{\text{rt},\gamma} d_z}{v_k}, -1 \right), 1 \right) \right) \quad (4.112)$$

where  $v_k$  is the kinematic speed and  $k_{\text{rt},\gamma}$  is again a tuning parameter which is chosen to be 0.06.

Note, at the end of the retraction path a flare maneuver is initiated as long as the airspeed of the aircraft is above a tuned threshold value, denoted with  $v_a$ . This maneuver reduces the ground speed of the aircraft through a conversion of kinetic into potential energy and allows a smoother transition into the figure of eight. The flare maneuver is defined by two parameters. The first parameter defines where on the retraction path the flare is initiated, here denoted with  $x_{f,i}$  (=50 m before the target point), the second parameter defines the final descend/ascend angle, here denoted with  $\gamma_f$  (=10°). Note, for a higher robustness only the x component in the W frame is used, hence it is not required that the aircraft is close to the target point in all three dimensions before the transition phase is triggered. In this case the adaption of the path angle during the flare maneuver is a function of the x coordinate of the aircraft position ( $p_{x,W}^G$ ). The overall descend angle command during the retraction phase is then defined by:

$$\gamma_{k,c} = \begin{cases} \gamma_{k,\text{path}} + \frac{\gamma_{k,\text{path}} - \gamma_f}{x_{f,i} - p_{t,x,W}} (p_{x,W}^G - x_{f,i}), & \text{for } p_{x,W}^G \leq x_{f,i} \wedge v_a > v_a \\ \text{Eq.(4.112)}, & \text{otherwise} \end{cases} \quad (4.113)$$

where  $v_a$  is set to  $25 \text{ m s}^{-1}$ .

Due to the potentially lower kinematic speed during the retraction phase, the wind speed can be similar to the kinematic speed. This does not justify, at least theoretically, to set the kinematic equal to the aerodynamic entities. Therefore, in order to account for wind effects, the kinematic course and path angle commands  $\chi_{k,c}$  and  $\gamma_{k,c}$  are adjusted: The actual required aerodynamic path angle can be calculated using Eq. (4.114) and Eq. (4.115), which has been derived in [14, p. 20-23].

$$\chi_{a,c} = \chi_{k,c} + \beta_a - \arcsin \left( \frac{1}{v_a \cos \gamma_a} (v_{w,y,O} \cos \chi_{k,c} - v_{w,x,O} \sin \chi_{k,c}) \right) \quad (4.114)$$

$$\begin{aligned} \gamma_{a,c} &= \arcsin \left( \frac{v_k \sin \gamma_{k,c} + v_{w,z,O}}{v_a} \right) \\ &\approx \arcsin \left( \frac{v_k \sin \gamma_{k,c}}{v_a} \right) \end{aligned} \quad (4.115)$$

where  $v_{w,x,O}$ ,  $v_{w,y,O}$  and  $v_{w,z,O}$  are the components of the wind velocity in the O frame. Notice that the calculation of  $\gamma_a$  requires the knowledge of the wind component in  $z_O$  direction  $v_{w,z,O}$  which is, however, small compared to  $v_a$  and hence can be neglected. Note, in practice the benefit of being able to account for the wind in the calculation of the reference path angles needs to be traded off against the impact of wind measurement/estimation errors. If no wind measurements or estimations are available the correction can be removed which, however, will lead to a higher control effort.

### 4.3.3. Transition Strategy from the Retraction to the Traction Phase

In this section the transition strategy that connects the retraction phase with the traction phase is presented. The main challenge in this part of the pumping cycle is represented by the rising tether tension i.e. from low tension during the retraction to high tension during the traction phase. Furthermore, since both phases are fundamentally different from a control perspective, a transition strategy from straight line following (retraction) to path following on a virtual sphere (traction) needs to be implemented. In the following several elementary solutions will be discussed before the final method is presented.

The most basic approach is to directly switch into the figure of eight path following mode as soon as the end of the retraction path is reached which does not require any intermediate guidance strategy. Another option is to include a planar circular arc at the end of the retraction phase that defines the turning radius for the transition phase. This delays the activation of the traction mode until the aircraft is steered sufficiently back into the wind which can be defined by a waypoint on the arc. The drawback of the first approach is the reduced level of guidance and hence it is difficult to shape the transient behavior. Since the same controller for the transient as for the traction phase is used, in order to avoid unnecessary switching between different controllers, tuning of the controller for better transient behavior would also alter the controller for the traction phase. The downside of the second approach is that it requires additional parameters to be tuned such as the length and curvature of the arc. Modifying the figure of eight would most likely also require to modify the geometry of the arc. It can be seen that both approaches are complementary in terms of additional complexity and level of guidance.

The advantages of both approaches can be combined in the following third alternative. Instead of defining a new arc (or any other transition path segment), the same but rotated figure of eight curve that is used during the traction phase is utilized. This is similar to the first approach where the traction phase is directly triggered at the end of the retraction phase. However, instead of directly approaching the traction phase path at a low elevation angle (power zone) a figure eight curve at a high elevation angle is used to enable a higher degree of guidance (advantage of the second approach). During the transient the curve is rotated towards the desired elevation angle for the traction phase. In combination with a shaped tether force set point change a smooth transition from straight path following with low tether tension to figure of eight flight path following with high tether tension can be achieved. The mathematical implementation of this approach is discussed in the following.

The path shape is defined by Eq. (4.56). Transforming the path definition from spher-

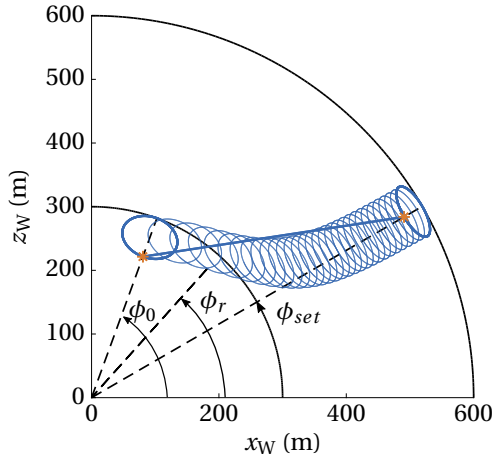


Figure 4.13: Side view of the reference path. The straight line that connects the orange dots represents the retraction path.

ical into Cartesian coordinates yields

$$(\mathbf{\Gamma})_P = \begin{pmatrix} \cos \lambda_\Gamma \cos \phi_\Gamma \\ \sin \lambda_\Gamma \cos \phi_\Gamma \\ \sin \phi_\Gamma \end{pmatrix} \quad (4.116)$$

where the subscript P denotes the path frame. It is essentially defined in the same way as the Wind reference frame W but is tilted by an angle  $\phi_r$  around the  $y_W$  axis. The reference path in the W frame is then given by

$$(\mathbf{\Gamma}^*)_W = \begin{pmatrix} \cos \phi_r & 0 & -\sin \phi_r \\ 0 & 1 & 0 \\ \sin \phi_r & 0 & \cos \phi_r \end{pmatrix} (\mathbf{\Gamma})_P \quad (4.117)$$

Note that this redefinition of the path requires also a small modification in the algorithm that finds the closest point on the path with respect to the current position. However, since the rotation matrix in Eq. (4.117) is constant with respect to  $s$ , the derivatives are not impacted and only the final result needs to be changed. Concretely, the target on the path as well as the tangent and its derivative with respect to  $s$  need to be rotated by  $\phi_r$  using the same rotation matrix as utilized in Eq. (4.117).

The transient of the rotation angle  $\phi_r$  is shaped using a first order filter with time constant  $\tau_r$  and set point  $\phi_{set}$  which corresponds to the reference elevation angle during the traction phase:

$$\dot{\phi}_r = \begin{cases} 0 & \text{if } \Delta\phi > \bar{\Delta}\phi \\ -\frac{1}{\tau_r}\phi_r + \frac{1}{\tau_r}\phi_{set}, & \phi_r(t=0) = \phi_0 \quad \text{else} \end{cases} \quad (4.118)$$

In order to avoid that the path is rotated too quickly, which would essentially render the transition strategy ineffectively,  $\dot{\phi}_r$  is set equal to zero as soon as the arc length on the unit sphere  $\Delta_\phi$  between the path and the current projected position of the aircraft exceeds a certain threshold  $\bar{\Delta}_\phi$ . This threshold is set to one degree for the subsequent simulations.  $\Delta_\phi$  is given by

$$\begin{aligned}\Delta_\phi &= \tilde{\phi}^G - \tilde{\phi}^t \\ \tilde{\phi}^G &= \arccos \left( \frac{(\mathbf{p}_{xy}^G)_W^\top (\mathbf{p}^G)_W}{\|(\mathbf{p}_{xy}^G)_W\|_2 \|(\mathbf{p}^G)_W\|_2} \right) \\ \tilde{\phi}^t &= \arccos \left( \frac{(\mathbf{p}_{xy,t})_W^\top (\mathbf{p}_t)_W}{\|(\mathbf{p}_{xy,t})_W\|_2 \|(\mathbf{p}_t)_W\|_2} \right)\end{aligned}\quad (4.119)$$

where  $(\mathbf{p}_{xy}^G)_W$  and  $(\mathbf{p}_{xy,t})_W$  are the normal projections onto the  $x_W y_W$  plane of the aircraft position  $(\mathbf{p}^G)_W$  and the target on the path  $(\mathbf{p}_t)_W$ , respectively. All vectors are given in the wind reference frame.

The time constant  $\tau_r$  in Eq. (4.118) is a tuning parameter that defines how quickly the path is rotated into the power zone. In the limit, as  $\tau_r$  goes to zero the transition scenario without guidance is reached. Contrarily, for large time constants the aircraft will fly most of the time at high elevation angles which will reduce the power output. Hence, the parameter value reflects the trade-off between robustness (large  $\tau_r$ ) and larger power output (small  $\tau_r$ ). This is discussed in more detail in chapter 6. Note, the initial condition is usually chosen smaller than 90 degrees (between 70 and 80 degrees) otherwise this would cause the aircraft to overfly the ground station. The filter is reset at the beginning of the transition phase.

## 4.4. Path Following Loop

Two different path following loops are implemented. The first loop calculates the attitude commands based on the outputs of the traction and transition guidance module. The second loop uses the outputs of the retraction phase guidance to calculate the attitude commands. The attitude commands are calculated using a nonlinear dynamic inversion strategy based on the point mass dynamics of the aircraft.

### 4.4.1. Traction Phase

In the path loop the commanded course and path angles as well as their corresponding rates, which are the outputs of the guidance module, are used to calculate the set points for the attitude loop. The overall pseudo control inputs are given in a proportional-differential form:

$$\begin{aligned}v_\chi &= \dot{\chi}_{k,c} + k_{p,\chi_k} (\chi_{k,c} - \chi_k) \\ v_\gamma &= \dot{\gamma}_{k,c} + k_{p,\gamma_k} (\gamma_{k,c} - \gamma_k)\end{aligned}\quad (4.120)$$

The set points of the attitude controller can then be derived using the inverted model for the path dynamics (see Eq. (2.10)) and inserting the pseudo control inputs given by

Eq. (4.120). The inverted model can be derived as follows: The total acceleration of the aircraft in the kinematic frame can be written as

$$(\dot{\mathbf{v}}_k)_K^O = \begin{pmatrix} \dot{v}_k \\ 0 \\ 0 \end{pmatrix}_K + (\boldsymbol{\omega})_K^{OK} \times \begin{pmatrix} v_k \\ 0 \\ 0 \end{pmatrix}_K = \begin{pmatrix} \dot{v}_k \\ \dot{\chi}_k \cos \gamma_k v_k \\ -\dot{\gamma}_k v_k \end{pmatrix}_K = \begin{pmatrix} a_{x,K} \\ a_{y,K} \\ a_{z,K} \end{pmatrix}_K \quad (4.121)$$

The path dynamic are then defined according to

$$m_a \begin{pmatrix} a_{x,K} \\ a_{y,K} \\ a_{z,K} \end{pmatrix}_K = (\mathbf{F}_a)_K + (\mathbf{F}_g)_K + (\mathbf{F}_t)_K \quad (4.122)$$

involving the aerodynamic force  $(\mathbf{F}_a)_K \in \mathbb{R}^{3 \times 1}$ , gravitational force  $(\mathbf{F}_g)_K \in \mathbb{R}^{3 \times 1}$  as well as the tether force  $(\mathbf{F}_t)_K \in \mathbb{R}^{3 \times 1}$  in the K frame, where gravity and tether force are calculated with

$$(\mathbf{F}_g)_K = \begin{pmatrix} -\sin \gamma_k m_a g \\ 0 \\ \cos \gamma_k m_a g \end{pmatrix} \quad (4.123)$$

and

$$(\mathbf{F}_t)_K = -\mathbf{M}_{KO} \frac{(\mathbf{p})_O}{\|(\mathbf{p})_O\|_2} F_t \quad (4.124)$$

Note, in order to keep the dimension of the resulting control law low, a straight line tether approximation is utilized. Solving for the aerodynamic force yields

$$\begin{pmatrix} f_{a,x,K} \\ f_{a,y,K} \\ f_{a,z,K} \end{pmatrix}_K = m_a \begin{pmatrix} a_{x,K} \\ a_{y,K} \\ a_{z,K} \end{pmatrix}_K - (\mathbf{F}_g)_K - (\mathbf{F}_t)_K = (\mathbf{F}_a)_K \quad (4.125)$$

The last two rows can be written as

$$\begin{aligned} f_{a,y,K} &= \cos \mu_k f_{a,y,\bar{K}} - \sin \mu_k f_{a,z,\bar{K}} \\ f_{a,z,K} &= \sin \mu_k f_{a,y,\bar{K}} + \cos \mu_k f_{a,z,\bar{K}} \end{aligned} \quad (4.126)$$

where  $\mu_k$  is the kinematic bank angle, i.e. the rollangle around the kinematic velocity vector and

$$\begin{aligned} f_{a,y,\bar{K}} &= -\cos \alpha_k \sin \beta_k f_{a,x,B} \\ &\quad + \cos \beta_k f_{a,y,B} - \sin \alpha_k \sin \beta_k f_{a,z,B} \\ f_{a,z,\bar{K}} &= -\sin \alpha_k f_{a,x,B} + \cos \alpha_k f_{a,z,B} \end{aligned} \quad (4.127)$$

Notice that  $\alpha_k$  and  $\beta_k$  are the kinematic angle of attack and kinematics sideslip angle. Since the inner loop controller actively controls the sideslip angle  $\beta_a$ , i.e. the aerodynamic sideslip angle, the aerodynamic side force  $f_{a,y,B}$  is approximately zero. Hence,

$$\begin{aligned} f_{a,y,\bar{K}} &= -\cos \alpha_k \sin \beta_k f_{a,x,B} - \sin \alpha_k \sin \beta_k f_{a,z,B} \\ f_{a,z,\bar{K}} &= -\sin \alpha_k f_{a,x,B} + \cos \alpha_k f_{a,z,B} \end{aligned} \quad (4.128)$$

Note, in the traction phase the kinematic speed is usually much higher than the wind speed. Therefore, in order to design the traction phase control law it is assumed that the kinematic angles can be approximated by the aerodynamic angles. This assumption is dropped for the retraction phase where the kinematic speed can be similar to the wind speed in magnitude. Therefore, the set point for the kinematic bank angle, corresponding to the required course and path angle rate as well as the tether force set point, is calculated by solving Eq. (4.126) with  $\beta_k \approx \beta_a \approx 0$  for  $\mu_k$  and inserting the pseudo-control signals for the course and path angle rates:

$$\mu_{a,c} \approx \mu_{k,c} = \arctan \left( \frac{m_a v_\chi \cos \gamma_k v_k - f_{t,y,K}}{m_a v_\gamma v_k + m_a g \cos \gamma_k + f_{t,z,K}} \right) = \arctan \left( \frac{\bar{f}_{y,K}}{\bar{f}_{z,K}} \right) \quad (4.129)$$

Under the assumption that the kinematic frame and the rotated aerodynamic frame are nearly identical in the traction phase, the commanded bank angle rotates the lift vector by  $\mu_{k,c}$ . In this case the numerator and denominator in Eq. (4.129) allow to estimate the required lift force to track the pseudo-control signals  $v_\chi$  and  $v_\gamma$  as well as to compensate the weight of the aircraft and the tether tension. This approach is originally presented in [68] for an untethered aircraft. In this case the required lift force can be approximated by

$$L_c \approx \sqrt{\bar{f}_{y,K}^2 + \bar{f}_{z,K}^2} \quad (4.130)$$

Note, due to the wind influence this is only an approximation which, however, works well during the traction phase where the kinematic speed is sufficiently higher compared to the wind speed. Since the lift is a function of the angle of attack the required lift force can be first translated into a required lift coefficient according to:

$$C_{L,c}(\alpha_a) = \frac{L_c}{\bar{q} S_{\text{ref}}} \quad (4.131)$$

where  $\bar{q}$  is the dynamic pressure. Finally, inverting the lift coefficient yields the angle of attack command:

$$\alpha_{a,c} = C_{L,c}^{-1} \left( \frac{L_c}{\bar{q} S_{\text{ref}}} \right) \quad (4.132)$$

Note, since only a proportional feedback part of the course and path angle tracking error is used no anti-windup or hedging is required in this loop. The numerical values of the outer loop controller are summarized in Table 4.1.

For the linear inner loop controllers an additional kinematic transformation is required that transforms the kinematic bank angle into the corresponding tangential plane role angle  $\Phi_{\tau,c}$  which is then tracked by the inner loop. The transformation strategy is as

Table 4.1: Tuned parameters of the outer loop traction phase controller.

$k_{p,\chi_k}$	$k_{p,\gamma_k}$
1	1

follows. First, the orientation of the  $\bar{\mathbf{K}}$  frame with respect to the tangential plane is determined. Then a componentwise comparison of the left and right hand side of Eq. (4.133) is used to translate the kinematic bank angle with respect to the tangential plane into the tangential plane roll angle.

$$\mathbf{M}_{\tau B} = \mathbf{M}_{\tau \bar{\mathbf{K}}} \mathbf{M}_{\bar{\mathbf{K}} B} \quad (4.133)$$

The kinematic bank angle with respect to the tangential plane is simply given by:

$$\mu_{k,\tau,c} = \mu_{k,c} - \mu^* \quad (4.134)$$

where  $\mu^*$  can be calculated with Eq. (4.102). Equation (4.134) simply represents the relationship between the three kinematic frames as depicted in Fig. 2.9. Finally, using the component-wise comparison of both sides of Eq. (4.133) yields the following formula to calculate the tangential plane roll angle:

$$\Phi_{\tau,c} = \arcsin \left( \frac{\cos \gamma_{k,\tau} \cos \beta_k (\sin \mu_{k,\tau,c} - \tan \gamma_{k,\tau} \tan \beta_k)}{\cos \Theta_\tau} \right) \quad (4.135)$$

#### 4.4.2. Retraction Phase

For the retraction phase the course and path angle controllers are designed similarly to the traction phase controllers. However, since the kinematic speed and the wind speed can be similar in this operational phase, the assumption that the kinematic angles are approximately the same as the aerodynamic angles needs to be dropped. In this case it is more convenient to derive the bank angle and angle of attack commands using the point mass dynamics given in the rotated aerodynamic frame which are defined in Eq. (2.17). The last two rows of Eq. (2.17) can be written as:

$$\begin{aligned} m_a v_a \dot{\chi}_a \cos \gamma_a &= f_{t,y,\bar{\mathbf{A}}} + \sin \mu_a L \\ m_a v_a \dot{\gamma}_a &= -\cos \gamma_a m_a g + f_{t,z,\bar{\mathbf{A}}} + \cos \mu_a L \end{aligned} \quad (4.136)$$

Note, the tether force components  $f_{t,y,\bar{\mathbf{A}}}$  and  $f_{t,z,\bar{\mathbf{A}}}$  are a function of position,  $\chi_a$ ,  $\gamma_a$  and the tether tension  $F_t$ . Equivalently,

$$\begin{aligned} m_a v_a \dot{\chi}_a \cos \gamma_a - f_{t,y,\bar{\mathbf{A}}} &= \sin \mu_a L \\ m_a v_a \dot{\gamma}_a + \cos \gamma_a m_a g + f_{t,z,\bar{\mathbf{A}}} &= \cos \mu_a L \end{aligned} \quad (4.137)$$

In order to calculate the bank angle command and the required lift,  $\dot{\chi}_a$  and  $\dot{\gamma}_a$  need to be replaced by the pseudo-control inputs of the retraction phase  $v_{\chi_a}$  and  $v_{\gamma_a}$  (Eq. (4.115))

Table 4.2: Tuned parameters of the outer loop retraction phase controller.

$\omega_{0,\chi_a}$	$\omega_{0,\gamma_a}$	$k_{p,\chi_a}$	$k_{i,\chi_a}$	$k_{p,\gamma_a}$	$k_{i,\gamma_a}$
1.5	1	0.6	0.06	2.4	0.05

and Eq. (4.114)). The two pseudo control inputs are calculated according to

$$\begin{aligned} v_{\chi_a} &= v_{\chi_a,\text{ref}} + k_{p,\chi_a} (\chi_{a,\text{ref}} - \chi_a) + k_{i,\chi_a} \int_0^t (\chi_{a,\text{ref}} - \chi_a) d\tau \\ v_{\gamma_a} &= v_{\gamma_a,\text{ref}} + k_{p,\gamma_a} (\gamma_{a,\text{ref}} - \gamma_a) + k_{i,\gamma_a} \int_0^t (\gamma_{a,\text{ref}} - \gamma_a) d\tau \end{aligned} \quad (4.138)$$

This yields

$$\begin{aligned} \mu_{a,c} &= \arctan \left( \frac{m_a v_a v_{\chi_a} \cos \gamma_a - f_{t,y,\bar{A}}}{m_a v_a v_{\gamma_a} + \cos \gamma_a m_a g + f_{t,z,\bar{A}}} \right) = \arctan \left( \frac{\bar{f}_{y,\bar{A}}}{\bar{f}_{z,\bar{A}}} \right) \\ L_c &= \sqrt{\bar{f}_{y,\bar{A}}^2 + \bar{f}_{z,\bar{A}}^2} \end{aligned} \quad (4.139)$$

The angle of attack command is then again obtained by inverting the corresponding lift coefficient given the current airspeed.

The reference signals for the course and the path angle  $\chi_{a,\text{ref}}$  and  $\gamma_{a,\text{ref}}$  are generated with linear reference filters. Although first order filters would be sufficient second order filters smooth additionally the commanded signal (see also [83]) and are therefore also utilized in this work. Since for the retraction controller an integral feedback part is implemented an anti-windup scheme in form of PCH is implemented. With the hedging signal  $v_{\chi_{a,h}}$  the equations of the second order filter, here exemplary displayed for the course, are defined by

$$\begin{aligned} \dot{v}_{\chi_a} &= -2\zeta\omega_{0,\chi_a} v_{\chi_a} + \omega_{0,\chi_a}^2 (\chi_{a,c} - \chi_{a,\text{ref}}) \\ \dot{\chi}_{a,\text{ref}} &= v_{\chi_a} - v_{\chi_{a,h}} \end{aligned} \quad (4.140)$$

Note, these equations can also be written as two in series connected first order filters. For an aperiodic filter, i.e.  $\zeta = 1$ , the bandwidth of the filter that smooths the commanded signal is  $0.5\omega_{0,\chi_a}$  and the second first order filter bandwidth is  $2\omega_{0,\chi_a}$ . Figure 4.14 depicts the structure of the reference filter. The path angle filter is implemented analogously. Note, the course reference angle as well as the course tracking error itself need to be wrapped to  $\pm\pi$  which is indicated by the wrap2pi blocks in Fig. 4.14. The numerical values of the outer loop retraction flight controller are summarized in Table 4.2.

Similar to the traction phase attitude command a kinematic transformation is required for the linear inner loop controllers. Hence, the commanded bank angle needs to be transformed into the corresponding roll angle which is then tracked by the inner loop retraction phase controller. Note, in this case the roll angle with respect to the ground (i.e. O frame) is required. The transformation is given by

$$\Phi_c = \arcsin \left( \frac{\cos \gamma_a \cos \beta_a (\sin \mu_{a,c} - \tan \gamma_k \tan \beta_a)}{\cos \Theta} \right) \quad (4.141)$$

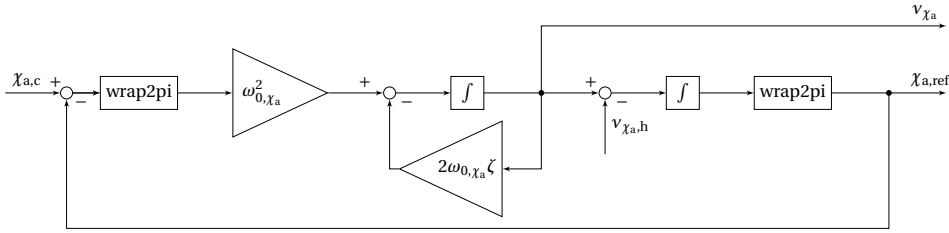


Figure 4.14: Second order reference filter for first order inversion with hedging signal.

## 4.5. Winch Controller

In this section a simple but effective winch controller is introduced that tracks the current tether force set point. Only the mechanical part (i.e. the winch) of the ground station is modeled. Modeling the electrical drive system is important if the overall power plant efficiency is analyzed but for the pumping cycle control part it does not play a significant role since the time constant of the electrical drive system is much lower compared to the mechanical part. Under this assumption the ground station dynamics are represented by a first order system. The input to the system is on the one hand the mechanical torque generated by the tether force (load) and on the other hand the torque generated by the electrical drive system. In this work the winch controller calculates the required torque that needs to be tracked by the drive control system. Since the electrical drive is not modeled it is assumed that this torque is directly applied to the winch.

The control objective of the winch is to track a high tension in the tether during the traction phase and a low tension set point in the retraction phase. This is achieved using a low-pass filtered proportional-integral controller that uses the tether force tension tracking error as an input and outputs the desired torque. The control law, stated as a transfer function, is then given by:

$$M_{W,c} = \frac{s k_{p,w} \omega_{0,w} + k_{i,w} \omega_{0,w}}{s(s + \omega_{0,w})} (F_{t,m} - F_{t,set}) \quad (4.142)$$

where  $s$  is the Laplace variable,  $\omega_{0,w}$  is the bandwidth of the low pass filter,  $k_{p,w}$  is the proportional gain,  $k_{i,w}$  is the integral gain,  $F_{t,m}$  is the measured tether force on the ground and  $F_{t,set}$  is the tether force set point. With this control law the winch accelerates if  $F_{t,m} - F_{t,set} > 0$  which leads to a higher reeling out speed, hence a lower airspeed and as a result the tension in the tether will drop. Contrarily, if the tension in the tether is below the set point i.e.  $F_{t,m} - F_{t,set} < 0$  the winch decelerates, hence the reeling speed reduces which leads to an increase in airspeed and as a result the tether force will increase. Although simple, this control law leads to an acceptable tracking performance in different wind conditions. Since the tether tension is directly controlled, it can more reliably keep the tether force below its maximum limit compared to a winch controller that tracks for instance a speed set point. The latter approach is usually encountered in the literature as reviewed in section 1.3. The winch control parameters are listed in Table 4.3.

Table 4.3: Tuned winch controller gains and filter bandwidths.

$k_{p,w}$	$k_{i,w}$	$\omega_{0,w}$ (rad/s)	$\omega_{0,ft}$ (rad/s)
0.48	0.026	12.6	0.25

Note that additionally the tether force set point change from the retraction to the traction phase is smoothed using a critically damped second order filter given by

$$F_{t,set} = \frac{\omega_{0,ft}^2}{s^2 + 2\omega_{0,ft}s + \omega_{0,ft}^2} F_{t,set,unfiltered} \quad (4.143)$$

where  $\omega_{0,ft}$  is the natural frequency of the filter as defined in Table 4.3.

Note that the set point change from traction to retraction is not smoothed in order to quickly reduce the tension in the tether. Otherwise, if the tether is still under high tension the aircraft would first gain altitude while flying into the wind as soon as the retraction guidance module is activated. As explained before, this is counteracted by letting the aircraft still follow the figure of eight path until the tether tension drops below a chosen threshold. In order to keep this transition short the set point change is not filtered.

## 4.6. Outer Loop Controller Verification

The last part of the second step in the control system design guideline (see Fig. 1.8) represents the verification of the outer loop using the 3-DoF model derived in section 2.3. More specifically, it is assessed in this step if the controller is able to guide the aircraft with sufficient accuracy along the traction as well the retraction reference flight paths. The outer loop calculates the set points based on the inversion of the point mass dynamics as well as the pseudo-control inputs. In order to smooth large set point changes, the commanded bank angle and angle of attack are low pass filtered with a bandwidth of  $\omega_{0,\mu,em} = 3 \text{ rad s}^{-1}$  and  $\omega_{0,\alpha,em} = 3 \text{ rad s}^{-1}$ . The same filter bandwidths for the traction and retraction attitude commands are used. Note that these low pass filters also emulate, in some sense, the delay between the commanded attitude angles and the actual attitude which is present in the 6-DoF model and defined by the time constants of the closed-loop dynamics. In the 3-DoF model these filtered states are regarded as the current "real" attitude angles of the aircraft. In addition, a perfect sideslip angle regulation is assumed (i.e.  $\beta_a=0$ ).

The controller performance is assessed based on the path following error and/or the tracking performance of the course and path angles as well as the required bank angle and angle of attack commands. Note that it is not reasonable to try to achieve perfect tracking performance through time consuming gain tuning at this stage. Rather an acceptable performance should be aimed for. Ultimately, the fine tuning of the controller is done in step 4 and 5 of the control design methodology. Furthermore, since the outer loop is independent of the inner loop controller, the obtained results can be used to check if the chosen trim points, that are used for the linear inner loop design, frame a reasonable part of the flight envelop. In fact, it is also possible to derive requirements for

Table 4.4: Averaged quantile values for the wind speed during a pumping cycle for two different shear profiles.

Average quantile	$v_{w,\text{ref}} = 4 \text{ m s}^{-1}$	$v_{w,\text{ref}} = 9 \text{ m s}^{-1}$
$\hat{q}_{0.05}$	$5.94 \text{ m s}^{-1}$	$14.51 \text{ m s}^{-1}$
$\hat{q}_{0.5}$	$6.92 \text{ m s}^{-1}$	$16.11 \text{ m s}^{-1}$
$\hat{q}_{0.95}$	$7.66 \text{ m s}^{-1}$	$17.47 \text{ m s}^{-1}$

the required flight envelope based on the results obtained with the point mass simulations in the first place. Note, the point mass model can also be used to optimize the high level parameters such as the path shape and tether force set points. This optimization approach is discussed later on in more detail.

The outer-loop controller is verified in a low and a high wind speed condition scenario. The utilized shear profile and atmospheric turbulence model are described in chapter 2. The two different wind speed conditions are then defined by the wind speed at the reference altitude (i.e. 6 m). For the low wind speed condition a reference wind speed of  $4 \text{ m s}^{-1}$  is chosen, for the high wind speed condition the reference wind speed is set to  $9 \text{ m s}^{-1}$ . The corresponding wind speed profiles are depicted in Fig 2.11 as a function of altitude. In order to get a better understanding of the actually encountered wind speed at the aircraft during a pumping cycle the  $q_{0.05}$ -quantile, the median and the  $q_{0.95}$ -quantile are calculated based on generic pumping cycle simulations. The quantiles obtained from different simulation runs are eventually averaged which leads to the values that are displayed in Table 4.4.

For each of the two wind speed conditions three different reference path shapes are defined. The paths are ordered with respect to their "compactness". In that sense paths with higher compactness lead to higher curvature peaks. On the one hand, this allows to analyze the impact of the path shape on the required attitude commands and hence allows to make a statement about the flight dynamical implications of the path geometry. On the other hand, it allows to assess how significant the specific path shape is on the average pumping cycle power.

#### Low Wind Speed Conditions

The results for two consecutive pumping cycles in low wind speed conditions and for the three path shapes are displayed in Fig. 4.15a-Fig. 4.15f. For every scenario the resulting pumping cycle flight path is displayed as projections of the 3D path into the xy and xz plane of the W frame. The dashed line represents the reference flight path. It can be observed that during the traction phase an excellent path following performance is achieved for all three paths. During the retraction phase an offset between aircraft position and reference path is observable which could be reduced by further tuning of the outer loop controller gains. However, since the offset does not impact the overall capability of flying the pumping cycle this offset is regarded as acceptable at this design stage.

In Fig. 4.16a-Fig. 4.16f the evolution of the tether force as well as the airspeed is displayed for the three path shapes. It can be observed that with increasing path compact-

ness the frequency of the tether force oscillation around the set point increases. This can be explained as follows. In the segments where the aircraft flies against gravity it slows down which leads to a loss in airspeed and hence to a reduction in tether tension. Similarly, during the segments where the aircraft flies towards the ground it accelerates which increases the airspeed and hence the tension in the tether. Since the winch controller can only counteract this periodic disturbance within its bandwidth, as well as within the physical limitations of the winch, no perfect tracking is possible. Note that the figure of eight time period decreases with path compactness. Ultimately, this leads to the increased frequency of the tether force oscillation for more compact paths. Additionally, due to the termination of the crosswind maneuver, as soon as the state machine switches from traction into retraction mode, a large tether tension tracking error occurs. This is not avoidable and a result of the winch's speed and acceleration limits. However, for all three path shapes this error can be reduced to an acceptable value before the traction mode is triggered again. Therefore no attempt to reduce the retraction phase tether force tracking error is made.

In Fig. 4.17a-Fig. 4.17f the evolution of the bank angle as well as the angle of attack is displayed for the three path shapes. The commanded angle of attack reference values vary between  $-6^\circ$  and  $10^\circ$  for all three path shapes. As expected, the flight controller commands high angle of attacks during the traction phase for high lift and hence high tether tension. In the retraction phase the angle of attack is decreased to reduce the tension in the tether and to glide back towards the ground station. Note that paths with high compactness are more demanding flight dynamically. More specifically, the results show that for paths with higher compactness the bank angle peaks increase. The larger bank angle peaks are due to the fact that more aerodynamic force is required parallel to the turning plane to create the required centripetal force. In general, one would also expect higher angle of attack peaks to increase also the aerodynamic force in magnitude. However, the angle of attack is already saturating in all three scenarios therefore the effect of a higher required maneuver force is only visible in the bank angle peaks. In general, higher attitude angles bring the aircraft closer to its flight dynamical limits, hence the margins for robustness decrease. Therefore, less compact flight paths are desirable if robustness is the main design driver.

Finally, the mean mechanical power for all three path shapes is nearly identical as can be observed in Fig. 4.18. With the most compact path the average power of the two consecutive pumping cycles is 2.145kW. The path with medium compactness leads to a mean power of 2.023kW and the least compact path yields 2.018kW. Hence, in the low wind speed conditions (see Fig. 4.18b-Fig. 4.18d) the path shape, if varied alone, has only a negligible impact on the average power output.

#### High Wind Speed Conditions

The resulting flight paths in the high wind speed conditions are shown in Fig. 4.19a-Fig. 4.19f. In general, the path following capability in high wind speed conditions is acceptable. Slightly larger deviations compared to the low wind speed conditions occur, especially during the up-turns, but this is expected due to the larger variations in the wind speed (see Fig. 4.22b-Fig. 4.22d). Due to the higher wind speed the winch reels out faster in order to track the tether force set point. This has two effects on the resulting flight path shapes. The first observation is that the path becomes stretched and, hence,

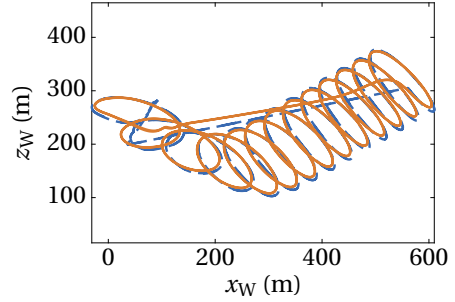
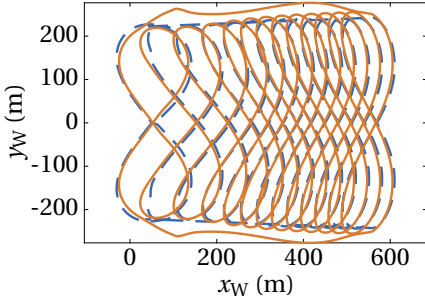
fewer figures of eight are flown per pumping cycle compared to the low wind speed scenario. The second observation in the high wind speed scenario is that if the transition rate, i.e. the rotational speed of the reference flight path towards lower elevation angles, is kept constant the resulting reference flight path will not reach its set point, since the radial velocity is significantly faster. Therefore, the retraction is triggered before the reference path reaches the defined traction phase elevation angle. However, it turns out that this effect adds an adaptive component to the reference flight path with respect to the wind conditions. This offers the benefit that it is not required to define different elevation angles for different wind speeds, since this is automatically achieved with the transition strategy.

Notice that since the change of tether length per half figure of eight increases, the retraction phase might be triggered long before the maximum tether length is reached. This is inevitable due to the conservative design of the high level decision logic which is implemented such that the maximum tether length is not allowed to be exceeded and the retraction points are fixed at the outer points of the paths (i.e.  $s = \frac{\pi}{2}$  or  $s = \frac{3\pi}{2}$ ). Since it only constitutes a design decision it can be adapted if desired in two ways. First, one could allow to trigger the retraction phase at any point on the path as soon as the maximum tether length is reached. However, this would introduce additional randomness into the pumping cycle flight path which increases the verification effort and, hence, makes it more challenging to arrive at a robust control solution. Second, the two fixed retraction points are maintained but the retraction is only triggered if the maximum tether length is reached. However, in this case it is not guaranteed anymore that the tether length is not exceeding its maximum value. Since both drawbacks are regarded as undesirable from a reliability point of view the drawback of triggering the retraction phase sometimes too early is regarded as the more reasonable solution.

Similarly to the low wind speed conditions the tether force oscillates around the set point and the frequency correlates again with the path compactness. Moreover, the largest tracking errors occur during the retraction phase which is again a results of the winch's speed and acceleration limits. Similar to the tether force the airspeed oscillates due to the up and down flight segments (see Fig. 4.20a-Fig. 4.20f).

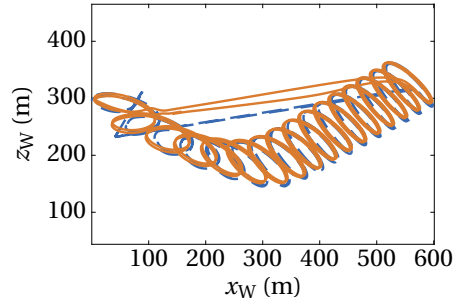
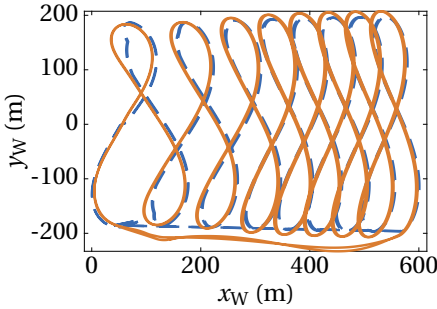
The bank angle varies within the defined boundaries and similar to the low wind speed conditions the bank angle peaks correlate with the path compactness (see Fig. 4.21a-Fig. 4.21e). Eventually, the mean power output of the two consecutive pumping cycles obtained with the three path shapes is calculated. For the path with the highest compactness an average pumping cycle power of 4.6kW is obtained, the medium sized path yields 5kW and the path with the lowest compactness leads to an average power output of 5.2kW. This result shows again the low sensitivity of the average pumping cycle power output towards the path shape.

— Reference — Flight path



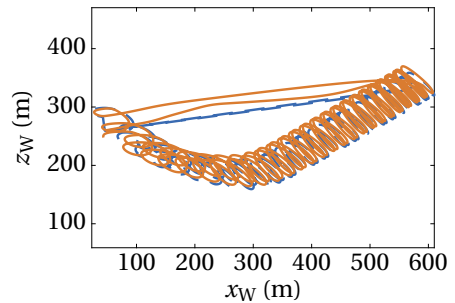
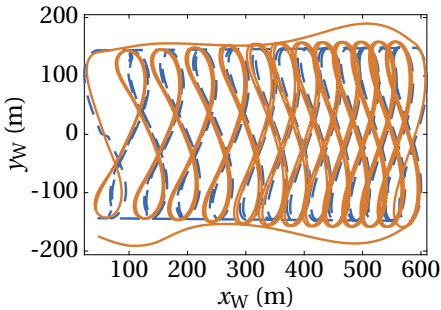
(a) Projected flight path in the  $xy$  plane of the wind frame with  $a_{\text{path}} = 0.8$  and  $b_{\text{path}} = 250$ .

(b) Projected flight path in the  $xz$  plane of the wind frame with  $a_{\text{path}} = 0.8$  and  $b_{\text{path}} = 250$ .



(c) Projected flight path in the  $xy$  plane of the wind frame with  $a_{\text{path}} = 0.6$  and  $b_{\text{path}} = 200$ .

(d) Projected flight path in the  $xz$  plane of the wind frame with  $a_{\text{path}} = 0.6$  and  $b_{\text{path}} = 200$ .



(e) Projected flight path in the  $xy$  plane of the wind frame with  $a_{\text{path}} = 0.4$  and  $b_{\text{path}} = 150$ .

(f) Projected flight path in the  $xz$  plane of the wind frame with  $a_{\text{path}} = 0.4$  and  $b_{\text{path}} = 150$ .

Figure 4.15: Flight path projections in low wind speed conditions and with different reference path shapes. The dashed line represents the reference.

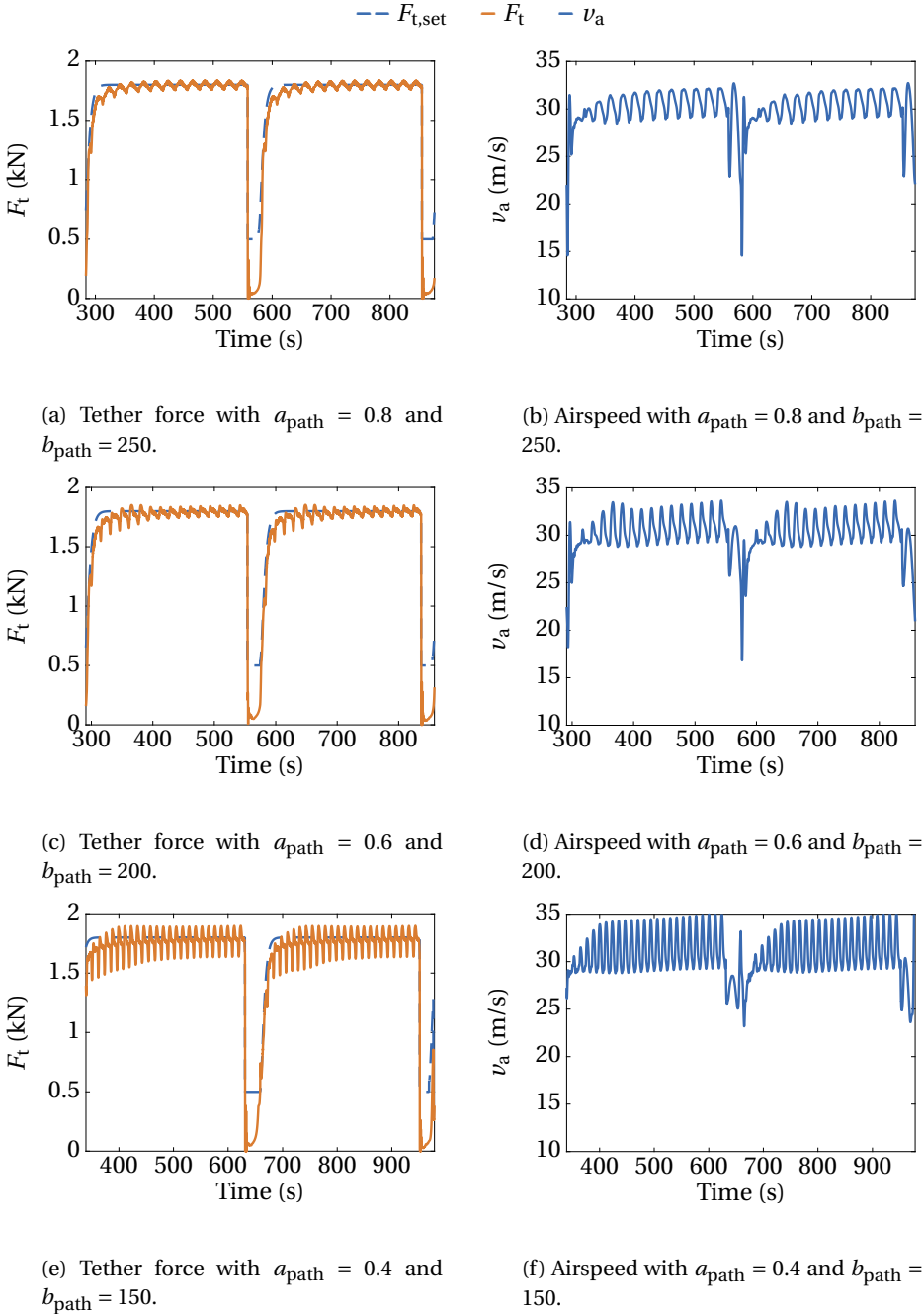
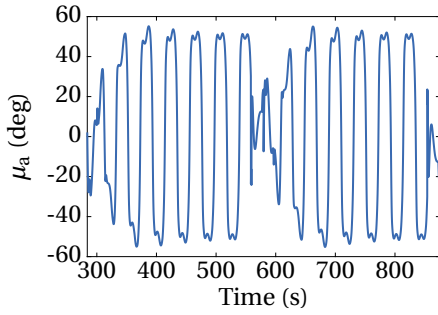
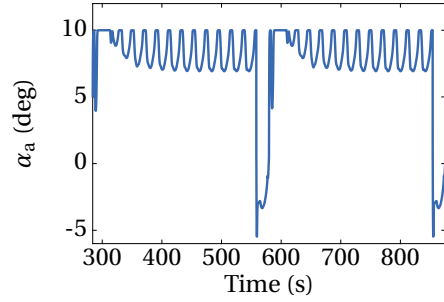


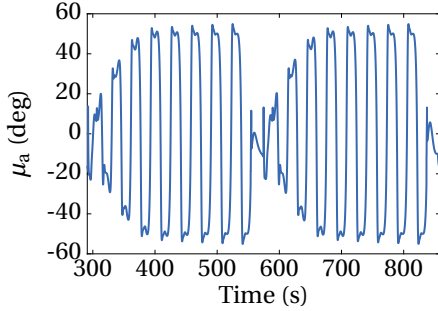
Figure 4.16: Evolution of tether force and airspeed in low wind speed conditions.



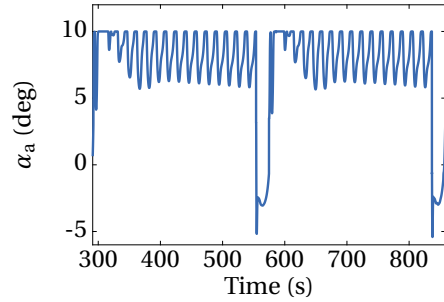
(a) Bank angle with  $a_{\text{path}} = 0.8$  and  $b_{\text{path}} = 250$ .



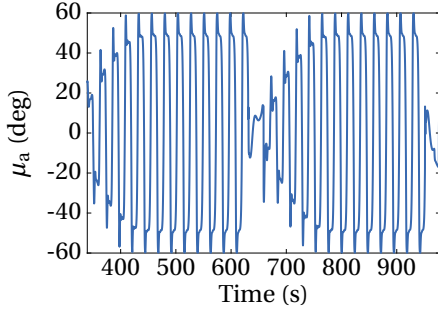
(b) Angle of attack with  $a_{\text{path}} = 0.8$  and  $b_{\text{path}} = 250$ .



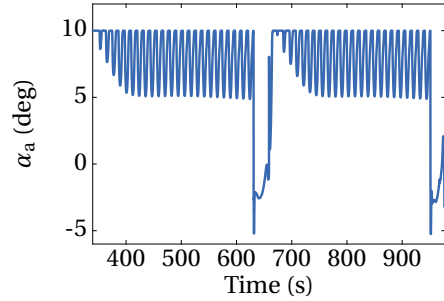
(c) Bank angle with  $a_{\text{path}} = 0.6$  and  $b_{\text{path}} = 200$ .



(d) Angle of attack with  $a_{\text{path}} = 0.6$  and  $b_{\text{path}} = 200$ .

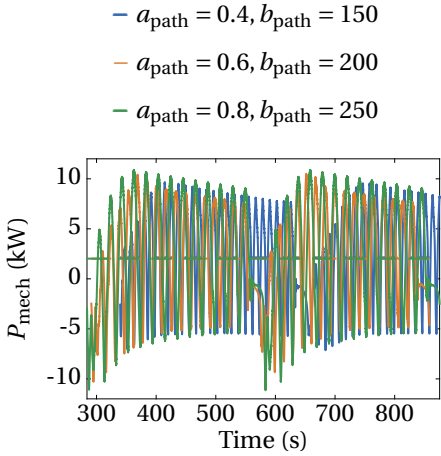


(e) Bank angle with  $a_{\text{path}} = 0.4$  and  $b_{\text{path}} = 150$ .

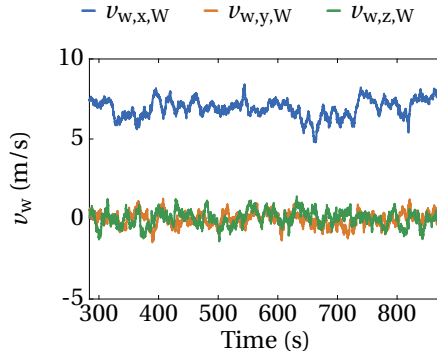


(f) Angle of attack with  $a_{\text{path}} = 0.4$  and  $b_{\text{path}} = 150$ .

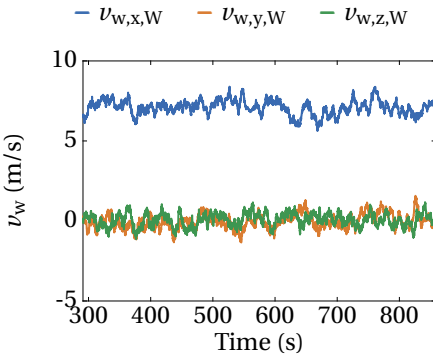
Figure 4.17: Evolution of aerodynamic bank angle and angle of attack in low wind speed conditions.



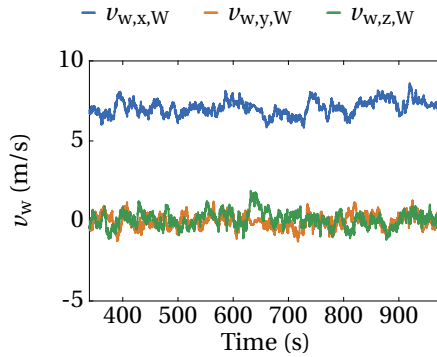
(a) Generated mechanical power w.r.t. the different path shapes. The dashed line indicates the median.



(b) Turbulent wind field with  $a_{\text{path}} = 0.4$  and  $b_{\text{path}} = 150$ .



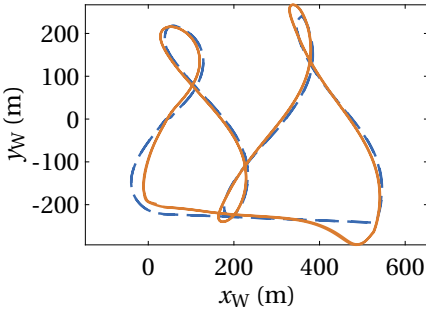
(c) Turbulent wind field with  $a_{\text{path}} = 0.6$  and  $b_{\text{path}} = 200$ .



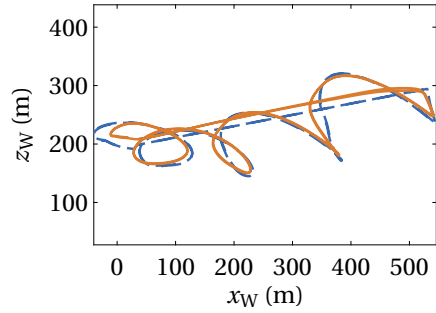
(d) Turbulent wind field with  $a_{\text{path}} = 0.8$  and  $b_{\text{path}} = 250$ .

Figure 4.18: Mechanical power output and turbulent wind fields in low wind speed conditions.

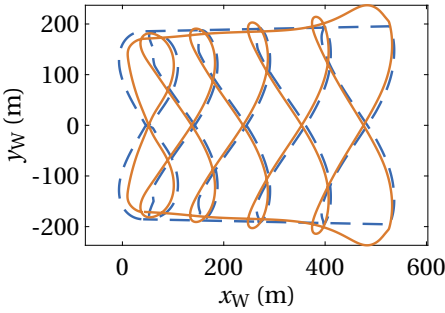
— Reference — Flight path



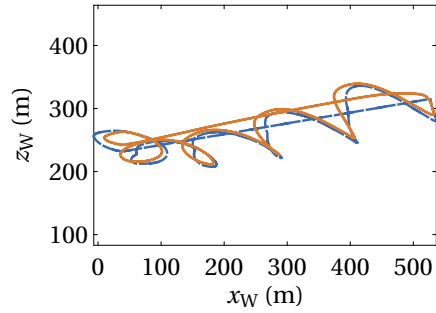
(a) Projected flight path in the  $xy$  plane of the wind frame with  $a_{\text{path}} = 0.8$  and  $b_{\text{path}} = 250$ .



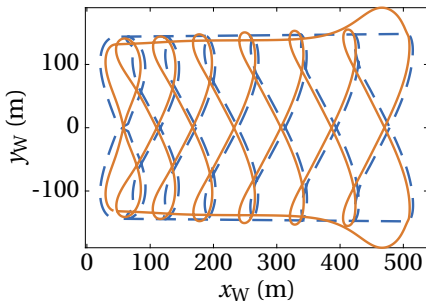
(b) Projected flight path in the  $xz$  plane of the wind frame with  $a_{\text{path}} = 0.8$  and  $b_{\text{path}} = 250$ .



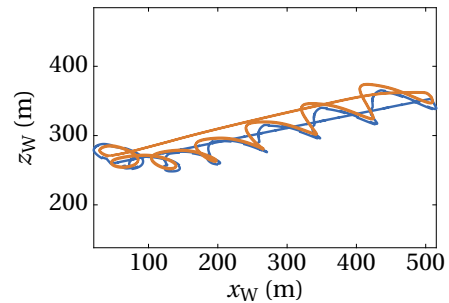
(c) Projected flight path in the  $xy$  plane of the wind frame with  $a_{\text{path}} = 0.6$  and  $b_{\text{path}} = 200$ .



(d) Projected flight path in the  $xz$  plane of the wind frame with  $a_{\text{path}} = 0.6$  and  $b_{\text{path}} = 200$ .

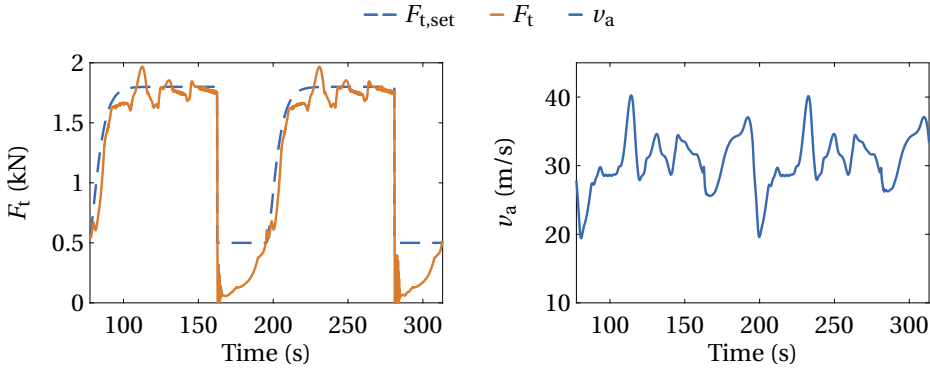


(e) Projected flight path in the  $xy$  plane of the wind frame with  $a_{\text{path}} = 0.4$  and  $b_{\text{path}} = 150$ .



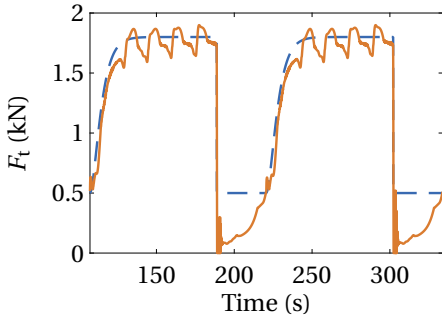
(f) Projected flight path in the  $xz$  plane of the wind frame with  $a_{\text{path}} = 0.4$  and  $b_{\text{path}} = 150$ .

Figure 4.19: Flight path projections in high wind speed conditions and with different reference path shapes. The dashed line represents the reference.

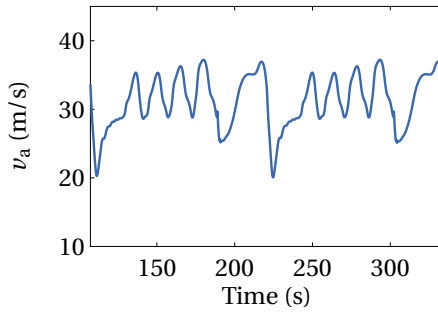


(a) Tether force with  $a_{\text{path}} = 0.8$  and  $b_{\text{path}} = 250$ .

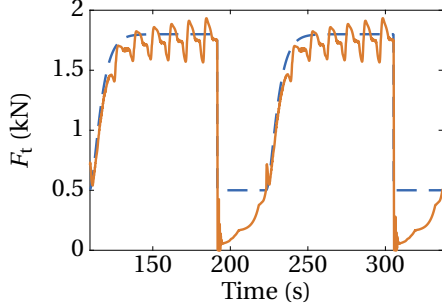
(b) Airspeed with  $a_{\text{path}} = 0.8$  and  $b_{\text{path}} = 250$ .



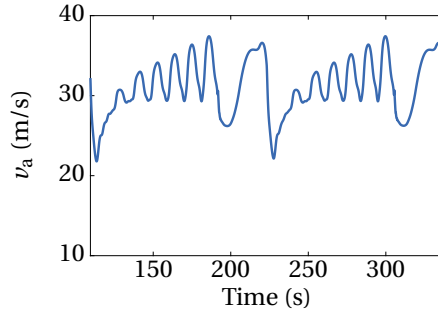
(c) Tether force with  $a_{\text{path}} = 0.6$  and  $b_{\text{path}} = 200$ .



(d) Airspeed with  $a_{\text{path}} = 0.6$  and  $b_{\text{path}} = 200$ .

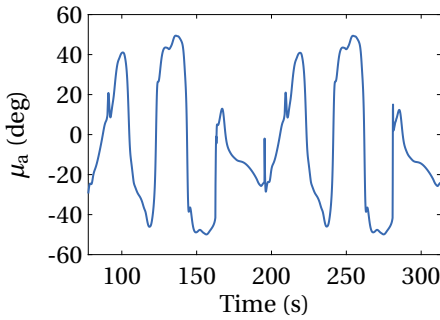


(e) Tether force with  $a_{\text{path}} = 0.4$  and  $b_{\text{path}} = 150$ .

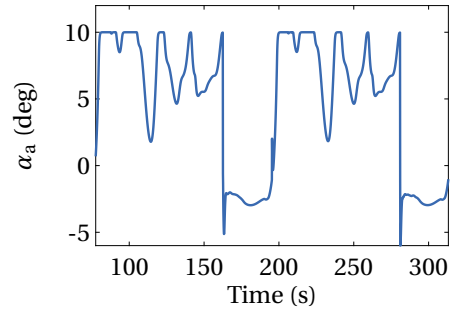


(f) Airspeed with  $a_{\text{path}} = 0.4$  and  $b_{\text{path}} = 150$ .

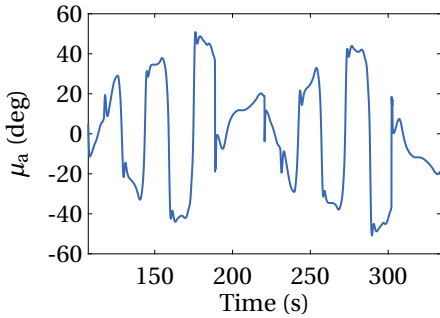
Figure 4.20: Evolution of tether force and airspeed in high wind speed conditions.



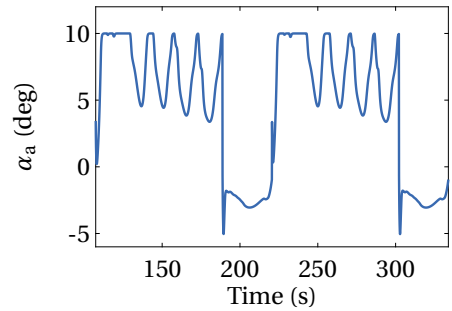
(a) Bank angle with  $a_{\text{path}} = 0.8$  and  $b_{\text{path}} = 250$ .



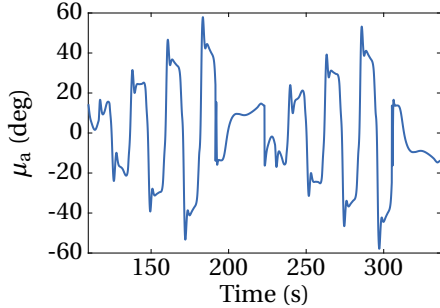
(b) Angle of attack with  $a_{\text{path}} = 0.8$  and  $b_{\text{path}} = 250$ .



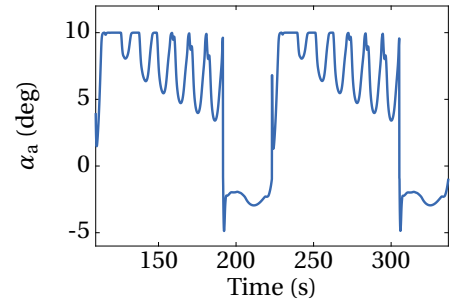
(c) Bank angle with  $a_{\text{path}} = 0.6$  and  $b_{\text{path}} = 200$ .



(d) Angle of attack with  $a_{\text{path}} = 0.6$  and  $b_{\text{path}} = 200$ .



(e) Bank angle with  $a_{\text{path}} = 0.4$  and  $b_{\text{path}} = 150$ .



(f) Angle of attack with  $a_{\text{path}} = 0.4$  and  $b_{\text{path}} = 150$ .

Figure 4.21: Evolution of aerodynamic bank angle and angle of attack in high wind speed conditions.

Based on these results, obtained with the 3-DoF model and the outer loop controller, the following conclusions can be drawn. The outer loop is able to successfully guide the aircraft during the pumping cycle in low as well as high wind speed conditions along paths with varying compactness (i.e. varying curvature peaks). The limited commanded set points allow to fly the figure of eight pattern during the traction phase as well as the straight gliding path during the retraction phase. Therefore, the required aerodynamic forces can be created in magnitude as well as orientation to track the tether tension set point as well as the required maneuver forces. In both wind speed conditions the impact of the path shape on the average power is not significant and hence the path should be chosen based on the overall control performance requirement. This motivates to choose paths with lower compactness since they are less demanding from a flight dynamic point of view as discussed in this section. Note, paths with very low compactness are also not desirable since they limit the amount of AWE systems that can be operated in a limited space. For this reason the medium sized path shape is chosen for the remainder of the work.

In light of the subsequent section it needs to be noted that the evolution of the air-speed, angle of attack and tether force, obtained with the 3-DoF simulations, can be used to frame a reasonable part of the flight envelope that characterizes nominal pumping cycle operation. This information can be used for the linear inner loop control design which requires to linearize the model in distinct operating points. The linear controllers can then be derived based on the obtained linear state-space models. This is the content of the subsequent section.

## 4.7. Linear Inner Loop Design

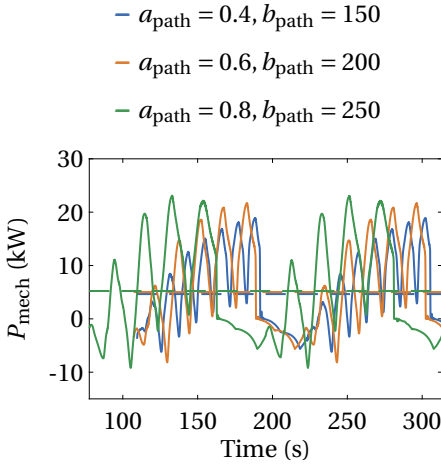
In this section three different linear inner loop designs are presented. All three controllers are characterized by the same structure but require different design steps. Based on the linear flight dynamic analysis in chapter 3 it can be concluded that decoupling of the longitudinal and lateral dynamics is justified if in the traction phase the attitude is parameterized with respect to the tangential plane. A similar conclusion can be drawn for the retraction phase. Since during the retraction phase the attitude is parameterized with respect to the ground, the traction and retraction phase controllers are derived separately in the subsequent two sections.

In total, the linear inner loop design task consists of four sub-tasks. First, operating points are determined and the nonlinear model is linearized in these operating points. This is already explained in detail in chapter 3. Next, the linear design models for the longitudinal and lateral motion are used to design and tune the controllers with respect to rise time, overshoot and settling time for a step input. Lastly, the robustness of the obtained controllers with respect to modeling uncertainties is assessed using the structured singular value and perturbed state-space models.

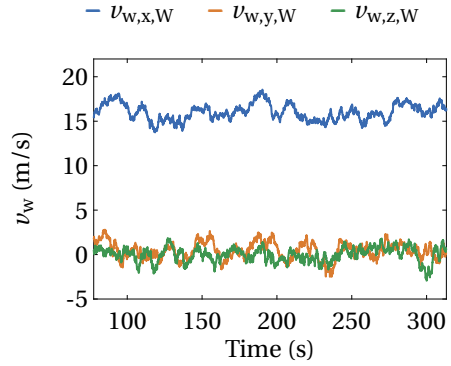
### 4.7.1. Traction Phase

#### Longitudinal Control System

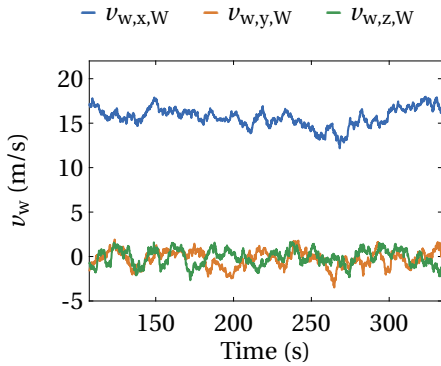
In this section the longitudinal controller is derived. It is designed and tuned with respect to its step response characteristics as well as its robustness towards parametric



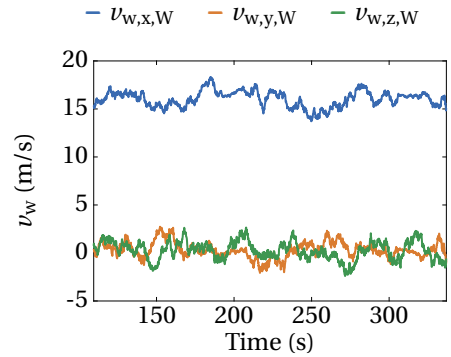
(a) Generated mechanical power w.r.t. the different path shapes. The dashed line indicates the median.



(b) Turbulent wind field with  $a_{\text{path}} = 0.8$  and  $b_{\text{path}} = 250$ .



(c) Turbulent wind field with  $a_{\text{path}} = 0.6$  and  $b_{\text{path}} = 200$ .



(d) Turbulent wind field with  $a_{\text{path}} = 0.4$  and  $b_{\text{path}} = 150$ .

Figure 4.22: Mechanical power output and turbulent wind fields in high wind speed conditions.

Table 4.5: Open loop analysis of the state-space model defined in Eq. (4.144).

Mode	Eigenvalue	Relative Damping $\zeta$	Natural Frequency $\omega_0$ (rad/s)
Short period	$-4.71 \pm 4.21$	0.75	6.32
Phygoid	$-0.04 \pm j1.7$	0.03	1.7

uncertainties in the state-space model. Since the longitudinal model has only one input and one output that needs to be tracked, no input/output decoupling is necessary. Robust tracking performance of the angle of attack is necessary since it has an immediate effect on controlling the magnitude of the lift and hence the tension in the tether. Furthermore, as stated in chapter 1, AWE systems are operated at high angles of attack, hence, close to the stall point of the aircraft. This makes a robust longitudinal control system paramount to achieve a high degree of reliability. Note, it is common in flight control applications to control the angle of attack using only the short period approximation. In this case, however, airspeed is controlled separately using the throttle as an additional input which allows to control phygoid and short period mode separately. In AWE such an airspeed control approach is obviously not available and the airspeed can only be stabilized but not tracked with only one control input. Therefore, in order to guarantee stability of the airspeed dynamics, the complete longitudinal model is required for the control design such that phygoid and short period mode can be controlled simultaneously.

Two design approaches are considered. First, a linear quadratic regulator with servomechanism for robust angle of attack tracking is designed. The chosen operating point is represented by  $F_t = 1.8 \text{ kN}$ ,  $\alpha_a = 7^\circ$  ( $v_a = 31.35 \text{ m s}^{-1}$ ) at a wind speed of  $12.5 \text{ m s}^{-1}$ , which corresponds to a quasi-stationary point approximately in the center of the operational envelope. For the controller design the state-space model is augmented by an integral error state which eventually allows to track angle of attack commands through the design of a linear state feedback controller. The resulting state-space model at this operating point is given by

$$\begin{pmatrix} \dot{v}_a \\ \dot{\alpha}_a \\ \dot{\Theta}_\tau \\ \dot{q} \\ \dot{e}_{i,\alpha} \end{pmatrix} = \begin{pmatrix} -0.43 & 34.19 & -53.9 & -0.42 & 0 \\ -0.11 & -6.00 & 0.10 & 0.90 & 0 \\ 0.003 & -0.01 & 0.01 & 0.99 & 0 \\ -0.01 & -19.4 & 0 & -3.06 & 0 \\ 0 & -1 & 0 & 0 & 0 \end{pmatrix} \begin{pmatrix} v_a \\ \alpha_a \\ \Theta_\tau \\ q \\ \int_0^t e_\alpha d\tau \end{pmatrix} + \begin{pmatrix} -1.71 \\ -0.48 \\ 0 \\ -31.9 \\ 0 \end{pmatrix} \delta_e + \begin{pmatrix} 0 \\ 0 \\ 0 \\ 0 \\ 1 \end{pmatrix} \alpha_{a,c} \quad (4.144)$$

with  $e_\alpha = \alpha_{a,c} - \alpha_a$ ,  $e_{i,\alpha} = \int_0^t e_\alpha d\tau$ . The open loop poles, relative damping and natural frequencies of the two oscillatory modes are shown in Table 4.5. The open loop dynamics at this linearization point are characterized by a well damped short period mode and a poorly damped Phygoid mode. The Phygoid's open loop eigenvalue pair is close to the imaginary axis, hence clearly indicating that the controller needs to shift them more into

Table 4.6: Closed loop properties of the state-space model defined in Eq. (4.144) with negative feedback using the LQR gains defined in Eq. (4.145).

Mode	Eigenvalue	Relative Damping $\zeta$	Natural Frequency $\omega_0$ (rad/s)
Short period	$-10.9 \pm 3.34$	0.96	11.4
Phygooid	$-0.7 \pm j2.1$	0.32	2.18

the left complex half plane to increase the damping and the robustness margins. For the servo-LQR at this operating point the following weighting matrices are chosen:

$$\begin{aligned} \mathbf{Q}_{\text{LQR,long,traction}} &= \text{diag}(0, 30, 0, 0.6, 45) \\ R_{\text{LQR,long,traction}} &= 3 \end{aligned} \quad (4.145)$$

where the "diag" operator creates a diagonal matrix out of its arguments. This yields the following feedback gain matrix:

$$\mathbf{K}_{\text{long,LQR}} = \begin{pmatrix} 0.0406 & -0.8808 & -1.0163 & -0.4552 & 3.8730 \end{pmatrix} \quad (4.146)$$

Closing the loop with this gain yields the closed-loop properties listed in Table 4.6. The closed loop has now an almost aperiodic short period mode ( $\zeta = 0.96$ ) and the phygooid mode pole is moved more into the left half plane which improves the relative damping. Also the natural frequency of the phygooid is slightly higher in the closed loop.

The second control design strategy for the longitudinal controller uses the linear matrix inequality approach presented in section 4.1.1. This approach is denoted as the LMI approach from now on. It allows to consider several operating points simultaneously for the controller design. Four operating points are chosen that enclose a reasonable part of the operational envelope. In addition, the same operating point at the center of this area, which corresponds to the design point of the LQR, is added. The operating points are defined in the first column of Table 4.8. The numerical values of the state-space matrices are given in the appendix A. The weighting matrices for the LMI controller synthesis are given by Eq. (4.147):

$$\begin{aligned} \mathbf{Q}_{\text{LMI,long,traction}} &= \text{diag}(0, 30, 0, 0.6, 60) \\ R_{\text{LMI,long,traction}} &= 3 \end{aligned} \quad (4.147)$$

Compared to the LQR design the  $\mathbf{Q}_{\text{LMI,long,traction}}$  is slightly altered to achieve approximately the same nominal step response as the LQR at its design point  $p_3$ . This leads to the following controller gains:

$$\mathbf{K}_{\text{long,traction,LMI}} = \begin{pmatrix} 0.0512 & -0.8663 & -1.2365 & -0.5174 & 4.4721 \end{pmatrix} \quad (4.148)$$

The closed-loop properties at  $p_3$  are summarized in Table 4.7. The LMI controller moves the closed loop poles to slightly different locations in the complex plane compared to the LQR. At  $p_3$  it transforms the short period mode into two aperiodic modes. The closed

Table 4.7: Closed loop properties of the state-space model defined in Eq. (4.144) with negative feedback using the gains of the LMI controller defined in Eq. (4.147).

Mode	Eigenvalue	Relative Damping $\zeta$	Natural Frequency $\omega_0$ (rad/s)
Aperiodic mode 1	-12.3	1	12.3
Aperiodic mode 2	-11.2	1	11.2
Phygoid	$-0.81 \pm j2.1$	0.36	2.25

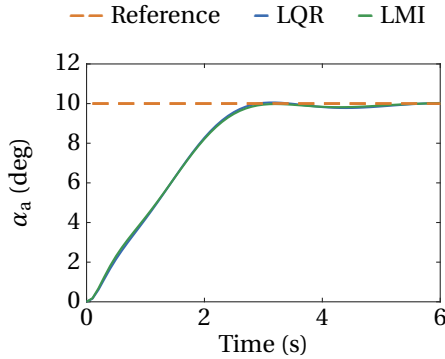


Figure 4.23: Step responses with LQR and LMI controller at the design point  $p_3$  of the traction phase.

loop phygoid motion using the LMI controller is similar to the LQR but slightly higher damped. On the other hand, both step responses to a  $10^\circ$  angle of attack reference step, displayed in Fig. 4.23, are approximately identical.

The robustness of the two longitudinal controllers with respect to parametric plant uncertainties is verified using the structured singular value (SSV, see [140, p.306-312]) which is calculated for a parameterized uncertainty model of the longitudinal plant dynamics. The SSV, denoted with  $\mu_\Delta$ , provides a sufficient and necessary condition for robust stability. Concretely, it allows to calculate the smallest uncertainty that leads to an unstable closed loop system. In fact, this uncertainty is given by the inverse of the SSV. For a precise mathematical definition see for instance [140, p.308]). The uncertainty model is created by defining a multiplicative uncertainty for each element in the state-space model of the form

$$\tilde{c}' = c' (1 + \delta_{mp}) \quad (4.149)$$

here  $c'$  represents a generic, nominal parameter value in the state-space model. To keep the preliminary robustness analysis as simple as possible the same uncertainty range for every parameter is defined as  $\delta_{mp} = \pm 0.3$  (i.e. 30% uncertainty on every element in the state-space model). The SSV is calculated for the five different state-space models ( $p_1$  to  $p_5$ ). The guaranteed margins are summarized in Table 4.8. The SSV is calculated using the *robstab* routine which is part of the robust control toolbox in Matlab (see [143]). The routine returns a lower as well as an upper bound. The lower bound is the guar-

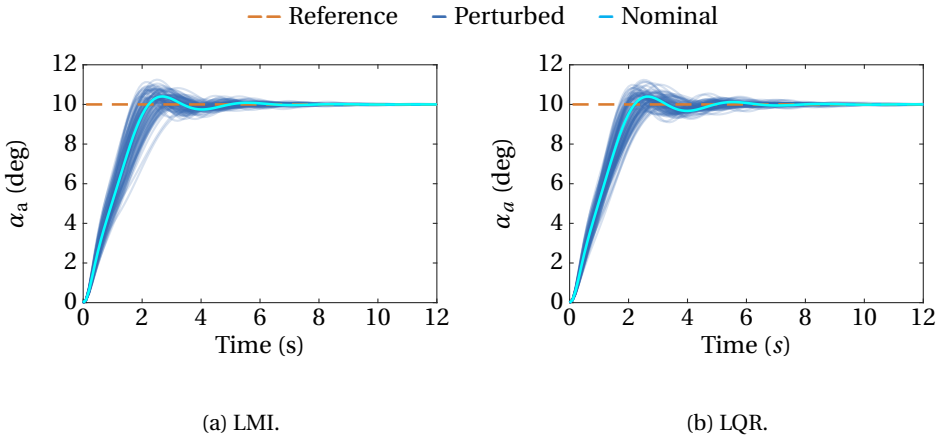
Table 4.8: Robustness margins for the LQR and the LMI based longitudinal control system. The quasi-stationary point is characterized by specific values for airspeed, angle of attack and tether force (values in brackets are in that order). The design point is highlighted in orange.

Quasi steady point	LB LQR	UB LQR	LB LMI	UB LMI
$p_1$ (27.70 m s <sup>-1</sup> , 10°, 1.6 kN)	0.90	0.90	0.99	1.00
$p_2$ (30.56 m s <sup>-1</sup> , 10°, 2 kN)	0.93	0.94	1.03	1.04
$p_3$ (31.35 m s <sup>-1</sup> , 7°, 1.8 kN)	1.08	1.12	1.16	1.21
$p_4$ (32.91 m s <sup>-1</sup> , 4°, 1.6 kN)	1.26	1.35	1.33	1.42
$p_5$ (36.32 m s <sup>-1</sup> , 4°, 2 kN)	1.29	1.38	1.37	1.46

anteed stability bound i.e. the systems remains stable for any uncertainty combination with magnitudes no larger than the lower bound. The upper bound guarantees that the stability bound is with certainty not larger than this value. Note, a value larger than 1 indicates that stability is guaranteed for the specified uncertainty interval times the margin value. Values lower than 1 indicate the fraction of the specified uncertainty interval for which stability can be still guaranteed. The results of the  $\mu_\Delta$ -analysis are summarized in Table 4.8. If the value is larger than one the controller can tolerate more uncertainty than specified. It can be observed that both controllers provide acceptable robust stability properties and the robustness correlates positively with airspeed. Concretely, the LQR guarantees stability up to 90% parametric uncertainty for the specified uncertainty interval at  $p_1$  and 93% parametric uncertainty at  $p_2$ . For all other points the LQR allows parametric uncertainties above the specified uncertainty interval. The LMI controller achieves already 99% parametric uncertainty at  $p_1$ . For all other operating points the guaranteed robustness margins are higher than the specified uncertainties. In general, the LMI controller leads to larger robustness margins than the LQR. This result is expected since the LMI controller simultaneously stabilizes a set of plants and therefore captures intrinsically parameter variations as a result of the different operating conditions that need to be stabilized.

Besides robust stability it needs to be analyzed how the controller performance degrades in presence of model uncertainties. Therefore, the step response properties are analyzed statistically for 1000 randomly sampled state-space models. To summarize the results of the statistical analysis in a single number the 0.95th quantile  $q_{0.95}$  is calculated for rise time, overshoot and settling time. It represents a threshold below which 95% of the obtained values lie. For the LQR the statistical results are summarized in Table 4.9 and for the LMI in Table 4.10. The step responses itself are visualized in Fig. 4.24a-Fig. 4.28b. In these figures the cyan colored line indicates the nominal response to the reference value indicated by the dashed orange line. The step responses of the randomly sampled state-space models are indicated by the dark blue lines.

With the nominal models the rise time increases with increasing airspeed for both

Figure 4.24: Step responses for the perturbed models at  $p_1$  of the traction phase.

controllers. Simultaneously, the overshoot decreases with increasing airspeed. This can be explained by the positive correlation of airspeed and natural damping. Comparing the rise time of the LQR with the LMI controller shows that the LMI controller is slightly slower but only in the order of 0.1 s. At  $p_1$  the LMI controller leads to a higher overshoot

Table 4.9: Statistical step response characteristics for all five perturbed state-space models and the LQR designed at  $p_3$ . Rise time is defined as the point where the signal reaches 95% of the reference value, overshoot is calculated with respect to the set point and settling time is defined as the point where the signal stays within  $\pm 2\%$  around the reference value. The values in brackets are obtained with the nominal model.

Characteristic	$q_{0.95}^{p1}$	$q_{0.95}^{p2}$	$q_{0.95}^{p3}$	$q_{0.95}^{p4}$	$q_{0.95}^{p5}$
Rise time $\alpha_a$ (s)	2.65 (1.99)	3.12 (2.02)	3.92 (2.39)	5.27 (3.21)	5.76 (4.20)
Overshoot $\alpha_a$ (%)	9.93 (3.98)	5.74 (0.79)	5.42 (0.37)	2.98 (0)	0.29 (0)
Settling time $\alpha_a$ (s)	6.53 (4.48)	5.09 (4.05)	5.47 (4.46)	6.70 (5.05)	7.35 (5.23)

Table 4.10: Statistical step response characteristics for all five perturbed state-space models and the LMI controller designed at  $p_3$ . Rise time is defined as the point where the signal reaches 95% of the reference value, overshoot is calculated with respect to the set point and settling time is defined as the point where the signal stays within  $\pm 2\%$  around the reference value. The values in brackets are obtained with the nominal model.

Characteristic	$q_{0.95}^{p1}$	$q_{0.95}^{p2}$	$q_{0.95}^{p3}$	$q_{0.95}^{p4}$	$q_{0.95}^{p5}$
Rise time $\alpha_a$ (s)	2.74 (2.01)	3.15 (2.04)	4.01 (2.44)	5.53 (3.42)	6.18 (4.30)
Overshoot $\alpha_a$ (%)	9.67 (4.03)	6.04 (0.53)	4.68 (0.18)	2.36 (0)	0.09 (0)
Settling time $\alpha_a$ (s)	5.84 (4.38)	4.80 (3.93)	5.34 (4.19)	7.01 (5.00)	7.94 (5.34)

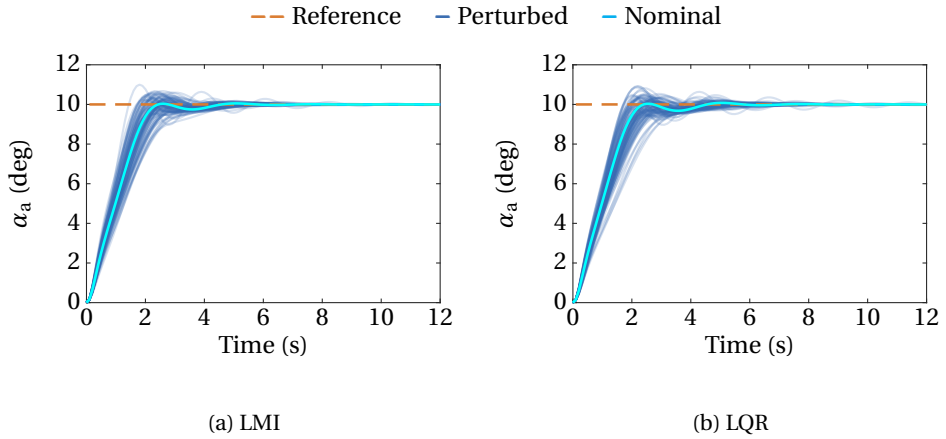


Figure 4.25: Step responses for the perturbed models at the design point  $p_2$  of the traction phase.

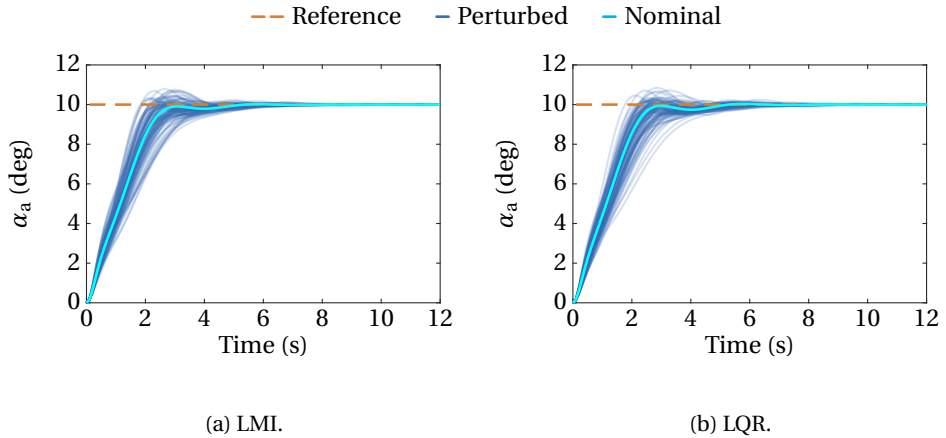


Figure 4.26: Step responses for the perturbed models at the design point  $p_3$  of the traction phase.

(4.03%) compared to the LQR (3.98%). However, at all other operating points the LMI controller is able to better damp the overshoot. The difference is however below 1% and hence negligible. The settling time for both controllers first decreases and then increases again. This effect is due to the increased damping and hence the lower overshoot which slows down the response time and hence increases the settling time. The corresponding settling times of LQR and LMI deviate only within the order of 0.1 s.

The results of the statistical simulations using the perturbed state-space models lead qualitatively to the same results. The rise time increases and the overshoot decreases with airspeed. The LQR leads at all operating points to a quicker response while except at  $p_2$  the LMI is achieving a higher damping. This is consistent with the closed loop eigenmode analysis summarized in Table 4.7. Similar to the nominal case the settling

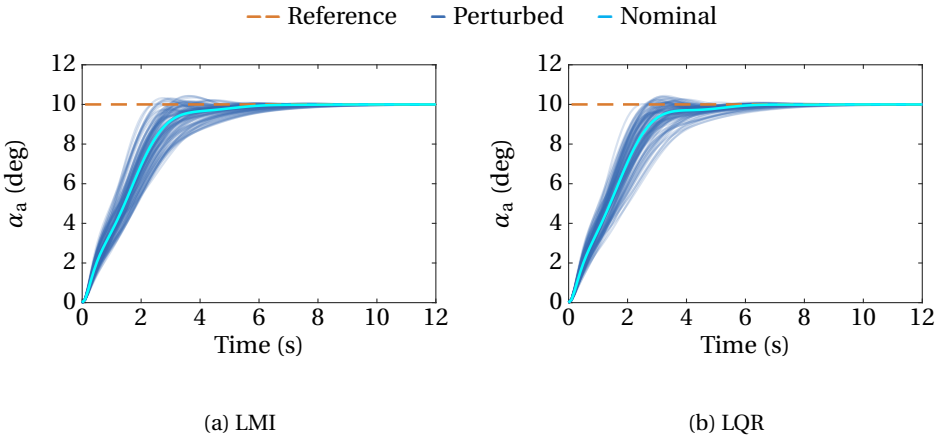


Figure 4.27: Step response for the perturbed models at the design point  $p_4$  of the traction phase.

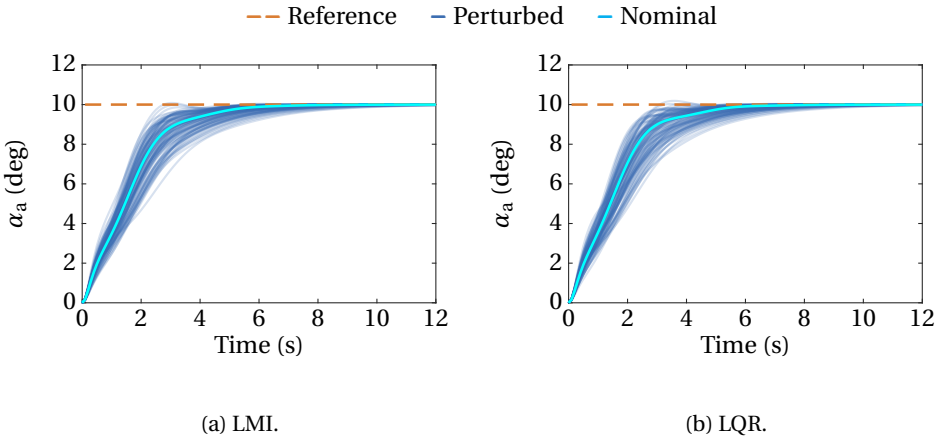


Figure 4.28: Step responses for the perturbed models at the design point  $p_5$  of the traction phase.

time for both controllers first decreases and then increases again from  $p_3$  to  $p_5$  due to the higher damping. The differences between the LQR and the LMI in terms of settling time are again not significant.

Overall the following conclusion can be drawn: Based on the  $\mu_\Delta$ -analysis the LMI controller leads to a more robust controller. This is expected due to the simultaneous design at several operating points. A significant performance loss of the LMI controller compared to the LQR, due to higher robustness margins, cannot be observed. Although small differences between the statistical step response characteristics occurred, these deviations are not significant. Ultimately, since the LMI controller does not introduce any additional complexity, i.e. it has exactly the same structure as the LQR, it is decided to use the LMI controller to control the longitudinal dynamics for the remainder of this

work, due to the higher guaranteed stability margins.

### Lateral Control System

In this section the design of the lateral control system for the traction phase is presented. Two different approaches to design the controller gains are compared. On the one hand, a design based on eigenstructure assignment (ESA) and, on the other hand, a similar LMI based controller as for the longitudinal dynamics is derived.

As presented in chapter 3, the state-space model corresponding to the lateral dynamics consists of the four states  $\beta_a$ ,  $\Phi_\tau$ ,  $p$ , and  $r$ . The aircraft is linearized at the center of the figure of eight and the quasi-stationary point is determined with the boundary conditions  $F_t = 1.8 \text{ kN}$ ,  $\alpha_a = 7^\circ$  ( $v_a = 31.35 \text{ ms}^{-1}$ ) and  $v_w = 12.5 \text{ ms}^{-1}$  (same as for the longitudinal controller). This point lies approximately in the center of the trimmed flight envelope shown in Fig. 3.1a and seems also to be a representative state based on the results obtained with the 3-DoF model.

In order to track the tangential plane roll angle command  $\Phi_{\tau,c}$  and to regulate the sideslip angle to zero the state-space model is augmented with integral error states. This leads, at this specific operating point, to the augmented state-space model given by:

$$\begin{pmatrix} \dot{\beta}_a \\ \dot{\Phi}_\tau \\ \dot{p} \\ \dot{r} \\ \dot{e}_{i,\beta} \\ \dot{e}_{i,\Phi_\tau} \end{pmatrix} = \begin{pmatrix} -0.40 & 1.76 & 0.11 & -0.97 & 0 & 0 \\ -0.08 & 0 & 1 & 0.04 & 0 & 0 \\ -24.7 & 0 & -19.6 & 9.14 & 0 & 0 \\ 8.19 & 0 & -2.77 & -0.72 & 0 & 0 \\ -1 & 0 & 0 & 0 & 0 & 0 \\ 0 & -1 & 0 & 0 & 0 & 0 \end{pmatrix} \begin{pmatrix} \beta_a \\ \Phi_\tau \\ p \\ r \\ e_{i,\beta} \\ e_{i,\Phi_\tau} \end{pmatrix} + \begin{pmatrix} -0.08 & 0.16 \\ 0 & 0 \\ -97.9 & 1.55 \\ 0.06 & -7.3 \\ 0 & 0 \\ 0 & 0 \end{pmatrix} \begin{pmatrix} \delta_a \\ \delta_r \end{pmatrix} + \begin{pmatrix} 0 & 0 \\ 0 & 0 \\ 0 & 0 \\ 0 & 0 \\ 1 & 0 \\ 0 & 1 \end{pmatrix} \begin{pmatrix} \beta_{a,c} \\ \Phi_{\tau,c} \end{pmatrix} \quad (4.150)$$

with  $e_\beta = \beta_{a,c} - \beta_a$ ,  $e_{i,\beta} = \int_0^t e_\beta d\tau$ ,  $e_{\Phi_\tau} = \Phi_{\tau,c} - \Phi_\tau$  and  $e_{i,\Phi_\tau} = \int_0^t e_{\Phi_\tau} d\tau$ . The following state feedback controllers stabilize the lateral dynamics defined by Eq. (4.150) and ensure steady-state tracking of  $\Phi_{\tau,c}$  and  $\beta_{a,c}$ .

### Design based on Eigenstructure Assignment

The first controller is derived using the eigenstructure assignment algorithm presented in section 4.1. For the controller design the desired eigenvalues and eigenvectors need to be defined. It is instructive to first analyze the open loop characteristics at this specific operating point in more detail and then only alter specific eigenmodes if necessary.

Naturally, this analysis is done without the integrator states in Eq. (4.150). The eigenvalues of the open loop plant as well as the corresponding natural frequencies and relative damping terms are listed in Table 4.11. As already discussed in chapter 3 the lateral dynamics in the traction phase consist, equivalently to the dynamics of an untethered aircraft, of two aperiodic and one periodic mode. The relative damping of the periodic mode (i.e. dutch-roll) is with 0.34 not well enough damped. Hence, the poles for the dutch-roll mode are altered within the eigenstructure assignment to achieve a damping of  $\frac{1}{\sqrt{2}}$ . The natural frequency of the dutch-roll as well as the roll mode is not altered. The spiral mode as well as the additional eigenvalues coming from the integrator states are regarded as auxiliary tuning parameters. The numerical values are listed in Table 4.12. where the desired eigenvalue for the dutch-roll is calculated using the desired damping and unchanged natural frequency with Eq. (4.151):

$$\lambda_{DR} = \omega_{0,DR} \left( -\zeta_{DR}^* \pm j\sqrt{1 - (\zeta_{DR}^*)^2} \right) \tag{4.151}$$

In the next step, the eigenmotions are further shaped by defining the desired eigenvectors. Since two inputs are available, two elements of each eigenvector can be specified as explained in section 4.1. In the following a "\*" symbol defines an unspecified element that the algorithm is choosing automatically and therefore is not user specified. The specification of the eigenvector elements is used to decouple the roll and yaw motion. Hence, depending on the eigenmotion that an eigenvector belongs to, the elements of the vector that correspond to the states that should not influence this mode are set to

Table 4.11: Open loop analysis of the state-space model defined in Eq. (4.150).

Mode	Eigenvalue	Relative Damping $\zeta$	Natural Frequency $\omega_0$ (rad/s)
Roll mode	-18.4	1	18.4
Dutch-roll mode	-1.35±j3.81	0.34	4.04
Spiral mode	0.375	-1	0.375

Table 4.12: Desired eigenvalues of the closed loop system.

Mode	Eigenvalue	Relative Damping $\zeta$	Natural Frequency $\omega_0$ (rad/s)
Roll mode	-18.4	1	18.4
Dutch-roll mode	-2.86 ±j2.86	$\frac{1}{\sqrt{2}}$	4.04
Spiral mode	-5	1	5
" $e_{i,\beta}$ "	-4	1	4
" $e_{i,\phi}$ "	-4	1	4

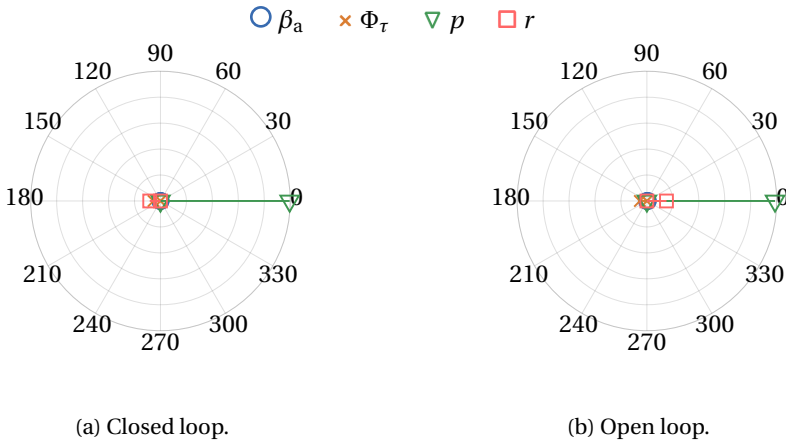


Figure 4.29: Eigenvector components corresponding to the roll mode.

zero. This yields the following set of eigenvectors:

$$\begin{aligned}
 \mathbf{v}_{\text{Roll}}^{\top} &= \begin{pmatrix} 0 & * & * & 10^{-4} & * & * \end{pmatrix} \\
 \mathbf{v}_{\text{DR}}^{\top} &= \begin{pmatrix} * & 0 & 10^{-4} & * & * & * \end{pmatrix} \\
 \mathbf{v}_{\text{DR}}^{\top} &= \begin{pmatrix} * & 0 & 10^{-4} & * & * & * \end{pmatrix} \\
 \mathbf{v}_{\text{Spiral}}^{\top} &= \begin{pmatrix} 0 & * & * & 10^{-4} & * & * \end{pmatrix} \\
 \mathbf{v}_{\beta,i}^{\top} &= \begin{pmatrix} 1 & 0 & * & * & * & * \end{pmatrix} \\
 \mathbf{v}_{\phi,i}^{\top} &= \begin{pmatrix} 0 & 1 & * & * & * & * \end{pmatrix}
 \end{aligned} \tag{4.152}$$

Note, it is not possible to set both selected elements in the eigenvectors to zero since this would lead to  $\mathbf{l}_j = 0$  (see Eq. (4.17)) and hence would render  $(\mathbf{v}_1^{\top} \dots \mathbf{v}_r^{\top})$  singular. Consequently, the controller gain is in this case not defined (see Eq. (4.21)). For this reason one of the two elements is set to a small, but larger than zero, value instead. With these design choices the following controller gain matrix is obtained:

$$\mathbf{K}_{\text{lat,ESA}} = \begin{pmatrix} 0.3184 & -1.8772 & -0.0710 & -0.1193 & -0.1130 & 3.7744 \\ 3.8427 & 1.7525 & 0.5879 & -1.0874 & -9.0269 & 0.6663 \end{pmatrix} \tag{4.153}$$

The designed controller is able to improve the decoupling of the roll and yaw motion which can be shown by comparing the eigenvector stars of the open loop and closed loop system which are displayed in Fig. 4.29a-Fig. 4.31b. As desired, the roll motion is nearly unchanged and is a mode that is mainly influence by the roll rate. Contrarily, the dutch-roll is now mainly a yaw motion and the controller is able to remove the dependency on

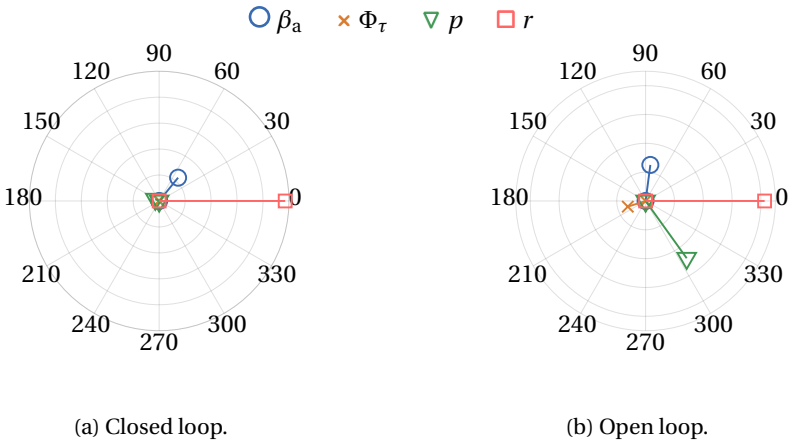


Figure 4.30: Eigenvector components corresponding to the dutch-roll mode.

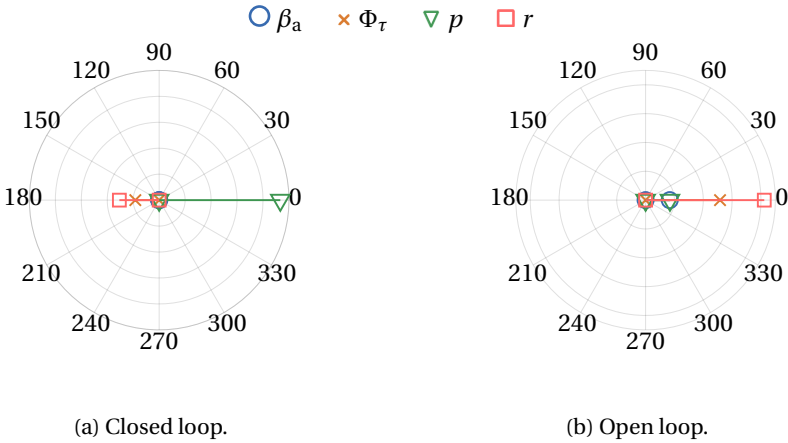


Figure 4.31: Eigenvector components corresponding to the spiral mode.

the roll rate. The spiral mode is altered the most, which is expected, since the controller stabilizes it and increases its natural frequency. In the open loop case the spiral mode is mainly a function of the yaw rate and the tangential plane roll angle. The controller is able to transform it into a second roll mode as desired through the choice of the elements of the corresponding eigenvector.

In the following, robust stability of this controller design is further analyzed as well as its performance using the step response characteristics. Robust stability of the lateral controller with respect to parametric plant uncertainties is verified analogously to the longitudinal controller using the SSV ( $\mu_\Delta$ -analysis). The SSV is calculated for the closed-loop plant models that are obtained with the controller and the state-space models derived for the same five operating points as for the longitudinal case. The numerical

Table 4.13: Robustness margins for the ESA controller. The quasi-stationary point is characterized by specific values for airspeed, angle of attack and tether force (values in brackets are in that order). The design point is highlighted in orange.

Quasi steady point	Lower bound	Upper bound
$p_1$ (27.70 ms <sup>-1</sup> , 10°, 1.6 kN)	1.19	1.20
$p_2$ (30.56 ms <sup>-1</sup> , 10°, 2 kN)	1.28	1.29
$p_3$ (31.35 ms <sup>-1</sup> , 7°, 1.8 kN)	1.53	1.58
$p_4$ (32.91 ms <sup>-1</sup> , 4°, 1.6 kN)	1.67	1.88
$p_5$ (36.32 ms <sup>-1</sup> , 4°, 2 kN)	1.72	1.96

values for the state-space models can be found in the appendix of this work (see Appendix A) and the results of the  $\mu_\Delta$ -analysis are summarized in Table 4.13. It can be observed that the controller is robustly stabilizing all five plants. In general, the robustness increases with airspeed. This can be explained by the increase in control authority at higher airspeed, due to the higher dynamic pressure.

In addition to the  $\mu_\Delta$ -analysis also a statistical analysis, analogously to the longitudinal case, is conducted in order to assess how the step response characteristics change if the state-space models are randomly perturbed. Roll angle and sideslip angle step inputs of  $\beta_{a,c} = 10^\circ$  and  $\Phi_{\tau,c} = 10^\circ$  are commanded and the resulting values for rise time, overshoot and settling time are determined. Besides the nominal step response also the robust performance of the controller is analyzed using perturbed state-space models. To summarize the outcome of the statistical experiments the 0.95-quantile  $q_{0.95}$  is again utilized. Additionally, the quantile for the induced sideslip angle due to a roll maneuver is calculated in order to quantify the decoupling capability of the controller. The statistical assessment is conducted at all five operating points. The step responses are displayed in Fig. 4.32a-Fig. 4.36b and the precise values of the step response characteristics as well as the corresponding quantile values are listed in Table 4.14. In the figures the nominal responses are indicated by the light green and cyan colored curves. The responses obtained with the perturbed model are indicated by the dark blue and dark green colored curves. It can be observed, as expected from the  $\mu_\Delta$ -analysis, that all sampled models are stable with the designed controller in the loop and in the defined uncertainty interval. Regarding the nominal step response characteristics the following observations can be made. For both sideslip angle and roll angle the rise time slightly increases with increasing airspeed. This can be attributed to the higher damping for a larger airspeed which also leads to a smaller overshoot. Since the roll motion is an aperiodic mode, no overshoot occurs across all five operating points. The settling time for the sideslip varies only slightly. It first decreases and then slightly increases again due to the almost overdamped behavior at  $p_4$  and  $p_5$ . Note, this "nonlinear" behavior needs also to be attributed to the definition of the settling time which in this case corresponds to the point in time where the signal stays within a  $\pm 2\%$  interval around the set point. Hence, as long as the overshoot is below 2% it will result in a lower settling time than a more

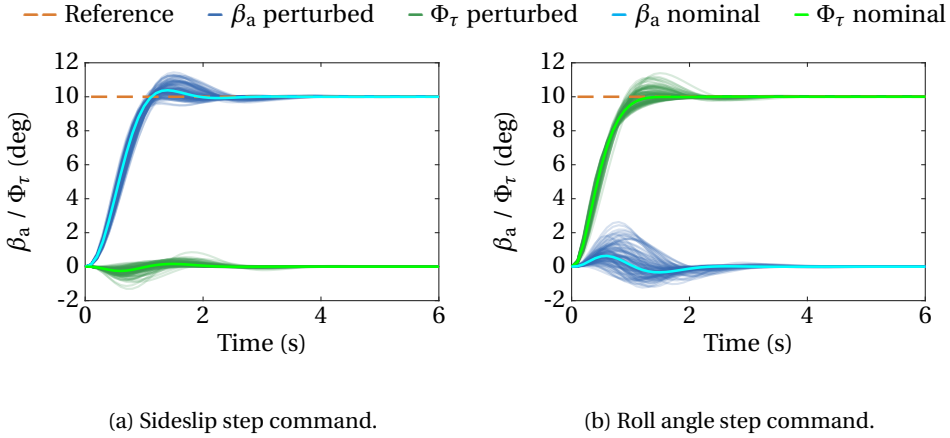


Figure 4.32: Step response of the ESA lateral controller using the nominal and the perturbed models at the design point  $p_1$  of the traction phase.

damped step response. This explains the minimum of the settling time for the sideslip angle at  $p_3$ . Due to the aperiodicity of the roll motion the settling time correlates with the rise time and hence increases with rising airspeed. An important design goal was to reduce the induction of a sideslip angle during a roll maneuver. The maximum induced roll angle during a step command for the sideslip angle at all operating points is shown in the last line of the Table 4.14. In the nominal case the induced sideslip stays below  $1^\circ$  at all operating points while at the design point the minimum is reached and almost no sideslip ( $0.04^\circ$ ) is induced. This result demonstrates the successful decoupling properties of the ESA design approach.

Table 4.14: Statistical step response characteristics for all five perturbed state-space models and the ESA controller designed at  $p_3$ . Rise time is defined as the point where the signal reaches 95% of the reference value, overshoot is calculated with respect to the set point and settling time is defined as the point where the signal stays within  $\pm 2\%$  around the reference value. The values in brackets are obtained with the nominal model.

Characteristic	$q_{0.95}^{p1}$	$q_{0.95}^{p2}$	$q_{0.95}^{p3}$	$q_{0.95}^{p4}$	$q_{0.95}^{p5}$
Rise time $\beta_a$ (s)	1.11 (1.01)	1.17 (1.05)	1.26 (1.08)	1.39 (1.12)	1.42 (1.16)
Rise time $\Phi_\tau$ (s)	1.24 (0.99)	1.29 (1.05)	1.33 (1.13)	1.35 (1.19)	1.40 (1.24)
Overshoot $\beta_a$ (%)	10.82 (3.82)	8.78 (2.37)	7.30 (1.35)	5.83 (0.49)	4.05 (0.34)
Overshoot $\Phi_\tau$ (%)	8.78 (0.00)	7.00 (0.00)	3.99 (0.00)	1.99 (0.00)	1.04 (0.00)
Settling time $\beta_a$ (s)	2.58 (1.68)	2.31 (1.64)	2.29 (1.18)	2.24 (1.24)	2.26 (1.31)
Settling time $\Phi_\tau$ (s)	2.00 (1.14)	1.97 (1.25)	1.87 (1.38)	1.79 (1.49)	1.81 (1.58)
$\Phi_\tau$ to $\beta_a^{\max}$ (deg)	1.83 (0.63)	1.96 (0.59)	1.27 (0.04)	1.20 (0.53)	1.18 (0.49)

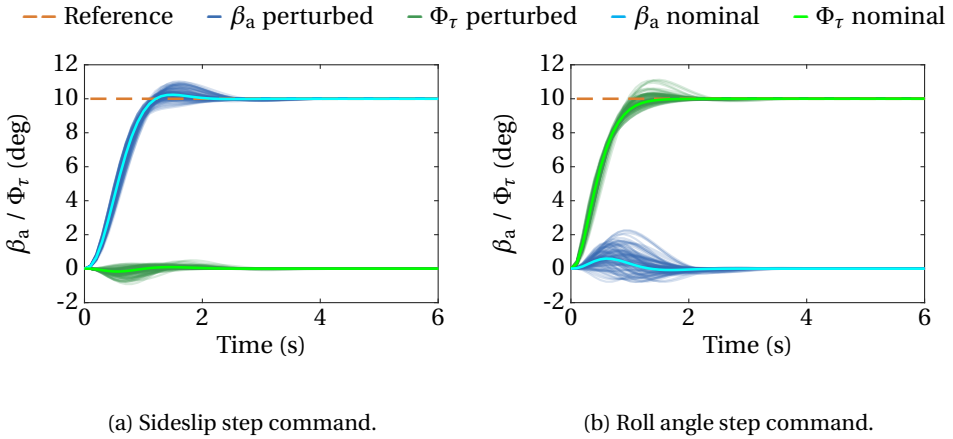


Figure 4.33: Step response of the ESA lateral controller using the nominal and the perturbed models at the design point  $p_2$  of the traction phase.

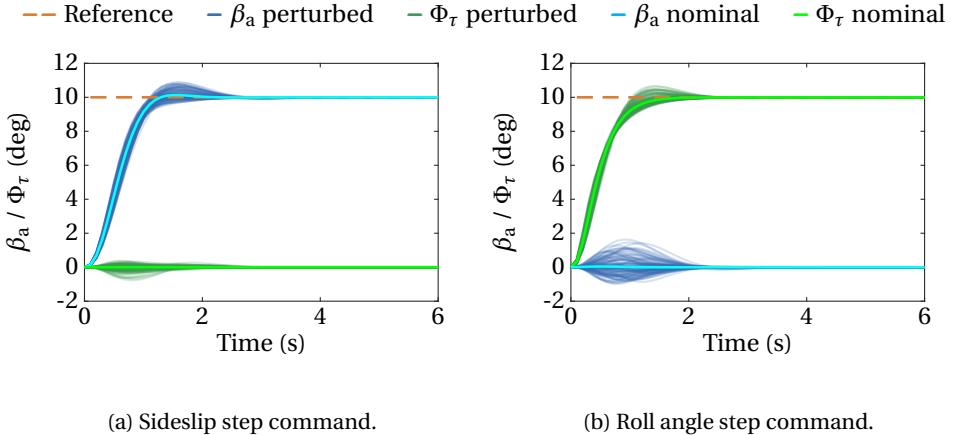


Figure 4.34: Step response of the ESA lateral controller using the nominal and perturbed models at the design point  $p_3$  of the traction phase.

The statistical results of the step responses using the perturbed state-space models lead qualitatively to similar results. The rise time for both sideslip and roll angle changes only slightly and increases with airspeed. The most significant difference can be observed in the overshoot. Especially at low airspeeds the low natural damping leads to a 95% quantile value of 10.82% for the sideslip angle and 8.78% for the roll angle. The design goal was set to be 10% however since this limit is only violated slightly it is decided that this design is acceptable. The settling time for both states is again similar to the nominal case. The induced sideslip angle is higher compared to the nominal case which is attributed to the fact that the uncertainties can amplify coupling effects that the controller is not able to compensate as effectively as in the nominal case. However,

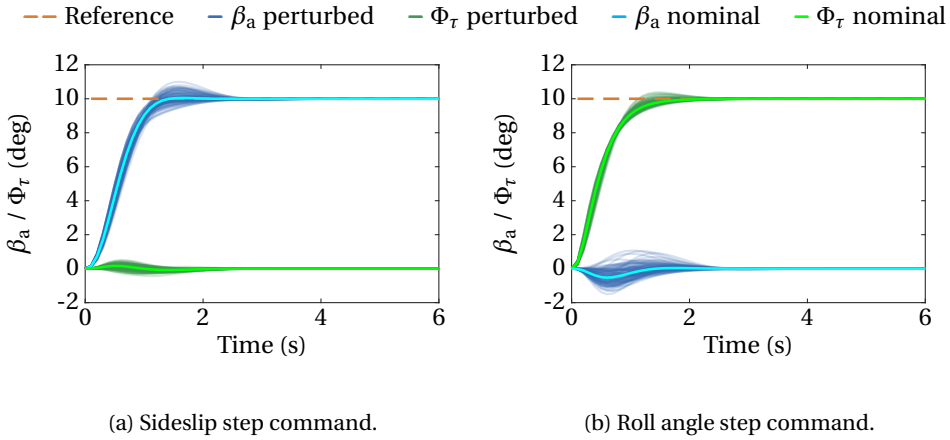


Figure 4.35: Step response of the ESA lateral controller using the nominal and the perturbed models at the design point  $p_4$  of the retraction phase.

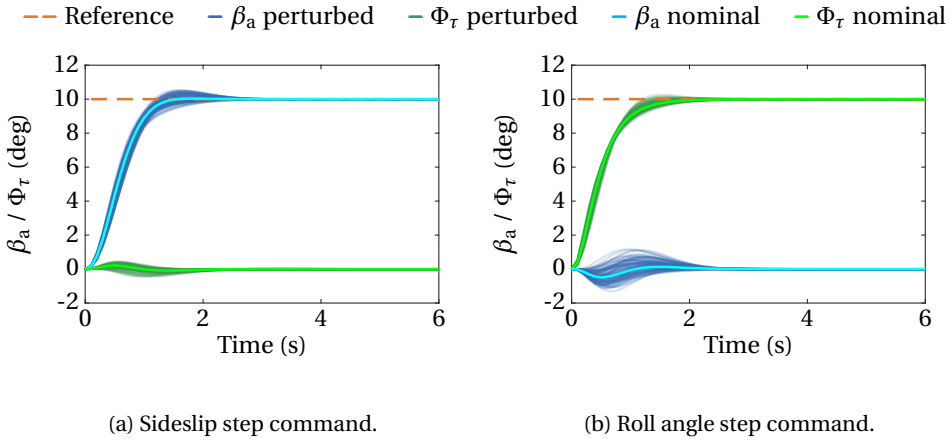


Figure 4.36: Step response of the ESA lateral controller using the nominal and the perturbed models at the design point  $p_5$  of the traction phase.

at all operating points the maximum quantile value for the maximum sideslip induction is below  $2^\circ$  which is regarded as an acceptable result. Note, based on the  $\mu_\Delta$ -analysis it can be observed that the robustness of the controller increases with airspeed. The same conclusion can be drawn regarding the robust performance using the statistical step response characteristics. The large overshoot at the operating point with the lowest airspeed is the most critical performance variation observed in the analysis with the perturbed state-space models.

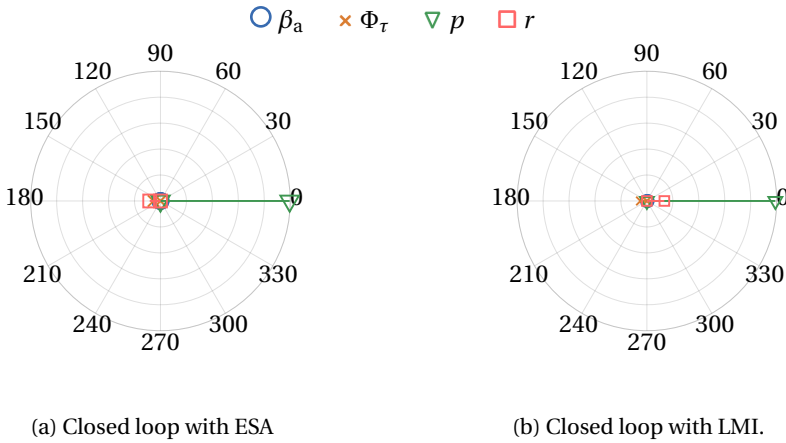


Figure 4.37: Eigenvector components corresponding to the roll mode.

#### Design based on Linear Matrix Inequalities

For the lateral dynamics also an LMI based controller is derived and compared to the ESA controller with respect to its robustness and performance properties. Similar to the derivation of the longitudinal controller the gains are synthesized by taking into account five plant models simultaneously for the controller synthesis. The numerical values for the state-space models can be found in the appendix of this work (see Appendix A). The weighting matrices are chosen to be:

$$\begin{aligned} \mathbf{Q}_{\text{LMI,lat}} &= \text{diag}(0, 0, 0, 0, 60, 60) \\ \mathbf{R}_{\text{LMI,lat}} &= \text{diag}(1, 1) \end{aligned} \quad (4.154)$$

This leads to the following controller gain matrix:

$$\mathbf{K}_{\text{lat,LMI,traction}} = \begin{pmatrix} -1.5027 & -2.3145 & -0.1122 & 0.0079 & 5.6412 & 5.3082 \\ 1.7277 & -1.9885 & 0.0073 & -0.6581 & -5.3082 & 5.6412 \end{pmatrix} \quad (4.155)$$

The ESA approach allows to systematically shape the modes of the closed loop system and hence allows to decouple the roll and yaw motion. The LMI design approach is more abstract and ultimately tries to minimize the  $H_2$ -norm of the closed loop system, hence the closed-loop dynamics are not as intuitively shaped as with the ESA controller. Therefore, it is instructive to analyze the resulting decoupling capabilities of the LMI controller and compare it with the ESA controller. This analysis is conducted using again the eigenvector stars shown in Fig. 4.37a-Fig. 4.39b. For convenience, the eigenvector stars corresponding to the closed-loop plant obtained with the ESA controller are again displayed.

As expected, the results indicate that the LMI controller is not able to decouple the roll and yaw motion as effectively as the ESA controller. Both approaches have a similar, unchanged compared to the open loop, roll mode which is dominated by the roll rate. However, the oscillatory mode (i.e. dutch-roll) is with the ESA controller only dominated

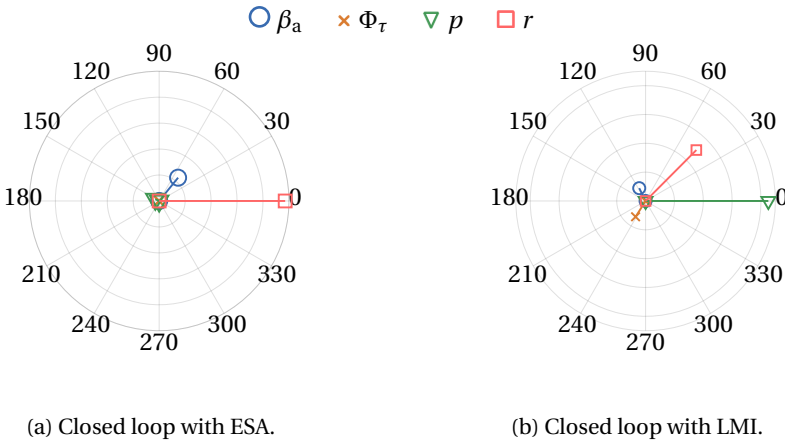


Figure 4.38: Eigenvector components corresponding to the dutch-roll mode.

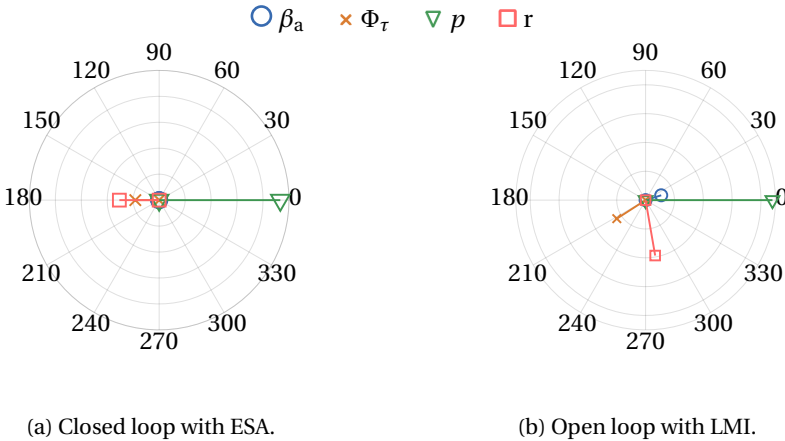


Figure 4.39: Eigenvector components corresponding to the spiral mode.

by the sideslip and the yaw rate which are both yaw motion states. The second aperiodic lateral mode is dominated by the roll rate which is obviously a roll motion state. Contrarily, with the LMI controller the oscillatory mode is dominated mostly by the roll rate but also the yaw rate has a non-negligible contribution. Similar state contributions can be observed for the second aperiodic mode.

Robust stability of the lateral LMI controller is assessed using again the  $\mu_\Delta$ -analysis. The results are displayed in Table 4.15. The LMI controller is robustly stabilizing the plant at all considered operating points within the specified uncertainty intervals. For the two operating conditions  $p_1$  and  $p_2$  the LMI controller is providing higher robustness margins than the ESA controller. At the ESA design point both controllers yield almost identical stability margins whereas for the operating points  $p_4$  and  $p_5$  the ESA controller

Table 4.15: Robustness margins of the LMI based lateral control system. The quasi-stationary point is characterized by specific values for airspeed, angle of attack and tether force (values in brackets are in that order). The orange line indicates the operating point that is selected for the ESA design.

Quasi steady point	Lower bound	Upper bound
$p_1$ (27.70 ms <sup>-1</sup> , 10°, 1.6 kN)	1.38	1.58
$p_2$ (30.56 ms <sup>-1</sup> , 10°, 2 kN)	1.47	1.70
$p_3$ (31.35 ms <sup>-1</sup> , 7°, 1.8 kN)	1.51	1.85
$p_4$ (32.91 ms <sup>-1</sup> , 4°, 1.6 kN)	1.49	1.87
$p_5$ (36.32 ms <sup>-1</sup> , 4°, 2 kN)	1.56	1.96

leads to higher robustness margins. Therefore, it is expected that the LMI controller is more robust in the low airspeed range, while the ESA controller is more robust in the high airspeed range.

Finally, the robust performance of the controller is analyzed using 1000 randomly sampled state-space models of the lateral dynamics. The step response characteristics are summarized in Table 4.16. First the nominal responses are analysed and compared with the ESA controller. Compared to the ESA controller the LMI controller leads to a lower rise time, which stays almost identical across all five operating points. In contrast to that the rise time of the tangential plane roll angle is lower for the ESA controller at the first four operating points. At  $p_5$  the rise time of the LMI controller is slightly higher. The LMI controller leads to a lower sideslip angle overshoot at all operating points. In fact, except at  $p_1$  no overshoots occur. However, the ESA controller achieves lower roll

Table 4.16: Statistical step response characteristics for all five perturbed state-space models and the LMI designed at  $p_3$ . Rise time is defined as the point where the signal reaches 95% of the reference value, overshoot is calculated with respect to the set point and settling time is defined as the point where the signal stays within  $\pm 2\%$  around the reference value. The values in brackets are obtained with the nominal model.

Characteristic	$q_{0.95}^{p1}$	$q_{0.95}^{p2}$	$q_{0.95}^{p3}$	$q_{0.95}^{p4}$	$q_{0.95}^{p5}$
Rise time $\beta_a$ (s)	0.86 (0.74)	1.04 (0.77)	1.13 (0.76)	1.22 (0.74)	1.25 (0.80)
Rise time $\Phi_\tau$ (s)	1.31 (1.12)	1.34 (1.14)	1.36 (1.16)	1.38 (1.17)	1.45 (1.23)
Overshoot $\beta_a$ (%)	7.73 (1.96))	5.23 (0)	5.71 (0)	5.48 (0)	3.46 (0)
Overshoot $\Phi_\tau$ (%)	9.01 (3.99)	6.53 (1.93)	4.47 (0.83)	2.51 (0.00)	1.03 (0.00)
Settling time $\beta_a$ (s)	1.74 (0.79)	1.64 (0.86)	1.64 (0.84)	1.67 (1.40)	1.58 (1.31)
Settling time $\Phi_\tau$ (s)	2.49 (2.02)	2.37 (1.25)	2.17 (1.28)	1.82 (1.34)	1.78 (1.47)
$\Phi_\tau$ to $\beta_a^{\max}$ (deg)	2.69 (1.91)	2.57 (1.86)	2.14 (1.47)	1.69 (1.04)	1.68 (1.05)

angle overshoot. The settling times for the sideslip angle are slightly shorter with the LMI controller except for the operating point  $p_4$ . The settling time for the roll angle is shorter with the ESA controller at  $p_1$  and  $p_2$ . At  $p_3$ ,  $p_4$  and  $p_5$  the LMI controller achieves a quicker settling time. Moreover, the roll-angle command induced sideslip angle is lower with the ESA controller at all five operating points, due to the better decoupling capabilities of the ESA controller. Nevertheless, also with the LMI controller the induced sideslip angle stays below  $2^\circ$  which is regarded as acceptable.

The statistical simulations lead to qualitatively similar results. The rise times for both sideslip and roll angle are only slightly higher than the nominal values. Similar to the ESA controller the largest performance loss is observed in terms of the overshoot. Here, the LMI controller leads again to a lower maximum overshoot than the ESA controller. No significant differences between the settling times of the nominal and the stochastic simulations can be observed. The same holds also for the induced roll angle in presence of model uncertainties. Here only a slight increase, i.e. less than  $+1^\circ$ , in the induced roll angle can be observed.

To sum it up, the LMI controller leads to similar results compared to the ESA controller. It offers slightly higher robustness margins at lower airspeeds but lower margins at higher airspeeds. No significant differences between the step responses (i.e. robust performance) between the two control approaches can be observed. Due to the similarities both control approaches are considered as final candidates to control the lateral dynamics. A final recommendation is later on given based on the results obtained with the nonlinear simulations.

#### 4.7.2. Retraction Phase

The inner loop retraction phase flight controller consists similarly to the traction phase controller of a longitudinal controller that tracks angle of attack commands as well as a lateral controller that tracks sideslip and roll angle commands. The retraction phase resembles a gliding flight state for untethered aircraft since the tension in the tether is kept low to minimize the required power consumption while reeling in the tether. Note, in contrast to the traction phase the conventional Euler angles with respect to the ground are controlled.

##### Longitudinal Control System

Similar to the traction phase a linear quadratic controller with servo mechanism is designed. In addition, a LMI based  $H_2$ -norm optimal controller is derived for a set of plants that envelope a relevant part of the retraction phase state-space. Note, similar to the longitudinal case a comparison between a single model LQR and the LMI based approach has been conducted but a detailed comparison is omitted here since similar results as for the traction phase controller were obtained that show higher robustness margins for the LMI controller with equivalent nominal step response characteristics (i.e. performance) compared to the simple LQR.

Based on the quasi-stationary analysis presented in chapter 3, and the 3-DoF simulations, three quasi-stationary points are chosen to design the controller. The first quasi-steady point ( $p_1$ ) is defined by  $v_a = 28.75 \text{ m s}^{-1}$  and  $\alpha_a = -3^\circ$ , the second quasi-steady point ( $p_2$ ) is defined by  $v_a = 32.29 \text{ m s}^{-1}$  and  $\alpha_a = -3.5^\circ$  and the third quasi-steady point

Table 4.17: Open loop analysis at the retraction phase operating point  $p_2$ .

Mode	Eigenvalue	Relative Damping $\zeta$	Natural Frequency $\omega_0$ (rad/s)
Short period at $p_2$	$-6.25 \pm 2.80$	0.91	6.85
Phygooid $p_2$	$-0.12 \pm j0.35$	0.34	0.36

( $p_3$ ) is defined by  $v_a = 37.73 \text{ ms}^{-1}$  and  $\alpha_a = -4^\circ$ . All three states require low tether tensions of  $F_t = 45.47 \text{ N}$ ,  $F_t = 66.36 \text{ N}$ , and  $F_t = 105.71 \text{ N}$ , respectively. The design steps are equivalent to the previous section. First, the step response characteristics are used to tune the controller gains. Second, a  $\mu_\Delta$ -analysis is conducted to calculate guaranteed stability bounds using perturbed state-space models. In the last step a statistical analysis of the step response characteristics is performed by simulating randomly picked perturbed state-space models within a specified uncertainty set. In general, during the retraction phase the aircraft is not required to fly dynamic maneuvers, hence more emphasis can be put on a robust controller design. The numerical values of the three utilized state-space models are listed in the appendix. Exemplary, the state-space model at  $p_2$  is shown in Eq. (4.156).

$$\begin{pmatrix} \dot{v}_a \\ \dot{\alpha}_a \\ \dot{\Theta} \\ \dot{q} \\ \dot{e}_{i,\alpha} \end{pmatrix} = \begin{pmatrix} -0.15 & 29.45 & -14.19 & -0.18 & 0 \\ -0.02 & -9.43 & 0.22 & 0.90 & 0 \\ 0 & 0 & 0 & 1 & 0 \\ 0 & -19.87 & 0 & -3.16 & 0 \\ 0 & -1 & 0 & 0 & 0 \end{pmatrix} \begin{pmatrix} v_a \\ \alpha_a \\ \Theta \\ q \\ \int_0^t e_\alpha d\tau \end{pmatrix} + \begin{pmatrix} 0.09 \\ -0.51 \\ 0 \\ -34.2 \\ 0 \end{pmatrix} \delta_e + \begin{pmatrix} 0 \\ 0 \\ 0 \\ 0 \\ 1 \end{pmatrix} \alpha_{a,c} \quad (4.156)$$

with  $e_\alpha = \alpha_{a,c} - \alpha_a$ ,  $e_{i,\alpha} = \int_0^t e_\alpha d\tau$ . The open loop mode characteristics are summarized exemplary for  $p_2$  in Table 4.5. It can be observed that at this operating point the plant is characterized by a well damped short period mode. The phygooid mode is less damped which needs to be improved through the feedback controller.

For the controller design the following waiting matrix is chosen:

$$\begin{aligned} \mathbf{Q}_{\text{LMI,long,retraction}} &= \text{diag}(0, 15, 0, 0, 40) \\ R_{\text{LMI,long,retraction}} &= 1.1 \end{aligned} \quad (4.157)$$

which results in the following controller gain matrix:

$$\mathbf{K}_{\text{long,retraction,LMI}} = \begin{pmatrix} 0.0072 & -1.4949 & -0.0851 & -0.1977 & 6.0302 \end{pmatrix} \quad (4.158)$$

The resulting closed-loop plant characteristics are listed in Table 4.18. The state feedback controller increases the natural frequency of the short period mode by moving the real part more into the left complex half plane. This leads to a reduction of the relative damping which is now only slightly higher than the optimal damping given by  $\frac{1}{\sqrt{2}}$ . On

Table 4.18: Closed loop analysis of the state-space models defined in Eq. (4.156) and the feedback controller defined in Eq. (4.158).

Mode	Eigenvalue	Relative Damping $\zeta$	Natural Frequency $\omega_0$ (rad/s)
Short period at $p_2$	$-9.2 \pm 6.87$	0.80	11.5
Phygoid at $p_2$	$-0.21 \pm j0.55$	0.35	0.59
Integrator at $p_2$	-1.46	1	1.46

the other hand, the phygoid damping is only slightly increased, however, the real parts of the eigenvalues are moved more into the left complex half plane which increases the natural frequency of the plant.

The  $\mu_\Delta$ -analysis yields the results depicted in Table 4.19. The results show that the controller guarantees robust stability within the modeled uncertainty interval. The robustness increases with rising airspeed which can be explained by the raising control authority.

The step responses are visualized in Fig. 4.40b and Fig. 4.41. The numerical values obtained with the statistical simulations are summarized in Table 4.20. The rise time increases from low to high airspeed. A significant increase at  $p_3$  can be explained by the step response shown in Fig. 4.41. The initial reaction is similar to the step responses at  $p_1$

Table 4.19: Robustness margins for the LMI based longitudinal controller for the retraction phase. The quasi-stationary point is characterized by airspeed, angle of attack and tether force (values in brackets are in that order).

Quasi steady point	LB LMI	UB LMI
$p_1 (28.75 \text{ ms}^{-1}, -3^\circ, 45.47 \text{ kN})$	1.00	1.04
$p_2 (32.29 \text{ ms}^{-1}, -3.5^\circ, 66.36 \text{ kN})$	1.19	1.26
$p_3 (37.73 \text{ ms}^{-1}, -4^\circ, 105.71 \text{ kN})$	1.39	1.55

Table 4.20: Statistical step response characteristics for all five perturbed state-space models and the LMI controller. Rise time is defined as the point where the signal reaches 95% of the reference value, overshoot is calculated with respect to the set point and settling time is defined as the point where the signal stays within  $\pm 2\%$  around the reference value. The values in brackets are obtained with the nominal model.

Characteristic	$q_{0.95}^{p1}$	$q_{0.95}^{p2}$	$q_{0.95}^{p3}$
Rise time $\alpha_a$ (s)	3.81 (2.10)	5.31 (2.74)	7.41 (5.67)
Overshoot $\alpha_a$ (%)	7.55 (1.09)	2.78 (0.90)	2.10 (1.16)
Settling time $\alpha_a$ (s)	13.24 (2.69)	8.79 (4.99)	10.72 (7.04)

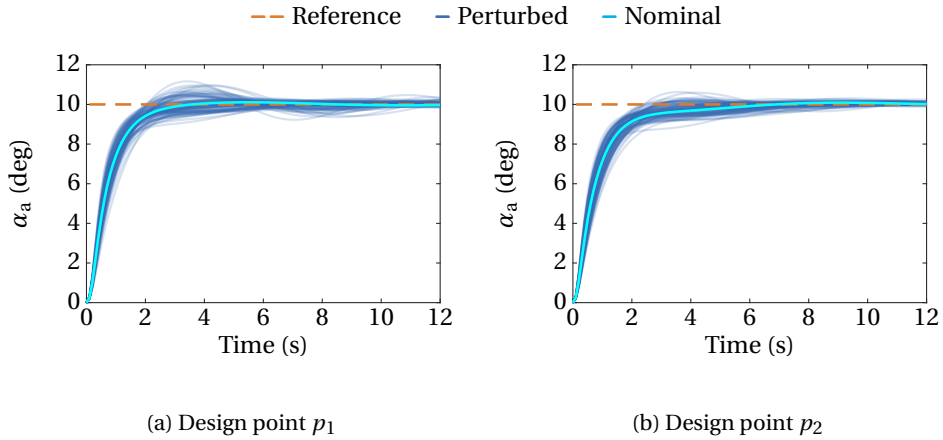


Figure 4.40: Step responses for the nominal as well as the perturbed models at different retraction phase operating points using the LMI controller.

and  $p_2$  (see Fig. 4.40a and Fig. 4.40b). However, it takes longer for the controller to converge to the steady state value. This can be explained by the smaller natural frequency associated with the integrator state at  $p_3$  (see Table 4.18). Only a negligible overshoot is present for all three operating points.

### Lateral Control System

In this section the lateral controller for the retraction phase is derived. Similar to the traction phase controller the gains are derived using the ESA algorithm and the LMI based approach. The controller gains are derived from the state-space models obtained through linearization around the same quasi-stationary operating points as for the longitudinal controller. The numerical values of the three utilized state-space models are listed in the appendix. Exemplary, the state-space model at  $p_2$  is shown in Eq. (4.159).

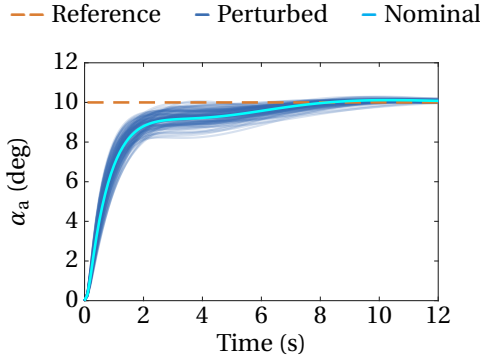


Figure 4.41: Step responses obtained with the nominal as well as the perturbed models at the retraction phase point  $p_3$  using the LMI controller .

$$\begin{aligned}
 p_2 : \begin{pmatrix} \dot{\beta}_a \\ \dot{\Phi} \\ \dot{p} \\ \dot{r} \\ \dot{e}_{i,\beta} \\ \dot{e}_{i,\Phi} \end{pmatrix} &= \begin{pmatrix} -0.39 & 0.35 & -0.07 & -0.98 & 0 & 0 \\ 0 & 0 & 1.0 & -0.14 & 0 & 0 \\ -26.28 & 0 & -20.13 & 5.07 & 0 & 0 \\ 11.61 & 0 & -0.18 & -0.87 & 0 & 0 \\ -1.0 & 0 & 0 & 0 & 0 & 0 \\ 0 & -1.0 & 0 & 0 & 0 & 0 \end{pmatrix} \begin{pmatrix} \beta_a \\ \Phi \\ p \\ r \\ e_{i,\beta} \\ e_{i,\Phi} \end{pmatrix} \\
 &+ \begin{pmatrix} -0.08 & 0.16 \\ 0 & 0 \\ -104.24 & 1.75 \\ 4.02 & -7.42 \\ 0 & 0 \\ 0 & 0 \end{pmatrix} \begin{pmatrix} \delta_a \\ \delta_r \end{pmatrix} + \begin{pmatrix} 0 & 0 \\ 0 & 0 \\ 0 & 0 \\ 0 & 0 \\ 1 & 0 \\ 0 & 1 \end{pmatrix} \begin{pmatrix} \beta_{a,c} \\ \Phi_c \end{pmatrix}
 \end{aligned} \tag{4.159}$$

with  $e_\beta = \beta_{a,c} - \beta_a$ ,  $e_{i,\beta} = \int_0^t e_\beta d\tau$ ,  $e_\Phi = \Phi_c - \Phi$  and  $e_{i,\Phi} = \int_0^t e_\Phi d\tau$ . The open-loop mode characteristics are shown in Table 4.21. The results indicate a low damped dutch roll which needs to be improved by the controller. The roll mode is regarded as sufficiently fast.

#### Design based on ESA

The ESA design objective is similar to the one stated for the traction phase. The lowly damped dutch-roll mode (see Table 4.21) needs to be improved by setting the desired relative damping of the closed-loop system to  $\frac{1}{\sqrt{2}}$  while the natural frequency of the

open-loop system is maintained. Similarly, the natural frequency of the roll mode is not modified. At the design point of the ESA controller ( $p_2$ ) the spiral mode is slightly unstable, hence, the controller needs to stabilize it. The desired natural frequency of the spiral mode is a tuning parameter and is set to  $5 \text{ rad s}^{-1}$ . The eigenvalues corresponding to the integrator states are set to  $-4$ . Overall, the design parameters are summarized in Table 4.22. The desired eigenvectors are chosen equivalently to the ones chosen for the traction phase controller with the goal to decouple the roll and yaw modes (see Eq. (4.152)). These design decisions result in the following controller gain matrix:

$$\mathbf{K}_{\text{lat,ESA,retraction}} = \begin{pmatrix} 0.3380 & -1.8352 & -0.0747 & -0.0387 & -0.1817 & 3.6859 \\ 2.6689 & 3.4529 & 0.4611 & -1.0759 & -6.7871 & -6.4944 \end{pmatrix} \quad (4.160)$$

The designed controller is able to improve the decoupling of the roll and yaw motion which can be shown by comparing the eigenvector stars of the open loop and closed loop system which are displayed in Fig. 4.42a-Fig. 4.44b. Note, that the roll mode has a small contribution of the yaw-rate (see Fig. 4.42a). This is due to the fact that the corresponding element in the eigenvector cannot be chosen to be exactly zero as explained in the previous section, since this results in a singularity and yields no valid controller. The resulting dutch roll and also the spiral mode are transformed into mainly a yaw motion and into a second roll mode as expected.

In the next step, the robustness of the controller is analysed using the SSV. The results are summarized in Table 4.23. It can be seen that the controller robustly stabilizes the plant at all three operating points. Furthermore, the robust performance is analyzed

Table 4.21: Open loop analysis of the state-space models defined in Eq. (4.159).

Mode	Eigenvalue	Relative Damping $\zeta$	Natural Frequency $\omega_0$ (rad/s)
Roll mode at $p_2$	-20.2	1	20.2
Dutch-Roll mode at $p_2$	$-0.58 \pm 3.49$	0.17	3.53
Spiral mode at $p_2$	0.003	-1	0.003

Table 4.22: Desired eigenvalues of the closed loop system at  $p_2$  and with the gain matrix defined in Eq. (4.160).

Mode	Eigenvalue	Relative Damping $\zeta$	Natural Frequency $\omega_0$ (rad/s)
Roll mode	-20.2	1	20.2
Dutch-roll mode	$-2.5 \pm j2.5$	$\frac{1}{\sqrt{2}}$	3.53
Spiral mode	-5	1	5
" $e_{i,\beta}$ "	-4	1	4
" $e_{i,\phi}$ "	-4	1	4

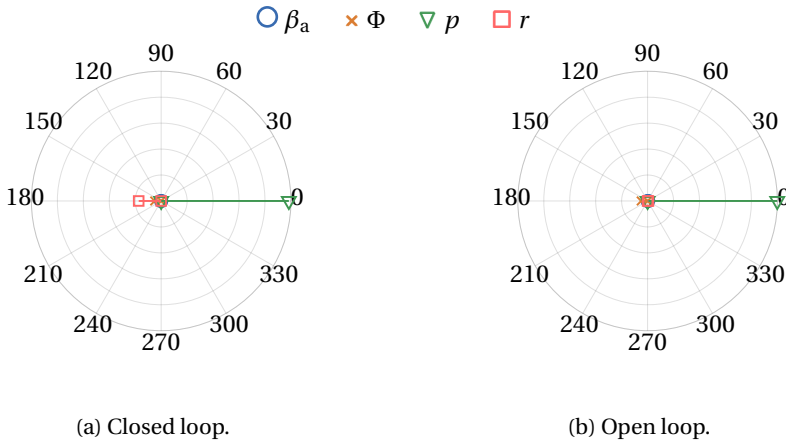


Figure 4.42: Eigenvector components corresponding to the roll mode using the ESA controller.

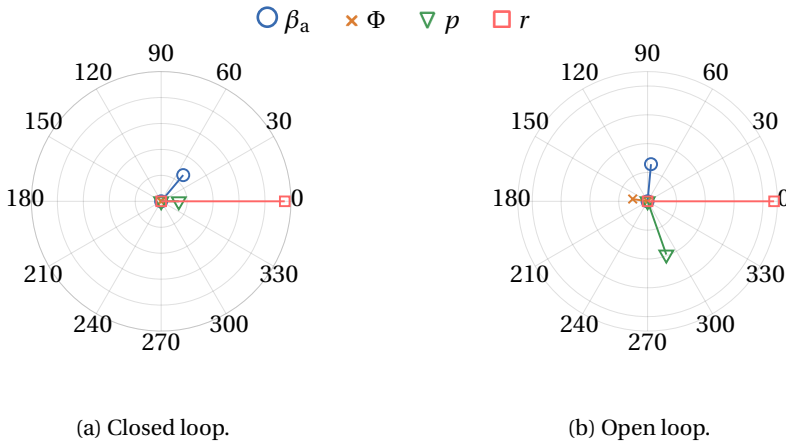


Figure 4.43: Eigenvector components corresponding to the dutch-roll mode using the ESA controller.

Table 4.23: Robustness margins for the ESA retraction phase lateral controller. The quasi-stationary point is characterized by specific values for airspeed, angle of attack and tether force (values in brackets are in that order).

Quasi steady point	Lower bound	Upper bound
$p_1 (28.75 \text{ m s}^{-1}, -3^\circ, 45.47 \text{ kN})$	1.40	1.50
$p_2 (32.29 \text{ m s}^{-1}, -3.5^\circ, 66.36 \text{ kN})$	1.47	1.60
$p_3 (37.73 \text{ m s}^{-1}, -4^\circ, 105.71 \text{ kN})$	1.54	1.71

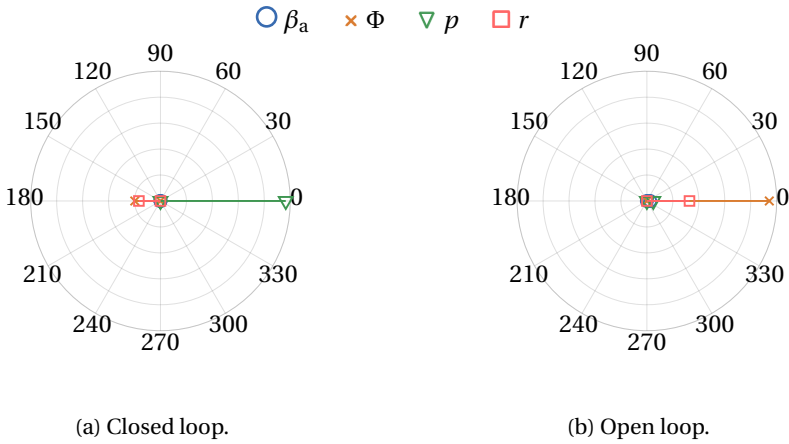


Figure 4.44: Eigenvector components corresponding to the spiral mode using the ESA controller.

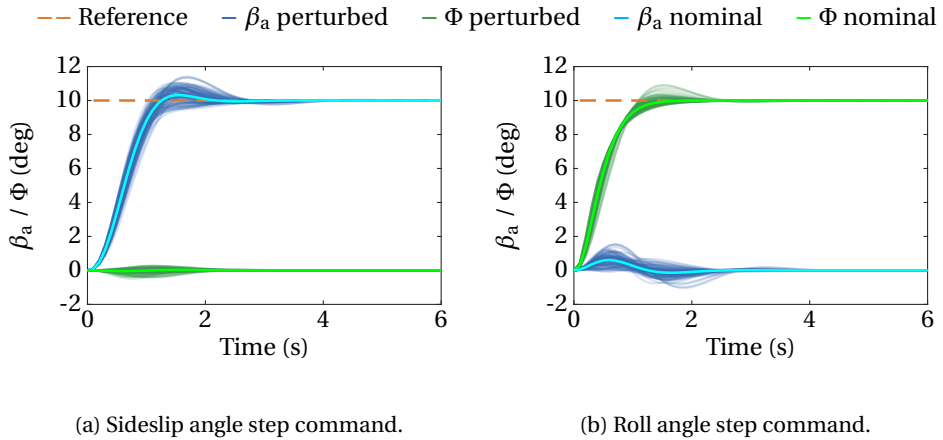


Figure 4.45: Step responses for the nominal as well as the perturbed lateral retraction phase models at  $p_1$  using the ESA controller.

again using a Monte Carlo approach with 1000 randomly sampled state-space models. The step responses are displayed in Fig. 4.45a- Fig. 4.47a and their properties are summarized in Table 4.24. For both sideslip and roll angle the rise time increases slightly for increasing airspeed. Due to the increased damping the overshoot decreases with airspeed. As a result, the settling time increases as well. The controller is able to attenuate the creation of a sideslip angle induced by a roll maneuver which results in sideslip angles well below one degree. Similar results are obtained with the statistical simulations.

#### Design based on LMIs

Similar to the traction phase a lateral controller using the LMI approach is derived and compared to the ESA controller with respect to robustness and performance. The chosen

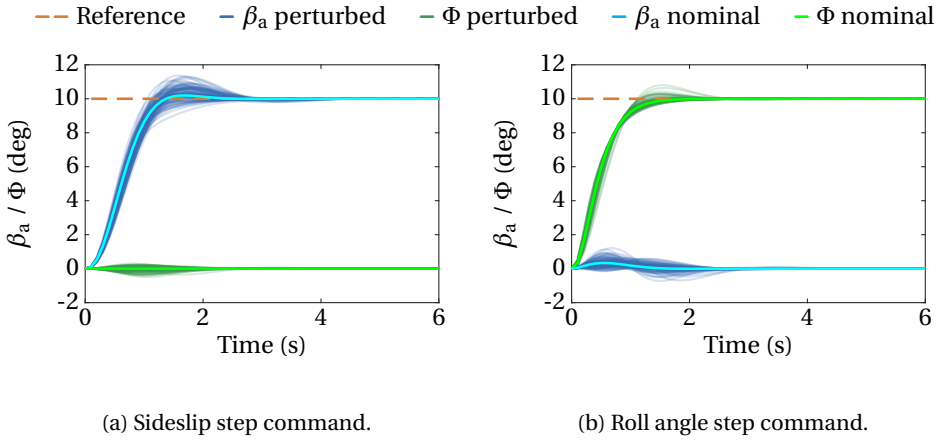


Figure 4.46: Step responses for the nominal as well as the perturbed lateral retraction phase models at  $p_2$  using the ESA controller.

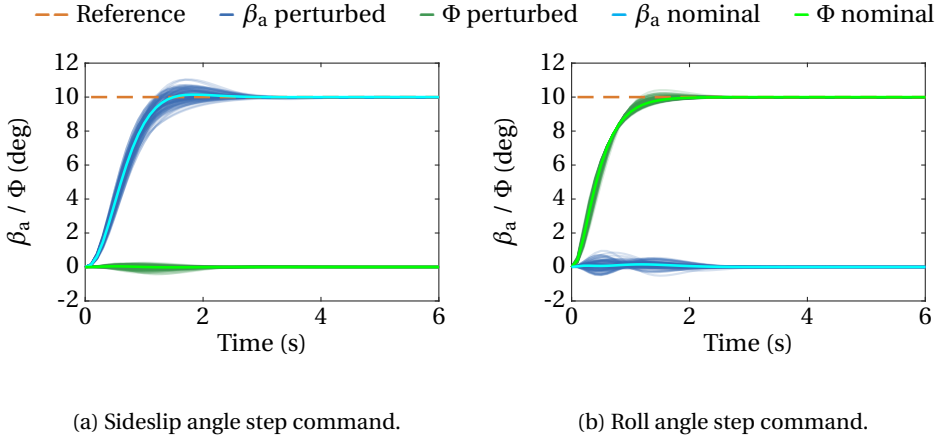


Figure 4.47: Step responses for the nominal as well as the perturbed lateral retraction phase models at  $p_3$  using the ESA controller.

weighting matrices are given by:

$$\begin{aligned} \mathbf{Q}_{\text{LMI,long,traction}} &= \text{diag}(1, 1, 1, 1, 50, 50) \\ \mathbf{R}_{\text{LMI,long,traction}} &= \text{diag}(12, 4) \end{aligned} \tag{4.161}$$

This leads to the following controller gain matrix:

$$\mathbf{K}_{\text{lat,retraction,LMI}} = \begin{pmatrix} -0.0176 & -1.4671 & -0.2071 & 0.0296 & 0.3475 & 2.0115 \\ 1.4422 & -0.1683 & -0.0133 & -0.7742 & -3.4839 & 0.6018 \end{pmatrix} \tag{4.162}$$

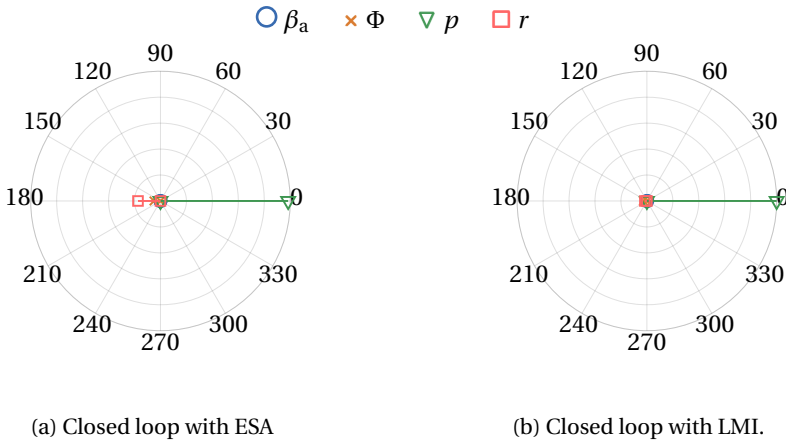


Figure 4.48: Eigenvector components corresponding to the roll mode using the LMI controller.

To compare the decoupling capabilities of the LMI controller the eigenvector stars of LMI and ESA controller are compared to each other. Notice that the LMI controller leaves the roll motion nearly unchanged in contrast to the ESA controller where the yaw rate has a small contribution (see Fig. 4.48a and Fig. 4.48b). Contrarily, the ESA controller is better able to decouple the dutch-roll mode while the LMI controller only slightly reduces the contribution of the roll rate in this mode (see Fig. 4.49a and Fig. 4.49b). The biggest difference is visible in the spiral mode which is transformed into a pure yaw motion with the LMI controller and a roll motion if the ESA controller closes the loop (see Fig. 4.50a and Fig. 4.50b).

Table 4.24: Statistical step response characteristics for all five perturbed state-space models and the ESA controller designed at the retraction phase point  $p_2$ . Rise time is defined as the point where the signal reaches 95% of the reference value, overshoot is calculated with respect to the set point and settling time is defined as the point where the signal stays within  $\pm 2\%$  around the reference value. The values in brackets are obtained with the nominal model.

Characteristic	$q_{0.95}^{p1}$	$q_{0.95}^{p2}$	$q_{0.95}^{p3}$
Rise time $\beta_a$ (s)	1.42 (1.12)	1.52 (1.17)	1.61 (1.24)
Rise time $\Phi$ (s)	1.23 (1.08)	1.26 (1.13)	1.29 (1.17)
Overshoot $\beta_a$ (%)	12.80 (3.20)	9.62 (1.95)	8.52 (1.45)
Overshoot $\Phi$ (%)	4.49 (0.00)	2.72 (0.00)	1.42 (0.00)
Settling time $\beta_a$ (s)	3.08 (1.81)	2.54 (1.27)	2.62 (1.36)
Settling time $\Phi$ (s)	1.99 (1.29)	1.79 (1.37)	1.68 (1.46)
$\Phi$ to $\beta_a^{\max}$ (deg)	1.36 (0.61)	0.92 (0.33)	0.59 (0.15)

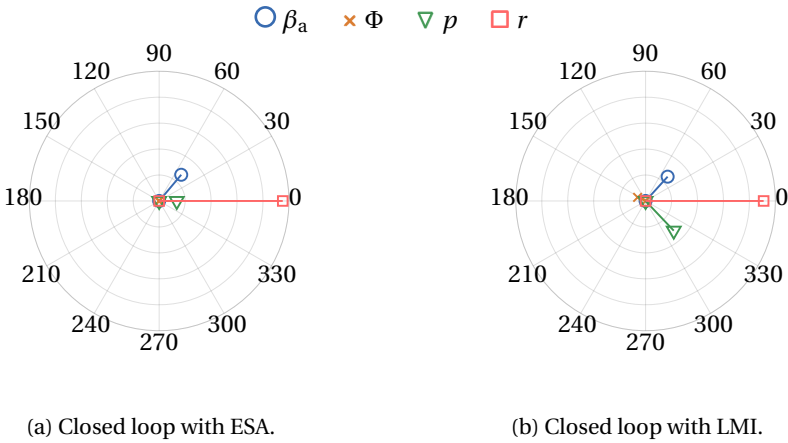


Figure 4.49: Eigenvector components corresponding to the dutch-roll mode using the LMI controller.

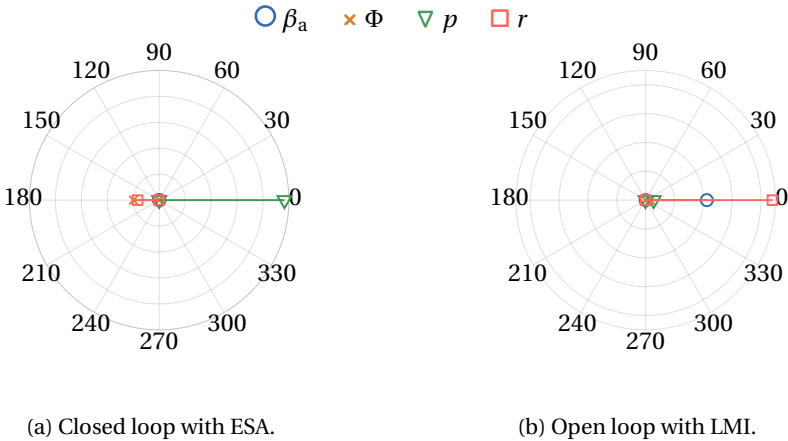


Figure 4.50: Eigenvector components corresponding to the spiral mode using the LMI controller.

In the next step robust stability of the LMI controller is investigated using the SSV. The results are summarized in Table 4.25. The LMI controller is able to guarantee robust stability across all three operating conditions. In fact, it allows even larger uncertainties than the ESA controller and hence can be regarded as a more robust control solution for the retraction phase.

In the last step the robust performance of the LMI controller is analyzed using the statistical step response characteristics. Note, to limit the scope only the numerical values are discussed in the following, since the step response plots are similar to the ones obtained with the ESA controller. The results are displayed in Table 4.26. Similar to the ESA controller the rise time increases with airspeed. However, the LMI controller is slightly less responsive leading to a longer, but acceptable, rise time for both sideslip and

Table 4.25: Robustness margins of the LMI retraction phase lateral flight controller. The quasi-stationary point is characterized by specific values for airspeed, angle of attack and tether force (values in brackets are in that order).

Quasi steady point	Lower bound	Upper bound
$p_1$ (28.75 m s <sup>-1</sup> , -3°, 45.47 kN)	1.58	1.76
$p_2$ (32.29 m s <sup>-1</sup> , -3.5°, 66.36 kN)	1.62	1.82
$p_3$ (37.73 m s <sup>-1</sup> , -4°, 105.71 kN)	1.65	1.89

## 4

roll angle. In terms of overshoot the LMI controller is performing better in regulating the sideslip angle but leads to higher roll angle overshoots. The overshoots are, however, less than 2% and hence acceptable. The settling time for the sideslip angle increases with airspeed if the LMI controller is used. This result fits to the increasing rise time and the zero overshoot property. Similarly, the settling time of the roll angle is increasing. Note, that the overshoot is below 2% which is within the interval that is used to define the settling time. Therefore, the rising settling time for the roll angle is also a result of the increasing rise time. This is different compared to the sideslip angle tracking properties of the ESA controller. In this case the settling time first decreases but the rise time increases. This phenomenon can be explained by the decreasing overshoot. As soon as the overshoot is within the interval that defines the settling time (i.e. 2%) the settling time increases again with increasing rise time. An important result is the better suppression of an induced sideslip angle due to a roll maneuver. In this case the LMI controller outperforms the ESA controller at all three operating points. These results hold qualitatively for both the nominal as well as the perturbed state-space models.

Table 4.26: Statistical step response characteristics for all five perturbed state-space models and the LMI controller designed at  $p_2$ . Rise time is defined as the point where the signal reaches 95% of the reference value, overshoot is calculated with respect to the set point and settling time is defined as the point where the signal stays within  $\pm 2\%$  around the reference value. The values in brackets are obtained with the nominal model.

Characteristic	$q_{0.95}^{p1}$	$q_{0.95}^{p2}$	$q_{0.95}^{p3}$
Rise time $\beta_a$ (s)	2.56 (1.59)	2.59 (1.72)	2.61 (1.83)
Rise time $\Phi$ (s)	1.65 (1.51)	1.66 (1.53)	1.71 (1.56)
Overshoot $\beta_a$ (%)	7.72 (0)	5.87 (0)	4.17 (0)
Overshoot $\Phi$ (%)	7.15 (1.75)	5.98 (1.08)	4.18 (0.5)
Settling time $\beta_a$ (s)	3.25 (1.86)	3.31 (2.09)	3.35 (2.21)
Settling time $\Phi$ (s)	3.33 (1.67)	3.22 (1.71)	2.99 (1.78)
$\Phi$ to $\beta_a^{\max}$ (deg)	0.57 (0.23)	0.43 (0.12)	0.32 (0.12)

To sum it up, both ESA and LMI controller satisfy the robust stability criteria and also achieve acceptable robust performance properties. The LMI controller offers a slightly higher robustness towards the parametric uncertainties compared to the ESA controller. A rather surprising result is the fact that the LMI controller, although not implicitly designed to decouple yaw and roll motion, is better able to damp the induced sideslip angle due to a roll maneuver compared to the ESA controller. Both designs are further investigated in terms of their control performance and robustness on the nonlinear model in the subsequent sections.

## 4.8. Nonlinear Inner Loop Design

In this section a nonlinear inner loop controller that is based on the work published by the author of this thesis in [119] is presented. It utilizes the same nonlinear guidance strategy as the linear inner loop controller but uses a cascaded nonlinear dynamic inversion approach to track the reference commands of the guidance loop. It consists of an attitude loop, rate loop and a control allocation part which are introduced in the following sections.

### 4.8.1. Attitude Loop

The attitude and the rate loop as well as the control allocation are identical for the traction and the retraction phase. This is an advantage of the nonlinear inner loop controller over the linear controllers since no additional control law switching is required. The pseudo-control inputs for the attitude to rate inversion are determined based on the filtered bank angle and angle of attack commands calculated by the outer loop and are given by

$$\begin{aligned}
 v_{\mu_a} &= v_{\mu_a,ref} + k_{p,\mu_a} (\mu_{a,ref} - \mu_a) + k_{i,\mu_a} \int_0^t (\mu_{a,ref} - \mu_a) d\tau \\
 v_{\alpha_a} &= v_{\alpha_a,ref} + k_{p,\alpha_a} (\alpha_{a,ref} - \alpha_a) + k_{i,\alpha_a} \int_0^t (\alpha_{a,ref} - \alpha_a) d\tau \\
 v_{\beta_a} &= k_{p,\beta_a} (\beta_{a,ref} - \beta_a) + k_{i,\beta_a} \int_0^t (\beta_{a,ref} - \beta_a) d\tau
 \end{aligned} \tag{4.163}$$

where  $v_{\mu_a,ref}$ ,  $v_{\alpha_a,ref}$  and all other reference signals are calculated with an equivalent reference filter as defined for the course angle in Eq. (4.140). Note, no " $v_{\beta_a,ref}$ " appears since the set point for the sideslip angle is at all times set to zero, hence no reference model that shapes set point changes is required. The inversion of the attitude to rate dynamics is given by

$$(\boldsymbol{\omega}_c)_B^{OB} = \mathbf{M}_{B\bar{A}} \begin{pmatrix} -\dot{\chi}_a \sin \gamma_a \\ \dot{\gamma}_a \\ \dot{\chi}_a \cos \gamma_a \end{pmatrix}_{\bar{A}} + (\boldsymbol{\omega})_B^{\bar{A}B} \tag{4.164}$$

with

$$(\boldsymbol{\omega})_{\text{B}}^{\bar{\text{A}}\text{B}} = \begin{pmatrix} \cos \alpha_a \cos \beta_a v_{\mu_a} + v_{\beta_a} \sin \alpha_a \\ \sin \beta_a v_{\mu_a} + v_{\alpha_a} \\ \sin \alpha_a \cos \beta_a v_{\mu_a} - \cos \alpha_a v_{\beta_a} \end{pmatrix}_{\text{B}} \quad (4.165)$$

The matrix  $\mathbf{M}_{\bar{\text{A}}\text{B}}$  can be constructed with the transformation matrices listed in the appendix A of this work.  $\dot{\chi}_a$  and  $\dot{\gamma}_a$  can be estimated in two ways. Either by numerically differentiating Eq. (4.114) and Eq. (4.115) or simply by using the points mass model equations as defined in Eq. (2.17). In this work the model equations are used to avoid errors induced by differentiating a potentially noisy signal.

## 4

### 4.8.2. Rate Loop

Note, since it is assumed that the tether is connected close to the center of gravity of the aircraft, the rate loop of the tethered aircraft can be implemented analogously to the rate loop of an untethered aircraft. Of course, this assumption can also be dropped which would simply add another moment term in the inversion law (as shown below) In this work a conventional first order dynamic inversion controller with second order reference filters is used. The commanded attitude rates calculated by Eq. (4.164) are filtered and the resulting rate accelerations are added to a PI control part analogously to Eq. (4.163) yielding the pseudo-control input  $\mathbf{v}_\omega$  for the inversion of the rate dynamics. The required moment to track the rate commands is then given by:

$$\mathbf{M}_c = \mathbf{J}\mathbf{v}_\omega + (\boldsymbol{\omega})_{\text{B}}^{\text{OB}} \times \mathbf{J}(\boldsymbol{\omega})_{\text{B}}^{\text{OB}} \quad (4.166)$$

### 4.8.3. Control Allocation

In the utilized model the control surface deflections appear affine in the aerodynamic moment equation. Therefore, a direct inversion of the moment equation with respect to the surface deflection is possible. Note, in general the moment equation might not be globally invertible and in this case an incremental control allocation as presented for instance in [68] needs to be used. With the utilized model in this work the resultant moment with respect to the center of gravity (CG) can be written as

$$\mathbf{M}_a = \mathbf{M}_0 + \mathbf{M}_{a,0}(\alpha_a, \beta_a, (\boldsymbol{\omega})_{\text{B}}^{\text{OB}}, v_a) + \mathbf{M}_{a,\delta}(\alpha_a, v_a, \delta_a, \delta_e, \delta_r) \quad (4.167)$$

Note, since for the control design it is assumed that the tether is attached to the CG and also no moment induced by a propulsion system is present, the term  $\mathbf{M}_0$  can be set to zero. The inversion of the rate dynamics yields the required moment  $\mathbf{M}_c$  to track the pseudo control input  $\mathbf{v}_\omega$ . Subtracting the currently acting aerodynamic moment part that does not depend on  $\delta_a, \delta_e$  or  $\delta_r$  leads to the moment increment  $\mathbf{M}_{a,\delta}^*$  that needs to be created through an adaption of the control surface deflections:

$$\mathbf{M}_{a,\delta}^* = \mathbf{M}_c - \mathbf{M}_{a,0} \quad (4.168)$$

What remains is to invert  $\mathbf{M}_{a,\delta}^*$  with respect to the control surface deflections which leads in this case to:

$$\begin{pmatrix} \delta_{a,c} \\ \delta_{e,c} \\ \delta_{r,c} \end{pmatrix} = \frac{1}{\bar{q}S_{\text{ref}}} \begin{pmatrix} 1/b & 0 & 0 \\ 0 & 1/\bar{c} & 0 \\ 0 & 0 & 1/b \end{pmatrix} \begin{pmatrix} C_{l\delta_a}(\alpha_a) & 0 & C_{l\delta_r}(\alpha_a) \\ 0 & C_{m\delta_e}(\alpha_a) & 0 \\ C_{n\delta_a}(\alpha_a) & 0 & C_{n\delta_r}(\alpha_a) \end{pmatrix}^{-1} \mathbf{M}_{a,\delta}^* \quad (4.169)$$

where  $C_{l\delta_a}(\alpha_a)$ ,  $C_{l\delta_r}(\alpha_a)$ ,  $C_{m\delta_e}(\alpha_a)$ ,  $C_{n\delta_a}(\alpha_a)$  and  $C_{n\delta_r}(\alpha_a)$  denote the control derivatives that are modeled as a function of the angle of attack. As an anti-windup strategy pseudo-control hedging is implemented as presented in section 4.1.3. The hedging command is calculated by passing the commanded surface deflections through an actuator model and then simply going the inversion backwards. Concretely, the achievable aerodynamic moment, given the actuator limitations, is given by

$$\hat{\mathbf{M}}_{a,\delta} = \bar{q}S_{\text{ref}} \begin{pmatrix} b & 0 & 0 \\ 0 & \bar{c} & 0 \\ 0 & 0 & b \end{pmatrix} \begin{pmatrix} C_{l\delta_a}(\alpha_a) & 0 & C_{l\delta_r}(\alpha_a) \\ 0 & C_{m\delta_e}(\alpha_a) & 0 \\ C_{n\delta_a}(\alpha_a) & 0 & C_{n\delta_r}(\alpha_a) \end{pmatrix} \begin{pmatrix} \delta_{a,a} \\ \delta_{e,a} \\ \delta_{r,a} \end{pmatrix} \quad (4.170)$$

where  $\delta_{a,a}$ ,  $\delta_{e,a}$  and  $\delta_{r,a}$  are the outputs of the actuator model. Note, in order not to make the controller dependent on the exact actuator model the hedging signal will only account for actuator saturation. The total achievable aerodynamic moment is then given by

$$\hat{\mathbf{M}}_c = \mathbf{M}_{a,0} + \hat{\mathbf{M}}_{a,\delta} \quad (4.171)$$

This eventually yields the hedging signal:

$$\mathbf{v}_{\omega,h} = \mathbf{v}_{\omega} - \mathbf{J}^{-1} \left( -(\boldsymbol{\omega})_B^{\text{OB}} \times \mathbf{J}(\boldsymbol{\omega})_B^{\text{OB}} + \hat{\mathbf{M}}_c \right) \quad (4.172)$$

which is then used to adapt the reference filter signal.

#### 4.8.4. Filter and Gain Design

For the design of the NDI controller in total 17 parameters need to be chosen. The attitude control loop consists of two second order, aperiodically dampened, reference filters with the bandwidths  $\omega_{0,\mu}$  and  $\omega_{0,\alpha}$  as well as the error feedback gains  $k_{p,\mu}$ ,  $k_{p,\alpha}$ ,  $k_{p,\beta}$ ,  $k_{i,\mu}$ ,  $k_{i,\alpha}$  and  $k_{i,\beta}$ . The rate loop consists of three second order, aperiodically dampened, reference models with filter bandwidths  $\omega_{0,p}$ ,  $\omega_{0,q}$  and  $\omega_{0,r}$  as well as the error feedback gains  $k_{p,p}$ ,  $k_{p,q}$ ,  $k_{p,r}$ ,  $k_{i,p}$ ,  $k_{i,q}$  and  $k_{i,r}$ . For the gains the subscript "p" indicates the proportional gain and "i" the integral gain. For an initial design all integral gains can be set to zero since they are only required to ensure reference tracking at steady state.

For the NDI controller only the inner most loop, i.e. the rate loop, is tuned in this step using only the rate dynamics. The attitude loop is tuned in the subsequent step since it requires through the transformation from the pseudo-control input to the commanded rates also the derivatives of  $\chi_a$  and  $\gamma_a$  and hence the full 6-DoF dynamics. In this case the commands for the bank angle and the angle of attack cannot be freely chosen but

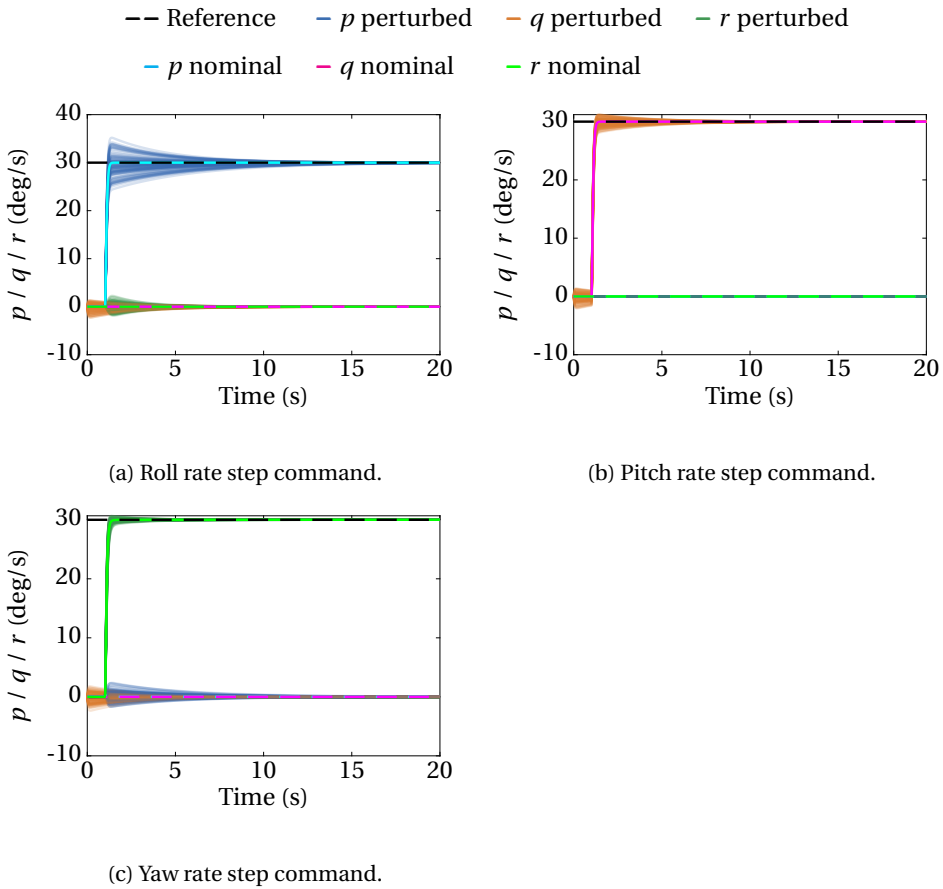


Figure 4.51: Step response using the NDI controller at  $p_3$  (traction phase).

need to be adapted according to the current airspeed which is not controlled in the NDI approach.

For the rate loop the robustness towards modeling uncertainties is assessed by sampling uniformly multiplicative uncertainties of the aerodynamic coefficients. In total 100 uncertainty combinations are sampled. To analyze the step response characteristics the same five traction phase trim point conditions as well as the three retraction phase trim point conditions as for the linear controllers are utilized. The step responses for  $30^\circ \text{s}^{-1}$  reference steps of the body-rates  $p$ ,  $q$  and  $r$  are shown only exemplary for the trim point  $p_3$  (traction phase point) in Fig. 4.51a, since all the step responses are very similar across all five operating points. The detailed numerical values for the step response characteristics across all five trim points are shown in Table 4.27 and Table 4.28. Due to the perfect inversion of the inner loop (without model uncertainties) the plant response follows accurately the reference except in case of saturation of the control signal. In this case the hedging signal adapts the reference model. This is indeed the case at  $p_1$  for the

rudder command which leads to a rise time of 0.26 seconds with the nominal model instead of the 0.24 seconds that are achieved at all other operating points. This is also the case for the settling time of the yaw rate at  $p_1$ ,  $p_2$  and  $p_3$ . The effect of rudder saturation at  $p_2$  and  $p_3$  on the rise time of the yaw rate is not visible due to the rounding error of the displayed values. Since the same reference models are chosen for roll, pitch and yaw, which is simply a result of the tuning phase, the nominal step response characteristics are the same except in case of actuator saturation.

Since the NDI controller is highly dependent on the model, the step response properties deteriorate if the model parameters are perturbed. The controller is especially sensible in the roll channel where the rise time increases from 0.24s to above 4.4s at all operating conditions. Moreover, the overshoot increases significantly for the roll channel and is above 10% at all operating points. The overshoots in the pitch channel is around 4% and for the yaw channel around 2%. Similarly, the settling time increases significantly and is around 10s for the roll rate, between 4s and 5s for the pitch rate and around 1.6s for the yaw rate. Despite the model uncertainties the NDI controller is still able to decouple the dynamics sufficiently which can be seen in the step response plots.

Qualitatively, similar results are obtained at the three retraction phase operating points. In the nominal case nearly the same step responses are obtained which is expected due to the perfect inversion. Small differences only appear in the yaw rate step responses due to the aforementioned saturation of the rudder control input. Similar to the traction phase trim points the roll channel is the least robust control channel in presence of model uncertainties and leads to overshoots up to 13.7%. Due to the large overshoots also the settling time increases significantly.

The final values for the controller gains and filter bandwidths of the NDI controller

Table 4.27: Statistical step response characteristics for all five perturbed state-space models and the NDI controller. Rise time is defined as the point where the signal reaches 95% of the reference value, overshoot is calculated with respect to the set point and settling time is defined as the point where the signal stays within  $\pm 2\%$  around the reference value. The values in brackets are obtained with the nominal model.

Characteristic	$q_{0.95}^{p1}$	$q_{0.95}^{p2}$	$q_{0.95}^{p3}$	$q_{0.95}^{p4}$	$q_{0.95}^{p5}$
Rise time p (s)	4.44 (0.24)	4.90 (0.24)	5.00 (0.24)	5.18 (0.24)	5.66 (0.24)
Rise time q (s)	0.72 (0.24)	1.22 (0.24)	0.81 (0.24)	0.48 (0.24)	0.86 (0.24)
Rise time r (s)	0.35 (0.26)	0.33 (0.24)	0.33 (0.24)	0.33 (0.24)	0.33 (0.24)
Overshoot p (%)	11.0 (0)	12.3 (0)	12.6 (0)	13.3 (0)	14.9 (0)
Overshoot q (%)	4.13 (0)	4.90 (0)	4.26 (0)	3.80 (0)	4.49 (0)
Overshoot r (%)	1.75 (0)	1.96 (0)	1.85 (0)	1.84 (0)	2.04 (0)
Settling time p (s)	9.65 (1.29)	10.2 (1.29)	10.3 (1.29)	10.5 (1.29)	11.0 (1.29)
Settling time q (s)	4.53 (1.29)	5.03 (1.29)	4.64 (1.29)	4.26 (1.29)	4.69 (1.29)
Settling time r (s)	1.58 (1.31)	1.67 (1.30)	1.59 (1.30)	1.58 (1.29)	1.68 (1.29)

are displayed in Table 4.29.

## 4.9. Inner Loop Performance during Figure of Eight Flight

In the previous section two types of inner loop flight controllers are derived: Two linear controllers, that both assume decoupled longitudinal and lateral dynamics, as well as a nonlinear controller are proposed. The performance and robustness properties of the linear controllers were already assessed using the step response characteristics as well as the structured singular value at different operation points. Similarly, the rate loop of the nonlinear controller is assessed using its step response characteristics at the same operating points. In this section the fourth step of the design methodology is presented

4

Table 4.28: Statistical step response characteristics at all three retraction phase operating points and with the NDI controller. Rise time is defined as the point where the signal reaches 95% of the reference value, overshoot is calculated with respect to the set point and settling time is defined as the point where the signal stays within  $\pm 2\%$  around the reference value. The values in brackets are obtained with the nominal model.

Characteristic	$q_{0.95}^{p1}$	$q_{0.95}^{p2}$	$q_{0.95}^{p3}$
Rise time $p$ (s)	4.68 (0.24)	5.23 (0.24)	6.00 (0.24)
Rise time $q$ (s)	0.29 (0.24)	0.30 (0.24)	0.31 (0.24)
Rise time $r$ (s)	0.34 (0.25)	0.33 (0.24)	0.33 (0.24)
Overshoot $p$ (%)	10.1 (0)	11.4 (0)	13.7 (0)
Overshoot $q$ (%)	2.18 (0)	2.49 (0)	2.81 (0)
Overshoot $r$ (%)	1.49 (0)	1.65 (0)	1.93 (0)
Settling time $p$ (s)	9.89 (1.29)	10.5 (1.29)	11.4 (1.29)
Settling time $q$ (s)	2.33 (1.29)	2.69 (1.29)	3.14 (1.29)
Settling time $r$ (s)	1.49 (1.31)	1.52 (1.29)	1.57 (1.29)

Table 4.29: Tuned gains and filter bandwidths for the inner loop NDI controller.

State	$k_p$	$k_i$	$\omega_0$
$\mu_a$	10	0	3
$\alpha_a$	5	1	3
$\beta_a$	1	0	-
$p$	40	10	20
$q$	30	10	20
$r$	10	5	20

where all three controllers are tested on the nonlinear model in combination with the outer loop controller. Since the traction phase is flight dynamically the more demanding operational mode, the inner loop performance is only tested for the traction phase. In fact, the aim of this section is to verify that the inner loop controllers are able to track the commands coming from the guidance module in order to fly figure of eight patterns. Although the step response analysis of the previous section represents a sufficient tool to create a first control design it does not allow to draw a conclusion about how well the inner loop controller is able to stabilize the nonlinear dynamics and how well it is able to track time varying reference signals calculated by the outer-loop especially during dynamic maneuvers such as the figure of eight flight during the traction phase.

Since the winch controller is already designed in Step 2 using the 3-DoF model, the focus in this step is again on the flight controller performance verification. Hence, the tether and the winch dynamics are removed and perfect tether force tracking conditions are emulated by applying a constant tether force pointing to the ground station. Since tether drag has a significant impact on the airspeed the straight line tether drag approximation is added as presented in 2.3.2. Essentially, this simplification, i.e. removing the tether dynamics, is the same that has been used to calculate the quasi-stationary operating points to generate the linear models for the linear controller design and therefore seems to be an appropriate simplification to further verify the flight controller designs.

Note, this intermediate step offers a convenient way to identify possible issues with the guidance algorithm as well as the inner loop controllers. Possible issues could be for instance unfeasible figure of eight shapes that are not flyable due to constraints that are only present in the 6-DoF model (e.g. actuator limitations or other nonlinear effects). Naturally, the controller can immediately be tested on the full simulation model including the tether dynamics but this makes it more difficult to trace back flight control performance issues to its source. If the controller is not working as expected on the simple nonlinear model with perfect radial control performance it is very unlikely that it will work on the complete simulation model. The inverse does obviously not necessarily hold but it at least results in a control design that is closer to the final design that can be applied to the complete system. Another advantage of this intermediate step is that it does not depend on any high level control strategy for the complete pumping cycle if only the figure of eight path following performance is investigated. The simulation model is simply initialized at a trim point on the figure of eight or close to it. This allows to test new flight control strategies for the traction phase conveniently.

Besides the removed complexity introduced by the tether dynamics and the winch controller also turbulence and time delays can be deactivated. Naturally, if it is desired to assess the effect of turbulence solely on the path following performance it is reasonable to also add the turbulence model already in this step of the controller analysis. Also, the impact of time delays can be already assessed in this step along with other sources of uncertainty. There should be, however, a clear justification to add this additional complexity already in this step and not in the final control assessment step using the complete model.

The set points calculated by the outer loop are influenced by the path shape, since the guidance module calculates course and flight path angle rates directly based on the path curvature. For paths with a high curvature more dynamic flight maneuvers with

especially higher bank angles need to be flown. This could already be observed with the 3-DoF model and its impact on the inner loop tracking performance is further assessed in the next section.

#### 4.9.1. Comparison of Path Following Capabilities

The path following capability of each of the three inner loops (LMI, ESA and NDI) is investigated for three path shapes with different path compactness and in low as well as high wind speed conditions equivalent to the investigations conducted with the 3-DoF model. As a reminder, "LMI" denotes an inner loop in which both longitudinal and lateral dynamics are controlled with the LMI controller. "ESA" denotes the case where the lateral dynamics are controlled with the ESA controller but the longitudinal dynamics with the LMI controller. The path following performance is assessed qualitatively using the projection of the resulting flight path into the  $yz$  plane of the path frame. The results are depicted in Fig. 4.52-Fig. 4.54.

It can be observed that all three inner loop controllers achieve a similar path following performance in low wind conditions (see first column of Fig. 4.52-Fig. 4.54). As expected, the path following performance deteriorates with increasing path compactness. In high wind speed conditions the linear inner loops achieve a similar performance with only slightly higher deviations from the reference flight path compared to the low wind speed condition case. The path following performance of the NDI controller deteriorates significantly in high wind speed conditions compared to the low wind speed condition case for all three path shapes. A possible reason for this behavior is that the NDI controller does not control the airspeed dynamics in contrast to the linear controller. Higher variations in the airspeed in high wind speed conditions can be indeed observed by comparing the evolution of the airspeed obtained with the LMI and the NDI controller using for instance the path with medium compactness in low and high wind speed conditions. These results are depicted in Fig. 4.55a and Fig. 4.55b. In the high wind speed conditions the mean airspeed obtained with the NDI or the LMI controller in the loop is almost identical. More specifically, with the NDI controller a mean airspeed of  $32.8 \text{ m s}^{-1}$  and with the LMI a mean airspeed of  $33.1 \text{ m s}^{-1}$  is obtained. With the LMI controller the airspeed is oscillating around the mean value between approximately  $32 \text{ m s}^{-1}$  and  $34.5 \text{ m s}^{-1}$ . With the NDI controller the variations of the airspeed are more significant. It turns out that during the turns the airspeed drops below  $30 \text{ m s}^{-1}$  and then raises to above  $35 \text{ m s}^{-1}$ . In the low wind speed conditions the variance of the airspeed obtained with both controllers is similar. In this case the mean airspeed of the LMI controller is  $30.6 \text{ m s}^{-1}$  and of the NDI controller  $30.7 \text{ m s}^{-1}$ . In both cases the airspeed oscillates between  $29 \text{ m s}^{-1}$  and  $32 \text{ m s}^{-1}$  or  $31.5 \text{ m s}^{-1}$ , respectively. Based on this result, the lack of a stabilizing feedback for the airspeed dynamics can be regarded as a disadvantage of the NDI controller compared to the linear feedback controllers. Consequently, the NDI controller is not able to damp the peaks in the airspeed as effectively as the linear controllers especially in higher wind speed conditions.

In addition, due to the time scale separation between the attitude and the rate loop reference model, the overall bandwidth of the NDI controller is reduced. The linear controller does not have this issue since the outer loop commands are directly mapped into actuator deflections using the linear feedback law.

Lastly, the NDI controller tries to shape the dynamics of the plant according to the implemented reference models. Usually, and also in this work, linear reference models are used. Based on the obtained results in high wind speed conditions it is debatable if the choice of fixed linear reference models is justified. Imposing a linear behavior on the nonlinear system might lead in the end to a worse performance than applying a linear controller to control the nonlinear dynamics in the first place.

## 4.10. Optimization of High Level Parameters

Although the goal of this thesis is not to propose another optimization method for AWE systems a strategy to automatize the determination of the control parameter values is presented. In section 1.3 several optimal control strategies are reviewed. If optimal control theory is applied the control problem is solved by calculating the control inputs such that a given cost function is minimized. In this case the entire system dynamics are incorporated as a whole into the optimal control problem in form of constraints. In some cases, and especially in an industrial setting, the control structure is often given and it is desired to optimize the parameters of the controller for instance in order to maximize the average pumping cycle power. Note, this section mainly intends to present a pitfall if the optimization strategy discards stochastic uncertainties especially in the context of this work. The results can be used to motivate further research in this direction.

In this section an evolutionary algorithm, concretely the Covariance Matrix Adaption Evolution Strategy (CMA-ES), is used to optimize a specified set of controller parameters (see [63]). The optimization framework that is utilized in this dissertation and that implements the CMA-ES algorithm is based on the work published in [47] and [48]. Note that the following results are partially an outcome of a collaboration project between the main author of [47] and [48] as well as the author of this dissertation.

In general, the advantage of evolutionary optimization strategies is that they can be applied to any non-convex and discontinuous system where gradient based optimization strategies will fail. The clear disadvantage is that they can become computationally expensive if the cost function evaluations are time consuming and a large parameter set is optimized. The to be optimized parameters in this work are listed in Table 4.30. To demonstrate the drawback of the optimization strategy the results for the high wind speed conditions i.e. for the wind speed profile with a wind speed of  $9\text{ m s}^{-1}$  at the reference height are presented in the following. Notice that the initial values correspond to the manually tuned parameters that led to acceptable robustness properties of the control system.

The utilized cost function consists of terms that penalize the violation of constraints such as the maximum tether tension  $F_{t,\max} = 2.16\text{ kN}$ , maximum angle of attack (here conservatively defined by  $\alpha_{a,\max} = 12^\circ$ ), large sideslip angles ( $\beta_a > 20^\circ$ ) or large deviations from the flight path ( $e_p > 60\text{ m}$ ). Furthermore, the winch activity is penalized through the variance of the required winch acceleration ( $\text{var}(a_w)$ ). In order to account for large tether force tracking errors, deviations beyond  $100\text{ N}$  relative to the current set point are penalized. Note, this penalty is only considered during the traction phase, since an initial tracking error during the retraction phase is inevitable due to the aforementioned winch limitations. The overall cost is reduced through the generated average pumping cycle power,  $\bar{P}_{\text{mech}}$ . In case a simulation is not completed, e.g. because the

aircraft crashed, a large penalty results. Mathematically, the cost is then calculated according to:

$$\text{cost} = -\bar{P}_{\text{mech}} + c_{\alpha} + c_{F_t} + c_{\beta} + c_{e_{p,t}} + c_{e_{p,r}} + \text{var}(a_W) + c_{e_{F_t}} \quad (4.173)$$

The calculation of the individual cost terms can be found in the appendix of this work (Appendix A.3). For each parameter combination a pumping cycle simulation is launched that uses the 6-DoF model including the winch and the tether dynamics. Several pumping cycles are flown until the change in the average power converges. Considering only the converged pumping cycle reduces the impact of the simulation initialization on the cost. The logged values of the last pumping cycle are then used to evaluate the cost function. The optimization usually runs several thousand pumping cycles until the cost function converges. The corresponding converged parameter values are subsequently denoted as the "optimized" parameters.

With the initial parameter set an average pumping cycle power of 5.01 kW is achieved. In the same wind field the average power output using the optimized parameter values is 6.45 kW which correspond to an increase of 28%. The difference in the power output is best explained utilizing the flight path projections into the xz plane, as shown in Fig. 4.56b. It can be observed, consistent to the values listed in Table 4.30, that the optimizer forces the aircraft to fly at lower elevation angles. On the one hand, this is achieved by a lower mean elevation angle of the reference path ( $\phi_{\text{set}}$ ) and on the other hand, by a faster rotation of the reference path during the transition from the retraction to the traction phase ( $\tau_r$ ). Furthermore, the duration of the pumping cycle is prolonged by increasing the distance between minimum  $l_{t,\text{min}}$  and maximum tether length  $l_{t,\text{max}}$ . The path following capability is improved by reducing the compactness of the path (see Fig. 4.56a). The winch controller is more aggressive due to the larger controller gains ( $k_{p,W}$  and  $k_{i,W}$ )

Table 4.30: Considered parameters with initial and optimized values.

Parameter	Initial value	Optimized value
$a_{\text{path}}$	0.6	0.875
$b_{\text{path}}$	200	268.5
$\phi_{\text{set}}$	0.5236	0.4893
$\tau_r$	10	2.35
$k_{p,W}$	0.483	8.232
$k_{i,W}$	0.026	0.383
$\omega_{0,W}$	12.6	15.5
$F_{t,\text{set},\text{retraction}}$	500	297.9
$l_{t,\text{max}}$	700	768
$l_{t,\text{min}}$	300	231

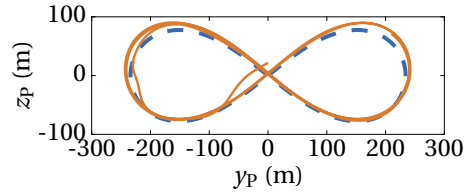
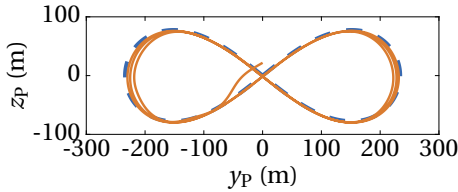
as well as the small increase of the controller bandwidth ( $\omega_{0,W}$ ). The consumed power during the retraction phase is reduced by decreasing the retraction phase set point of the tether tension ( $F_{t,\text{set},\text{retraction}}$ ). The more aggressive tether tension tracking performance, achieved with the optimized parameter set, is visible in Fig. 4.57b. Clearly, the optimized controller tracks the tether tension more accurately, in particular during the transition.

The higher average pumping cycle power, however, comes at the cost of a significant robustness decrease compared to the initial, less optimal, parameter set. This can be shown by activating the atmospheric turbulence model which leads to the results in Fig. 4.58a (initial parameter values) and Fig. 4.58b (optimized parameter values). With the optimized parameter set the tether force peaks increase significantly and even violate the maximum tether force value in 3 out of 5 pumping cycles. In contrast to that, the controller with the initial parameter values leads to a tether force tracking performance that is more consistent with the results obtained without turbulence. This indicates that the deterministic formulation of the optimization problem can lead to practically unfeasible solutions. Robust optimization could improve the results by explicitly taking into account uncertainty and stochasticity. More specifically, the average cost function value for a given parameter combination could be optimized. This way variation of the wind field due to turbulence can be incorporated into the optimization. This is, however, not investigated further in this work and is therefore suggested for future research.

Note, although the resulting controller is non-robust towards uncertainties it could also serve as a starting point for further (manual) robustness optimizations. For instance, in the presented example the winch controller is aggressively tracking the tether tension. It could be investigated how decreasing the winch controller gains can reduce the tether force peaks and how this will impact the optimized power output. Since also the same controller parameters (gains and high level parameters) are used for all wind conditions, a rather conservative controller is utilized that is most likely not exploiting the full potential of the power generation capability in all wind conditions. This could be improved in the future by scheduling the parameters over the mean wind speed.

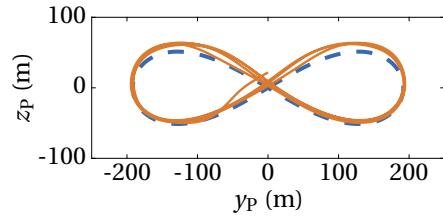
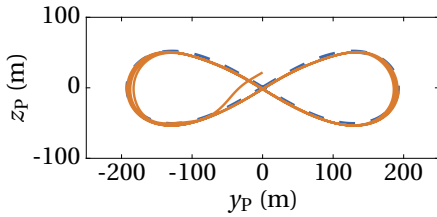
Note that in the subsequent chapter the robust and manually tuned parameter values are utilized since the optimized parameters do not meet the desired robustness criteria.

— Reference — Flight path



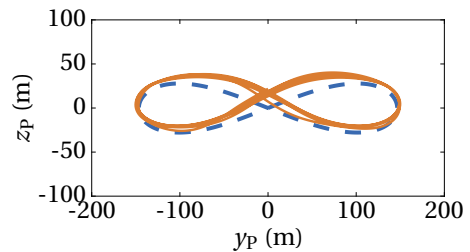
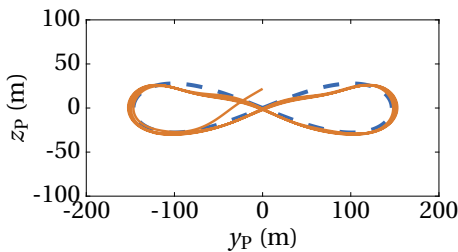
(a) Reference path defined with  $a_{\text{path}} = 0.8$  and  $b_{\text{path}} = 250$ . Low wind speed condition.

(b) Reference path defined with  $a_{\text{path}} = 0.8$  and  $b_{\text{path}} = 250$ . High wind speed condition.



(c) Reference path defined with  $a_{\text{path}} = 0.6$  and  $b_{\text{path}} = 200$ . Low wind speed condition.

(d) Reference path defined with  $a_{\text{path}} = 0.6$  and  $b_{\text{path}} = 200$ . High wind speed condition.

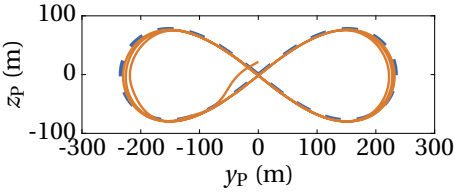


(e) Reference path defined with  $a_{\text{path}} = 0.4$  and  $b_{\text{path}} = 150$ . Low wind speed condition.

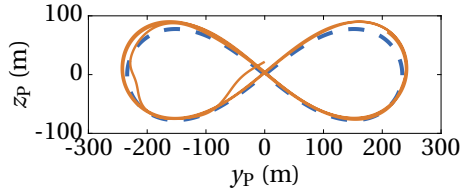
(f) Reference path defined with  $a_{\text{path}} = 0.4$  and  $b_{\text{path}} = 150$ . High wind speed condition.

Figure 4.52: Path following capabilities of the ESA inner loop controller in low (left column) as well as high wind speed conditions (right column).

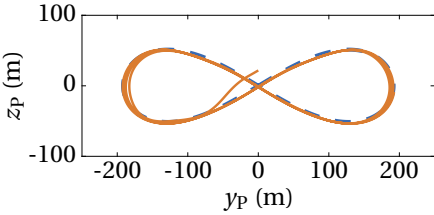
— Reference — Flight path



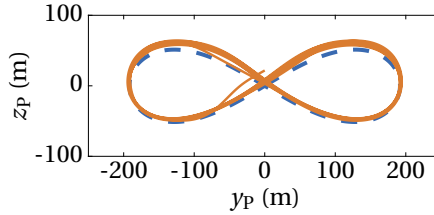
(a) Reference path defined with  $a_{\text{path}} = 0.8$  and  $b_{\text{path}} = 250$ . Low wind speed condition.



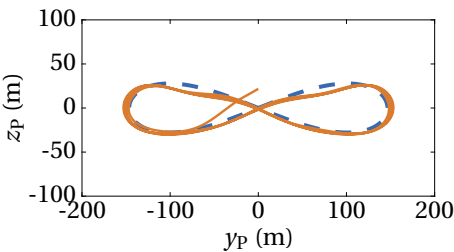
(b) Reference path defined with  $a_{\text{path}} = 0.8$  and  $b_{\text{path}} = 250$ . High wind speed condition.



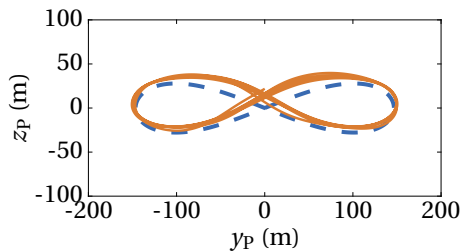
(c) Reference path defined with  $a_{\text{path}} = 0.6$  and  $b_{\text{path}} = 200$ . Low wind speed condition.



(d) Reference path defined with  $a_{\text{path}} = 0.6$  and  $b_{\text{path}} = 200$ . High wind speed condition.



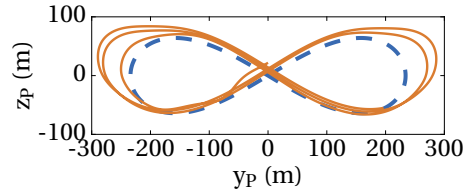
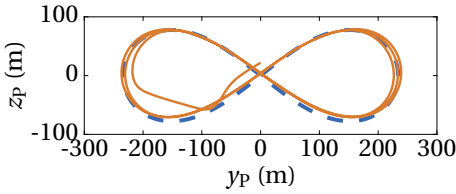
(e) Reference path defined with  $a_{\text{path}} = 0.4$  and  $b_{\text{path}} = 150$ . Low wind speed condition.



(f) Reference path defined with  $a_{\text{path}} = 0.4$  and  $b_{\text{path}} = 150$ . High wind speed condition.

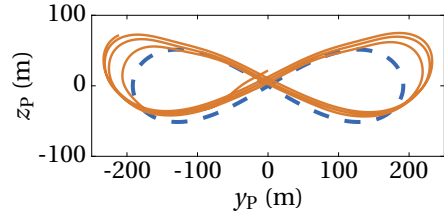
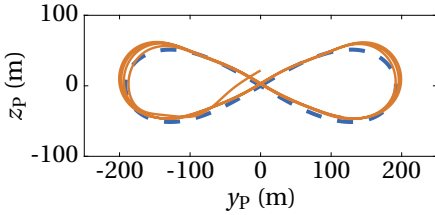
Figure 4.53: Path following capabilities of the LMI inner loop controller in low (left column) as well as high wind speed conditions (right column).

--- Reference    - Flight path



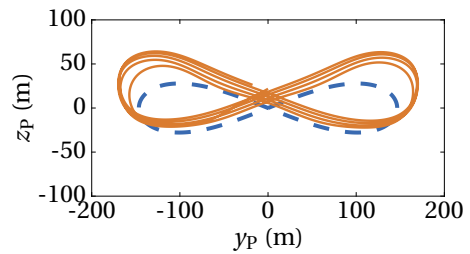
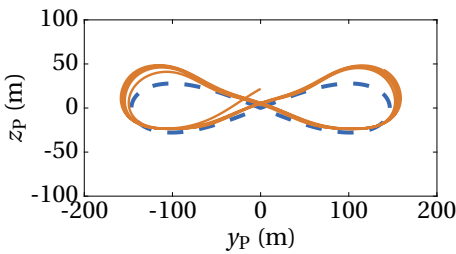
(a) Reference path defined with  $a_{\text{path}} = 0.8$  and  $b_{\text{path}} = 250$ . Low wind speed condition.

(b) Reference path defined with  $a_{\text{path}} = 0.8$  and  $b_{\text{path}} = 250$ . High wind speed condition.



(c) Reference path defined with  $a_{\text{path}} = 0.6$  and  $b_{\text{path}} = 200$ . Low wind speed condition.

(d) Reference path defined with  $a_{\text{path}} = 0.6$  and  $b_{\text{path}} = 200$ . High wind speed condition.



(e) Reference path defined with  $a_{\text{path}} = 0.4$  and  $b_{\text{path}} = 150$ . Low wind speed condition.

(f) Reference path defined with  $a_{\text{path}} = 0.4$  and  $b_{\text{path}} = 150$ . High wind speed condition.

Figure 4.54: Path following capabilities of the NDI inner loop controller in low (left column) as well as high wind speed conditions (right column).

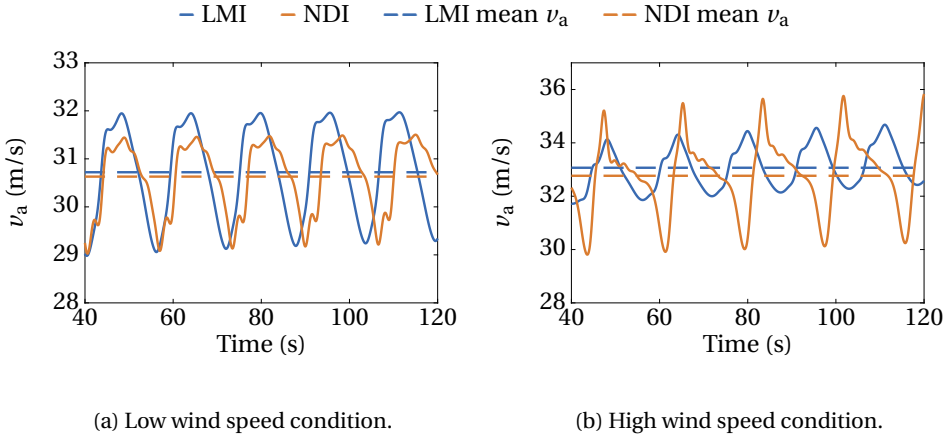


Figure 4.55: Evolution of the airspeed in low and high wind speed conditions using either the LMI or the NDI controller. The reference path is defined by  $a_{\text{path}} = 0.6$  and  $b_{\text{path}} = 200$ .

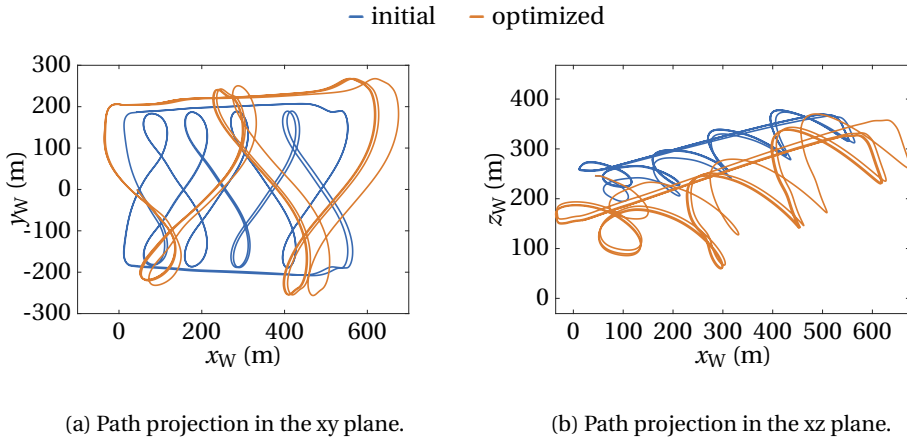


Figure 4.56: Comparison of the initial and the optimized flight path.

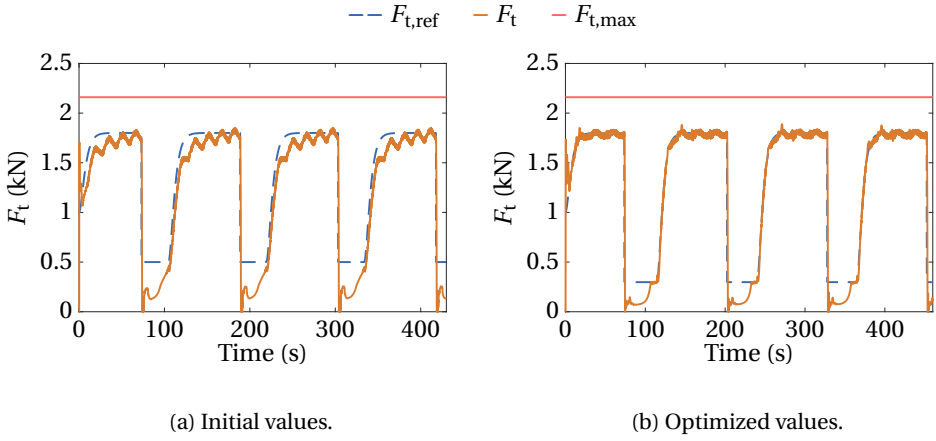


Figure 4.57: Tether force tracking performance with the initial and the optimized parameter values without turbulence.

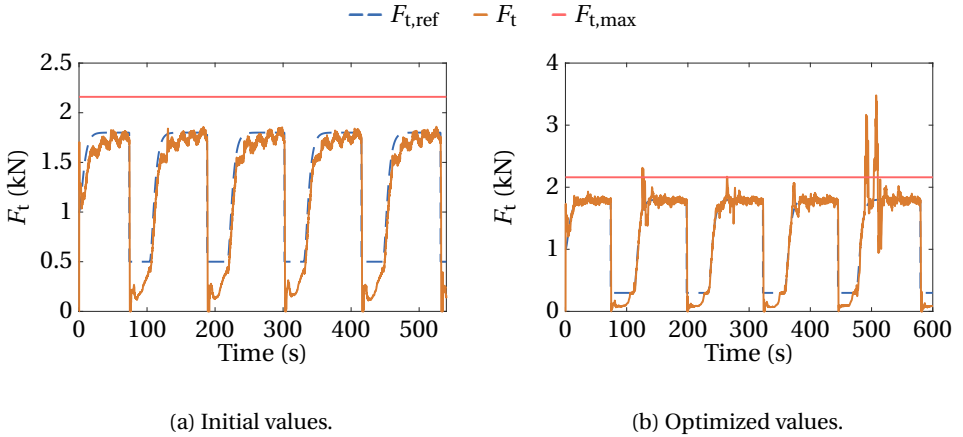


Figure 4.58: Tether force tracking performance with the initial and the optimized parameter values with turbulence.

## 4.11. Summary

In this chapter the AWE control system is derived. First, the high-level state machine is introduced that controls the operational modes during a pumping cycle. Next, the guidance strategies are presented that allow to fly figure-8 patterns during the traction phase and straight flight paths during the retraction phase. Furthermore, a transition strategy to guide the AWE system from the retraction to the traction phase is proposed. A simple winch controller is presented that tracks a high tether force set point during the traction and a low tether force set point during the retraction phase. Moreover, different inner loop flight controllers are derived and a preliminary robustness and performance study is conducted that can be included in an iterative control design process for AWE systems. In the last section, a global parameter optimization strategy is presented including a discussion of the limitations imposed by deterministic models.

The overall control system architecture with linear inner loop (LMI or ESA) is depicted in Fig. 4.59. Similarly, the control architecture with the NDI inner loop is depicted in Fig. 4.60. In both figures the blue blocks indicate control modules that are active during the traction phase whereas the orange blocks represent active modules during the retraction phase. All other blocks are active during the traction as well as the retraction phase. Note that in the figures the feedback paths are not depicted for the sake of clarity. The figures show graphically the main benefit as well as the main drawback of the NDI inner loop approach. On the one hand, the NDI controller consists of only one inner loop controller whereas in the case of linear inner loops two separate controllers are necessary. On the other hand, Fig. 4.60 also visualizes the larger required cascaded structure of the NDI controller compared to the approach with linear inner loops. This is a drawback since a larger cascade leads to an overall smaller bandwidth due to the necessary time scale separation of adjacent modules.

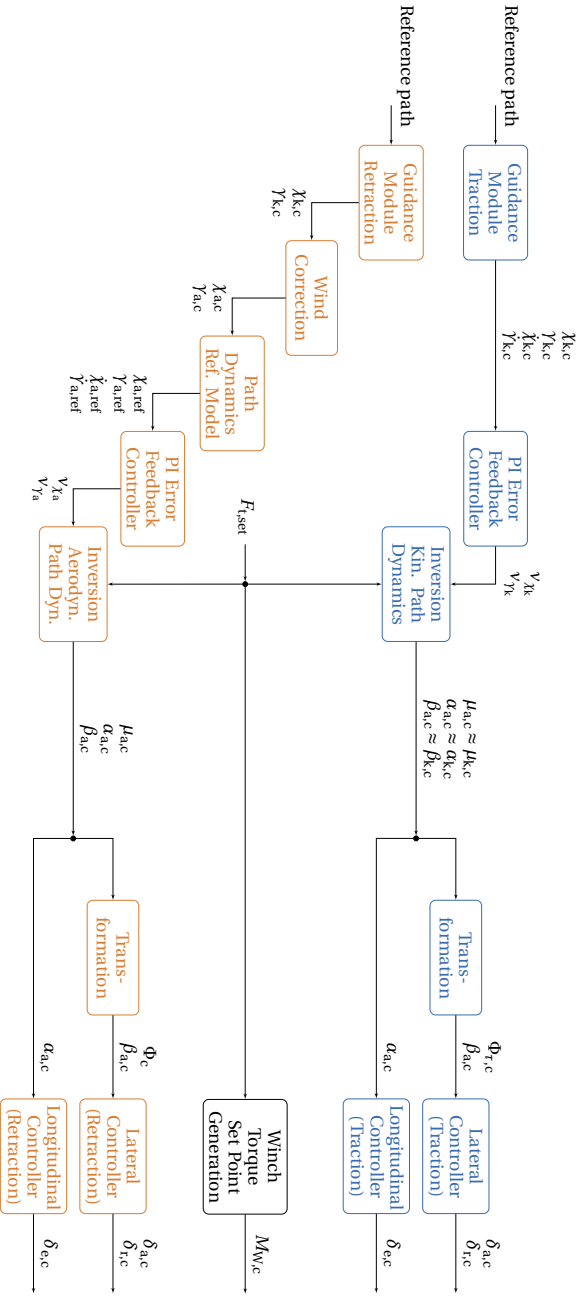


Figure 4.59: Cascaded flight and winch control system architecture with linear inner loop. Feedback paths are omitted in the figure. The highlighted blocks in blue are active during the traction phase, the orange highlighted blocks are active during the retraction phase. All other blocks are active in both phases.

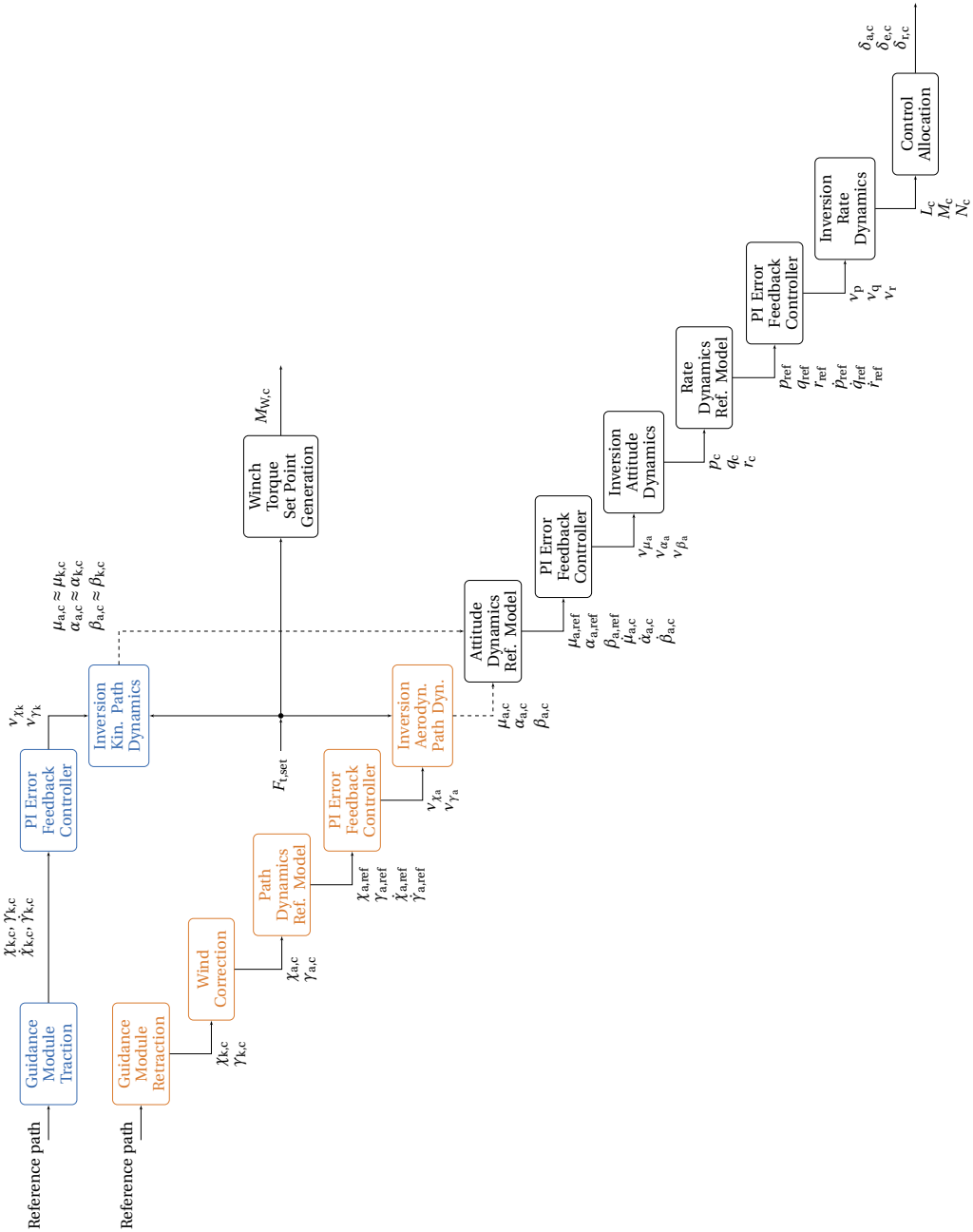


Figure 4.60: Cascaded NDI flight and winch control system architecture. Feedback paths are omitted in the figure. The highlighted blocks in blue are active during the retraction phase, the orange highlighted blocks are active during the retraction phase. All other blocks are active in both phases.



# 5

## Control Performance Analysis in Presence of Uncertainty

In this chapter the derived controllers are implemented in the nonlinear simulation environment. A detailed statistical analysis is conducted to assess the performance and robustness properties with respect to atmospheric turbulence, time delays and model uncertainties. Furthermore, a sensitivity analysis is presented that allows to determine influential uncertainties with respect to the robustness of a specific controller.

### 5.1. Preliminaries

In chapter 4 inner and outer loop flight control systems that enable autonomous pumping cycle operation are derived. Moreover, the inner loop flight controllers are assessed with respect to tracking performance and robustness towards modeling uncertainties. For the linear inner loop controllers, on the one hand, the structured singular value is used to calculate guaranteed robustness margins and, on the other hand, a Monte Carlo step response analysis is conducted to quantify the robust performance statistically. Although these results provide a preliminary understanding of the performance and the robustness properties of the closed loop system they cannot ensure that the system achieves its performance properties or even remains stable if deployed on the complete nonlinear system while performing pumping cycles. Therefore, in the last part of the previous section the combination of the outer and the inner flight control loop is tested on the 6-DoF model with respect to its capability to follow a figure of eight shaped path. However, in this case the radial control objective is simplified since the tether dynamics are neglected and perfect tether tension tracking is assumed. Furthermore, the impact of model uncertainties is not investigated. Note, this intermediate step is suggested to only verify if the inner loop design is able to track the outer loop commands subject to the nonlinearities and actuator dynamics which are present in the full 6-DoF simulation model. In general, the verification steps in chapter 4 use models with the same or similar fidelity as the design models. This allows to incorporate them in the iterative control

design process since the simulation runs are computationally cheap and errors are easier to trace back to their sources. Nonetheless, it turns out that if the controllers perform well in these intermediate verification tests the amount of control design iterations using the 6-DoF model with the highest fidelity can be reduced.

If an acceptable control design with respect to robustness and performance is obtained in step 5 of the design workflow a statistical analysis using the simulation model with the highest complexity, including the dynamics of all subsystems, modeling uncertainties and different environmental conditions, needs to be conducted. Due to the high complexity of this system, an analytical approach to verify the controller performance and robustness is no longer feasible. Instead, a statistical approach is chosen using again Monte Carlo simulations. The benefit of this approach is that the scope of real world effects is basically unlimited and only restricted by the additional computational burden. This is the main drawback of this approach and hence makes it only partially suited in an early stage of the controller design process (i.e. step 5).

Parametric uncertainties are already considered during the iterative control design process in chapter 4. However, for the linear controllers these uncertainties are only associated with the elements in the state-space models. In contrast to that, the uncertainty model used for the iterative NDI design already considered uncertainties directly in the nonlinear aerodynamic model. However, since in this case only the attitude and rate dynamics are required for the step response analysis, uncertainties such as the tether attachment point location or uncertainties in the aerodynamic force model are not considered. A more complete uncertainty model is utilized in this section and all control designs are compared with each other regarding their robustness towards these uncertainties using statistical techniques.

Uncertainties and disturbances are usually modeled as random variables that are sampled for instance from a Gaussian or a uniform distribution. Depending on the prior knowledge of the model parameters an appropriate distribution can be selected. The most conservative distribution to model a parametric uncertainty is the uniform distribution. It is used if one simply assumes that a parameter lies within a specified interval. A Gaussian distribution allows to incorporate prior confidence in the initial parameter value. The Gaussian PDF can be centered around the initial parameter value and the variance of the distribution specifies the confidence in this value i.e. a large variance indicates a low confidence and a small variance indicates a high confidence. Note, in case a Gaussian distribution is used to model parametric uncertainties it is common to additionally limit the support of the distribution. Otherwise, it is possible that, although with very low probability, unrealistically large or small parameter values are sampled. In this work a conservative approach is chosen and all parametric uncertainties are sampled from a uniform distribution.

Prior to the statistical controller assessment it is important to define a set of metrics which are used to decide whether the control design has satisfactory robust performance properties or not. In this work these metrics are, on the one hand, the maximum tether force and, on the other hand, the maximum angle of attack value. In other words, a tether rupture or a stalling aircraft are considered as failures and in some sense indicate controller instability. The reason for choosing these metrics is that both might lead to a loss of the system. If the tether breaks the AWE system is no longer able to continue its

operation. A contingency maneuver can try to recover the system which will experience a significant acceleration in radial direction as soon as the tether breaks. This is due to the sudden loss of the radial motion constraining tether force. In the best case scenario the aircraft can be recovered and a landing maneuver can be initiated. After a successful landing the tether needs to be replaced and possible damaged parts on the aircraft need to be repaired before the system is operational again. In any case, pumping cycle operation is no longer possible for a certain amount of time. Therefore, it is desirable to reduce the probability of a tether rupture to an acceptable value. Besides tether rupture, stall is considered as an additional violation of the robustness requirement. Although a stalled aircraft can be recovered (see e.g. [152, p.4.2–p.4.24]) it should be ensured that this event happens with an acceptable low probability due to the higher chance of loss of control in this flight state. Furthermore, predicting the behavior in the post stall regime is difficult in simulations. The aircraft model utilized in this work is not created for the post stall regime and hence the controller should keep the aircraft in the regime where the model has been validated. Among these two metrics the tether rupture requirement is considered to be more critical since it will with certainty lead to an abortion of the current operation. In addition, due to the limited model accuracy a conservative limit for the angle of attack is chosen.

In the following, a controller is denoted as "robust" if the probabilities that the tether force or the angle of attack exceed their limits are acceptable. Note, due to its stochastic nature, the system can never achieve 100% reliability. Usually the desired robustness level is defined a priori and the system needs to be designed with respect to this level. However, since there is no consensus in the community yet how robust (i.e. reliable) an AWE system needs to be, the results in this section are generated with a conservative controller that sacrifices power output for robustness up to a level that is defined to be acceptable. This leads obviously to subjective requirement choices that need to be challenged by other researchers in the future. This design philosophy reoccurs throughout this work and represents a strong contrast to the existing literature where maximizing the average power output is the main design driver.

Additional metrics such as the path following errors during the traction and the retraction phase can be defined, however, for the following analysis they will not be discussed in detail. The reason for this decision is that the violation of other metrics most of the time leads eventually to a maximum tether force peak and/or angle of attack peak limit violation anyway. Therefore, if the system is able to carry out the pumping cycles while keeping the tether force and angle of attack below their peak limits other performance metrics are assumed to be satisfied as well. Note, path following error metrics might become more important in the future if additional top level requirements are defined that demand that the AWE system needs to stay within a prescribed space at the operational side to avoid collision with neighboring AWE systems. However, this is not considered in this work.

The considered limits for the tether force and angle of attack peak in this chapter are summarized in Table 5.1. Since there is no information available about the real tensile force limit of the tether, its limit is defined to be 20% above the tether force traction phase set point. Although in [98] it is stated that the maximum force is 1800 N, flight test data, which is unfortunately confidential, shows that also a tether force beyond this limit

Table 5.1: Tether force and angle of attack limits and the associated requirements.

Metric	Limit	Requirement
$F_{t,\max}$	$F_{t,\text{set}} \cdot 1.2 = 2160 \text{ N}$	$F_t \leq F_{t,\max}$
$\alpha_{a,\max}$	$\frac{\alpha_{a,\text{ref},\max} + \alpha_{a,\text{stall}}}{2} = 14^\circ$	$\alpha_a \leq \alpha_{a,\max}$

was measured. Note, since in [98] the trajectory is optimized, the tether force constraint is most likely corresponding to the traction phase set point definition in this thesis, i.e.  $F_{t,\text{set}} = 1800 \text{ kN}$ . Similarly, [98] states that stall occurs beyond  $18^\circ$  but a limit of  $10^\circ$  is used. In this thesis the maximum commanded reference value is also set to  $10^\circ$  but the requirement is set to the mean value of the stall angle and the maximum reference value to allow controller overshoot without violating the requirement. In any case the angle of attack limit is chosen conservatively due to the questionable model accuracy close to the stall point.

The statistical experiments that are used to assess the controller robustness are conducted as follows. In total  $n_s$  pumping cycles are simulated for each controller. After each pumping cycle simulation run the tether force and angle of attack peaks are determined. This yields in total  $n_s$  tether force and angle of attack peak values. For a more convenient comparison of different designs it is required to summarize the obtained values in a representative way. One option would be to use the sample average. However, the sample average is usually sensitive towards outliers and also does not provide any further information about the distribution of the metric. An alternative is to use a quantile function plot which represents the inverse of the sample cumulative distribution function. It conveniently allows to determine, for an arbitrarily selected threshold value, the probability that the actual value is equal or smaller than this value. This approach offers a simple but effective way to compare different control designs with each other and also allows to verify if the control system satisfies its performance metrics in a statistical sense. Note, in contrast to the SSV approach which is used to assess the robustness of the linear controllers in chapter 4, the quantile approach contains uncertainty. Like in any statistical experiment, however, this uncertainty decreases with larger sample sizes. In order to quantify the expected uncertainty of the quantile function plot, confidence intervals are estimated that allow to infer the expected variation of the quantile plot across different experiments. Asymptotic confidence intervals (CI) for a quantile  $q_i$  are calculated according to

$$CI = q_i \pm \tilde{\Phi}^{-1}(1 - \alpha) \frac{\sqrt{Pr_i(1 - Pr_i)}}{\sqrt{n_s} \hat{f}_X(q_i)} \quad (5.1)$$

where  $\tilde{\Phi}^{-1}$  is the inverse of a normal Gaussian CDF, the choice of  $\alpha$  reflects the confidence level i.e.  $1 - \alpha = 0.95$  corresponds to the 95% confidence interval,  $Pr_i$  equals the probability of being lower than the quantile  $q_i$ ,  $n_s$  is the sample size i.e. the number of samples of the metric for which the quantile is calculated and  $\hat{f}_X(q_i)$  is the estimation of the probability density function of the corresponding metric. For a detailed derivation it is referred to [139, p.77–p.79]. The derivation is also reproduced in appendix A.4 of this



## 5.2. Results

This section is subdivided into five parts. In the first part, the impact of different time delays on the tether force and angle of attack peaks is investigated. This is done in a statistical sense where the time delays at different positions in the control system are regarded as uncertainties sampled from uniform distributions. In the second part, the time delay is fixed and only the impact of turbulence is investigated. In the third part, the robustness towards model uncertainties is assessed. In the fourth part, the most influential model uncertainties are determined using a sensitivity analysis. Overall, the goal of this chapter is to determine the controller that yields the lowest probabilities of exceeding the tether force and angle of attack limits in presence of the discussed uncertainties. A more detailed performance analysis is then conducted with the most robust controller and the results are presented in the last section of this chapter.

### 5.2.1. Impact of Time Delays

Since no information about the expected measurement and control delays are publicly available for the considered system, a stochastic assessment of the time delay margins is conducted. Time delays are considered at four different positions in the closed loop system. Measurements at the aircraft, the flight control commands, measurements on the ground and the winch control commands are delayed. The goal of the analysis in this section is, on the one hand, to investigate where large time delays are most critical and, on the other hand, how the time delay margins vary among the three different controllers. For each controller and for both low as well as high wind speed conditions, including turbulence, around 5000 pumping-cycles are used to create the time delay margins. The time delays are sampled uniformly in the interval 1 ms to 100 ms.

The time delay margin is defined in this work as a linear separation boundary between samples that satisfy or violate a requirement. A requirement is violated if either the tether force or the angle of attack is larger than the limits defined in Table 5.1. In order to obtain a conservative margin, the separation boundary is chosen such that all samples that lead to a requirement violation lie in the half-space above the decision boundary. Note, in some cases it might be reasonable to define outliers which will move the decision boundary more towards the set that contains samples that lead to a requirement violation. Outliers occur since also the turbulence is sampled which can be regarded as process noise. The supporting point of the separation plane can be calculated by projecting every point that violates one of the constraint into the direction of the normal vector of the separating plane located in the origin. It turns out that an orientation of the separation plane of  $45^\circ$  with respect to the horizontal can be chosen. This is of course without restriction to generality and also the orientation of the plane could be further optimized but this is not investigated further in this work. The supporting point is ultimately defined by the sample that yields the shortest projected vector length.

#### Time Delay Margins of the LMI Controller in Low Wind Speed Conditions

The results for the LMI controller are depicted in Fig. 5.3a-5.4b for both the tether force and the angle of attack requirement. It turns out that the flight control system (FCS) delays suffice as features to create the decision boundary. Therefore, the delay combinations of the FCS and of the winch control system (WCS) are depicted in separate scatter

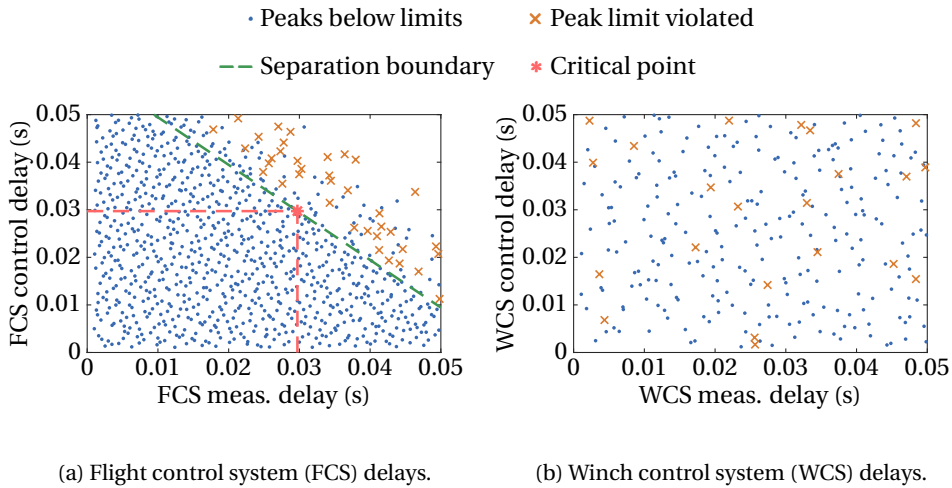


Figure 5.3: Impact of time delays on the tether force peak in low wind speed conditions and with the LMI controller.

plots. The green dashed line indicates the time delay margin. The time delay margin is higher for the tether force than for the angle of attack requirement. Below a maximum combined delay of 29 ms the LMI controller robustly keeps the tether force below its maximum value. In order to comply with the angle of attack requirement, however, the largest delay that still satisfies the requirement is 18 ms. To obtain these results one outlier is identified which is indicated by the black square in Fig. 5.4a. For the winch controller no separation boundary can be found which shows that the FCS delays are dictating the robustness of the control system. Note, it seems that above the separation boundary in Fig. 5.3a samples are missing. However, this is caused by the fact that for large time delays the AWE system was not able to finish the two pumping cycles and hence these results are immediately discarded and not depicted in the figures.

#### Time Delay Margins of the ESA Controller in Low Wind Speed Conditions

Similarly, the robustness of the ESA controller towards time delays can be analyzed. The time delay margin for the tether force requirement is slightly lower (27 ms) compared to the LMI controller and significantly lower for the angle of attack requirement (9 ms). Similarly to the LMI controller, the ESA controller is insensitive towards WCS delays in the considered delay interval (see Fig. 5.5a- Fig. 5.6b).

#### Time Delay Margins of the NDI Controller in Low Wind Speed Conditions

With the NDI controller a time delay margin of 31 ms for the tether force requirement is obtained. The time delay margin corresponding to the angle of attack requirement is slightly higher, i.e. 31 ms. Similar to the LMI and ESA controller the time delay margin is driven by the FCS delays (see Fig. 5.7a- Fig. 5.8b) in the considered interval.

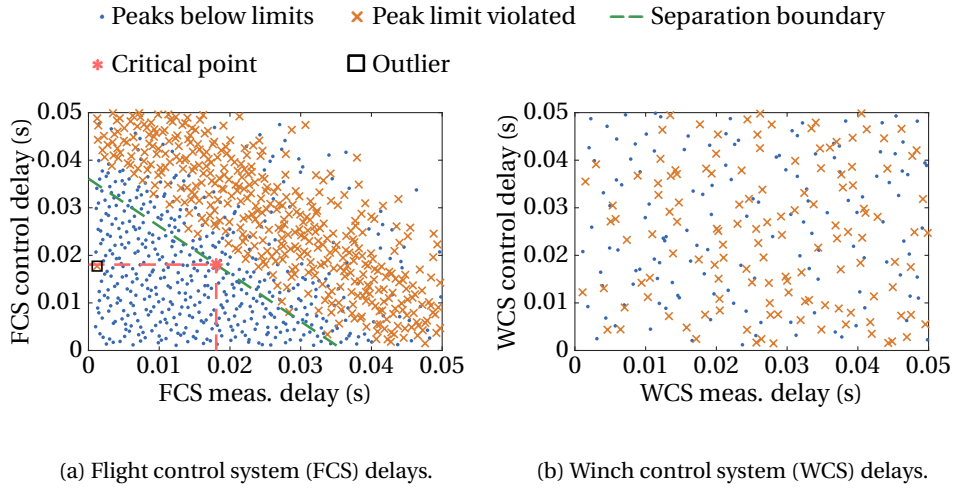


Figure 5.4: Impact of time delays on the angle of attack peak in low wind speed conditions and with the LMI controller.

#### Time Delay Margins of the LMI Controller in High Wind Speed Conditions

The results for the LMI controller obtained in high wind speed conditions are depicted in Fig. 5.9a- Fig. 5.10b. The time delay margin of the FCS is with 23 ms lower than the one obtained in low wind speed conditions, whereas in high wind speed conditions the controller is more robust towards delays with respect to the angle of attack requirement and offers a time delay margin of 21 ms .

#### Time Delay Margins of the ESA Controller in High Wind Speed Conditions

The ESA controller in high wind speed conditions is more robust towards FCS control system time delays with respect to the tether force and the angle of attack requirement compared to the results obtained in low wind speed conditions. It achieves time delay margins of 27 ms and 20 ms, respectively. The AWE system is again insensitive to winch control delays (see Fig. 5.11a-Fig. 5.11b) in the considered interval.

#### Time Delay Margins of the NDI Controller in High Wind Speed Conditions

Finally, the robustness of the NDI controller towards time delays in high wind speed conditions is analyzed. The results are depicted in Fig. 5.13a-5.14b. The NDI controller provides a time delay margin with respect to the tether force requirement of 18 ms in this wind condition, which is significantly lower compared to the low wind speed condition case. On the other hand, it offers a high time delay margin of 47 ms with respect to the angle of attack requirement. As for the linear controllers the AWE system is insensitive towards winch control delays in the considered time delay interval.

The results of the time delay analysis for the two wind conditions and the three controllers are summarized in Table 5.2. In general, the linear controllers tolerate higher

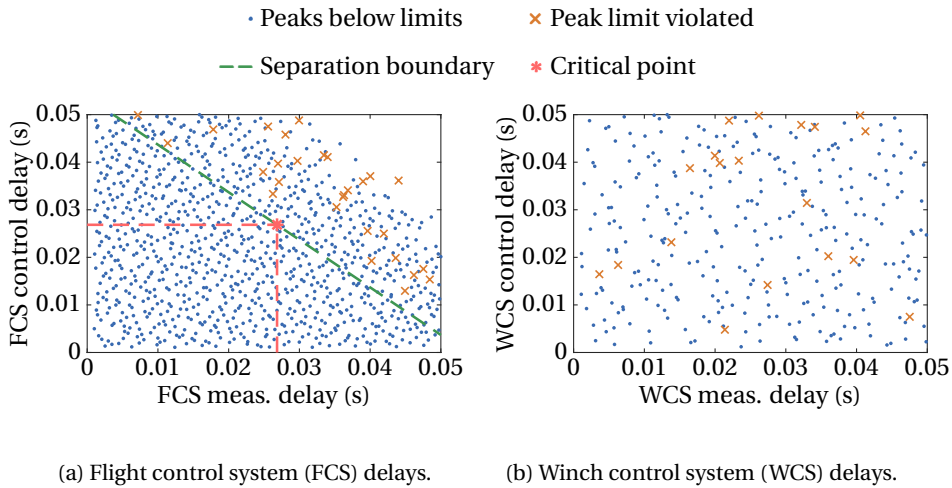


Figure 5.5: Impact of time delays on the tether force peak in low wind speed conditions and with the ESA controller.

time delays with respect to the tether force requirement compared to the tolerable delays with respect to the angle of attack requirement in both wind conditions. In the low wind speed condition case the NDI controller allows the highest delay while still complying with both requirements. In the high wind speed condition case the NDI controller provides the lowest delay margin among the three controllers with respect to the tether force requirement. For all three controllers the FCS delays are the more critical delays compared to the WCS delays. This is shown by the fact that the separation boundary can always be calculated using only the FCS delays.

Except for the ESA controller time delay margin with respect to the angle of attack requirement in low wind speed conditions, the obtained margins for the three controllers are sufficient in both wind conditions. Note, the low ESA controller time delay margin could also be caused by outliers. If the three samples closest to the decision boundary are regarded as outliers the time delay margin increases to about 15 ms.

For the following analysis the four time delays are fixed and set to 15 ms which is regarded as a reasonable control and measurement delay. Disregarding the outliers all controllers are able to satisfy the two requirements in both wind conditions for these or lower time delays. This allows subsequently to study the impact of turbulence and model uncertainties on the controller robustness in more detail.

### 5.2.2. Impact of Turbulence

In this section the impact of atmospheric turbulence on the pumping cycle operation is assessed for each of the three controllers in both low and high wind speed conditions. The controller performance and robustness is quantified using the introduced quantile function plots that are created using 5000 pumping cycle simulations with randomly sampled turbulence fields. In addition, the impact of turbulence on the power output

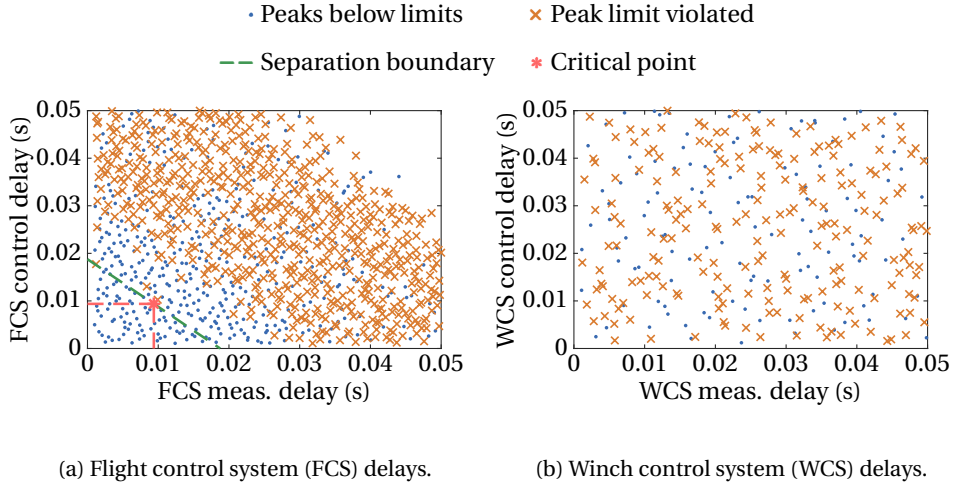


Figure 5.6: Impact of time delays on the angle of attack peak in low wind speed conditions and with the ESA controller.

5

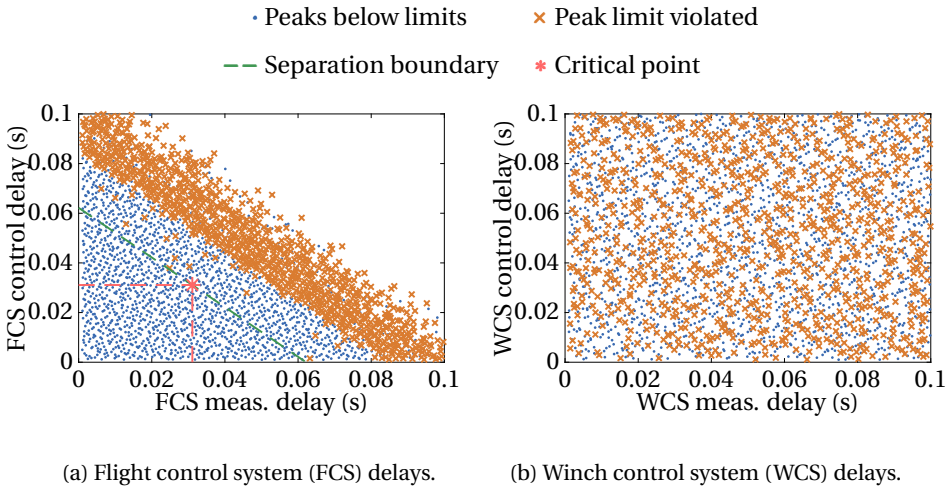


Figure 5.7: Impact of time delays on the tether force peak in low wind speed conditions and with the NDI controller.

is investigated. In the following, first the high wind speed conditions are assessed and based on the results a small high level modification of the original controller is introduced that increases the robustness towards tether rupture in the transition from the retraction to the traction phase. Note, the time delay analysis presented in the previous section is conducted with the already implemented modification.

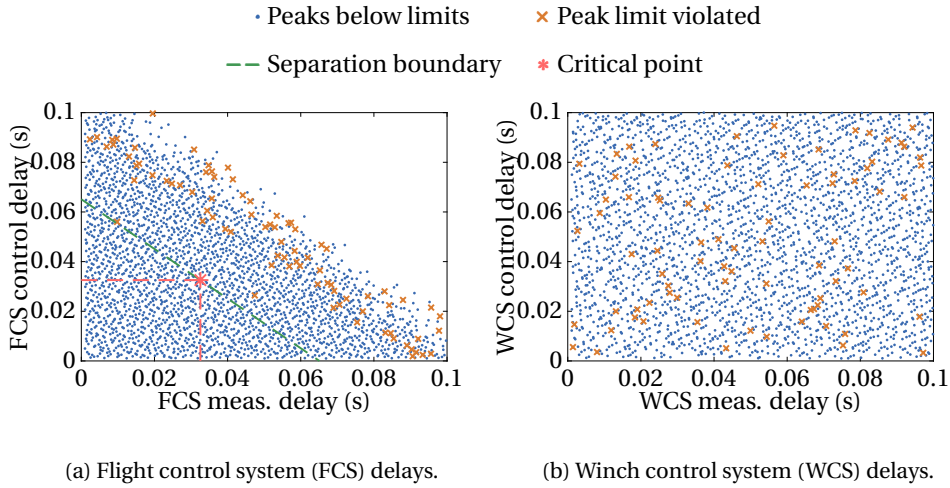


Figure 5.8: Impact of time delays on the angle of attack peak in low wind speed conditions and with the NDI controller.

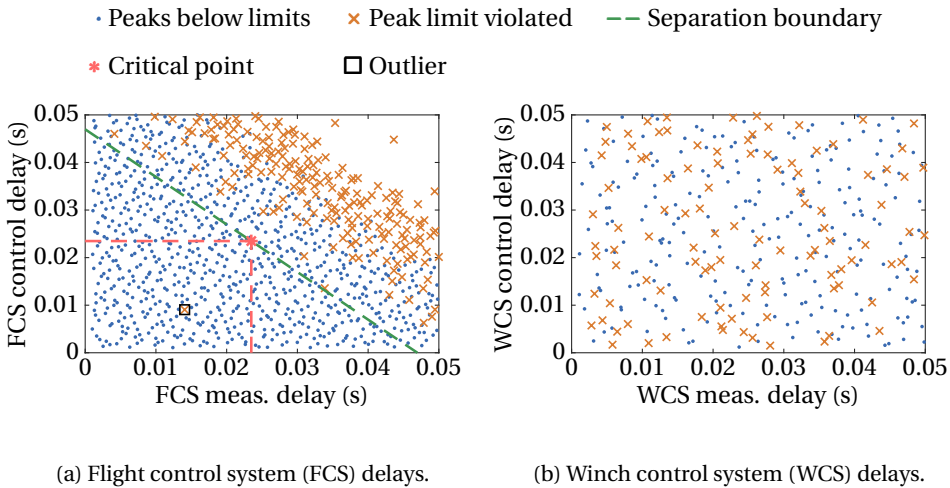


Figure 5.9: Impact of time delays on the tether force peak in high wind speed conditions with the LMI controller.

### High Wind Speed Conditions with the LMI Controller

The quantile plots for the tether force peaks as well as the angle of attack peaks obtained with the LMI controller are depicted in Fig. 5.15a and Fig. 5.15b. Based on the quantile function plot in Fig. 5.15b it can be concluded that the controller is able to keep the angle of attack below the critical threshold. Contrarily, the tether force exceeds the threshold with a probability of around 3%. Assuming that this probability is not acceptable the root cause needs to be identified and mitigated by modifying the controller. In order to

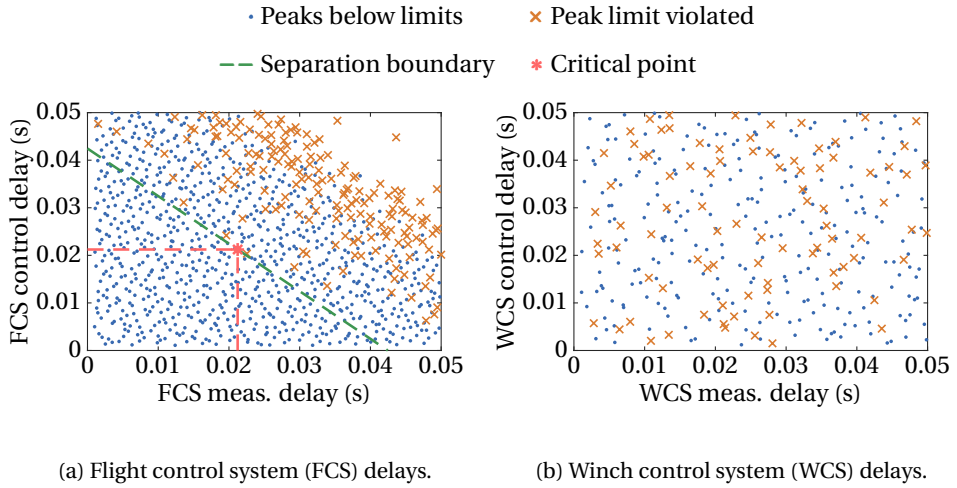


Figure 5.10: Impact of time delays on the angle of attack peak in high wind speed conditions and with the LMI controller.

5

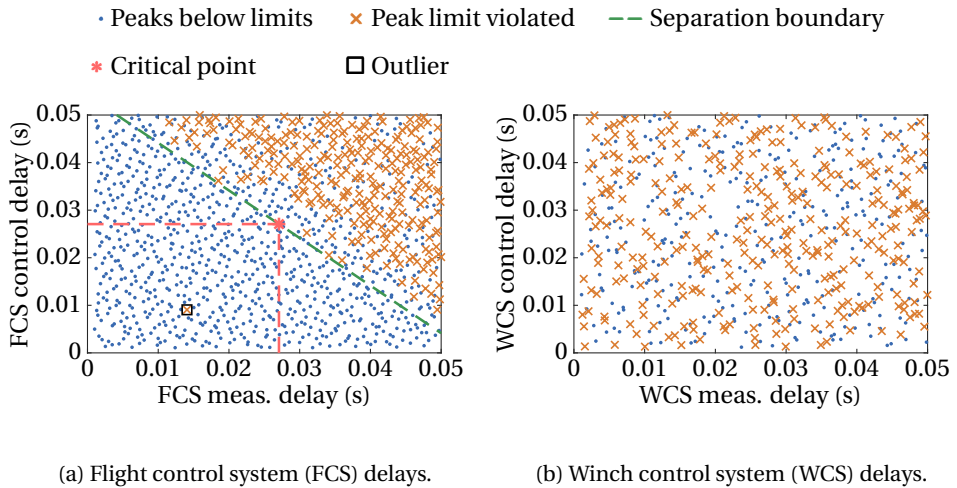


Figure 5.11: Impact of time delays on the tether force peak in high wind speed conditions and with the ESA controller.

identify where in the operational cycle the controller fails, the obtained Monte Carlo simulation results are analyzed in more detail. In the first step, the differences between the simulation runs that do not violate the tether force peak requirement and the runs with requirement violation are identified. In general, instead of analyzing every run individually, which is impossible for the 5000 simulation runs, it is better to use the distribution of a characteristic metric. In this specific example the distribution of the airspeed peak is utilized. The reason to choose this metric is that the tether force is generated by the

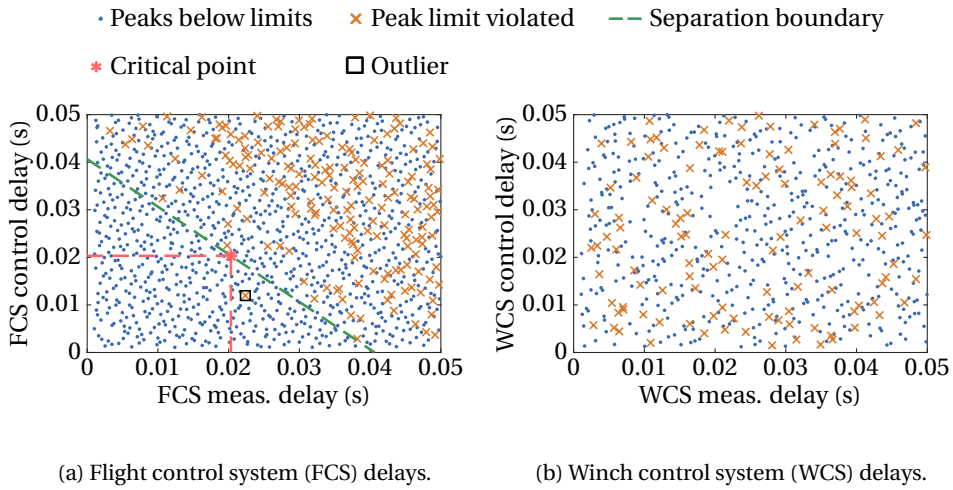


Figure 5.12: Impact of time delays on the angle of attack peak in high wind speed conditions and with the ESA controller.

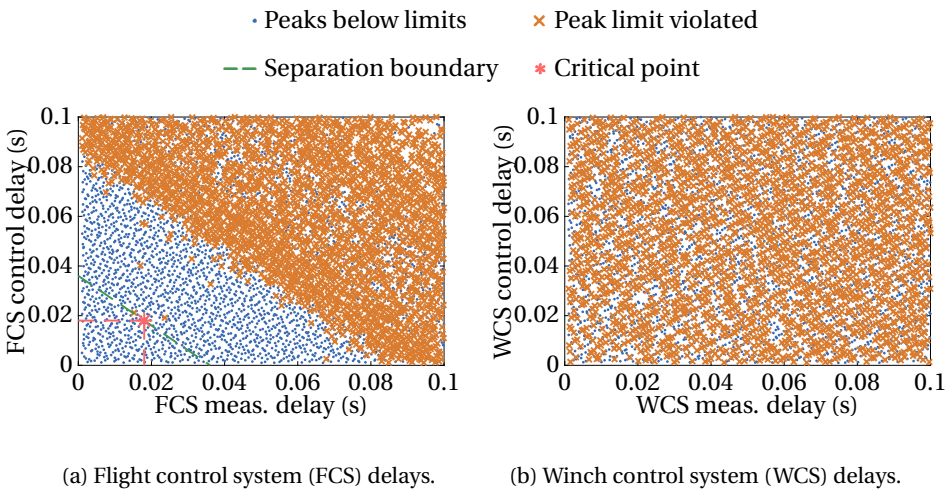


Figure 5.13: Impact of time delays on the tether force peak in high wind speed conditions and with the NDI controller.

aerodynamic force, and in particular by the lift force of the aircraft. Besides the angle of attack, the airspeed is the main contributing state that defines the magnitude of the lift. Since the angle of attack is robustly controlled within the defined limit it is likely that a large airspeed overshoot causes the violation of the tether force requirement. For this specific example the distribution of the maximum airspeed across the 5000 pumping cycles is depicted in Fig. 5.16a which is complemented by the quantile function plot shown in Fig. 5.16b. These results lead to the following observations: On the one hand,

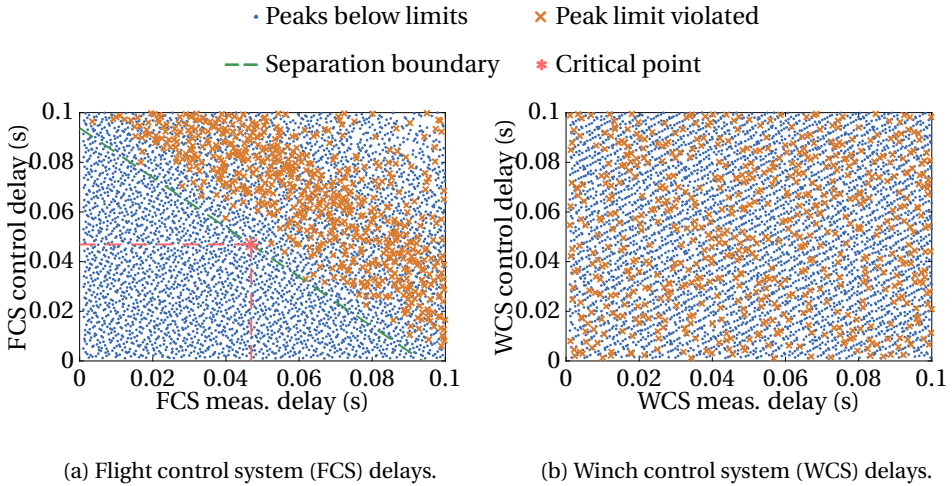


Figure 5.14: Impact of time delays on the angle of attack peak in high wind speed conditions and with the NDI controller.

Table 5.2: Overview of the time delay margins in low and high wind speed conditions. Possible outliers in the data are neglected and the same delay margins for measurements and controls are assumed.

Wind condition	Controller	$\bar{\tau}_{FCS, F_t}$	$\bar{\tau}_{FCS, \alpha_a}$	Figure
low	LMI	29 ms	18 ms	5.3a & 5.4a
low	ESA	27 ms	9 ms	5.5a & 5.6a
low	NDI	31 ms	33 ms	5.13a & 5.14a
high	LMI	23 ms	21 ms	5.9a & 5.10a
high	ESA	27 ms	20 ms	5.11a & 5.12a
high	NDI	18 ms	47 ms	5.13a & 5.14a

in around 30% of the failed runs the airspeed peak is equal or larger than  $40 \text{ m s}^{-1}$  which is only the case in around 6% of the nominal flights. Airspeed peaks during the nominal flights that are larger or equal to  $42 \text{ m s}^{-1}$  occurred with 0% probability, but in 12% of the failed flights.

Besides the maximum airspeed value it is also instructive to analyze where in the operational cycle the peak occurs. It turns out that in this specific example all tether force peaks exceeded the critical value during the transition phase. This correlates with the airspeed peaks which occur in 92.5% of these flights in the transition as well. Contrarily, during the flights without requirement violation the peak occurs in 97% of the flights at the beginning of the retraction phase. This observation is further visualized in Fig. 5.17. In the scatter plot the orange crosses correspond to maximum airspeed and tether force

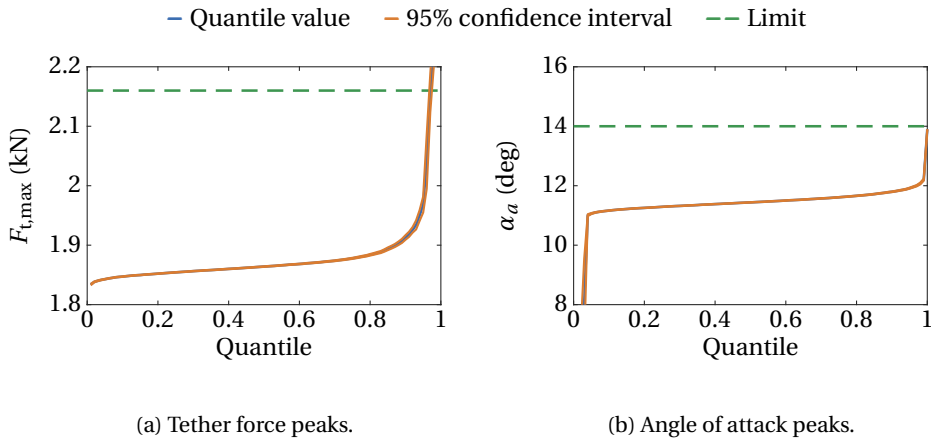


Figure 5.15: Impact of turbulence on angle of attack and tether force peaks in high wind speed conditions and with the LMI controller.

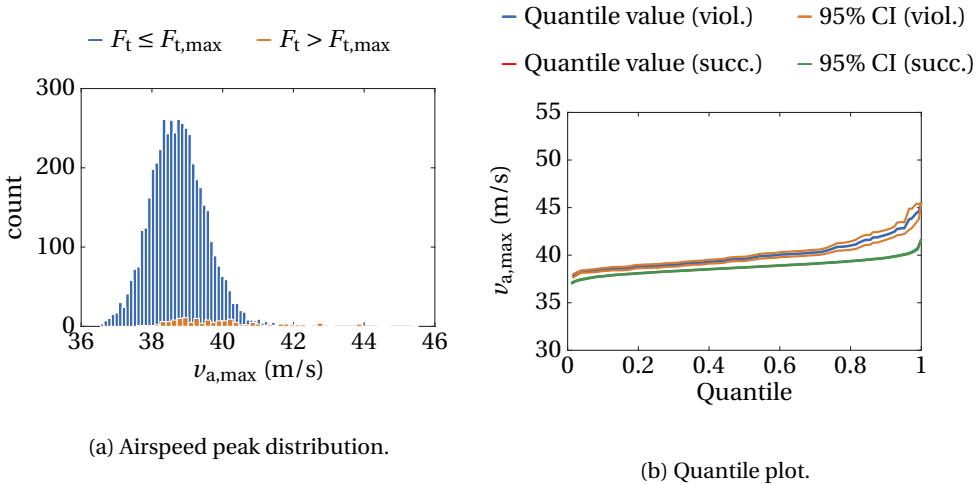


Figure 5.16: Distribution and quantile function plot of the maximum airspeed for nominal and failed flights. Results are obtained with the LMI controller in high wind speed conditions and with turbulence.

set point pairs in flights where the tether force requirement is violated. The blue dots correspond to flights where the tether force stays below its limit. In the transition phase the tether force set point is increased from 0.5kN to 1.8kN. Hence, points in the plot with a tether force set point between 0.5kN and 1.8kN correspond to a transition state.

Based on the results it can be concluded that the tether force peak during the transition correlates with the airspeed peak. In the following a randomly selected sample is analyzed in more detail, in order to propose a modification that renders the controller more robust with respect to the tether force requirement. The obtained tether force and

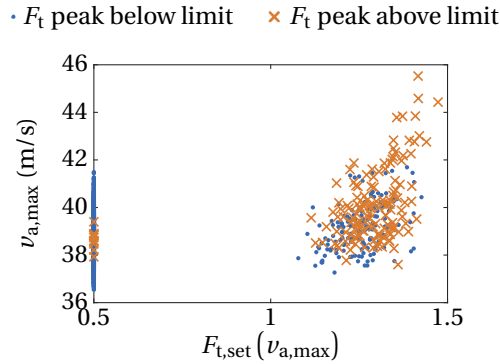


Figure 5.17: Maximum airspeed plotted over corresponding tether force set point. Results are obtained in high wind speed conditions and with the LMI controller.

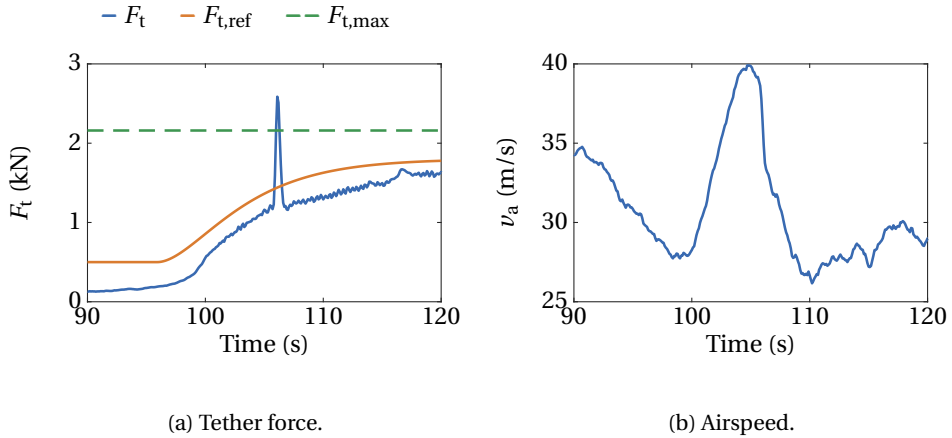


Figure 5.18: Tether force and airspeed plots obtained with the LMI controller with requirement violation in high wind speed conditions with turbulence.

airspeed plots are visualized in Fig. 5.18a and Fig. 5.18b. At around 98s the transition is triggered, hence the tether force set point is increasing. At the same time the airspeed starts to rise (see Fig. 5.18b). This is expected since the increasing tether force set point leads to a faster reeling in of the tether which accelerates the aircraft against the wind. However, this result reveals a flaw in the transition set point calculator. It demands an increase in tether force regardless of the current airspeed. Therefore, a reasonable modification of the set point generator is to only increase the tether force set point as long as the airspeed is below a critical threshold. The threshold value that triggers this safety mechanism can be defined using the results in Fig. 5.17. Since below  $35\text{ms}^{-1}$  no tether force requirement violation occurs, this value represents a reasonable decision boundary. As an additional counter measure the current tether force set point can be reduced which forces the winch to reel out the tether (or reel in slower) and hence can reduce the

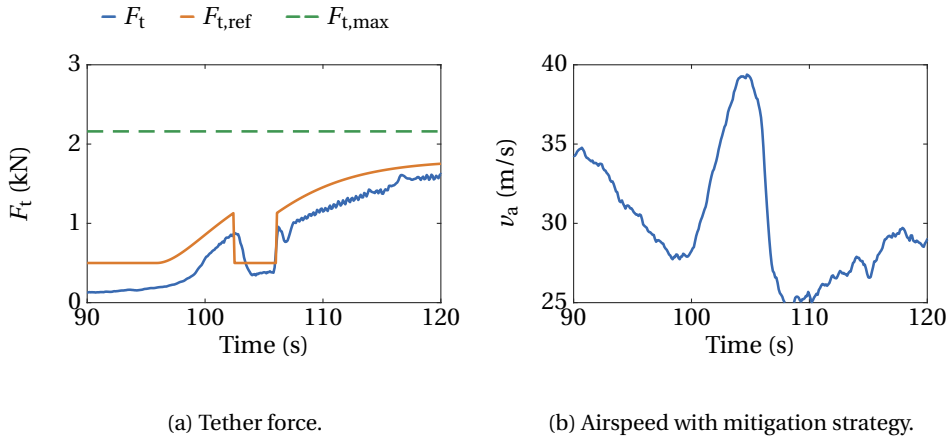
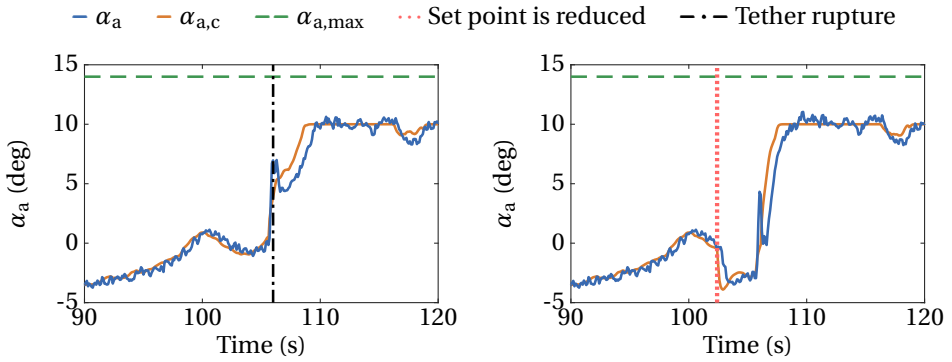


Figure 5.19: Tether force and airspeed plots obtained with the LMI controller with mitigation strategy in high wind speed conditions with turbulence.

tension in the tether even if the airspeed is further increasing. This offers the additional advantage that the lower tether force set point also reduces the commanded angle of attack and therefore not only the winch but also the flight controller itself contributes to the reduction of the tether tension actively.

In order to verify the mitigation strategy it is first tested using the boundary conditions of the previous simulation run that contained the tether force requirement violation. The results with modification are depicted in Fig. 5.19a and Fig. 5.19b. On the one hand, it can be observed that with the mitigation strategy the tether force requirement is no longer violated. On the other hand, based on the results shown in Fig. 5.19b, the airspeed peak is only reduced by  $1 \text{ m s}^{-1}$ . Hence, the drop in the tether force set point did not prevent a further increase in airspeed. In fact, the reduction of the tether tension is more effectively achieved through the adaption of the angle of attack set point (see Fig. 5.20a and Fig. 5.20b). In the present example the angle of attack at the breaking point is  $6.9^\circ$  which in combination with the airspeed of  $36 \text{ m s}^{-1}$  leads approximately to a lift force of 2.6 kN. This result is consistent with the tether force peak depicted in Fig. 5.18a. Hence, the combination of airspeed and angle of attack leads to a tether rupture in this flight phase. Contrarily, in the scenario with set point adaption the angle of attack set point is reduced to around  $-4^\circ$  as soon as the airspeed exceeds  $35 \text{ m s}^{-1}$ . This leads to a reduction of the generated lift and the tether force drops accordingly.

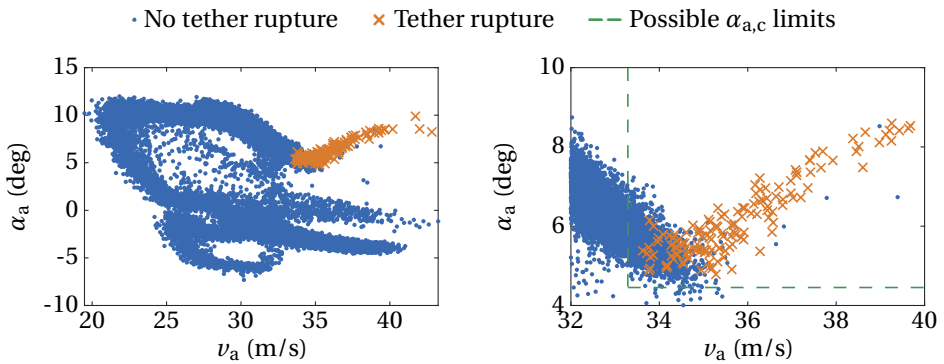
Additionally, it is instructive to analyze the airspeed and angle of attack combinations that actually resulted in the requirement violation. Randomly sampling angle of attack and airspeed pairs across flights without requirement violation and plotting them together with the pairs where the tether force exceeds the limit yields the results depicted in Fig. 5.21a and Fig. 5.21b. The scatter plots show that the airspeed and angle of attack pairs, at the point where the tether force exceeds the limit, form a visible cluster (orange crosses). The green dashed lines coarsely separate the two classes such that all requirement violations occur on the right hand side and above the separation lines. It



(a) Angle of attack without mitigation strategy. (b) Angle of attack with mitigation strategy.

Figure 5.20: Angle of attack evolution obtained with the LMI controller in high wind speed conditions and with turbulence.

5



(a) Complete sample set.

(b) Magnified part with a possible separation boundary as a function of airspeed and angle of attack.

Figure 5.21: Angle of attack and airspeed pairs at randomly sampled points during the transition phase.

can be observed that the tether force requirement violation is indeed not only a function of airspeed but also of angle of attack. For instance, below  $4^\circ$  the tether force did not exceed the limit independent of the observed airspeed. Notice that the airspeed maxima in flights with tether force requirement violation are beyond  $37 \text{ m s}^{-1}$  (see Fig. 5.17) which indicates that the airspeed can drop before the tether force exceeds its limit. Choosing the threshold value based on the maximum airspeed distribution offers therefore the advantage that it is more predictive than a threshold value selected based on the boundaries in Fig. 5.21b. For completeness also the maximum airspeed is plotted over

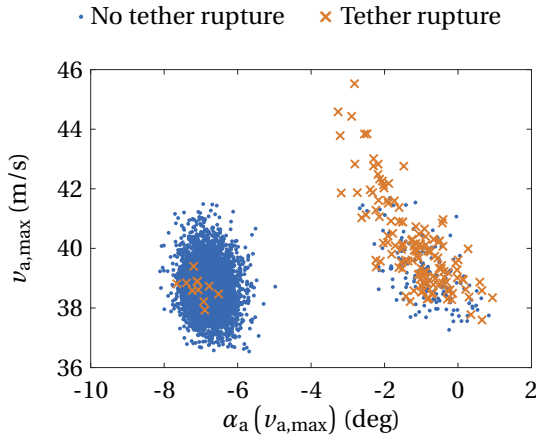


Figure 5.22: Maximum airspeed during a pumping cycles plotted over the corresponding angle of attack.

the corresponding angle of attack value and the result is depicted in Fig. 5.22. Similar to Fig. 5.17 the cluster corresponding to tether force requirement violations is clearly visible. This result could be used to further specify the threshold value not only as a function of airspeed but also of angle of attack. For safety reasons, however, the conservative value of  $35 \text{ m s}^{-1}$  independent of the angle of attack is chosen in the following.

It is paramount to conduct another Monte Carlo simulation run to see if the mitigation strategy is indeed improving the robustness across a large sample set and not only in one specific wind field. The results obtained with the controller modification are summarized in the quantile function plots shown in Fig. 5.23a and Fig. 5.23b. The results demonstrate indeed the effectiveness of the controller modification which reduces the amount of tether force violations to zero. The angle of attack requirement is still satisfied across all flights. Therefore, it can be concluded that the mitigation strategy is effective and is, hence, utilized to generate the remaining results.

Finally, the impact of turbulence on the mean power output in this wind condition and with the LMI controller is quantified. The results are again presented in form of a quantile function plot which is displayed in Fig. 5.24. With the current controller setting and in the utilized high wind speed condition case the system generates between 5kW and 5.6kW per pumping cycle in 50% of the flights. Characterizing the power output of an AWE system using a quantile function plot has the advantage that it allows to determine the probability that the average power output is within a specific interval conveniently by subtracting the corresponding quantile values. It therefore also allows to quantify the sensitivity of the AWE performance towards stochastic disturbances. Furthermore, confidence intervals can be used to investigate the expected variation of the quantile function plot across different experiments given a fixed sample size. In this example the average power output varies due to turbulence between 4.3kW and 5.6kW which corresponds to variations up to 30% using the same wind speed profile (but changing turbulence). This indicates that it is paramount to include the effect of turbulence not only to verify the controller robustness but also to more accurately quantify the



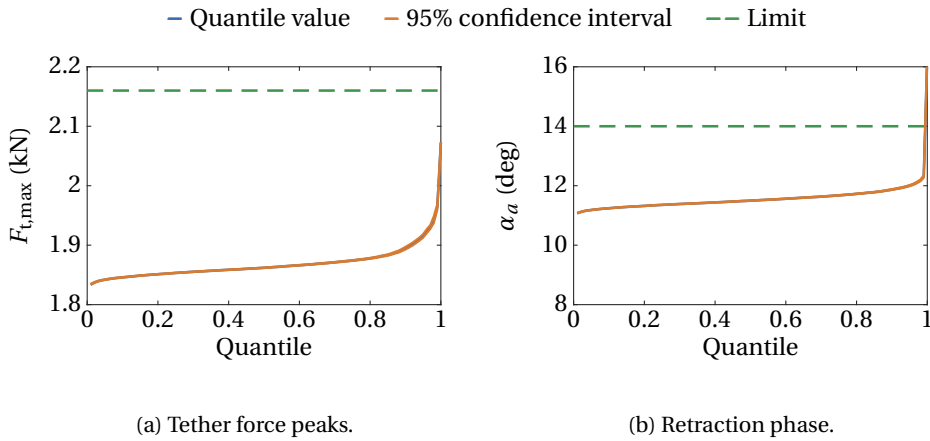


Figure 5.25: Impact of turbulence on angle of attack and tether force peaks in high wind speed conditions and with the ESA controller.

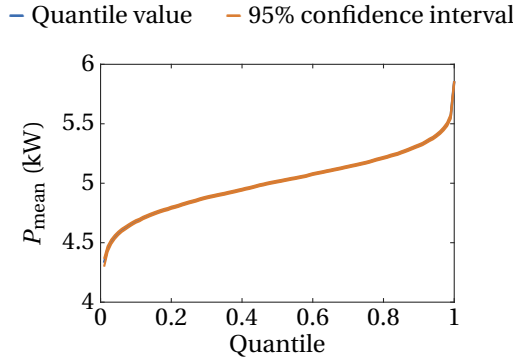


Figure 5.26: Quantile plot for the mean power in high wind speed conditions and with the ESA controller.

Fig. 5.25b and Fig. 5.26. Similar to the LMI controller, no tether rupture occurred during the 5000 simulations. However, the probability of encountering an angle of attack value beyond the limit in one pumping cycle is estimated to be 0.4%. Moreover, the ESA controller leads to a slightly higher maximum power output. In the analyzed flights the mean pumping cycle power output varies between 4.3 kW and 5.8 kW which corresponds to a variation of up to 35% due to turbulence.

High Wind Speed Conditions with the NDI Controller

Finally, the results obtained with the NDI controller in high wind speed conditions are presented. The corresponding quantile plots are displayed in Fig. 5.27a, Fig. 5.27b and Fig. 5.28. On the one hand, the NDI controller achieves reliable angle of attack tracking. On the other hand, the tether force peak requirement is violated in 0.2% of the flights. Note, the maximum force peak is at 2.19 kN which is only 30 N above the criti-

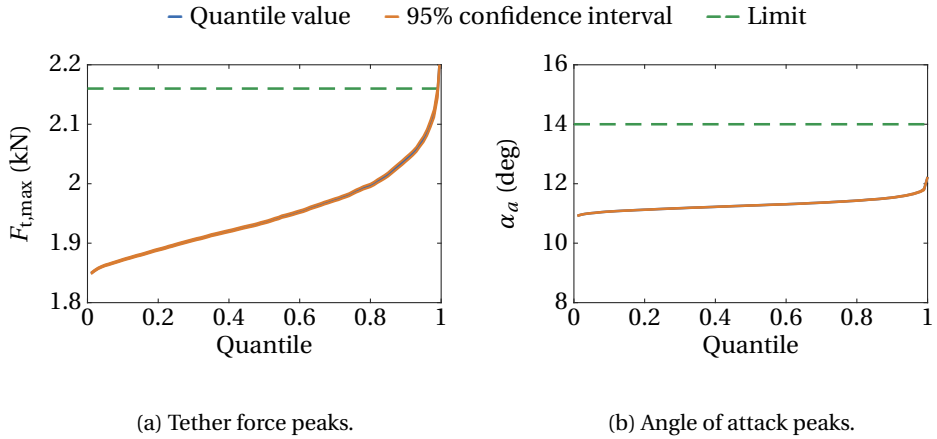


Figure 5.27: Impact of turbulence on angle of attack and tether force peaks in high wind speed conditions and with the NDI controller.

5

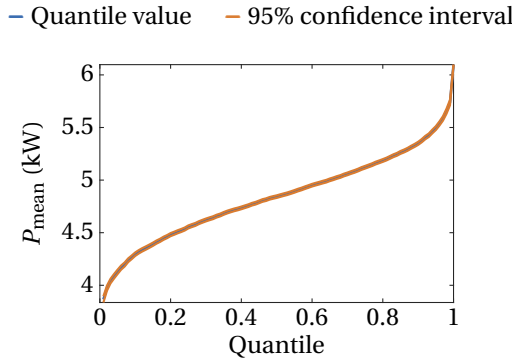


Figure 5.28: Quantile function plot of the mean power in high wind speed conditions and with the NDI controller.

cal threshold, hence this is still regarded as an acceptable result. In general, the quantiles of the tether force peak correspond to higher tether force values compared to the quantile function values obtained with the linear controllers. For instance, with the NDI controller more than 70% of the flights have a tether force peak larger than 1.9kN which is only the case for around 10% of the flights with the LMI or ESA controller. The NDI controller achieves a similar power output compared to the ESA controller. In 50% of the flights the power output is between 4.8kW and 6.1 kW which corresponds to a variation of up to 27% due to turbulence.

Low Wind Speed Conditions with the LMI Controller

With the LMI based controller the results depicted in Fig. 5.29a, Fig. 5.29b and Fig. 5.30 are obtained in low wind speed conditions. The tether force tracking performance of the

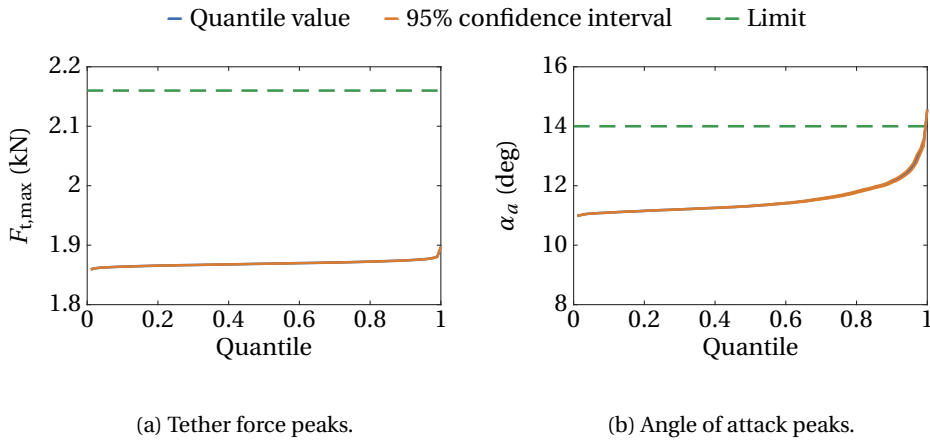


Figure 5.29: Impact of turbulence on angle of attack and tether force peaks in low wind speed conditions and with the LMI controller.

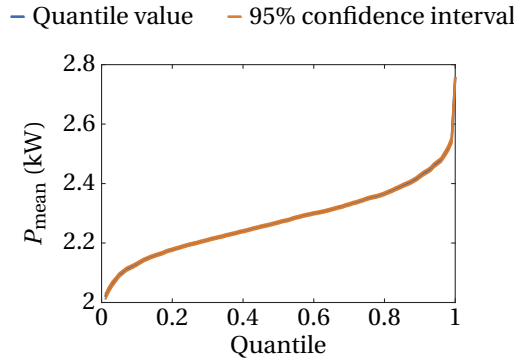


Figure 5.30: Quantile plot of the mean power obtained in low wind speed conditions and with the LMI controller.

LMI controller increases in low wind speed conditions and the largest observed peak is below 1.9kN. On the other hand, a low probability of 0.4% exists that the angle of attack exceeds the limit slightly (overshoot is below 1°). As expected the power output drops in low wind speed conditions. In the analyzed flights the on average generated power varies between 2kW and 2.8kW which corresponds to a variation of up to 40% due to turbulence.

**Low Wind Speed Conditions with the ESA Controller**

The ESA controller yields in low wind speed conditions the results displayed in Fig. 5.31a-Fig. 5.32a. On the one hand, a low tether rupture probability of 0.32% is obtained. On the other hand, the probability of an angle of attack requirement violation increases significantly (29.3%). This large deterioration compared to the high wind speed conditions

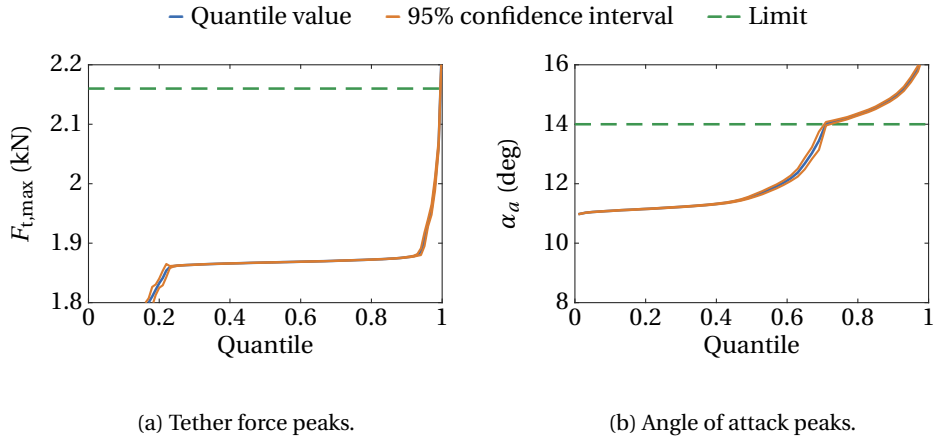


Figure 5.31: Impact of turbulence on angle of attack and tether force peaks in low wind speed conditions and with the ESA controller.

5

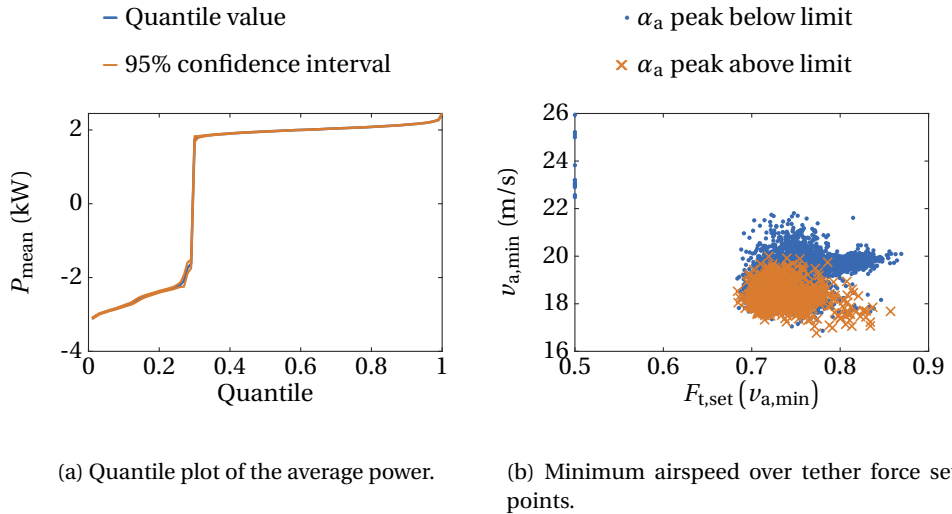
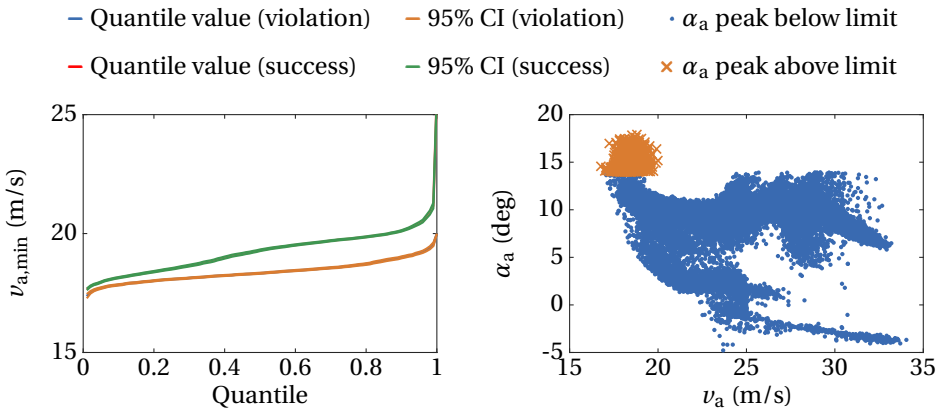


Figure 5.32: Quantile plot of the average power as well as the distribution of the minimum airspeed over tether force set points. Results are obtained in low wind speed conditions with the ESA controller.

is not expected and is investigated more in detail. The first observation is that the angle of attack peaks that exceed the limit of  $14^\circ$  occur all in the transition phase from the retraction into the traction phase. This conclusion can be drawn based on the results depicted in Fig. 5.32b. In the figure the orange crosses, corresponding to flights with angle of attack peaks higher than the limit, are all obtained at points during the pumping cycle where the tether force set point is in between the retraction and the traction phase set point (0.5 kN and 1.8 kN, respectively). In addition, since the angle of attack requirement



(a) Quantile plots for the minimum airspeed.

(b) Randomly sampled angle of attack and airspeed pairs during the transition.

Figure 5.33: Distribution of the angle of attack and airspeed pairs during the transition in low wind speed conditions and with the ESA controller.

violation is investigated, the minimum airspeed is a reasonable metric to investigate the cause for high angle of attacks during the transition. In Fig. 5.32b all the angle of attack peaks beyond the threshold correspond to an airspeed below  $20 \text{ m s}^{-1}$ . This result shows that if the airspeed drops below  $20 \text{ m s}^{-1}$  the angle of attack can exceed its limit value with a high probability. This again reveals the drawback of not controlling the airspeed explicitly in the proposed control architecture. An auxiliary backup propulsion system could be implemented that is activated in the event of an airspeed drop below, for instance,  $20 \text{ m s}^{-1}$  which would most likely increase the robustness of the ESA controller in low wind speed conditions. This has, however, not been investigated further in the present work. Note that both LMI and ESA controllers are not designed for this low airspeed in the first place, as shown in chapter 4. However, the LMI controller, which leads already in the linear analysis to higher robustness margins at the operating points with lower airspeed (i.e.  $p_1$  and  $p_2$ ), is also able to guarantee a successful flight without requirement violation even in wind conditions outside its design space.

The obtained power output with the ESA controller in low wind speed conditions is slightly lower than with the LMI controller (see Fig. 5.32a). The power varies between 1.6kW and 2.2kW which corresponds to variations up to 38%, due to turbulence. Note, however, that the result is not very representative due to the significant amount of flights where the angle of attack limit is violated.

#### Low wind speed conditions with the NDI Controller

Finally, the results for the NDI controller in low wind speed conditions are presented. The corresponding quantile plots are displayed in Fig. 5.34a, Fig. 5.34b and Fig. 5.35. In the low wind speed condition case with turbulence the NDI controller leads to the best performance among the three controllers. According to the quantile function plots no

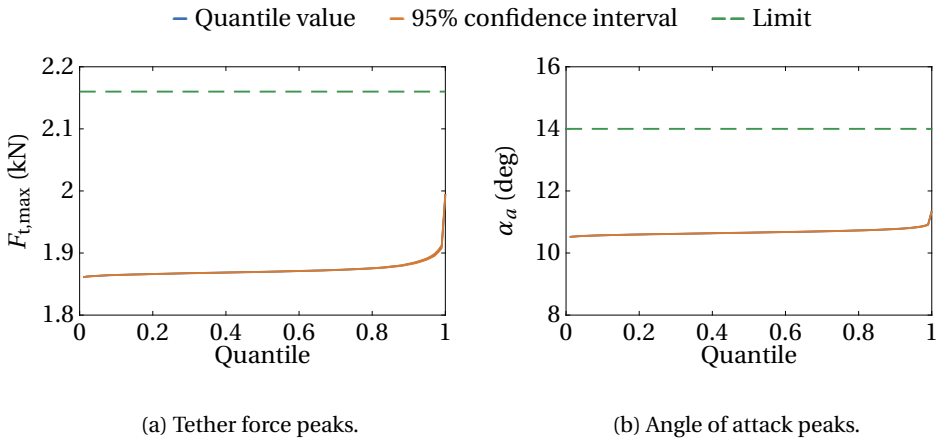


Figure 5.34: Impact of turbulence on angle of attack and tether force peaks in low wind speed conditions and with the NDI controller.

5

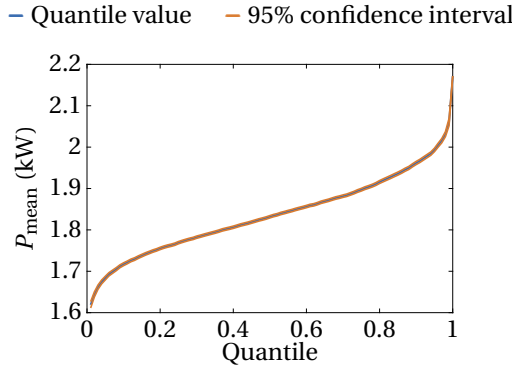


Figure 5.35: Quantile plot for the mean power in low wind speed conditions and with the NDI controller.

tether rupture and no angle of attack peak requirement violation occurred. The power output varies between 1.6kN and 2.2kN which leads to variation of up to 38% due to turbulence.

The presented results of LMI, ESA and NDI controller in only turbulent wind conditions and without any additional uncertainties are summarized in Table 5.3. Except for the high probability of violating the angle of attack constraint with the ESA controller in low wind speed conditions, the results show acceptable robustness properties of the controllers towards atmospheric turbulence.

The robustness of the linear controllers could be improved by additionally using gain scheduling such that the flight controller is more robust in the airspeed range between  $v_{a,min} = 15 \text{ ms}^{-1}$  and  $v_{a,min} = 20 \text{ ms}^{-1}$  as well as above  $35 \text{ ms}^{-1}$ . This would especially be beneficial for the ESA controller where most of the angle of attack violations occurred in the low airspeed range. Naturally, it is also possible to increase the size of the covered

Table 5.3: Overview of the angle of attack peak requirement violation and tether rupture probabilities with sampled turbulence for LMI, ESA and NDI controller. As usual around 5000 samples are used.

Wind						
condition	Controller	Metric	Traction	Retraction	Transition	Total
low	LMI	$\alpha_a > \alpha_{a,\max}$	0%	0%	100%	0.4%
low	LMI	$F_t > F_{t,\max}$	0%	0%	0%	0%
low	ESA	$\alpha_a > \alpha_{a,\max}$	0%	0%	100%	29.3%
low	ESA	$\nu_{a,\min}^{\alpha_a > \alpha_{a,\max}}$	0%	0%	100%	-
low	ESA	$F_t > F_{t,\max}$	0%	0%	100%	0.32%
low	NDI	$\alpha_a > \alpha_{a,\max}$	0%	0%	0%	0%
low	NDI	$F_t > F_{t,\max}$	0%	0%	0%	0%
high	LMI	$\alpha_a > \alpha_{a,\max}$	0%	0%	0%	0%
high	LMI	$F_t > F_{t,\max}$	0%	0%	0%	0%
high	ESA	$\alpha_a > \alpha_{a,\max}$	0%	0%	0%	0%
high	ESA	$F_t > F_{t,\max}$	0%	0%	100%	0.2%
high	NDI	$\alpha_a > \alpha_{a,\max}$	0%	0%	0%	0%
high	NDI	$F_t > F_{t,\max}$	100%	0%	0%	0.2%

flight envelope within the LMI controller synthesis by simply adding more state space models to the optimization problem. However, this can result in a conservative controller with worse performance even in the nominal case. This is due to the fact that a large range of airspeed conditions need to be stabilized while the  $H_2$ -norm needs to be minimized with a single controller gain.

In the last chapter of this thesis an additional approach to avoid tether rupture during the traction phase in turbulent wind conditions is presented and tested with the NDI controller. It uses a coordinated roll-pitch maneuver to reduce the lift magnitude and the radial component of the aerodynamic force. As a result the tether tension can be reduced efficiently with the flight controller without having to abort the pumping cycle operation even if the winch is saturating.

Furthermore, the results show that the average pumping cycle power output varies significantly due to turbulence. In low wind speed conditions variations of up to 40%, 38% and 38% with the LMI, ESA as well as the NDI controller can be observed, respectively. In high wind speed conditions the effect of turbulence decreases slightly but nevertheless resulted in variations of up to 30%, 35% as well as 27% with the same controllers.

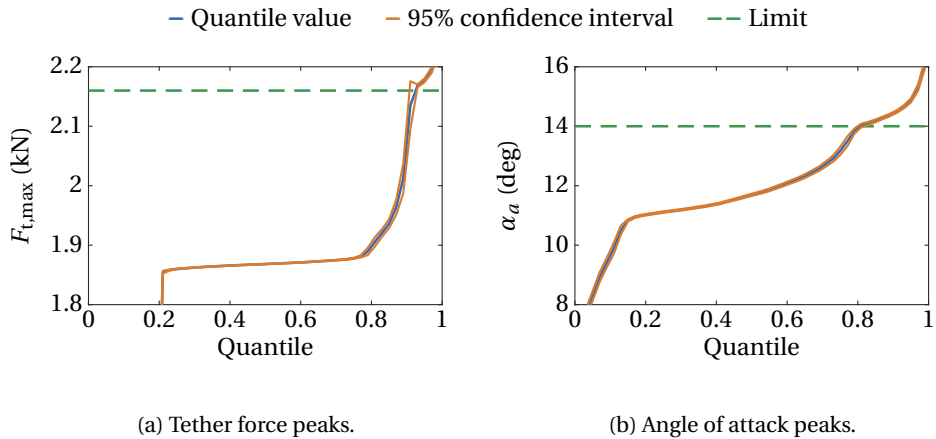


Figure 5.36: Impact of model uncertainties (up to  $\pm 20\%$ ) on angle of attack and tether force peaks in low wind speed conditions and with the LMI controller.

5

### 5.2.3. Impact of Model Uncertainties

The utilized aerodynamic model is given in form of polynomials that are a function of the angle of attack as described in section 2. The inexact knowledge of the polynomial coefficients is modeled in this section using multiplicative uncertainties. For instance, the uncertainty of the "constant" part of the force coefficient in z direction, given in the body-fixed reference frame, is modeled as:

$$C_{z,0}(\alpha_a) = C_{z,0,0}(1 + X_1) + C_{z,0,\alpha}(1 + X_2)\alpha_a + C_{z,0,\alpha^2}(1 + X_2)\alpha_a^2 \quad (5.2)$$

Each  $X_i$  is a uniformly distributed random variable with a constant probability density function in the interval  $[-\Delta_X, +\Delta_X]$ . For simplicity, and also because it is reasonable at this stage that every aerodynamic parameter is known with equal certainty, the same intervals for all aerodynamic uncertainties are used. In the following  $\Delta_X = 0.2$  (i.e.  $\pm 20\%$  uncertainty on the parameter values) is chosen. This results in 72 aerodynamic model uncertainties. Additionally, in order to investigate the impact on the robustness of a tether attachment point that is not exactly located in the CG, the tether attachment point location is modeled as an additional uncertainty. The tether location is varied in x and z direction by up to 5 cm and in y direction by 1 cm relative to the CG. Hence, 75 uniformly distributed uncertainties are considered in total. The analysis is again conducted in low and high wind speed conditions for each of the three controllers. Note, the analysis also includes sampled turbulence fields which, similar to the time delay analysis, can be regarded as process noise.

#### Low Wind Speed Conditions with the LMI Controller

The quantile function plots for the tether force and the angle of attack peaks obtained with 5000 simulations using the LMI controller in low wind speed conditions are shown in Fig. 5.36a and Fig. 5.36b. In the low wind speed condition case the tether rupture

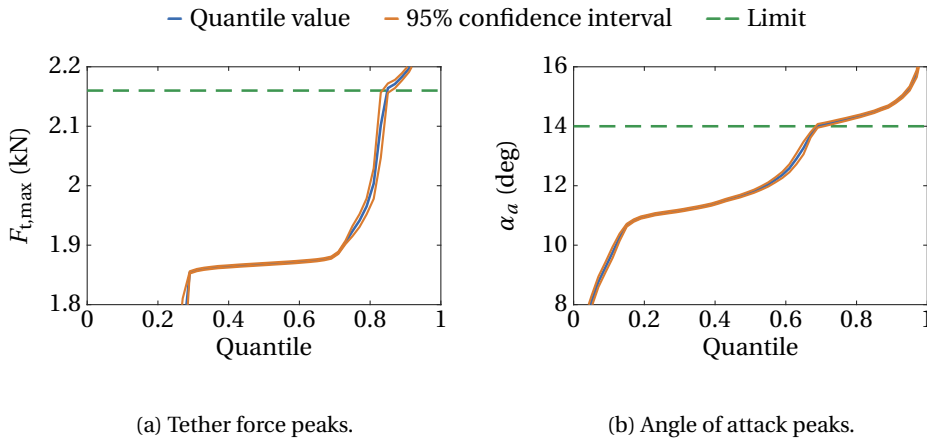


Figure 5.37: Impact of model uncertainties (up to  $\pm 20\%$ ) on angle of attack and tether force peaks in low wind speed conditions and with the ESA controller.

probability increases to 8.7%. The angle of attack limit is violated in 20% of the simulation runs. The simulation results show further that all tether force peaks beyond the critical value are obtained during the traction phase. In contrast, in flights where the angle of attack limit is violated, 99% of the limits were exceeded during the transition from retraction to traction and in 1% of the flights during the traction phase.

#### Low Wind Speed Conditions with the ESA Controller

The results obtained with the ESA controller in low wind speed conditions are displayed in Fig. 5.37a and Fig. 5.37b. It can be observed that the ESA controller, in low wind speed conditions, is less robust compared to the LMI controller. The angle of attack limit is violated in 31.7% of the flights and the tether force limit is exceeded in 16.2% of the flights. Note that the ESA controller led already without modeling uncertainties to a significantly higher probability of exceeding the angle of attack peak limit compared to the LMI controller. Hence, this result is expected. Similar to the LMI controller the angle of attack requirement is violated most of the time (97%) during the transition, whereas the tether force requirement is violated in 64.8% of the cases in the traction phase, and in 21.9% of the flights it is violated in the transition phase. In both cases the airspeed minima and maxima are obtained in the same operational mode where the requirements are violated. This is analyzed in more detail later in this section.

#### Low Wind Speed Conditions with the NDI Controller

The results obtained with the NDI controller in low wind speed conditions are displayed in Fig. 5.38a and Fig. 5.38b. The probability of a tether rupture is around 10.7% and the angle of attack limit is violated in 0.32% of the flights. Most of the angle of attack violations (62.5%) occur in the traction phase and in 37.5% of the flights during the transition. The tether force peak violations occur in 100% of the flights during the traction phase. Again, the airspeed minima and maxima are obtained in the same operational mode where the requirements are violated.

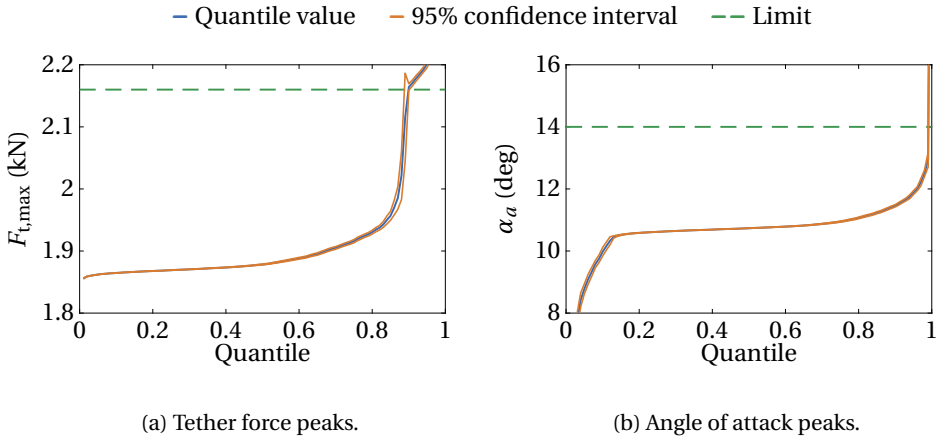


Figure 5.38: Impact of model uncertainties (up to  $\pm 20\%$ ) on angle of attack and tether force peaks in low wind speed conditions and with the NDI controller.

5

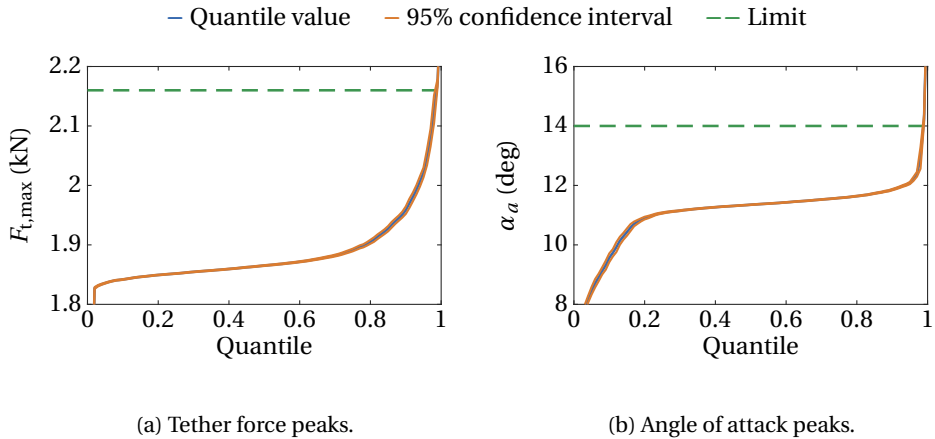


Figure 5.39: Impact of aerodynamic uncertainties (up to  $\pm 20\%$ ) on angle of attack and tether force peaks in high wind speed conditions and with the LMI controller.

### High Wind Speed Conditions with the LMI Controller

The results obtained with the LMI controller in high wind speed conditions and with model uncertainties are shown in Fig. 5.39a and Fig. 5.39b. In contrast to the low wind speed condition case, the tether ruptures with a lower probability (1.6%). Similarly, the angle of attack limit is violated in only 1.52% of the flights. These results already indicate that the LMI controller is more robust towards modeling uncertainties in high wind speed conditions than in low wind speed conditions.



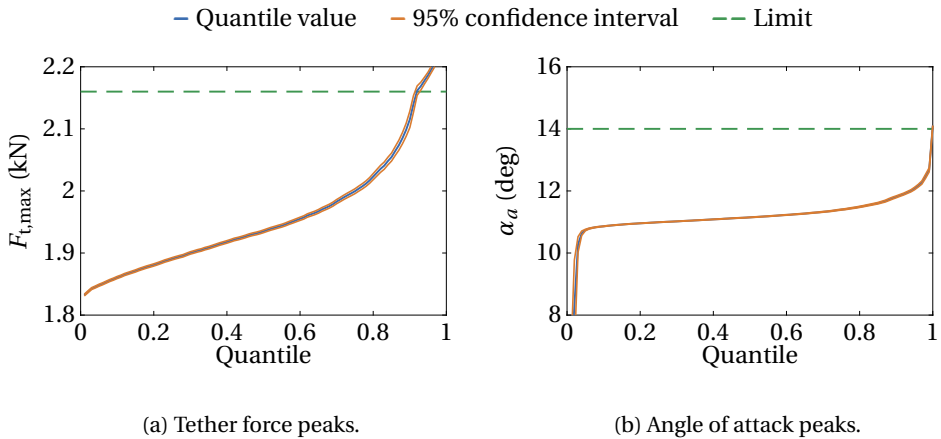


Figure 5.41: Impact of aerodynamic uncertainties (up to  $\pm 20\%$ ) on angle of attack and tether force peaks in high wind speed conditions and with the NDI controller.

5

controller leads to a most robust angle of attack tracking performance. Even in presence of modeling uncertainties the probability of violating the angle of attack limit is well below 1% in both wind conditions. Both results are consistent to the results obtained without modeling uncertainties.

Notice one might be able to reduce the significant probability of violating the angle of attack requirement for the linear controllers by lifting the corresponding constraint. Although this approach seems to simply bypass the issue it could be justified by the conservative choice of the current limit value with respect to the expected stall point ( $\approx 18^\circ$ ). In fact, if the requirement limit is set to the stall point, the probability of violating the angle of attack requirement is reduced to 0.04% with the LMI controller and to 0.56% with the ESA controller. Lifting the requirement limit, however, requires to increase the confidence in the aerodynamic model of the aircraft in the high angle of attack regime. Besides this result, and except for the tether rupture probability achieved with the ESA controller in low wind speed conditions, the obtained probabilities are regarded as acceptable.

For completeness the same analysis can be conducted for a lower uncertainty level. For instance, assuming uncertainties up to  $\pm 10\%$  leads to the results depicted in Table 5.4. It can be observed that with the LMI and the NDI controller this uncertainty level leads only to a small increase in the probability of violating one the two requirements compared to the results obtained without model uncertainties. In low wind speed conditions zero tether force requirement violations occurred with the LMI and the NDI controller. In addition, the NDI controller does not violate the angle of attack requirement in both wind conditions. With the LMI controller the probability of a tether force requirement violation is 0.06% in high wind speed conditions. Furthermore, the LMI controller violates the angle of attack requirement with a probability of 0.4% and 0.22% in low and high wind speed conditions, respectively. Especially the reduced probability in low wind speed conditions compared to the result obtained with the larger uncertainty

Table 5.4: Overview of the angle of the attack peak requirement violation and tether rupture probabilities with sampled turbulence and uncertainties up to  $\pm 10\%$  for LMI, ESA and NDI controller. As usual 5000 samples are used to calculate the probabilities.

Wind			
condition	Controller	Metric	Total
low	LMI	$\alpha_a > \alpha_{a,\max}$	0.4%
low	LMI	$F_t > F_{t,\max}$	0%
low	ESA	$\alpha_a > \alpha_{a,\max}$	29.6%
low	ESA	$F_t > F_{t,\max}$	1.76%
low	NDI	$\alpha_a > \alpha_{a,\max}$	0%
low	NDI	$F_t > F_{t,\max}$	0%
high	LMI	$\alpha_a > \alpha_{a,\max}$	0.22%
high	LMI	$F_t > F_{t,\max}$	0.06%
high	ESA	$\alpha_a > \alpha_{a,\max}$	0.28%
high	ESA	$F_t > F_{t,\max}$	0.23%
high	NDI	$\alpha_a > \alpha_{a,\max}$	0%
high	NDI	$F_t > F_{t,\max}$	0.3%

level ( $\pm 20\%$ ) is significant. In high wind speed conditions the NDI controller violates the tether force requirement with a probability of 0.3% which is, however, only slightly higher than without uncertainties (0.2%). Hence, also in this case the impact of the uncertainties on the robustness is not significant.

Contrarily, even with the lower uncertainty level the ESA controller leads to a high probability of violating the angle of attack requirement in low wind speed conditions (29.6%). The probability of violating the tether force requirement is reduced from 16.2% to 1.76% but still yields the highest failure probability across the three controllers. In high wind speed conditions both probabilities are reduced, but also in this wind condition the least robust angle of attack tracking performance is provided by the ESA controller (0.28%). The tether force requirement is violated with a slightly lower probability compared to the NDI controller (0.23%).

In general, the positive correlation between robustness and wind speed of the linear controllers can be explained by looking at the distributions of the minimum airspeed: The quantile function values obtained in low wind speed conditions, depicted in Fig. 5.42a and Fig. 5.42b, are below the quantile function values that are obtained in the high wind speed condition flights. Notice that the results presented in chapter 4 show that the robustness decreases with airspeed due to the lower control authority. In addition, it is shown in the previous section that the ESA controller leads to a high probability

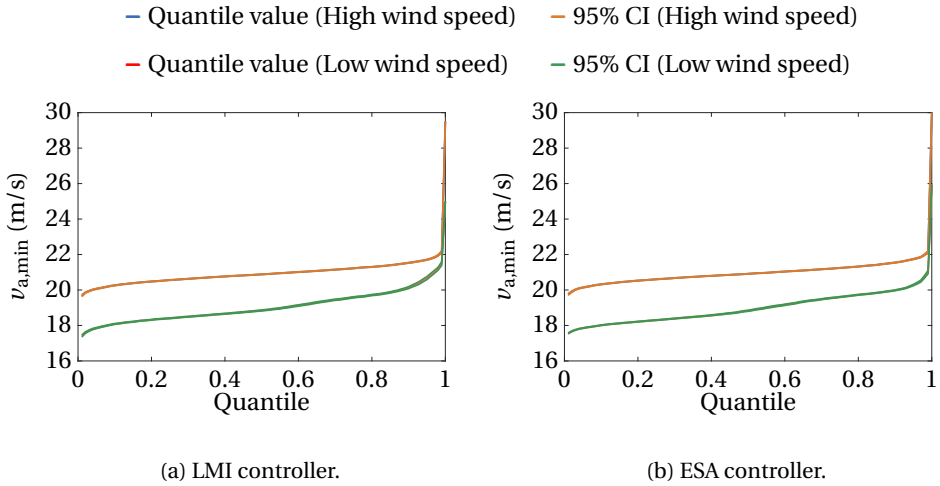


Figure 5.42: Quantile function plots of the minimum airspeed during pumping cycle operation in low as well as high wind speed conditions.

of violating a requirement if the airspeed is below  $20 \text{ m s}^{-1}$ . In low wind speed conditions the minimum airspeed is with around 90% chance below  $20 \text{ m s}^{-1}$  whereas in high wind speed conditions around 95% of the airspeed minima are above  $20 \text{ m s}^{-1}$ . Therefore, the lower minimum airspeed in low wind speed conditions can be used to explain the higher probability of violating either the angle of attack or the tether force requirement. Moreover, the similarity between the curves shown in Fig. 5.42a and Fig. 5.42b indicates once more the higher robustness of the LMI controller also for airspeeds outside its design interval ( $27.70 \text{ m s}^{-1} - 36.32 \text{ m s}^{-1}$ ).

In the following section a sensitivity analysis is performed that can help to identify the uncertainties that drive the requirement violations. These insights can then be used to further improve the robustness of a specific controller with respect to the uncertainties it is most sensitive to.

#### 5.2.4. Sensitivity Analysis

Based on the presented results in the last section it can be confirmed that model uncertainties increase the probability of encountering a violation of the maximum tether force or the angle of attack limit. Since the uncertainty model is high dimensional (75 uncertainties) it is instructive to systematically determine the uncertainties that drive the failure probability. For this task the approach presented in [113] is utilized. It is appealing due to its simplicity but at the same time it is build up on a sound theoretical foundation. Furthermore, it can be easily integrated into an existing verification toolchain since the algorithm requires only an interface at the uncertainty generation level. The authors in [113] reformulate the problem of detecting influential uncertainties in Monte Carlo simulations into a hypothesis test. The null hypothesis is that every parameter is not influential. After the experiment is conducted it is verified, for each parameter, if the

Table 5.5: Overview of the requirement violation probabilities across the uncertainty models with up to  $\pm 20\%$  model uncertainties and sampled turbulence. The results for all three controllers LMI, ESA and NDI are displayed for comparison. As usual around 5000 samples are used to generate the results.

Wind						
condition	Controller	Metric	Traction	Retraction	Transition	Total
low	LMI	$\alpha_a > \alpha_{a,\max}$	1%	0%	99%	20%
low	LMI	$\nu_{a,\min}^{\alpha_a > \alpha_{a,\max}}$	1%	0%	99%	-
low	LMI	$F_t > F_{t,\max}$	100%	0%	0%	8.7%
low	LMI	$\nu_{a,\max}^{F_t > F_{t,\max}}$	100%	0%	0%	-
high	LMI	$\alpha_a > \alpha_{a,\max}$	0%	18.4%	81.6%	1.52%
high	LMI	$\nu_{a,\min}^{\alpha_a > \alpha_{a,\max}}$	0%	0%	100%	-
high	LMI	$F_t > F_{t,\max}$	77.5%	1.3%	21.2%	1.6%
high	LMI	$\nu_{a,\max}^{F_t > F_{t,\max}}$	72.5%	11.3%	16.3%	-
low	ESA	$\alpha_a > \alpha_{a,\max}$	0.4%	2.6%	97%	31.7%
low	ESA	$\nu_{a,\min}^{\alpha_a > \alpha_{a,\max}}$	0.27%	3.6%	96.2%	-
low	ESA	$F_t > F_{t,\max}$	64.8%	13.3%	21.9%	16.2%
low	ESA	$\nu_{a,\max}^{F_t > F_{t,\max}}$	65.7%	22.6%	11.7%	-
high	ESA	$\alpha_a > \alpha_{a,\max}$	0%	16.7%	83.3%	4.4%
high	ESA	$\nu_{a,\min}^{\alpha_a > \alpha_{a,\max}}$	0%	8.0%	92.0%	-
high	ESA	$F_t > F_{t,\max}$	44.3%	41.5%	14.2%	7.8%
high	ESA	$\nu_{a,\max}^{F_t > F_{t,\max}}$	47.9%	39.2%	12.9%	-
low	NDI	$\alpha_a > \alpha_{a,\max}$	62.5%	0%	37.5%	0.32%
low	NDI	$\nu_{a,\min}^{\alpha_a > \alpha_{a,\max}}$	62.5%	0%	37.5%	-
low	NDI	$F_t > F_{t,\max}$	100%	0%	0%	10.7%
low	NDI	$\nu_{a,\max}^{F_t > F_{t,\max}}$	100%	0%	0%	-
high	NDI	$\alpha_a > \alpha_{a,\max}$	100%	0%	0%	0.02%
high	NDI	$\nu_{a,\min}^{\alpha_a > \alpha_{a,\max}}$	0%	0%	100%	-
high	NDI	$F_t > F_{t,\max}$	72.4%	19.4%	8.2%	8.3%
high	NDI	$\nu_{a,\max}^{F_t > F_{t,\max}}$	81.1%	6.2%	12.7%	-

outcome is statistically significant in which case the null hypothesis is rejected and the parameter is identified as influential.

The algorithm is concisely summarized in the following. For a detailed derivation it is referred to the original publication [113]. Note, in [112] a simplified approach to [113] is proposed which uses a normal approximation of the hyper-geometric distribution and hence avoids the calculation of binomial coefficients. The authors suggest this modification to reduce the computational burden which is required to calculate the binomial coefficients. In the present work the computational effort was acceptable therefore the original exact approach is utilized to derive the following results. Note, the sensitivity analysis is only carried out for the LMI controller exemplary. It is noteworthy, that this sensitivity analysis can also be applied to any other parameter choices beyond the model uncertainties e.g. high level control parameter choices or even aircraft design choices. However, this is out of the scope of this work and is, hence, left for future work.

The first step of the algorithm consists of an initial Monte Carlo simulation run where the uncertainties are sampled individually from their marginal distributions. For the following it is assumed that the sampled uncertainties of the  $i$ th simulation are represented by the vector  $\boldsymbol{\eta}_{T,i}$ . In the second step all  $\boldsymbol{\eta}_{T,i}$ s are identified that correspond to a simulation where the considered requirement (e.g. tether force limit) is violated. In the third step, new uncertainty vectors are generated based on the identified  $\boldsymbol{\eta}_{T,i}$ s. The new vectors are generated by choosing the  $j$ th parameter from the seed vector  $\boldsymbol{\eta}_{T,i}$  with a probability specified by  $r$  (i.e. flipping a biased or fair coin) and with a probability of  $1 - r$  the  $j$ th element of the new vector is set to zero (i.e. the nominal value of this parameter is not perturbed). In this work a value of 0.5 for  $r$  is chosen but [113] suggests that also slightly biased "coin flips", i.e.  $r=0.4$  or  $r=0.6$ , lead to reasonable results. The outcome of this step is a matrix of uncertainty vectors (i.e. test vectors) constructed from the  $\boldsymbol{\eta}_{T,i}$ s that led to a requirement violation. In the fourth step the second round of Monte Carlo simulations is started using the newly constructed uncertainty vectors. The fifth step involves counting of the failures  $n_f$  among the  $n_{mc}$  simulation runs. Next, the number of times each nominal parameter value is perturbed in the Monte Carlo simulation run is determined (denoted with  $n_{mc,j}$ ). The obtained number should match approximately  $r$  times  $n_{mc}$  since  $r$  is the probability that a parameter is picked in one test vector. Eventually, for each parameter the number  $n_{f,j}$  of failures the parameter is involved in is counted. Based on these results a hyper-geometric distribution is used to model the probability of  $z_j$  failures of the  $j$ th parameter among  $n_{mc,j}$  total occurrences of this parameter. The probability mass function of the hyper-geometric distribution is in this case given by:

$$p_{Z_j}(z_j) = \frac{\binom{n_f}{z_j} \binom{n_{mc} - n_f}{n_{mc,j} - z_j}}{\binom{n_{mc}}{n_{mc,j}}} \quad (5.3)$$

where the brackets indicate binomial coefficients.  $Z_j$  corresponds to the hyper-geometrically distributed random variable associated to the  $j$ th element of an uncertainty vector. Eventually, the following hypothesis test is proposed by [113]: If the p-value of encountering  $z_j$  or more failures is smaller than a prescribed level of significance  $\alpha$  the null hypothesis

is rejected and the parameter is assumed to be influential. As proposed in [113] the level of significance is calculated according to

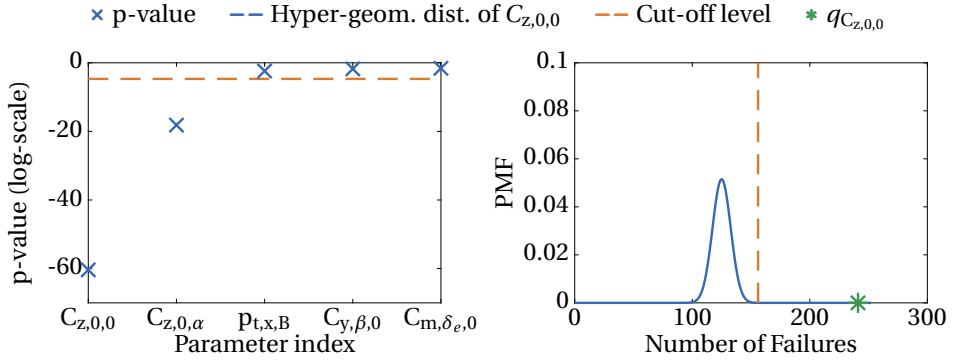
$$\alpha = \frac{1}{10n_{mc}} \quad (5.4)$$

In the last step of the sensitivity analysis a third round of Monte Carlo simulations is launched with an independent set of uncertainty vectors (randomly sampled). However, this time the determined influential uncertainties are set to zero. This should result in a significant reduction of the number of requirement violations if the removed uncertainties are indeed driving the analyzed requirement violation probability.

This method is subsequently applied to determine the influential model uncertainties that influence the probabilities of violating either the tether force or the angle of attack limit requirements. Naturally, both requirements can also be investigated separately. For the analysis all 72 aerodynamic as well as the three tether attachment location uncertainties are considered which leads, as before, to a total of 75 uniformly distributed uncertainties. The sensitivity analysis is conducted for the low and the high wind speed conditions separately.

Based on the simulations conducted with the LMI controller in high wind speed conditions, which led to the results depicted in Fig. 5.39a and Fig. 5.39b, the specific sample values of the uncertainties that are involved in either a tether rupture or an angle of attack peak requirement violation are extracted. New test vectors are created, a new Monte Carlo simulation is started using the test vectors and the hypothesis test is conducted using the new results. For the high wind speed condition case, it turns out that with the defined confidence level in Eq. (5.4) only two out of 75 uncertainties reject the null hypothesis and are hence regarded as influential. Tracing back the uncertainties to the aerodynamic model identifies  $C_{z,0,0}$  and  $C_{z,0,\alpha}$  as the uncertainties that influence significantly the probability of violating either the maximum allowable tether force or angle of attack value. From a physical point of view this makes sense since these coefficients belong to the longitudinal dynamics which are directly linked to the tether force as well as the angle of attack dynamics. Uncertainties in the longitudinal model reduce the performance of the angle of attack tracking controller and hence increase the chance of a requirement violation. The lowest five p-values are depicted in Fig. 5.43a. Since the orders of magnitude vary significantly across the parameters, a log-scale for the p-values is chosen. The cutoff level (here  $2 \cdot 10^{-5}$ ) is indicated by the orange dashed line which seems to be a reasonable decision level since the orders of magnitude of the p-values beyond the cut-off level are similar. For illustrative purposes the hypergeometric distribution corresponding to the  $C_{z,0,0}$  is plotted along with the confidence level (dashed). The actual number of failures, where the uncertainty on  $C_{z,0,0}$  is nonzero, is indicated by the green asterisk. Since the cutoff level is on the left hand side of the number of failures, a statistically significant result is obtained and the parameter is defined to be influential. The numerical values are listed in Table 5.6 for completeness.

In order to verify that the controller is indeed most sensitive towards uncertainties in  $C_{z,0,0}$  and  $C_{z,0,\alpha}$  a third Monte Carlo simulation run is launched with completely new uncertainty samples. This time, however, the uncertainties for  $C_{z,0,0}$  and  $C_{z,0,\alpha}$  are set to zero. The sanity check provides the results displayed in Fig. 5.44a and Fig. 5.44b. It



(a) p-values corresponding to the uncertainties (log-scale).

(b) Hypergeometric distribution corresponding to  $C_{z,0,0}$ . The asterisk indicates the corresponding quantile.

5

Table 5.6: The p-values indicate influential uncertainties with respect to tether rupture. The corresponding aerodynamic coefficients are listed in the left column and their p-value in the right column. The parameter below the line is the first non-influential parameter. Results are generated with 4992 samples which leads to a cut-off level of  $2 \cdot 10^{-5}$ .

Parameter	p-value
$C_{z,0,0}$	$4.14 \cdot 10^{-61}$
$C_{z,0,\alpha}$	$6.82 \cdot 10^{-19}$
$p_{t,x,B}$	$0.04 \cdot 10^{-1}$
$C_{y,\beta,0}$	0.02
$C_{m,\delta_e,0}$	0.03

can be observed that the tether rupture probability is decreased to zero. Note, there is still a small chance (i.e. 0.26%) that the angle of attack limit is violated. Nevertheless, the probability of violating the angle of attack peak requirement is reduced compared to the case with the full uncertainty model where the probability is 1.52%), hence approximately an order of magnitude higher. This result shows that the hypothesis test is indeed able to determine the most influential parameters that are responsible for an increased probability of violating a critical requirement.

The same analysis is conducted for the low wind speed condition scenario. The results of the sensitivity analysis, with respect to the tether force and the angle of attack requirement violation, are depicted in Table 5.7. Similar, to the high wind speed condition case the z-force coefficients  $C_{z,0,0}$  and  $C_{z,0,\alpha}$  are among the influential parameter. In addition, the static roll-damping coefficient  $C_{l,p,0}$  is, according to the hypothesis test, an influential parameters. This result can be interpreted as follows: In the previous section

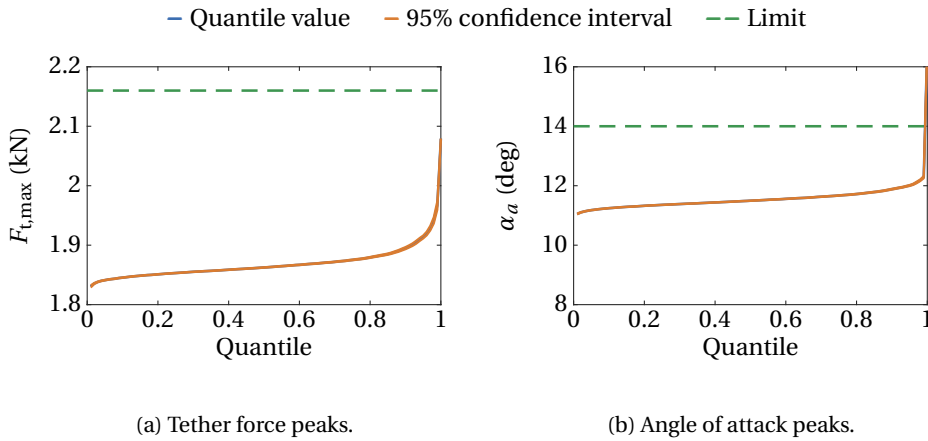


Figure 5.44: Results for high wind speed conditions and LMI controller with uncertainties (up to  $\pm 20\%$ ) excluding the influential uncertainties of  $C_{z,0,0}$  and  $C_{z,0,\alpha}$ .

it could be observed that the angle of attack requirement is violated with high probability (99%) during the transition phase where also the minimum airspeed is reached with the same probability. During the transition the aircraft needs to turn, which in case of a significant difference between the roll damping coefficient of the model as well as the real system can reduce the performance of the lateral controller even further. Not being able to accurately track the roll commands can increase the coupling between the longitudinal and lateral dynamics which eventually increases the failure probability. In that sense the uncertainty on the static roll-damping coefficient can have indeed an impact on the stability which is even further amplified in presence of low dynamic pressure and hence in low wind speed conditions. For completeness, the lowest five p-values are depicted in Fig. 5.45a and the hyper-geometric distribution for  $C_{z,0,0}$  is depicted in 5.45b. Note, for the low wind speed condition analysis a high number of failures resulted in presence of model uncertainties (see Table 5.5). For this reason a larger number of new test vectors needs to be created to approximate all possible combinations of influential parameters. In total, 9912 test vectors are created to conduct the hypothesis test.

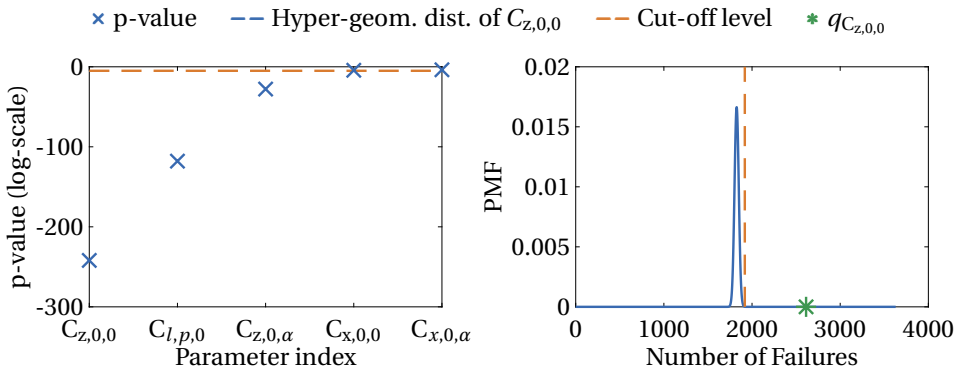
Re-simulating with the perturbed models but removing the three influential uncertainties leads to a significant reduction in both failure probabilities. In fact, only one tether rupture occurred in 5000 simulations (0.02%) compared to 8.7% using the full perturbed model (see Table 5.5). The probability of violating the angle of attack peak is reduced to 7.3% compared to 20% on the fully perturbed model. The quantile function plots for the sanity check are displayed in Fig. 5.46a and Fig. 5.46b.

The results of this section indicate that the probability of violating either the tether force peak requirement or the probability of exceeding the angle of attack limit is mainly driven by three model parameters. Combining the results of the hypothesis test obtained in the high and low wind speed conditions yields the force coefficient in z direction  $C_{z,0,0}$  and  $C_{z,0,\alpha}$  as well as the static roll-damping coefficient  $C_{l,p,0}$  as the main influential parameters. Indeed, the results show that removing the corresponding uncertainties can

Table 5.7: The p-values indicate influential uncertainties with respect to either a tether force peak or a angle of attack peak requirement violation. The corresponding aerodynamic coefficients are listed in the left column and their p-value in the right column. The parameter below the line is the first non-influential parameter. The jump in the p-value is significant. Results are generated with 9912 samples which leads to a cut-off level of  $1 \cdot 10^{-5}$ .

Parameter	p-value
$C_{z,0,0}$	$1.10 \cdot 10^{-242}$
$C_{l,p,0}$	$1.21 \cdot 10^{-118}$
$C_{z,0,\alpha}$	$1.48 \cdot 10^{-28}$
$C_{x,0,0}$	$4.55 \cdot 10^{-5}$
$C_{x,0,\alpha}$	$1.82 \cdot 10^{-4}$

5



(a) p-values corresponding to the uncertainties (log-scale).

(b) Hypergeometric distribution corresponding to  $C_{z,0,0}$  with cut-off level.

reduce the requirement violation probabilities significantly. This insight could be used to reiterate through the linear control design process. For instance, the expected model uncertainty associated to these coefficients can be increased for the calculation of the SSV. Optimizing the SSV leads then to a controller that is more robust in particular towards uncertainties in these three parameters. This approach could of course be formalized in the context of  $\mu$ -synthesis. Furthermore, additional state-space models could be added to the LMIs that are used for the controller design. These state-space models could be obtained through large perturbations of the nominal state-space models at the locations corresponding to the influential parameters. The most straightforward way to do this is to linearize the perturbed nonlinear model around the same operating points and then add the resulting state-space models to the LMIs that are used for the controller synthesis.

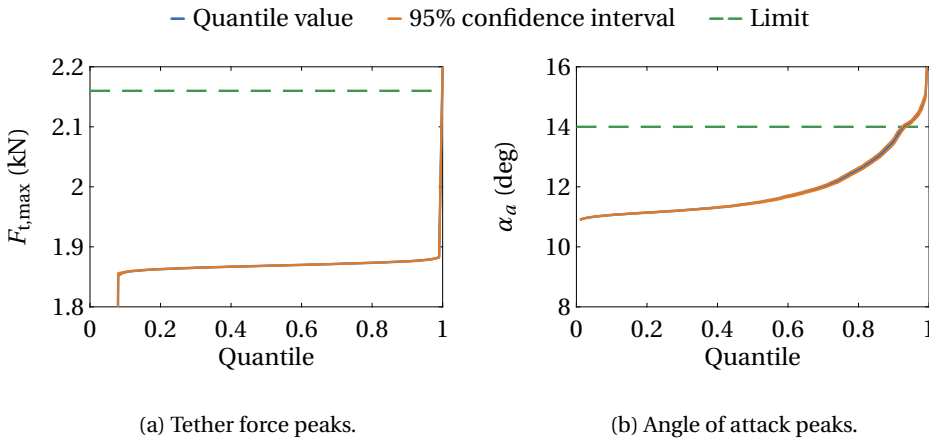


Figure 5.46: Results for high wind speed conditions and LMI controller with uncertainties (up to  $\pm 20\%$ ) excluding the influential uncertainties of  $C_{z,0,0}$ ,  $C_{z,0,\alpha}$  and  $C_{l,p,0}$ .

### 5.2.5. Detailed Control Performance Analysis

Based on the statistical analysis it can be concluded that the ESA controller provides overall the lowest level of robustness. In low wind speed conditions it leads to the highest probability of exceeding the angle of attack limit (31.7%) as well as to the highest probability of exceeding the tether tension limit (16.2%). Similarly, in high wind speed conditions it leads to the highest probability of exceeding the angle of attack limit (4.4%). The probability of exceeding the tether force limit in high wind speed conditions is slightly lower compared to the NDI controller (7.8% compared to 8.3%). Based on these results the ESA controller, at least in the presented form, is not a recommended inner loop control strategy. Contrarily, comparing the performance and robustness properties of the LMI with the NDI controller leads not to a clear decision which controller performs better. Therefore, both controllers are in this section further analyzed in detail based on a single simulation run consisting of several consecutively flown pumping cycles. Similar to the last section the results in low and in high wind speed conditions are presented. The results are generated with sampled turbulence but without any additional uncertainties.

#### Low Wind Speed Conditions with the LMI controller

The evolution of the wind velocity at the aircraft during the pumping cycle operation is component wise displayed in Fig. 5.47a. The component of the wind velocity in x direction (blue) varies approximately between  $5.2 \text{ m s}^{-1}$  and  $9 \text{ m s}^{-1}$ . The components  $v_{w,y,W}$  (orange) and  $v_{w,z,W}$  (green), representing side wind and updrafts/downdrafts due to the atmospheric turbulence in the W frame, vary between  $-1.5 \text{ m s}^{-1}$  and  $1.4 \text{ m s}^{-1}$ . The wind speed defined by the wind speed profile is indicated by the red line. Note, the blue line consists of the turbulence superimposed to the wind speed profile. It can be observed that the shear effect, i.e. the altitude dependence of the wind speed, has only a minor impact on the variation of the wind speed in  $x_W$  direction in this specific simulation run.

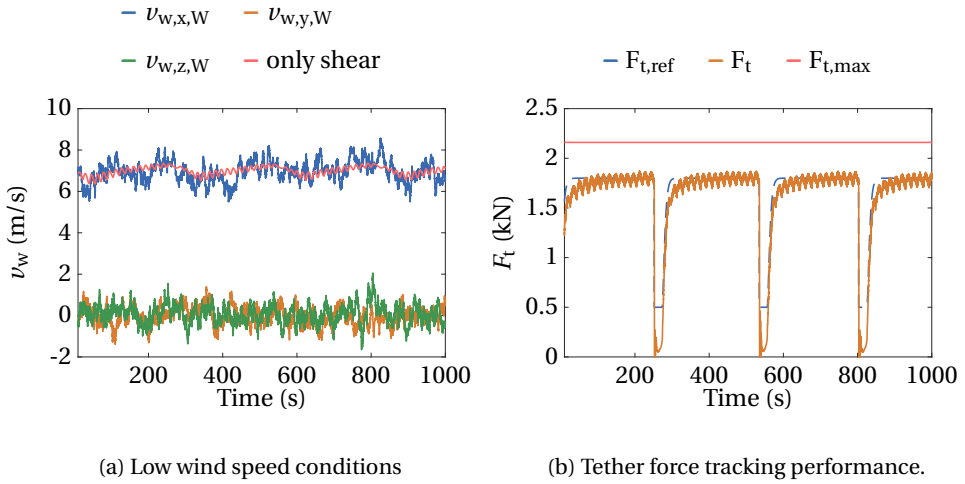


Figure 5.47: Low wind speed conditions and tether force tracking performance with the LMI controller

The evolution of the tether force is displayed in Fig. 5.47b. The blue dashed line is the filtered set point of the tether force that is tracked by the winch controller. The tracking performance of the tether force in the traction phase ( $F_{t,set} = 1.8\text{ kN}$ ) is acceptable and the tension is kept in the vicinity of the set point. During the retraction phase the controller is not able to track the reference accurately. This is due to the fact that at the beginning of the retraction phase the winch reeling in speed is saturating (see Fig. 5.48) and hence the requested tension cannot be tracked. However, as soon as the winch speed leaves the saturation state the accurate tension tracking performance is recovered. Note, this behavior can also be observed in the 3-DoF simulations and, hence, is most likely not caused by the inner loop controller. The tracking error during the retraction phase could be reduced by adapting the tether tension set point. However, since this tracking error has no impact on the overall capability of performing the pumping cycle operation it is regarded as acceptable.

The inner loop flight control performance is analyzed with respect to the tracking accuracy of the path loop reference signals  $\mu_{a,c}$ ,  $\alpha_{a,c}$  and  $\beta_{a,c}$ . The (aerodynamic) bank angle reference (blue, dashed) is tracked acceptably (see Fig. 5.49a). The reference values stay within the defined boundaries (green, dotted-dashed line) which indicates that the control objective is well posed. A magnified part of the bank angle tracking performance is displayed in Fig. 5.49b showing indeed good tracking behavior with only small bank angle tracking errors during the turns.

Furthermore, it can be observed that the flight controller is able to track the angle of attack command acceptably (see Fig. 5.50a). Overshoots up to 2 degrees occur when the reference set point is saturating. As expected from the statistical analysis in the previous section the angle of attack peak is not exceeding its limit value (red line) within the displayed 3.5 pumping cycles (exceedance probability is 0.4%). Note, however, that

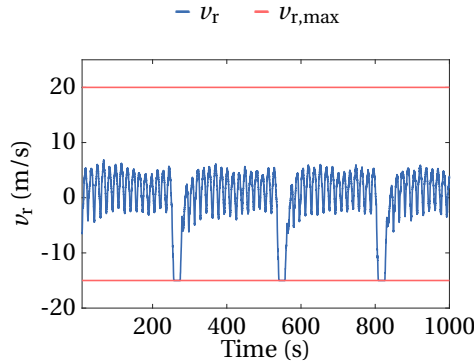
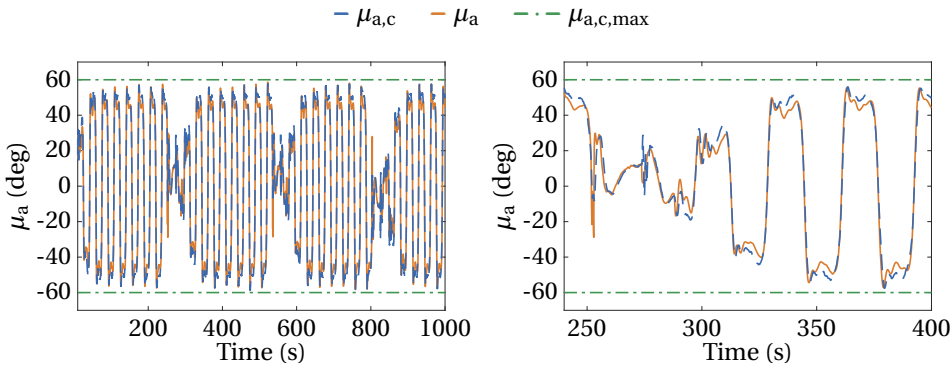


Figure 5.48: Tether reeling speed in high wind speed conditions and with the LMI controller.

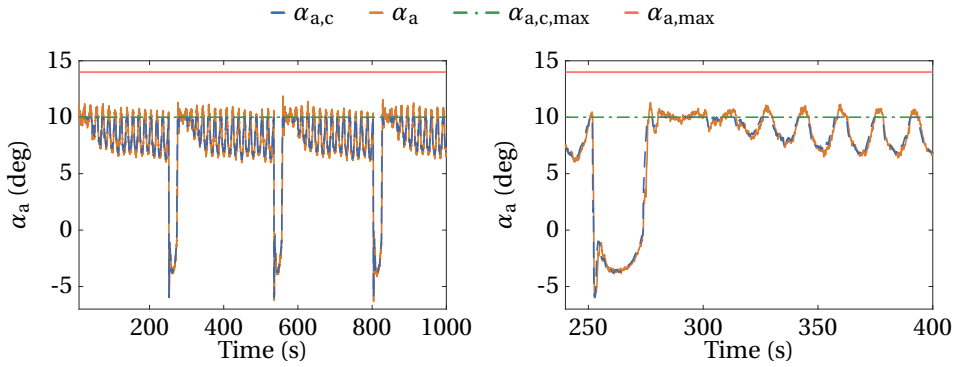


(a) Tracking performance during consecutive pumping cycles.

(b) Magnified part of Fig. 5.49a.

Figure 5.49: Bank angle tracking performance of the LMI controller in high wind speed conditions.

the overshoots of up to  $2^\circ$  at the end of the retraction phase fit to the statistical results which show that the largest peaks indeed happen with high probability in the transition phase. A magnified part of the angle of attack signal is displayed in Fig. 5.50b. It might be worth investigating if the reference angle of attack limit of  $10^\circ$  is too conservative, since the reference angle of attack is saturating during a large part of the traction phase. From a safety point of view this might be possible, since stall is expected only beyond  $18^\circ$ . This has not been investigated further and also might require to obtain more information about the aerodynamic model accuracy in the high angle of attack range. Note that this limit (i.e.  $10^\circ$ ) is chosen based on the maximum angle of attack definition in [96]. Moreover, the sideslip angle is well regulated during the traction phase and stays within  $\pm 1.5$  degrees around zero during the figure of eight flight. Sideslip angle peaks occur in the transitions, however the peaks stay within  $\pm 10$  degrees around zero and are quickly regulated back to zero (see Fig. 5.51) which is an acceptable result.



(a) Tracking performance during consecutive pumping cycles.

(b) Magnified part of Fig. 5.50a.

Figure 5.50: Angle of attack tracking performance of the LMI controller in low wind speed conditions.

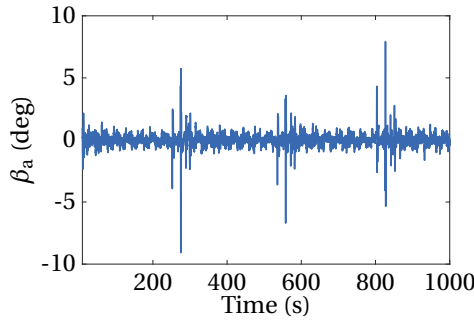


Figure 5.51: Sideslip angle tracking performance in low wind speed conditions and with the LMI controller

The outputs of the actuators are displayed in Fig. 5.52a, Fig. 5.52b and Fig. 5.53. The aileron deflection saturates only during the transition from retraction to traction but only for a short amount of time. During the traction and retraction phase it stays well below the deflection limits indicated by the red line. The elevator deflection has the lowest variance among the actuator deflections and never saturates during the displayed pumping cycles. Similar to the aileron, the rudder deflection saturates during the transition from retraction to traction phase but stays below the limits for the rest of the figure of eight flight.

The flight path itself is displayed in Fig. 5.54. The adaption of the path during the transition from retraction to traction phase is visible where the figure of eight pattern rotates from high to low elevation angles. The projection of the flight path in the  $xy$  plane shows that the path "width" stays within  $\pm 200\text{m}$  with respect to the  $x_W$  axis. Also the "height" of the figure of eight remains consistent as shown by the projection onto the  $xz$  plane. The highest altitude in these pumping cycles is 370m, the lowest point is at

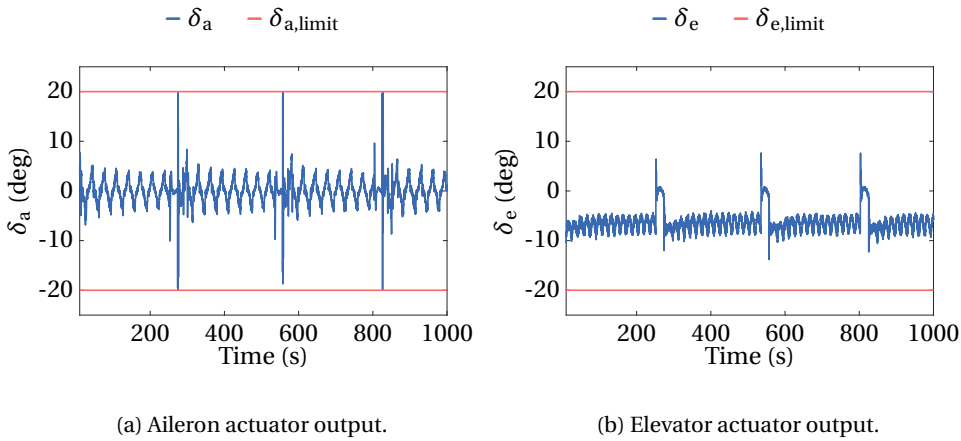


Figure 5.52: Aileron and elevator actuator outputs in low wind speed conditions and with the LMI controller.

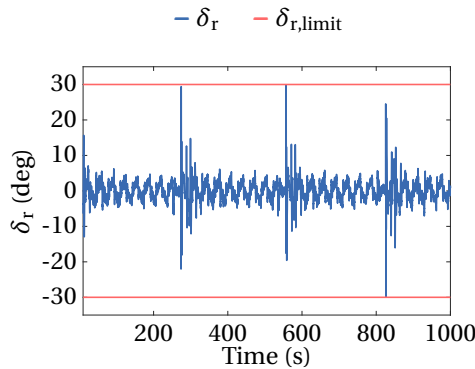


Figure 5.53: Rudder actuator output in low wind speed conditions and with the LMI controller.

110m altitude. Overall, the controller achieves a very repetitive flight pattern despite the turbulent wind conditions, which proves the satisfactory path following performance.

Finally, the evolution of the mechanical power is depicted in Fig. 5.55 (orange, solid line). The mean power is indicated by the blue, dashed line. Due to the low wind speed conditions and the high tether tension set point the winch needs to reel in during the upward flights to compensate the deceleration of the aircraft due to gravity. This leads to negative power segments also in the traction phase. The mean power is 2.4kW which, according to the statistical result depicted in Fig. 5.30, corresponds approximately to the 0.85 quantile. The peak power in this scenario is about 12.3kW and during the retraction phase the highest consumed power is  $-9.6\text{kW}$ .

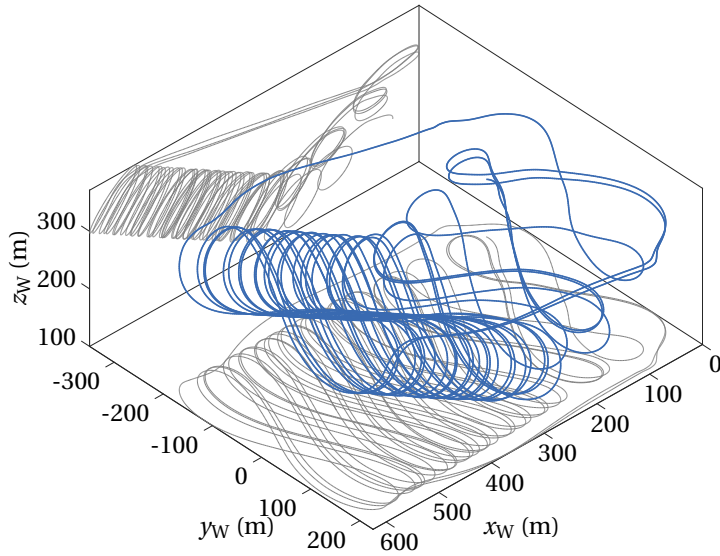


Figure 5.54: Flight path in low wind speed conditions and with the LMI controller.

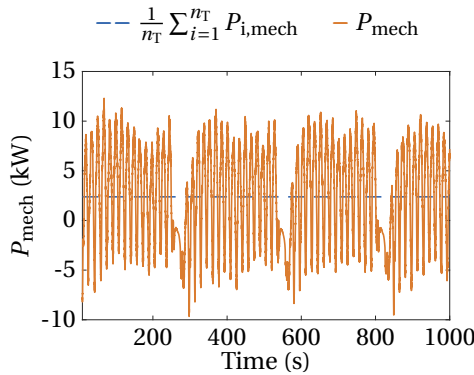


Figure 5.55: Mechanical power output in low wind speed conditions and with the LMI controller.

### Low Wind Speed Conditions with the NDI controller

Based on the statistical analysis presented in the previous section it could be concluded that the NDI controller leads to the same level of reliability as the LMI controller in the low wind speed condition scenario. Hence, it is expected that the subsequently presented detailed pumping cycle control performance of the NDI controller is similar to the one achieved with the LMI controller.

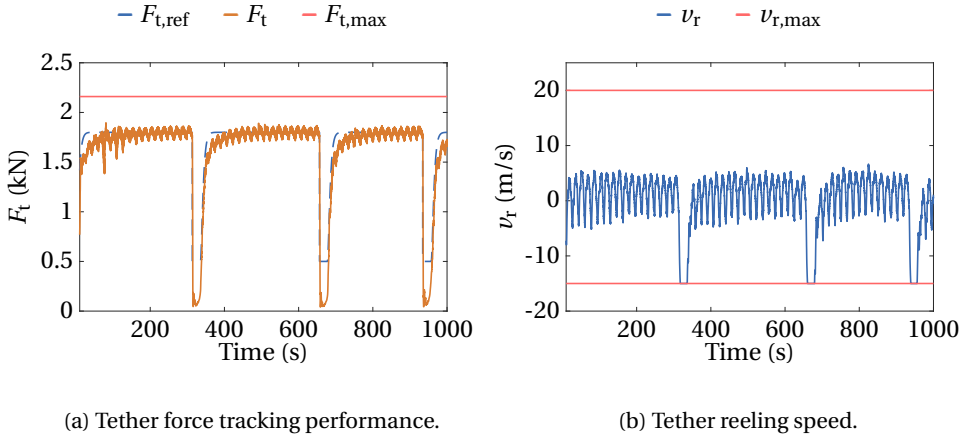


Figure 5.56: Tether force tracking performance and reeling speed in low wind speed conditions and with the NDI controller.

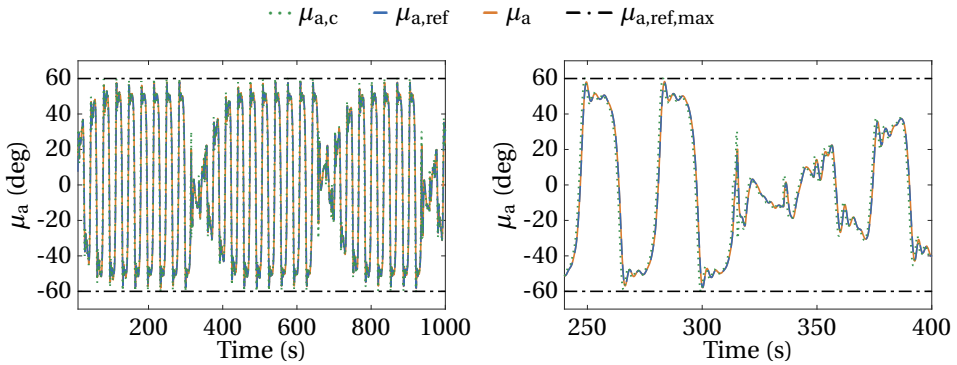
The evolution of the tether force is displayed in Fig. 5.56a. Similar to the result obtained with the LMI controller the highest tether force tracking errors occur during the retraction phase due to the saturation of the winch reeling speed (see Fig. 5.56b). During the transition as well as during the traction phase satisfactory tether force tracking is achieved.

The NDI controller is more accurately tracking the bank angle reference values as shown in Fig. 5.57a as well as in Fig. 5.57b compared to the LMI controller in similar wind conditions. Also the angle of attack tracking performance is better across all pumping cycles (see Fig. 5.58a and Fig. 5.58b). This is consistent with the statistical analysis where the NDI controller never violated the angle of attack peak limit in contrast to the LMI controller (0.4% of the flights violate the angle of attack requirement). Moreover, the NDI controller offers a better sideslip angle regulation. In contrast to the LMI controller no large peaks, due to the controller switching, can be observed and the sideslip angle stays at all times below  $5^\circ$  (see Fig. 5.59a).

The outputs of the actuators are displayed in Fig. 5.59b, Fig. 5.60a and Fig. 5.60b. Compared to the LMI controller the aileron deflection peaks are lower and during the analyzed pumping cycles the aileron actuator is not saturating. During the traction phase the elevator deflections are similar to the ones required by the LMI controller though the peaks, in particular when the state machine switches from traction to retraction phase, are lower. The rudder actuator deflections are comparable to the ones required by the LMI controller.

The resulting flight path is depicted in Fig. 5.61. The reoccurring flight path pattern is in particular visible in the  $xz$ -plane projection of the path. Moreover, the path stays in crosswind direction within  $\pm 200$  m indicating reliable path-following performance. The lowest altitude during the pumping cycle is 116 m and the highest 383 m, which is similar to the LMI controller (110 m and 370 m).

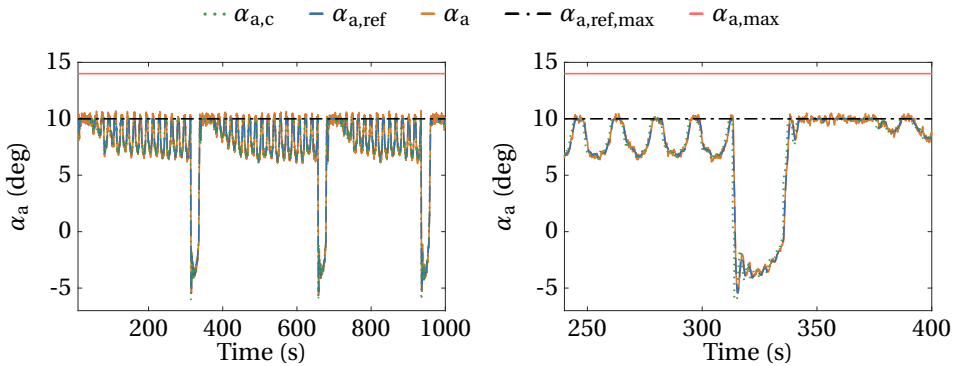
Finally, the evolution of the mechanical power is shown in Fig. 5.62. In these simu-



(a) Tracking performance during consecutive pumping cycles.

(b) Magnified part of Fig. 5.57a.

Figure 5.57: Bank angle tracking performance of the NDI controller in low wind speed conditions.



(a) Tracking performance during consecutive pumping cycles.

(b) Magnified part of Fig. 5.58a.

Figure 5.58: Angle of attack tracking performance of the NDI controller in low wind speed conditions.

lations the mean mechanical power output is 1.9kW which corresponds approximately to the 0.78 quantile. The peak power is 12.25kW and the maximum consumed power is -11 kW.

### High Wind Speed Conditions with the LMI controller

In the following the results for the high wind speed condition scenario are presented. The encountered wind conditions, here for the LMI controller, are shown in Fig. 5.63a. Similarly to the low wind speed condition scenario the variations in the wind velocity components are dominated by the atmospheric turbulence. The shear effect leads to

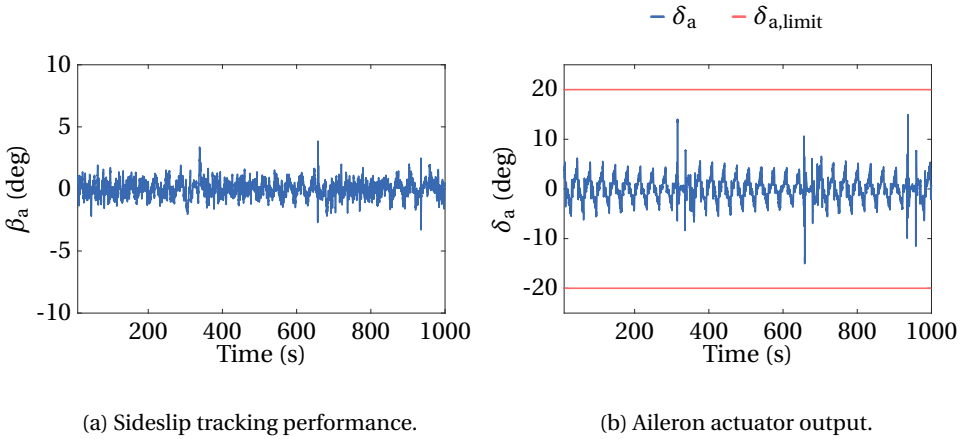


Figure 5.59: Sideslip angle tracking performance and aileron actuator outputs in low wind speed conditions and with the NDI controller.

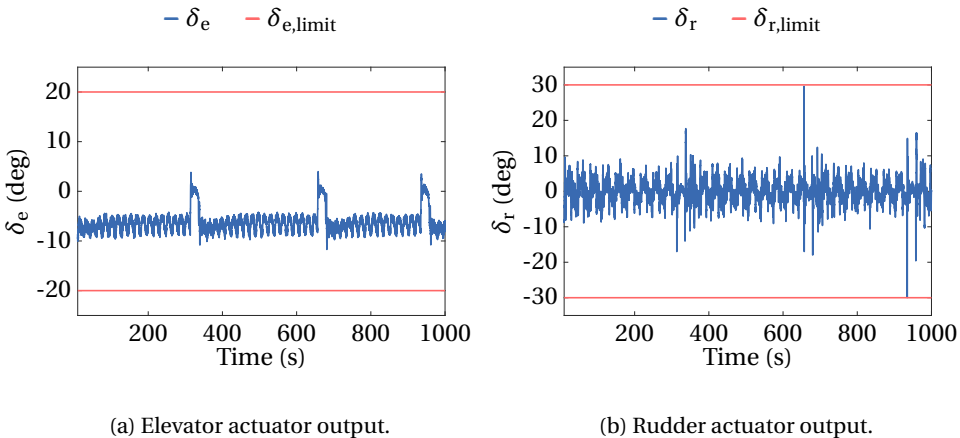


Figure 5.60: Elevator and rudder actuator outputs in low wind speed conditions and with the NDI controller.

only a small change in the wind speed in  $x_W$  direction during the pumping cycles (red line). With turbulence the wind speed varies in  $x_W$  direction between  $13.5\text{ m s}^{-1}$  and  $19.6\text{ m s}^{-1}$ . The crosswind as well as the down-/updraft components (orange and green lines) vary during these pumping cycles between  $-3.5\text{ m s}^{-1}$  and  $2.9\text{ m s}^{-1}$ .

Qualitatively, the tether force tracking performance is similar to the low wind speed condition case (see Fig. 5.63b). Also in the high wind speed conditions the tether force set point during the retraction phase cannot be tracked due to the saturation of the winch reeling speed which is visualized in Fig. 5.64. As expected, based on the statistical analysis, the tether force peak stays well below its limit in all shown pumping cycles. Note that

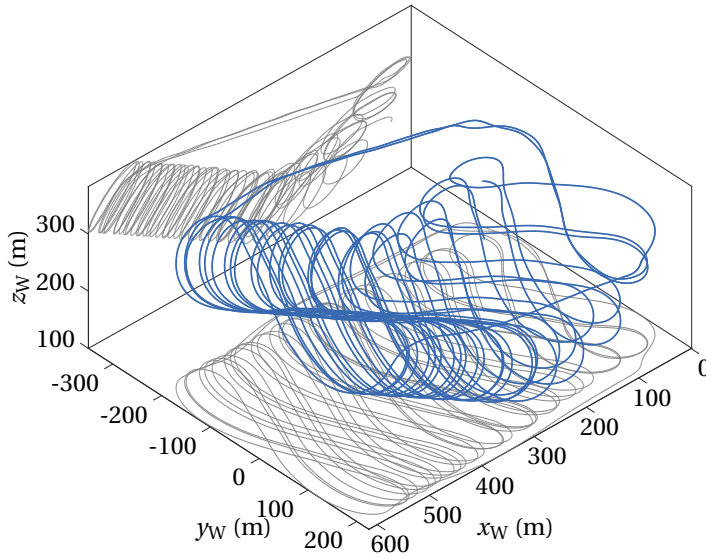


Figure 5.61: Flight path in low wind speed conditions and with the NDI controller.

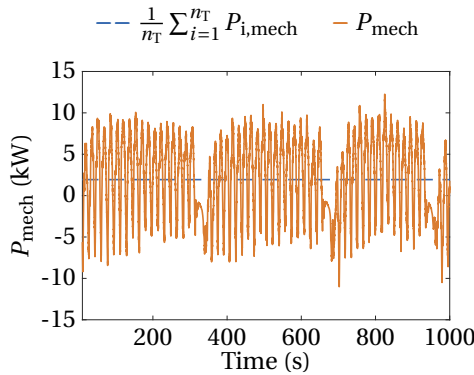
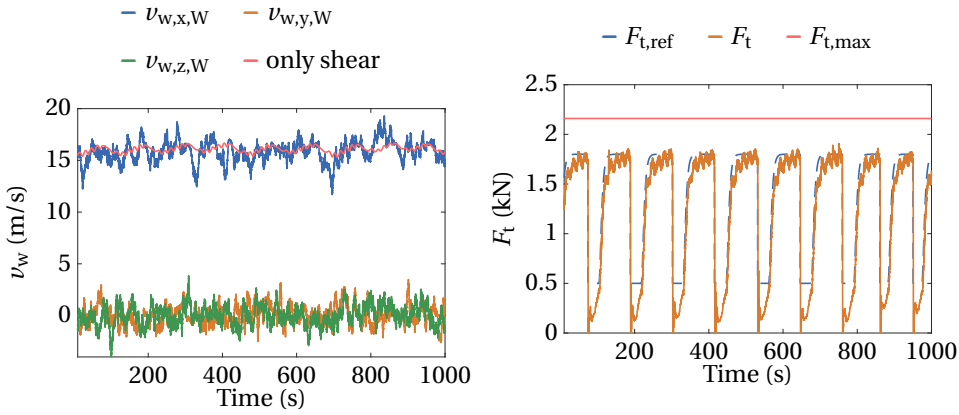


Figure 5.62: Mechanical power output in low wind speed conditions and with the NDI controller.

due to the high wind speed the winch needs to reel out faster than in low wind speed conditions which leads to shorter pumping cycles.

Qualitatively, the flight controller achieves a satisfactory tracking performance for the bank angle in high wind conditions (see Fig. 5.65a). Zooming in on the evolution of the bank angle command yields the result in Fig. 5.65b. The tracking performance deteriorates slightly in the high wind speed condition case but the deviations are still



(a) Wind speed components, given in the W frame, at the aircraft.

(b) Tether force tracking performance.

Figure 5.63: Wind velocity and tether force tracking with the LMI controller in high wind speed conditions.

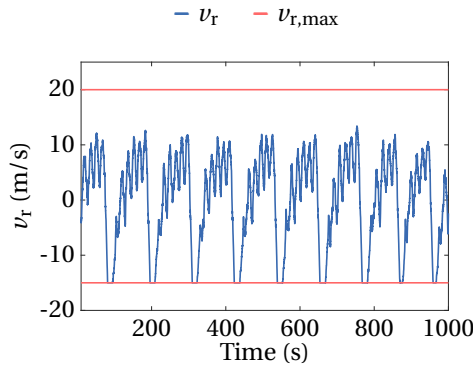
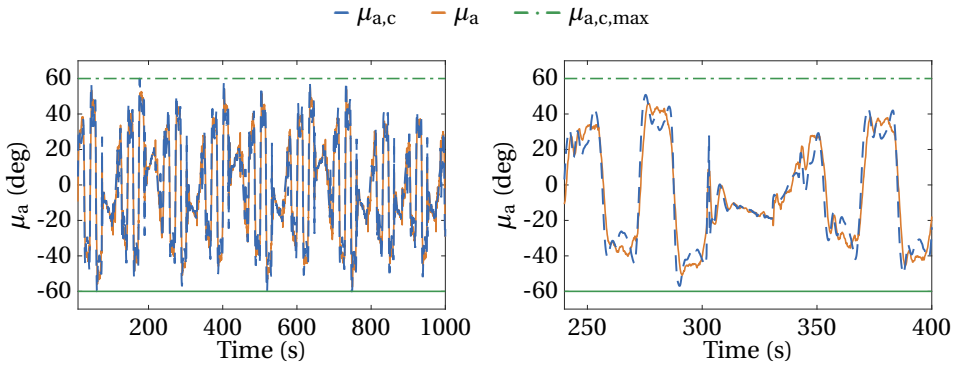


Figure 5.64: Tether reeling speed in high wind speed conditions and with the LMI controller.

acceptable and stay within the set point limits. The evolution of the angle of attack is displayed in Fig. 5.66a and a magnified part is displayed in Fig. 5.66b. In contrast to the bank angle the angle of attack performance does not deteriorate visibly. Moreover, the evolution of the sideslip angle is displayed in Fig. 5.67a. In the high wind condition case the sideslip angle peaks are lower and rarely exceed 5 degrees. In general, the better tracking performance can be explained by the higher dynamic pressure and hence higher control authority in high wind speed conditions.

The actuator outputs are displayed in Fig. 5.67b, Fig. 5.68a and Fig. 5.68b. The control effort rises in terms of the variance of the signals which can be explained by the larger turbulence components in the wind field that act as disturbances on the system which need to be compensated. The peaks of the rudder deflections are reduced, which again

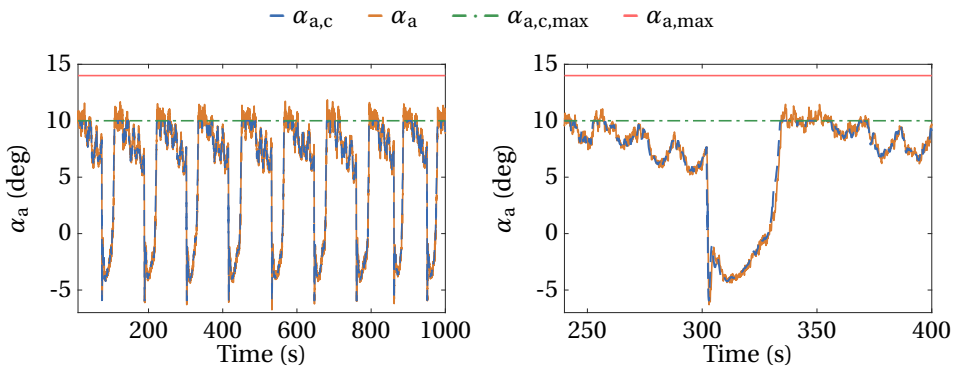


(a) Tracking performance during consecutive pumping cycles.

(b) Magnified part of Fig. 5.65a.

Figure 5.65: Bank angle tracking performance of the LMI controller in high wind speed conditions.

5



(a) Tracking performance during consecutive pumping cycles.

(b) Magnified part of Fig. 5.66a.

Figure 5.66: Angle of attack tracking performance of the LMI controller in high wind speed conditions.

is a result of the higher control authority. Overall the deflections stay most of the time within the limits. Saturation occurs only for a short amount of time, similar to the low wind speed condition scenario.

The resulting flight path in high wind speed conditions is depicted in Fig. 5.69. Also in these wind conditions the figure of eight patterns are consistent and reoccurring which is an indication for the robustness of the path following controller towards the increased level of turbulence. The highest point during the pumping cycle is at 405 m and the lowest point at 207 m. The flight path projection in the xy plane shows that similar to the low wind speed conditions the pumping cycles are flown within the space defined by the

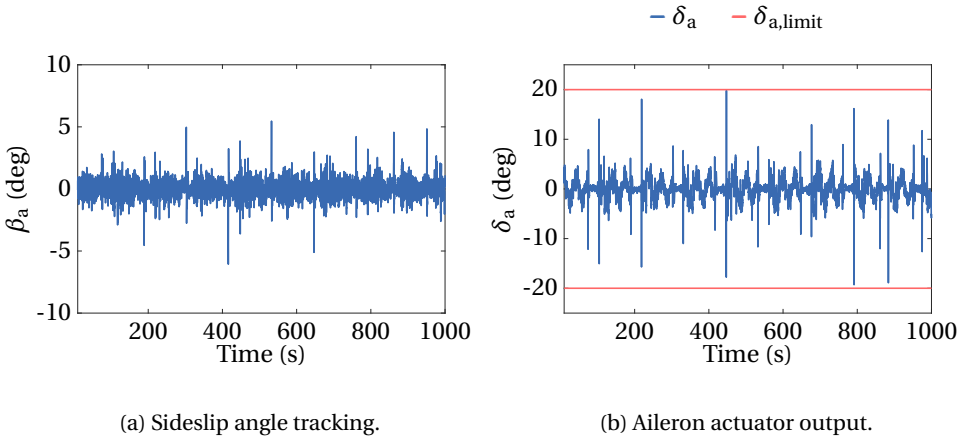


Figure 5.67: Sideslip angle tracking and aileron actuator outputs in high wind speed conditions and with the LMI controller.

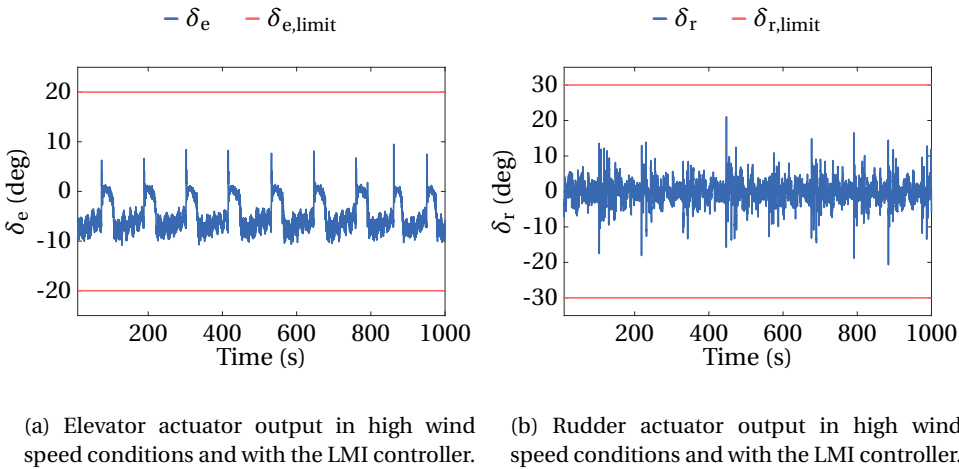


Figure 5.68: Elevator and rudder actuator outputs in high wind speed conditions and with the LMI controller.

width of the figure of eight ( $\pm 200$  m). The major difference is that due to the high reeling out speed, and the same rotational speed of the reference path from high to low elevation angles, the aircraft flies on average at higher elevation angles which also explains the higher altitude minimum. This behavior is also observed in the 3-DoF simulations and was identified as a beneficial intrinsic reference path adaption as a function of wind speed.

The evolution of the mechanical power in high wind speed conditions is depicted in Fig. 5.70. In this scenario the mean power output is around 5 kW. Comparing this result

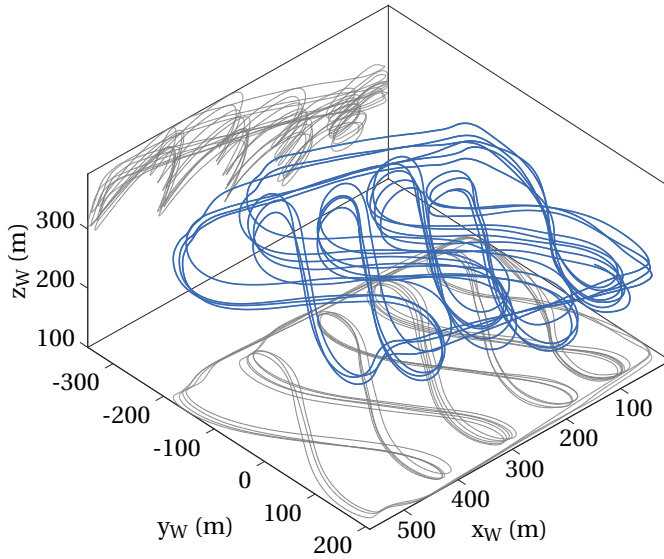


Figure 5.69: Flight path in high wind speed conditions and with the LMI controller.

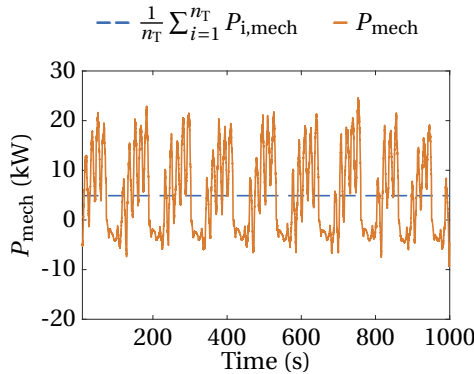


Figure 5.70: Mechanical power in high wind speed conditions and with the LMI controller.

with the statistical results depicted in Fig. 5.24 shows that this power output represents approximately the 0.5 quantile (i.e. the median). The peak power in this scenario is about 24.6 kW and during the retraction phase the highest consumed power is -9.4 kW.

#### High Wind Speed Conditions with the NDI Controller

Based on the Monte Carlo simulation results obtained with the NDI controller one can conclude that the tether tracking performance with the NDI controller is worse com-

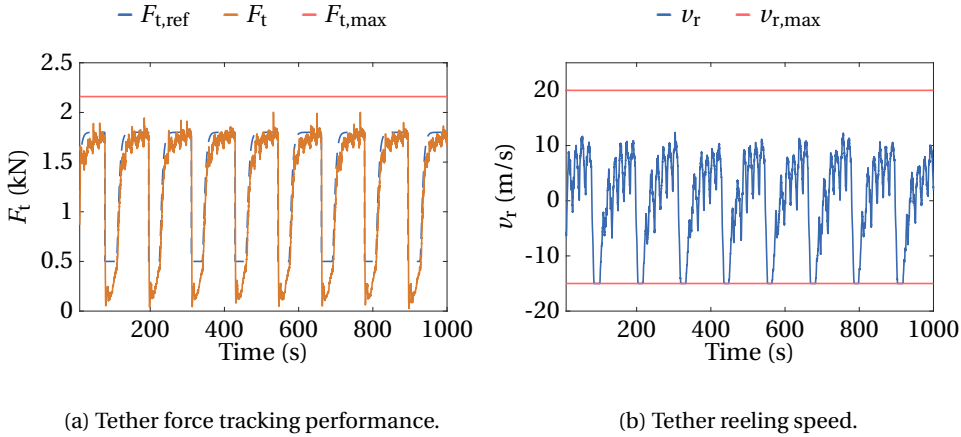
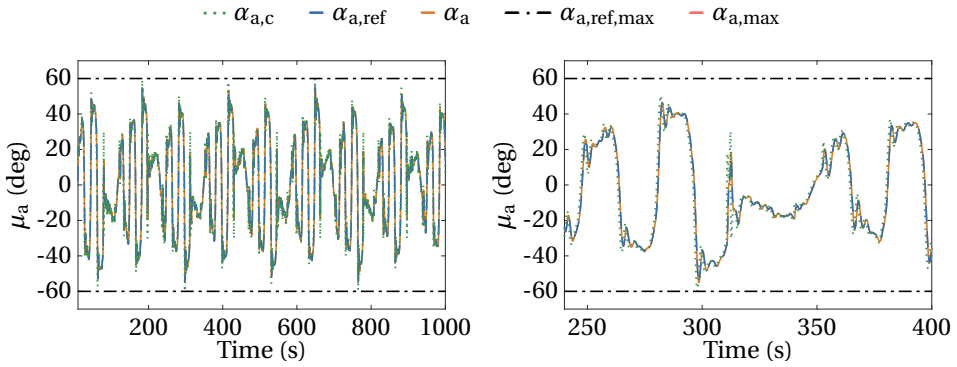


Figure 5.71: Tether force and reeling speed in high wind speed conditions and with the NDI controller.

pared to the case where the inner loop is regulated with the LMI controller. This can also be deduced from the results depicted in Fig. 5.71a. Although the maximum tether force limit (red line) is not exceeded, large overshoots towards the end of the traction phase, in particular in the 5th, 6th and 7th depicted traction phase, are clearly visible. In addition, the already observed large tether force tracking errors during the retraction phase occur. This can again be explained by the winch limitations, in particular the lower reeling speed limit which is reached during the retraction phase (see Fig. 5.71b). Accurate roll angle tracking can be observed in Fig. 5.72a and Fig. 5.72b. Although the tracking performance slightly deteriorates compared to the low wind speed conditions it still outperforms the LMI controller. The NDI controller yields the highest robustness level towards inadvertently exceeding the angle of attack limit. The accurate angle of attack tracking performance is visible in Fig. 5.73a and Fig. 5.73b. Moreover, the evolution of the sideslip angle is displayed in Fig. 5.74a. With the NDI controller slightly higher sideslip angle peaks occur compared to the LMI controller. However, all peaks are below  $10^\circ$  and are regulated quickly back to zero, hence this is regarded as an acceptable result.

The actuator outputs are displayed in Fig. 5.74b, Fig. 5.75a and Fig. 5.75b. The required aileron deflections are similar to the ones obtained with the LMI controller. Within the analyzed simulation run the ailerons did not saturate. Similarly, nearly identical elevator deflections are required compared to the LMI controller with slightly lower peaks at the transition points of traction to retraction phase. The biggest difference occurs in the rudder deflections where in case of the NDI controller larger peaks with short periods of actuator saturation occur.

The resulting flight path in high wind speed conditions is depicted in Fig. 5.69. Qualitatively, a similar repetitive flight path pattern is achieved compared to the path obtained with the LMI controller. In the crosswind direction the path stays within  $\pm 200$  m. The path pattern is less overlapping in the  $x$  and  $z$  plane. These varying overshoots in the "upturns" are also visible in the results obtained with the 3-DoF model in chapter 4. The lowest point during the pumping cycles is at approximately 190 m, the highest

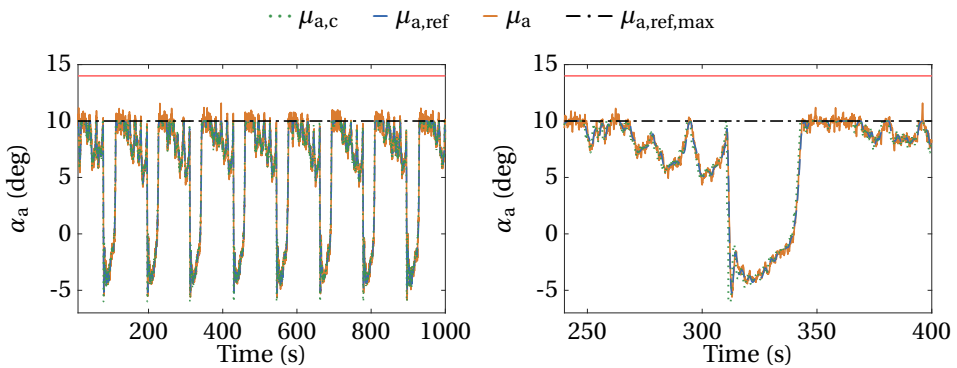


(a) Tracking performance during consecutive pumping cycles.

(b) Magnified plot of Fig. 5.72a.

Figure 5.72: Bank angle tracking performance of the NDI controller in high wind speed conditions.

5



(a) Tracking performance during consecutive pumping cycles.

(b) Magnified part of Fig. 5.73a.

Figure 5.73: Angle of attack tracking performance of the NDI controller in high wind speed conditions.

point at around 400 m, similar to the lowest and highest path points reached by the LMI controller (207 m and 405 m).

Finally, the evolution of the mechanical power is depicted in Fig. 5.77. In this scenario the mean power output is around 5.4 kW which corresponds to the 0.7 quantile. The peak power in this scenario is about 22.39 kW and during the retraction phase the highest consumed power is -10.87 kW.

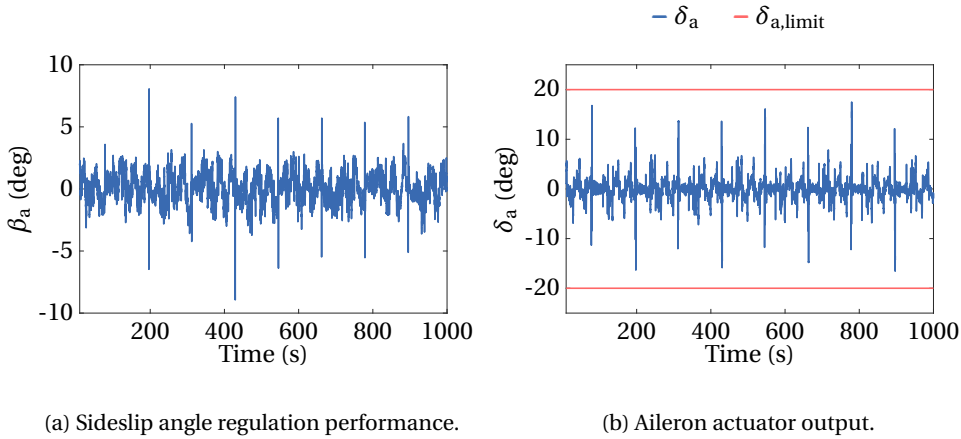


Figure 5.74: Sideslip angle and aileron actuator output in high wind speed conditions and with the NDI controller.

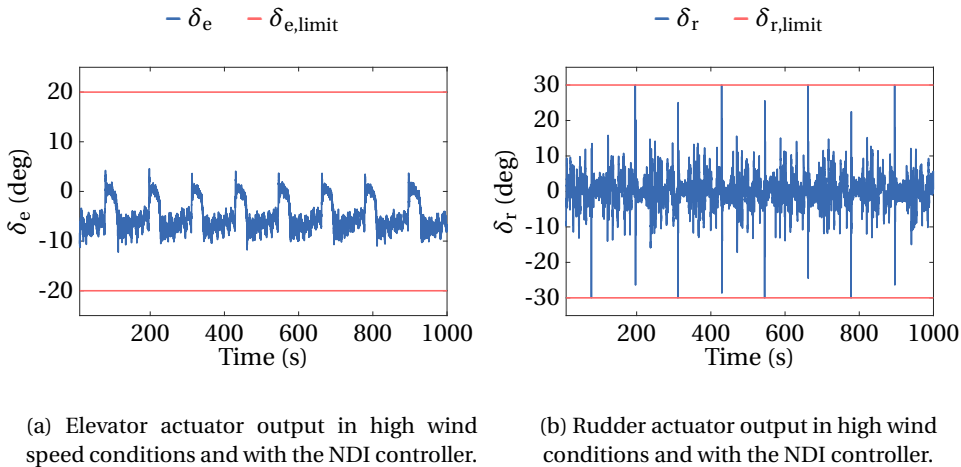


Figure 5.75: Elevator and rudder output in high wind speed conditions and with the NDI controller.

### 5.3. Summary

In this chapter the performance and robustness properties of the different controller designs derived in the previous chapter are studied in detail. The main goal of this chapter is to assess how the performance of the different controllers deteriorates in presence of atmospheric turbulence, time delays, as well as model uncertainties. Quantile function plots and asymptotic confidence intervals are utilized to capture the robustness properties statistically. It is shown that a deterministic analysis greatly overestimates the performance and robustness of the derived controllers. This shows that a statistical reliability

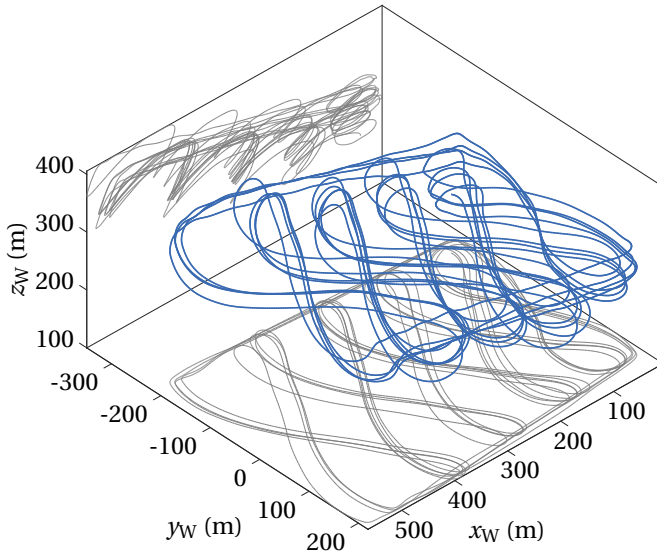


Figure 5.76: Flight path in high wind speed conditions and with the NDI controller.

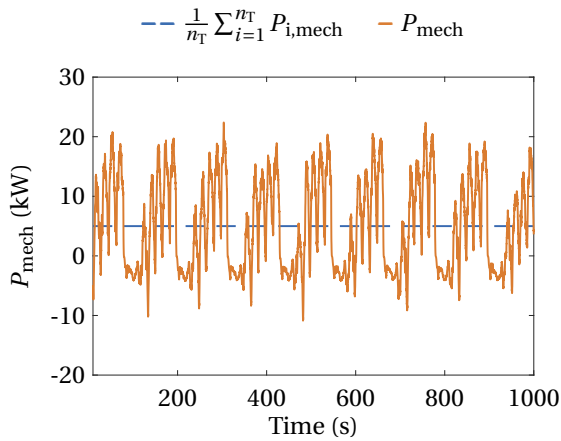


Figure 5.77: Mechanical power output in high wind speed conditions and with the NDI controller.

analysis of AWE systems is paramount if different control strategies are compared with each other. In addition, a sensitivity analysis is presented that can be used to identify the parametric uncertainties a particular controller is least robust to using hypothesis testing. The results can help to design controllers in the future that are in particular robust

with respect to variations in the corresponding model parameter values. In the last section, the performance of the LMI and the NDI controller is studied in more detail using a single simulation run with several consecutively flown pumping cycles. Both controllers achieve a similar performance but since the LMI controller is simpler to design and implement it is the recommended choice.



# 6

## Upset Condition Generation, Prediction and Avoidance

In this chapter a methodology is proposed that allows to systematically sample uncertainties that lead to a control system failure. Based on the generated data a prediction model can be constructed that is able to foresee critical flight conditions which eventually allows to avoid the failure. Note, the entire chapter is based on published work of the author of this dissertation (see [116]).

### 6.1. Preliminaries

AWE systems need to operate in varying environmental conditions such as slowly varying wind speeds due to the altitude dependent mean wind speed profile but also need to cope with rapid changes due to wind gusts and turbulence. Because of the inherent stochastic nature of the wind conditions it is difficult to explicitly include them in the control design process. In practice, the closed loop system is verified a posteriori for randomly generated wind conditions as presented in the previous chapter. If the controller fails to satisfy all requirements, it either needs to be re-tuned or completely re-designed. The results presented in the previous chapter show that in order to create enough confidence, that the controller achieves its objective, a large amount of simulations is necessary (i.e. direct Monte Carlo simulation approach [121, p. 83f]). Essentially, with the direct Monte Carlo approach a random walk is performed hoping to encounter sufficiently many wind conditions in order to statistically assess the robustness of the controller. Naturally, the accuracy of the results depend on the quality of the model itself and can lead to too optimistic (i.e. too low failure probability) or to too conservative (i.e. too high failure probability) results.

Besides the computational burden of this type of control system verification process it is often difficult to efficiently create counter examples where the control system fails. For example a wind model might create a critical wind gust with a probability of  $10^{-6}$ . Hence, it requires on average  $10^6$  simulation runs until it is encountered once. Notice

that in reality such a gust could occur with a much lower probability due to the model uncertainty. Therefore, it might be also of interest to analyze wind conditions that, according to the model, have a low probability of occurrence. Ultimately, the more information about the conditions that lead to control system failures is available, the more reliably they can be predicted and prevented in the future. If enough data about counter examples is available, a model that runs in parallel to the control system can be constructed that monitors the current flight state. It can then be used to predict how likely it is that the current flight condition leads to an upset and if necessary triggers a maneuver that avoids it. Creating such a predictor requires a significant amount of data that can not be generated efficiently using the direct Monte Carlo method due to the aforementioned computational burden. Therefore, a different approach is chosen in this chapter which is based on *subset simulations* (SS). It is an algorithm that has been developed originally to estimate small failure probabilities of high dimensional stochastic systems [9]. Recently SS has already been applied to small failure probability estimation in the context of flight control system verification (see [99] and [156]). In the context of this work the algorithm will not only be used to estimate rare event probabilities but also to generate systematically a knowledge base for external disturbances that lead to a specified control system failure, denoted as an upset. The generated conditions will then be used to train a binary classifier which is either based on a fixed threshold prediction strategy or a *support vector machine* (SVM). These surrogate models are able to predict and eventually prevent the occurrence of a failure beforehand with the overall goal to improve the fail-operational characteristic of the AWE system.

This chapter is subdivided into the following parts. First, a generic framework is presented that systematically generates conditions in which the control system fails. Second, two different prediction strategies are presented that are either based on a simple threshold approach or a binary time series classification technique to predict upset conditions. Third, a loss rate function is derived that allows to trade off the prediction performance with respect to the induced economic loss of false positives and false negatives. In the last part of this chapter the framework is applied to predict and prevent tether rupture, a common failure scenario in the context of AWE. A tailored avoidance maneuver is proposed that prevents this specific upset and keeps the system operational.

## 6.2. Upset Condition Generation, Prediction and Avoidance Framework

The framework consists of three steps denoted with A, B and C. The different steps can be designed to a large extent independently, which allows to improve the framework in the future in a modular manner. In step A (Upset Condition Generation) the subset simulation (SS) algorithm is utilized to systematically generate samples that lead to a specific upset condition. In step B (Upset Condition Prediction) the prediction model is designed based on the created samples from step A in order to learn to distinguish between upset and nominal conditions. Finally, in step C (Upset Condition Avoidance) the avoidance maneuver is designed. The complete framework is visualized in Fig. 6.1 where the highlighted rectangles enclose the tasks associated to every individual step. The three steps are discussed generically and in more detail in the subsequent paragraphs. In section 6.3

the framework is applied to generate, predict and prevent tether rupture during pumping cycle operation.

### 6.2.1. Upset Condition Generation

In this work upset conditions are generated using the SS algorithm. The introduction of SS in this section follows [170]. Further details about SS and mathematical proofs can also be found in [9]. In general, SS is a popular algorithm to estimate small event probabilities for high dimensional systems [9]. An event, or failure, probability is a function of a multidimensional random variable  $\Theta$ . As a function of its probability density function  $f_{\Theta}$  a failure can be written as a multidimensional integral:

$$p_f = \int_{\Theta_{sp}} \mathcal{I}_F(\theta) f_{\Theta}(\theta) d\theta \quad (6.1)$$

where  $\Theta_{sp}$  represents the entire space of  $\theta$ ,  $\mathcal{I}_F(\theta)$  is the indicator function that is either one if a certain realization  $\theta$  leads to a failure or zero otherwise. Furthermore, in the context of SS it is usually assumed that the random variables are identically and independently (iid) distributed; hence,

$$f_{\Theta}(\theta) = \prod_{k=1}^{d_{\theta}} f_{\Theta_k}(\theta_k) \quad (6.2)$$

where  $d_{\theta}$  is the dimension of the random variable vector  $\Theta$ . In addition, it is assumed that the random variables are iid standard normal random variables with probability density function  $f'$ . Directly evaluating the integral in Eq. (6.1) analytically or even numerically is not feasible for complex high dimensional systems due to the curse of dimensionality [9]. One approach to calculate this integral is using direct Monte Carlo methods that randomly sample from the parameter marginal distributions, evaluating the indicator function by simulation and using eventually the sample average to approximate the failure probability. If  $p_f$  is small this can require an unfeasible amount of simulation runs which is especially critical if one simulation run is time consuming i.e. several minutes or more. Contrarily, in the context of SS  $p_f$  is written as a product of conditional probabilities which involves the definition of intermediate failure domains. The main idea behind this strategy is that transitioning from one intermediate failure domain to the next has a higher chance than directly transitioning from nominal conditions into the failure domain. The failure probability can then equivalently be expressed as a product of conditional probabilities

$$p_f = \Pr(F_1) \prod_{i=1}^{m_s-1} \Pr(F_{i+1} | F_i) \quad (6.3)$$

The first intermediate failure probability  $\Pr(F_1)$  is obtained via a direct Monte Carlo approach where  $n_s$  samples are generated at random. Next, a limit function  $Y$  that characterizes how close the current sample is to the failure is evaluated for each sample. The limit function is defined such that a higher value indicates a sample that is closer to the actual failure defined by  $Y^*$ . The current intermediate failure domain is defined by a

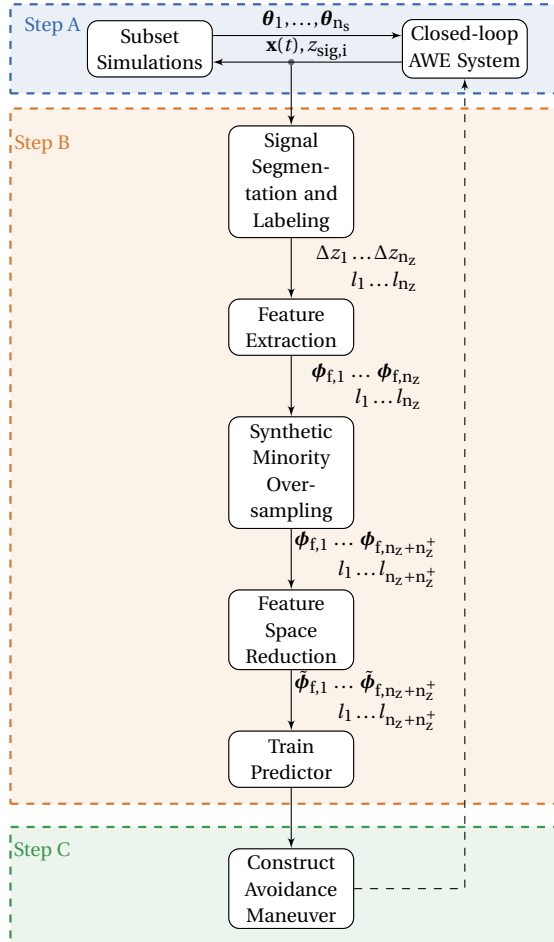


Figure 6.1: Workflow of the proposed framework.

threshold  $\mathcal{T}$  for the limit function which is in general smaller than the critical value  $\Upsilon^*$ . Given the current sample set of size  $n_s$  the threshold  $\mathcal{T}$  is calculated by splitting the  $n_s$  samples into two subsets. One that contains the  $n_s \cdot p_s$  samples with the highest limit function values and one that contains the remaining  $n_s - n_s \cdot p_s$  samples. Then  $\mathcal{T}$  is the average of the limit function values that separate the two sets. If the threshold values of the limit function are arranged in descending order then the intermediate threshold value is defined by

$$\mathcal{T} = \frac{\Upsilon^{n_s \cdot p_s} + \Upsilon^{n_s \cdot p_s + 1}}{2} \quad (6.4)$$

where  $\Upsilon^{n_s \cdot p_s}$  and  $\Upsilon^{n_s \cdot p_s + 1}$  denote the limit function values of the  $n_s \cdot p_s$ th and  $(n_s \cdot p_s + 1)$ -th largest samples with respect to their limit function values in the current sample set. In that case, the transition probabilities  $\Pr(F_{i+1} | F_i)$  are by definition equal to  $p_s$  which is usually set to 0.1 [9]. In order to populate an intermediate failure domain with new samples a Markov chain Monte Carlo method, such as the modified Metropolis algorithms (Algorithm 1), is used. The algorithm is briefly introduced in the following based on [9]. In the context of SS the task of the Metropolis algorithm is to populate an intermediate failure domain with samples that also belong to the current intermediate failure domain i.e.  $\tilde{\theta} \in F_i$ . This means that  $\tilde{\theta}$  leads to a limit function value that is larger than the current intermediate threshold  $\mathcal{T}$ . As soon as  $n_s$  samples are contained in the current domain  $F_i$  the subsequent intermediate failure domain  $F_{i+1}$  will be defined. First, the new threshold  $\mathcal{T}$  using Eq. (6.4) is calculated and afterwards new Markov chains are created to populate  $F_{i+1}$ . New samples, conditioned on an existing sample  $\theta$  in an intermediate

---

**Algorithm 1** Modified Metropolis Algorithm
 

---

- 1: Pick  $\theta \in F_i$
  - 2: **for** each coordinate  $k = 1 \dots d_\theta$  in  $\theta$  **do**
  - 3:   Sample  $\tilde{\theta}_k \sim \tilde{f}(\cdot | \theta_k)$
  - 4:   Compute  $\alpha_{ss} = \frac{f'(\tilde{\theta}_k)}{f'(\theta_k)}$
  - 5:   Accept  $\tilde{\theta}_k$  if  $\alpha_{ss} > 1$  or if  $\alpha_{ss} > u$  with  $u \sim \mathcal{U}(0, 1)$
  - 6: **end for**
  - 7: Accept  $\tilde{\theta}$  if  $\tilde{\theta} \in F_i$  o.w. set  $\tilde{\theta} = \theta$
  - 8: **return**  $\tilde{\theta}$
- 

failure domain  $F_i$ , are created by centering a symmetric proposal function  $\tilde{f}$  around each coordinate  $\theta_k$  of  $\theta$ . In this work a Gaussian proposal function is used. Its variance can be calculated adaptively as described in [115]. This results in  $n_s \cdot p_s$  Markov chains with  $\frac{1}{p_s} - 1$  elements. An accept/reject strategy, as defined in line 5 of the algorithm, leads to a non-greedy random walk around the previous state in the Markov chain. Since the intermediate thresholds are selected adaptively with respect to the most promising samples (higher limit function value) and new samples are only accepted if they are contained in the current intermediate failure domain (line 7) the algorithm will return at every stage inputs that drive the system more towards an upset condition (critical limit function value). This procedure is repeated until more than  $n_s \cdot p_s$  samples lie in the actual failure

domain. The actual failure probability can then be approximated by

$$p_f \approx p_s^{m_s-1} \frac{n_{f,ss}}{n_s} \quad (6.5)$$

where  $n_{f,ss} > n_s \cdot p_s$  is the number of samples that lie in the actual failure domain and  $m_s$  are the number of epochs in the SS run.

Applying the SS algorithm in the context of this work requires to define the upset conditions formally in form of a scalar limit function. All samples that lead to a limit function value that is beyond a defined threshold value are considered as upset conditions. The crucial part in modeling an upset condition is the allocation of the upset condition to a reasonable signal value or a combination of different signal values. For instance, if the analyzed upset is stall, the angle of attack represents the obvious choice as a limit function. Since this framework is mostly applicable to control system failure, finding the right limit function is usually done by taking the complement of the control objective. For instance, as described in section 1.2, the control objective for AWE systems operated in pumping cycle mode can be decomposed into a path-following problem (tangential direction control) and a tether force tracking problem (radial direction control). Hence, the limit function should be able to describe a failure in the tangential or radial direction control objective. The performance of the tangential direction control objective is reflected by the path-following tracking error, which suggests to choose this signal as a limit function to generate conditions in which the controller is not able to keep the aircraft close enough to the flight path. Similarly, in the radial direction the controller needs to track a high tension in the tether for maximum power production while keeping the tether force below the maximum tensile force that the aircraft and the tether itself can still support. An upset condition in this case can then be defined as a condition where the tension in the tether exceeds this critical value. The latter example is investigated in depth in section 6.3. Depending on the model fidelity, more complex upset conditions such as too high wing bending or vibrations with certain amplitudes in a certain frequency range can be analyzed, where the external excitation is generated using SS. Ultimately, a wide range of different upset conditions can be converted into a scalar function  $Y(\theta)$  with a threshold value beyond which the upset occurs. Note that the choice of this limit function is not limited to a specific functional form. It can be represented by an arbitrary nonlinear scalar function that just needs to be tailored to the specific upset condition. The only constraint is that the function needs to be monotonous such that maximizing the functional value indeed drives the system towards the considered upset condition. In most cases it is dependent on the aircraft states and outputs (e.g. angle of attack, airspeed, wing bending, tether tension,...). Having defined the limit function the SS algorithm can be applied to sample  $\theta$ s in order to drive  $Y$  into the specific upset  $Y > Y^*$ .

### 6.2.2. Upset Condition Prediction

In this section two prediction approaches are presented. Since it is assumed that an upset can be defined by the value of the corresponding limit function, a first intuitive prediction approach is to predict an upset solely based on the current functional value of  $Y$ . Due to the stochastic nature of the system the values of  $Y$  will fluctuate according to the

joint distribution of the uncertainties. Threshold values can then be selected based on the distribution of the maximum  $Y$  values obtained from Monte Carlo simulations. For the sole purpose of classification it is obvious that selecting a threshold value arbitrarily close to the maximum limit function value will yield the highest prediction accuracy (least conservative). However, due to the inertia of the system as well as time delays this will in most cases not allow to avoid the upset condition. Contrarily, if the threshold value decreases the false positive rate will grow (more conservative). For this reason different threshold values need to be tested and a benchmark strategy as presented at the end of this section can be used to identify the best threshold.

In addition to the fixed threshold approach an alternative strategy based on binary time series classification is proposed. The main motivation for this approach is that also the time history of certain states and outputs contains information which can be exploited for prediction. This approach is especially beneficial in the context of controls since critical disturbances often cause an oscillatory behavior prior to the actual upset. Obviously, oscillations can only be detected by analyzing the time and frequency content of a signal in a certain time window which is not possible if the simple threshold approach is utilized. In this work the time series classifier is realized as a *support vector machine* (SVM) which is optimized based on the generated samples in step A of the framework. In the following a concise description of the SVM algorithm is given which is based on [12, p.383-387]. More details about SVMs can also be found in [28].

The goal of the SVM algorithm is to find a hyperplane for each class such that the margin between the two planes is maximized. The two spaces defined by the hyperplanes can be defined as

$$\boldsymbol{\eta}^\top \boldsymbol{\phi}_{f,i} + bias \begin{cases} \geq 1 & \text{if } \boldsymbol{\phi}_{f,i} \text{ belongs to class 1} \\ \leq -1 & \text{otherwise} \end{cases} \quad (6.6)$$

where  $\boldsymbol{\eta}$  is the normal vector of both hyperplanes. The distance between the two hyperplanes is given by  $\frac{2}{\sqrt{\boldsymbol{\eta}^\top \boldsymbol{\eta}}}$ . In order to maximize the distance between the two planes the scalar product  $\boldsymbol{\eta}^\top \boldsymbol{\eta}$  needs to be minimized which leads to the following quadratic programming problem [12, p.384]:

$$\begin{aligned} & \text{minimise} && \frac{1}{2} \boldsymbol{\eta}^\top \boldsymbol{\eta} \\ & \text{subject to} && l_i (\boldsymbol{\eta}^\top \boldsymbol{\phi}_{f,i} + bias) \geq 1, \quad i = 1, \dots, n \end{aligned} \quad (6.7)$$

with  $l_i \in \{-1, 1\}$ . The optimization problem can be rewritten in terms of its Lagrangian as defined in [12, p.386]. It will contain the input vector only as the scalar product  $\boldsymbol{\phi}_{f,i}^\top \boldsymbol{\phi}_{f,i}$  which allows to apply the kernel trick. The kernel function essentially maps the input parameter into a higher dimensional space in which both classes are linearly separable [12, p.382]. A common kernel is the radial basis function, or Gaussian kernel, which is also used in this work. Ultimately, the SVM is used to solve a binary classification problem where a given data set  $\mathcal{D} = \{(\boldsymbol{\phi}_{f,i}, l_i), i = 1, \dots, n_{\text{train}}\}$  is used to construct a model that can predict if a certain input vector belongs to class -1 or 1. The predictor equation

that is eventually added to the control system is given by

$$\hat{f}_P = \sum_{j=1}^{m_{LM}} \alpha_{L,j} l_j e^{-\left(\frac{(\phi_{r,i} - \phi_{SV,j})^T (\phi_{r,i} - \phi_{SV,j})}{\sigma_{SVM}^2}\right)} \quad (6.8)$$

where the  $\alpha_{L,j}$ 's are the  $m_{LM}$  non-zero Lagrange multipliers of the corresponding support vectors  $\phi_{SV,j}$  as well as their class labels  $l_j$ , and  $\sigma_{SVM}^2$  is the variance of the Gaussian kernel which is a hyperparameter that needs to be tuned.  $\phi_{r,i}$  corresponds to the current feature vector. The class label is then determined based on the condition

$$\hat{l} = \begin{cases} 1 & \text{if } \hat{f}_P \geq 0 \\ -1 & \text{else} \end{cases} \quad (6.9)$$

In this work an upset is defined by a label value of -1 and a nominal condition by a label value of +1. Estimated quantities are indicated by the "hat" operator in this chapter.

The inputs to the SVM based predictor will be specific estimations of aircraft states and wind conditions. Note, it will be assumed that the utilized signal values can be measured at a specific rate, no state estimation is performed. The approach can however be extended by including a state estimator in between the predictor and the sensor outputs.

Instead of capturing the complete time history of each signal, specific signal statistics are extracted and collected in a finite dimensional feature vector. Therefore, each signal is cut into smaller segments according to a chosen time window size. For instance, the highlighted green area in Fig. 6.2 indicates a time window with length 10s of an arbitrary signal denoted here with  $z_{sig}$  which has a hypothetical maximum value  $z_{sig,max}$  of 1.8 (orange, dashed line). At around 67s the signal content between 57s and 67s, denoted with  $\Delta z_1$  is translated into a feature vector. To create the training examples the time window will be moved from either the final logged data point to the first data point, or if the complete signal contains an upset i.e.  $Y(\theta) > Y^*$ , in this example  $Y(\theta) = z_{sig} > z_{sig,max}$ , the segmentation starts where the first upset occurs minus a shift  $\Delta T_r$  as depicted in Fig. 6.2. The additional shift is required otherwise the predictor might fail to forecast an upset prior to its occurrence. The signal segmentation contains overlaps between the segments, hence the first time window is only shifted by  $\Delta T_s$  and not by the window length. Note, only the first segment in Fig. 6.2 would be labeled as an upset i.e.  $l = -1$ , the following segments starting with  $\Delta z_2$  belong all to the non-upset class and are labeled with  $l = 1$ . Note, the time shifts are hyperparameters that need to be tuned to improve the classifier performance.

If a binary classifier is trained based on the generated data, the prediction accuracy can be improved by balancing the training data set. Although the SS algorithm will systematically generate upset conditions, the segmentation of the logged signals within a pumping cycle will always lead to more non-upset than upset conditions and hence to an extremely imbalanced data set. In fact, most of the simulated pumping cycles will not contain a single upset. One approach, which belongs to the data-level methods of learning from imbalanced data (see [89]), suggests to use a similar amount of samples from both classes. In this case randomly chosen non-upset samples are removed from the training data set (undersampling). This has the disadvantage that samples are thrown

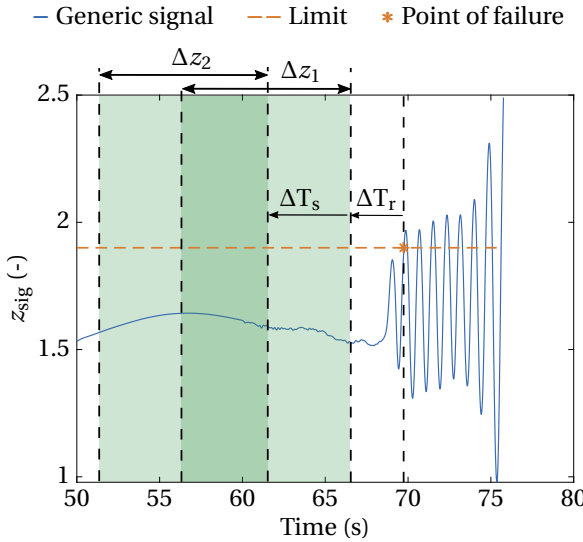


Figure 6.2: Training example with reaction time definition for a hypothetical signal.

away. Another more sophisticated approach is to synthetically create more samples of the minority class. This can be achieved using the so called "Synthetic minority over-sampling technique" (SMOTE) [23]. The algorithm randomly picks a sample from the minority class, determines its  $k$ -nearest neighbors, picks one of the  $k$  neighbors at random and interpolates again randomly between the two samples to synthesize a new minority class sample. Since the variances vary strongly between the different features the  $k$ -nearest neighbors are determined based on the Mahalanobis distance which normalizes the Euclidean distance between two samples using the sample covariance matrix of the training set. This process is repeated until a specified amount of minority class samples has been created. Note, SMOTE can also be applied to the uncertainty vector  $\theta$ . In that case the synthesized input vectors can be tested by simulation if they indeed lead to an upset and hence belong to the minority class. If a synthesized input vector is not leading to an upset it is discarded. This is an advantage over the approach where SMOTE is used to synthesize new feature vectors. In this case it is not guaranteed with certainty that a new feature vector indeed belongs to the upset class. A drawback of applying SMOTE to the input vectors is that it requires significantly more time to create more samples of the minority class since every synthesized sample requires an additional simulation run. In this work SMOTE is applied directly to the feature space to save training time.

Based on the balanced training set a greedy forward feature selection algorithm as described in [56] is proposed to identify the most relevant features. The relevance of a feature is determined using 10-fold cross-validation and as a metric the average Matthews correlation coefficient (MCC) is used to measure classification performance. The MCC is defined as

$$\text{MCC} = \frac{n_{TP} \cdot n_{TN} - n_{FP} \cdot n_{FN}}{\sqrt{(n_{TP} + n_{FP})(n_{TP} + n_{FN})(n_{TN} + n_{FP})(n_{TN} + n_{FN})}} \quad (6.10)$$

where  $n_{TP}$ ,  $n_{TN}$ ,  $n_{FP}$  and  $n_{FN}$  denote the number of true positives, true negatives, false positives and false negatives, respectively. The MCC is the preferred performance measure in binary classification problems since it condenses information of all four quadrants of the confusion matrix in one single number. This is not the case if other measures are used such as accuracy or F1 score which is discussed in detail in [25]. Ultimately, each continuous time series segment is condensed in a  $\mathbb{R}^{m_f}$  dimensional vector  $\tilde{\phi}_{f,i}$  and the predictor is optimized based on the relationship

$$\begin{pmatrix} \tilde{\phi}_{f,1} \\ \tilde{\phi}_{f,2} \\ \vdots \\ \tilde{\phi}_{f,n_z+n_z^+} \end{pmatrix} \rightarrow \begin{pmatrix} l_1 \\ l_2 \\ \vdots \\ l_{n_z+n_z^+} \end{pmatrix} \quad (6.11)$$

where  $l_i \in \{-1, 1\}$ . Note, the "tilde" operator indicates the reduced feature vector,  $n_z$  indicates the amount of samples generated by the SS algorithm and  $n_z^+$  is the amount of additionally synthesized samples using SMOTE. In this work the SVM is trained using the Matlab Statistics and Machine Learning Toolbox [143].

In the previous paragraphs two prediction strategies are presented. On the one hand, a simple threshold based predictor and on the other hand a time series classification prediction strategy. One open question to be answered is how the performance of the prediction methods can be compared to each other in the context of upset condition prediction for an AWE system. Besides the classical metrics such as accuracy, F1 score or MCC it is beneficial to associate weights to false positives and false negatives that reflect the practical impact on the system performance. Since in practice false positives and false negatives have in general a different impact, ranking predictors simply based on their prediction accuracy is not a recommended approach. In the context of AWE a solution is to weight both terms proportionally to the resulting economic loss. In case of a false positive this loss equals the energy loss due to the triggered emergency maneuver  $E_{FP} = E_{em}$ . The loss stemming from a false negative  $E_{FN}$  is more difficult to estimate since it requires a cost model that is able to predict the energy loss due to system downtime, repair costs and material costs in case the upset damaged the system. In order to combine the impact of false negatives and false positives in a single number, an economic loss rate is introduced which is defined as the weighted linear combination:

$$E_{tot} = w_{FP}E_{FP} + w_{FN}E_{FN} \quad (6.12)$$

where  $E_{FP}$  and  $E_{FN}$  are the associated energy losses in kWh due to false predictions. In this work, the weights  $w_{FP}$  and  $w_{FN}$  are derived based on the probabilities of false predictions. Mathematically, the occurrence of either a FP or a FN is modeled as a Poisson process. The Poisson process that models the arrivals of FPs runs until the first arrival time within the Poisson process that models the arrival of a FN. The expected value of the arrival time of a FN allows then to estimate the amount of FPs until that point in time and hence the resulting energy loss. The rate for the process that models the occurrence

of a FN is given by

$$\begin{aligned}\lambda_{\text{FN}} &= \Pr(\hat{l} = 1, l = -1) \\ &= \Pr(\hat{l} = 1 \mid l = -1) \Pr(l = -1) \\ &= \frac{n_{\text{FN}}}{n_{\text{FN}} + n_{\text{TP}}} p_f\end{aligned}\quad (6.13)$$

The conditional probability is simply given by the false positive rate of the prediction strategy. The probability that  $l = -1$  is the upset condition probability which is independent of the prediction approach. Estimating the conditional probability is done by re-simulating upset conditions for each of the different predictors using the results from the SS run in step A. Note, it is paramount here to use a different SS run than the one used to train the predictor. With the estimated FN rate the number of pumping cycles until the first expected FN occurs is then given by

$$n_{\text{pc}} = \frac{1}{\lambda_{\text{FN}}}\quad (6.14)$$

The expected number of FP up to the first FN is given by the expected value of the corresponding Poisson process defined by

$$\begin{aligned}n_{\text{FP}} &= \lambda_{\text{FP}} n_{\text{pc}} \\ &= \Pr(\hat{l} = -1, y = 1) n_{\text{pc}}\end{aligned}\quad (6.15)$$

With the SVM based predictor the probability of encountering a false positive per pumping cycle can be estimated by counting falsely predicted upsets in a separate Monte Carlo simulation run. With a fixed threshold predictor this probability can be directly calculated using Eq. (6.16).

$$\Pr(\hat{y} = -1, y = 1) = 1 - F_{\tilde{Y}(\boldsymbol{\theta})}(Y_T) - p_f\quad (6.16)$$

where  $Y_T$  represents the chosen threshold value and  $F_{\tilde{Y}(\boldsymbol{\theta})}$  is the cumulative distribution function of the maximum values of  $Y(\boldsymbol{\theta})$  which are calculated for each simulation run. Note, the threshold value represents a quantile of the distribution of  $\tilde{Y}(\boldsymbol{\theta})$  and hence the false positive probability is the corresponding area under the PDF right from the threshold minus the upset probability.

If a FN occurs the system will not be operational for a specific amount of time  $\Delta T_{\text{nop}}$ . It reflects the required time to conduct a possible emergency landing, maintenance and relaunching. This mainly leads to a power loss in terms of missed pumping cycles. Assuming an average pumping cycle time of  $t_{\text{pc}}$  the number of missed pumping cycles is

$$n_{\text{mpc}} = \frac{\Delta T_{\text{nop}}}{t_{\text{pc}}}\quad (6.17)$$

The expected energy loss per pumping cycle due to predictions errors is eventually given by

$$\begin{aligned}E_{\text{tot}} &= w_{\text{FP}} E_{\text{FP}} + w_{\text{FN}} E_{\text{FN}} \\ &= \frac{1}{n_{\text{pc}} + n_{\text{mpc}}} (n_{\text{FP}} P_{\text{em}} t_{\text{pc}} + n_{\text{mpc}} P_{\text{pc}} t_{\text{pc}} + E_{\text{misc}})\end{aligned}\quad (6.18)$$

This expression can be normalized by the average energy  $E_{pc} = P_{pc} t_{pc}$  converted in one pumping cycle which yields

$$\frac{E_{tot}}{E_{pc}} = \frac{1}{n_{pc} + n_{mpc}} \left( n_{FP} \frac{P_{em}}{P_{pc}} + n_{mpc} + \frac{E_{misc}}{E_{pc}} \right) \quad (6.19)$$

$E_{misc}$  combines all additional losses involved with a FN such as replacement costs of damaged parts. Equation (6.19) allows to rank different predictors with respect to their expected energy loss relative to the average converted energy in one pumping cycle. This metric is better suited to assess prediction performance because it associates weights to false positives and negatives that have a practical meaning. This is not the case if standard metrics for prediction performance are used. Note, at this stage only guesses about the average downtime  $\Delta T_{nop}$  as well as the additional involved costs, summarized in  $E_{misc}$ , can be made. Furthermore, due to the lack of a comprehensive cost model for AWE systems, Eq. (6.19) is only an approximation of the monetary loss that might be encountered in reality. In the future, and as soon as more data becomes available, a more accurate cost model should replace the simple model defined in Eq. (6.19).

Moreover, note that the features used by the SVM based predictor are selected with respect to the achieved MCC. One could also directly choose Eq. (6.19) to rank the performance of feature combinations. However, this requires to rank the features as a function of the parameter values in the loss function for which only rough estimations are available at the moment. For this reason the MCC is used to optimize the SVM and Eq. (6.19) is only used to compare different prediction strategies after the design phase. Based on these results the best predictor can be chosen and deployed on the real system.

## 6

### 6.2.3. Upset Condition Avoidance

In step C of the framework the avoidance maneuver is defined. Due to the possibility of false positives it is desirable that the impact of the maneuver on the pumping cycle operation is minimized. One generic approach for upset avoidance during the pumping cycle is to abort the current traction or retraction phase and use the onboard propulsion system to either land the aircraft or to go into a loiter mode from which the normal operation can again be initiated. Both approaches, however, reduce the average power output of the system significantly. A more efficient upset avoidance strategy needs to be tailored to the upset condition itself, which is demonstrated in the next section for the case of tether rupture.

## 6.3. Application: Generate, Predict and Avoid Tether Rupture

### 6.3.1. Setup

In this section the the three steps A, B and C of the framework are applied to the case of tether rupture which is an important upset condition in the field of AWE. Due to the complex interaction between ground station and flight control system, wind, tether as well as the aircraft dynamics it is basically impossible to analytically derive conditions that lead to this critical event. Furthermore, assuming that a reliable control system is implemented tether rupture has a low probability of occurrence which makes it a suitable example to demonstrate the methodology proposed in this work. Additionally, since this

event has a high relevance for the AWE community, the cause for tether rupture based on the obtained results is investigated in depths.

In step A the SS algorithm is used to generate systematically conditions that drive the tether force peak within a pumping cycle beyond its maximum allowable value. The limit function is in this case given by

$$Y(\boldsymbol{\theta}) = F_t \quad (6.20)$$

In the present example the stochastic excitation is limited to the uncertainties in the wind conditions. It is arguably also the highest uncertainty that makes AWE systems difficult to control. Of course, the framework can be easily extended in order to include model parameter uncertainties, sensor noise or hardware failures but this is left for future work. The wind conditions in the simulations are generated using the Dryden Turbulence model that has as input standard Gaussian distributed random variables  $\theta_k$  that are filtered to recover the Dryden turbulence spectrum. In total  $d = T_{\text{sim}} f_s$  random variables are sampled per run where  $T_{\text{sim}}$  is the simulation run-time and  $f_s$  the sampling frequency which is set to 10 Hz. Further possible variations in the wind field such as discrete gusts or changes in the wind speed profile and the mean wind direction are not considered in this work and are also left for future research. In general, upset conditions for a complete pumping cycle, or even several pumping cycles in a row can be generated with the proposed framework. However, since the dimension of the joint probability density function from which the wind condition is sampled grows linearly with simulation time all the results are generated for only one pumping cycle per sample. For this specific example the SS algorithm created 4221 tether ruptures and around  $7.1 \cdot 10^5$  segments without tether rupture are extracted. The results are created with one SS run that included in total  $3 \cdot 10^4$  pumping cycle simulations. The selected time window size for one segment is 5 s and the reaction time shift  $\Delta T_r$  is set to 0.2 s.

In step B reasonable state and output variables are selected to predict the upset and the predictor is designed based on the results of step A. In this example only signals that are available at the aircraft are considered in order to avoid communication delays between the ground station and the aircraft. Specifically, the following signals are chosen:

- wind speed components  $v_{w,x,W}$ ,  $v_{w,y,W}$ , and  $v_{w,z,W}$
- aircraft acceleration in radial direction  $a_{z,\tau}$
- Tether force  $F_t$
- angle of attack  $\alpha_a$
- path following error  $e_p$

Following section 6.2.2, each signal is discretized into smaller overlapping time windows and statistical properties in the time and frequency domain are calculated. The utilized features that are calculated for each of the signals in the time domain are: mean, median, rms-value, variance, maximum, minimum, maximum peak-to-peak ratio, skewness, kurtosis, crest factor, median absolute deviation, range of the cumulative sum, the

time-reversal asymmetry statistic given by Eq. (6.21) and the maximum signal slope. The time-reversal asymmetry statistic is defined by [56]

$$\Xi = \frac{\mathbb{E}((\Delta z_i(t) - \Delta z_i(t - \tau_{\text{TRA}}))^3)}{(\mathbb{E}((\Delta z_i(t) - \Delta z_i(t - \tau_{\text{TRA}}))^2))^{\frac{3}{2}}} \quad (6.21)$$

where different values for  $\tau_{\text{TRA}}$  are considered. In the frequency domain the following characteristics are calculated: median and maximum amplitude, and additionally the maximum amplitude above 1 Hz using a fast Fourier transform. Note, this set of features is created heuristically. The individual features are chosen because they are computationally cheap to evaluate and easy to comprehend or because they turned out to be useful features in other applications (e.g. the time-reversal statistic in [56]). It is shown later in this section that an optimized subset, which is derived from the initial feature pool, leads to an acceptable prediction performance. Note, it is always possible to add more features to the initial feature pool for instance if the initial prediction performance is poor. However, the larger the initial feature pool, the longer it takes to optimize the smaller subset. Therefore, it is recommended to only gradually increase the size of the feature pool and always check if an acceptable classification performance can be achieved before new features are added.

In order to balance the data set additional feature vectors are created using the SMOTE algorithm and afterwards the feature selection algorithm is applied to reduce the dimension of the original feature space. With SMOTE around  $6 \cdot 10^5$  feature vectors are synthesized from the 4221 original samples created by the SS algorithm in step A. Note, in contrast to the original feature vectors it cannot be guaranteed that the synthesized feature vectors indeed belong to the set of feature vectors that lead to tether rupture. One reason is that the set corresponding to a tether rupture is not necessarily convex. Hence, an interpolated feature vector can also end up outside the non-convex set.

The optimized subset of features is displayed in Table 6.1 (ordered according to significance). Note, the MCC value in the second column is the cumulative MCC value. In Fig. 6.3 the convergence of the selection process is displayed. Convergence is defined as the point where the relative change in the MCC after adding a feature to the list is smaller than  $10^{-4}$ . This convergence criteria is also proposed in [56]. With the optimized feature list the SVM predictor is trained as explained in section 6.2.2.

Additionally, fixed thresholds are selected based on the estimated distribution of the tether force peaks using the results of the first stage of the SS run (direct Monte Carlo run). In this case the thresholds are selected with respect to the tether force set point in the traction phase. The thresholds  $F_{t,\text{set}} + 8\%$ ,  $F_{t,\text{set}} + 10\%$ ,  $F_{t,\text{set}} + 12\%$ ,  $F_{t,\text{set}} + 14\%$  and  $F_{t,\text{set}} + 16\%$  are considered which are all larger than the 0.99-quantile of the tether force peak distribution which corresponds to  $F_{t,\text{set}} + 7\%$ . The set point  $F_{t,\text{set}}$  itself is chosen to be  $-20\%$  of the maximum allowable tether tension which is set to 2 kN.

In step C of the framework the avoidance maneuver is designed. In case of a predicted tether rupture the contingency maneuver must reduce the current tension in the tether as quickly as possible. It turns out that with the underlying control system this can be achieved with a set point change for the tether force. On the one hand, the tension in the tether is tracked by the winch controller via the reeling out/in speed and on the other hand by the flight path controller through the angle of attack and bank angle.

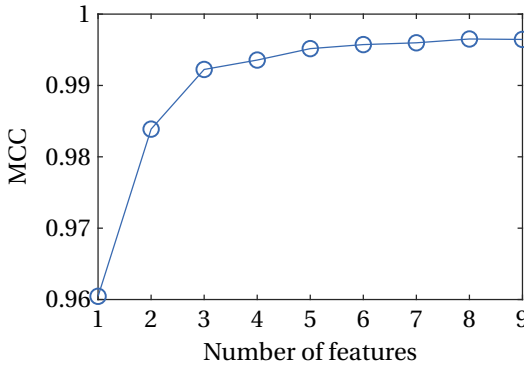


Figure 6.3: Maximization of the MCC using greedy feature selection.

Therefore, changing the set point for the tether force leads to an adaptation of the winch reeling speed but also of the angle of attack and bank angle commands  $\alpha_{a,c}$  and  $\mu_{a,c}$ , respectively. Since it is desired that the aircraft continues following the flight path the set point change for the attitude angles should only reduce the tether tension but not the maneuver forces. Hence, the reference values for  $\alpha_a$  and  $\mu_a$  are still calculated using the inversion of the path-dynamics as defined in Eq. (4.132) and Eq. (4.129).

Note, in order to track the tether force the angle of attack and bank angle commands are calculated using the tether force set point  $F_{t,set}$  and not the measured tether force currently acting on the aircraft. The tether force set point enters the path-dynamics via Eq. (4.124). During nominal operation this allows to effectively keep the tether under the desired tension. As soon as an upset is predicted this set point will be reduced to a low value ( $F_{t,set} = 10\text{N}$ ). As a result the aircraft will correct the current bank and angle of attack commands accordingly while still creating enough lift to continue following the reference path. This allows to reliably reduce the tension in the tether quickly even if the winch is currently saturating which is discussed in the next section. As soon as the tether force drops below a second threshold value, i.e.  $F_t \leq c \cdot 10\text{N}$  with for instance  $c = 1.2$ , and the predictor output switches from  $\hat{l} = -1$  (upset) back to  $\hat{l} = 1$  (no upset) the force set point is reset again to the original traction phase set point.

### 6.3.2. Results

It is important to note that the results of this section were generated with an older version of the nonlinear control system compared to the one presented in chapter 4. Time delays are not considered and the winch control input is not low pass filtered. This led to a more optimistic control performance and hence the resulting failure probabilities are lower than the ones presented in chapter 5. Nevertheless, the results demonstrate how to apply the framework to generate, predict and prevent important failure conditions for AWE systems. Therefore, the specific controller implementation is of secondary importance.

Before the actual results are presented some additional findings regarding the transition strategy and its impact on the tether rupture probability are discussed in the following. The transition strategy from the retraction to the traction phase, realized as a

Table 6.1: Ordered feature list.

Feature	MCC
Crest factor $F_t$	9.60
$\Xi$ for $e_p$ Eq. (6.21) with $\tau_{\text{TRA}} = 1$ s	9.83
Maximum $F_t$ slope	9.92
Mean of $F_t$	9.935
Maximum amplitude above 1 Hz of $\alpha_a$	9.951
Median amplitude of $F_t$	9.957
Minimum $\alpha_a$	9.959
Variance $a_{z,\tau}$	9.965
Variance of $F_t$	9.965

## 6

controlled rotation of the reference flight path from high to low elevation angles, has an important impact on the overall probability of tether rupture and on the power output. In fact, the choice of the bandwidth  $\omega_r$ , that defines how quickly the path is rotated from higher to lower elevation angles during the transition from retraction to traction phase, allows to trade off robustness against performance. In Fig. 6.4 the results of three independent subset simulations are presented with three different choices for  $\omega_r$ . As a reference  $\omega_r = 0.05$  is chosen which leads to an approximate tether rupture probability during a pumping cycle of  $p_f \approx 2 \cdot 10^{-7}$ . Increasing the reference value by a factor of 1.5 and 2 increases the power output by 28% and 33% but also leads to a significant increase of the tether rupture probability by a factor of approximately  $1.9 \cdot 10^3$  and  $1.3 \cdot 10^4$ , respectively. Since there is no external standard that defines the allowable tether rupture probability the conservative value of  $\omega_r = 0.05$  is chosen to generate the subsequent results. The corresponding low probability also justifies using SS to generate this type of upset condition in the first place, whereas the other two controller settings defined by  $1.5\omega_r$  and  $2\omega_r$  lead to tether rupture probabilities that might be analyzed with simple Monte Carlo simulations. Given a desired level of reliability  $\omega_r$  can be adapted in the future accordingly.

The performance of the different prediction strategies (SVM and thresholds) is tested on a separately generated data set that is not used to construct the predictors. The test data set is generated in the same manner as the training data set using the SS algorithm. In the first part of this section the effectiveness of the avoidance maneuver is analyzed. Subsequently, the prediction and prevention performance among the different predictors is assessed using Eq. (6.19).

The effectiveness of the prediction and avoidance strategy is demonstrated and explained in detail using the results of one sample of the test set that contains a tether rupture. To that end, the same simulation is carried out twice once with prediction

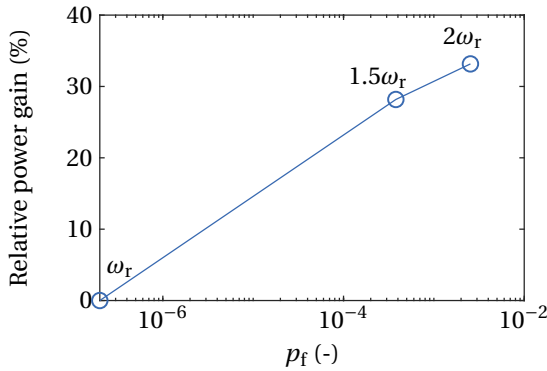


Figure 6.4: Relative gain in pumping cycle power over tether rupture probability as a function of multiples of the path rotation constant  $\omega_r$ .

and avoidance method and once without. To limit the scope of the result section only the results using the SVM prediction strategy are displayed and analyzed. The resulting flight path of both scenarios is displayed in Fig. 6.5a, the corresponding projection in the  $x_W y_W$ -plane is depicted in Fig. 6.5b. The blue path shows one complete pumping cycle where the tether rupture is prevented using the proposed avoidance maneuver. It can be observed that the system is able to continue its operation and the avoidance maneuver has no visible impact on the path following performance. The green cross indicates the point where the tether breaks and as a result, in the scenario without avoidance strategy, the aircraft is ejected from the reference flight path and is no longer able to continue the pumping cycle. The evolution of the tether force in both scenarios is depicted in Fig. 6.6. At around 69s the avoidance maneuver is triggered which leads to a significant tether tension reduction as indicated by the blue solid line. In contrast to that, without the avoidance maneuver the tether tension continues to oscillate and at around 70.5s the tether breaks.

The control system performance during the avoidance maneuver is analyzed in more detail using the evolution of the aerodynamic bank angle and the angle of attack. In Fig. 6.7a the impact of the tether tension set point change is clearly visible in the evolution of the commanded bank angle  $\mu_{a,c}$  (blue, solid line). At around 69s the commanded value drops to around  $-30^\circ$ . Since the controller uses a dynamic inversion based control strategy the set point is filtered (orange, dashed line) and the actual bank angle is controlled such that it follows the corresponding reference model (green, dotted line). A similar behavior results for the angle of attack  $\alpha_{a,c}$ . Also in this case the tether tension set point change leads to a drop in the commanded angle of attack. The actual angle of attack follows the corresponding reference model with an overshoot of approximately  $2.3^\circ$ .

The adaption of the bank angle and the angle of attack leads to an adaption of the aircraft attitude with respect to the tangential plane. Therefore, besides the change in lift magnitude through the adaption of the angle of attack also the rotation of the lift force leads to a tether force reduction. If the aircraft is flying in the tangential plane most of

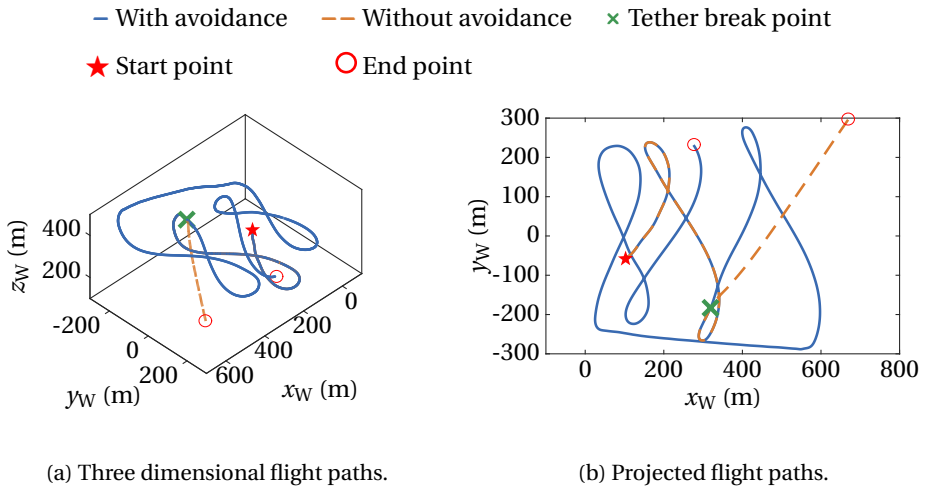


Figure 6.5: Pumping cycle flight paths with and without tether rupture avoidance

## 6

the lift force is pointing in the radial direction. Increasing the attitude angles (absolute value) with respect to the tangential plane by a simultaneous roll and pitch maneuver can reduce the tension in the tether since the component of the lift vector perpendicular to the tether direction increases. This behavior can be observed in Fig. 6.8a and Fig. 6.8b. Both plots demonstrate that due to the tether force set point change the aircraft is indeed rotated into the tangential plane (blue, solid line). The roll angle  $\Phi_r$  is reduced from a nearly horizontal attitude (with respect to the tangential plane) to  $-50^\circ$ , the pitch angle  $\Theta_r$  is reduced from around  $-5^\circ$  to  $-25^\circ$ . Without the avoidance maneuver (orange, dashed line) the roll angle stays nearly constant and the pitch angle starts to oscillate and to increase. The red dotted line indicates the point where the tether breaks.

For the case with tether rupture avoidance the resulting trajectory is again displayed in Fig. 6.9a. The blue line represents the flight path of one pumping cycle, of which only the part around the prevented tether rupture is displayed in Fig. 6.9b. The tether is shown as a solid gray line connecting the aircraft with the ground station. Additionally, a simple aircraft visualization (colored rectangle) is added to the figure which represents the orientation of the aircraft wing. The aircraft visualization color changes from green to orange as soon as the avoidance maneuver is triggered. The resulting attitude change is visible in the beginning of the maneuver where the aircraft rolls negatively, with respect to the body-fixed frame x-axis, into the tangential plane. The color changes back to green as soon as the avoidance maneuver is finished. In this case the end of the avoidance maneuver is defined as the first time the tether force set point reaches again 90% of the original traction phase tether tension set point. A visible drawback of the avoidance maneuver is that the aircraft flies about a quarter of the figure of eight at low tether tension which results in a power loss. Hence, the amount of falsely predicted upsets (i.e. false positives) needs to be traded off against the power loss associated with a tether rupture. On the other hand, a visible deviation from the flight path cannot be observed

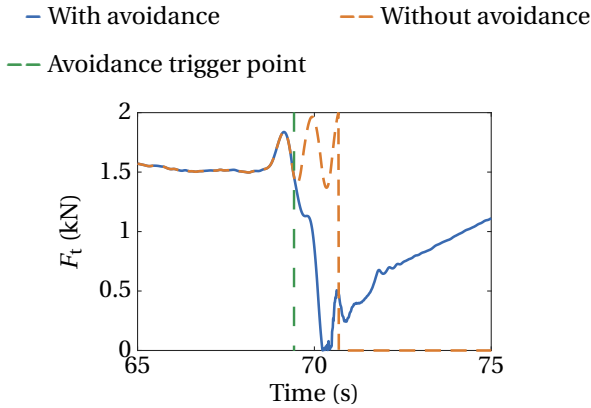
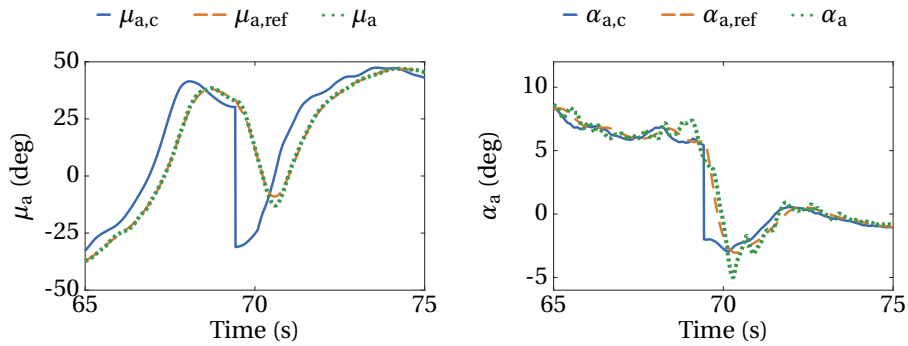


Figure 6.6: Evolution of the tether tension with and without prediction and avoidance strategy.

and the aircraft continues the traction phase without interruption which is an advantage over strategies that need to abort the current operational mode in order to prevent tether rupture.

The actual reason for the tether break can be found by looking at the evolution of the tether, or winch, acceleration measured on the ground. In Fig. 6.10a the winch acceleration for the scenario without avoidance maneuver is displayed. The dashed orange line indicates the point where the tether breaks. Before the tether breaks the winch acceleration saturates at around 68s and starts to jump between the maximum and the minimum acceleration limit with increasing frequency until the maximum supported tension is exceeded and the tether breaks. In contrast, Fig. 6.10b shows the winch acceleration for the scenario with avoidance maneuver. In this case, the oscillation is prevented and instead the winch stays in the upper saturation limit leading to a fast reeling out of the tether. The start of the avoidance maneuver is indicated by the dashed green line. The corresponding winch speed for the flight with tether rupture is displayed in Fig. 6.11a. It can be observed that the winch speed itself is not saturating but also starts to oscillate due to the saturated acceleration. In contrast, with the avoidance maneuver the reeling out speed continues to increase after a small kink at the prediction point (see Fig. 6.11b) and tether rupture is prevented. As soon as the avoidance maneuver is completed the winch starts reeling out slower according to the increasing tether force set point at around 70.2s (see Fig. 6.6).

For completeness the mean wind speed at the aircraft around the point in time at which the avoidance maneuver is triggered is displayed in Fig. 6.12b and the wind speed evolution of the flight without avoidance maneuver in the same time window is displayed in Fig. 6.12a. The evolution of the wind speed before the avoidance maneuver is triggered or before the tether ruptures does not show any visible changes compared to wind speed after the avoidance maneuver and after tether rupture. This indicates that the tether rupture is not caused by an easy to comprehend change in the wind conditions at the aircraft but rather is a result of the complex interaction between aircraft and winch dynamics, as well as the control system and the wind conditions. This is consis-



(a) Evolution of the aerodynamic bank angle. (b) Evolution of the angle of attack with set point  $\mu_{a,c}$ , reference  $\mu_{a,ref}$  and achieved point  $\alpha_{a,c}$ , reference filter state  $\alpha_{a,ref}$  and achieved angle of attack  $\alpha_a$ .

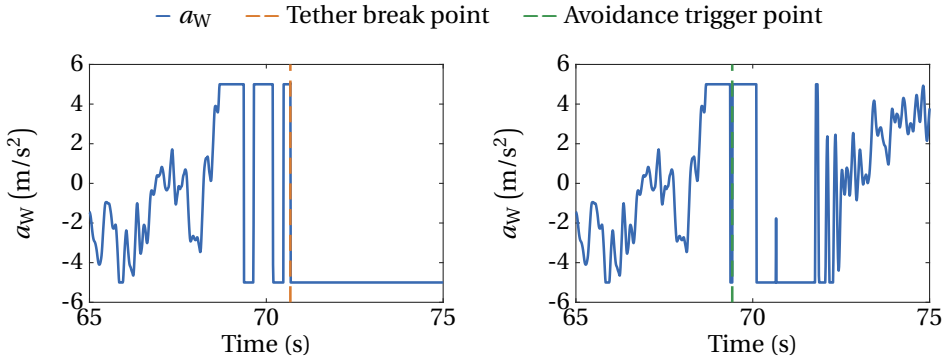
Figure 6.7: Attitude tracking performance during the avoidance maneuver.

tent with the results displayed in Table 6.1 where no metric corresponding to the wind conditions is among the selected features.

6

In the previous paragraph the winch acceleration limits are identified as one cause for the tether rupture. However, a second factor represented by a specific airspeed and angle of attack combination can be identified. This can be shown by analyzing the distribution of airspeed and angle of attack pairs for simulation runs with and without tether rupture. Note, for the upset case the values at the point of tether rupture are taken and for the nominal flight the values are picked at randomly chosen positions on the flight path. The results are displayed in Fig. 6.13a and Fig. 6.13b. In total 22200 simulations without tether rupture and 5749 simulations with tether rupture from three different subset simulation runs are used to approximate the distributions. The red solid line in both figures represents the same optimized separation boundary. The distributions itself are plotted in two different figures for visualization purposes. It can be observed that most of the samples above the boundary are simulation runs where the tether ruptured whereas most of the simulation runs below the boundary are flight without tether rupture. The color gradient represents the conditional probability of a specific airspeed and angle of attack combination given a tether rupture or given no tether rupture. The results show that a perfect separation between the two distributions is not possible. This is however to be expected since using only airspeed and angle of attack to distinguish tether rupture conditions from nominal flights reduces the dimension of the problem significantly. However, except some minor overlap in the tails the two modes of the distributions are indeed distinguishable (brighter color). Furthermore, above an airspeed of  $37 \text{ m s}^{-1}$  there is a high chance that a sample belongs to the upset class independently of the angle of attack value. Similarly, below  $30 \text{ m s}^{-1}$  and independent of the angle of attack no tether rupture will occur with a high probability. This result suggests an additional strategy to avoid tether rupture by limiting the angle of attack set point as a function of airspeed according to the plotted linear decision boundary. However, this is

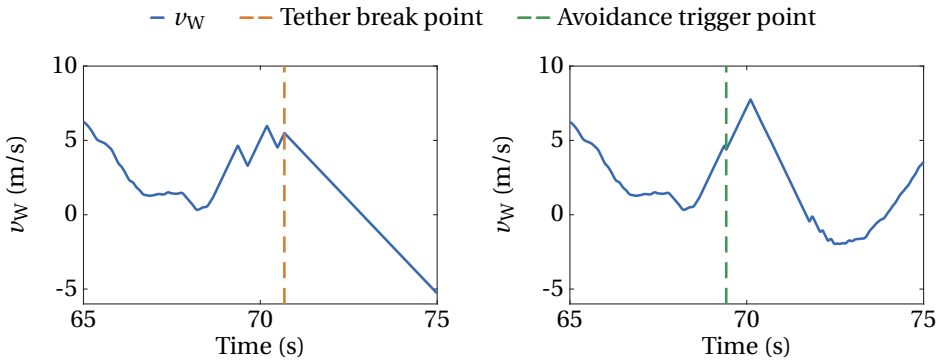




(a) Evolution of the winch acceleration without (b) Evolution of the winch acceleration with tether rupture avoidance.

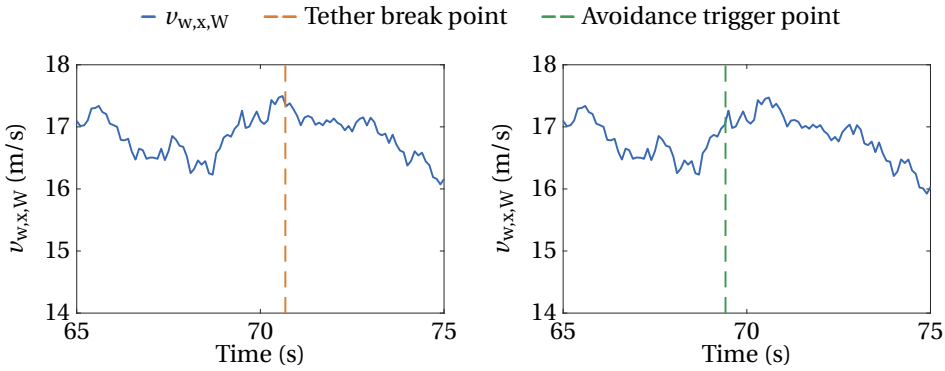
Figure 6.10: Winch acceleration.

## 6



(a) Evolution of the winch speed without tether (b) Evolution of the winch speed with tether rupture avoidance.

Figure 6.11: Winch reeling out/in speed.



(a) Evolution of wind speed in mean wind direction without avoidance maneuver. (b) Evolution of wind speed in mean wind direction with avoidance maneuver.

Figure 6.12: Mean wind speed at the aircraft.

not investigated in this work further and is left for future research.

In the following the performance of different predictors will be investigated with respect to classical performance metrics as well as the introduced economic loss rate given by Eq. (6.19). In total, five different threshold based predictors and one SVM based predictor are compared to each other. The results are visualized in Fig. 6.14 where the conditional probabilities of not detecting and preventing tether rupture is plotted over the probability of a false positive. The blue, solid line with circular markers connects the performance pairs of the five threshold strategies. The performance of the SVM predictor is represented by the orange asterisk. The numerical values are listed in Table 6.2. The false negative rates are estimated based on 764 flights with tether rupture and the false positive probability is estimated based on 20803 samples without tether rupture. For the fixed thresholds the probability of a FP is negatively correlated with the probability of a

Table 6.2: Upset detection performance.

Method	Pr (FP)	Pr ( $\hat{l} = 1 \mid l = -1$ )
$F_{t,set} + 8\%$	0.48%	0%
$F_{t,set} + 10\%$	0.13 %	0%
$F_{t,set} + 12\%$	0.04%	0.26%
$F_{t,set} + 14\%$	0.01%	1.44%
$F_{t,set} + 16\%$	0%	7.20%
SVM	0%	0.79%

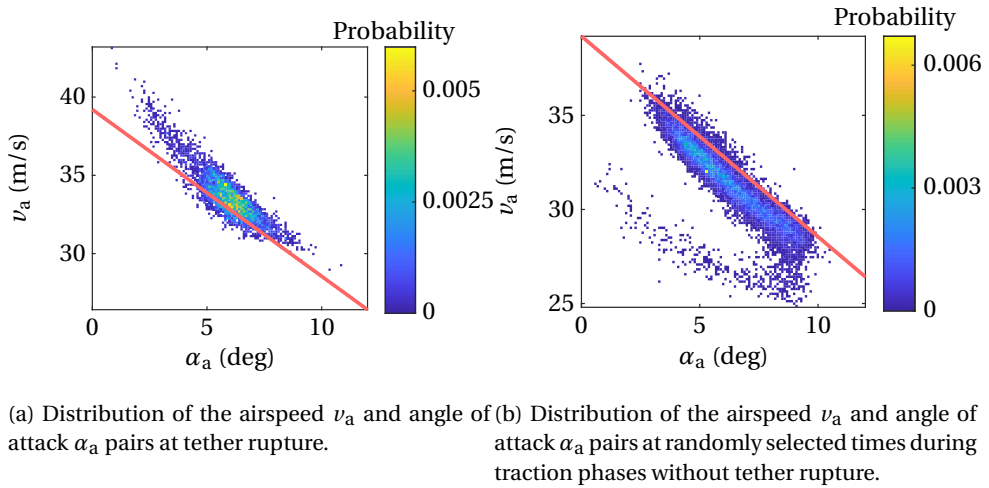


Figure 6.13: Airspeed and angle of attack distribution.

## 6

not correctly identified/prevented tether rupture, as expected. The closer the threshold value is selected to the critical value the more likely it is that the tether rupture cannot be prevented due to the inertia of the system. In contrast to that, the more conservative the threshold is chosen, i.e. closer to the set point, the more likely it is to prevent a tether rupture but at the cost of an increasing false positive rate. Based on the numerical values and also based on Fig. 6.14 it is difficult to decide which is the best prediction strategy. The SVM achieves the best performance with respect to false positives together with the highest threshold which however has an almost 10 times higher probability of not avoiding a tether rupture. Between the thresholds  $F_{t,set} + 14\%$  and  $F_{t,set} + 12\%$  the largest threshold value can be found that outperforms the SVM in terms of the false negative rate. However, this predictor and predictors below this threshold lead to higher false positive rates. Therefore, selecting the right prediction strategy solely based on these results is difficult because no reasonable acceptable FP and FN rate can be defined a priori and both metrics are not equally important from a practical point of view.

The energy loss rate defined in Eq. (6.19) tries to solve the aforementioned issue by assigning weights to the FP and FN rate proportionally to the associated performance loss. Since no reasonable estimation of the term  $E_{misc}$  can be made at this stage of the research,  $E_{misc}$  is set to zero in the following analysis. Note, in this case a false negative impacts the performance loss only through the power loss due to the number of missed pumping cycles during the downtime of the system. The expected downtime after a tether rupture is not available either but a reasonable range of values can be defined and the losses can be plotted over the selected range. All other parameter values can be estimated using sample averages from the Monte Carlo simulations. The numerical values are listed in Table 6.3.

In Fig. 6.15 the performance loss rate per average converted energy per pumping

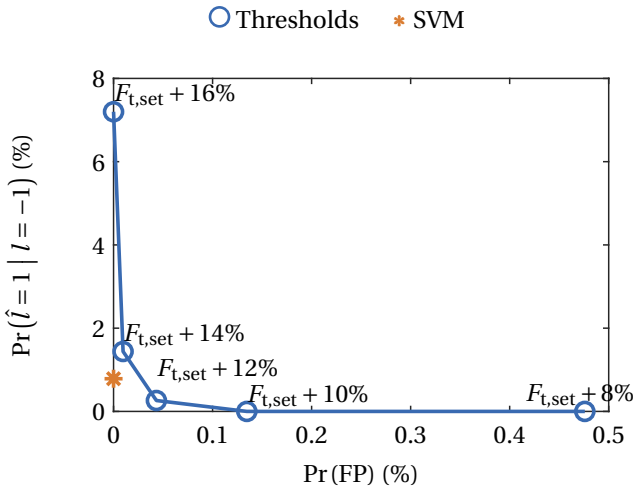


Figure 6.14: Conditional probability of not preventing tether rupture given a tether rupture for different prediction thresholds and the SVM predictor.

cycle  $E_{pc}$  is displayed as a function of system downtime using Eq. (6.19). The results show that without prevention strategy (dashed line) the relative performance loss grows quickly with increasing system downtime even for the estimated low probability of tether rupture. For the thresholds  $F_{t,\text{set}} + 8\%$  and  $F_{t,\text{set}} + 10\%$  the loss rate remains constant since their false negative rate is zero and hence the downtime has no impact on the loss. The other thresholds and the SVM predictor loss rates remain nearly constant as well due to the overall small probability of false negatives among the predictors. The SVM leads to the lowest loss rate among the predictors in the considered time window.

### 6.3.3. Discussion of Model Validity

The presented framework uses models of the AWE system as well as the wind to create, predict and prevent upset conditions. The accuracy of the models is critical in order to be able to project the results to reality. The aircraft model has been validated to some extent as described in [96] and [111] but especially for quick changes in the wind condi-

Table 6.3: Average parameter values.

Parameter	Value	Unit
$P_{em}$	0.4	kW
$P_{pc}$	3.9	kW
$t_{pc}$	2.5	minutes
$p_f$	$2 \times 10^{-7}$	-

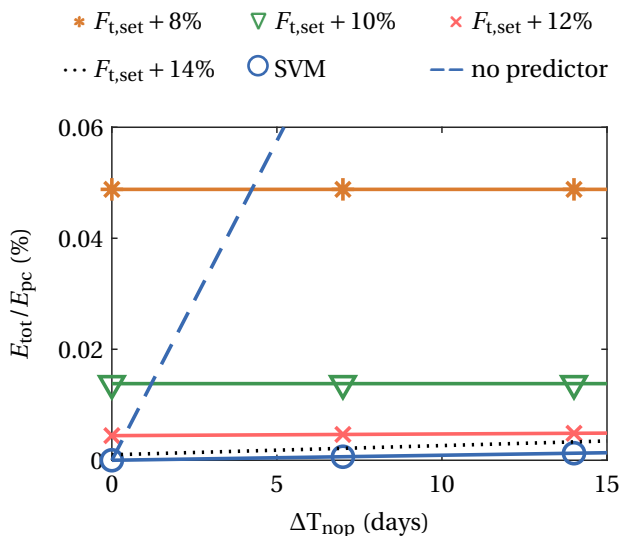


Figure 6.15: Comparison of loss rates across different predictors.

## 6

tions the aerodynamic model is probably too aggressive since changes in the local flow immediately change the resulting lift force. It is expected that with a more realistic aerodynamic model an additional time delay between changes in the local flow field around the aircraft and the resulting change of the tether force is present which might alter the presented results in the previous section. The present model can hence be regarded as conservative and it is expected that the prediction accuracy can be further improved with a more realistic model. Testing the framework with a more realistic aircraft model is therefore regarded as the main suggestion for future work. This will also allow to investigate further upset conditions related to the structural and aerodynamic integrity of the aircraft. For instance, wind conditions that lead to critical wing bending or severe vibrations can be generated using the SS algorithm and a data-driven predictor such as the SVM predictor can be used to trigger a load and/or vibration alleviation strategy if necessary. Finally, it needs to be emphasized that the presented results are strongly dependent on the specific controller. In order to investigate how well the results generalize it is recommended to apply the presented methodology to a different closed loop system model in the future. Moreover, additional data-driven methods for the predictor can be tested to further decrease both false positive and negative rates and hence the economic loss. Finally, if more information about the terms in Eq. (6.19) is available the SVM should be optimized with respect to the loss and not the MCC.

### 6.4. Summary

In this chapter a framework to generate, predict and prevent upset conditions that jeopardize the long term reliability of AWE systems is presented. The SS method is used to systematically sample uncertainties that lead to a specified requirement violation. The

obtained samples are then used to construct a binary classifier that monitors the current state of the AWE system during flight. The classifier can trigger an avoidance maneuver that ultimately prevents the requirement violation and keeps the system operational. The feasibility of the framework is successfully demonstrated using the example of tether rupture in the last part of this chapter.



# 7

## Conclusion and Perspective

In this last chapter the most important findings are presented and further research directions are proposed.

### 7.1. Conclusion

In this thesis a control system design workflow for rigid wing Airborne Wind Energy (AWE) systems operated in pumping cycle mode is presented. The proposed control approach is characterized by a cascaded and hence modular architecture which is derived by dividing the AWE system into slower and faster dynamics as well as by separating the radial and tangential control objectives. In addition, instead of designing the AWE control system immediately for the 6-DoF dynamics, including flight and winch control system, a step wise approach is pursued. On the one hand, this makes the controller synthesis easier since simpler models can be used to design the controllers. On the other hand, the verification task is simplified since encountered control system failures can be traced back to their source more conveniently. Lastly, it allows to design, modify or even augment parts of the control system without having to change the complete control architecture. For instance, different inner loop control strategies can be designed that can share the same outer loop or the winch control strategy can be modified without the necessity to alter the flight controller. Eventually, statistical experiments are conducted to verify the performance and robustness properties of all designed controllers. Moreover, in the last chapter of this thesis a methodology is presented that allows to systematically generate conditions in which the control system is failing. The generated knowledge is leveraged to build a predictor that can foresee a specific control system failure condition which triggers an avoidance maneuver to prevent it.

The generated and presented results of the previous chapters allow to answer the research questions stated in section 1.4. For convenience the questions are repeated in the following.

1. What makes AWE systems more difficult to control than conventional UAVs?

The robustness of the control system in this work is defined by the probability of exceeding either the maximum tether tension or the maximum angle of attack. Based on the analysis of the simulation runs that contained a violation of at least one of the two limits it can be concluded that the lack of a direct airspeed control strategy impairs the robustness of the AWE control system. In conventional UAV flight control a defined airspeed can explicitly be tracked using the thrust lever. Disturbances that alter the speed can then simply be countered by adjusting the throttle setting and a desired lift force required to follow a reference path can be tracked more accurately. Such a direct airspeed control approach is usually not part of an AWE control system, which makes the airspeed an internal state that can only be controlled indirectly through the adaption of the reeling speed. This makes it more difficult to control the lift force and consequently the tether tension.

## 2. How should robustness and performance of AWE control systems be assessed?

The results in chapter 5 show that the stochastic environment in which AWE systems are operated can have a significant impact on the robustness and performance. On the one hand, robust control design and analysis techniques for linear systems can be applied to take into account uncertainties explicitly in the control design phase of the inner loop. In this work the structured singular value as well as the linear matrix inequality design approach turned out to be effective techniques to synthesize a controller with acceptable performance and robustness properties. Since these tools are computationally cheap and easy to calculate they can be conveniently included in the iterative control design process. On the other hand, since these techniques are limited to linear systems they only provide an initial level of confidence that the controller will also work on the nonlinear system as well as in presence of time varying and stochastic disturbances coming from the wind. Therefore, the linear robust design and analysis tools need to be augmented with statistical analysis techniques. Using quantile function plots turned out to be a convenient way to summarize the performance and robustness properties of the controller during pumping cycle operation. Confidence intervals can be used to quantify the expected variability of the quantile function plots across multiple runs of the statistical experiment.

Clearly, assessing control systems, not only in the context of AWE, solely based on single run simulations and without uncertainties leads to a distorted view of the actual controller performance and robustness. This has especially been demonstrated using the optimized controller that achieved excellent control performance in the deterministic setting but failed immediately if the environmental conditions were changed. Calculating optimal trajectories is helpful to assess the overall power generation capability of the system but if uncertainties are not explicitly considered in the optimization process the resulting controller is most likely prone to failure in a stochastic, hence more realistic, environment.

## 3. How can the derivative term in the pseudo-control input for the inversion of the path-dynamics during figure-8 flight be calculated without relying on linear reference filters?

The inner loop attitude commands are generated by determining the required lift force to compensate the weight of the tether and aircraft in order to create the required tether tension but also the required maneuver forces to follow the reference flight path. Since in the traction phase the flight path is characterized by a non-constant curvature, the required maneuver forces change continuously as a function of the target position on the path. Since the geometry of the path is known as well as the kinematic speed of the aircraft, it is possible to derive the required turning rate given by the rate of the directional change of the tangent on the path without requiring any numerical approximation for instance using a linear filter. If the aircraft is on the path and tracks this turning rate it will follow the path perfectly. In this sense the geometrically calculated course rate represents a nonlinear reference model that is defined by the path geometry itself.

4. How can decoupled linear state feedback flight controllers for robust figure-8 flight be systematically designed and how do they perform compared to a nonlinear flight controller?

During the figure of eight flight the attitude angles of the aircraft vary significantly between approximately  $\pm 60^\circ$  with respect to the ground. This makes a linear inner loop control design difficult. However, if instead the attitude is parameterized with respect to the tangential plane and the transport rate of the tangential plane is considered in the attitude propagation equation it turns out that the flight of the aircraft on the virtual sphere resembles a straight flight state of an untethered aircraft with respect to the Earth surface. Ultimately, this allows to determine quasi-stationary operating points given a certain angle of attack and tether force set point. Linearizing the aircraft equations of motion in these operating points allows to derive state-space models that can be used to synthesize the inner loop controllers.

In addition, it turned out that it is possible to decouple the longitudinal and the lateral aircraft dynamics even during the dynamic figure of eight flight. On the one hand, this is proven by looking at the eigenvalue locations in the complex plain using the coupled as well as the two decoupled models. The results show that the eigenvalue locations indeed coincide sufficiently. On the other hand, the eigenvector stars can be used to determine if the state contributions to the different modes are similar using the coupled as well as the decoupled models. This is indeed the case. Both results indicate that the lateral and longitudinal dynamics can be regarded as decoupled, hence the two controllers can be designed separately.

Promising results are obtained with a linear matrix inequality based strategy to derive  $H_2$ -norm optimal longitudinal and lateral controller gains. This approach allows to incorporate several state space models, derived at different operating points, simultaneously in the control synthesis process. The structured singular value can then additionally be used to calculate guaranteed robustness margins towards modeling uncertainties.

Although at first the traction phase control objective appears to be very nonlinear, the linear controllers achieve a similar or even better performance compared to the nonlinear controller. One identified disadvantage of the nonlinear controller

is that it is only controlling the attitude angles. The attitude angle tracking performance, and in particular the angle of attack tracking performance, of the nonlinear controller is indeed more robust compared to the linear controllers especially in presence of model uncertainties. This is reflected in the achieved lower probability of inadvertently exceeding the angle of attack peak limit during pumping cycle operations. However, the nonlinear controller is not stabilizing the airspeed dynamics. This leads to airspeed oscillations with higher amplitudes during the figure of eight flight and eventually makes the nonlinear controller less robust towards tether rupture. Moreover, due to the required time scale separation of the attitude and rate loop the nonlinear controller leads to larger crosstrack errors during the figure of eight flight. An additional disadvantage of the nonlinear controller is that it is significantly more complex to implement. Hence, the simplicity of the LMI controller combined with its acceptable robustness properties makes it the recommended inner loop control solution for both traction and retraction phase.

5. How can the transition from the retraction to the traction phase be shaped in order to damp tether tension peaks during the transients and how does the transition strategy enable to trade-off performance and robustness?

The transition from the retraction to the traction phase is arguably the most critical flight phase during pumping cycle operation. On the one hand, the controller needs to switch from straight line following to figure of eight path following. On the other hand, the tether tension needs to be increased from a low set point value during the retraction phase to a high value during the traction phase. It is paramount that a smooth transition is achieved to avoid aggressive maneuvers. These can cause large attitude angle variations that lead to tether force peaks that cannot be compensated quickly enough, due to the limitations of the winch, and therefore can potentially lead to tether rupture. The proposed transition strategy in this work led to a smooth transition by intercepting the figure of eight reference path at high elevation angles. In this case, the aircraft transitions into the figure of eight path nearly horizontally and is then guided through a controlled rotation of the reference path to lower elevation angles.

Based on a statistical analysis the choice of the time constant of the transition enables to trade off robustness (i.e. the capability to perform pumping cycles while complying with all requirements) against the average power output. With small time constants the scenario without transition strategy is reached in the limit. In this case the aircraft is directly flying into the power zone and due to the significant acceleration the interception of the flight path becomes more challenging. On the other hand, with large time constants the aircraft is following a flight path that is most of the time characterized by a mean elevation angle higher than the target elevation angle. This enables a smoother transition into the path without significant accelerations but reduces the power output significantly. In practice it is important to state the required level of reliability beforehand and then tune the time constant accordingly.

6. How can upset conditions in the context of AWE be defined and systematically

generated if the probability of encountering one per pumping cycle is low in simulations and how can they be predicted and prevented?

Upset conditions in this work are regarded as discrete, binary events. For instance, tether rupture is an upset that leads to the abortion of the pumping cycle operation and in the worst case to a loss of the system. What makes upset conditions in particular challenging in AWE is the way AWE systems are operated. A pumping cycle lasts roughly two minutes which leads to 720 pumping cycles per day. To make AWE systems commercially feasible the probability of an upset needs to be low. Specifically, "low" could be for instance a probability of  $10^{-4}$  of encountering one upset condition per cycle. This corresponds approximately to one upset in two weeks of pumping cycle operation. Trying to achieve an even higher level of reliability requires to design and tune the controller to improve its resilience towards these "rare" failure conditions. Hence a strategy to efficiently generate conditions in which the controller fails is required. Using direct Monte Carlo simulations can be a first approach to tackle this challenge but especially if the computational time to simulate a pumping cycle is high, this approach is limited. Instead, more sophisticated approaches can be used such as the *subset simulation* method utilized in this work. It allows to generate conditions that occur with low probability and in which the controller violates a requirement in a more systematic way. Ultimately, the created counter examples can be used to create a surrogate model that is able to predict these conditions before they lead to an upset. The results show that already simple prediction strategies, optimized based on the generated counter examples, can improve the overall reliability of the AWE system.

In order to trade off false positive and false negative rates a cost function is introduced in this work that is better suited to rank predictor performances than conventional classification measures. It allows to associate an average energy loss rate to each of the two prediction error types and hence weights prediction errors according to their practical impact. The *support vector machine* based predictor achieves the lowest loss in the investigated scenario but more accurate information about the involved parameters in the cost function such as system downtime, repair costs, maintenance costs and so on is required in the future to improve the validity of the loss rate function.

Finally, for well tuned control systems upset conditions occur with low probability which poses the question if accepting upsets is better than preventing them and therefore avoiding any prediction error induced costs. However, the results in this work show that in the long run also rare upset conditions can have an impact on the average power output, hence augmenting AWE baseline control systems with an upset tailored prediction and prevention strategy, such as the one presented in this work, is recommended.

## 7.2. Perspective

In this section possible future research directions are outlined.

### More Realistic Environmental Conditions

In the literature and also in this work it is assumed that the wind speed profile and the wind direction is constant during the pumping cycle operation. This is of course a simplification which needs to be dropped in future analyses. Although it is straightforward to rotate the wind reference frame according to the time varying wind direction (as long as it is measured or estimated) this might lead to transients that can jeopardize the controller reliability, for instance because the target points on the reference paths might jump if the reference path is rotated too quickly. Furthermore, the wind direction can change with altitude (twist). This twist of the wind speed profile could be treated in two ways. First, the reference path is not adapted which means that the crosswind component and hence the harmful part of the wind field is growing which might reduce the reliability of the system as well as the power output. Second, the reference path could be rotated as a function of the twist. This might, however, lead to a more challenging retraction phase control problem, since the retraction phase reference flight path might then also be required to be implemented as a curved path.

### High-level Modification for Improved Robustness

In order to improve the reliability of AWE systems the following system level modifications can be considered. Tether rupture occurs mainly at high airspeed, which could be mitigated through air/speed breaks. The angle of attack requirement is mostly violated if the airspeed drops below a minimum value. This could be mitigated using a backup propulsion system that could be switched on if the airspeed drops below a defined threshold. These threshold limits can be either extracted from the quasi-stationary analysis or from the statistical experiments.

Alternatively, a modification of the radial control objective can be implemented. Instead of using the winch to track a tether force set point it could be used to track an airspeed set point instead. Using limitations on commanded airspeed and angle of attack constraints the created lift and hence ensures that the resulting tether force is not exceeding its critical value. This approach has the advantage that similar to a conventional flight control system not only the attitude but also the speed is explicitly controlled. The downside of tracking an airspeed instead of a tether tension set point is that it requires a reliable communication channel between the aircraft and the ground station.

### Stochastic and Robust Optimization

Optimization routines offer a convenient way to automatize the controller gain design process. One drawback, which is described in detail in this work, is that the optimized controllers can fail if the operating conditions are changed. In this work this is especially the case if the controller is optimized in a deterministic wind field and then verified in turbulent wind conditions. The latter can lead to a significant reduction of the controller reliability. Therefore, as a possible research direction it is recommended to investigate how statistical i.e. robust optimization approaches can be used to optimize the parameters of the AWE control system. A brute force way to do this would be to use again a global optimization method, but instead of treating the output of the cost function as a deterministic value a sample average could be calculated. In this case the samples are generated by evaluating the cost function multiple times with the same parameter vector

but re-sampled uncertainties (e.g. different wind conditions). Naturally, this simple approach increases the required cost function evaluations significantly. Therefore, a more sophisticated approach needs to be found. The ultimate goal is to further automatize the gain design such that the optimized controller is not only robust but also maximizes the average pumping cycle power output.

Alternatively, more sophisticated cost functions can be derived. For instance, it can be shown that by taking into account not only one specific wind speed profile but several profiles can increase the robustness of the optimized controller. Further modifications of the cost function need to put even more emphasize on robustness. This could also include the linear control design step where for instance the structured singular value (SSV) is added to the cost function such that larger SSV values decrease the cost.

### Simulation Models

The presented simulation framework in chapter 5 of this thesis uses models of the AWE system as well as the wind to create, predict and prevent upset conditions. The accuracy of the models is critical in order to be able to project the results to reality. The aircraft model has been validated to some extent as described in [96] and [111] but especially for quick changes in the wind conditions the aerodynamic model is probably too aggressive, since changes in the local flow immediately change the resulting lift force. It is expected that with a more realistic aerodynamic model an additional time delay between changes in the local flow field around the aircraft and the resulting change of the tether force is present which might alter the presented results in the previous chapter. The utilized model in this work can hence be regarded as conservative and it is expected that the prediction accuracy can be further improved with a more realistic model. Testing the framework with a more realistic aircraft model is therefore regarded as another suggestion for future work. This will also allow to investigate further upset conditions related to the structural and aerodynamic integrity of the aircraft. For instance, wind conditions that lead to critical wing bending or severe vibrations can be generated using the SS algorithm and a data-driven predictor such as the SVM predictor can be used to trigger a load and/or vibration alleviation strategy if necessary.

### Launching and Landing

Since in this work only a pumping cycle controller is developed, further research could also include the development of a launching and landing control system which is then combined with the pumping cycle controller. Due to the cascaded control structure the inclusion of a launching and landing controller will be straight forward. Scenarios that need to be investigated are emergency landings, triggered at randomly chosen points during operation, where the pumping cycle is aborted and the aircraft is safely landed.



# Bibliography

- [1] *Aerospace Toolbox*. The MathWorks, Natick, MA, USA. 2018b.
- [2] E. Ahbe, T. A. Wood, and R. S. Smith. “Transverse Contraction-Based Stability Analysis for Periodic Trajectories of Controlled Power Kites with Model Uncertainty”. In: *2018 IEEE Conference on Decision and Control (CDC)*. 2018, pp. 6501–6506. DOI: [10.1109/CDC.2018.8619106](https://doi.org/10.1109/CDC.2018.8619106).
- [3] Uwe Ahrens, Moritz Diehl, and Roland Schmehl, eds. *Airborne Wind Energy*. Green Energy and Technology. Berlin Heidelberg: Springer, 2013. DOI: [10.1007/978-3-642-39965-7](https://doi.org/10.1007/978-3-642-39965-7).
- [4] Altaeros Energies. URL: <http://www.altaerosenergies.com/> (visited on 01/24/2021).
- [5] Ampyx Power B.V. URL: <http://www.ampyxpower.com/> (visited on 01/24/2021).
- [6] Joel A E Andersson et al. “CasADi - A software framework for nonlinear optimization and optimal control”. In: *Mathematical Programming Computation* 11.1 (2019). Ed. by S Forth et al., pp. 1–36. DOI: [10.1007/s12532-018-0139-4](https://doi.org/10.1007/s12532-018-0139-4). URL: [http://link.springer.com/10.1007/978-3-642-30023-3{\\\_}27](http://link.springer.com/10.1007/978-3-642-30023-3{\_}27).
- [7] P. J. Antsaklis, K. M. Passino, and S. J. Wang. “An introduction to autonomous control systems”. In: *IEEE Control Systems Magazine* 11.4 (1991), pp. 5–13. DOI: [10.1109/37.88585](https://doi.org/10.1109/37.88585).
- [8] I. Argatov, P. Rautakorpi, and R. Silvennoinen. “Estimation of the mechanical energy output of the kite wind generator”. In: *Renewable Energy* 34.6 (June 2009), pp. 1525–1532. DOI: [10.1016/j.renene.2008.11.001](https://doi.org/10.1016/j.renene.2008.11.001). URL: <https://doi.org/10.1016/j.renene.2008.11.001>.
- [9] Siu-Kui Au and James L. Beck. “Estimation of small failure probabilities in high dimensions by subset simulation”. In: *Probabilistic Engineering Mechanics* 16.4 (2001), pp. 263–277. ISSN: 0266-8920. DOI: [https://doi.org/10.1016/S0266-8920\(01\)00019-4](https://doi.org/10.1016/S0266-8920(01)00019-4). URL: <http://www.sciencedirect.com/science/article/pii/S0266892001000194>.
- [10] Mark Aull, Andy Stough, and Kelly Cohen. “Design Optimization and Sizing for Fly-Gen Airborne Wind Energy Systems”. In: *Automation* 1.1 (2020), pp. 1–16. ISSN: 2673-4052. DOI: [10.3390/automation1010001](https://doi.org/10.3390/automation1010001). URL: <https://www.mdpi.com/2673-4052/1/1/1>.
- [11] J. H. Baayen and W. J. Ockels. “Tracking control with adaption of kites”. In: *IET Control Theory and Applications* 6.2 (2012), pp. 182–191. DOI: [10.1049/iet-cta.2011.0037](https://doi.org/10.1049/iet-cta.2011.0037).
- [12] D. Barber. *Bayesian Reasoning and Machine Learning*. Cambridge, England: Cambridge University Press, 2012. DOI: <https://doi.org/10.1017/CBO9780511804779>.

- [13] Florian Bauer et al. “On Multicopter-Based Launch and Retrieval Concepts for Lift Mode Operated Power Generating Kites”. In: *Book of Abstracts of the International Airborne Wind Energy Conference 2015*. Ed. by Roland Schmehl. Delft, The Netherlands: Delft University of Technology, June 15–16, 2015, pp. 92–93. ISBN: 978-94-6186-486-4. DOI: [10.4233/uuid:7df59b79-2c6b-4e30-bd58-8454f493bb09](https://doi.org/10.4233/uuid:7df59b79-2c6b-4e30-bd58-8454f493bb09). Presentation video recording available from: <https://collegerama.tudelft.nl/Mediasite/Play/a303417db9114a9f876819208bd889c71d>.
- [14] Randal W. Beard and Timothy W. McLain. *Small Unmanned Aircraft: Theory and Practice*. Princeton, NJ, USA: Princeton University Press, 2012. ISBN: 9780691149219. DOI: [10.1515/9781400840601](https://doi.org/10.1515/9781400840601).
- [15] Morgan Behrel et al. “Performance measurement of a 50-square-meter kite setup on a 13-meter trawler”. In: *La Houille Blanche* (Dec. 2019), pp. 67–69. DOI: [10.1051/lhb/2019036](https://doi.org/10.1051/lhb/2019036).
- [16] Eelke Bontekoe. “Up! How to Launch and Retrieve a Tethered Aircraft”. MA thesis. Delft University of Technology, 2010. URL: <http://resolver.tudelft.nl/uuid:0f79480b-e447-4828-b239-9ec6931bc01f>.
- [17] J. Booth. *A Treatise on Some New Geometrical Methods: The geometrical properties of elliptic integrals, rotatory motion, the higher geometry, and conics derived from the cone, with an appendix to the first volume*. A Treatise on Some New Geometrical Methods. Longmans, Green, Reader, and Dyer, 1873.
- [18] Joseph S. Brinker and Kevin A. Wise. “Stability and flying qualities robustness of a dynamic inversion aircraft control law”. In: *Journal of Guidance, Control, and Dynamics* 19.6 (Nov. 1996), pp. 1270–1277. DOI: [10.2514/3.21782](https://doi.org/10.2514/3.21782). URL: <https://doi.org/10.2514/3.21782>.
- [19] Rudolf Brockhaus, Wolfgang Alles, and Robert Luckner. *Flugregelung*. Berlin Heidelberg: Springer-Verlag, 2011. DOI: [10.1007/978-3-642-01443-7](https://doi.org/10.1007/978-3-642-01443-7).
- [20] Thilo Bronnenmeyer. *Optimal Control for Multi-Kite Emergency Trajectories (MSc thesis)*. Stuttgart, Germany: University of Stuttgart, 2018.
- [21] M. Canale, L. Fagiano, and M. Milanese. “High Altitude Wind Energy Generation Using Controlled Power Kites”. In: *IEEE Transactions on Control Systems Technology* 18.2 (2010), pp. 279–293. ISSN: 1063-6536. DOI: [10.1109/TCST.2009.2017933](https://doi.org/10.1109/TCST.2009.2017933).
- [22] M. Canale et al. “Control of tethered airfoils for a new class of wind energy generator”. In: *Proceedings of the 45th IEEE Conference on Decision and Control*. 2006, pp. 4020–4026. DOI: [10.1109/CDC.2006.376775](https://doi.org/10.1109/CDC.2006.376775).
- [23] Nitesh V. Chawla et al. “SMOTE: Synthetic Minority over-Sampling Technique”. In: *J. Artif. Int. Res.* 16.1 (June 2002), 321–357. ISSN: 1076-9757.
- [24] Antonello Cherubini et al. “Airborne Wind Energy Systems: A review of the technologies”. In: *Renewable and Sustainable Energy Reviews* 51 (2015), pp. 1461–1476. DOI: [10.1016/j.rser.2015.07.053](https://doi.org/10.1016/j.rser.2015.07.053).
- [25] Davide Chicco and Giuseppe Jurman. “The advantages of the Matthews correlation coefficient (MCC) over F1 score and accuracy in binary classification evaluation”. In: *BMC Genomics* 21.1 (Jan. 2020). DOI: [10.1186/s12864-019-6413-7](https://doi.org/10.1186/s12864-019-6413-7).

- [26] M. Cobb et al. “An Iterative Learning Approach for Online Flight path Optimization for Tethered Energy Systems Undergoing Cyclic Spooling Motion”. In: *2019 American Controls Conference (ACC)*. 2019, pp. 2164–2170. DOI: [10.23919/ACC.2019.8814773](https://doi.org/10.23919/ACC.2019.8814773).
- [27] M. Cobb et al. “Iterative Learning-Based Path Optimization for Repetitive Path Planning, with Application to 3-D Crosswind Flight of Airborne Wind Energy Systems”. In: *IEEE Transactions on Control Systems Technology* 28.4 (2019), pp. 1447–1459. DOI: [10.1109/TCST.2019.2912345](https://doi.org/10.1109/TCST.2019.2912345).
- [28] Nello Cristianini and John Shawe-Taylor. “Support Vector Machines”. In: *An Introduction to Support Vector Machines and Other Kernel-based Learning Methods*. Cambridge, England: Cambridge University Press, 2000, 93–124. DOI: [10.1017/CBO9780511801389.008](https://doi.org/10.1017/CBO9780511801389.008).
- [29] Anirban DasGupta. *Asymptotic Theory of Statistics and Probability*. New York, NY: Springer New York, 2008, pp. 91–100. ISBN: 978-0-387-75971-5. DOI: [10.1007/978-0-387-75971-5\\_7](https://doi.org/10.1007/978-0-387-75971-5_7).
- [30] Jochem De Schutter et al. *awebox: Modelling and optimal control of single- and multiple-kite systems for airborne wind energy*. URL: <https://github.com/awebox/awebox> (visited on 07/03/2020).
- [31] Tarek N. Dief et al. “Adaptive Flight Path Control of Airborne Wind Energy Systems”. In: *Energies* 13.3 (Feb. 2020), p. 667. DOI: [10.3390/en13030667](https://doi.org/10.3390/en13030667). URL: <https://doi.org/10.3390/en13030667>.
- [32] M. Diehl. “Real-Time Optimization for Large Scale Nonlinear Processes”. PhD thesis. University of Heidelberg, 2001. URL: <http://archiv.ub.uni-heidelberg.de/volltextserver/1659/>.
- [33] M. Diehl, H. G. Bock, and J. P. Schlöder. “A Real-Time Iteration Scheme for Nonlinear Optimization in Optimal Feedback Control”. In: *SIAM Journal on Control and Optimization* 43.5 (2005), pp. 1714–1736. DOI: [10.1137/S0363012902400713](https://doi.org/10.1137/S0363012902400713). URL: [http://epubs.siam.org/sicon/resource/1/sjcodc/v43/i5/p1714\\_s1](http://epubs.siam.org/sicon/resource/1/sjcodc/v43/i5/p1714_s1).
- [34] Moritz Diehl, Lalo Magni, and Giuseppe De Nicolao. “Efficient NMPC of unstable periodic systems using approximate infinite horizon closed loop costing”. In: *Annual Reviews in Control* 28.1 (2004), pp. 37–45. DOI: [10.1016/j.arcontrol.2004.01.011](https://doi.org/10.1016/j.arcontrol.2004.01.011).
- [35] S. S. Diwale, I. Lympelopoulou, and C. N. Jones. “Optimization of an Airborne Wind Energy system using constrained Gaussian Processes”. In: *2014 IEEE Conference on Control Applications (CCA)*. 2014, pp. 1394–1399. DOI: [10.1109/CCA.2014.6981519](https://doi.org/10.1109/CCA.2014.6981519).
- [36] Geir E. Dullerud and Fernando Paganini. *A Course in Robust Control Theory*. Springer New York, 2000. DOI: [10.1007/978-1-4757-3290-0](https://doi.org/10.1007/978-1-4757-3290-0). URL: <https://doi.org/10.1007/978-1-4757-3290-0>.
- [37] Enerkite GmbH. URL: <http://www.enerkite.com/> (visited on 01/14/2016).

- [38] Dale Enns et al. “Dynamic inversion: an evolving methodology for flight control design”. In: *International Journal of Control* 59.1 (Jan. 1994), pp. 71–91. DOI: [10.1080/00207179408923070](https://doi.org/10.1080/00207179408923070). URL: <https://doi.org/10.1080/00207179408923070>.
- [39] M. Erhard and H. Strauch. “Theory and Experimental Validation of a Simple Comprehensible Model of Tethered Kite Dynamics Used for Controller Design”. In: *Airborne Wind Energy*. Ed. by Uwe Ahrens, Moritz Diehl, and Roland Schmehl. Green Energy and Technology. Berlin Heidelberg: Springer, 2013. Chap. 8, pp. 141–165. DOI: [10.1007/978-3-642-39965-7\\_8](https://doi.org/10.1007/978-3-642-39965-7_8).
- [40] Michael Erhard and Hans Strauch. “Control of Towing Kites for Seagoing Vessels”. In: *IEEE Transactions on Control Systems Technology* 21.5 (2013), pp. 1629–1640. DOI: [10.1109/TCST.2012.2221093](https://doi.org/10.1109/TCST.2012.2221093). arXiv: [1202.3641](https://arxiv.org/abs/1202.3641) [cs.DS].
- [41] Michael Erhard and Hans Strauch. “Flight control of tethered kites in autonomous pumping cycles for airborne wind energy”. In: *Control Engineering Practice* 40 (2015), pp. 13–26. DOI: [10.1016/j.conengprac.2015.03.001](https://doi.org/10.1016/j.conengprac.2015.03.001).
- [42] L. Fagiano and S. Schnez. “On the Take-off of Airborne Wind Energy Systems Based on Rigid Wings”. In: *Renewable Energy* 107 (2015), pp. 473–488. DOI: [10.1016/j.renene.2017.02.023](https://doi.org/10.1016/j.renene.2017.02.023).
- [43] L. Fagiano et al. “Automatic control of tethered wings for airborne wind energy: design and experimental results”. In: *Proceedings of the European Control Conference (ECC13)*. Zurich, Switzerland, July 17–19, 2013. DOI: [10.23919/ECC.2013.6669174](https://doi.org/10.23919/ECC.2013.6669174).
- [44] L. Fagiano et al. “Automatic crosswind flight of tethered wings for airborne wind energy: modeling, control design and experimental results”. In: *IEEE Transactions on Control Systems Technology* 22.4 (2014), pp. 1433–1447. DOI: [10.3182/20140824-6-ZA-1003.01896](https://doi.org/10.3182/20140824-6-ZA-1003.01896).
- [45] L. Fagiano et al. “Automatic crosswind flight of tethered wings for airborne wind energy: modeling, control design and experimental results”. In: *IEEE Transactions on Control Systems Technology* 22.4 (2014), pp. 1433–1447. DOI: [10.3182/20140824-6-ZA-1003.01896](https://doi.org/10.3182/20140824-6-ZA-1003.01896).
- [46] Lorenzo Fagiano et al. “Autonomous Take Off and Flight of a Tethered Aircraft for Airborne Wind Energy”. In: *IEEE transactions on control systems technology* 26.1 (2018), pp. 151–166. DOI: [10.1109/TCST.2017.2661825](https://doi.org/10.1109/TCST.2017.2661825).
- [47] U Fasel et al. “Aerostructural optimization of a morphing wing for airborne wind energy applications”. In: *Smart Materials and Structures* 26.9 (Aug. 2017), p. 095043. DOI: [10.1088/1361-665x/aa7c87](https://doi.org/10.1088/1361-665x/aa7c87). URL: <https://doi.org/10.1088/1361-665x/aa7c87>.
- [48] Urban Fasel et al. “Reduced-Order Dynamic Model of a Morphing Airborne Wind Energy Aircraft”. In: *AIAA Journal* 57.8 (Aug. 2019), pp. 3586–3598. DOI: [10.2514/1.j058019](https://doi.org/10.2514/1.j058019). URL: <https://doi.org/10.2514/1.j058019>.
- [49] U. Fechner et al. “Dynamic Model of a Pumping Kite Power System”. In: *Renewable Energy* 83 (2015), pp. 705–716. DOI: [10.1016/j.renene.2015.04.028](https://doi.org/10.1016/j.renene.2015.04.028). arXiv: [1406.6218](https://arxiv.org/abs/1406.6218) [cs.SY].

- [50] Uwe Fechner. “A Methodology for the Design of Kite-Power Control Systems”. PhD thesis. Delft University of Technology, 2016. DOI: [10.4233 / uuid:85efaf4c-9dce-4111-bc91-7171b9da4b77](https://doi.org/10.4233/uuid:85efaf4c-9dce-4111-bc91-7171b9da4b77).
- [51] Uwe Fechner and Roland Schmehl. “Feed-Forward Control of Kite Power Systems”. In: *Journal of Physics: Conference Series* 524 (June 2014), p. 012081. DOI: [10.1088 / 1742 - 6596 / 524 / 1 / 012081](https://doi.org/10.1088/1742-6596/524/1/012081). URL: <https://doi.org/10.1088/1742-6596/524/1/012081>.
- [52] Uwe Fechner and Roland Schmehl. “Flight Path Control of Kite Power Systems in a Turbulent Wind Environment”. In: *Proceedings of the 2016 American Control Conference (ACC)*. Boston, MA, USA: IEEE, July 6–8, 2016, pp. 4083–4088. DOI: [10.1109/ACC.2016.7525563](https://doi.org/10.1109/ACC.2016.7525563).
- [53] Manuel C.R.M. Fernandes, Luís Tiago Paiva, and Fernando A.C.C. Fontes. “Heading Angle Control for Path-following Guidance with Large Domain of Attraction of a Pumping Kite Generator”. In: *Book of Abstracts of the International Airborne Wind Energy Conference 2019*. Glasgow, United Kingdom: University of Strathclyde, Oct. 15–16, 2019, p. 87. URL: <http://resolver.tudelft.nl/uuid:a9d8f367-f52f-4358-a40e-8bd0977a1a45>.
- [54] Hans Joachim Ferreau et al. “Real-Time Control of a Kite-Model using an Auto-Generated Nonlinear MPC Algorithm”. In: *IFAC Proceedings Volumes* 44.1 (2011). 18th IFAC World Congress, pp. 2488–2493. ISSN: 1474-6670. DOI: <https://doi.org/10.3182/20110828-6-IT-1002.01117>. URL: <http://www.sciencedirect.com/science/article/pii/S147466701643987X>.
- [55] *Flying Qualities of Piloted Airplanes*. U.S. Military Specification MIL-F-8785C. November 5, 1980.
- [56] B. D. Fulcher and N. S. Jones. “Highly Comparative Feature-Based Time-Series Classification”. In: *IEEE Transactions on Knowledge and Data Engineering* 26.12 (2014), pp. 3026–3037. ISSN: 2326-3865. DOI: [10.1109/TKDE.2014.2316504](https://doi.org/10.1109/TKDE.2014.2316504).
- [57] Otto Föllinger. *Regelungstechnik*. 12th ed. Berlin, Germany: VDE Verlag GmbH, 2016. ISBN: 978-3-8007-4201-1.
- [58] “Global Wind Report 2019”. In: *Global Wind Energy Council* (2019).
- [59] Alfred Gray. *Modern Differential Geometry of Curves and Surfaces with Mathematica*. 1st. Boca Raton, FL, USA: CRC Press, Inc., 1996. ISBN: 0849371643.
- [60] Sébastien Gros, Mario Zanon, and Moritz Diehl. “Orbit control for a power generating airfoil based on nonlinear MPC”. In: *2012 American Control Conference (ACC)*. IEEE, 2012, pp. 137–142. DOI: [10.1109/ACC.2012.6315367](https://doi.org/10.1109/ACC.2012.6315367).
- [61] A. Hably, J. Dumon, and G. Smith. “Control of an airborne wind energy system with a Magnus effect”. In: *2016 American Control Conference (ACC)*. 2016, pp. 4978–4983. DOI: [10.1109/ACC.2016.7526142](https://doi.org/10.1109/ACC.2016.7526142).
- [62] Ahmad Hably et al. “Observer-based control of a tethered wing wind power system: indoor real-time experiment”. In: *Proceedings of the 2013 American Control Conference*. Washington, DC, USA, June 17–19, 2013. DOI: [10.1109 / ACC.2013.6580368](https://doi.org/10.1109/ACC.2013.6580368).

- [63] Nikolaus Hansen and Andreas Ostermeier. “Completely Derandomized Self-Adaptation in Evolution Strategies”. In: *Evolutionary Computation* 9.2 (June 2001), pp. 159–195. DOI: [10.1162/106365601750190398](https://doi.org/10.1162/106365601750190398).
- [64] Haocheng Li, D. J. Olinger, and M. A. Demetriou. “Attitude tracking control of an Airborne Wind Energy system”. In: *2015 European Control Conference (ECC)*. 2015, pp. 1510–1515. DOI: [10.1109/ECC.2015.7330752](https://doi.org/10.1109/ECC.2015.7330752).
- [65] Haocheng Li, D. J. Olinger, and M. A. Demetriou. “Control of an airborne wind energy system using an aircraft dynamics model”. In: *2015 American Control Conference (ACC)*. 2015, pp. 2389–2394. DOI: [10.1109/ACC.2015.7171090](https://doi.org/10.1109/ACC.2015.7171090).
- [66] Stefan Haug. “Design of a Kite Launch and Retrieval System For a Pumping High Altitude Wind Power Generator”. MA thesis. University of Stuttgart, 2012. DOI: [10.18419/opus-3936](https://doi.org/10.18419/opus-3936).
- [67] O. Hoegh-Guldberg et al. “The human imperative of stabilizing global climate change at 1.5°C”. In: *Science* 365.6459 (Sept. 2019). DOI: [10.1126/science.aaw6974](https://doi.org/10.1126/science.aaw6974). URL: <https://doi.org/10.1126/science.aaw6974>.
- [68] F. Holzapfel and G. Sachs. “Dynamic Inversion Based Control Concept with Application to an Unmanned Aerial Vehicle”. In: *AIAA Guidance, Navigation, and Control Conference and Exhibit*. Providence, Rhode Island, Aug. 16–19, 2004. DOI: [10.2514/6.2004-4907](https://doi.org/10.2514/6.2004-4907).
- [69] Florian Holzapfel. “Nichtlineare adaptive Regelung eines unbemannten Fluggerätes”. PhD thesis. Technical University of Munich, 2004. URL: <https://mediatum.ub.tum.de/doc/601905/601905.pdf>.
- [70] Florian Holzapfel et al. “Development of a Lateral-Directional Flight Control System for a New Transport Aircraft”. In: *AIAA Guidance, Navigation, and Control Conference and Exhibit*. American Institute of Aeronautics and Astronautics, Aug. 2006. DOI: [10.2514/6.2006-6222](https://doi.org/10.2514/6.2006-6222). URL: <https://doi.org/10.2514/6.2006-6222>.
- [71] Greg Horn, Sébastien Gros, and Moritz Diehl. “Numerical Trajectory Optimization for Airborne Wind Energy Systems Described by High Fidelity Aircraft Models”. In: *Airborne Wind Energy*. Ed. by Uwe Ahrens, Moritz Diehl, and Roland Schmehl. Green Energy and Technology. Berlin Heidelberg: Springer, 2013. Chap. 11, pp. 205–218. DOI: [10.1007/978-3-642-39965-7\\_11](https://doi.org/10.1007/978-3-642-39965-7_11).
- [72] B. Houska and M. Diehl. “Optimal Control for Power Generating Kites”. In: *Proceedings of the European Control Conference (ECC)*. Kos, Greece, 2007, pp. 3560–3567. DOI: [10.23919/ECC.2007.7068861](https://doi.org/10.23919/ECC.2007.7068861).
- [73] Boris Houska and Moritz Diehl. “Robustness and Stability Optimization of Power Generating Kite Systems in a Periodic Pumping Mode”. In: *Proceedings of the IEEE Multi-Conference on Systems and Control*. Yokohama, Japan, Sept. 8–10, 2010, pp. 2172–2177. DOI: [10.1109/CCA.2010.5611288](https://doi.org/10.1109/CCA.2010.5611288).
- [74] K. Hussen et al. *Study on challenges in the commercialisation of airborne wind energy systems*. Tech. rep. PP-05081-2016, prepared by Ecorys BV for the European Commission’s DG Research and Innovation. Brussels, 2018. DOI: [10.2777/87591](https://doi.org/10.2777/87591).

- [75] A. Ilzhöfer, B. Houska, and M. Diehl. “Nonlinear MPC of kites under varying wind conditions for a new class of large-scale wind power generators”. In: *International Journal of Robust and Nonlinear Control* 17.17 (2007), pp. 1590–1599. DOI: [10.1002/rnc.1210](https://doi.org/10.1002/rnc.1210).
- [76] Intergovernmental Panel on Climate Change (IPCC). *Global Warming of 1.5°C. An IPCC Special Report on the impacts of global warming of 1.5°C above pre-industrial levels and related global greenhouse gas emission pathways, in the context of strengthening the global response to the threat of climate change, sustainable development, and efforts to eradicate poverty*. IPCC, 2018. URL: <https://www.ipcc.ch/sr15/>.
- [77] International Renewable Energy Agency. *Climate Change and Renewable Energy: National policies and the role of communities, cities and regions*. Abu Dhabi: International Renewable Energy Agency, 2019. URL: [https://www.irena.org/-/media/Files/IRENA/Agency/Publication/2019/Jun/IRENA\\_G20\\_climate\\_sustainability\\_2019.pdf](https://www.irena.org/-/media/Files/IRENA/Agency/Publication/2019/Jun/IRENA_G20_climate_sustainability_2019.pdf).
- [78] Massimo Ippolito. *KiteGen Carousel*. 2009. URL: <http://www.kitegen.com/en/products/kite-gen-carousel/>.
- [79] Alberto Isidori. *Nonlinear Control Systems*. Springer London, 1995. DOI: [10.1007/978-1-84628-615-5](https://doi.org/10.1007/978-1-84628-615-5). URL: <https://doi.org/10.1007/978-1-84628-615-5>.
- [80] Claudius Jehle and Roland Schmehl. “Applied Tracking Control for Kite Power Systems”. In: *AIAA Journal of Guidance, Control, and Dynamics* 37.4 (2014), pp. 1211–1222. DOI: [10.2514/1.62380](https://doi.org/10.2514/1.62380).
- [81] Eric N. Johnson. “Limited Authority Adaptive Flight Control”. PhD thesis. Georgia Institute of Technology, 2000. URL: <http://hdl.handle.net/1853/12953>.
- [82] B. Karg and S. Lucia. “Learning-based approximation of robust nonlinear predictive control with state estimation applied to a towing kite”. In: *2019 18th European Control Conference (ECC)*. 2019, pp. 16–22. DOI: [10.23919/ECC.2019.8796201](https://doi.org/10.23919/ECC.2019.8796201).
- [83] E. Karlsson et al. “Automatic flight path control of an experimental DA42 general aviation aircraft”. In: *2016 14th International Conference on Control, Automation, Robotics and Vision (ICARCV)*. 2016, pp. 1–6. DOI: [10.1109/ICARCV.2016.7838566](https://doi.org/10.1109/ICARCV.2016.7838566).
- [84] Tomas Kellner. *A Towering Achievement: This Summer In Holland, GE Will Build The World's Largest Wind Turbine*. 2019. URL: <https://www.ge.com/news/reports/towering-achievement-summer-holland-ge-will-build-worlds-largest-wind-turbine>.
- [85] Tomas Kellner. *Making Waves: GE Unveils Plans To Build An Offshore Wind Turbine The Size Of A Skyscraper, The World's Most Powerful*. 2018. URL: <https://www.ge.com/news/reports/making-waves-ge-unveils-plans-build-offshore-wind-turbine-size-skyscraper-worlds-powerful>.
- [86] Kitemill AS. URL: <http://www.kitemill.no/> (visited on 07/16/2015).

- [87] Jonas Koenemann et al. “Modeling of an airborne wind energy system with a flexible tether model for the optimization of landing trajectories”. In: *IFAC-PapersOnLine* 50.1 (2017), pp. 11944–11950. ISSN: 24058963. DOI: [10.1016/j.ifacol.2017.08.1037](https://doi.org/10.1016/j.ifacol.2017.08.1037).
- [88] Jonas Koenemann et al. “OpenOCL-The Open Optimal Control Library”. In: *Airborne Wind Energy Conference 2019*. Glasgow, Scotland, UK, 2019. URL: <https://openocl.org/>.
- [89] Bartosz Krawczyk. “Learning from imbalanced data: open challenges and future directions”. In: *Progress in Artificial Intelligence* 5.4 (2016), pp. 221–232. ISSN: 2192-6360. DOI: [10.1007/s13748-016-0094-0](https://doi.org/10.1007/s13748-016-0094-0). URL: <https://doi.org/10.1007/s13748-016-0094-0>.
- [90] M Kruijff and R Ruiterkamp. “A Roadmap Towards Airborne Wind Energy in the Utility Sector”. In: *Airborne Wind Energy – Advances in Technology Development and Research*. Ed. by R Schmehl. Green Energy and Technology. Singapore: Springer, 2018. Chap. 26, pp. 643–662. DOI: [10.1007/978-981-10-1947-0\\_26](https://doi.org/10.1007/978-981-10-1947-0_26).
- [91] Eugene Lavretsky and Kevin A. Wise. *Robust and adaptive control*. Springer-Verlag London, 2013. ISBN: 978-1-4471-4395-6. DOI: [10.1007/978-1-4471-4396-3](https://doi.org/10.1007/978-1-4471-4396-3).
- [92] R. Leuthold et al. “Operational Regions of a Multi-Kite AWE System”. In: *2018 European Control Conference (ECC)*. 2018, pp. 52–57. DOI: [10.23919/ECC.2018.8550199](https://doi.org/10.23919/ECC.2018.8550199).
- [93] H. Li, D. J. Olinger, and M. A. Demetriou. “Attitude tracking control of a Ground-Gen airborne wind energy system”. In: *2016 American Control Conference (ACC)*. 2016, pp. 4095–4100. DOI: [10.1109/ACC.2016.7525565](https://doi.org/10.1109/ACC.2016.7525565).
- [94] Haocheng Li, David J. Olinger, and Michael A. Demetriou. “Attitude Tracking Control of an Airborne Wind Energy System”. In: *Airborne Wind Energy*. Springer Singapore, 2018, pp. 215–239. DOI: [10.1007/978-981-10-1947-0\\_10](https://doi.org/10.1007/978-981-10-1947-0_10). URL: [https://doi.org/10.1007/978-981-10-1947-0\\_10](https://doi.org/10.1007/978-981-10-1947-0_10).
- [95] G Licitra et al. “Optimal Control for Minimizing Power Consumption During Holding Patterns for Airborne Wind Energy Pumping System”. In: *Proceedings of the European Control Conference (ECC)*. 2016. DOI: [10.1109/ECC.2016.7810515](https://doi.org/10.1109/ECC.2016.7810515).
- [96] Giovanni Licitra. “Identification and Optimization of an Airborne Wind Energy System”. PhD thesis. University of Freiburg, 2018. URL: <https://freidok.uni-freiburg.de/data/16226>.
- [97] Giovanni Licitra et al. “Aerodynamic model identification of an autonomous aircraft for airborne wind energy”. In: *Optimal Control Applications and Methods* 40.3 (Jan. 2019), pp. 422–447. DOI: [10.1002/oca.2485](https://doi.org/10.1002/oca.2485). URL: <https://doi.org/10.1002/oca.2485>.
- [98] Giovanni Licitra et al. “Optimal input design for autonomous aircraft”. In: *Control Engineering Practice* 77 (2018), pp. 15–27. DOI: [10.1016/j.conengprac.2018.04.013](https://doi.org/10.1016/j.conengprac.2018.04.013).

- [99] David Löbl and Florian Holzapfel. “Subset Simulation for Estimating Small Failure Probabilities of an Aerial System Subject to Atmospheric Turbulences”. In: *AIAA Atmospheric Flight Mechanics Conference*. American Institute of Aeronautics and Astronautics, 2015. DOI: [10.2514/6.2015-0236](https://doi.org/10.2514/6.2015-0236).
- [100] J. Löfberg. “YALMIP : a toolbox for modeling and optimization in MATLAB”. In: *2004 IEEE International Conference on Robotics and Automation*. IEEE. DOI: [10.1109/cacsd.2004.1393890](https://doi.org/10.1109/cacsd.2004.1393890). URL: <https://doi.org/10.1109/cacsd.2004.1393890>.
- [101] G. Looye. “Design of Robust Autopilot Control Laws with Nonlinear Dynamic Inversion”. In: *at - Automatisierungstechnik* 49.12/2001 (Jan. 2001). DOI: [10.1524/auto.2001.49.12.523](https://doi.org/10.1524/auto.2001.49.12.523). URL: <https://doi.org/10.1524/auto.2001.49.12.523>.
- [102] Miles L. Loyd. “Crosswind kite power”. In: *Journal of Energy* 4.3 (1980), pp. 106–111. DOI: [10.2514/3.48021](https://doi.org/10.2514/3.48021).
- [103] Miles L. Loyd. “Foreword”. In: *Airborne Wind Energy*. Ed. by Uwe Ahrens, Moritz Diehl, and Roland Schmehl. Green Energy and Technology. Berlin Heidelberg: Springer, 2013. ISBN: 978-3-642-39964-0. DOI: [10.1007/978-3-642-39965-7](https://doi.org/10.1007/978-3-642-39965-7). URL: <http://link.springer.com/10.1007/978-3-642-39965-7>.
- [104] Miles L. Loyd. “Wind driven apparatus for power generation”. U.S. pat. US 4,251,040. 1978.
- [105] Rogelio Lozano et al. “Energy production control of an experimental kite system in presence of wind gusts”. In: *Proceedings of the 2013 IEEE/RSJ International Conference on Intelligent Robots and Systems*. IEEE. Tokyo, Japan, Nov. 3–7, 2013, pp. 2452–2459. DOI: [10.1109/IROS.2013.6696701](https://doi.org/10.1109/IROS.2013.6696701).
- [106] Rolf H. Luchsinger et al. “Closing the Gap: Pumping Cycle Kite Power with Twings”. In: *Book of Abstracts of the International Airborne Wind Energy Conference 2015*. Ed. by Roland Schmehl. Delft, The Netherlands: Delft University of Technology, June 15–16, 2015, pp. 26–28. ISBN: 978-94-6186-486-4. DOI: [10.4233/uuid:7df59b79-2c6b-4e30-bd58-8454f493bb09](https://doi.org/10.4233/uuid:7df59b79-2c6b-4e30-bd58-8454f493bb09). Presentation video recording available from: <https://collegerama.tudelft.nl/Mediasite/Play/646b794e7ac54320ba48ba9f41b-41f811d>.
- [107] Rolf H. Luchsinger et al. “TwingTec’s Roadmap From Full Proof of Concept to the First Commercial Product”. In: *Book of Abstracts of the International Airborne Wind Energy Conference 2019*. Ed. by Roland Schmehl and Oliver Tulloch. Glasgow, United Kingdom: University of Strathclyde, Oct. 15–16, 2019, pp. 103–107. URL: <http://resolver.tudelft.nl/uuid:c5838af6-a0dd-4beeb-b5e7-6c97ef74bd0a>.
- [108] S. Lucia and S. Engell. “Control of towing kites under uncertainty using robust economic nonlinear model predictive control”. In: *2014 European Control Conference (ECC)*. 2014, pp. 1158–1163. DOI: [10.1109/ECC.2014.6862335](https://doi.org/10.1109/ECC.2014.6862335).
- [109] Makani Power. URL: <http://www.makanipower.com/why-airborne-wind/> (visited on 07/11/2012).
- [110] Makani Power Inc. URL: <http://www.makanipower.com> (visited on 07/04/2013).

- [111] Elena C. Malz et al. “A reference model for airborne wind energy systems for optimization and control”. In: *Renewable Energy* 140 (2019), pp. 1004–1011. DOI: [10.1016/j.renene.2019.03.111](https://doi.org/10.1016/j.renene.2019.03.111).
- [112] Toshikazu Motoda. “Simplified Approach to Identifying Influential Uncertainties in Monte Carlo Analysis”. In: *Journal of Spacecraft and Rockets* 41.6 (Nov. 2004), pp. 1071–1075. DOI: [10.2514/1.10265](https://doi.org/10.2514/1.10265). URL: <https://doi.org/10.2514/1.10265>.
- [113] Toshikazu Motoda and Yoshikazu Miyazawa. “Identification of Influential Uncertainties in Monte Carlo Analysis”. In: *Journal of Spacecraft and Rockets* 39.4 (July 2002), pp. 615–623. DOI: [10.2514/2.3851](https://doi.org/10.2514/2.3851). URL: <https://doi.org/10.2514/2.3851>.
- [114] M. Pachter and P. R. Chandler. “Challenges of autonomous control”. In: *IEEE Control Systems Magazine* 18.4 (1998), pp. 92–97. DOI: [10.1109/37.710883](https://doi.org/10.1109/37.710883).
- [115] Jason Papaioannou et al. “MCMC algorithms for Subset Simulation”. In: *Probabilistic Engineering Mechanics* 41 (2015), pp. 89–103. ISSN: 0266-8920. DOI: <https://doi.org/10.1016/j.probengmech.2015.06.006>. URL: <http://www.sciencedirect.com/science/article/pii/S0266892015300205>.
- [116] Sebastian Rapp and Roland Schmehl. “Enhancing Resilience of Airborne Wind Energy Systems Through Upset Condition Avoidance”. In: *Journal of Guidance, Control, and Dynamics* (Nov. 2020), pp. 1–15. DOI: [10.2514/1.g005189](https://doi.org/10.2514/1.g005189). URL: <https://doi.org/10.2514/1.g005189>.
- [117] Sebastian Rapp and Roland Schmehl. “Vertical Takeoff and Landing of Flexible Wing Kite Power Systems”. In: *AIAA Journal of Guidance, Control, and Dynamics* 41.11 (2018), pp. 2386–2400. DOI: [10.2514/1.G003535](https://doi.org/10.2514/1.G003535).
- [118] Sebastian Rapp et al. “A Modular Control Architecture for Airborne Wind Energy Systems”. In: *Proceedings of the AIAA Scitech 2019*. San Diego, California: AIAA, Jan. 7–11, 2019. DOI: [10.2514/6.2019-1419](https://doi.org/10.2514/6.2019-1419).
- [119] Sebastian Rapp et al. “Cascaded Pumping Cycle Control for Rigid Wing Airborne Wind Energy Systems”. In: *AIAA Journal of Guidance, Control, and Dynamics* 42.11 (2019), pp. 2456–2473. DOI: [10.2514/1.G004246](https://doi.org/10.2514/1.G004246).
- [120] Jacob Reiner, Gary J. Balas, and William L. Garrard. “Robust Dynamic Inversion for Control of Highly Maneuverable Aircraft”. In: *Journal of Guidance, Control, and Dynamics* 18.1 (Jan. 1995), pp. 18–24. DOI: [10.2514/3.56651](https://doi.org/10.2514/3.56651). URL: <https://doi.org/10.2514/3.56651>.
- [121] Christian P. Robert and George Casella. *Monte Carlo Statistical Methods (Springer Texts in Statistics)*. Berlin, Heidelberg: Springer-Verlag, 2005. ISBN: 0387212396. DOI: [10.1007/978-1-4757-4145-2](https://doi.org/10.1007/978-1-4757-4145-2).
- [122] *Robust Control of Linear Systems Subject to Uncertain Time-Varying Parameters*. Springer Berlin Heidelberg, 2006. DOI: [10.1007/3-540-33276-6](https://doi.org/10.1007/3-540-33276-6). URL: <https://doi.org/10.1007/3-540-33276-6>.
- [123] N. Rontsis et al. “Improved path following for kites with input delay compensation”. In: *2015 54th IEEE Conference on Decision and Control (CDC)*. 2015, pp. 656–663. DOI: [10.1109/CDC.2015.7402304](https://doi.org/10.1109/CDC.2015.7402304).

- [124] Richard Ruiterkamp and Sören Sieberling. “Description and Preliminary Test Results of a Six Degrees of Freedom Rigid Wing Pumping System”. In: *Airborne Wind Energy*. Ed. by Uwe Ahrens, Moritz Diehl, and Roland Schmehl. Green Energy and Technology. Berlin Heidelberg: Springer, 2013. Chap. 26, pp. 443–458. DOI: [10.1007/978-3-642-39965-7\\_26](https://doi.org/10.1007/978-3-642-39965-7_26).
- [125] Volkan Salma, Felix Friedl, and Roland Schmehl. “Improving reliability and safety of airborne wind energy systems”. In: *Wind Energy* 23.2 (Dec. 2019), pp. 340–356. DOI: [10.1002/we.2433](https://doi.org/10.1002/we.2433).
- [126] Gonzalo Sánchez-Arriaga. *Lagrangian Kite SimulAtors (LAKSA)*. URL: <https://github.com/apastor3/laksa> (visited on 07/03/2020).
- [127] Ramiro Saraiva, Marcelo De Lellis, and Alexandre Trofino. “Passive Phase Design of a Pumping Kite Wind Generator”. In: *IFAC Proceedings Volumes* 47.3 (2014), pp. 6764–6769. ISSN: 14746670. DOI: [10.3182/20140824-6-ZA-1003.01338](https://doi.org/10.3182/20140824-6-ZA-1003.01338). URL: <https://linkinghub.elsevier.com/retrieve/pii/S1474667016426753>.
- [128] Ramiro Saraiva et al. “Dynamics Identification, Filtering and Control Design for Power Kites.” In: *IFAC-PapersOnLine* 50.1 (July 2017), pp. 11938–11943. DOI: [10.1016/j.ifacol.2017.08.1036](https://doi.org/10.1016/j.ifacol.2017.08.1036). URL: <https://doi.org/10.1016/j.ifacol.2017.08.1036>.
- [129] Audrey Schanen et al. “Take-off and landing of an AWE system using a multi-copter”. In: *2020 American Control Conference (ACC)*. IEEE, July 2020. DOI: [10.23919/acc45564.2020.9148035](https://doi.org/10.23919/acc45564.2020.9148035). URL: <https://doi.org/10.23919/acc45564.2020.9148035>.
- [130] Jürgen Scheffran and Antonella Battaglini. “Climate and conflicts: the security risks of global warming”. In: *Regional Environmental Change* 11.S1 (Nov. 2010), pp. 27–39. DOI: [10.1007/s10113-010-0175-8](https://doi.org/10.1007/s10113-010-0175-8). URL: <https://doi.org/10.1007/s10113-010-0175-8>.
- [131] R. Schmehl. *Airborne Wind Energy – An introduction to an emerging technology*. Accessed 30 June 2020. URL: <http://www.awesco.eu/awe-explained/>.
- [132] Roland Schmehl, ed. *Airborne Wind Energy – Advances in Technology Development and Research*. Green Energy and Technology. Singapore: Springer, 2018. DOI: [10.1007/978-981-10-1947-0](https://doi.org/10.1007/978-981-10-1947-0).
- [133] Roland Schmehl. *Rupture of the weak link during a mast-based launch attempt of the V3 kite*. 2020. URL: <https://doi.org/10.5446/46845> (visited on 08/21/2020).
- [134] Roland Schmehl. *Rupture of the weak link during a mast-based launch attempt of the V3 kite*. 2020. URL: <https://doi.org/10.5446/46849>.
- [135] Roland Schmehl and Oliver Tulloch, eds. *Book of Abstracts of the International Airborne Wind Energy Conference 2019*. Glasgow, United Kingdom: University of Strathclyde, Oct. 15–16, 2019, p. 164. DOI: [10.4233/uuid:57fd203c-e069-11e9-9fcb-441ea15f7c9c](https://doi.org/10.4233/uuid:57fd203c-e069-11e9-9fcb-441ea15f7c9c).
- [136] E. Schmidt et al. “In-Flight Estimation of the Aerodynamics of Tethered Wings for Airborne Wind Energy”. In: *IEEE Transactions on Control Systems Technology* 28.4 (2020), pp. 1309–1322. DOI: [10.1109/TCST.2019.2907663](https://doi.org/10.1109/TCST.2019.2907663).

- [137] J. D. Schutter, R. Leuthold, and M. Diehl. “Optimal Control of a Rigid-Wing Rotary Kite System for Airborne Wind Energy”. In: *2018 European Control Conference (ECC)*. 2018, pp. 1734–1739. DOI: [10.23919/ECC.2018.8550383](https://doi.org/10.23919/ECC.2018.8550383).
- [138] Peter Schwartz and Doug Randall. “An abrupt climate change scenario and its implications for United States national security”. In: *Oil, Gas & Energy Law Journal (OGEL)* 2.1 (2004). URL: <https://www.ogel.org/article.asp?key=1135>.
- [139] Robert J. Serfling. *Approximation Theorems of Mathematical Statistics*. New York: Wiley, 2001. ISBN: 0471219274.
- [140] Sigurd Skogestad and Ian Postlethwaite. *Multivariable Feedback Control: Analysis and Design*. Hoboken, NJ, USA: John Wiley and Sons, Inc., 2005. ISBN: 0470011688.
- [141] SkySails GmbH. URL: <http://www.skysails.info/english/company/> (visited on 12/10/2012).
- [142] SkySails GmbH. *SkySails Antrieb für Frachtschiffe*. 2014. URL: <http://www.skysails.info/deutsch/skysails-marine/skysails-antrieb-fuer-frachtschiffe/bedienung/> (visited on 05/30/2016).
- [143] *Statistics and Machine Learning Toolbox*. The MathWorks, Natick, MA, USA. 2018b.
- [144] Julia Sternberg et al. “Robust and Stable Periodic Flight of Power Generating Kite Systems in a Turbulent Wind Flow Field”. In: *Proceedings of the 15th IFAC Workshop on Control Applications of Optimization*. Rimini, Italy: IFAC, Sept. 13–16, 2012. DOI: [10.3182/20120913-4-IT-4027.00009](https://doi.org/10.3182/20120913-4-IT-4027.00009).
- [145] Brian L. Stevens, Frank L. Lewis, and Eric N. Johnson. *Aircraft control and simulation*. 3rd ed. Hoboken, New Jersey: John Wiley & Sons Inc., 2016. ISBN: 978-1-118-87098-3. DOI: [10.1002/9781119174882](https://doi.org/10.1002/9781119174882).
- [146] *The Tallest 20 in 2020: Then and Now*. CTBUH Research Report. Council on Tall Buildings and Urban Habitat, 2020. URL: <https://global.ctbuh.org/resources/papers/download/4304-the-tallest-20-in-2020-then-and-now.pdf>.
- [147] The United Nations. “The Paris Agreement”. In: (2015). URL: [https://unfccc.int/files/essential\\_background/convention/application/pdf/english\\_paris\\_agreement.pdf](https://unfccc.int/files/essential_background/convention/application/pdf/english_paris_agreement.pdf).
- [148] D. Todeschini et al. “Control of vertical take off, dynamic flight and landing of hybrid drones for airborne wind energy systems”. In: *2019 American Control Conference (ACC)*. 2019, pp. 2177–2182. DOI: [10.23919/ACC.2019.8815202](https://doi.org/10.23919/ACC.2019.8815202).
- [149] Davide Todeschini et al. “Control of a Rigid Wing Pumping Airborne Wind Energy System in all Operational Phases”. In: *Control Engineering Practice* (2020). arXiv: [2006.11141](https://arxiv.org/abs/2006.11141) [eess.SY]. URL: <https://arxiv.org/abs/2006.11141>.
- [150] K. C. Toh, M. J. Todd, and R. H. Tütüncü. “SDPT3 — A Matlab software package for semidefinite programming, Version 1.3”. In: *Optimization Methods and Software* 11.1-4 (Jan. 1999), pp. 545–581. DOI: [10.1080/10556789908805762](https://doi.org/10.1080/10556789908805762). URL: <https://doi.org/10.1080/10556789908805762>.
- [151] *UpWind - Design limits and solutions for very large wind turbines*. 2011. URL: [http://www.ewea.org/fileadmin/ewea\\_documents/documents/upwind/21895\\_UpWind\\_Report\\_low\\_web.pdf](http://www.ewea.org/fileadmin/ewea_documents/documents/upwind/21895_UpWind_Report_low_web.pdf).

- [152] U.S. Department of Transportation. *Airplane Flying Handbook*. Federal Aviation Administration, 2016. Chap. 4. URL: [https://www.faa.gov/regulations\\_policies/handbooks\\_manuals/aviation/airplane\\_handbook/media/06\\_afh\\_ch4.pdf](https://www.faa.gov/regulations_policies/handbooks_manuals/aviation/airplane_handbook/media/06_afh_ch4.pdf).
- [153] Kimon P. Valavanis and George J. Vachtsevanos, eds. *Handbook of Unmanned Aerial Vehicles*. Dordrecht: Springer, 2014. DOI: [10.1007/978-90-481-9707-1](https://doi.org/10.1007/978-90-481-9707-1).
- [154] Rolf van der Vlugt, Johannes Peschel, and Roland Schmehl. “Design and Experimental Characterization of a Pumping Kite Power System”. In: *Airborne Wind Energy*. Ed. by Uwe Ahrens, Moritz Diehl, and Roland Schmehl. Green Energy and Technology. Berlin Heidelberg: Springer, 2013. Chap. 23, pp. 403–425. DOI: [10.1007/978-3-642-39965-7\\_23](https://doi.org/10.1007/978-3-642-39965-7_23).
- [155] M. Vukov et al. “Real-time Nonlinear MPC and MHE for a Large-scale Mechatronic Application”. In: *Control Engineering Practice* 45 (2015), pp. 64–78. DOI: <https://doi.org/10.1016/j.conengprac.2015.08.012>.
- [156] Mengmeng Wang et al. “Probabilistic Assessment of a Safety-Critical Backup Controller by Subset Simulation”. In: *AIAA Journal of Guidance, Control, and Dynamics* 42.5 (2019), pp. 1146–1156. DOI: [10.2514/1.g003901](https://doi.org/10.2514/1.g003901).
- [157] P. Williams, B. Lansdorp, and W. J. Ockels. “Nonlinear Control and Estimation of a Tethered Kite in Changing Wind Conditions”. In: *AIAA Journal of Guidance, Control and Dynamics* 31.3 (2008). DOI: [10.2514/1.31604](https://doi.org/10.2514/1.31604).
- [158] “Wind Technologies Market Report”. In: *U.S. Department of Energy* (2018).
- [159] “Wind turbines: How big? - [Opinion]”. In: *IEEE Spectrum* 56.11 (Nov. 2019), pp. 20–20. DOI: [10.1109/mspec.2019.8889907](https://doi.org/10.1109/mspec.2019.8889907). URL: <https://doi.org/10.1109/mspec.2019.8889907>.
- [160] T. A. Wood, H. Hesse, and R. S. Smith. “Predictive Control of Autonomous Kites in Tow Test Experiments”. In: *IEEE Control Systems Letters* 1.1 (2017), pp. 110–115. DOI: [10.1109/LCSYS.2017.2708984](https://doi.org/10.1109/LCSYS.2017.2708984).
- [161] Tony A. Wood et al. “Model-Based Path Planning and Tracking for Tethered Wings”. In: *Proc. of the IEEE Conference on Decision and Control* 54 (2015). DOI: [10.1109/CDC.2015.7403276](https://doi.org/10.1109/CDC.2015.7403276).
- [162] Tony A. Wood et al. “Modeling, Identification, Estimation and Adaptation for the Control of Power-Generating Kites”. In: *Proc. of the 18th IFAC Symposium on System Identification* 51 (2018), pp. 981–989. DOI: [10.1016/j.ifacol.2018.09.066](https://doi.org/10.1016/j.ifacol.2018.09.066).
- [163] Tony A Wood et al. “Predictive guidance control for autonomous kites with input delay”. In: *IFAC-PapersOnLine* 50.1 (2017), pp. 13276–13281. DOI: <https://doi.org/10.1016/j.ifacol.2017.08.1965>.
- [164] World Meteorological Organization. *WMO Statement on the State of the Global Climate in 2018*. World Meteorological Organization, 2019. URL: [https://library.wmo.int/doc\\_num.php?explnum\\_id=5789](https://library.wmo.int/doc_num.php?explnum_id=5789).
- [165] Mario Zanon, Sébastien Gros, and Moritz Diehl. “Model predictive control of rigid-airfoil airborne wind energy systems”. In: *Airborne wind energy*. Springer, 2013, pp. 219–233. DOI: [10.1007/978-3-642-39965-7\\_12](https://doi.org/10.1007/978-3-642-39965-7_12).

- [166] Mario Zanon et al. “Control of Dual-Airfoil Airborne Wind Energy systems based on nonlinear MPC and MHE”. In: *European Control Conference*. Strasbourg, France, July 17–19, 2013, pp. 1801–1806. DOI: [10.1109/ECC.2014.6862238](https://doi.org/10.1109/ECC.2014.6862238).
- [167] A. U. Zraggen, L. Fagiano, and M. Morari. “Automatic Retraction and Full-Cycle Operation for a Class of Airborne Wind Energy Generators”. In: *IEEE Transactions on Control Systems Technology* 24.2 (2016), pp. 594–608. ISSN: 1063-6536. DOI: [10.1109/TCST.2015.2452230](https://doi.org/10.1109/TCST.2015.2452230).
- [168] A. U. Zraggen, L. Fagiano, and M. Morari. “Real-Time Optimization and Adaptation of the Crosswind Flight of Tethered Wings for Airborne Wind Energy”. In: *IEEE Transactions on Control Systems Technology* 23.2 (2015), pp. 434–448. DOI: [10.1109/TCST.2014.2332537](https://doi.org/10.1109/TCST.2014.2332537).
- [169] Aldo U. Zraggen, Lorenzo Fagiano, and Manfred Morari. “Real-Time Optimization and Adaptation of the Crosswind Flight of Tethered Wings for Airborne Wind Energy”. In: *IEEE Transactions on Control Systems Technology* 23.2 (2015), pp. 434–448. DOI: [10.1109/TCST.2014.2332537](https://doi.org/10.1109/TCST.2014.2332537).
- [170] Konstantin M. Zuev. “Subset Simulation Method for Rare Event Estimation: An Introduction”. In: *Encyclopedia of Earthquake Engineering*. Ed. by Michael Beer et al. Berlin, Heidelberg: Springer Berlin Heidelberg, 2021, pp. 1–25. ISBN: 978-3-642-36197-5. DOI: [10.1007/978-3-642-36197-5\\_165-1](https://doi.org/10.1007/978-3-642-36197-5_165-1). URL: [https://doi.org/10.1007/978-3-642-36197-5\\_165-1](https://doi.org/10.1007/978-3-642-36197-5_165-1).

# A

## Appendix

### A.1. Transformation Matrices

Note, all inverse transformations are naturally given by the corresponding transpose of the defined matrices below.

The transformation matrix that transforms a vector from the B into the O frame is given by (see [145, p. 12]):

$$\mathbf{M}_{OB} = \begin{pmatrix} \cos \Psi \cos \Theta & \cos \Psi \sin \Phi \sin \Theta - \cos \Phi \sin \Psi & \sin \Phi \sin \Psi + \cos \Phi \cos \Psi \sin \Theta \\ \cos \Theta \sin \Psi & \cos \Phi \cos \Psi + \sin \Phi \sin \Psi \sin \Theta & \cos \Phi \sin \Psi \sin \Theta - \cos \Psi \sin \Phi \\ -\sin \Theta & \cos \Theta \sin \Phi & \cos \Phi \cos \Theta \end{pmatrix} \quad (\text{A.1})$$

Equivalently, the transformation matrix that transforms a vector from the B into the  $\tau$  frame is given by:

$$\mathbf{M}_{\tau B} = \begin{pmatrix} \cos \Psi_{\tau} \cos \Theta_{\tau} & \cos \Psi_{\tau} \sin \Phi_{\tau} \sin \Theta_{\tau} - \cos \Phi_{\tau} \sin \Psi_{\tau} & \sin \Phi_{\tau} \sin \Psi_{\tau} + \cos \Phi_{\tau} \cos \Psi_{\tau} \sin \Theta_{\tau} \\ \cos \Theta_{\tau} \sin \Psi_{\tau} & \cos \Phi_{\tau} \cos \Psi_{\tau} + \sin \Phi_{\tau} \sin \Psi_{\tau} \sin \Theta_{\tau} & \cos \Phi_{\tau} \sin \Psi_{\tau} \sin \Theta_{\tau} - \cos \Psi_{\tau} \sin \Phi_{\tau} \\ -\sin \Theta_{\tau} & \cos \Theta_{\tau} \sin \Phi_{\tau} & \cos \Phi_{\tau} \cos \Theta_{\tau} \end{pmatrix} \quad (\text{A.2})$$

The transformation matrix that transforms a vector from the B into the A frame is given by (see [145, p. 77]):

$$\mathbf{M}_{AB} = \begin{pmatrix} \cos \alpha_a \cos \beta_a & \sin \beta_a & \sin \alpha_a \cos \beta_a \\ -\cos \alpha_a \sin \beta_a & \cos \beta_a & -\sin \alpha_a \sin \beta_a \\ -\sin \alpha_a & 0 & \cos \alpha_a \end{pmatrix} \quad (\text{A.3})$$

Equivalently, the transformation of a vector from the B into the  $\bar{K}$  frame is given by:

$$\mathbf{M}_{\bar{K}B} = \begin{pmatrix} \cos \alpha_k \cos \beta_k & \sin \beta_k & \sin \alpha_k \cos \beta_k \\ -\cos \alpha_k \sin \beta_k & \cos \beta_k & -\sin \alpha_k \sin \beta_k \\ -\sin \alpha_k & 0 & \cos \alpha_k \end{pmatrix} \quad (\text{A.4})$$

The transformation matrix that transforms a vector from the  $\bar{K}$  into the K frame is simply given by a rotation around the  $x_K$  axis:

$$\mathbf{M}_{K\bar{K}} = \begin{pmatrix} 1 & 0 & 0 \\ 0 & \cos \mu_k & -\sin \mu_k \\ 0 & \sin \mu_k & \cos \mu_k \end{pmatrix} \quad (\text{A.5})$$

Equivalently, the transformation matrix that transforms a vector from the  $K^*$  into the K frame is given by:

$$\mathbf{M}_{KK^*} = \begin{pmatrix} 1 & 0 & 0 \\ 0 & \cos \mu^* & -\sin \mu^* \\ 0 & \sin \mu^* & \cos \mu^* \end{pmatrix} \quad (\text{A.6})$$

The transformation matrix that transforms a vector from the A into the  $\bar{A}$  (note that the  $\bar{A}$  frame is defined analogously to the K frame) frame is given by:

$$\mathbf{M}_{\bar{A}A} = \begin{pmatrix} 1 & 0 & 0 \\ 0 & \cos \mu_a & -\sin \mu_a \\ 0 & \sin \mu_a & \cos \mu_a \end{pmatrix} \quad (\text{A.7})$$

The transformation matrix that transforms a vector from the W into the  $\tau$  frame is equivalent to the transformation matrix between the earth-centered-earth-fixed frame and the O frame (see [145, p. 31]):

$$\mathbf{M}_{\tau W} = \begin{pmatrix} -\sin \phi \cos \lambda & -\sin \phi \sin \lambda & \cos \phi \\ -\sin \lambda & \cos \lambda & 0 \\ -\cos \phi \cos \lambda & -\cos \phi \sin \lambda & -\sin \phi \end{pmatrix} \quad (\text{A.8})$$

The transformation matrix that transforms a vector from the W into the O frame is given by:

$$\mathbf{M}_{OW} = \begin{pmatrix} \cos \xi & \sin \xi & 0 \\ \sin \xi & -\cos \xi & 0 \\ 0 & 0 & -1 \end{pmatrix} \quad (\text{A.9})$$

where  $\xi$  is the wind direction measured from the  $x_O$  axis.

The transformation matrix that transforms a vector from the O to the K frame is given by (see [19, p. 58]):

$$\mathbf{M}_{KO} = \begin{pmatrix} \cos \chi_k \cos \gamma_k & \sin \chi_k \cos \gamma_k & -\sin \gamma_k \\ -\sin \chi_k & \cos \chi_k & 0 \\ \cos \chi_k \sin \gamma_k & \sin \chi_k \sin \gamma_k & \cos \gamma_k \end{pmatrix} \quad (\text{A.10})$$

Equivalently, the transformation matrix that transforms a vector from the  $\tau$  to the  $K^*$  frame is given by:

$$\mathbf{M}_{K^*\tau} = \begin{pmatrix} \cos \chi_\tau \cos \gamma_\tau & \sin \chi_\tau \cos \gamma_\tau & -\sin \gamma_\tau \\ -\sin \chi_\tau & \cos \chi_\tau & 0 \\ \cos \chi_\tau \sin \gamma_\tau & \sin \chi_\tau \sin \gamma_\tau & \cos \gamma_\tau \end{pmatrix} \quad (\text{A.11})$$

Equivalently, the transformation matrix that transforms a vector from the O to the  $\bar{A}$  frame is given by:

$$\mathbf{M}_{\bar{A}O} = \begin{pmatrix} \cos \chi_a \cos \gamma_a & \sin \chi_a \cos \gamma_a & -\sin \gamma_a \\ -\sin \chi_a & \cos \chi_a & 0 \\ \cos \chi_a \sin \gamma_a & \sin \chi_a \sin \gamma_a & \cos \gamma_a \end{pmatrix} \quad (\text{A.12})$$

## A.2. State-space Models for Control Design

### A.2.1. Traction Phase Longitudinal Dynamics

The state-space model at  $p_1$  is given by:

$$\begin{pmatrix} \dot{v}_a \\ \dot{\alpha}_a \\ \dot{\Theta}_\tau \\ \dot{q} \\ \dot{e}_{i,\alpha} \end{pmatrix} = \begin{pmatrix} -0.45 & 33.11 & -48.17 & -0.42 & 0 \\ -0.13 & -4.59 & 0.12 & 0.90 & 0 \\ 0 & -0.01 & 0.01 & 0.99 & 0 \\ -0.01 & -15.68 & 0 & -2.68 & 0 \\ 0 & -1.00 & 0 & 0 & 0 \end{pmatrix} \begin{pmatrix} v_a \\ \alpha_a \\ \Theta_\tau \\ q \\ \int_0^t e_\alpha d\tau \end{pmatrix} + \begin{pmatrix} -1.70 \\ -0.42 \\ 0 \\ -24.56 \\ 0 \end{pmatrix} \delta_e + \begin{pmatrix} 0 \\ 0 \\ 0 \\ 0 \\ 1 \end{pmatrix} \alpha_{a,c} \quad (\text{A.13})$$

The state-space model at  $p_2$  is given by:

$$\begin{pmatrix} \dot{v}_a \\ \dot{\alpha}_a \\ \dot{\Theta}_\tau \\ \dot{q} \\ \dot{e}_{i,\alpha} \end{pmatrix} = \begin{pmatrix} -0.50 & 40.27 & -58.82 & -0.47 & 0 \\ -0.13 & -5.07 & 0.13 & 0.90 & 0 \\ 0 & -0.0 & 0.01 & 0.99 & 0 \\ -0.01 & -19.09 & 0 & -2.96 & 0 \\ 0 & -1.0 & 0 & 0 & 0 \end{pmatrix} \begin{pmatrix} v_a \\ \alpha_a \\ \Theta_\tau \\ q \\ \int_0^t e_\alpha d\tau \end{pmatrix} + \begin{pmatrix} -2.07 \\ -0.46 \\ 0 \\ -29.90 \\ 0 \end{pmatrix} \delta_e + \begin{pmatrix} 0 \\ 0 \\ 0 \\ 0 \\ 1 \end{pmatrix} \alpha_{a,c} \quad (\text{A.14})$$

The state-space model at  $p_3$  is given by:

$$\begin{pmatrix} \dot{v}_a \\ \dot{\alpha}_a \\ \dot{\Theta}_\tau \\ \dot{q} \\ \dot{e}_{i,\alpha} \end{pmatrix} = \begin{pmatrix} -0.43 & 34.19 & -53.9 & -0.42 & 0 \\ -0.11 & -6.00 & 0.10 & 0.90 & 0 \\ 0.003 & -0.01 & 0.01 & 0.99 & 0 \\ -0.01 & -19.4 & 0 & -3.06 & 0 \\ 0 & -1 & 0 & 0 & 0 \end{pmatrix} \begin{pmatrix} v_a \\ \alpha_a \\ \Theta_\tau \\ q \\ \int_0^t e_\alpha d\tau \end{pmatrix} + \begin{pmatrix} -1.71 \\ -0.48 \\ 0 \\ -31.9 \\ 0 \end{pmatrix} \delta_e + \begin{pmatrix} 0 \\ 0 \\ 0 \\ 0 \\ 1 \end{pmatrix} \alpha_{a,c} \quad (\text{A.15})$$

The state-space model at  $p_4$  is given by:

$$\begin{pmatrix} \dot{v}_a \\ \dot{\alpha}_a \\ \dot{\Theta}_\tau \\ \dot{q} \\ \dot{e}_{i,\alpha} \end{pmatrix} = \begin{pmatrix} -0.40 & 31.690 & -49.01 & -0.37 & 0 \\ -0.09 & -7.20 & 0.07 & 0.90 & 0 \\ 0 & -0.01 & 0.01 & 0.99 & 0 \\ -0.01 & -20.91 & 0 & -3.22 & 0 \\ 0 & -1.0 & 0 & 0 & 0 \end{pmatrix} \begin{pmatrix} v_a \\ \alpha_a \\ \Theta_\tau \\ q \\ \int_0^t e_\alpha d\tau \end{pmatrix} + \begin{pmatrix} -1.33 \\ -0.51 \\ 0 \\ -35.51 \\ 0 \end{pmatrix} \delta_e + \begin{pmatrix} 0 \\ 0 \\ 0 \\ 0 \\ 1 \end{pmatrix} \alpha_{a,c} \quad (\text{A.16})$$

The state-space model at  $p_5$  is given by:

$$\begin{pmatrix} \dot{v}_a \\ \dot{\alpha}_a \\ \dot{\Theta}_\tau \\ \dot{q} \\ \dot{e}_{i,\alpha} \end{pmatrix} = \begin{pmatrix} -0.45 & 38.50 & -59.92 & -0.41 & 0 \\ -0.09 & -7.95 & 0.08 & 0.90 & 0 \\ 0 & -0.010.01 & 0.99 & 0 & 0 \\ -0.01 & -25.48 & 0 & -3.56 & 0 \\ 0 & -1.00 & 0 & 0 & 0 \end{pmatrix} \begin{pmatrix} v_a \\ \alpha_a \\ \Theta_\tau \\ q \\ \int_0^t e_\alpha d\tau \end{pmatrix} + \begin{pmatrix} -1.6300 \\ -0.5700 \\ 0 \\ -43.2600 \\ 0 \end{pmatrix} \delta_e + \begin{pmatrix} 0 \\ 0 \\ 0 \\ 0 \\ 1 \end{pmatrix} \alpha_{a,c} \quad (\text{A.17})$$

### A.2.2. Traction Phase Lateral Dynamics

The state-space model at  $p_1$  is given by:

$$\begin{aligned}
 \begin{pmatrix} \dot{\beta}_a \\ \dot{\Phi}_\tau \\ \dot{p} \\ \dot{r} \\ \dot{e}_{i,\beta} \\ \dot{e}_{i,\Phi_\tau} \end{pmatrix} &= \begin{pmatrix} -0.35 & 1.79 & 0.16 & -0.96 & 0 & 0 \\ -0.07 & 0 & 1.00 & 0.10 & 0 & 0 \\ -19.16 & 0 & -17.27 & 9.11 & 0 & 0 \\ 5.78 & 0 & -3.10 & -0.60 & 0 & 0 \\ -1.00 & 0 & 0 & 0 & 0 & 0 \\ 0 & -1.00 & 0 & 0 & 0 & 0 \end{pmatrix} \begin{pmatrix} \beta_a \\ \Phi_\tau \\ p \\ r \\ e_{i,\beta} \\ e_{i,\Phi_\tau} \end{pmatrix} \\
 &+ \begin{pmatrix} -0.07 & 0.14 \\ 0 & 0 \\ -75.44 & 1.19 \\ -0.77 & -5.69 \\ 0 & 0 \\ 0 & 0 \end{pmatrix} \begin{pmatrix} \delta_a \\ \delta_r \end{pmatrix} + \begin{pmatrix} 0 & 0 \\ 0 & 0 \\ 0 & 0 \\ 0 & 0 \\ 1 & 0 \\ 0 & 1 \end{pmatrix} \begin{pmatrix} \beta_{a,c} \\ \Phi_{\tau,c} \end{pmatrix}
 \end{aligned} \tag{A.18}$$

The state-space model at  $p_2$  is given by:

$$\begin{aligned}
 \begin{pmatrix} \dot{\beta}_a \\ \dot{\Phi}_\tau \\ \dot{p} \\ \dot{r} \\ \dot{e}_{i,\beta} \\ \dot{e}_{i,\Phi_\tau} \end{pmatrix} &= \begin{pmatrix} -0.39 & 1.97 & 0.16 & -0.96 & 0 & 0 \\ -0.08 & 0 & 1.00 & 0.09 & 0 & 0 \\ -23.32 & 0 & -19.06 & 10.05 & 0 & 0 \\ 7.03 & 0 & -3.42 & -0.67 & 0 & 0 \\ -1.00 & 0 & 0 & 0 & 0 & 0 \\ 0 & -1.00 & 0 & 0 & 0 & 0 \end{pmatrix} \begin{pmatrix} \beta_a \\ \Phi_\tau \\ p \\ r \\ e_{i,\beta} \\ e_{i,\Phi_\tau} \end{pmatrix} \\
 &+ \begin{pmatrix} -0.08 & 0.16 \\ 0 & 0 \\ -91.85 & 1.45 \\ -0.94 & -6.93 \\ 0 & 0 \\ 0 & 0 \end{pmatrix} \begin{pmatrix} \delta_a \\ \delta_r \end{pmatrix} + \begin{pmatrix} 0 & 0 \\ 0 & 0 \\ 0 & 0 \\ 0 & 0 \\ 1 & 0 \\ 0 & 1 \end{pmatrix} \begin{pmatrix} \beta_{a,c} \\ \Phi_{\tau,c} \end{pmatrix}
 \end{aligned} \tag{A.19}$$

The state-space model at  $p_3$  is given by:

$$\begin{aligned}
 \begin{pmatrix} \dot{\beta}_a \\ \dot{\Phi}_\tau \\ \dot{p} \\ \dot{r} \\ \dot{e}_{i,\beta} \\ \dot{e}_{i,\Phi_\tau} \end{pmatrix} &= \begin{pmatrix} -0.40 & 1.76 & 0.11 & -0.97 & 0 & 0 \\ -0.08 & 0 & 1 & 0.04 & 0 & 0 \\ -24.7 & 0 & -19.6 & 9.14 & 0 & 0 \\ 8.19 & 0 & -2.77 & -0.72 & 0 & 0 \\ -1 & 0 & 0 & 0 & 0 & 0 \\ 0 & -1 & 0 & 0 & 0 & 0 \end{pmatrix} \begin{pmatrix} \beta_a \\ \Phi_\tau \\ p \\ r \\ e_{i,\beta} \\ e_{i,\Phi_\tau} \end{pmatrix} \\
 &+ \begin{pmatrix} -0.08 & 0.16 \\ 0 & 0 \\ -97.9 & 1.55 \\ 0.06 & -7.3 \\ 0 & 0 \\ 0 & 0 \end{pmatrix} \begin{pmatrix} \delta_a \\ \delta_r \end{pmatrix} + \begin{pmatrix} 0 & 0 \\ 0 & 0 \\ 0 & 0 \\ 0 & 0 \\ 1 & 0 \\ 0 & 1 \end{pmatrix} \begin{pmatrix} \beta_{a,c} \\ \Phi_{\tau,c} \end{pmatrix}
 \end{aligned} \tag{A.20}$$

The state-space model at  $p_4$  is given by:

$$\begin{aligned}
 \begin{pmatrix} \dot{\beta}_a \\ \dot{\Phi}_\tau \\ \dot{p} \\ \dot{r} \\ \dot{e}_{i,\beta} \\ \dot{e}_{i,\Phi_\tau} \end{pmatrix} &= \begin{pmatrix} -0.42 & 1.51 & 0.06 & -0.97 & 0 & 0 \\ -0.08 & 0.01 & 1.00 & -0.01 & 0 & 0 \\ -27.33 & 0 & -20.66 & 8.35 & 0 & 0 \\ 9.89 & 0 & -2.13 & -0.80 & 0 & 0 \\ -1.00 & 0 & 0 & 0 & 0 & 0 \\ 0 & -1.00 & 0 & 0 & 0 & 0 \end{pmatrix} \begin{pmatrix} \beta_a \\ \Phi_\tau \\ p \\ r \\ e_{i,\beta} \\ e_{i,\Phi_\tau} \end{pmatrix} \\
 &+ \begin{pmatrix} -0.08 & 0.17 \\ 0 & 0 \\ -108.69 & 1.74 \\ 1.24 & -8.00 \\ 0 & 0 \\ 0 & 0 \end{pmatrix} \begin{pmatrix} \delta_a \\ \delta_r \end{pmatrix} + \begin{pmatrix} 0 & 0 \\ 0 & 0 \\ 0 & 0 \\ 0 & 0 \\ 1 & 0 \\ 0 & 1 \end{pmatrix} \begin{pmatrix} \beta_{a,c} \\ \Phi_{\tau,c} \end{pmatrix}
 \end{aligned} \tag{A.21}$$

The state-space model at  $p_5$  is given by:

$$\begin{aligned}
 \begin{pmatrix} \dot{\beta}_a \\ \dot{\Phi}_\tau \\ \dot{p} \\ \dot{r} \\ \dot{e}_{i,\beta} \\ \dot{e}_{i,\Phi_\tau} \end{pmatrix} &= \begin{pmatrix} -0.47 & 1.67 & 0.06 & -0.97 & 0 & 0 \\ -0.09 & 0.01 & 1.00 & -0.02 & 0 & 0 \\ -33.30 & 0 & -22.80 & 9.22 & 0 & 0 \\ 12.05 & 0 & -2.35 & -0.8800 & 0 & 0 \\ -1.00 & 0 & 0 & 0 & 0 & 0 \\ 0 & -1.00 & 0 & 0 & 0 & 0 \end{pmatrix} \begin{pmatrix} \beta_a \\ \Phi_\tau \\ p \\ r \\ e_{i,\beta} \\ e_{i,\Phi_\tau} \end{pmatrix} \\
 &+ \begin{pmatrix} -0.09 & 0.19 \\ 0 & 0 \\ -132.42 & 2.11 \\ 1.51 & -9.75 \\ 0 & 0 \\ 0 & 0 \end{pmatrix} \begin{pmatrix} \delta_a \\ \delta_r \end{pmatrix} + \begin{pmatrix} 0 & 0 \\ 0 & 0 \\ 0 & 0 \\ 0 & 0 \\ 1 & 0 \\ 0 & 1 \end{pmatrix} \begin{pmatrix} \beta_{a,c} \\ \Phi_{\tau,c} \end{pmatrix}
 \end{aligned} \tag{A.22}$$

### A.2.3. Retraction Phase Longitudinal Dynamics

The state-space model at  $p_1$  is given by:

$$\begin{aligned}
 \begin{pmatrix} \dot{v}_a \\ \dot{\alpha}_a \\ \dot{\Theta} \\ \dot{q} \\ \dot{e}_{i,\alpha} \end{pmatrix} &= \begin{pmatrix} -0.18 & 41.05 & -15.81 & -0.2 & 0 \\ -0.02 & -11.21 & 0.25 & 0.9 & 0 \\ 0 & 0 & 0 & 1 & 0 \\ 0 & -27.16 & 0 & -3.69 & 0 \\ 0 & -1.0 & 0 & 0 & 0 \end{pmatrix} \begin{pmatrix} v_a \\ \alpha_a \\ \Theta \\ q \\ \int_0^t e_\alpha d\tau \end{pmatrix} + \begin{pmatrix} 0.25 \\ -0.59 \\ 0 \\ -46.63 \\ 0 \end{pmatrix} \delta_e + \begin{pmatrix} 0 \\ 0 \\ 0 \\ 0 \\ 1 \end{pmatrix} \alpha_{a,c}
 \end{aligned} \tag{A.23}$$

The state-space model at  $p_2$  is given by:

$$\begin{aligned}
 \begin{pmatrix} \dot{v}_a \\ \dot{\alpha}_a \\ \dot{\Theta} \\ \dot{q} \\ \dot{e}_{i,\alpha} \end{pmatrix} &= \begin{pmatrix} -0.15 & 29.45 & -14.19 & -0.18 & 0 \\ -0.02 & -9.43 & 0.22 & 0.90 & 0 \\ 0 & 0 & 0 & 1 & 0 \\ 0 & -19.87 & 0 & -3.16 & 0 \\ 0 & -1 & 0 & 0 & 0 \end{pmatrix} \begin{pmatrix} v_a \\ \alpha_a \\ \Theta \\ q \\ \int_0^t e_\alpha d\tau \end{pmatrix} + \begin{pmatrix} 0.09 \\ -0.51 \\ 0 \\ -34.2 \\ 0 \end{pmatrix} \delta_e + \begin{pmatrix} 0 \\ 0 \\ 0 \\ 0 \\ 1 \end{pmatrix} \alpha_{a,c}
 \end{aligned} \tag{A.24}$$

The state-space model at  $p_3$  is given by:

$$\begin{pmatrix} \dot{v}_a \\ \dot{\alpha}_a \\ \dot{\Theta} \\ \dot{q} \\ \dot{e}_{i,\alpha} \end{pmatrix} = \begin{pmatrix} -0.13 & 22.92 & -13.27 & -0.17 & 0 \\ -0.02 & -8.26 & 0.19 & 0.90 & 0 \\ 0 & 0 & 0 & 1 & 0 \\ 0 & -15.74 & 0 & -2.82 & 0 \\ 0 & -1 & 0 & 0 & 0 \end{pmatrix} \begin{pmatrix} v_a \\ \alpha_a \\ \Theta \\ q \\ \int_0^t e_\alpha d\tau \end{pmatrix} + \begin{pmatrix} 0 \\ -0.45 \\ 0 \\ -27.15 \\ 0 \end{pmatrix} \delta_e + \begin{pmatrix} 0 \\ 0 \\ 0 \\ 0 \\ 1 \end{pmatrix} \alpha_{a,c} \quad (\text{A.25})$$

#### A.2.4. Retraction Phase Lateral Dynamics

The state-space model at  $p_1$  is given by:

$$\begin{pmatrix} \dot{\beta}_a \\ \dot{\Phi} \\ \dot{p} \\ \dot{r} \\ \dot{e}_{i,\beta} \\ \dot{e}_{i,\Phi} \end{pmatrix} = \begin{pmatrix} -0.35 & 0.39 & -0.07 & -0.98 & 0 & 0 \\ 0 & 0 & 1.0 & -0.13 & 0 & 0 \\ -20.85 & 0 & -17.94 & 4.7 & 0 & 0 \\ 9.1 & 0 & -0.27 & -0.77 & 0 & 0 \\ -1.0 & 0 & 0 & 0 & 0 & 0 \\ 0 & -1.0 & 0 & 0 & 0 & 0 \end{pmatrix} \begin{pmatrix} \beta_a \\ \Phi \\ p \\ r \\ e_{i,\beta} \\ e_{i,\Phi} \end{pmatrix} + \begin{pmatrix} -0.07 & 0.15 \\ 0 & 0 \\ -82.76 & 1.38 \\ 3.04 & -5.91 \\ 0 & 0 \\ 0 & 0 \end{pmatrix} \begin{pmatrix} \delta_a \\ \delta_r \end{pmatrix} + \begin{pmatrix} 0 & 0 \\ 0 & 0 \\ 0 & 0 \\ 0 & 0 \\ 1 & 0 \\ 0 & 1 \end{pmatrix} \begin{pmatrix} \beta_{a,c} \\ \Phi_c \end{pmatrix} \quad (\text{A.26})$$

The state-space model at  $p_2$  is given by:

$$\begin{aligned}
 \begin{pmatrix} \dot{\beta}_a \\ \dot{\Phi} \\ \dot{p} \\ \dot{r} \\ \dot{e}_{i,\beta} \\ \dot{e}_{i,\Phi} \end{pmatrix} &= \begin{pmatrix} -0.39 & 0.35 & -0.07 & -0.98 & 0 & 0 \\ 0 & 0 & 1.0 & -0.14 & 0 & 0 \\ -26.28 & 0 & -20.13 & 5.07 & 0 & 0 \\ 11.61 & 0 & -0.18 & -0.87 & 0 & 0 \\ -1.0 & 0 & 0 & 0 & 0 & 0 \\ 0 & -1.0 & 0 & 0 & 0 & 0 \end{pmatrix} \begin{pmatrix} \beta_a \\ \Phi \\ p \\ r \\ e_{i,\beta} \\ e_{i,\Phi} \end{pmatrix} \\
 &+ \begin{pmatrix} -0.08 & 0.16 \\ 0 & 0 \\ -104.24 & 1.75 \\ 4.02 & -7.42 \\ 0 & 0 \\ 0 & 0 \end{pmatrix} \begin{pmatrix} \delta_a \\ \delta_r \end{pmatrix} + \begin{pmatrix} 0 & 0 \\ 0 & 0 \\ 0 & 0 \\ 0 & 0 \\ 1 & 0 \\ 0 & 1 \end{pmatrix} \begin{pmatrix} \beta_{a,c} \\ \Phi_c \end{pmatrix}
 \end{aligned} \tag{A.27}$$

The state-space model at  $p_3$  is given by:

$$\begin{aligned}
 \begin{pmatrix} \dot{\beta}_a \\ \dot{\Phi} \\ \dot{p} \\ \dot{r} \\ \dot{e}_{i,\beta} \\ \dot{e}_{i,\Phi} \end{pmatrix} &= \begin{pmatrix} -0.46 & 0.32 & -0.08 & -0.98 & 0 & 0 \\ 0 & 0 & 1.0 & -0.16 & 0 & 0 \\ -35.85 & 0 & -23.49 & 5.69 & 0 & 0 \\ 16.04 & 0 & -0.06 & -1.02 & 0 & 0 \\ -1.0 & 0 & 0 & 0 & 0 & 0 \\ 0 & -1.0 & 0 & 0 & 0 & 0 \end{pmatrix} \begin{pmatrix} \beta_a \\ \Phi \\ p \\ r \\ e_{i,\beta} \\ e_{i,\Phi} \end{pmatrix} \\
 &+ \begin{pmatrix} -0.10 & 0.19 \\ 0 & 0 \\ -142.08 & 2.39 \\ 5.74 & -10.1 \\ 0 & 0 \\ 0 & 0 \end{pmatrix} \begin{pmatrix} \delta_a \\ \delta_r \end{pmatrix} + \begin{pmatrix} 0 & 0 \\ 0 & 0 \\ 0 & 0 \\ 0 & 0 \\ 1 & 0 \\ 0 & 1 \end{pmatrix} \begin{pmatrix} \beta_{a,c} \\ \Phi_c \end{pmatrix}
 \end{aligned} \tag{A.28}$$

### A.3. Cost Function Terms

The cost terms in the optimization algorithm are defined and calculated as follows. The average pumping cycle power is simply given by the sample average:

$$\bar{P}_{\text{mech}} = \frac{1}{n} \sum_{i=1}^N P_{i,\text{mech}} \quad (\text{A.29})$$

where  $N$  is the number of samples and  $P_{i,\text{mech}}$  is the current mechanical power of sample  $i$ . The angle of attack penalty is calculated according to:

$$c_{\alpha} = p_{\alpha} \max \left( \max \left( \frac{\alpha_a}{\alpha_{a,\text{max}}} - 1, 0 \right) \right) \quad (\text{A.30})$$

In this form the angle of attack is penalized whenever it exceeds a defined maximum angle  $\alpha_{a,\text{max}}$  (here  $12^\circ$ ). Note, only the peaks are taken in one simulation run (holds for all penalties). Furthermore,  $p_{\alpha} = 10^5$ . Similarly, the penalty for the tether force peak is defined:

$$c_{F_t} = p_F \max \left( \max \left( \frac{F_t}{F_{t,\text{max}}} - 1, 0 \right) \right) \quad (\text{A.31})$$

with  $p_F = 10^4$  and  $F_{t,\text{max}} = 2160$  N. The sideslip angle is penalized according to:

$$c_{\beta} = p_{\beta} \max \left( \max \left( \frac{\beta_a}{\beta_{a,\text{max}}} - 1, 0 \right) \right) \quad (\text{A.32})$$

with  $p_{\beta} = 10^4$  and  $\beta_{a,\text{max}} = 20^\circ$ . Large path-following errors during the traction phase are penalized according to:

$$c_{e_{p,t}} = p_{e_{p,t}} \max \left( \max \left( \frac{e_{p,t}}{e_{p,t,\text{max}}} - 1, 0 \right) \right) \quad (\text{A.33})$$

where  $e_{p,t}$  is the path-following error during the traction phase and with  $p_{e_{p,t}} = 10^4$  and  $e_{p,t} = 60$  m. Large path-following errors during the retraction phase are penalized according to:

$$c_{e_{p,r}} = p_{e_{p,r}} \max \left( \max \left( \frac{e_{p,r}}{e_{p,r,\text{max}}} - 1, 0 \right) \right) \quad (\text{A.34})$$

where  $e_{p,r}$  is the path-following error during the retraction phase and with  $p_{e_{p,r}} = 10^4$  and  $e_{p,r} = 60$  m. Large tether force tracking errors  $e_{F_t}$  are penalized according to:

$$c_{e_{F_t}} = \max(F_t) \max \left( \max \left( \frac{e_{F_t}}{e_{F_t,\text{max}}} - 1, 0 \right) \right) \quad (\text{A.35})$$

with  $e_{F_t,\text{max}} = 100$  N.

### A.4. Asymptotic Confidence Interval for Quantiles

The asymptotic confidence interval for a quantile can be derived as follows. Note, the derivation is reproduced from [139, p.77–p.79].

Let  $X$  be a random variable with cumulative distribution function (CDF)  $F_X$ . For large  $n_s$ ,  $F_X$  can be approximated by

$$F_X(x) \approx \hat{F}_X(x) = \frac{1}{n_s} \sum_{i=1}^{n_s} \mathcal{I}(X_i \leq x) = \frac{1}{n_s} \sum_{i=1}^{n_s} Z_{\text{ber},i} \quad (\text{A.36})$$

where  $\mathcal{I}(X_i \leq x)$  is the indicator function that is either one or zero depending on its argument. Clearly,  $Z_{\text{ber},i}$  is one if  $X_i \leq x$  and zero otherwise. Hence,  $Z_{\text{ber},i}$  is a Bernoulli random variable with mean  $F_X(x)$  and variance  $F_X(x)(1 - F_X(x))$ . According to the Central Limit Theorem (applied to the sample average of  $Z_{\text{ber},i}$ ):

$$\sqrt{n_s} (\hat{F}_X(x) - F_X(x)) \xrightarrow{d} \mathcal{N}(0, F_X(x)(1 - F_X(x))) \quad (\text{A.37})$$

where  $d$  stands for "convergence in distribution" if  $n_s$  goes to infinity. Since the inverse of the CDF yields the quantile value  $q_i$  the asymptotic variance  $\mathcal{V}$  in Eq. (A.38) needs to be determined:

$$\sqrt{n_s} (F_X^{-1}(\hat{F}_X(x)) - F_X^{-1}(F_X(x))) \xrightarrow{d} \mathcal{N}(0, \mathcal{V}) \quad (\text{A.38})$$

In this form  $\mathcal{V}$  can be determined using the Delta-method (see e.g. [29, p.49]). The transformation is defined as:

$$g(\theta) = F_X^{-1}(\theta) \quad (\text{A.39})$$

To calculate the derivative of  $g(\theta)$  note that

$$g(\theta) = F_X^{-1}(\theta) \equiv F_X(g(\theta)) = \theta \rightarrow \frac{d\theta}{dg(\theta)} = f_X(g(\theta)) \quad (\text{A.40})$$

Hence,

$$\frac{dg(\theta)}{d\theta} = \frac{1}{f_X(g(\theta))} = \frac{1}{f_X(F_X^{-1}(\theta))} \quad (\text{A.41})$$

Using this results and invoking the Delta-method yields the asymptotic variance:

$$\mathcal{V} = \frac{F_X(x)(1 - F_X(x))}{(f_X(F_X^{-1}(F_X(x))))^2} = \frac{F_X(x)(1 - F_X(x))}{(f_X(x))^2} \quad (\text{A.42})$$

Note, if  $x = q_{1-\alpha}$  then  $F_X(q_{1-\alpha}) = 1 - \alpha$  or shorter  $F_X(q_i) = Pr_i$ . Furthermore, since the probability density function is not known (in general) it needs to be estimated. This yields an approximation for the asymptotic variance:

$$\mathcal{V} \approx \frac{Pr_i(1 - Pr_i)}{(\hat{f}_X(q_i))^2} \quad (\text{A.43})$$

Finally, this allows to calculate the standard error (SE):

$$SE = \sqrt{\frac{Pr_i(1 - Pr_i)}{n_s (\hat{f}_X(q_i))^2}} \quad (\text{A.44})$$

Which yields the confidence interval for the quantile  $q_i$ :

$$CI = q_i \pm \tilde{\Phi}^{-1}(1 - \alpha) SE \quad (\text{A.45})$$

where  $\tilde{\Phi}^{-1}(1 - \alpha)$  can be obtained from any standard normal distribution table since  $\tilde{\Phi}^{-1}$  is the inverse of the cumulative distribution function of a standard normally distributed random variable.



# Acknowledgements

First, I would like to thank all the members of my doctoral committee for accepting our invitation as well as for taking the time to read and assess my dissertation. Second, I would like to thank my promoter, Gerard van Bussel, for giving me the opportunity to conduct my research in his institute: Thank you very much for your feedback and for guiding me through my Ph.D. student journey. Of course, I would like to thank my co-promoter Roland Schmehl who enabled this research in the first place: Your enthusiasm about airborne wind energy, optimism and encouragement to solve challenging technical problems was inspiring. Thank you very much for taking the time, despite your busy schedule, to discuss my weekly progress and for your continuous feedback.

In general, I would like to thank everyone in our research group. In particular, Ashim, Ashwin, Bedassa, Carlos, Julia, Mark, Mihir, Mikko, Navi, Sebastian S., Vinit and Zi. I really liked our daily card game sessions, lunch and coffee breaks. Moreover, I want to thank Mark who helped me to translate the summary of this thesis as well as the propositions. In addition, I would like to thank Sylvia for her organizational efforts and support but also for keeping everything in order in the institute.

Furthermore, I would like to thank the whole AWESCO team. Our spring, summer and winter schools all around Europe belong definitely to the highlights of my time as a Ph.D. student. I hope we can arrange a reunion soon. In particular, thank you Thomas for helping me to implement your wind field model that I could then use in a publication. Furthermore, I would like to thank the whole Kitemill team who gave me the opportunity to visit their company in Norway, providing me with valuable insights regarding the practical challenges in airborne wind energy as well as data that I could publish in a paper. I would also like to thank Urban Fasel for inviting me to ETH Zurich, for our collaboration and for letting me use his optimization framework.

Sport always helps me to get back in balance after long working hours in the office. This is of course even more fun if you do not have to do this on your own. Therefore, thank you to all my workout buddies, especially Prateek and Navi.

This section would be incomplete without thanking my former house mates and friends Kris, Ronan, Tito and Toto. It was great fun living together with you guys! I hope we can meet up soon to celebrate all our Ph.D. degrees. Again, merci beaucoup to Ronan (and a bit to Toto) who helped me to lift my French to the next level by teaching me lots of useful expressions and for introducing me to, among others, Oxmo, le poète.

Last but not least, I would like to thank my family and especially my parents and their partners for supporting, encouraging and advising me throughout the past years.



# Curriculum Vitæ

Sebastian Rapp was born on 12 July 1988 in Albstadt-Ebingen, Germany. He received his Abitur in 2008 from Karl-Maybach-Gymnasium in Friedrichshafen, Germany. After high school he studied aerospace engineering at the Technical University of Munich and obtained his Bachelor of Science and Master of Science degrees in 2012 and 2015, respectively. During this period he also studied one year abroad at the Institute Supérieure de l'Aéronautique et de l'Espace in Toulouse. In 2016 he began his Ph.D. research in the field of automatic control for airborne wind energy systems at the Delft University of Technology. Since October 2020 he is a flight control algorithms engineer at MBDA in Germany.



# List of Publications

1. Chris Vermillion, Mitchell Cobb, Lorenzo Fagiano, Rachel Leuthold, Moritz Diehl, Roy S. Smith, Tony A. Wood, **Sebastian Rapp**, Roland Schmehl, David Olinger, and Michael Demetriou (2020). "Electricity in the Air: Insights From Two Decades of Advanced Control Research and Experimental Flight Testing of Airborne Wind Energy Systems". Annual Reviews in Control (under review).
2. **Sebastian Rapp**, Roland Schmehl (2020). "Enhancing Resilience of Airborne Wind Energy Systems Through Upset Condition Avoidance". In: AIAA Journal of Guidance, Control, and Dynamics 44.2 , pp. 251–265. DOI: 10.2514/1.G005189.
3. Dylan Eijkelhof, **Sebastian Rapp**, Urban Fasel, Mac Gaunaa and Roland Schmehl (2020). "Reference Design and Simulation Framework of a Multi-Megawatt Airborne Wind Energy System", 2020 J. Phys.: Conf. Ser. 1618 032020. DOI:10.1088/1742-6596/1618/3/032020.
4. **Sebastian Rapp**, Roland Schmehl (2019). "Rare Event Prediction for Enhanced Control System Reliability". Book of Abstracts of the International Airborne Wind Energy Conference.
5. **Sebastian Rapp**, Roland Schmehl, Espen Oland, Thomas Haas (2019). "Cascaded Pumping Cycle Control for Rigid Wing Airborne Wind Energy Systems". In: AIAA Journal of Guidance, Control, and Dynamics 42.11 , pp. 2456–2473. DOI: 10.2514/1.G004246.
6. **Sebastian Rapp**, Roland Schmehl, Espen Oland, Sture Smidt, Thomas Haas, Johan Meyers (2019). "A Modular Control Architecture for Airborne Wind Energy Systems". In: Proceedings of the AIAA Scitech 2019. San Diego, California: AIAA, Jan. 7–11, 2019. DOI: 10.2514/6.2019-1419.
7. **Sebastian Rapp**, Roland Schmehl (2018). "Vertical Takeoff and Landing of Flexible Wing Kite Power Systems". In: AIAA Journal of Guidance, Control, and Dynamics 41.11, pp. 2386–2400. DOI: 10.2514/1.G003535.
8. **Sebastian Rapp**, Roland Schmehl (2017). "Towards Robust Automatic Operation of Rigid Wing Kite Power Systems". Book of Abstracts of the International Airborne Wind Energy Conference.